University of Southampton

FACULTY OF NATURAL AND ENVIRONMENTAL SCIENCE

SCHOOL OF CHEMISTRY

Probing the Molecular Level Details of Bacterial Outer Membrane Vesicles and Their Parent Bacteria: A Simulation Approach

by

Damien Francis Jefferies

Thesis for the degree of Doctor of Philosophy

September 2019

UNIVERSITY OF SOUTHAMPTON

Abstract

FACULTY OF NATURAL AND ENVIRONMENTAL SCIENCE

Computational Chemistry

Thesis for the degree of Doctor of Philosophy

Probing the Molecular Level Details of Bacterial Outer Membrane Vesicles and Their Parent Bacteria: A Simulation Approach

Damien Francis Jefferies

Gram-negative bacteria have an unusual cell envelope that contains an inner cytoplasmic lipid membrane and an outer bacterial lipid membrane. The outer bacterial lipid membrane produces outer membrane vesicles that regulate bacterial pathogenesis processes. The outer membrane vesicles transport virulence factors from bacteria to host cell surfaces and the vesicles then move into the host cell cytosol. Computer simulations were conducted here in this thesis to understand how outer membrane vesicles pass through host cell surfaces independently of any membrane protein effects. The simulations suggest that outer membrane vesicles enter cells via lipid-mediated endocytosis processes and interestingly, that the host membrane wrapping interactions depend on the length of the lipopolysaccharide macromolecules. Additional simulations were conducted to understand how polymyxin B1 peptides affect the inner and outer membranes of Gram-negative bacteria and how cohesive intermolecular interactions between lipopolysaccharide lipids can affect the durability of Gram-negative bacterial membranes. The simulation studies are by no means disparate; the simulations provide general insights into disease transmission. The simulations clarify how lipopolysaccharide macromolecules promote the spread of disease and conversely how antibiotics can curb it.

Table of Contents

List of Tables

List of Figures

for a time Δt (bottom). (C) The E. coli outer membrane model that contains the central vitamin B12 transporter (BtuB) integral membrane protein. The structure was assembled with the CHARMM-GUI construction tool (top) and simulated for a time Δt (bottom). The inner leaflet lipids are blue, white, and black. The outer leaflet lipids are pink, orange, gold, cyan and gray. The BtuB protein is yellow and green. The ions are represented as small spheres that are not covalently linked with the lipids or protein molecules. Image source: 10.1021/acs.jctc.8b01066 (DOI) [229].

Figure 5: *(A) Model of the E. coli cell envelope that includes the inner cytoplasmic membrane (IM), the outer membrane (OM), peptidoglycan (cell wall), Braun's lipoprotein (Lpp) and integral membrane proteins. The lipids are gray and the peptidoglycan is blue and green. The proteins have different color schemes to help readers to distinguish between them. (B-D) Representative states of the peptidoglycan cell wall composite when it is relaxed (B), stretched to 1.5x of its original area (C) and stretched to 2x its original area (D). The glycan strands are blue, the peptide cross-links are green and the borders of the simulation cell are represented as a thin dashed line. The image sources are: 10.106/j.bbamem.2018.09.020 (DOI) [312] and 10.1371/journal.pcbi.1003475 (DOI) [309].*

Figure 6: *Implementation of the CHARMM-GUI Martini Maker module. (A) The initial random placement of 20 LPS lipids and the subsequent self-assembly of the lipids into a unilamellar or bilamellar bacterial membrane fragment. (B) The initial construction of an LPS micelle and the subsequent transformation of the micelle to become a unilamellar bacterial membrane. (C) The initial construction of an LPS micelle with embedded OmpF protein and the subsequent transformation of the micelle into a multicomponent unilamellar bacterial membrane. (D) The final frame snapshots of molecular dynamics simulations of asymmetric bacterial membrane models that were generated with the CHARMM-GUI Martini Maker. The bilayers contained only lipids (OM) or lipids and the OmpA integral membrane protein (OM-OmpA). (E) Snapshots of OMV simulation systems that contained only lipids or lipids and an embedded outer membrane protein. The systems were made with the CHARMM-GUI Martini Maker module. The proteins are red, the acyl tails are yellow, the core sugars are violet, the choline and phosphate groups are blue and purple and the unsaturated bonds are cyan. Image source: 10.1002/jcc.24895 (DOI) [151].*

Figure 7: *Understanding the properties of lipid rafts through the application of molecular dynamics simulations. (A) Formation of separate liquid-ordered (green) and liquid-disordered (red) nanodomains that are enriched in saturated lipids (green) and cholesterol (black), or polyunsaturated lipids (red). (B) Top view snapshots showing how the cholesterol molecules were distributed within the multicomponent membrane simulation system and the (C) radial distribution function for the cholesterol-cholesterol intermolecular separation distances. (D) Snapshots of GM1 ganglioside and POPC lipids that were simulated in two-component membranes. The membrane became more rigid and raft-like as the concentration of the ganglioside molecules was*

increased from 10% through to 30%. The Image sources are: 10.1073/pnas.0807527105 (DOI) [335] and 10.1016/j.bpj.2016.09.021 (DOI) [362].

Figure 8: *The structure of four phospholipids. (A) The structure of a phosphatidylcholine lipid (16:0/18:1(9Z)) that consists of two acyl tails bonded via an ester linkage to glycerol, a negatively charged phosphate group and a terminal positively charged choline section. (B) The structure of phosphatidylserine lipid (16:0/18:1(9Z)) that consists of two acyl chains bonded via an ester linkage to glycerol, a negatively charged phosphate group and a terminal serine moiety. (C) The structure of a phosphatidylethanolamine lipid (16:0/18:1(9Z)) that consists of two acyl chains covalently bonded through an ester link to central glycerol and phosphate groups, and a terminal ethanolamine section. (D) The structure of a phosphatidylglycerol lipid (16:0/18:1(9Z)) that consists of two acyl tails bonded via an ester linkage to glycerol, a negatively charged phosphate group and a terminal glycerol group. Image source: https://avantilipids.com*

Figure 9: *The properties and molecular dynamics simulations of cholesterol. (A) The chemical composition of cholesterol molecules and a simplified schematic illustration showing how the polar-headgroup-to-hydrophobic-body cross sectional area ratio gives cholesterol an effective conical structure. (B) Schematic illustrations showing how lipid shape, defined by the hydrophilic-headgroup-to-hydrophobic-lipid-component, is expected to affect preferences for spontaneous curvature generation. (C) Molecular dynamics simulations that show how cholesterol molecules can regulate membrane curvature and the membrane stress distribution by flipping between the apposed membrane leaflets on a nanosecond timescale. (D) Schematic illustration showing how lipid sorting can be induced by membrane curvature, but also how induced lipid sorting can affect local preferences for spontaneous membrane curvature generation. (E) Plasma membrane molecular dynamics simulations that demonstrated curvature-induced cholesterol molecule sorting. The cholesterol molecules moved to negatively curved membrane domains during production time. The image sources are: Wikipedia Commons, 10.3389/fmicb.2014.00220 (DOI) (439) 10.1021/ja903529f (DOI) [437] 10.1146/annurev.cellbio.20.010403.095451 (DOI) [440] 10.1002/adts.201800034 (DOI) [364].*

Figure 10: *The structure and molecular dynamics simulations of hopanoids. (A-C) The structure of three hopanoids: hopane (A), diploptene (B), and bacteriopanetetrol (C). (D) Martini coarse-grained molecular dynamics simulations of multicomponent membranes that included either hopane (yellow), diploptene (green), or bacteriohopanetetrol (purple) with POPC lipids. The POPC phosphate headgroups are orange to show the position of the membrane-water interface. The image sources are: Wikipedia Commons and 10.1063/1.4937783 (DOI) [451].*

Figure 11: *The structure of PIP_2 molecules and the interaction of PIP_2 molecules with integral membrane proteins. (A) The skeletal structure of the*

PIP_2 lipid that includes the phosphate groups (red), the inositol ring and the anchoring saturated and unsaturated acyl chains (blue). (B-C) The binding positions of PIP_2 lipids on Kir2.2 channel proteins that were identified from X-ray crystallography (B) and molecular dynamics simulation studies (C). The PIP_2 lipids are represented as green and red spheres and the protein residues are represented as violet chains. (D) The S1P1 GPCR molecule that has been colored according to its interactions with the PIP_2 phosphoryl headgroup in coarse-grained molecular dynamics simulations. The interaction number color bar ranges from white through to red. The image sources are: Wikipedia Commons, 10.1038/nature10370 (DOI) 10.1021/bi301350s (DOI) [470] and 10.1021/jacs.5b08048 (DOI) [76].

Figure 12: *The chemical structure of three simple sphingolipids. (A) The chemical structure of sphingosine. (B) The chemical structure of a ceramide. The variable fatty acid moiety is red and the sphingosine backbone is black. (C) The chemical structure of a sphingomyelin molecule. The variable fatty acid moiety is red, the sphingomyelin backbone is black and the phosphocholine group is blue. Image source: Wikipedia Commons.*

Figure 13: *The ganglioside lipid structure and representations of how ganglioside molecules can induce spontaneous curvature generation. (A) Biosynthetic pathway for some of the smallest and simplest ganglioside molecules i.e. GM3, GM2 and GM1. Ganglioside molecules consist of a core ceramide unit that is bonded to glycan headgroups that contain monosaccharides such as glucose (Glc), galactose (Gal), N-acetylgalactosamine (GalNAc), and sialic acid residues (Sia). Additional monosaccharide units can be added onto GM3, GM2 and GM1 molecules to create larger and more complex ganglioside molecules. (B) The skeletal formula of the GM3 lipid. The ceramide domain is highlighted gray and the Glc, Gal, and Sia units are highlighted blue, yellow and maroon. (C-D) Molecular dynamics simulations showing how molecular dynamics simulations have demonstrated that GM1 molecules can reshape asymmetric biomembranes. The phospholipids are blue and the GM1 molecules are red. The graphic contains both top view and side view snapshots. (E-F) Molecular dynamics simulations showing how cholera toxin B subunit (CTxB) can induce local curvature generation within biomembrane mimetics. (E) The DOPC lipids are green and the GM1 lipids are purple. (F) The membrane has been refitted to a thin surface for easier visualization of the induced membrane curvature. The image sources are: 10.3389/fimmu.2014.00325 (DOI) [426] 10.1038/nchembio0209-71 (DOI) [535] 10.1073/pnas.1722320115 (DOI) [536] 10.1002/2211-5463.12321 (DOI) [537].*

Figure 14: *Pathogens and pathogenic products can bind ganglioside lipids and this interaction promotes endocytosis. (A) SV40 coat protein VP1 pentamer cocrystallized with GM1 pentasaccharide. The coat protein is green and the pentasaccharides are red. (B) Cholera toxin β subunit cocrystallized with GM1 pentasaccharide. (C) E. coli enterotoxin β subunit cocrystallized with nitrophenyl-galactoside. (D) Shiga toxin β subunit cocrystallized with GB3 trisaccharide. (E) Pentameric E. coli Shigalike toxin β subunit cocrystallized*

with a GB3 analog. (F) Binding of SV40 to GM1 lipids in a multicomponent membrane. (G) The formation of a lipid raft (dark blue band) and the demonstration of actin-dependent immobilization. (H) The invagination of the plasma membrane mimetic due to interactions with SV40. The interactions between SV40 and the plasma membrane mimetic generate a caveola structure. (I) Scission machinery facilitating endocytosis after the production of a flask-shaped lipid raft structure (i.e. caveola). (J) The formation of a vacuole and the transport of the vacuole through the intracellular space. The image source is: 10.1101/cshperspect.a004721 (DOI) [542].

Figure 15: *Schematic representation of a single molecule of smooth LPS from E. coli bacteria. The illustration includes the conserved Lipid A domain, which is a phosphorylated glucosamine disaccharide decorated with multiple fatty acid chains. Lipid A is bonded to the core oligosaccharide section, which includes hexose sugars such as keto-deoxyoctulosonate (Kdo), glucose (Glc), mannoheptose (Hep), N-acetyl-D-glucosamine (GlcNac), galactose (Gal) and phosphate groups. The length of the core domain determines rough LPS nomenclature e.g. Re and Ra mutants are shown using red and pink skeletal structures. Smooth LPS lipids additionally contain terminal O-antigen chain units. Smooth LPS lipids can contain multiple repeats of the repetitive O-antigen chain polymer unit. The length and composition of the O-antigen chain varies among different bacterial species and depends on the bacterial growth conditions. The image is based on work from the 10.1021/acs.jctc.8b01059 manuscript (DOI) [315].*

Figure 16: *Schematic illustration of the cell envelope of (A) Gram-negative and (B) Gram-positive bacteria. Phospholipids are orange spheres attached to two acyl chains, LPS lipids are orange ovals attached to six acyl chains and terminal red square polymers, teichoic acids are green circle polymers attached to orange heptagons, proteins are gray circle and oval composites, and peptidoglycan is the repeating blue and purple hexagon-square composite. (C) The chemical structure of the peptidoglycan unit. (D) The chemical structure of teichoic acid. The different cell wall structures affect how bacteria interact with the external milieu and thereby, their response to the Gram stain procedure. The image source is: 10.1021/acs.chemrev.8b00538 (DOI) [59].*

Figure 17: *Host-pathogen interface interactions. The OMVs are liposomes that contain an outer leaflet that is predominantly comprised of lipopolysaccharide lipids and an inner leaflet that is predominantly comprised of phospholipids. The OMVs deliver luminal cargo and virulence factors to host cells as they pass through or fuse with the host cell (eukaryotic) plasma membranes. The OMVs can enter cells through clathrin-dependent endocytosis and alternative lipid-mediated internalization uptake pathways that involve lipid rafts, but the precise biomolecular interactions that underpin these processes are not entirely understood. Here, the OMV outer leaflet is cyan, the inner leaflet is orange, the outer membrane proteins are yellow, the host plasma membrane is pink, the lipid raft is blue and the clathrin molecules are purple and red.*

Figure 18: *Overview of AMP membrane breakdown processes. (A) The AMPs initially bind to the host membrane surfaces through a combination of electrostatic and hydrophobic protein-lipid interactions. The AMPs adopt orientations that maximize the number of attractive peptide-lipid electrostatic and hydrophobic interactions. (B) In the barrel-stave model the hydrophobic AMP moieties are oriented toward the encompassing acyl chains and this creates a transmembrane water pore. The encompassing acyl chains maintain a transmembrane orientation (i.e. align with the membrane normal axes) and the AMPs oligomerize to effectively form a pore that has one hydrophobic surface and one hydrophilic surface. (C) In the toroidal-pore model the intracellular (inner) and extracellular (outer) monolayers distort when they interact with the oligomerized AMPs and this creates a transmembrane water pore whose surface is comprised of lipid headgroups and protein residues. (D) In the carpet model the AMPs stay on the membrane surface and induce membrane rupture as they change the structure of the membrane. The image source is: 10.1007/s10989-009-9180-5 (DOI) [673].*

Figure 19: *The structure and simulations of the Polymyxin B antimicrobial peptide. (A) The lipopeptide contains a cyclic component that is made of seven amino acids and a non-cyclic section that contains three amino acids with terminal fatty acid chain moiety. The lipopeptide contains five cationic diaminobutyric acid (Dab) residues that impart a net (+5) positive charge to the molecule and this positive electrostatic charge promotes PMB1 interactions with anionic lipids. The fatty acid chain, isobutyl group, and phenylalanine side chains confer hydrophobicity and they promote PMB1 interactions with hydrophobic acyl chain moieties. (B-C) Results from molecular dynamics simulations. The cholesterol concentration affected how the simulated PMB1 peptides interacted with the multicomponent membranes. There was indentation of the bilayers and an overall increase in permeability when the cholesterol content was zero (B). There was significantly less membrane damage when the membranes contained high concentrations of cholesterol (C). The water molecules are red and white, the lipid tails are thin cyan strands, the phosphate groups are orange and the polymyxin molecules are represented using a space-filling van der Waals model. The image sources are: Wikipedia Commons and 10.1016/j.bpj.2017.09.013 (DOI) [728].*

Figure 20: *Schematic representation of the non-bonded interaction energy term components. (A) Lennard-Jones component that is used to approximate repulsive electron overlap forces at short-range, and attractive dispersion forces at long-range. The well depth is provided by ε, and σ is the distance where the potential reaches its minimum. (B) Coulombic interaction energy experienced by two point charged particles. Coulomb forces are appreciable at both short- and long-ranges given that they decay according r^{-1}, where r is the distance between two charged particles.*

Figure 21: *The components of the molecular dynamics forcefield bonded potential. (A) The component for bond stretching: atoms i and j oscillate about an equilibrium bond distance r_{eq}. (B) The component for valence angles:*

atoms i, j, and k flex about an equilibrium valence angle θ_{eq}. (C) The improper torsion angle component: the angle between the two intersecting planes (ijk) and (jkl) oscillates about an equilibrium improper torsion angle ω_{eq}. (D) The proper dihedral component describes the angular spring between the planes (ijk) and (jkl) that is formed of four consecutively bonded atoms.

Figure 22: *Some of the different resolution levels that can be used in molecular dynamics simulations. (A) An all-atom model for the DPPC lipid. The carbon (cyan), oxygen (red), nitrogen (blue), and hydrogen (white) atoms are represented here explicitly. (B) The GROMOS united-atom forcefield model for the DPPC lipid. The hydrogen atoms are clustered into neighboring carbon atoms to produce a less computationally demanding representation for the DPPC lipid. (C) The coarse-grained Martini forcefield model for the DPPC lipid. Here, multiple neighboring heavy atoms have been clustered into single pseudo-atom interaction centers to substantially reduce the computational load and make the lipid simulations less computationally demanding. The Martini beads have the following color scheme: carbon tail (cyan), glycerol (pink), phosphate (brown), and choline (blue).*

Figure 23: *Schematic illustration of a single particle (red circle) passing through the borders of a periodic unit cell (black lines). The use of periodic representations provides a more accurate mimic of bulk systems given the removal of a well-defined, simulation cell boundary. The simulated atoms can freely traverse the space-filling box and as they pass through one border of the unit cell, they instantaneously re-enter through the opposite face.*

Figure 24: *Illustration showing how the leap-frog algorithm operates. The computation of particle positions is shown with a blue line and the computation of particle velocities is shown with a red line. Simulation time is represented with a black arrow; the time step is user-defined and should be calibrated to ensure that molecular dynamics simulations are both efficient and realistic. There is a lack of synchronization between the particle position and velocity calculations: if particle positions are calculated at $t + n\Delta t$, then particle velocities are calculated at $t + \frac{n}{2}\Delta t$, where $n \in \mathbb{N}$.*

Figure 25: *Representative harmonic potential used to enforce (standard) position restraints in molecular dynamics simulations. The potential energy rises as particles drift from a user-defined reference position. The magnitude of the potential energy is a function of the distance between the atom and the user-defined reference position.*

Figure 26: *Coarse-grained models for PMB1 and Re LPS. (A) coarse-grained model for PMB1. The Martini beads are shown as translucent spheres and the underlying united-atom particles are shown as opaque spheres. The carbon atoms are ice blue, the oxygen atoms are red, the nitrogen atoms are blue and the hydrogen atoms are white. (B) The coarse-grained model for Re LPS. The carbon tails are white, the glucosamine and glycerol groups are pink, the phosphate groups are blue, and the remaining core saccharides are cyan. The*

Re LPS lipid is divided into its component Lipid A anchor and keto-deoxyoctulosonate (Kdo) dimer sections for clarity.

Figure 27: *Voronoi tessellation of the Re LPS bilayers that were simulated with either Na^+ or Ca^{2+} ions. (A, B) The two-dimensional Voronoi tessellations were used to determine the projected surface areas distributions for the Re LPS bilayers that were simulated with either (A) Na^+ or (B) Ca^{2+} ions. The mean area values are represented with dashed red lines and the standard deviation (σ) and skew (S) values are shown in the top right-hand corner. (C, D) The observed data sets are compared with Gaussian distributed data sets of equivalent σ and S values. The linear association between the Gaussian (blue) and observed data (black) sets was calculated with the standard Pearson product-moment correlation coefficient (r).*

Figure 28: *The properties of the Re LPS bilayers that with simulated with either Na^+ or Ca^{2+} ions. (A, B) The wave-number-dependent viscosity η(k) was determined from the transverse current autocorrelation function for the Re LPS bilayers that were simulated with either Na^+ (blue triangles) or Ca^{2+} (black squares) ions. The values of η(k) were determined by considering (A) the entire Re LPS lipids in the viscosity calculations or by considering (B) only their phosphate groups. The data were fit to the Padé approximant: $\eta(k) = (1 + bk^2)^{-1}$; the fitting parameters (a, b) are shown with the optimized expressions for η(k) (dashed lines). The inset image shows η(k) as $k \rightarrow 0$. Blue lines represent the simulations with Na^+ ions; black lines represent the simulations with Ca^{2+} ions. (C, D) The radial distribution functions (RDF) were determined for the Re LPS phosphate groups in the simulations with (C) Ca^{2+} and (D) Na^+ ions. (E-H) The velocity autocorrelation functions C(t) were determined for (E, G) the whole Re LPS lipids or for their (F, H) phosphate groups. The data are presented for the bilayers with either (E, F) Na^+ or (G, H) Ca^{2+} ions.*

Figure 29: *The translocation of the PMB1 peptide through the bacterial membrane mimetic depended on the type of ambient ions that were used to conduct the molecular dynamics simulations. (A, B) The contact number for interactions between the PMB1 Dab residue side chains and the Re LPS lipid phosphate groups as a function of simulation time. The cut-off distance was 0.47 nm (the effective size of a coarse-grained Martini bead); data were collated for all of the unbiased simulations. (A) The data for the bilayers that were simulated with Na^+ ions and for (B) the bilayers that were simulated with Ca^{2+} ions. (C, D) The final-frame snapshots of the PMB1 peptides (green) interacting with the Re LPS bilayers that were loaded with (C) Na^+ or (D) Ca^{2+} ions. The Re LPS lipids are colored according to Fig. 26 and the Na^+, Ca^{2+}, and water particles are omitted for clarity. (E-H) The radial distribution functions for the phosphate (black lines) and carboxylate (blue lines) groups of the Re LPS lipids with respect to the position of the PMB1 Dab residue side chains. The data are shown for both the (E, F) Na^+, and (G, H) Ca^{2+} ion simulation systems. The data were sampled during the last 100 ns of simulation time.*

Figure 30: *The PMB1 benzyl group penetrates the lipid core. (A) Position of the Re LPS phosphate groups and a single PMB1 benzyl group are shown with black and blue lines, respectively. The coordinates are with respect to the bilayer normal and the distances are relative to the bilayer center. The temperature was 310 K, the pressure was 1 bar and the membranes were simulated with divalent Ca^{2+} ions. (B) Side view snapshot showing how the PMB1 peptide enters into the bacterial membrane mimetic; the perspective is reversed relative to Fig. 30A for clarity. The inset image shows the two-dimensional Voronoi tessellation for the Re LPS headgroups as the PMB1 peptide enters into the lipid core. The projected polygons are colored cyan if they represent lipids that were adjacent to the embedded PMB1 benzyl group. (C) The area per lipid for the five Re LPS lipids that were adjacent to the benzyl group when it moved into the bilayer interior (3390-3480 ns). The average projected surface area of the five Re LPS headgroups was higher than the bilayer average (1.60 ± 0.004 nm^2).*

Figure 31: *The free energy profile for PMB1 translocation into the membrane interior. The free energy profiles are shown for the simulation systems with (A, C) Na^+ or (B, D) Ca^{2+} ions. (A, B) The PMF profiles for PMB1 as a function of distance from the bilayer center. The PMF profiles are shown for the system temperatures: 320 K (solid cyan lines), 310 K (solid blue lines), and 300 K (solid black lines). (C, D) The free energy profiles ΔG that were computed at 310 K were decomposed into entropic $-T\Delta S$ (solid red lines) and enthalpic ΔH (solid green lines) components. The dashed black lines show the average position of the Re LPS phosphate groups from the bilayer center. (E) The configurational entropy for the PMB1 peptides was evaluated with the Schlitter formula (S) and the quasi-harmonic approximations (Q) as a function of distance from the bilayer center. The cyan and black lines show the data for the simulations with Na^+ ions and the red and blue lines represent the data for simulations with Ca^{2+} ions.*

Figure 32: *The vitreous dynamics of the Re LPS lipids. The lipid dynamics of the Re LPS lipids were different when they were simulated with (A-D) Na^+ and (E-H) Ca^{2+} ions. (A, E) The trajectories of single representative Re LPS phosphate groups are presented here as red lines. The background snapshots of the Re LPS lipids are shown with the scale bar to provide a sense of distance. The background snapshots clarify how far the representative Re LPS lipids have moved in Fig. 32A and Fig. 32E or in other words, how long the red line trajectories are. The simulations were conducted with a simulation temperature of 310 K and the analysis was performed for 1 μs. (B-C, F-G) Streamline visualization analysis for arbitrarily selected simulation frames to capture the collective, heterogeneous relaxation dynamics that give rise to the so-called "blob-and-channel" trajectories that are a hallmark of vitreous systems. (D, H) The self-part of the van Hove correlation function that is defined as the probability that a particle that is at r_0 at time zero can be found at position r_0+t at time t. The figures show how the Re LPS lipid trajectories change when they are simulated with different types of ions.*

Figure 33: *The Re LPS diffusion was affected by the PMB1 peptides. (A, E) The trajectories of single representative Re LPS phosphate groups was visualized over the course of 1 μs long umbrella sampling simulations. The sampled windows correspond to the minimum of the 310 K PMF profiles from Fig. 31A. The trajectories of single representative Re LPS phosphate groups are presented here as red lines. The background snapshots of the Re LPS lipids are shown with the scale bar to provide a sense of distance. The background snapshots clarify how far the representative Re LPS lipids have moved in Fig. 33A and Fig. 33E or in other words, how long the red line trajectories are. (A) When the Na^+ ion simulation system was simulated with a PMB1 peptide there was a shift away from the clustered-continuous-time-random walk processes (see Figure 32A for comparison) towards the localized oscillatory and rattling motions that have been noted for ions in rigid crystals. (E) When the Ca^{2+} ion simulation system was simulated with a PMB1 peptide there was a more significant shift away from clustered-continuous-time-random walk processes (see Figure 32E for comparison) towards localized oscillatory motions. The Re LPS phosphate groups were confined to membrane domains that were approximately 2 nm^2 during the last 1 μs of simulation time. (B-C, F-G) Streamline visualization analyses of arbitrarily selected simulation frames to clarify the collective Re LPS headgroup relaxation dynamics in the presence of the PMB1 peptide. The Re LPS trajectories are noticeably different from the relaxation dynamics of the Re LPS phosphate groups when they were not simulated with PMB1 peptides (see Figure 32B-C and Figure 32F-G for comparison). There is an approximate order of magnitude reduction in the headgroup displacements per simulation step (see adjoining color bars for clarity). (D, H) Self-part of the van Hove correlation function for the Re LPS phosphate groups. Comparisons between Figure 32D, 32H and Figure 33D, 33H reveal significant differences in the relative mobility of the Re LPS molecules when they interact with a PMB1 peptide.*

Figure 34: *The lateral diffusion coefficients D(z) for the Re LPS phosphate groups as a function of PMB1 distance from the bilayer center. The blue line shows the data for the systems with Na^+ ions and the black line shows the data for the systems with Ca^{2+} ions. The diffusion coefficients D(z) were determined by linear regression of the mean square displacement and error bars have been included for each data point. The lateral diffusion coefficient axis is logarithmic.*

Figure 35: *The PMB1 peptide induces the glass-to-crystal transformation. (A, B) Top view snapshots of the Re LPS bilayer when it was simulated with (A) water and ions and (B) when it was simulated with water, ions and a PMB1 peptide. The Re LPS phosphate groups are presented as opaque blue spheres and the other sections of the Re LPS molecules are depicted as translucent spheres. The red quadrilaterals are used to draw attention to the crystalline packing of the Re LPS phosphate groups. These membrane systems were simulated at 310 K with Na^+ ions. (C-F) Voronoi tessellation analyses of the Re LPS phosphate groups when they were simulated (C, E) with water and ions and (D, F) when they were simulated with water, ions and the PMB1 peptide. (D, F) The figures were created by sampling data from the umbrella sampling*

window that was positioned at the location of the 310 K PMF minimum (see Figure 31A for reference). (C, D) The plots show the area per phosphate group. The color scale bars are used for clarity. It should be noted that each Re LPS lipid has two phosphate groups. (E, F) The plots show the number of whole Re LPS lipids that are counted for each of the tessellated Voronoi cells (see adjoining color scale bars for clarity). (F) The number of 3 Re LPS neighbors (corresponding to 6 phosphate groups), is indicative of hexagonal packing, which has previously been observed in experimental studies when Gram-negative outer membrane mimetics were strained or placed under high surface pressures [121]. (G, H) The heat capacity change as a function of distance between the PMB1 peptide and the bilayer center. The data are determined for the membrane that with simulated with (G) Na^{+} and (H) Ca^{2+} ions.

Figure 36: (*A) Final frame (top view) snapshot of the Gram-negative inner membrane mimetic. The lipids have the following color scheme: POPE (cyan) and POPG (white). (B) The visualization of the POPG number density during the last 10 ns of the simulation. (C, D) The corresponding visualization of the POPG number densities in the upper (C) and lower (D) bilayer leaflets.*

Figure 37: *(A) The distance of the upper leaflet POPE and POPG phosphate groups from the membrane midplane is shown with a black line. The distance between a single (representative) PMB1 peptide and the bilayer center is shown with a blue line. (B) The area per lipid for each one of the upper leaflet phosphate group at 460 ns i.e. the time when the PMB1 peptide passed through the phosphate group domain. The arrow shows the pore that the PMB1 peptide tunneled when it moved into the membrane interior. (C) Final frame (side view) snapshot that shows the position of the PMB1 peptides in the Gram-negative inner membrane mimetic.*

Figure 38: *(A) The POPG lipid number density during the last 10 ns of the molecular dynamics simulation. The projected number density map is decomposed into the contributions from the upper and lower leaflets (inset). (B) The associated PMB1 peptide particle number density during the last 10 ns of the molecular dynamics simulation. (C, D) The thickness of the upper bilayer leaflet during the last 10 ns of the molecular dynamics simulation. The figures show thickness data for the simulation systems with water and ions (C) and for the simulation systems with water, ions and peptides. There is approximately one PMB1 peptide for every 27 phospholipids (D).*

Figure 39: *(A) Snapshot of a single unit of the E. coli O1 O-antigen chain that was simulated with the GROMOS 53A6 united-atom forcefield. The atoms have the following color scheme: carbon atoms (cyan), nitrogen atoms (blue), oxygen atoms (red) and hydrogen atoms (white). (B) The corresponding coarse-grained Martini forcefield model. (C) Comparison of the radius of gyration values for the O-antigen chain units in the comparative united-atom and coarse-grained molecular dynamics simulations. (D) Comparison of the end-to-end lengths for the O-antigen chain units in the comparative united-atom and coarse-grained molecular dynamics simulations. (E) The probability*

distribution for a single O-antigen chain bond length in the comparative united-atom and coarse-grained molecular dynamics simulations. (E) The probability distribution for a single angle in the comparative united-atom and coarse-grained molecular dynamics simulations. The united-atom simulation data are presented with black lines and the corresponding coarse-grained molecular dynamics simulation data are presented with red lines.

Figure 40: *(A) Side view snapshot of system OANT, with (B) a single smooth LPS lipid extracted from the bilayer to show the orientation of the acyl chains and O-antigen chain sugars. The bond that anchors the O-antigen chain to the Lipid A and core sugar domains is termed here as "O-anchor" to make the discussion of LPS headgroup orientation clearer. (C) Side view snapshot of system MIXED_POPE, with (D) a single smooth LPS lipid extracted from the bilayer to show the orientation of the smooth LPS acyl chains and O-antigen chain sugars. The acyl tails are white, the phosphate groups are blue, the glycerol and glucosamine sugars are pink, the core sugars are cyan, the terminal O-antigen chains are red and the water molecules are omitted for clarity. (E) The average order parameters that were calculated for the backbone chain beads of the O-antigen chain sugars in systems OANT (black), OANT_POPE (red), MIXED (green), and MIXED_POPE (blue). (F) The angle distribution for the angle that was formed between the O-anchor bond and the terminal O-antigen chain sugar in systems OANT (black), OANT_POPE (red), MIXED (green) and MIXED_POPE (blue).*

Figure 41: *(A) Two smooth LPS lipids from system MIXED_POPE that were initially separated by ~4 nm and subsequently formed a dimer after the flexible O-antigen chains interacted with each other. (B) The corresponding time series that shows the distance between the two smooth LPS lipids as a function of sampled simulation time. (C) Snapshot of the large smooth LPS lipid aggregate that formed after additional smooth LPS lipids interacted with the smooth LPS lipid dimer. (D-E) The O-antigen chain number density in systems OANT (D) and MIXED_POPE (E) after 500 ns. The inset images show the corresponding top view snapshots.*

Figure 42: *(A) Top view snapshot of a larger analogue of system MIXED_POPE after 15 μs. The POPE and rough LPS lipids are omitted for clarity. The periodic borders are represented with a thin blue line and the periodic images are presented with different shades of red and cyan for clarity. The smooth LPS lipids formed a single contiguous network that spanned the entire length of the simulation cell. (B) The corresponding two-dimensional projection of the O-antigen chain number density (sampled during the last 100 ns). (C) Snapshot of the two O-antigen chain aggregates after 15 μs of simulation time. One of the O-antigen chain aggregates is green and the other one is orange. (D) The number of glycan polymers in each of these O-antigen chain aggregates.*

Figure 43: *(A) Surface tension-areal strain curves. (B) Lateral pressure against areal strain. (C) Lateral pressure against membrane thickness. (D) Lateral pressure against acyl tail order parameters. Data are shown for the*

OANT (black), OANT_POPE (red), MIXED (green), and MIXED_POPE (blue) simulation systems. Readers should note that the dependent variables were plotted on the y-axis in Figure 43A and Figure 43B even though it is customary to plot the independent variable on the x-axis and the dependent variable of the y-axis. The unusual presentation of the simulation data enables readers to more easily identify the relationship between the applied mechanical stress and the membrane stress response. The presentation of the simulation data has been used to study for example, how phospholipid membranes respond to applied mechanical stress [977] and it is therefore easier to compare the data that are presented here with data from previous molecular dynamics simulation studies.

Figure 44: *(A) The average order parameters for the O-antigen chains in system OANT as the lateral pressure component magnitude was incrementally increased. The color scheme is as follows: -10 bar (red), -30 bar (green), -50 bar (blue), -70 bar (yellow), -90 bar (brown), -110 bar (cyan) and -130 bar (violet). (B, C) The two-dimensional projection of the O-antigen chain particle number density for system OANT when it was simulated with a lateral pressure magnitude of 1 bar (B) and -130 bar (C). (D) The partial mass density plots for system OANT when it was simulated with a lateral pressure of 1 bar (red and blue lines) and -130 bar (cyan and green lines). The data for the lipid phosphate groups are red and green and the data for the water molecules are blue and cyan. (E) Snapshot that shows the spontaneous formation of a transmembrane pore in system OANT when it is simulated with a lateral pressure magnitude of -150 bar. The water particles are blue and the LPS lipids follow the color scheme of Figure 40.*

Figure 45: *(A) The starting configuration for the smooth OMV equilibration simulations. The POPE and POPG lipids are silver and the LPS lipids have the color scheme: Lipid A and core sugars (cyan) and O-antigen chain (red). The water and ions were removed to make the figure clearer. The periodic cell boundaries are represented with a blue line. The periodic images are shown using different color shades for clarity. The lipids were extended along the bilayer normal to ensure that lipid clustering was not biased during the molecular dynamics simulations. Water pores were maintained along the (x/y/z) coordinate axes to facilitate interleaflet flip-flop for small phospholipids. (B) Area per lipid for LPS (red) and POPE (magenta) lipids in the smooth OMV (during the last 0.25 μs); area per lipid for LPS (cyan) and POPE (magenta) lipids in the rough OMV. (C) Membrane thickness for the smooth (red) and rough (cyan) OMVs during the last 0.25 μs; the average membrane thickness values were 3.58 ± 0.01 nm (smooth OMV) and 3.72 ± 0.01 nm (rough OMV). (D) Area per lipid for POPE (orange) and POPG (green) lipids in the POPE-POPG phospholipid vesicle during the last 0.25 μs. (E) The corresponding membrane thickness values for the POPE-POPG phospholipid vesicle.*

Figure 46: *(A) Smooth and rough OMVs—atoms are represented using a volumetric density map. The POPE and POPG lipids are silver and the LPS molecules have the color scheme: Lipid A and core sugars (cyan), O-antigen*

chain (red). (B) The terminal sugar particles are assigned a BGR color based on their radial height (extension). (C) The LPS molecule is divided into its constituent Lipid A anchor, core sugar domain, and terminal O-antigen chain. The Lipid A phosphate groups are green to clarify the position of the water-lipid interface that is referenced throughout this chapter. The atoms are represented with a volumetric density map (left) and a simpler ball-and-stick model (right).

Figure 47: *Schematic illustration of the smooth OMV that has been used to understand the different topology of the rough and smooth OMVs. The LPS lipids are orange, the outer leaflet POPE molecules are magenta and inner leaflet lipids are omitted throughout. The radial heights are labelled as follows: r_m (middle of the hydrophobic membrane core), r_1 (outer leaflet phosphate group boundary), r_2 (termini of the LPS core sugars), and r_3 (termini of the LPS O-antigen chains). The lipids are treated as axisymmetric cylinders, for example, the LPS macromolecules have constant cross-sectional area A_L and volume $V_l = \pi(r - r_m)(d_L/2)^2$, where d_L is the cylinder diameter and $r_m \leq r \leq r_3$.*

Figure 48: *(A-B) Smooth and rough OMVs at the POPC bilayer. (C) The axis components of the radius of gyration for the rough OMV (bottom); the phosphate group (BGR) height map after 2 μs (top). (D) The POPC lipid shell population for the rough OMV (5 nm cutoff). (E) The LPS-POPC contact number (0.6 nm cutoff). (F) The fraction of simulation frames—during the last 0.25 μs—with registered LPS-POPC contacts (per rough LPS molecule). (G) The axis components of the radius of gyration for the smooth OMV (top); the phosphate group (BGR) height map after 2 μs (bottom). (H) The fraction of simulation frames—during the last 0.25 μs—with registered LPS-POPC contacts (per smooth LPS molecule). (I) The POPC lipid shell population for the smooth OMV; (J) the LPS-POPC contact number. Figures I-J and Figures D-E are measured from the point of OMV-host membrane first contact and thus, are non-zero from the start.*

Figure 49: *The area per lipid (BPR) color-height map for the upper (extracellular) leaflet of the POPC bilayer after it was simulated with the smooth OMV for 2 μs. The mean area per lipid for this color-height map is 0.54 nm^2; for comparison, the area per lipid is 0.68 nm^2 for POPC membranes that are not strained.*

Figure 50: *(A) Smooth OMV and the host plasma membrane (5 nm shell). The phosphate groups are assigned a (BSR) color based on their height (z-axis coordinate); the ganglioside molecules are magenta. In the inset, the ganglioside head groups are magenta and the lipid tails are white. (B) The phosphate group (BGR) height map after 2 μs. (C) The terminal sugar particles are assigned are a (BGR) color based on their endpoint radial height. (D) The LPS-GM3 contact duration projected onto the phosphate group density map; the data are shown for the last 0.25 μs of simulation time. (E) The fraction of simulation frames—during the last 0.25 μs—that LPS-GM3*

contacts were registered for each one of the 615 smooth LPS molecules in the OMV outer leaflet. Put simply, the graph shows the fraction of sampled simulation time that each smooth LPS lipid was bonded to GM3 lipids (based on a 0.6 cutoff). Once the LPS-GM3 interactions were formed they were almost always maintained thereafter.

Figure 51: *(A) Top view snapshot of the smooth OMV after it was simulated for 2 μs with the multicomponent plasma membrane model. (B) The same top view snapshot with the smooth OMV removed for clarity. The ganglioside lipids within 5 nm of the smooth OMV are magenta and the ganglioside lipids beyond this 5 nm cutoff are white. The POPE, POPC, POPS, PIP_2, cholesterol, and sphingomyelin molecules are omitted throughout. The trajectories are shown for the magenta ganglioside lipids during the last 0.25 μs. The trajectory paths were assigned colors to link the sampled simulation time with lipid diffusion. The early frame positions are red, the late frame positions are blue and the intermediary frame positions are white. (C) Snapshot of the multicomponent plasma membrane when it was simulated without any OMVs. The trajectories are shown for randomly selected ganglioside lipids during the last 0.25 μs. When Figures A-B are compared with Figure C it becomes apparent that OMVs have the capacity to immobilize ganglioside lipids through zipper-like interlinking at the wrapping interface.*

Figure 52: *(A) The POPE-POPG vesicle that was used in the control experiments—the atoms are represented using a volumetric density map. The POPE lipids are orange and the POPG lipids are green. (B) The phosphate group (BGR) height map for the POPE-POPG vesicle after it bounced off the host POPC membrane. (C) The endpoint conformation for the simulation of the POPE-POPG vesicle and the multicomponent plasma membrane model. The POPE molecules are orange, the POPG molecules are green, and the host plasma membrane lipids that are within 0.5 nm of these lipids are purple. The vesicle fused with the host plasma membrane to form a lipid-lined pore that promoted lipid exchange between the plasma membrane and the POPE-POPG vesicle.*

Figure 53: *Comparison of the smooth and rough OMVs at the plasma membrane surface at 2 μs of simulation time. The smooth OMV retained its spherical shape and generated moderate curvature and the rough OMV lost its spherical shape and generated larger curvatures at the spreading front. Sphericity is denoted here with the Ψ_n symbols.*

Figure 54: *(A) The ganglioside molecules (pink), which are confined to the upper (extracellular) leaflet, create non-negligible stress in plasma membranes that promotes spontaneous bilayer curvature. (B) The energy barriers for bilayer reshaping are reduced when ganglioside molecules aggregate and form clusters that have high intrinsic positive curvature. The ganglioside lipid aggregates can reduce the line tension between membrane domains of different widths due to their conical shape. (C-D) Schematic illustrations showing how smooth OMVs affect bilayer shape and composition.*

The sphingomyelin are yellow rectangles, the PIP_2 lipids are orange triangles, the cholesterol molecules are inverted green triangles and the POPS, POPC, and POPE lipids are omitted for clarity. After simulation time of Δt there a significant number of (GM3) ganglioside molecules that have interlinked the smooth LPS lipid headgroups (based on a 0.6 nm cutoff) and consequently, there is a change in the local lipid composition and bilayer curvature. (E) The abundance of ganglioside monomers and aggregates that were detected during the last 100 ns of simulation time when the plasma membrane mimetic was simulated without any OMVs.

Acknowledgments

The Sansom group (Oxford University) provided the coarse-grained plasma membrane model.

The Im group (Lehigh University) integrated the coarse-grained lipopolysaccharide molecular dynamics simulation models into the CHARMM-GUI Martini Maker module.

The Khalid (Southampton University) and Bond (Bioinformatics Institute A*STAR) groups helped with simulation set up and the production of both theses and co-authored scientific articles.

Max Crispin (Southampton University) and Mark Sansom (Oxford University) were my internal and external examiners.

DECLARATION OF AUTHORSHIP

I, Damien Jefferies

declare that this thesis and the work presented in it are my own and has been generated by me as the result of my own original research.

Probing the Molecular Level Details of Bacterial Outer Membranes and Their Parent Bacteria: A Simulation Approach

I confirm that:

1. This work was done wholly or mainly while in candidature for a research degree at this University;
2. Where any part of this thesis has previously been submitted for a degree or any other qualification at this University or any other institution, this has been clearly stated;
3. Where I have consulted the published work of others, this is always clearly attributed;
4. Where I have quoted from the work of others, the source is always given. With the exception of such quotations, this thesis is entirely my own work;
5. I have acknowledged all main sources of help;
6. Where the thesis is based on work done by myself jointly with others, I have made clear exactly what was done by others and what I have contributed myself;
7. Parts of this work have been published as:

D. Jefferies, S. Khalid, To infect or not to infect: molecular determinants of bacterial outer membrane vesicle internalization by host membranes. J. Mol. Biol. 2020, 432, 1251-1264
D. Jefferies, S. Khalid, Atomistic and coarse-grained simulations of membrane proteins: A practical guide. Methods 2020, In press
D. Jefferies, PC. Hsu, S. Khalid, Through the lipopolysaccharide glass: a potent antimicrobial peptide induces phase changes in membranes. Biochemistry 2017, 56, 1672-1679
D. Jefferies, J. Shearer, S. Khalid, Role of O-antigen in response to mechanical stress of the E. coli outer membrane: insights from coarse-grained MD simulations. J. Phys. Chem. B 2019, 123, 3567-3575

Signed: ……

Date: ……

List of Abbreviations

3D FFT	Three-dimensional fast Fourier transform
AA	All-Atom
AFM	Atomic force microscopy
ALA	Alanine
AMBER	Assisted Model Building with Energy Refinement
AMOEBA	Atomic Multipole Optimized Energetics for Biomolecular Application
AMP	Antimicrobial peptide
ATP	Adenosine triphosphate
BGR	Blue Green Red
BHT	Bacteriohopanetetrol
BPR	Blue Purple Red
BSR	Blue Silver Red
BtuB	Vitamin B12 transporter
Cer	Ceramide
CG	Coarse-grained
CHARMM	Chemistry at Harvard Macromolecular Mechanics
CHIKV	Chikungunya virus
Chrys-3	Chrysophsin-3
CL	Cardiolipin
CTxB	Cholera toxin B subunit
Dab	Diaminobutyric acid
DM	Dimyristoyl
DMPC	Dimyristoyl-phosphatidylcholine
DMPE	Dimyristoyl-phosphatidylethanolamine
DMPS	Dimyristoyl-phosphatidylserine
DNA	Deoxyribonucleic acid
DO	Dioleoyl
DOPC	Dioleoyl-phosphatidylcholine
DOPG	Dioleoyl-phosphatidylglycerol
DOI	Digital Object Identifier
DP	Dipalmitoyl
DPPC	Dipalmitoyl-phosphatidylcholine
DPPE	Dipalmitoyl-phosphatidylethanolamine
DPPG	Dipalmitoyl-phosphatidylglycerol
EDTA	Ethylenediaminetetraacetic acid
FhuA	Ferrichrome outer membrane transporter
FRET	Fluorescence Resonance Energy Transfer
FT-IR	Fourier-transform infrared spectroscopy
Gal	Galactose
Glc	Glucose
GlcNAc	N-acetylglucosamine
GLY	Glycine
GAFF	General Amber ForceField
GM	Ganglioside
GM1	Monosialotetrahexosylganglioside
GM2	Disialotetrahexosylganglioside

GM3	Monosialodihexosylganglioside
GPCR	G protein-coupled receptor
GROMOS	GROningen Molecular Simulation
Hep	Mannoheptose
HF	Hartree-Fock
IL	Inner leaflet
IM	Inner Membrane
Kdo	Keto-deoxyoctulosonate
L-BFGS	Limited-memory Broyden-Fletcher-Goldfarb-Shanno
Ld	Liquid-disordered
Lo	Liquid-ordered
LPP	Braun's lipoprotein
LPS	lipopolysaccharide
LYS	Lysine
ManNAc	N-acetyl-D-mannosamine
Mcr	Mobilized colistin resistance
MD	Molecular dynamics
MIC	Minimum inhibitory concentration
MP	Møller-Plesset
MP2	Møller-Plesset to second order
mPy	Mouse polyoma virus
MTTK	Martyna-tuckerman-tobias-klein
MurNac	N-Acetylmuramic acid
NMR	Nuclear magnetic resonance
NPT	Isothermal-isobaric ensemble
NVE	Micro-canonical ensemble
NVT	Canonical ensemble
OL	Outer leaflet
OM	Outer membrane
OMP	Outer membrane protein
OmpA	Outer membrane protein A
OmpF	Outer membrane protein F
OmpLA	Outer membrane phospholipase A
OmpX	Outer membrane protein X
OMV	Outer membrane vesicle
OPLS	Optimized Potentials for Liquid Simulations
OPLS-AA	Optimized Potentials for Liquid Simulations All-Atom
PC	Phosphatidylcholine
PE	Phosphatidylethanolamine
PG	Phosphatidylglycerol
PIP	Phosphoinositides
PIP_2	Phosphatidylinositol 4,5-bisphosphate
PIP_3	Phosphatidylinositol 3,4,5-trisphosphate
PmB	Polymyxin B
PMB1	Polymyxin B1
PME	Particle mesh Ewald
PMF	Potential of mean force
PO	Palmitoyloleoyl
POPC	Palmitoyloleoyl-phosphatidylcholine

POPE	Palmitoyloleoyl-phosphatidylethanolamine
POPG	Palmitoyloleoyl-phosphatidylglycerol
POPS	Palmitoyloleoyl-phosphatidylserine
PS	Phosphatidylserine
QS	Quasistatic stretching
RDF	Radial distribution function
Ra	Ra mutant
Rc	Rc mutant
Rd	Rd mutant
Re	Re (deep-rough) mutant
Rha	Rhamnose
RNA	Ribonucleic acid
RMSD	Root-mean-square deviation
SCD	Deuterium order parameter
SCG	Supra coarse-grained
SEDM	Stimulated emission depletion microscopy
Sia	Sialic acid
SV40	Simian vacuolating virus 40
US	Unsteady stretching
VMD	Visual Molecular Dynamics
WHAM	Weighted Histogram Analysis Method

Chapter 1: Introduction

1.1 Biological Membranes (Overview and Current Understanding)

All living organisms contain biological membranes, which are semipermeable barriers that regulate the movement of molecules from one region of space to another region through passive and energy-dependent processes [1-6]. Cellular membranes form the boundary between the intracellular and extracellular environments and delineate “self” and “non-self” biomolecular interactions. Cellular membranes regulate the uptake of nutrients from the outside of cells and at the same time they facilitate the export of waste products from the intracellular cytosol [7-9]. Cellular membranes underpin all basic cell functioning and they are inextricably linked to the most basic concepts of living organism and the most basic definitions of “life”. It is theorized that the very first lifeforms comprised little more than a single lipid bilayer encasing a relatively unsophisticated matrix whose primary function was to produce more phospholipids [10-13].

Cellular biological membranes can be sub-divided into three types: eukaryotic cell membranes, prokaryotic cell membranes, and archaeal cell membranes [14-16]. Eukaryotic cell membranes compartmentalize the eukaryotic cellular cytosol and consist of a single phospholipid bilayer with a complex combination of anchored integral membranes proteins (e.g. transporters, linkers and receptors) and less tightly anchored peripheral membranes proteins (e.g. enzymes, lipid clamps and electron carriers) [17-19]. Prokaryotic cell membranes compartmentalize the prokaryotic cellular cytosol and have an altogether different composition that varies from one class of bacteria to another. Gram-positive bacteria contain a single phospholipid bilayer that is interlinked with a thick wall of peptidoglycan, whereas Gram-negative bacteria have two cellular membranes and a thin wall of peptidoglycan that is wedged between them [20-22]. Archaeal membranes contain unusually long phospholipids that can span the entire

membrane normal axis and the lipids can contain two, rather than one, hydrophilic headgroups [23-25].

Biological membranes also compartmentalize biological matter within subcellular organelles and isolate subcellular organelle functions from the encompassing cellular cytoplasm (Figure 1A). Subcellular lysosomes are membrane-bound organelles that compartmentalize hydrolytic enzymes that are capable of breaking down proteins, nucleic acids, lipids and complex sugars at physiological temperature and pressure [26-28]. Lysosomes contain an acidic lumen that activates the hydrolytic enzymes and enhances the digestion of complex macromolecules into smaller and more useful biomolecules. Mitochondria are perhaps an even more interesting representative organelle since they are described as semiautonomous double-membrane-bound organelles; they contain their own genome and even have the capacity to independently generate chemical energy through the action of enzymes [29-31]. Mitochondria are surrounded by two membranes and the inner membrane has substantial infoldings called cristae that resemble the textured outer surface of alpha-proteobacteria [32-33]. The inner membrane and matrix contain high concentrations of the enzymes that are necessary for aerobic respiration and the production of adenosine triphosphate (ATP) [34-35]. Given that mitochondria resemble proteobacteria, that they contain bacterial lipids and also that the inner and outer membranes effectively compartmentalize cytosolic organelle functions, it has been theorized that mitochondria were originally prokaryotic cells that became endosymbionts living inside eukaryotic cells [36-38]. It is clear then that lipid membranes effectively compartmentalize entire cellular cytosols and also effectively delineate subcellular organelle functions from the encompassing cellular cytoplasm.

Lipid membranes can also form vesicles either within or outside of eukaryotic, prokaryotic, or archaeal cellular membranes. Vesicles are nanoscopic spheric structures that consist of at least one lipid membrane that encases a liquid or cytoplasmic core [37-39]. Vesicles form naturally within

the plasma membrane during the expulsion (exocytosis), uptake (endocytosis) and transport of organic and non-organic materials [40-41]. Vesicles are also formed within the cellular cytoplasm where they traffic biomolecules from one organelle to another, or even from one subcellular organelle to the cellular membrane where they are expelled into the extracellular space and can subsequently enter into neighbouring cells or rupture at a distance far away from the parent cells. Synaptic vesicles are specialized nanocarriers that mediate interactions between adjacent neurons and relay nerve impulses from one dendritic cell to another [42-43]. Synaptic vesicles are located at the presynaptic terminal and fuse with one cellular membrane when a signal moves along an axon. The neurotransmitters are released into the synaptic cleft, where they can move into a neighboring neuron and propagate the nerve impulse [44-45].

Vesicles are also formed within Gram-negative bacterial cell surfaces and given their structure and composition, i.e. an external leaflet of lipopolysaccharide (LPS) molecules and an internal leaflet of phospholipids, the nanospheres are termed “outer membrane vesicles” (OMVs) [46-47]. OMVs are involved in diverse cellular functions including trafficking bacterial cell signalling biochemicals, sequestering metals and biomolecules, nutrient scavenging, forming bacterial biofilms and even mediating bacterial pathogenesis [48-51]. OMVs traffic pathogenic cargo from parent bacteria to host eukaryotic membranes where they move into the host cell cytosol and induce disease transmission processes [52-53]. The precise nanoscopic biomolecular interactions that underpin OMV entry into host cell cytosols are not entirely understood, although some important insights will be provided here in the penultimate chapter of this thesis.

While it is evident that the production of vesicles *in vivo* underpins intercellular signalling, nutrient scavenging, subcellular trafficking, bacterial pathogenesis, etc. It is important to appreciate that synthetic vesicles are also regularly manufactured within laboratories and then they are used in biochemical and biophysical studies. Homogeneous phospholipid vesicle

suspensions can be prepared for example, through extrusion, sonification, or alternatively, by injecting a suspension of phospholipids into water [54-55]. Phospholipid vesicles can be produced with relatively simple experimental apparatus and used as suitable surrogates for more complex realistic biological membrane systems.

Biological membranes regulate many important biological functions and they contain multiple different types of constituent biomolecules. Cellular membranes ordinarily contain at the very least, a complex combination of lipids, proteins and sugars [56]. But cellular membranes can comprise tens of thousands of different lipids and an inordinate number of different integral and peripheral membrane proteins [57-58]. The interactions between these lipids and proteins are only now beginning to be understood through the use of molecular simulation methods [59] (Figure 1B) but the simulated membrane mimetics have generally been overly simplistic. The models generally contain just a few different types of proteins and lipids and the membrane mimetics almost always omit important biomolecular matter such as the glycocalyx or the "pericellular matrix", which is a glycoprotein and glycolipid covering that surrounds the cell membranes of some epithelia and bacterial cells [60-62]. Characterizing the structure of such inordinately complex cellular membranes has proved difficult and a clear, indisputable representation of cellular membrane structure stills remains elusive [63]. Several rudimentary models were proposed to explain cellular membrane structure in the 20th century and one of the better-known hypotheses was the fluid mosaic model; now commonly known as the Singer-Nicolson model (1972).

The fluid mosaic model assumed that cellular membranes contained different types of lipids and proteins that would diffuse laterally from one position within the membrane plane to another [64-65]. The constituent protein and lipid molecules were hypothesized to be the "membrane mosaic tiles" that together would form a contiguous bilayer structure. The proteins and lipids were assumed to have considerable degrees of freedom and their lateral and

rotational movement was effectively unrestrained in the fluid mosaic model [66-67]. The proteins and lipids would undergo continuous lateral diffusion and the membrane would be more or less homogeneous with the proteins and lipids being uniformly distributed throughout the membrane bilayer. This hypothesis was however, in conflict with publications from the 1970s that proposed that cellular membranes were full of lateral heterogeneities [68-70]. There was an increasing number of publications that contested the hypothesis that lipids and proteins were arranged relatively uniformly throughout biological membranes. Newer data suggested that there were lateral lipid composition fluctuations within biological membranes and that the membranes could not be both homogenous and equally fluid throughout. It was becoming increasingly apparent that there was lateral segregation, domain formation, and lipid-protein interactions associated with functional membrane domains within biological membranes [71-72]. The mounting evidence called into question the fluid-mosaic model and by 1997, Simons and Ikonen popularized the raft hypothesis [73]. Lipid rafts are of special interest here, since data form the penultimate chapter of this thesis suggests that OMVs might promote the formation of curved lipid rafts, i.e. caveolae [74], in mammalian membrane mimetics when they interact with host cell (GM3) ganglioside molecules.

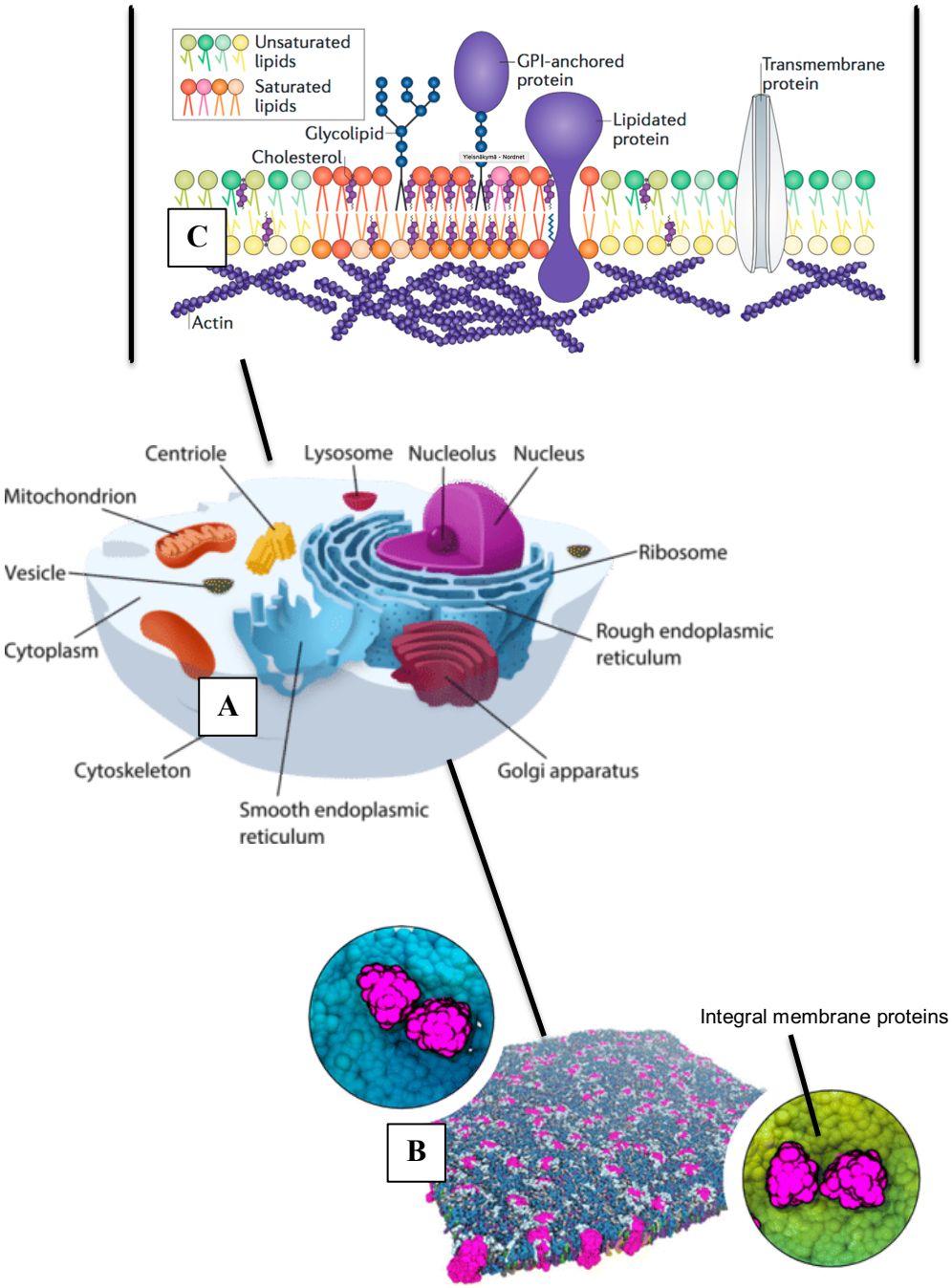

Figure 1. Introduction to the structure of animal cells. (A) Eukaryotic subcellular membrane-bound organelles (e.g. mitochondria and lysosomes) that are encased by the peripheral cellular membrane. The cellular membrane delineates "self" and "non-self" cellular interactions and the organelle membranes isolate organelle functions from the encompassing cytoplasmic space. The labels are used to show how the subcellular organelles are distributed throughout the cellular cytoplasm. (B) Modern molecular dynamics simulation graphics that represent how molecular modelling has been used to understand the clustering of integral membrane proteins. The integral membrane proteins are pink and the lipid membrane is either blue or yellow. (C) Schematic representation of the eukaryotic cellular membrane structure that includes a central liquid-ordered membrane raft domain and two liquid-disordered membrane domains either side of this. Saturated lipids are red and orange, unsaturated lipids

are yellow and green, cholesterol molecules are the curved purple structures. The macromolecules can be identified by the different refence labels. Image sources are: Encyclopaedia Britannica, and papers (i) 10.1038/nrm.2017.16 (DOI) [75]; and (ii) 10.1021/jacs.5b08048 (DOI) [76].

The membrane raft model (Figure 1C) proposed that biological membranes are interspersed with cholesterol- and sphingolipid-rich nanodomains that are associated with specific cellular functions and cell signalling [77-79]. It had already been theorized that under the appropriate conditions, cholesterol could co-couple with saturated phospholipids to generate cholesterol-rich liquid ordered domains within multicomponent membranes [80]. The areas that were enriched with cholesterol would be termed liquid-ordered (Lo) domains and the areas that were depleted of cholesterol molecules would be termed liquid-disordered (Ld) domains. The raft hypothesis was however, significantly more specific in its characterization of lipid segregation and the composition of lateral membrane heterogeneities. The membrane raft model posited that cholesterol molecules would pair with sphingolipids, saturated phospholipids and proteins to form a structure whose biophysical parameters differed from the encompassing membrane environment [81-84]. The so-called "lipid rafts" would facilitate for example, intercellular signalling and membrane budding events [85-87].

After more than a decade of research, it was concluded that lipid rafts are transient functional structures or in other words, they are fluctuating functional nanoscale assemblies that regulate important biological functions [88]. Stimulated emission depletion microscopy (SEDM) has been refined to analyze membrane structures on spatial scales as small as 10-20 nm [75]. When SEDM was used to analyze biological membrane mimetics it was found that nanoscopic raft-like assemblies self-assembled through the attractive interactions of proteins and lipids. The experimental groups observed nanoscopic multicomponent biomolecular structures that consisted of small (3-6 nm) membrane proteins with encompassing pools of lipids (~5 nm) [89]. Experimental evidence has generally corroborated the raft hypothesis and it

is now considered to be a reasonably accurate representation of generic mammalian membrane structure [90-91].

The raft hypothesis is however, inadequate for accurately describing the composition of bacterial membranes and in particular, the inner and outer membranes of Gram-negative bacteria [92-95]. Gram-negative bacteria are prokaryotic lifeforms that are typically a few micrometers in length [96-98] and unlike eukaryotic cells, the bacteria usually lack large membrane-bound organelles in their cytoplasm such as mitochondria and a nucleus (Figure 2A) [99-100]. Gram-negative bacteria have an unusual cell envelope that contains two distinct lipid membranes and a layer of peptidoglycan that is situated between them [101-102]. The inner and outer membranes of Gram-negative bacteria differ in terms of chemical composition and structure but importantly, neither membrane contains cholesterol or conventional membrane raft structures [103]. The Gram-negative cell envelope is tripartite and it contains: (i) the cytoplasmic membrane; (ii) the outer bacterial membrane; and (iii) interstitial layers of peptidoglycan that are situated between them [95,101]. The chemical composition of the inner and outer membranes is already reasonably well-known [103] but the specific organization and interactions of the constituent components still needs clarifying [104-106]. In 2018 Turner et al. used atomic force microscopy (AFM) to analyze the structure of the *Escherichia coli* peptidoglycan cell wall [107]. It was previously assumed that the layers of peptidoglycan formed a highly ordered crystalline material [108-110] but the AFM experiments demonstrated that peptidoglycan is much less ordered than was previously depicted and also, that the specify morphology of the peptidoglycan chains depends of the shape of the parent bacteria. The form of the peptidoglycan layer is itself still debated and the interactions of the peptidoglycan network with bacterial membrane proteins (e.g. Braun's lipoprotein) are even less clear [111-112]. AFM techniques can be applied to evaluate the general structural characteristics of peptidoglycan networks but the fast interactions between membrane proteins and peptidoglycan molecules transpires on a

spatiotemporal scale that is beyond the scope of conventional experimental analysis methods [113].

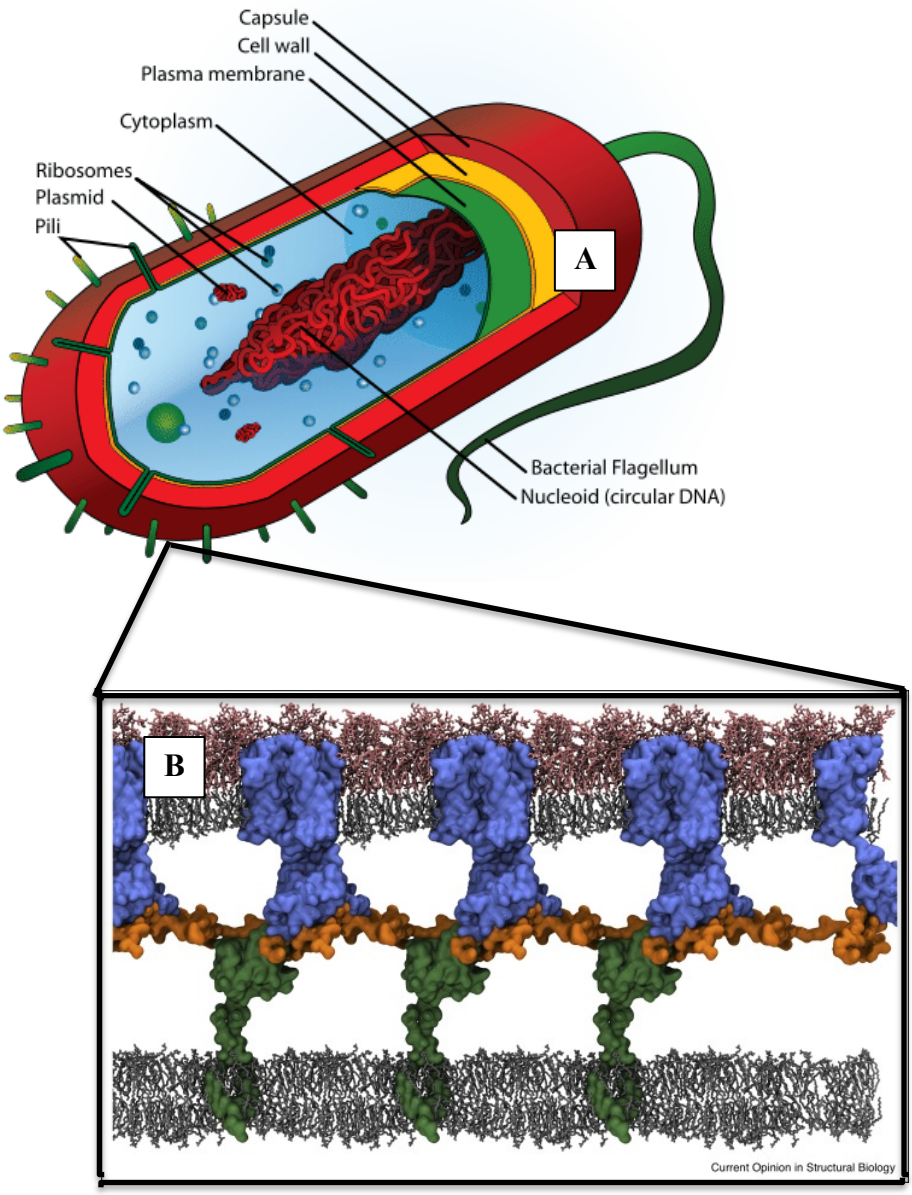

Figure 2. The structure of Gram-negative bacteria. (A) Schematic illustration that shows the structure of the Gram-negative bacterial cell organelles and how these subcellular structures are encased by the peripheral cell envelope. (B) Tripartite structure of the Gram-negative cell envelope that includes the inner cytoplasmic membrane (black), the outer bacterial membrane (black and pink), peptidoglycan (orange) and the anchoring proteins that stretch across the periplasm (green and blue). The structure was determined from complementary experimental and computational analyses. The image sources are: Wikipedia Commons and paper 10.1016/j.sbi.2019.12.017 (DOI) [53].

The coupling of outer membrane proteins both with each other and with encompassing lipids has similarly been difficult to assess through experimental analysis and their general oligomeric form is only now becoming fully apparent [114]. Sansom et al. have recently combined experimental analysis methods with computer simulation techniques to understand how outer membrane proteins (OMPs) co-couple to form long oligomeric networks that can span several tens of nanometers [115]. The combination of computer simulation and experimental analysis techniques enabled the group to elucidate the spatiotemporal organization of large OMP clusters in unprecedented detail and also to understand how oligomeric protein network might be formed *in vivo*.

The conventional understanding of the outer membrane of Gram-negative bacteria is being revised due to mounting experimental and complementary computer simulation data (Figure 2B) [116-118]. Clifton et al. showed for example, that the position of outer membrane lipids can depend of the availability of divalent (e.g. Ca^{2+}) cations [119-120]. The intracellular and extracellular lipids were found to rotate about the membrane midplane when stabilizing divalent cations were sequestered with EDTA. Neutron reflectivity and isotopic labelling were used to show that the outer membrane became more homogenous once the stabilizing cations were displaced. The EDTA chemical destabilized the asymmetric structure of the bacterial outer membrane and the constituent LPS lipids flipped about the membrane midplane into the intracellular leaflet, while the intracellular phospholipids flipped about the membrane midplane into the extracellular leaflet. The analyses showed that the outer membrane can become distorted if the concentration of ambient divalent cations is low.

Bacterial membrane mimetics were also analyzed in 2013 via X-ray and neutron reflectometry with grazing incidence X-ray diffraction and Brewster angle microscopy [121]. It was found that bacterial membrane lipids (Rc LPS) can form highly ordered monolayers that display an oblique hexagonal unit cell at surface pressures of 20 nNm^{-1} and above. The bacterial membrane

mimetics adopted relatively rigid hexagonal grid packing that is comparable to the packing of ions within a crystalline material [122-123]. Ongoing experimental analysis continues to corroborate the inference that the Gram-negative bacterial outer membrane can form a relatively rigid and ordered structure under the right conditions [124-128].

Experimental data are also being used to understand how membrane-active antimicrobial agents can affect the stability and morphology of bacterial outer membrane mimetics [129-133]. Membrane-active antimicrobial agents (e.g. antimicrobial peptides) are known to disrupt the integrity of lipid membrane bilayers but the biomolecular and biophysical interactions that underpin these disruption pathways still need to be elucidated [134-136]. Our understanding of bacterial membranes is simplistic, but our understanding of the interactions between bacterial membranes and antimicrobial agents is even more basic. Neutron reflectometry was applied under multiple contrast conditions to understand how the sugar groups of bacterial LPS lipids protect the phosphate-rich inner core region from electrostatic interactions with antimicrobial peptides. By analyzing the interactions of the protein antibiotic colicin N with two different rough LPS lipids, it was shown that the uncharged sugars of LPS lipids can block short-range electrostatic interactions between cationic antimicrobials and the vulnerable anionic LPS phosphate groups [137]. Lakey et al. used other interesting experimental methods to understand the general biophysical and biochemical properties of colicin N antimicrobial peptides and to rationalize how the peptides can destroy pathogenic microbes [138-143]. Experiments were additionally applied to investigate the interactions of antimicrobial polymyxin B molecules with Gram-negative bacterial outer membrane mimetics. It was shown through the combination of neutron reflectometry and infrared spectroscopy that the physical state of the lipid matrix can regulate interactions with polymyxin peptides [144-146]. The analyses revealed that the translocation of polymyxin molecules into the bacterial outer membrane mimetics was dependent on the phase transition of bacterial lipids (LPS) from the gel to the liquid crystalline state. The insertion of polymyxin moieties into bacterial

membranes is well-known to mediate disruptive interactions [147-150] but the factors that control how effectively the hydrophobic moieties could penetrate bacterial membrane cores was poorly understood before this pioneering publication. Collectively, the experimental analyses are clarifying the precise morphology of the Gram-negative bacterial cell envelope and how antimicrobial agents and mechanical stress can affect its form and structural stability.

From this thesis subsection it is evident that experimental techniques are approaching a spatiotemporal scale where they can be used to detect the presence of fluctuating nanoscale assemblies [75,89] and the overarching morphology of the Gram-negative cell envelope [107-112, 92-96]. But it is nonetheless challenging to understand many biomolecular interactions that occur both within, and at the surface of, cellular membranes since the interactions can occur on sub-nanometer and sub-nanosecond spatiotemporal scales [116-117]. It can be challenging to understand the lipid and protein interactions that drive the formation of flat lipid rafts, caveola, and other fluctuating lipid heterogeneities without using some combination of the most advanced experimental analysis techniques and the most sophisticated complementary computational tools. Computer simulation methods are necessary for understanding how mammalian membranes are organized at the molecular level and for understanding the general biophysical parameters of fluctuating lipid heterogeneities, e.g. lipid rafts [114]. Computer simulation methods are necessary for understanding the interactions that transpire within Gram-negative bacterial cell envelopes including the interactions between the LPS lipids themselves [104,116-117,119-120], the interactions between LPS lipids and antimicrobial agents [105] and the properties of OMVs that erupt from bacterial cell surfaces [151]. There is a spatiotemporal resolution that is relatively inaccessible with conventional experimental techniques and this scale is more easily accessed with molecular dynamics simulation methods.

1.2 Analysis of Biological Membrane Models with Molecular Dynamics Simulations (Brief Overview)

Some of the first molecular dynamics simulations were conducted in 1957 and they were performed in an attempt to investigate the interactions of simplistic hard-sphere models [152]. Seven years later (1964) more realistic molecular dynamics simulations were conducted to simulate the interactions of an argon liquid [153]. After a few more years of method development, MacCammon et al. studied the interactions of a small bovine pancreatic trypsin inhibitor protein over what now seems to be an unacceptably short simulation timeframe (8.8 ps) but at the time was pioneering [154]. Protein folding was being simulated for an entire microsecond in 1998 due to exponential increases in computer processing power and the development of more advanced molecular dynamics simulation forcefields [155-156].

The attention of the simulation community was at this time gravitating more and more toward the simulation of lipid assemblies and lipid membrane mimetics [59]. The first molecular dynamics simulations of biological membrane mimetics focused on simplified lipid bilayers without explicit solvent (water) [157], simplified lipid monolayers [158] and small lipid micelles that were immersed in water [159]. The simulations provided some interesting molecular level insights but it was desirable to simulate greater spatiotemporal scales and effectively bridge the gap between experimental and computational research. Larry Scott et al. began to combine molecular dynamics simulation algorithms with Monte Carlo methods to develop new simulation techniques that could be used to simulate unprecedented spatiotemporal scales [160-162]. There was also an ongoing attempt to correct any noted inadequacies of common molecular dynamics simulation forcefields and make them more suitable for accurately representing the properties of lipid membranes. Scientific research groups would produce one relatively crude molecular dynamics simulation forcefield and once these forcefields were benchmarked, they would be refined so that they could more accurately mimic the properties of lipid membranes. The older simulation forcefields could be used as an effective “starting-point” for generating

entirely new and improved types of molecular dynamics simulation forcefields [163-167].

For example, Egberts et al. designed a model for DPPC lipids in 1994 that was based on the GROMOS-87 molecular dynamics simulation forcefield [168]. The forcefield seemed to be inappropriately calibrated; when the DPPC lipids were simulated at physiological pressure and temperature they inaccurately transitioned into the gel phase. The partial charges on the GROMOS-87 lipids were halved and the dihedral potential of the acyl chains was transformed into the Ryckaert-Belleman representation to compensate for the incorrect lipid properties. When the DPPC lipids were simulated with the reparametrized forcefield they correctly entered into the liquid-disordered Ld membrane phase [169]. Berger went on to systematically reparametrize the original Egberts et al. parameters by applying the optimized potential for liquid simulations (OPLS) parameters that were used in an earlier model for DMPC lipids [170]. The Lennard-Jones parameters for CH_2 and CH_3 moieties were carefully calibrated to match known experimental data for volume and heat of vaporization energies [171]. The Berger lipids became the "minimal standard" in molecular dynamics simulations of lipid membranes [59]. The method of using so-called Berger lipids for molecular dynamics simulations is only now, decades later, becoming uncommon and scientists are opting instead to use more sophisticated molecular dynamics simulation forcefields such as the CHARMM36 all-atom forcefield [172-173,104].

The advent of sophisticated forcefields that explicitly represented each constituent atom of a given biomolecule was pioneering and as molecular dynamics simulations continued to produce more interesting biophysical data, it was becoming clear that molecular dynamics simulation forcefields could be modified to not only increase their overall accuracy but also to increase their scope and spatiotemporal resolution. The molecular dynamics simulation forcefields could be modified to effectively bridge the length and timescale gaps between experimental and molecular simulation analysis methods [114, 59, 174-178]. Rather than directly supersede sophisticated

atomistic force fields, low resolution force fields, or coarse-grained force fields, were designed to complement them [179-180]. The simulation community could use sophisticated all-atom resolution molecular dynamics simulation forcefields (e.g. CHARMM36) for the accurate reproduction of sub-nanometer and sub-nanosecond biomolecular interactions in one instance, and then lower resolution coarse-grained forcefields for the simulation of biological processes on much larger spatiotemporal scales in another instance (Figure 3A) [181].

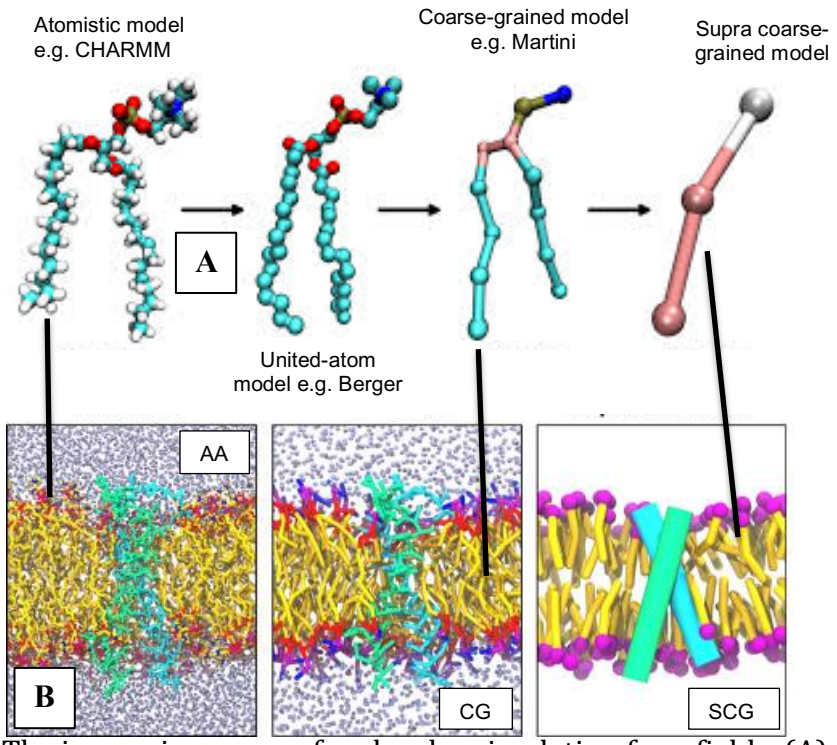

Figure 3. The increasing scope of molecular simulation forcefields. (A) Comparison between an atomistic CHARMM forcefield lipid model, a united-atom Berger forcefield lipid model, a coarse-grained Martini forcefield lipid model, and a supra coarse-grained forcefield lipid model. Each constituent particle of the four lipid models represents a single molecular dynamics simulation interaction center. (B) Sideview snapshots of a multicomponent membrane being simulated with an atomistic or "all-atom" resolution forcefield (AA), a coarse-grained resolution forcefield (CG), and a supra coarse-grained resolution simulation forcefield (SCG). Transmembrane proteins are cyan and green, water is blue and the other molecules represent the simulation lipids. The image sources are: 10.1021/acs.chemrev.8b00460 (DOI) [114] and 2015.igem.org.

Molecular dynamics simulation forcefields are now being used to complement experimental analysis techniques and resolve biological

interactions that are barely accessible by any other means. Let us first consider some of the molecular dynamics simulations that have provided a clearer understanding of the Gram-negative cell envelope structure and the interactions between Gram-negative membrane mimetics and AMPs (e.g. Chrysophsin-3) or antimicrobial nanomaterials (e.g. buckminsterfullerene). After that, we can consider how molecular dynamics simulation methods have been used to provide insights into the nature of fluctuating lipid heterogeneities, lipid rafts, the structure and interactions of mammalian plasma membranes, and the self-association and self-assembly of biological membrane proteins and lipids (Figure 3B). Taken together, the descriptions will provide a brief account of how molecular dynamics simulations are being used to elucidate the properties of membranes and the nature of membrane interactions. It should be noted however, that this summary is kept intentionally brief and more comprehensive reviews are regularly published to provide more scope for biophysical scientists; for example, see [182-188].

The outer-membrane of Gram-negative bacteria has been simulated repeatedly using high-level molecular dynamics simulation forcefields to the point that scientific research groups have created an identity for themselves that involves almost exclusively, the production and simulation of Gram-negative bacterial membranes with specific molecular dynamics simulation forcefields (e.g. the CHARMM suite of forcefields [189-197, etc.]). The Im group are now firmly established as scientists who probe all aspects of the Gram-negative bacterial inner and outer membranes using high-level atomistic forcefields and to a lesser extent, the Martini coarse-grained molecular dynamics simulation forcefield [104,198-210]. Early pioneering simulation studies were used to determine the structural parameters of the Gram-negative bacterial outer membrane; the group determined different lipid packing parameters such as area per lipid, membrane thickness, lipid acyl chain order parameters, and structure and orientation metrics for LPS lipid moieties [211]. It was found that the area per lipid, membrane thickness, and acyl chain order parameters depended on the size of the LPS chemotype that was being simulated. Shorter forms of LPS lipids occupied less lateral

surface area, tended to have less ordered acyl chains, and tended to have a thicker hydrophobic core membrane domain. More interestingly, it was found that the orientation of the terminal headgroup moieties also depended on the local membrane environment. More heterogeneous membrane environments promoted lipid headgroup splay, and the terminal LPS sugar moieties stretched out over the membrane surface when they were surrounded by small lipid molecules. This is interesting to note since LPS headgroup splay is connected to LPS lipid clustering in chapter 4 of this thesis. Molecular dynamics simulations are applied in chapter 4 and it is demonstrated that LPS lipid headgroups can each other and progressively form LPS nanodomains when they are surrounded by small lipid molecules.

The conformational dynamics of the terminal sugar moieties was later investigated by the Im group with the CHARMM36 atomistic forcefield and their simulation data was combined with NMR experimental data. The simulations focused on homogenous single-component LPS lipid leaflets and it was found that the LPS lipid headgroup moieties adopted an approximately lamellar alignment. The tilt angle of the most peripheral LPS headgroup saccharide moieties was determined to be as small as ~10° [212].

The Im group have also analyzed how outer membrane lipids interact with outer membrane proteins. In 2014 they performed atomistic resolution molecular dynamics simulations to analyze the interactions of outer membrane phospholipase A (OmpLA) with Gram-negative outer membrane lipids [213]. It is important to state here that the LPS lipid molecules were relatively short form chemotypes that lacked terminal O-antigen chain polymers. It is also important to clarify that OmpLA is a porin protein that consists of a 12-stranded antiparallel beta-barrel with a convex and flat side [214-218]. The convex side enables semi-specific secretion of biomolecules, including bacteriocins. It was found that specific protein moieties (i.e. L1, L4, and L6 loops) covered the interior of the protein barrel in a way that would prevent pore function *in vivo*. It was resolved that the omitted LPS headgroup sugar units would, in some way, intervene and through unaccounted for

intermolecular interactions, they would affect the position of the protein loops and thereby the function of the porin protein. The insights regarding the effects of the lipid environment on the conformation of the embedded protein are themselves quite interesting, but equally interesting data was collated to assess how the embedded protein perturbed the encompassing pool of lipids. It was found that the membrane protein changed the thickness of the encompassing lipids. In general, energetically unfavourable mismatch between transmembrane protein domains and hydrophobic bilayer cores is relieved through adaptation of the bilayer (i.e. local thinning or thickening), or through changes in protein orientation [219-222]. In the simulations conducted by the Im group it was found that the local OmpLA membrane thinning was location specific. There was more thinning adjacent to specific portions of the embedded OmpLA protein surface, rather than the membrane thinning being a simple function of distance between lipids and the protein surface.

The Im group have, and still are, developing web-based tools that simplify the construction of Gram-negative bacterial membrane mimetics (Figure 4A) [223-227]. Users can select the relative abundances of upper and lower membrane leaflet lipids and the CHARMM-GUI Membrane Builder [228-230] will generate a structure file that has these molecules optimally organized about the membrane midplane (Figure 4B). Further, one can opt to place appropriately oriented outer membrane proteins between these lipids and create a structure file that contains a complex combination of (asymmetrically distributed) lipids and protein (Figure 4C). The associated simulation parameter files are provided in a directory for users to unpack and use one after another. Given the previous discussions of atomistic bacterial membrane simulations it is unsurprising that the CHARMM-GUI modules were at first only customized for the production of atomistic structure files [231]. The scope of the CHARMM-GUI module has since increased beyond atomistic simulations alone and the online modules now additionally simplify the construction of lower resolution coarse-grained outer membrane mimetics [151, 232]. What is more, the construction tools can be used to

produce more than just flat lipid membranes or conventional planar lipid geometries. The CHARMM-GUI Martini Maker was customized for the production of spheric micelles, spheric vesicles, discoidal nanodisc geometries, flat membrane mimetics and more. The module is used in the penultimate chapter to assemble OMVs and is also used in chapter 4 to generate flat bacterial membrane mimetics.

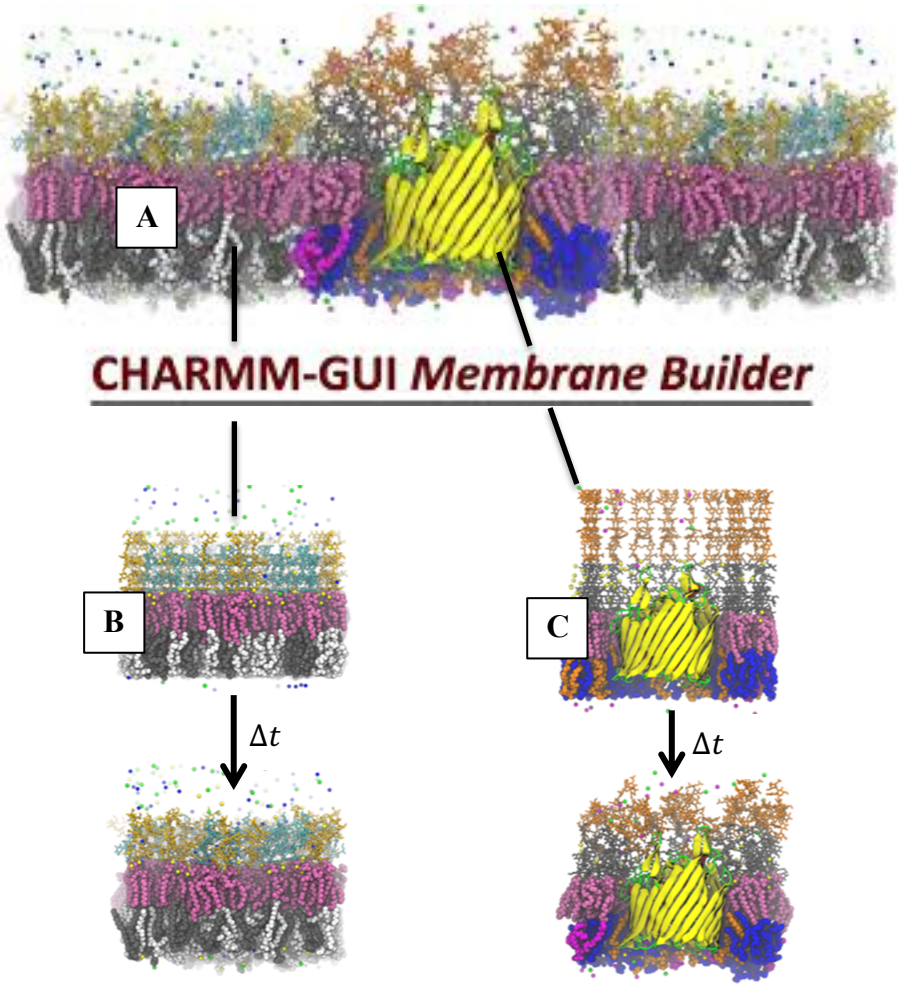

Figure 4. (A) Visualization of a complex asymmetric Gram-negative outer membrane mimetics that were created with the CHARMM-GUI web-based construction tool. (B) The *Campylobacter jejuni* outer membrane model that was assembled with the CHARMM-GUI construction tool (top) and simulated for a time Δt (bottom). (C) The *E. coli* outer membrane model that contains the central vitamin B12 transporter (BtuB) integral membrane protein. The structure was assembled with the CHARMM-GUI construction tool (top) and simulated for a time Δt (bottom). The inner leaflet lipids are blue, white, and black. The outer leaflet lipids are pink, orange, gold, cyan and gray. The BtuB protein is yellow and green. The ions are represented as small spheres that are not covalently linked with the lipids or protein molecules. Image source: 10.1021/acs.jctc.8b01066 (DOI) [229].

Lins et al. are also firmly established as a scientific research group who are interested in understanding Gram-negative bacterial outer membranes interactions with atomistic resolution molecular dynamics simulation forcefields. The team were conducting atomistic resolution molecular dynamics simulations as early as 2001 [233] that were based on the AMBER95 [234] and GLYCAM_93 [235] forcefields with geometry optimizations being conducted with Hartree-Fock self-consistent field calculations at the 6-31G* level [236-239]. The simulations revealed that calcium ions (Ca^{2+}) were predominantly hexacoordinated with the anionic LPS macromolecule phosphate groups. Most of the calcium ions were confined to a domain ~2 nm thick in the inner core region of the LPS bacterial outer membrane mimetics. The analyses showed that the bacterial outer membrane mimetics were divided quite clearly into positively and negatively charged domains along the membrane normal axis. The charge distribution was the result of the calcium ions being spatially restricted to specific portions of the Gram-negative outer membrane model [240]. Lins et al. would subsequently analyze the structure and electrostatics of the *Pseudomonas aeruginosa* bacterial outer membrane seven years later in 2008 [241-242]. The molecular dynamics simulations demonstrated that the LPS headgroup and acyl chain domains can have different dynamic interactions; averaged diffusion constants can be two orders of magnitude larger for the LPS headgroup domains when comparisons are made with the anchoring acyl chain domain. Molecular dynamics simulations were additionally conducted in 2017 to analyze the interactions of polymyxin B molecules with the LPS Lipid A anchor [243]. It is important to state here that Lipid A molecules consist of just two glucosamine sugar units, in an $\beta(1\rightarrow6)$ linkage, with the covalently bonded LPS acyl chains [244-245]. Lipid A is the smallest LPS lipid variant and it is used to understand the interactions of larger and more complex LPS lipid variants. The simulated polymyxin B antimicrobials were able to interact with the vulnerable anionic Lipid A phosphate groups. It was found that the polymyxin B peptides displaced the stabilizing cations from the bacterial membrane surface when they interacted with the LPS lipid membrane. The simulations provided atomistic level insights for processes

that had already been hypothesized but had arguably never been proved outright [147-150]. The positively charged polymyxin diaminobutyric acid (Dab) residues interacted with the anionic LPS lipids phosphate groups and this interaction induced bilayer damage as the stabilizing divalent cations moved from the water-lipid interfacial domain into the simulated water domain. The group have used molecular dynamics simulation methods to make other equally important connections between ion valence and LPS lipid properties [246-247]. The group has additionally produced molecular dynamics simulation forcefields and analysis tools that help users to produce and analyze LPS lipid molecular dynamics simulations; for example, see [248-252].

Significantly more simulations were conducted to assess the interactions of antimicrobial agents with Gram-negative bacterial membrane mimetics. The field of antimicrobial agent based molecular dynamics simulations is vast and it should be appreciated that the following publications, and the publications that are listed in sections 1.7 and 1.8, constitute just a small fraction of all the simulation studies that were conducted to understand some aspect of antimicrobial interactions through the use of molecular dynamics simulation forcefields. The coarse-grained Martini forcefield was used to study the interactions of the antimicrobial peptide (AMP) Chrysophsin-3 (chrys-3) [253-255] with different phospholipid bilayers, including an inner Gram-negative (*E. coli*) bacterial membrane mimetic that contained POPE and POPG lipids [255]. It was found that the chrys-3 molecules aggregated at the lipid membrane surface and that this process induced the formation of large lipid protrusions. The protrusions could be considered micellization intermediates since the deformation would lower barriers for micellization processes and membrane rupture processes [256-259]. The simulations were corroborated by experimental data that suggested that chrysophsin molecules primarily disrupted membranes through pore formation processes [260-264]. It was also found the chrys-3 molecules had preferential interactions for the negatively charged PG lipids within the two-component Gram-negative inner membrane mimetics and it was hypothesized that

electrostatic interactions could play an important role in the antimicrobial action of the cationic chrys-3 peptide. This hypothesis was corroborated by comparable Martini forcefield simulations that explored the interactions of different types of cationic AMPs with different models for the inner membrane of Gram-negative bacteria. Take for example, the coarse-grained simulations that sought to clarify the interactions of α-helical Latarcin AMPs [265-269] with the inner membrane of Gram-negative bacteria [270, 271]. The Gram-negative bacterial inner membrane mimetic was arranged with PE and PG lipids an approximate 7:3 number ratio to make it comparable with realistic bacterial membrane systems [272-274]. The α -helical AMPs preferentially interacted with the anionic PG lipids despite the significant surplus of neutrally charged PE lipids. It was similarly noted in experimental studies that the Latarcin AMPs could induce membrane reorganization within plasma membrane mimetics [275], that the Latarcin AMPs have preferential interactions for anionic liposomes [276] and that the Latarcin AMPs can induce membrane damage when they interact with host membrane lipids [277-280]. The coarse-grained molecular dynamics simulations of the chrys-3 and Latarcin AMPs corroborate data from chapter 3 where it is shown that polymyxin molecules have preferential interactions for anionic lipids and that these preferential interactions can induce lipid segregation, anionic domain registration about the membrane midplane, and bilayer thinning processes.

Grossfield et al. performed comparable coarse-grained [281-282] and atomistic [283] molecular dynamics simulations but this time the group explored the interactions of the C16-KGGK cationic peptides [284-285] with Gram-negative inner membrane mimetics that contained POPE and POPG lipids in a 2:1 number ratio. Here again it was shown that the cationic AMPs had preferential interactions with the anionic PG lipids despite their relatively low concentration within the multicomponent bacterial membrane mimetics. Over the course of a 1 μs simulation it was found that the C16-KGGK molecules had approximately twice as many interactions with the negatively charged PG lipids compared with the neutrally charged PE lipids. Unusually, the simulations also found that the C16-KGGK molecules formed a large

multicomponent cluster before interacting with the Gram-negative inner bacterial membrane model and also, that this cluster induced crystalline packing of the PG lipid headgroups when it was interacting with the membrane surface. Higher resolution atomistic forcefield simulations were recently conducted by Poger et al. (2018) [286] and the results not only corroborate, but also add to, earlier simulations that demonstrated preferential interactions between cationic AMPs and anionic PG phospholipids. Through the application of molecular dynamics simulations, it was found that the preferential interactions between cationic AMPs (aurein 1.2) and negatively charged lipids can not only promote spontaneous positive curvature and bilayer buckling but also that cardiolipin lipids, which have intrinsic negative curvature, have the capacity to suppress spontaneous membrane curvature generation during membrane interactions with AMPs. This is particularly intriguing since it might also explain why high concentrations of cardiolipin lipids suppress the ability of Gram-positive bacterial membrane-active proteins (e.g. daptomycin) to lyse, disrupt, or porate bacterial membrane mimetics [287-291]. There have been several other supporting computational and experimental publications that have explored the membrane disrupting properties of aurein 1.2; for example, see [292-296].

Molecular dynamics simulations methods were applied just a few years ago to understand how antimicrobial Buckminsterfullerene (C_{60}) nanoparticles [297-299] interact with Gram-negative bacterial outer membrane mimetics [300-301]. The simulations revealed that the LPS core saccharide units tend to significantly impede the trajectories of the C_{60} nanoparticles and that the nanoparticles could only access the membrane core through bilayer surface areas that were concentrated in shorter LPS chemotypes or PE phospholipids. The C_{60} nanoparticles preferentially gravitated towards the interfacial membrane domains once they had penetrated the water-lipid interfacial domain, i.e. to areas that divided distinct PE and LPS lipid clusters, suggesting that the nanoparticles were line-active linactants [302-304] and that they have the capacity to affect interfacial line tension energies. Taken together,

the simulation studies are quite important since they corroborate simulation data from chapter 4. Within chapter 4 it is demonstrated that cationic polymyxin molecules have preferential interactions with negatively charged PG phospholipids and further that these preferential interactions can change the multicomponent membrane organization and structure. There is not only the aggregation of negatively charged PG lipids within one leaflet of the bilayer, there is also the association, registration, or alignment, of the PG lipid clusters about the membrane midplane.

Gumburt et al. are also well-known for conducting molecular dynamics simulations to analyze the biophysical properties of the Gram-negative bacterial cell wall including the interactions between bacterial lipids and outer membrane proteins [305-308], the properties of peptidoglycan chains [309-310] and the properties of both the inner and outer Gram-negative bacterial membranes. Pioneering publications sought for example, to understand how the rod shape of Gram-negative bacteria is maintained during peptidoglycan remodelling [311]. The team developed ad hoc models for the constituent components of the Gram-negative bacterial cell wall to demonstrate how peptidoglycan remodelling enzymes, including transglycosylases, transpeptidases, and endopeptidases, are coordinated to remodel a sacculus several orders of magnitude larger than the enzymes themselves. The team found that top-down regulation of new peptidoglycan insertion sites was unnecessary, and that local coordination of peptidoglycan remodelling enzymes within discrete complexes was sufficient for maintaining the rod shape of the Gram-negative bacterial sacculus. In 2018 Gumburt et al. performed additional molecular dynamics simulations to assess how mechanical stress was distributed throughout the multicomponent *E. coli* cell envelope (Figure 5A) [312]. Molecular dynamics simulations were conducted to understand molecular level interactions within three domains of the Gram-negative cell envelope: (i) the inner membrane; (ii) the outer bacterial membrane; and (iii) the thin layer (or layers) of peptidoglycan that is wedged between them. The molecular dynamics simulation data was used to understand the mechanical properties

of each distinct domain of the Gram-negative bacterial cell envelope and comparisons were also made with complementary experimental data. The area compressibility modulus (K_A) [313-314] was used by Gumbart et al. to quantify the mechanical strength of each distinct domain of the Gram-negative bacterial cell envelope. There was close agreement between the calculated and experimentally resolved K_A values for the inner membrane models, but there were significant discrepancies between the calculated and experimentally resolved K_A values for the outer membrane models. The experimental analyses suggested that the inner membrane area compressibility had a magnitude of 238 mNm^{-1} and the molecular dynamics simulations suggested that the inner membrane area compressibility had a magnitude of 182 mNm^{-1}. The molecular dynamics simulations predicted a K_A value of 524 mNm^{-1} for the outer bacterial membrane model, whereas the experiments predicted a significantly lower magnitude of 233 mNm^{-1}. The addition or removal of integral membrane proteins was in general insignificant and the area compressibility magnitudes would be at most ~10% different between comparative simulation systems that included integral membrane proteins in one instance and excluded integral membrane proteins in another. The layer of peptidoglycan was more complex and it was found that K_A values varied substantially with the degree of peptidoglycan area expansion (Figure 4B-D). Compressibility magnitudes were negligible at low area expansions but they would rapidly exceed values of 200 mNm^{-1} when the expansion was 100%.

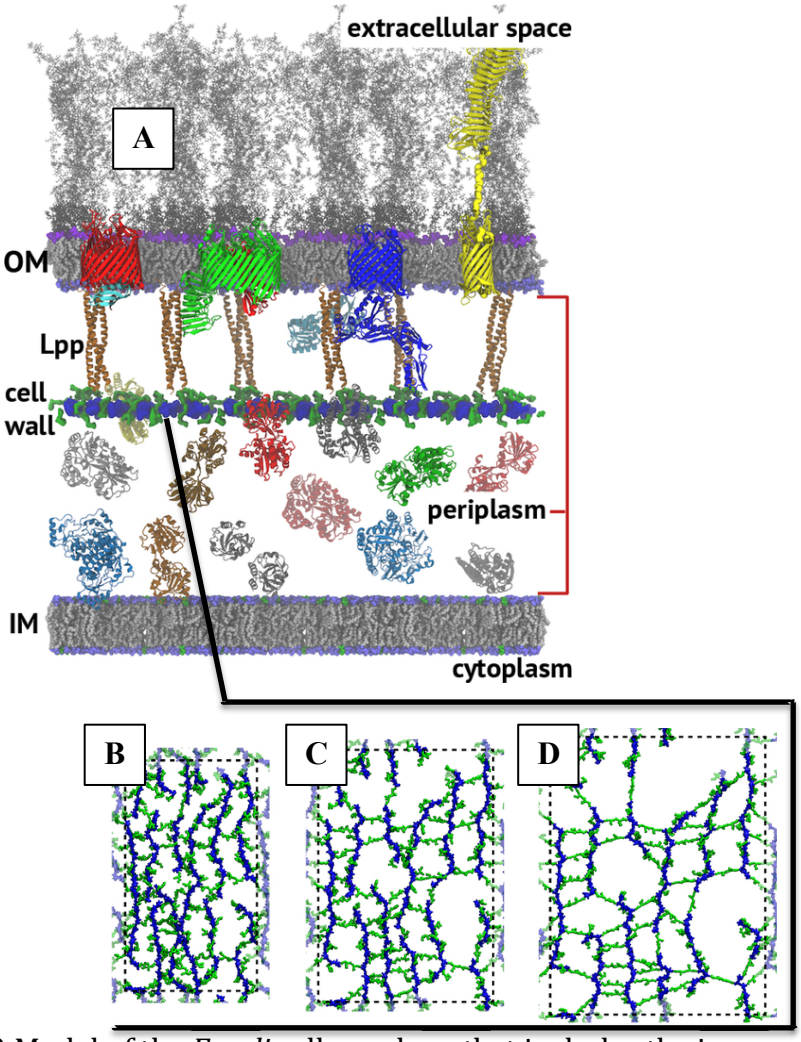

Figure 5. (A) Model of the *E. coli* cell envelope that includes the inner cytoplasmic membrane (IM), the outer membrane (OM), peptidoglycan (cell wall), Braun's lipoprotein (Lpp) and integral membrane proteins. The lipids are gray and the peptidoglycan is blue and green. The proteins have different color schemes to help readers to distinguish between them. (B-D) Representative states of the peptidoglycan cell wall composite when it is relaxed (B), stretched to 1.5x of its original area (C) and stretched to 2x its original area (D). The glycan strands are blue, the peptide cross-links are green and the borders of the simulation cell are represented as a thin dashed line. The image sources are: 10.106/j.bbamem.2018.09.020 (DOI) [312] and 10.1371/journal.pcbi.1003475 (DOI) [309].

Khalid et al. have conducted molecular dynamics simulations over the last couple of decades to understand various aspects of the Gram-negative cell envelope including interactions between lipids and outer membrane proteins [315-319], the interactions between peptidoglycan and outer membrane proteins [320-321], and the interactions between various components of the Gram-negative cell wall and AMPs and antimicrobial nanoparticles [301]. In

2019 the group used molecular dynamics simulation methods to understand how the *E. coli* inner membrane TolR protein interacts with periplasmic layers of peptidoglycan. It was demonstrated that TolR protein can bind the periplasmic peptidoglycan through electrostatic interactions when it transitions from an initially compressed conformation that is of one length, to an extended conformation that is approximately twice as long. The complementary interactions of the outer membrane OmpA proteins and the inner membrane TolR proteins with the periplasmic peptidoglycan can help to maintain the (peptidoglycan) cell wall structure [322]. The Khalid group have also conducted molecular dynamics simulations to understand how the TolC-AcrABZ efflux pump [323-324] simultaneously interacts with the inner and outer membranes of Gram-negative bacteria [325]. The mesoscale molecular dynamics simulations were conducted to understand how some of the largest efflux pumps can interact with the inner cytoplasmic membrane, the outer LPS membrane, and various integral membrane proteins all at the same time and also, how these interactions might affect the properties of the Gram-negative cell envelope. It was discovered that there was strong coupling between the trajectories of the proteins and lipids within the outer bacterial membrane but perhaps more interestingly, that the lipids were much less encumbered within the inner cytoplasmic membrane. It was additionally ascertained that the embedded membrane protein moieties affected the local membrane composition. Cardiolipin lipids were for example, significantly enriched within the vicinity of the multidrug efflux pump (AcrBZ) and also within the vicinity of the AqpZ water channels [326-327].

The Khalid group also used molecular dynamics simulation methods to understand how polymyxin molecules interact with both the inner and outer membranes of Gram-negative bacteria [328-329]. It was found that the outer membrane core saccharide sugars encumbered the antimicrobial polymyxin peptides and prevented them from passing through the phosphate group domain and into the hydrophobic bilayer interior or the “membrane core”. The outer membrane was not significantly disrupted and it was difficult to

extrapolate to obvious models for AMP-induced outer membrane breakdown processes. In stark contrast, it was found that the polymyxin molecules clearly affected the integrity of the inner membrane by reducing its transmembrane width. The polymyxin hydrophobic moieties entered into the bacterial membrane core as the polymyxin molecules adhered to the inner bacterial membrane mimetic surface and there was obvious correlation between the position of the attached polymyxin peptides and areas of membrane thinning. The localized reduction in membrane width and the associated increase in membrane permeability would inevitably affect bilayer stability on longer timescales [292,330-331]. It is quite interesting to note that Dupuy et al. showed, through the use of molecular dynamics simulations and X-ray and neutron scattering techniques, that colistin also contributes to the destabilization of the inner membrane of Gram-negative bacteria by affecting membrane parameters such as acyl tail order values and bilayer bending moduli [332]. These results are corroborated by molecular dynamics simulation data in chapter 4. We will see that polymyxin molecules tend to thin biological membranes in coarse-grained molecular dynamics simulations when they are simulated on long multimicrosecond timescales.

The Khalid group developed coarse-grained Martini LPS lipid models to overcome the limitations of computationally demanding atomistic resolution molecular dynamics simulation forcefields and more effectively bridge the gap between experimental and simulation spatiotemporal scales [151,301]. The LPS lipids were initially simulated with atomistic resolution molecular dynamics simulation forcefields and the resulting data were used to calibrate corresponding coarse-grained Martini forcefield parameter sets. The coarse-grained models were able to mimic the atomistic reference molecular dynamics simulation data remarkably accurately. The coarse-grained LPS area per lipid values were within 1-2% of the reference atomistic simulation values and the membrane thickness and acyl tail order parameters were within 10% and 0.2 of the target atomistic simulation data. The coarse-grained model was used to study the interactions of C_{60} nanoparticles with Gram-negative bacterial outer membrane mimetics and it was found that the

LPS lipid core saccharide domain was an effective barrier to the hydrophobic C_{60} nanoparticles. The C_{60} nanoparticles were unable to pass through the LPS core saccharide domain; however, the nanoparticles were able to enter into the bacterial membrane hydrophobic core through “bilayer defects” or in other words, membrane domains that were depleted of LPS lipid. The C_{60} nanoparticles could pass through areas of the bilayer surface that were depleted of LPS lipids and contained for example, small quantities of PE phospholipid. After the C_{60} nanoparticles had entered into the hydrophobic membrane core domain they acted as line-active linactants [333-334]and moved toward the interfacial membrane domains.

The coarse-grained models were subsequently integrated into the CHARMM-GUI Martini Maker module and have been used to generate LPS lipid micelles (Figure 6A-C), LPS lipid nanodiscs, LPS lipid membranes (Figure 4D), LPS OMVs (Figure 4E) etc. [151] The online Martini Maker module is used in the penultimate chapter of this thesis to generate both smooth and rough OMV simulation systems. The CHARMM-GUI Martini Maker module is also used in chapter 4 to create various Gram-negative bacterial membrane mimetics that contain different concentrations of smooth LPS lipids in the extracellular leaflet.

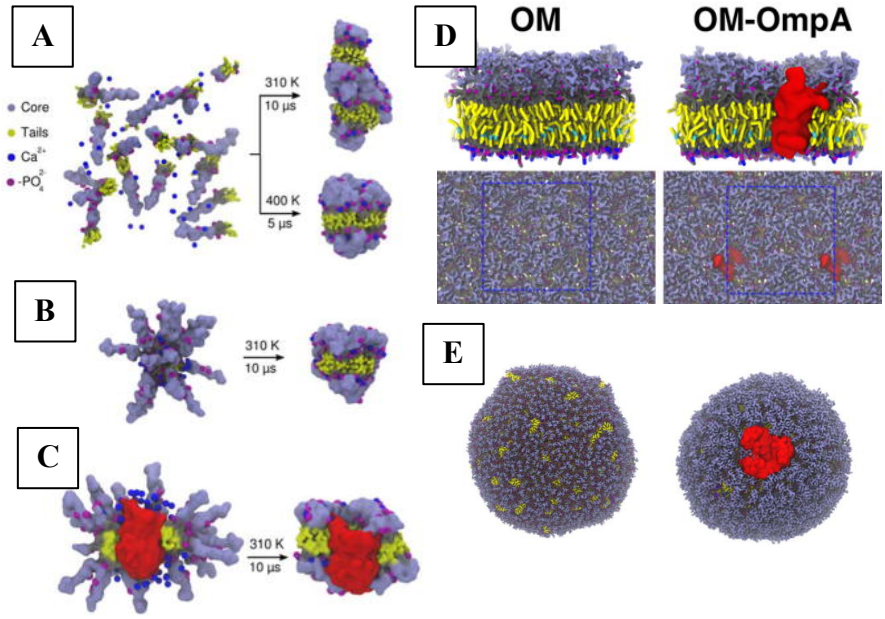

Figure 6. Implementation of the CHARMM-GUI Martini Maker module. (A) The initial random placement of 20 LPS lipids and the subsequent self-assembly of the lipids into a unilamellar or bilamellar bacterial membrane fragment. (B) The initial construction of an LPS micelle and the subsequent transformation of the micelle to become a unilamellar bacterial membrane. (C) The initial construction of an LPS micelle with embedded OmpF protein and the subsequent transformation of the micelle into a multicomponent unilamellar bacterial membrane. (D) The final frame snapshots of molecular dynamics simulations of asymmetric bacterial membrane models that were generated with the CHARMM-GUI Martini Maker. The bilayers contained only lipids (OM) or lipids and the OmpA integral membrane protein (OM-OmpA). (E) Snapshots of OMV simulation systems that contained only lipids or lipids and an embedded outer membrane protein. The systems were made with the CHARMM-GUI Martini Maker module. The proteins are red, the acyl tails are yellow, the core sugars are violet, the choline and phosphate groups are blue and purple and the unsaturated bonds are cyan. Image source: 10.1002/jcc.24895 (DOI) [151].

Let us now move away from Gram-negative outer membrane molecular dynamics simulations and consider how molecular dynamics simulations have been used to understand the formation of lipid raft-like structures. We can first consider pioneering coarse-grained simulations that explored the spontaneous formation of Lo and Ld domains in ternary membrane mixtures of cholesterol, saturated phospholipids and unsaturated phospholipids. Risselada and Marrink conducted molecular dynamics simulations in 2008 with the Martini coarse-grained forcefield to analyze the molecular level interactions that can induce the spontaneous formation of Lo and Ld

nanodomains within multicomponent plasma membrane mimetics [335]. It was found that uniformly distributed tripartite membranes progressively sequestered into two distinct nanodomains through stepwise self-associating lipid-lipid interactions (Figure 7A). The cholesterol molecules would predominantly co-couple with saturated phospholipids to progressively form raft-like assemblies and the unsaturated lipids would in turn, progressively form liquid-disordered (Ld) nanodomains (Figure 7B-C). It seemed that cholesterol's preference for saturated lipid chains drove phase segregation and the formation of raft-like assemblies that within these molecular simulations, were cut off by relatively diffuse borders. It was previously assumed that the Lo and Ld interface was rather sharply defined [336-338] but the coarse-grained Martini forcefield molecular simulations revealed that the boundaries were instead broad and dynamic. The work is corroborated by atomistic forcefield simulations that have assessed the biophysical properties of liquid-ordered nanodomains within multicomponent membranes [339-340]. The simulations were starting to demonstrate how molecular level interactions can induce phase segregation and the formation of lipid raft-like structures. More sophisticated phase diagrams were subsequently generated for binary lipid/cholesterol simulation systems as a function of simulation temperature using the coarse-grained Martini forcefield [341-342]. Carpenter et al. produced a ternary lipid phase diagram [343-344] that mimicked experimental phase diagrams [345] remarkably accurately, showing how molecular dynamics simulations can be used to understand how membrane phase behaviour is modulated. The formation of fluctuating lipid heterogeneities is being probed on unprecedented spatiotemporal scales and the resulting simulation data are being combined with results from experimental analysis techniques to produce a more comprehensive understanding of lipid raft structure and formation [346-348]. Indeed, the number of simulations that have explored the spontaneous production of liquid-ordered nanodomains is now quite significant and it has been found through molecular dynamics simulations, that phase segregation is affected by lipid saturation [349-353], hydrophobic mismatch [354], line-active linactants [355], lipid chain length [356], transmembrane peptides

[357-358], cholesterol flip-flop processes [359-360] lipid heterogeneity [361] and more.

Molecular simulations have also been used to understand how glycolipid co-coupling can induce the formation of raft-like nanodomains whose biophysical properties differ from the encompassing membrane environment. The Im group conducted all-atom molecular dynamics simulations to understand how different concentrations of (GM1) ganglioside molecules can affect the biophysical parameters of two-component lipid membrane systems (Figure 7D) [362]. The membranes contained three different concentrations GM1 lipids (10%, 20%, and 30%) and higher concentrations of POPC phospholipids (90%, 80%, and 70%). The all-atom molecular dynamics simulation data demonstrated that higher GM1 lipid concentrations can induce tighter lipid packing and at the same time, decrease energy barriers that would otherwise impede localized positive curvature generation. The ordered clusters segregated from the unordered membrane domain and formed a large percolated cluster when the GM1 concentration was high (i.e. 30%) and the simulation temperatures did not exceed a temperature of 330 K. Sansom et al. have demonstrated that positive curvature generation can be further enhanced when ganglioside molecules are simulated in multicomponent membranes that have multiple different types of lipid molecules (cholesterol, PIP_2, GM3 lipids etc.) [363]. When multicomponent membranes contain a diverse combination of both intrinsically positively and intrinsically negatively curved lipids, the intrinsically positively curved lipids can move to positively curved membrane domains and the intrinsically negatively curved lipids can move to negatively curved membrane domains and this process can lower local energies barriers that would otherwise impede spontaneous curvature generation and membrane reshaping processes [364]. Taken together, the molecular dynamics simulations are beginning to clarify why the outer rims of caveolae are highly concentrated in ganglioside lipids, whereas the central sections contain unusually high concentrations of cholesterol [365-367]. The self-association of ganglioside molecules tends to increase local preferences for

positive curvature generation and this phenomenon by itself causes plasma membranes to expand into the intracellular cytosol [368]. But the spontaneous production of a negatively curved inner plasma membrane domain is energetically unfavourable and consequently, the intrinsically negatively curved cholesterol molecules move into the expanding inner plasma membrane leaflet. These molecular level insights might help to explain why pathogens and pathogenic products have been found to enter into the host cell cytoplasmic space as they bind ganglioside lipid molecules and through this interaction, induce the aggregation of ganglioside molecules and the production of highly curved caveolae [368]. But this will be discussed in more depth in section 1.4.4 when glycolipids and ganglioside molecule properties are explained more thoroughly.

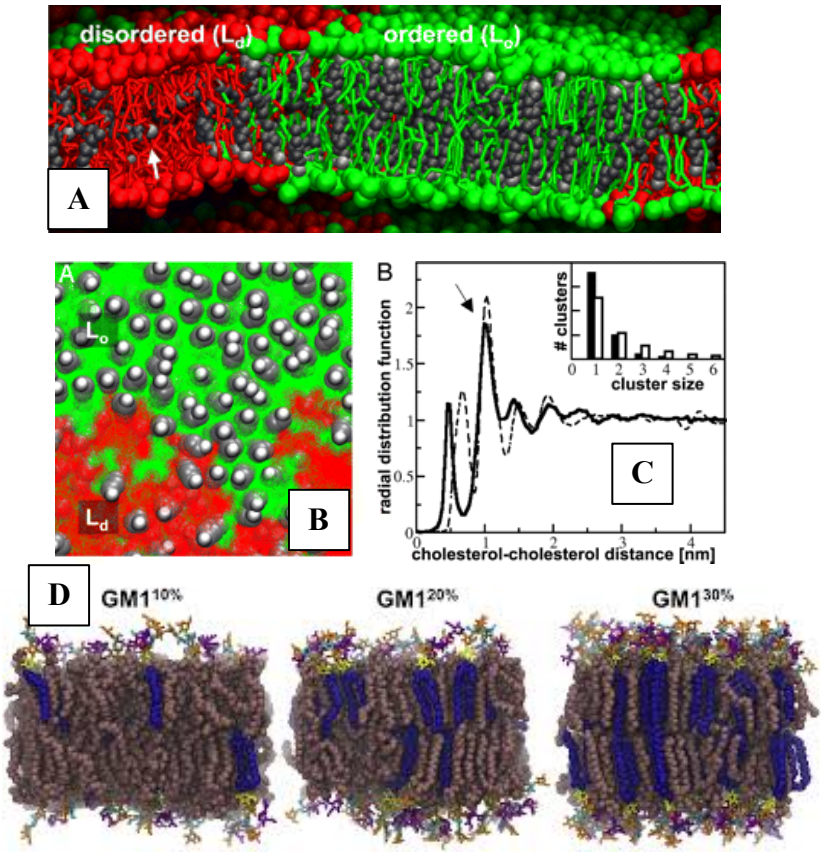

Figure 7. Understanding the properties of lipid rafts through the application of molecular dynamics simulations. (A) Formation of separate liquid-ordered (green) and liquid-disordered (red) nanodomains that are enriched in saturated lipids (green) and cholesterol (black), or polyunsaturated lipids (red). (B) Top view snapshots showing how the cholesterol molecules were distributed within the multicomponent membrane simulation system and the (C) radial distribution function for the cholesterol-cholesterol intermolecular separation distances. (D) Snapshots of GM1 ganglioside and

POPC lipids that were simulated in two-component membranes. The membrane became more rigid and raft-like as the concentration of the ganglioside molecules was increased from 10% through to 30%. The Image sources are: 10.1073/pnas.0807527105 (DOI) [335] and 10.1016/j.bpj.2016.09.021 (DOI) [362].

Perhaps it is even more impressive that molecular dynamics simulation forcefields were used to understand how lipids interact with integral membrane proteins and how these protein-lipid interactions can change the properties of the local membrane environment [369-371]. Understanding such elementary interactions is necessary for understanding how molecular self-association processes might take an otherwise homogeneous membrane toward a state of significant heterogeneity. The simulations were performed using either high-level atomistic forcefields, lower resolution coarse-grained forcefields, or even multiple different forcefields used one after another [372-373]. The protein-lipid simulations provided insights into previously poorly understood interactions e.g. reversible lipid-protein binding events that can occur on timescales of 10-100s of microseconds [114]. Arnarez et al. identified six protein binding sites for cardiolipin when it interacts with respiratory chain complex cytochrome bcl through the application of molecular dynamics simulation methods [374]. Other notable publications that have assessed protein-lipid interactions within biological membrane mimetics include simulation studies by Sansom et al.; for instance, simulations that identified the binding sites of PIP_2 molecules on the inwardly rectifying potassium (Kir) channels [375-376] and the binding sites of PIP_3 molecules on the pleckstrin homology domain [377].

Molecular dynamics simulation methods have also been used to understand how protein oligomerization processes can occur in model membranes [59,114]. Experimental analysis data was combined with computer simulation techniques to determine the organization of syntaxin clusters within plasma membrane mimetics [378] and show at the same time, how the oligomerization interactions are mediated by interactions between the PIP_2 lipids and the syntaxin protein surface. Periole et al. have similarly performed coarse-grained molecular dynamics simulations to show that G protein-

coupled receptors (GPCRs) [379] can cluster in model membranes and the group also showed that the localized adaptation of the membrane bilayer was most pronounced near transmembrane helices 2, 4, and 7. Comparable simulation studies were conducted to assess the properties and interactions of bacterial membrane proteins, i.e. the family of OMPs. In one instance, it was shown that OmpF proteins can self-associate and form oligomers that contain a few dozen membrane protein monomers [115]. In another instance it was shown that the combination of hydrophobic mismatch and curvature-based sorting might drive protein assembly in phospholipid vesicles [318]. Domanski et al. found that transmembrane WALP helical peptides can amplify non-ideal lipid mixing and Lo/Ld domain segregation processes [351]. The group simulated multicomponent plasma membrane mimetics that contained the following biomolecules: WALP peptides, saturated lipids, unsaturated lipids and cholesterol. The multicomponent membrane separated into distinct liquid-ordered and liquid-disordered nanodomains and interestingly, there was a high concentration of the transmembrane WALP helices within the liquid-disordered nanodomains. Ackerman and Feigenson similarly observed the growth of nanodomains around WALP transmembrane peptides [357] and further, that there is cross-correlation of the Lo/Ld nanodomains about the membrane midplane.

Newer generation molecular dynamics simulation forcefields are increasingly being used to investigate unprecedented spatiotemporal scales and obtain biomolecular level insights to explain previously poorly understood biological membrane phenomena. We have seen here how molecular dynamics simulation forcefields have been used to better understood fluctuating heterogeneities within biological membranes, the structure and characteristics of the Gram-negative bacterial cell envelope, specific protein-lipid interactions and the self-association of lipids and proteins. The same molecular dynamics simulation forcefields will be applied here throughout this work to understand previously unexplored biomolecular interactions between proteins, lipids, and lipid membranes and

thereby explain some long-standing uncertainties such as the different uptake rates of smooth and rough OMVs at host cell surfaces.

1.3 Main Aims of the Introduction

The primary focus of this thesis is OMVs and more precisely, how OMVs interact with eukaryotic plasma membrane models. Molecular dynamics simulation methods are used in this thesis to investigate the interactions of different types of OMVs with mammalian plasma membrane mimetics. The molecular dynamics simulations are conducted in order to determine the biophysical parameters of OMVs at host cell surfaces and to understand why some OMVs (i.e. smooth OMVs) pass through host cell membranes more effectively than others (i.e. rough OMVs) [52]. The OMVs contain three different types of lipid and the host cell mammalian membranes contain seven different types of lipid that are distributed asymmetrically about the membrane midplane. It is important that readers understand the chemical properties of each constitute membrane lipid and for this reason, each lipid will be mentioned in the forthcoming discussions. The chemical structure of each lipid type will be provided with an exploration of how the lipids have been simulated with different molecular dynamics simulation forcefields. For example, the structure of ganglioside molecules will be described in section 1.4.4 and there will also be a subsequent discussion of how ganglioside molecules have been simulated with molecular dynamics simulation forcefields [361-362]. Additional biomolecules (e.g. hopanoids) will be mentioned to provide a more thorough overview wherever it seems to be appropriate and beneficial for the readers of this thesis.

Chapters 3 and 4 focus on the interactions of Gram-negative bacterial membranes. The molecular dynamics simulation forcefields are applied to understand how lipid-lipid interactions can affect membrane mechanical strength parameters and also how bacterial membranes can interact with one of the simplest and most effective AMPs: polymyxin B1 (PMB1) [328,130]. It is therefore appropriate to discuss the structure of LPS lipids in section 1.4.5

and also to discuss how LPS lipid interactions have been investigated through the application of molecular dynamics simulation forcefields. Readers must be fully aware of the general compositional characteristics of LPS lipids and also which chemical moieties distinguish so-called “smooth” LPS lipid [242,315] variants from shorter forms of “rough” LPS lipids [233,241]. Other than this, it is necessary to discuss bacterial infections and multiple-drug resistant bacteria to explain why polymyxins are becoming increasingly necessary [147-150] for treating nosocomial infections and why they are being studied more and more with computational [180,329] and experimental analysis methods [144-145]. The precise chemical structure of the PMB1 peptide will be provided in section 1.8 and there will also be a detailed description of AMPs [187], the Gram staining process [95], the asymmetric structure of the Gram-negative cell envelope, and the asymmetric structure of both smooth and rough OMVs [20].

1.4 Lipids (Structure and Simulations)

1.4.1 Phospholipids

Phospholipids have a relatively simple structure; they contain hydrophobic acyl chains that are covalently bonded to a hydrophilic domain of a glycerol or sphingoid base and variable terminal chemical moieties [380-381]. Phosphatidylcholine (PC) is an example of a phospholipid that comprises the majority of plant [382-383] and animal membranes and the lipid contains two hydrocarbon acyl chains that are covalently bonded via an ester linkage to glycerol, a negatively charged phosphate group, and a terminal positively charged choline section (Figure 8A). The composition of the molecule makes it zwitterionic at physiological pH and it also confers an overall neutral electrostatic charge. The intracellular leaflet of mammalian plasma membranes additionally contains a moderate amount of the phosphatidylserine (PS) lipid [384-386], which is structurally similar to PC lipid but rather than there being a terminal positively charged choline section, there is a terminal serine moiety instead (Figure 8B) [387].

Bacterial membranes are particularly abundant in the phosphatidylethanolamine (PE) lipid molecule that contains two acyl chains covalently bonded through an ester linkage to central glycerol and phosphate groups and a terminal ethanolamine moiety (Figure 8C) [388-389]. The lipid has zwitterionic chemical characteristics and neutral electrostatic charge at physiological pH but the presence of the terminal ethanolamine group affects the physical properties of the molecule such that PC and PE lipids have different lateral diffusion constants, intramolecular motion parameters, bilayer packing properties, preferred bilayer orientation angles and different elasticity moduli [390].

Phospholipids have an overall positive or negative electrostatic charge when the phospholipid headgroups are terminated with neutrally charged chemical compounds. The phosphatidylglycerol (PG) lipid is a minor component of plant [391-392], animal [393] and bacterial membranes [394] and is similar to PE in terms of structure and physical parameters but the presence of a terminal glycerol group gives the lipid an overall negative electrostatic charge (Figure 8D). The dimeric cardiolipin (CL) molecule contains two PG molecules connected through a central glycerol backbone and two-fold net negative charge (at physiological pH). Cardiolipin molecules [395] have an unusual headgroup-to-acyl-chain cross-sectional area ratio and unusual biophysical interactions within biological membrane mimetics such as preferential interactions with Gram-negative integral membrane proteins [374,396] and the capacity to suppress spontaneous membrane curvature generation [286].

It is important to state here that PC, PS, PE, and PG phospholipids can be bonded to different combinations of acyl chain moieties [397]. The phospholipid headgroups can be bonded to acyl chains that differ in terms of saturation/unsaturation and the number of constituent carbon atoms. POPC, POPS, POPE and POPG phospholipids are usually used in molecular dynamics simulations to better understand biological membrane mimetics

[59,114,370,]. The molecules contain one saturated acyl chain and one monounsaturated acyl chain, i.e. the 16:0/18:1 acyl chain bonding scheme. The POPC, POPS, POPE, and POPG molecules are used throughout this thesis to mimic realistic eukaryotic and bacterial membranes, but it is important to appreciate that even minor modifications of the acyl chain structure can affect the biophysical parameters of lipid membrane bilayers [59]. It was recently even proposed that *E. coli* bacteria can survive the acidic conditions of the human stomach and subsequently multiple within the less acidic human colon when *fab*A and *fab*B genes instigate a cascade of reactions that merely alters the degree of Gram-negative membrane phospholipid acyl chain saturation [398].

Phospholipids were some of the first lipids to be simulated with molecular dynamics simulation forcefields and they have since become a staple of both atomistic and coarse-grained molecular dynamics simulations [174,182]. The phospholipids are combined to create simple biological membrane mimetics and these membrane models are simulated with AMPs [187], nanomaterials [399-401], integral and peripheral membrane proteins [369-371], dendrimers [402-403], carbohydrates [404-405], alcohols [406], capsaicin [407], and more. The simulated phospholipid bilayers are used as simplistic substitutes for realistic biological membranes and the molecular dynamics simulation forcefields are applied to understand how these multicomponent phospholipid membranes interact with different organic and nonorganic molecules on a range of distinct spatiotemporal scales. It is assumed that the simulations provide realistic and accurate data since the molecular dynamics simulation forcefields have been successively reparametrized over the course of several decades to accurately reproduce the experimentally determined properties of lipid membranes and at the same time, they have been refined to mimic higher level reference simulation data, i.e. *ab initio* quantum chemical calculations [163,167]. The additive all-atom CHARMM lipid forcefield [408] was for example, modified to more accurately reproduce the properties of different phospholipid bilayers including POPC and POPE lipid membranes. The area per lipid values of the simulated phospholipid

membranes matched reference PC and PE lipid surface area data on average to within 2% [409-413] and the density profiles matched reference data from neutron and X-ray diffraction experiments [414-417]. The acyl tail order parameters also provided proper splitting of the S_{CD} for the aliphatic carbon adjacent to the carbonyl for POPE and POPC bilayer membranes [409,418].

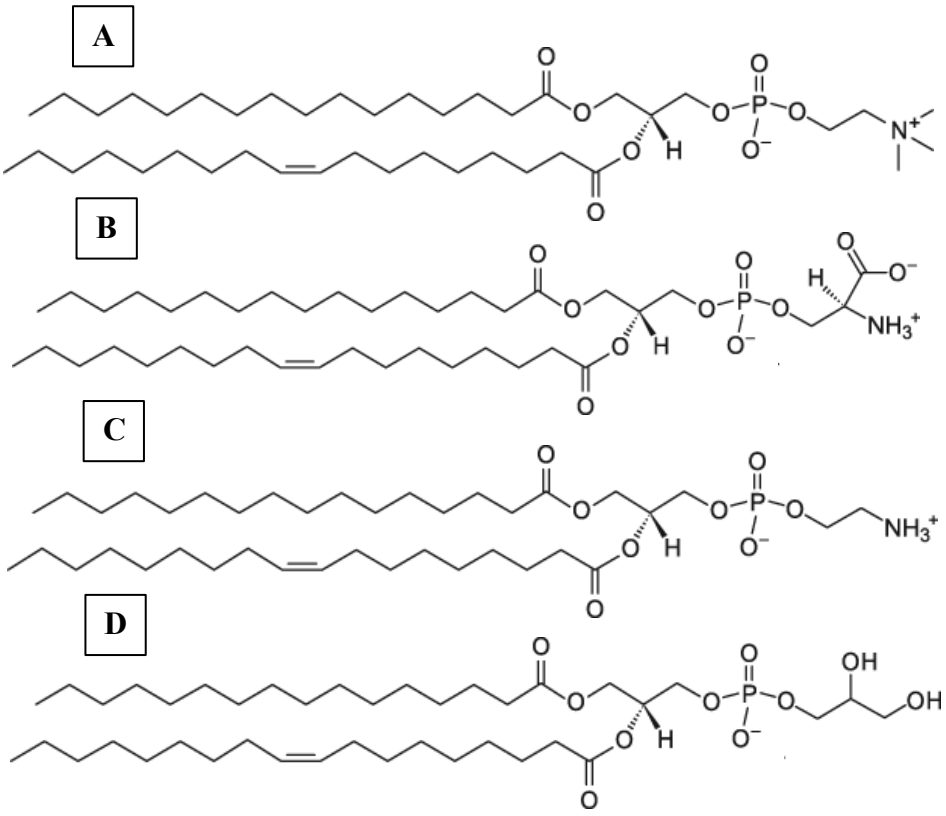

Figure 8. The structure of four phospholipids. (A) The structure of a phosphatidylcholine lipid (16:0/18:1(9Z)) that consists of two acyl tails bonded via an ester linkage to glycerol, a negatively charged phosphate group and a terminal positively charged choline section. (B) The structure of phosphatidylserine lipid (16:0/18:1(9Z)) that consists of two acyl chains bonded via an ester linkage to glycerol, a negatively charged phosphate group and a terminal serine moiety. (C) The structure of a phosphatidylethanolamine lipid (16:0/18:1(9Z)) that consists of two acyl chains covalently bonded through an ester link to central glycerol and phosphate groups, and a terminal ethanolamine section. (D) The structure of a phosphatidylglycerol lipid (16:0/18:1(9Z)) that consists of two acyl tails bonded via an ester linkage to glycerol, a negatively charged phosphate group and a terminal glycerol group. Image source: https://avantilipids.com

1.4.2 Sterols

Sterols are essential for the basic functioning of eukaryotic and prokaryotic cells and the eukaryotic and prokaryotic cellular membranes [14,419]. Cholesterol molecules are an important modulator of eukaryotic mammalian membrane fluidity [420] and ergosterol and hopanoid molecules tightly regulate the mechanical properties of fungal and bacterial membranes [421-422]. Sterol molecules contain a single short hydrocarbon chain and variable functional groups that are both bonded to a relatively rigid central body of pentagonal and hexagonal hydrocarbon rings [423-425]. The combination of multiple adjoining pentagonal and hexagonal hydrocarbon rings confers unusual biophysical parameters and biophysical properties (Figure 9A) [420]. It is now well-known that cholesterol lipids can order multicomponent membrane domains and also that cholesterol lipids regulate the formation of fluctuating lipid heterogeneities and lipid raft structures [73,83,88]. Cholesterol molecules induce the formation of lipid rafts through co-coupling intermolecular interactions with sphingolipids, saturated lipids and integral membrane proteins. The cholesterol molecules have an unusual shape that confers the molecule space-filling properties and the propensity to co-couple with intrinsically positively curved glycosphingolipids [426-427]. It seems important to define intrinsic curvature here since it is not only important for understanding the properties of cholesterol but also for understanding how OMVs induce membrane curvature generation in chapter 5. The intrinsic positive curvature magnitude of a molecule defines its propensity forming positively curved membrane domains [428-429] and is calculated as the lipid-headgroup-to-acyl-chain moiety cross-sectional area ratio (Figure 9B). Cholesterol has a lipid-headgroup-to-acyl-chain cross-sectional area ratio that is smaller than unity (one) and consequently it usually energetically preferable for cholesterol molecules to move into negatively curved multicomponent membrane domains. The morphology of the sterol not only promotes its movement to negatively curved membrane domains but also promotes its interactions with lipids that have complementary large headgroup-to-hydrophobic-moiety area ratios [364,430].

Cholesterol has been repeatedly simulated within biological membrane mimetics using a wide range of different atomistic and coarse-grained molecular dynamics simulation forcefields [431-435]. It has been found for example, that the interactions between cholesterol and saturated lipids can promote the formation of Lo membrane domains within tripartite plasma membrane mimetics [335]. It was also found that cholesterol molecules can flip about the membrane midplane on nanosecond timescales that are readily probed with low resolution coarse-grained molecular dynamics simulation forcefields [359,436] and even with the significantly more computationally demanding suite of high-level atomistic resolution simulation forcefields (Figure 9C) [437-438,360]. This not only corroborates results from experimental studies and validates molecular dynamics simulation studies of biological membranes, but also provides much needed molecular level insights that are otherwise inaccessible given the spatiotemporal constraints of conventional experimental analytical techniques. The molecular dynamics simulations have revealed that the compositional characteristics of multicomponent membranes affects the frequency of the cholesterol lipid flip-flop events and also the explicit chemical energy profiles that either impede or promote the movement of cholesterol molecules from one membrane leaflet to the other [360,437]. The coarse-grained molecular dynamics simulations have also demonstrated that cholesterol molecules have important roles in regulating the registration of Lo and Ld domains about the membrane midplane [359]. When cholesterol lipids freely flip about the membrane midplane they can promote the registration of liquid-ordered (Lo) and liquid-disordered (Ld) membrane domains about the membrane midplane.

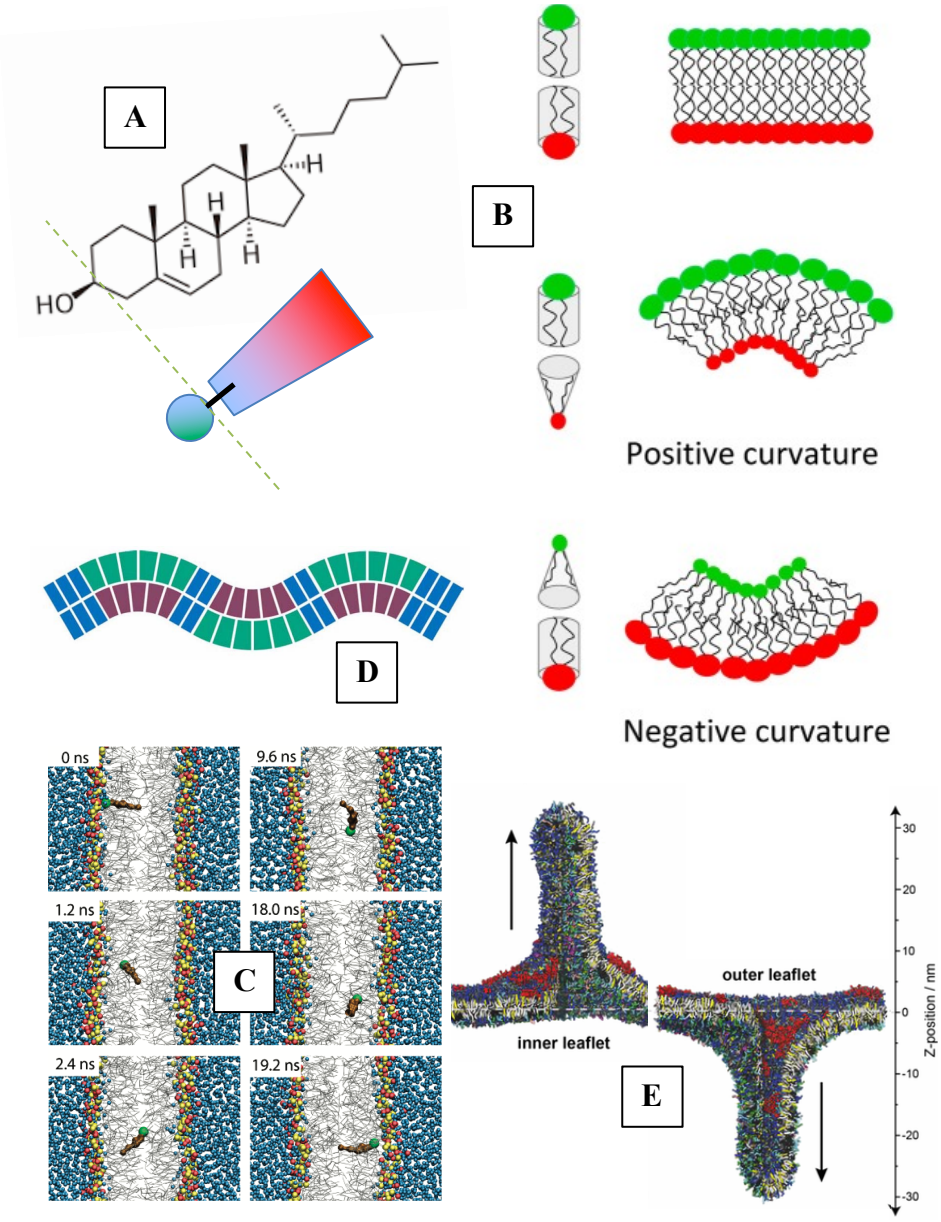

Figure 9. The properties and molecular dynamics simulations of cholesterol. (A) The chemical composition of cholesterol molecules and a simplified schematic illustration showing how the polar-headgroup-to-hydrophobic-body cross sectional area ratio gives cholesterol an effective conical structure. (B) Schematic illustrations showing how lipid shape, defined by the hydrophilic-headgroup-to-hydrophobic-lipid-component, is expected to affect preferences for spontaneous curvature generation. (C) Molecular dynamics simulations that show how cholesterol molecules can regulate membrane curvature and the membrane stress distribution by flipping between the apposed membrane leaflets on a nanosecond timescale. (D) Schematic illustration showing how lipid sorting can be induced by membrane curvature, but also how induced lipid sorting can affect local preferences for spontaneous membrane curvature generation. (E) Plasma membrane molecular dynamics simulations that demonstrated curvature-induced cholesterol molecule sorting. The cholesterol molecules moved to

negatively curved membrane domains during production time. The image sources are: Wikipedia Commons, 10.3389/fmicb.2014.00220 (DOI) (439) 10.1021/ja903529f (DOI) [437]
10.1146/annurev.cellbio.20.010403.095451 (DOI) [440]
10.1002/adts.201800034 (DOI) [364].

The molecular dynamics simulations of cholesterol molecules have also helped to validate curvature-induced lipid sorting models that stated, but had not proved outright, that lipid-lipid interactions are governed by the shape, or intrinsic positive curvature, of lipids in multicomponent membranes (Figure 9D) [440,364]. Cholesterol molecules have an intrinsic spontaneous negative curvature, i.e. a small headgroup-to-acyl-chain cross-sectional area ratio, and it has been found that cholesterol molecules preferentially move into the negatively curved domains of simulated multicomponent membranes. Cholesterol molecules were found for example, to move into the negatively curved domains of mesoscopic (~30 nm) plasma membrane mimetic tethers (Figure 9E) [430, 364]. These simulations are interesting not only because they help to validate long-standing hypothesis relating to spontaneous curvature generation in multicomponent membranes, but also because they help us to understand the results from chapter 5. Within chapter 5 it is found that cholesterol molecules preferentially move into the expanding inner leaflet of plasma membrane mimetics as the membrane bulges into the intracellular space and creates negatively curved membrane space. The movement of cholesterol molecules into negatively curved membrane domains has already been observed in coarse-grained molecular dynamics simulations and it is therefore easier to understand, through comparison, why we see cholesterol molecules move from one region of the simulated plasma membrane mimetics into another when they interact with the simulated OMVs.

It is interesting to draw comparisons with ergosterol and the different types of hopanoid molecules since the comparisons corroborate inferences made about cholesterol's space-filling properties and its tendency to increase the order and rigidity of localized multicomponent membrane domains. The ergosterol and cholesterol molecules have similar chemical structures; each

sterol contains four rigid pentagonal or hexagonal rings that are bonded to a short hydrocarbon acyl chain and terminal hydroxyl moiety [441-443]. The hopanoid molecules are natural pentacyclic compounds that are structurally comparable to the hopane triterpene compound (Figure 10A) but they additionally contain variable moieties that are bonded to the central body of the pentagonal and hexagonal hydrocarbon rings [444-445].

Sáenz et al. studied the properties of the simplest naturally occurring bacterial hopanoid, i.e. diplopterol, to understand how hopanoids affect the biophysical parameters of multicomponent bacterial membranes [446]. The diplopterol molecule is comprised of one pentagonal and four hexagonal hydrocarbon rings with terminal hydroxy group; it is found in prokaryotic membranes where it can co-couple with the Lipid A anchoring domain of LPS macromolecules [447-449]. The group demonstrated that diplopterol had the capacity to order saturated lipid tails and form a liquid-ordered (Lo) phase within multicomponent biological membrane mimetics. Sáenz et al. would later demonstrate that hopanoid molecules do not only promote the formation of liquid-ordered domains within multicomponent bacterial outer membrane models but also that these hopanoid molecules can affect multidrug transport processes [450]. The scientific research groups have shown that hopanoids can pair with glycolipids that have large headgroup-to-acyl-chain cross-sectional area ratios and that these progressive co-coupling interactions can generate highly ordered multicomponent membrane domains in a manner that is analogous to the co-coupling of sterols and glycosphingolipids within the mammalian eukaryotic plasma membrane.

There have been few (if any) molecular dynamics simulations that been conducted to understand the properties of hopanoids in realistic prokaryotic membrane mimetics that contain some combination of LPS lipids, phospholipids and integral membrane proteins, but molecular dynamics methods have been applied in the past to understand the properties of hopanoids within highly simplified bacterial membrane systems that contain

no more than two different types of organic molecules. Marrink et al. published an interesting publication in 2015 that expanded the coarse-grained Martini forcefield simulation library and provided theoreticians with coarse-grained Martini parameter sets for different sterols such as ergosterol [451]. The group provided coarse-grained parameter sets for different hopanoid molecules including hopane [452-454], diploptene (Figure 10B), and bacteriohopanetetrol (Figure 10C) [455] and additionally investigated the interactions of these coarse-grained models in simulated phospholipid membranes. The coarse-grained molecular dynamics simulations demonstrated that each type of hopanoid molecule preferentially adopts a unique arrangement along the membrane normal axis and therefore that each molecule has a unique partial mass density profile for the membrane normal axis. The hopane and diploptene molecules preferentially moved toward the hydrophobic membrane midplane, whereas the bacteriohopanetetrol molecules moved closer to the water-lipid interfacial domain that was formed of the hydrophilic POPC lipid headgroups (Figure 10D). The results are corroborated by earlier atomistic molecular dynamics simulations that sought to understand the relative effects of sterols and hopanoids on multicomponent lipid membranes. Poger et al. demonstrated that diploptene molecules preferentially partitioned between two hydrophobic membrane leaflets, close to the membrane midplane, and also that bacteriohopanetetrol molecules were aligned with the acyl chains and were preferentially situated closer to the hydrophilic headgroup domain [456].

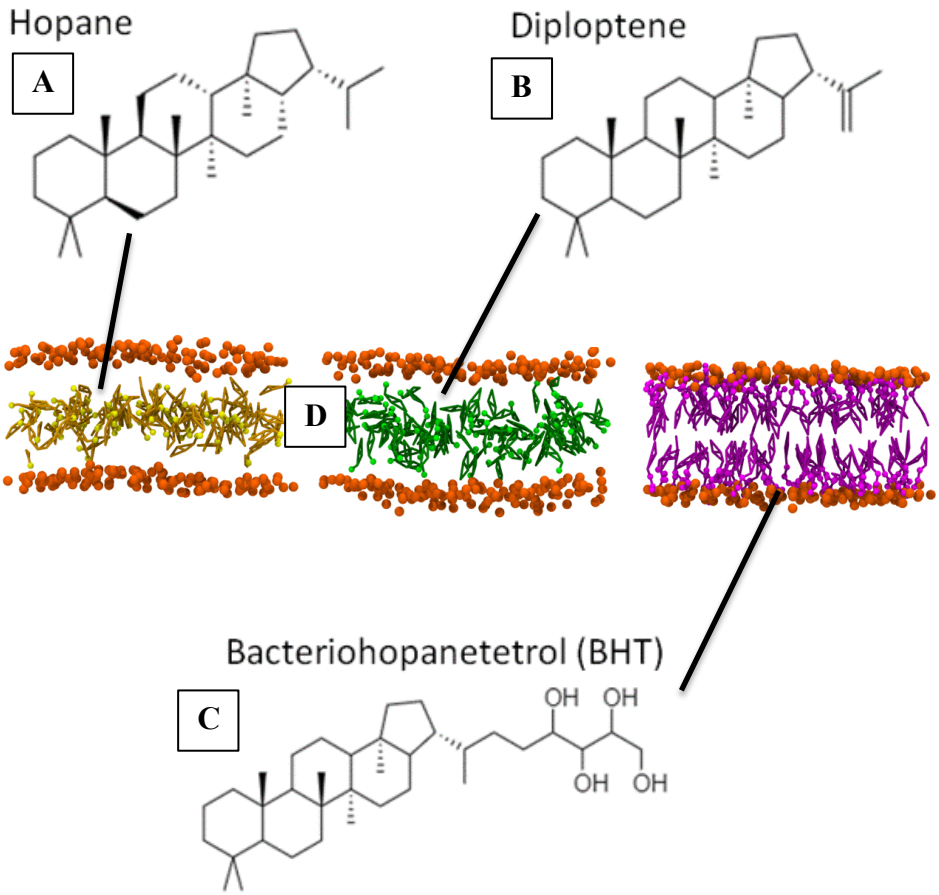

Figure 10. The structure and molecular dynamics simulations of hopanoids. (A-C) The structure of three hopanoids: hopane (A), diploptene (B), and bacteriopanetetrol (C). (D) Martini coarse-grained molecular dynamics simulations of multicomponent membranes that included either hopane (yellow), diploptene (green), or bacteriohopanetetrol (purple) with POPC lipids. The POPC phosphate headgroups are orange to show the position of the membrane-water interface. The image sources are: Wikipedia Commons and 10.1063/1.4937783 (DOI) [451].

1.4.3 PIP_2

Phospahtidylinositol (4,5)-bisphosphate (PIP_2) represents less than 1% of all membrane phospholipids [457] but nonetheless, the molecule modulates the function of several important integral membrane proteins [458-460], directs major independent signalling cascades [461-462] and affects the efficacy of endocytosis and exocytosis processes within cellular membranes [463-466]. PIP_2 is a phosphatidylinositol bisphosphate that consists of a phosphatidic acidic backbone linked via the phosphate group to a bisphosphorylated inositol (hexahydroxycyclohexane). Phosphatidylinositol bisphosphates are

generated as different kinases phosphorylate simpler phosphatidylinositol molecules [467]. The kinases add phosphate moieties onto positions 4 or 5 of the inositol ring, although position 3 can additionally be phosphorylated. Phosphatidylinositol bisphosphates can contain different combinations of fatty acid moieties at the C-1 and C-2 positions that vary in terms of length and the degree of saturation [468-469]. Here, the PIP_2 lipid is depicted with one of its acyl chains being saturated and another being unsaturated (Figure 11A).

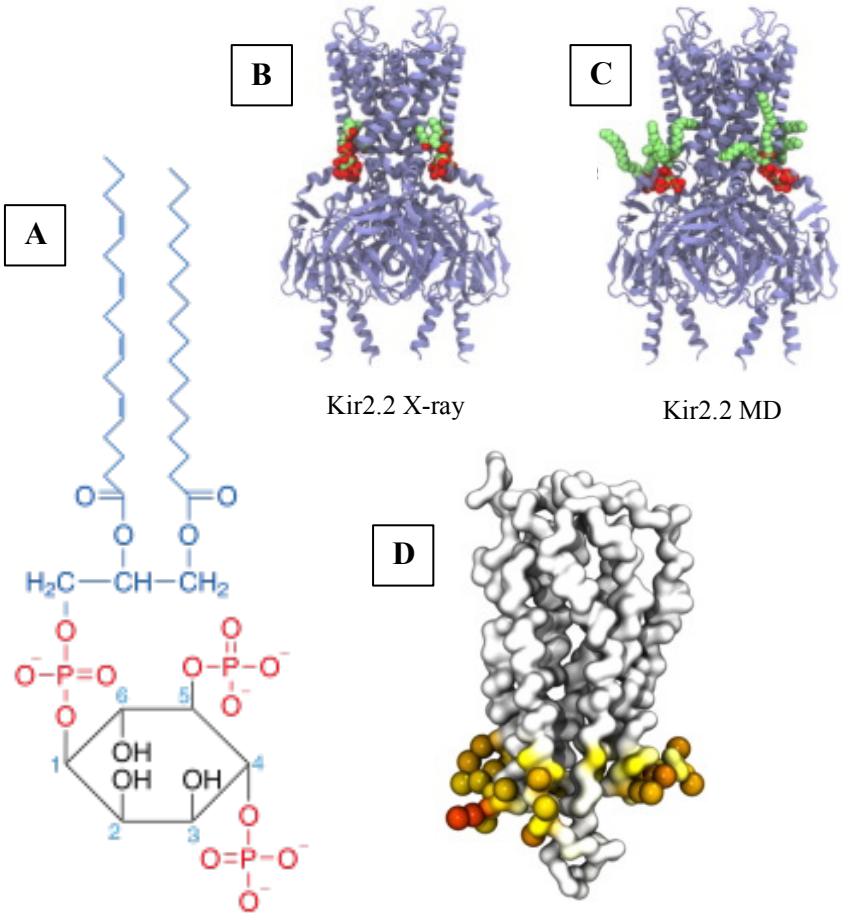

Figure 11. The structure of PIP_2 molecules and the interaction of PIP_2 molecules with integral membrane proteins. (A) The skeletal structure of the PIP_2 lipid that includes the phosphate groups (red), the inositol ring and the anchoring saturated and unsaturated acyl chains (blue). (B-C) The binding positions of PIP_2 lipids on Kir2.2 channel proteins that were identified from X-ray crystallography (B) and molecular dynamics (MD) simulation studies (C). The PIP_2 lipids are represented as green and red spheres and the protein residues are represented as violet chains. (D) The S1P1 GPCR molecule that has been colored according to its interactions with the PIP_2 phosphoryl headgroup in coarse-grained molecular dynamics simulations. The interaction number color bar ranges from white through to red. The image sources are: Wikipedia Commons, 10.1038/nature10370

(DOI) 10.1021/bi301350s (DOI) [470] and 10.1021/jacs.5b08048 (DOI) [76].

It is interesting to note that the inwardly rectifying potassium channels are gated by the interaction of their cytoplasmic region with PIP_2 lipids [471-475]. Inwardly rectifying potassium channels can constitute several hundreds of amino acid residues and one would not expect that they are activated by the much smaller PIP_2 lipids. Nonetheless, it is now quite clear that PIP_2 molecules can regulate ion channel activity when they interact with the cytoplasmic domain of the inwardly rectifying potassium channel (Figure 11B-C) and that PIP_2 lipids are an important cofactor for ion channel activity [458-460]. It has also been demonstrated that PIP_2 molecules can stabilize the active states of Class A GPCRs through direct bonding [475-477]. The PIP_2 lipids also recruit the G-protein-coupled kinase 2 enzyme to the plasma membrane by binding its large lobe [478] and that the molecule can also regulate the organization of filamentous actin (F-actin) when it interacts with regulatory proteins [479].

Emberhard et al. demonstrated that the phosphoinositides affected the rates of endocytosis and exocytosis processes when they applied phosphoinositide-specific phospholipase C into digitonin-permeabilized chromaffin cells and found that as this process decreased phosphoinositide levels, it inhibited calcium-triggered exocytosis processes [480]. Later studies would then be devised to identify the specific proteins, e.g. phosphatidylinositol transfer protein, that promoted the PIP_2 mediated endocytosis and exocytosis processes [481-482]. The authors demonstrated that PIP_2 specific antibodies had the capacity to strongly inhibit exocytosis processes and these experiments provided indisputable evidence that PIP_2 lipids can affect large dense core vesicle exocytosis processes.

It should not be too surprising that PIP_2 molecules have been simulated with both atomistic and coarse-grained resolution molecular dynamics simulation forcefields. The molecules have putative roles in modulating the function of integral membrane proteins and the PIP_2 molecules are also known to

facilitate endocytosis and exocytosis processes within host cell surfaces. Molecular dynamic simulation forcefields could be used by scientists to understand the molecular level interactions that drive these interesting and important macroscopic cellular functions. Molecular dynamics simulations were conducted via CHARMM with the C27r all-atom potential energy set to explore the biophysical properties of PIP_2 molecules when they were in POPC lipid bilayer membranes [483-408]. It was discovered that the position of the simulated PIP_2 ring phosphate groups were above the plane of the encompassing POPC lipid nitrogen atoms (~40° from the membrane normal) and this result was particularly interesting since it contested some earlier neutron diffraction experiments that were conducted to determine the orientation of inositol lipid headgroups in biological membrane mimetics [484-485]. The apparent mismatch between PIP_2 lipid conformations in experimental and computational publications would be a point of contention in ensuing publications.

Later works (2013) used a combination of quantum and all-atom molecular dynamics simulations to understand the orientation of the inositol ring and it was found that the PIP_2 lipid headgroup and anchoring acyl chains were approximately perpendicular to each other, indicating that the inositol ring should lie flat along the membrane surface if there were no other extraneous biomolecular interactions affecting the lipid headgroup orientation [486]. Interestingly, these atomistic molecular dynamics simulations additionally demonstrated that ion interactions can affect lipid headgroup behaviour and they also revealed how calcium ions can induce the formation of PIP_2 lipid clusters. Still, other molecular dynamics simulation groups were reporting that the inositol headgroup was oriented ~45° from the membrane normal in atomistic molecular dynamics simulations and further, that the PIP_2 lipids had complex interactions with encompassing pools of lipids and that the PIP_2 lipids could even affect the orientation of adjacent lipid headgroups [487]. PIP_2 molecules have since been simulated with membrane proteins in more complex multicomponent biological membrane mimetics [488-491] but it still seems to be challenging to accurately reproduce the conformational

characteristics of PIP_2 lipids with the computationally demanding and sophisticated suite of atomistic molecular dynamics simulation forcefields.

Phosphoinositides (PIP) molecules have been added to lower-level coarse-grained molecular dynamics simulation forcefields even though it can be challenging to accurately imitate the orientation and dynamics of realistic PIP_2 molecules with higher-level atomistic molecular dynamics simulation forcefields. PIP lipid models have been calibrated to replicate reference (target) atomistic simulation data and once acceptable predictions of this reference data was reproduced, the calibrated coarse-grained models were used to simulate more complex lipid-lipid and lipid-protein interactions within multicomponent plasma membrane models (Figure 11D) [492-496]. Martini coarse-grained simulations have been conducted to understand the spontaneous formation of PIP nanodomains [363-364, 497-498] and also how PIP molecules bind different integral membrane proteins including GPCR [475,499] and inwardly rectifying potassium channels [500-501] on unprecedented spatiotemporal scales. The coarse-grained simulations are generally corroborated by comparative molecular dynamics simulations that are conducted with atomistic resolution forcefields. There are similar patterns of PIP_2 lipid binding in comparative atomistic and coarse-grained resolution molecular dynamics simulations [369,470,376].

1.4.4 Glycolipids

Glycolipids have important roles in regulating cellular recognition, cellular adhesion and preserving the stable membrane bilayer structure [430,502-507]. The essential feature of a glycolipid is the presence of a monosaccharide or polysaccharide chain covalently linked to an anchoring lipid moiety. The lipid domain anchors the glycolipids into the hydrophobic core section of a biological membrane, whereas the terminal carbohydrate groups are exposed on the bilayer surface and they project outwards into the extracellular space [508-511].

The carbohydrate domain differs from one glycolipid to another and the chemical composition of the terminal polysaccharide chain depends on the cellular growth conditions and the state of the encompassing biological environment [512]. The variable monosaccharide or polysaccharide sections are however, almost always covalently linked to simpler glycerol or sphingosine backbones and conserved anchoring acyl chain domains [513-514]. One of the simplest glycolipids is sphingomyelin, which is especially abundant in the membranous myelin sheath that encases nerve cell axons [515-517]. The lipid consists of a single variable palmitoyl chain that is covalently linked to the central sphingosine backbone and terminal phosphocholine group (Figure 12A-C). Palmitoyl sphingomyelin is an interesting and relatively simple form of sphingomyelin that contains palmitate (16:0) at the variable acylation position. Palmitoyl sphingomyelin can interact with cholesterol in multicomponent membranes to form lipid raft structures [518-520]. The molecule has been the subject of thorough experimental [521-524] and computational [525-528] analyses and the molecule is used in chapter 5 (termed sphingolipid) for molecular dynamics simulations of simplified eukaryotic mammalian plasma membrane models. Ganglioside molecules have comparable structural characteristics to sphingomyelin molecules but the terminal phosphocholine headgroup is substituted with oligosaccharide residues and sialic acid units instead [512]. It is important to understand the biophysical properties of ganglioside lipids here because ganglioside molecules are hypothesized to instigate a complex cascade of molecular level interactions that promote OMV internalization in chapter 5 of this thesis [368].

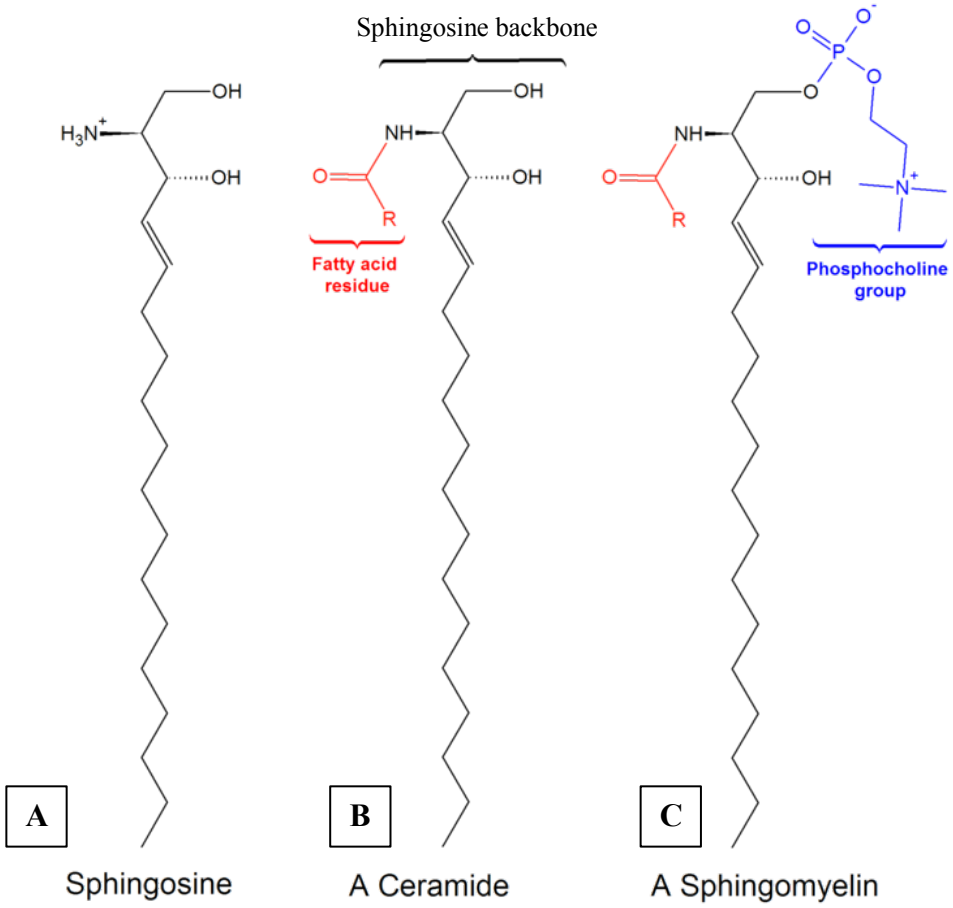

Figure 12. The chemical structure of three simple sphingolipids. (A) The chemical structure of sphingosine. (B) The chemical structure of a ceramide. The variable fatty acid moiety is red and the sphingosine backbone is black. (C) The chemical structure of a sphingomyelin molecule. The variable fatty acid moiety is red, the sphingomyelin backbone is black and the phosphocholine group is blue. Image source: Wikipedia Commons.

Ganglioside lipids were first discovered by Ernst Klenk in the 1940s and the term "ganglioside" was based on the high concentrations of the ganglioside glycolipids discovered within neurons or "Ganglionzellen" [426]. The ganglioside lipid anchors contain the long-chain amino alcohol sphingosine that is coupled through an amino group to a fatty acid chain to form a ceramide [512-513]. The glycan headgroup contains one or more sialic acid residues, which are carbohydrates with a nine-carbon backbone and a carboxylic acid moiety and there are also adjoining glucose, galactose, N-acetylgalactosamine units etc. GM3 lipid is one of the simplest ganglioside lipids that is present in almost all mammalian cell membranes [426,529-533]

and the molecule contains an anchoring ceramide unit that is covalently bonded to glucose, galactose, and sialic acid units (Figure 13A). GM3 lipid have the smallest ganglioside headgroup domain and they can be used to produce more complex ganglioside macromolecules [512,534]. For example, the addition of single adjoining N-acetylgalactosamine and galactose units transforms basic GM3 lipids into the larger GM2 and GM1 molecules, respectively (Figure 13B). Additional saccharide units can be added onto the GM3, GM2, and GM1 molecules to synthesize ganglioside macromolecules that have much larger headgroups, e.g. ganglioside lipids with seven or eight saccharide units per lipid headgroup.

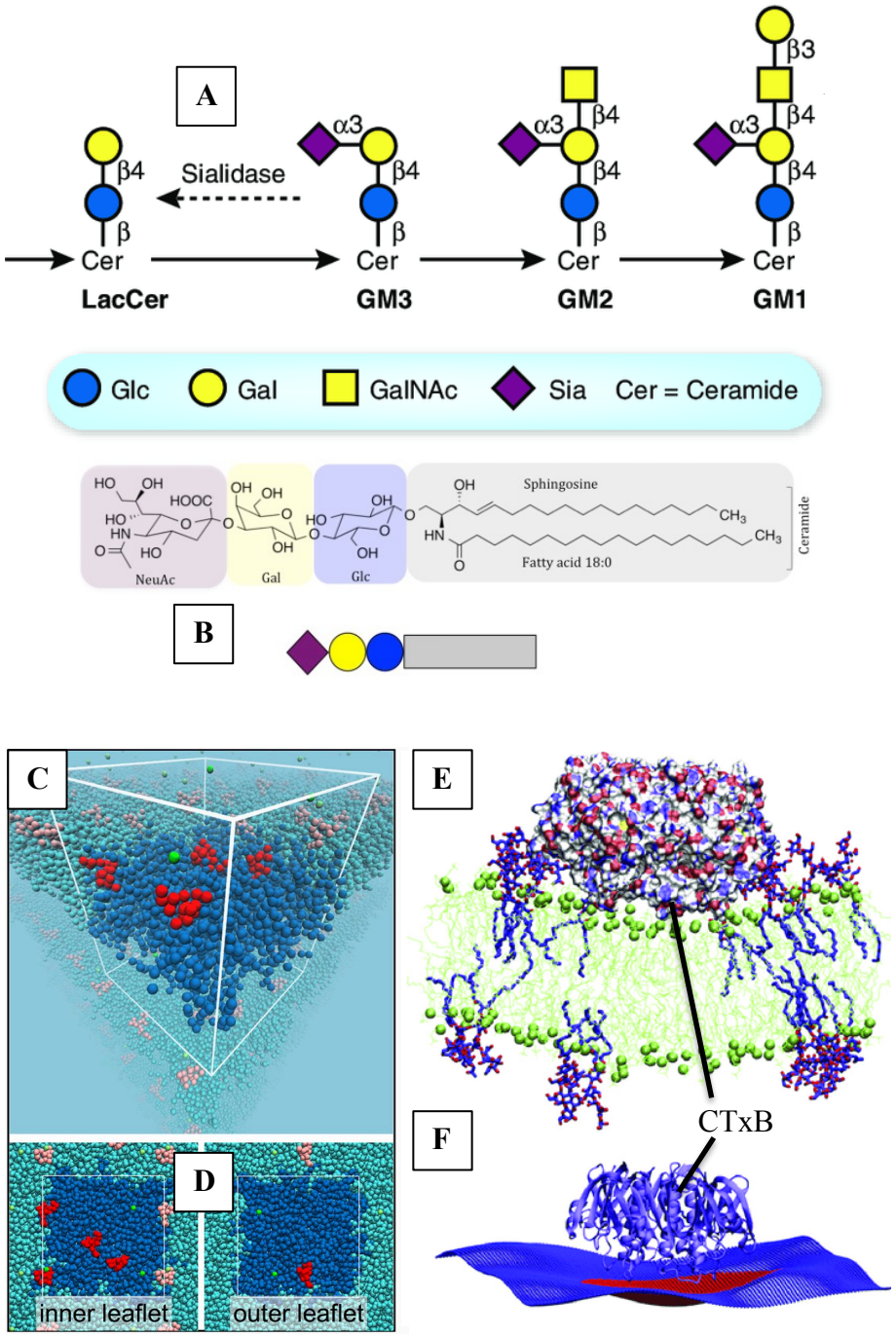

Figure 13. The ganglioside lipid structure and representations of how ganglioside molecules can induce spontaneous curvature generation. (A) Biosynthetic pathway for some of the smallest and simplest ganglioside molecules i.e. GM3, GM2 and GM1. Ganglioside molecules consist of a core ceramide unit that is bonded to glycan headgroups that contain monosaccharides such as glucose (Glc), galactose (Gal), N-acetylgalactosamine (GalNAc), and sialic acid residues (Sia). Additional monosaccharide units can be added onto GM3, GM2 and GM1 molecules to create larger and more complex ganglioside molecules. (B) The skeletal formula of the GM3 lipid. The ceramide domain is highlighted gray and the Glc, Gal, and Sia units are highlighted blue, yellow and maroon. (C-D) Molecular dynamics simulations showing how molecular dynamics simulations have demonstrated that GM1 molecules can reshape

asymmetric biomembranes. The phospholipids are blue and the GM1 molecules are red. The graphic contains both top view and side view snapshots. (E-F) Molecular dynamics simulations showing how cholera toxin B subunit (CTxB) can induce local curvature generation within biomembrane mimetics. (E) The DOPC lipids are green and the GM1 lipids are purple. (F) The membrane has been refitted to a thin surface for easier visualization of the induced membrane curvature. The image sources are: 10.3389/fimmu.2014.00325 (DOI) [426] 10.1038/nchembio0209-71 (DOI) [535] 10.1073/pnas.1722320115 (DOI) [536] 10.1002/2211-5463.12321 (DOI) [537].

GM3 and GM1 lipids have been used in atomistic and coarse-grained resolution molecular dynamics simulations to investigate the biophysical and biochemical properties of both shorter and longer forms of ganglioside molecules [426]. Dasgupta et al. used complementary molecular dynamics simulations and sophisticated experimental analyses to demonstrate that (GM1) ganglioside lipids can create non-negligible stress in POPC membranes that promotes, albeit moderately, spontaneous membrane curvature generation (Figure 13C-D) [536]. The membrane-modulating effects of ganglioside lipid become more pronounced when single ganglioside coalesce to form relatively rigid glycosphingolipid clusters that have high intrinsic positive curvature parameters [363]. Ganglioside molecules are generally confined to the extracellular leaflet of multicomponent plasma membranes and as they coalesce within just one membrane leaflet, the lipids can generate an appreciable preference for positive curvature generation and this can induce membrane reshaping processes [368].

One of the more interesting membrane reshaping events is the spontaneous production of curved lipid rafts, or caveolae, when ganglioside molecules coalesce within the extracellular leaflet of multicomponent plasma membranes [74,87,368]. The caveolae are produced when pathogens (e.g. bacteria and viruses) and pathogenic products (e.g. toxins and lectins) interact with host cell membrane ganglioside lipid headgroups (Figure 13E-F). Computer simulation and experimental analysis methods have been combined to demonstrate that SV40 virus [538-540], cholera toxin [368,537] and Shiga toxin (Figure 14A-E) [368,541] can enter into the host cell

cytoplasmic space when they interact with host cell ganglioside lipid headgroups. The pathogens and pathogenic products interact with the host cell surface and as they progressively sequester adjacent ganglioside lipid headgroups, they form large glycosphingolipid clusters that have high intrinsic positive curvature. The co-coupling glycosphingolipid interactions simultaneously induce localized membrane curvature and also increase the local concentrations of cholesterol, PIP lipids, sphingomyelin molecules, and saturated phospholipids [368]. The sequestered glycosphingolipids lower energy barriers that would otherwise impede spontaneous curvature generation and the raft-like plasma membrane domain bulges inwards into the intracellular matrix (Figure 14F-H) [542]. The inward bulging invaginations continue to expand into the cytoplasmic matrix and they can eventually form larger endocytosis intermediates (Figure 14I) that decouple from the cellular membrane on long timescales (Figure 14J). It is already well established that Shiga toxin, cholera toxin, and SV40 particles induce the formation of caveolae when they interact with host cell ganglioside lipid headgroups [368,542], but it stands to reason that other pathogenic products and synthetic macromolecules could be functionalized, either through natural selection or through chemical engineering processes, to exploit similar endocytosis uptake processes. The simulation data from chapter 5 suggests that OMVs have been functionalized to sequester ganglioside lipids and through this interaction, deform host cell surfaces so that they can enter into the host cell cytosol.

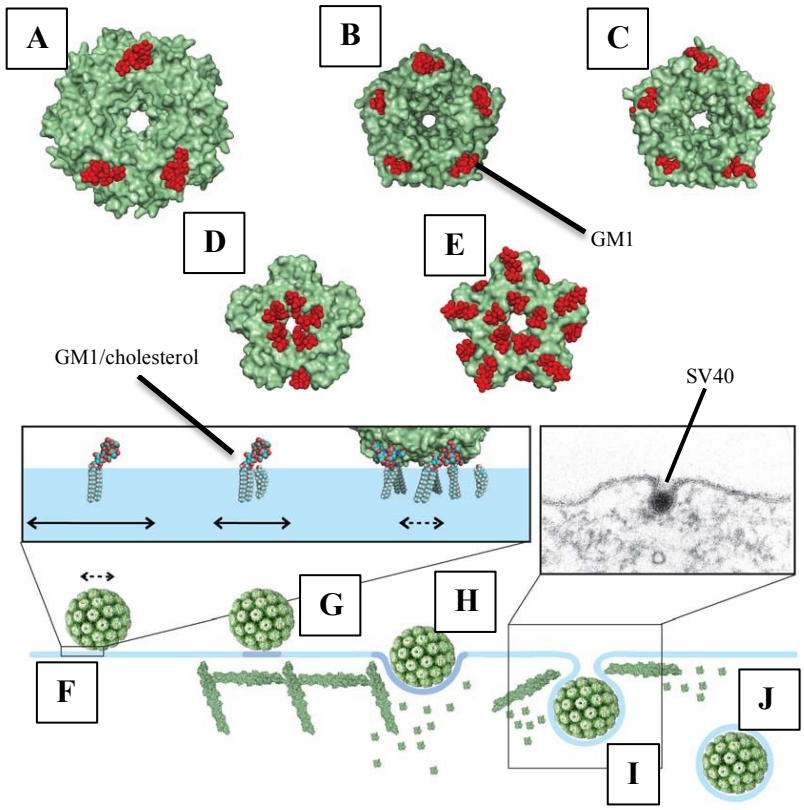

Figure 14. Pathogens and pathogenic products can bind ganglioside lipids and this interaction promotes endocytosis. (A) SV40 coat protein VP1 pentamer cocrystallized with GM1 pentasaccharide. The coat protein is green and the pentasaccharides are red. (B) Cholera toxin βsubunit cocrystallized with GM1 pentasaccharide. (C) E. coli enterotoxin βsubunit cocrystallized with nitrophenyl-galactoside. (D) Shiga toxin βsubunit cocrystallized with GB3 trisaccharide. (E) Pentameric *E. coli* Shigalike toxin βsubunit cocrystallized with a GB3 analog. (F) Binding of SV40 to GM1 lipids in a multicomponent membrane. (G) The formation of a lipid raft (dark blue band) and the demonstration of actin-dependent immobilization. (H) The invagination of the plasma membrane mimetic due to interactions with SV40. The interactions between SV40 and the plasma membrane mimetic generate a caveola structure. (I) Scission machinery facilitating endocytosis after the production of a flask-shaped lipid raft structure (i.e. caveola). (J) The formation of a vacuole and the transport of the vacuole through the intracellular space. The image source is: 10.1101/cshperspect.a004721 (DOI) [542].

1.4.5 Lipopolysaccharide

Lipopolysaccharide (LPS) macromolecules are unusually large glycolipids both in terms of end-to-end length and the lateral surface area that the molecules occupy in multicomponent bacterial membranes [104,543-545]. The macromolecules have a characteristic tripartite structure that consists of

the anchoring Lipid A domain, the core oligosaccharide section, and the repetitive glycan polymer O-antigen chain [546-548].

The anchoring Lipid A domain is a phosphorylated glucosamine disaccharide that is decorated with multiple fatty acid moieties [546,549-550]. The fatty acid moieties are embedded into the core of bacterial membranes and the glucosamine sugars extend outwards into the extracellular space. The phosphate groups are situated at the water-lipid interface; they have a net negative electrostatic charge and they readily interact with stabilizing divalent cations (e.g. Ca^{2+} and Mg^{2+} ions). The divalent cations can simultaneously coordinate multiple adjacent anionic Lipid A anchors and these bridging cations can effectively screen the repulsive electrostatic interactions between the adjacent anionic LPS phosphate groups that would otherwise promote electrostatic repulsion and membrane reshaping processes [119-120,551]. Garate and Oostenbrink (2013) simulated Lipid A molecules with water, octane and at the water-octane interface itself [552] using the CHARMM36 all-atom forcefield [553-554]. The Lipid A molecule was shown to have a larger gyration radius in the hydrophobic octane media compared with the polar solution of water or at the water-octane interface. Entire Lipid A membranes have been simulated by the Im group using the CHARMM36 all-atom forcefield [555], by Li et al. [556] using the GLYCAM06-based LPS forcefield [557-559] and by Lakshminarayanan et al. [560] using the GROMOS 53A6 forcefield [561-563]. The research groups showed that the simulated Lipid A membranes were stable at physiological pressure and temperature when they were interlinked with divalent cations, e.g. Ca^{2+} and Mg^{2+} ions.

The LPS lipid core domain contains an oligosaccharide chain that is linked to the anchoring Lipid A domain. The keto-deoxyoctulosonate (Kdo) sugar is a primary component of most LPS core saccharide sections [563] but non-carbohydrate components including amino acids, ethanolamine substituents, and phosphate groups can also be present [543,564]. The specific nomenclature used to describe LPS lipids depends predominantly on the

extension of the core saccharide section and the number of constituent saccharide units that are bonded to the anchoring Lipid A domain. Re LPS is the simplest LPS lipid that is found within realistic Gram-negative bacterial membranes and it consists of two Kdo saccharide units bonded to the Lipid A anchor [565-566]. The incorporation of additional saccharide units would transform Re LPS chemotypes to the larger Rd, Rc, Rb and Ra LPS chemotypes [567] that have different sets of biophysical parameters in multicomponent membranes. Khalid et al. performed some of the earliest molecular dynamics simulations of Rd LPS lipid membranes with the united-atom GROMOS53A6 forcefield to understand how electrostatic fields can disrupt multicomponent bacterial membranes [551]. The Rd LPS lipid membranes were found to have area per lipid magnitudes that were in line with predictions from X-ray diffraction analysis [568], but the LPS acyl tail order parameters were noticeably higher than experimentally derived acyl tail order parameters for comparative phospholipid membranes [569]. The Im group performed higher resolution molecular dynamics simulations of various LPS lipid chemotypes [211,223] with the CHARMM36 all-atom forcefield and they obtained more accurate estimates of the LPS acyl chain order parameters if we are benchmarking against reference DMPC membranes [569], but the predicted area per lipid values exceeded the upper limit of LPS area per lipid values (1.56 nm^2) predicted from experimental analyses [568]. Lins et al. also performed pioneering atomistic resolution simulations to understand the uptake of uranyl by LPS lipid membranes with minimal core saccharide domain [241]. The group did not provide lipid packing parameters and it is therefore more challenging to draw comparisons with experimental analysis data.

LPS lipids are increasingly being simulated in more realistic multicomponent Gram-negative outer membrane models that incorporate different outer membrane proteins [308] including gated outer membrane transporters [570-572] and β-barrel assembly machinery [573]. The LPS lipids that contain the Lipid A anchor and variable core saccharide sections are usually termed “rough” LPS lipid chemotypes [121,567] because bacterial colonies

have a rough appearance when they contain short forms of LPS lipid, i.e. LPS lipid without any terminal O-antigen chain units. Martini molecular dynamics simulation forcefields have been used to understand the properties of Gram-negative outer membrane models that contain different types of rough LPS lipids (e.g. the Re and Ra chemotypes) [301]. The coarse-grained molecular dynamics simulations have demonstrated that there is "communication" between the extracellular and intracellular leaflets of the Gram-negative outer membrane [574]. Areas of high acyl chain disorder in the extracellular leaflet were found to be correlated with areas of high acyl chain order in the intracellular leaflet. Martini coarse-grained simulations have also been used to demonstrate that LPS lipid nanodisc width decreases from nanodisc center to periphery and that LPS lipid micelle structure is significantly perturbed by large changes in simulation temperature (~90 K difference) [151].

The repetitive glycan polymer is termed the O-antigen chain and it can, in some circumstances, be the heaviest section of the LPS lipid macromolecular structure [575-576]. The composition of the O-antigen chain varies from one bacterial species to another. There are more than 160 different *E. coli* O-antigen glycan polymer chain structures alone, but there is found to be even more chemical heterogeneity when LPS lipids from one bacterial genus (e.g. *Escherichia*) are compared with LPS lipids from an entirely distinct genus (e.g. *Campylobacter* or *Pseudomonas*) [543]. The O-antigen chains are the peripheral moiety of the tripartite LPS macromolecular structure and they are in direct contact with the external milieu. When LPS lipids contain the Lipid A anchor with complete core saccharide section and the terminal O-antigen chain polymer they are termed "smooth" LPS lipid chemotypes [577] because bacterial colonies have a smooth appearance when they contain the longer forms of LPS lipid, i.e. LPS lipid with terminal O-antigen chain moieties. Smooth *E. coli* LPS lipid can contain for example, type 1 Lipid A anchor with R3 core sugar sequence and the terminal O1 O-antigen chain polymer (Figure 15) [315]. The O1 O-antigen chain subunit contains the five saccharide units arranged end-to-end: β N-acetyl-D-glucosamine, α D-galactose, α L-rhamnose, α L-rhamnose, and β N-acetyl-D-mannosamine [315]. Smooth LPS

lipids have been simulated in single-component bacterial membrane mimetics and also in more complex multicomponent membrane mimetics with atomistic resolution molecular dynamics simulation forcefields [104,198,211-212]. The OPLS-AA [170] and GLYCAM [246] molecular dynamics simulation forcefields have also been used to analyze the conformations of single O-antigen chain polymers in solution [578]. It was found that the conformation of the O-antigen chain was affected by the choice of the molecular dynamics simulation forcefield. When the O-antigen chain was simulated with the OPLS-AA forcefield it had large gyration radii and when it was simulated with the GLYCAM simulation forcefield the gyration radii were substantially smaller. Smooth LPS lipids have been simulated much less frequently with coarse-grained molecular dynamics simulation forcefields. However, in 2018 Khalid et al. used the Martini coarse-grained forcefield to understand how smooth LPS lipids interact with the following integral membrane proteins: OmpA, FhuA, OmpF, EstA, BtuB, and OmpX [315] and before this, the Martini coarse-grained forcefield had been used to understand how smooth LPS lipids interact with PE and PG phospholipids [579-581].

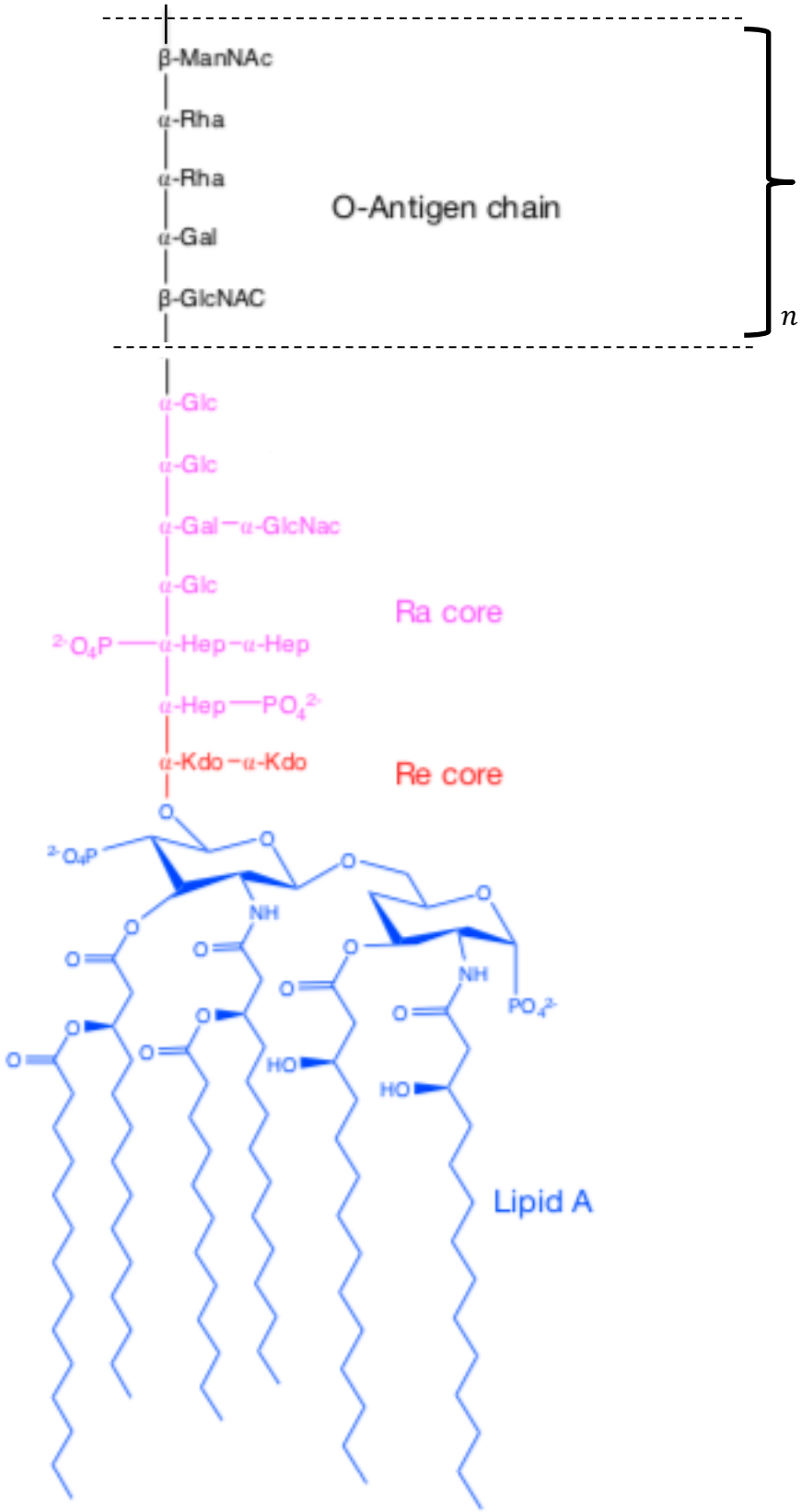

Figure 15. Schematic representation of a single molecule of smooth LPS lipid from *E. coli* bacteria. The illustration includes the type 1 Lipid A domain, which is a phosphorylated glucosamine disaccharide decorated with multiple fatty acid chains (blue). Lipid A is bonded to the R3 core oligosaccharide domain that includes hexose sugars such as keto-deoxyoctulosonate (Kdo), glucose (Glc), mannoheptose (Hep), N-acetyl-D-

glucosamine (GlcNac), galactose (Gal) and phosphate groups. The length of the core domain determines rough LPS nomenclature; Re LPS lipids contain the Re core domain (red) and Ra LPS mutants contain the complete core saccharide sequence (red and pink). Smooth LPS lipids additionally contain terminal O-antigen chain units (black). Smooth LPS lipids can contain multiple repeats of the repetitive O-antigen chain polymer unit. The CHARMM-GUI Martini Maker coarse-grained Re LPS lipid model contains the type 1 Lipid A domain with two Kdo sugars; the Ra LPS lipid model contains the type 1 Lipid A domain with complete core saccharide section; the coarse-grained smooth LPS lipid contains the type 1 Lipid A domain with complete R3 core saccharide section and four units of the terminal O1 O-antigen chain polymer. The image is based on work from the 10.1021/acs.jctc.8b01059 manuscript (DOI) [315].

1.5 Bacterial Infection and Multiple-Drug Resistance

Pathogenic bacteria spread disease as they pass through the four stages of infection: (i) colonization, (ii) invasion, (iii) proliferation and (iv) transmission [582-586]. The colonization of human tissues by pathogens is usually enhanced by adhesion molecules that are exposed on the bacterial cell surface [587-589]. The infectious microbes migrate toward target host cell surfaces in response to chemical gradients and then attach onto the membrane surfaces through the action of the exposed adhesion proteins. After the bacteria have colonized the target cells, they expel toxins that can damage the host human tissues (e.g. connective, muscle, and epithelial) and change the local physiological conditions. The microbes progressively sequester different biomolecules and metals that are needed for bacterial growth and the pathogenic microbes continue to multiply until they evoke an immune response that contributes to the transmission of the bacteria to new a host [590-592].

Antibiotics were used throughout the 20th century to prevent the spread of infectious bacteria and to effectively reduce the global rates of morbidity and mortality that are associated with infectious bacterial diseases [593-595]. Antibiotics are one of the most successful forms of chemotherapy and they have been used to treat nosocomial infections [596], to avoid complicated surgery [597], to prevent infection during incision-based surgery [598-599], to prevent infectious diseases among immunocompromised patients [598]

and they were even added to livestock feed to safeguard animal health and welfare [600-604]. The excessive and inappropriate use of antibiotics established a selective pressure that favored the proliferation of bacteria that were resistant to first-line antibiotic agents [593,605-606]. The drug-resistant bacteria thrived and their drug-resistant genes became more common [607-609]. These drug resistant genes have since been passed between infectious bacteria during the last few decades and there are now so-called multi-drug resistant bacteria that are unaffected by almost all available forms of antibiotic medication, e.g. methicillin-resistant *Staphylococcus aureus* (MRSA) and multidrug resistant strains of *Acinetobacter baumannii* [610-611]. Multidrug resistant bacteria are dangerous and they have the potential to not only increase the global rates of morbidity and mortality associated with infectious bacteria but also to increase national healthcare system spending [612-616]. Bacterial infections are becoming increasingly hazardous and there is an urgent need to synthesis new antibiotic medication that can be used to treat multi-drug resistant bacteria. The phenomenon is not unprecedented and clinicians had noted that Gram-positive cocci were developing resistance to sulphonamide group drugs in the first-half of the 20th [593]. Chemists synthesized novel derivatives of otherwise ineffective sulphonamide antimicrobials to make new antibiotic medication for the increasingly resistant strains of Gram-positive cocci bacteria [593, 617-621]. There was an effective arms race between chemists and microbes that has persisted ever since, sometimes increasing in rapidity and other times slowing as the volume of antimicrobial scientific research and scientific funding varied throughout the last century [622-623]. We are now at an interesting precipice where computational simulation methodologies have reached a level of sufficient complexity that they can be used to not only gain unprecedented molecular level insights into the action of effective antimicrobials [624] but also to streamline pipelines for drug-target interaction network analysis and to streamline pipelines to identify potentially novel antibiotic medication [625-629]. Molecular dynamics simulations are increasingly being applied to evaluate the

molecular level interactions of effective antimicrobial peptides and to gain insights into their antibacterial and membrane disrupting effects [630-631].

1.6 Gram-Negative and Gram-Positive Bacteria

1.6.1 Gram Staining

Bacteria are broadly classed as either Gram-positive or Gram-negative according to the structure of their cell envelope and how they respond to the Gram stain test. The Gram stain test is a relatively simple procedure that uses colored dyes to determine whether bacteria should be classed as either Gram-positive or Gram-negative [632-635]. Scientists initially apply primary crystal violet and iodine solution stains to a heat-fixed smear of the bacterial cell culture. The bacterial culture is subsequently decoloured with ethanol or acetone and counterstained with carbol fuchsin or safranin. Gram-positive and Gram-negative bacteria respond differently to the step-wise staining procedure [634]. Gram-negative bacteria are dyed pink by the carbol fuchsin or safranin, whereas Gram-positive bacteria retain the initial measure of the crystal violet stain. The different responses can be understood if we consider the different structure and composition of the Gram-positive and Gram-negative cell envelopes [20,636]. The Gram-negative bacterial cell envelope is tripartite and it contains the inner cytoplasmic membrane, the outer bacterial membrane, and layers of peptidoglycan that are located between them. The Gram-positive cell envelope is dipartite and rather than there being an outer membrane, there is only the cytoplasmic membrane and the layers of peptidoglycan that bonded to it through lipoteichoic acid. The Gram-positive and Gram-negative layers of peptidoglycan are differently exposed to the external milieu and they consequently have different responses to the Gram stain test.

1.6.2 Cell Envelopes

Gram-positive bacteria have a cytoplasmic lipid membrane that contains phospholipids and transmembrane proteins (Figure 16A). The cytoplasmic

membrane additionally contains interstitial lipoteichoic acids (Figure 16B) that act as chelating agents and bind the fluid lipid membrane to a relatively rigid wall of porous peptidoglycan (Figure 16C) [637-639]. The peptidoglycan layers are comprised of murein, a polymer of disaccharides that are cross-linked by short chains of amino acids [640-643]. The sugar component consists of alternating N-acetylglucosamine and N-acetylmuramic acid units that are attached to a chain of three to five amino acid units. The peptide chains can be cross-linked to form a 3D mesh-like network that is up to 80 nm thick and forms around 90% of the dry-weight of Gram-positive bacteria [644].

The Gram-negative bacterial cell envelope contains two membranes, the inner and outer lipid membrane bilayers, and layers of peptidoglycan that are located between them (Figure 16D) [59]. There are different types of phospholipid molecules within the inner cytoplasmic membrane including cardiolipin, PE and PG phospholipid [645-648]. There are various membrane proteins that are embedded throughout the inner cytoplasmic membrane including aquaporin AqpZ [648] and the lactose permease LacY transport protein [649]. The outer membrane has an asymmetric structure and there are significantly more phospholipids in the inner (intracellular) leaflet than the outer leaflet and correspondingly, significantly more LPS macromolecules in the outer (extracellular) leaflet than the inner leaflet. There is in effect, one extracellular LPS leaflet that interacts with the external milieu and an opposing phospholipid leaflet that interacts with the periplasmic matrix. There are also different types of transmembrane β-barrel porin proteins embedded throughout the outer membrane, e.g. the vitamin B12 transporter BtuB protein [650-651] and the ferrichrome outer membrane transporter FhuA [652]. Braun's lipoprotein is also embedded throughout the outer membrane and this 7.2 kDa macromolecule has the rather interesting and unusual property that it can connect the outer bacterial membrane to the layers of peptidoglycan in the periplasm [653-655].

Molecular dynamics simulations of the Gram-negative bacterial cell envelope have become larger, longer and significantly more complex during the last couple of decades [104-105,231]. Scientific research groups have successively calibrated different atomistic resolution simulation forcefields [163] to more accurately reproduce the properties of LPS containing bacterial outer membrane mimetics and these carefully calibrated lipidic systems have been simulated with different types of integral membrane proteins, e.g. the OMPs [308]. Molecular dynamics simulations were conducted with sophisticated atomistic resolution forcefields to understand the properties of bacterial cell wall mimetics that contain models for the inner cytoplasmic membrane, the outer bacterial membrane, the layers of peptidoglycan, and some of the different proteins that mediate interactions between them [320-321]. Atomistic simulations were similarly conducted to understand how mechanical stress is distributed throughout the constituent components of the Gram-negative bacterial cell envelope [312] and how the outer membrane is affected by membrane-active AMPs [328].

Coarse-grained molecular dynamics simulation forcefields were used in 2017 to probe previously unprecedented spatiotemporal scales and enable microsecond long simulations of mesoscopic bacterial cell wall composites that include models for the inner cytoplasmic membrane, the outer bacterial membrane, and a model for the large AcrABZ-TolC multidrug efflux pump protein that spans the entire periplasmic space and simultaneously interacts with both the inner and outer bacterial membranes [325]. Coarse-grained molecular dynamics simulations have also provided interesting insights into fundamental processes that underpin bacterial cell growth and bacterial cell division. Coarse-grained molecular dynamics simulations have explained how the rod-shaped structure of Gram-negative bacteria is preserved during bacterial cell growth [311] and how constrictive forces are necessary for promoting bacterial cell division [656].

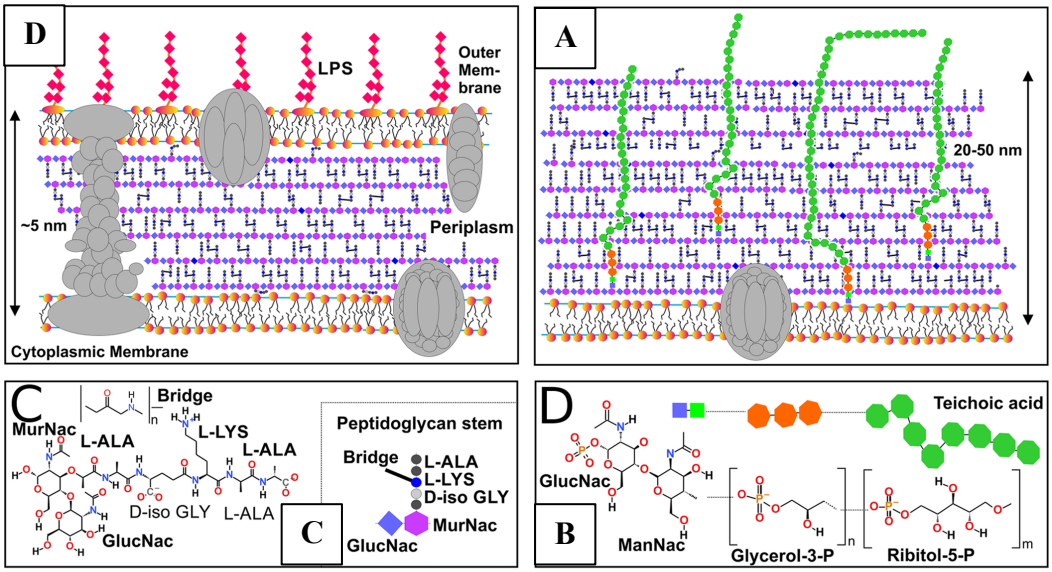

Figure 16. Schematic illustration of the cell envelope of (A) Gram-negative and (B) Gram-positive bacteria. Phospholipids are orange spheres attached to two acyl chains, LPS lipids are orange ovals attached to six acyl chains and terminal red square polymers, teichoic acids are green circle polymers attached to orange heptagons, proteins are gray circle and oval composites, and peptidoglycan is the repeating blue and purple hexagon-square composite. (C) The chemical structure of the peptidoglycan unit. (D) The chemical structure of teichoic acid. The different cell wall structures affect how bacteria interact with the external milieu and thereby, their response to the Gram stain procedure. The image source is: 10.1021/acs.chemrev.8b00538 (DOI) [59].

1.6.3 Outer Membrane Vesicle Biogenesis and Functions

The outer membrane of Gram-negative bacteria frequently swells and ruptures and this process generates outer membrane vesicles (OMVs) that can move into the extracellular space [47-51] and traffic molecular cargo from the periplasm of one bacterium to surface of another [51-52]. The stability of the Gram-negative cell envelope is affected by the number and strength of the non-covalent interactions between murein and the outer membrane proteins [312], and the covalent cross-links between Braun's lipoprotein and the rigid layers of peptidoglycan [320,657]. Areas of the bacterial outer membrane that are devoid or depleted of attachments to the layer of peptidoglycan are liable to swell and progressively protrude outwards until the membrane decouples entirely from the bacterial cell wall and subsequently forms spherical OMVs [51,658-659].

OMVs are small (~20-250 nm) spherical vesicles that contain a combination of different lipids that are distributed asymmetrically about the membrane midplane [660-661]. The outer leaflet is predominantly comprised of LPS lipids and the inner leaflet is predominantly comprised of phospholipids but there can also be integral membrane proteins that embedded throughout [662-663]. The structure and compositional characteristics of the OMVs are comparable to the structure and compositional characteristics of the parent Gram-negative bacterial outer membranes. OMVs have high concentrations of smooth LPS lipids when they bleb from the surface of smooth Gram-negative bacteria and similarly, OMVs have high concentrations of rough LPS lipids when they bleb from the surface of rough Gram-negative bacteria [664].

OMVs contain an inner periplasmic core and diverse luminal and surface exposed biomolecular cargo. The lumen can contain relatively high concentrations of degradative enzymes, which catalyze the decomposition of complex macromolecules, or instead contain high concentrations of genetic material (DNA and RNA) that can be transferred from one bacterial cell to another [47,665]. OMVs have also been found to traffic acquisition proteins from bacterial cell envelopes into the extracellular space, making them adept at performing nutrient scavenging roles [48]. It is becoming increasingly clear that OMVs additionally traffic pathogenic cargo (e.g. virulence factors) toward target mammalian cell membrane surfaces and that they have important roles in mediating bacterial pathogenies [48,52,664]. OMVs bleb from pathogenic Gram-negative bacterial cell surfaces and traffic toxins, hemolysin molecules, proteases, adhesin compounds etc. to host cell surfaces and this process contributes to the spread of infectious disease. The OMVs pass through the extracellular space and after initial interactions with host cell surfaces they enter into the host cell cytosol and release their pathogenic cargo [52,664]. When virulence factors are concentrated within OMVs they are afforded protection from the extracellular environment and consequently it can be more effective to deliver molecular cargo within OMVs compared with conventional soluble section processes [666-667].

Although it is well established that OMVs can enter into the host cell cytosol during infection, the precise biomolecular interactions that underpin host cell association and OMV uptake have not been determined [52,664]. It has been demonstrated that OMVs can deliver luminal cargo via clathrin dependent endocytosis mechanisms; the binding of the OMV ligands to the host cell surface receptors triggers the formation of clathrin coated pits that are up to 200 nm in diameter and are sufficiently wide to envelope most small, medium, and large sized OMVs that are released from Gram-negative bacterial cell surfaces [52,668-669]. Numerous studies have described roles for clathrin proteins in the active internalization of OMVs but generally with the caveat that OMV uptake still transpires even when clathrin proteins are absent or entirely inactivated. OMV uptake can occur independently of any membrane embedded proteins through endocytosis interactions that are mediated entirely by lipid-lipid interactions [664]. It is theorized that the OMVs initially dock onto plasma membranes and subsequently release their luminal cargo through direct membrane fusion as they interact with lipid rafts that form the host cell surface (Figure 17). The proposed model has not been proven through experimental analyses and the uptake model is consequently quite vague and unclear [52]. The observation that the lipid-mediated internalization dynamics depend on the presence and length of constituent LPS O-antigen chains makes the uptake pathway even less clear and more difficult to understand [664]. It seems appropriate therefore to briefly describe the compositional characterises of lipid rafts in the following paragraph and to describe how lipid rafts could promote direct membrane fusion or endocytosis uptake processes. Readers should be aware that lipid rafts have already been discussed more comprehensively when the raft hypothesis was first introduced in section 1.1.

Lipid rafts are transient fluctuating nanoscale assemblies that are predominantly comprised of glycosphingolipids, cholesterol, integral membrane proteins, and saturated phospholipids [73-75]. Lipid rafts have unusual molecular packing parameters (i.e. area per lipid and thickness), acyl

chain order values, and diffusion parameters that differ from the encompassing membrane environment [81-82,135,362]. Cholesterol molecules pair with sphingolipids and proteins and these co-coupling interactions form a relatively static and liquid-ordered raft structure (Lo) whose biophysical parameters differ the encompassing liquid-disordered membrane (Ld) [59]. Recent molecular dynamics simulations have proposed that the liquid-ordered (Lo)/liquid-disordered (Ld) phase boundary can facilitate direct membrane fusion if the Lo phase constituents have the larger negative spontaneous curvature [670]. In such a case, the presence of membrane fusion intermediates (i.e. highly curved fusion stalks) next to the less-ordered boundary region becomes energetically favourable.

However, it is also clear that caveolae promote spontaneous curvature generation and the production of endocytosis intermediates independently of direct membrane fusion interactions [74,368]. The word caveolae is Latin for "little caves" and the name seems to be appropriate since caveolae are small membrane invaginations that have a raft-like composition that includes glycosphingolipids, cholesterol, sphingolipid and saturated phospholipids [87,671-672]. Glycosphingolipids are especially abundant within the neck of the caveolae [366-367,673] because clusters of intrinsically positively curved glycosphingolipids have the capacity to lower line tension energies between neighboring flat and negatively curved membrane domains. In other words, it is energetically favourable for the clusters of glycosphingolipids to move toward the interfacial domains that separate adjacent flat and negatively curved membrane domains [430,536]. Cholesterol molecules are also present in unusually high concentrations within caveolae, but they are primarily situated within the central portion of the caveolae that bulges inwards into the intracellular space [673]. Viral particles are already known to induce endocytosis processes when they interact with glycosphingolipids within host cell membrane surfaces [538-540,674] and it is not unreasonable to assume that OMVs might also induce the formation of endocytosis intermediates (e.g. caveolae) when they bind and sequester host cell glycosphingolipids. The results from chapter 5 indicate that OMVs might

induce the formation of highly curved lipid raft-like assemblies when they bind (GM3) ganglioside molecules and that this interaction can promote the formation of raft-like endocytosis intermediates on long timescales.

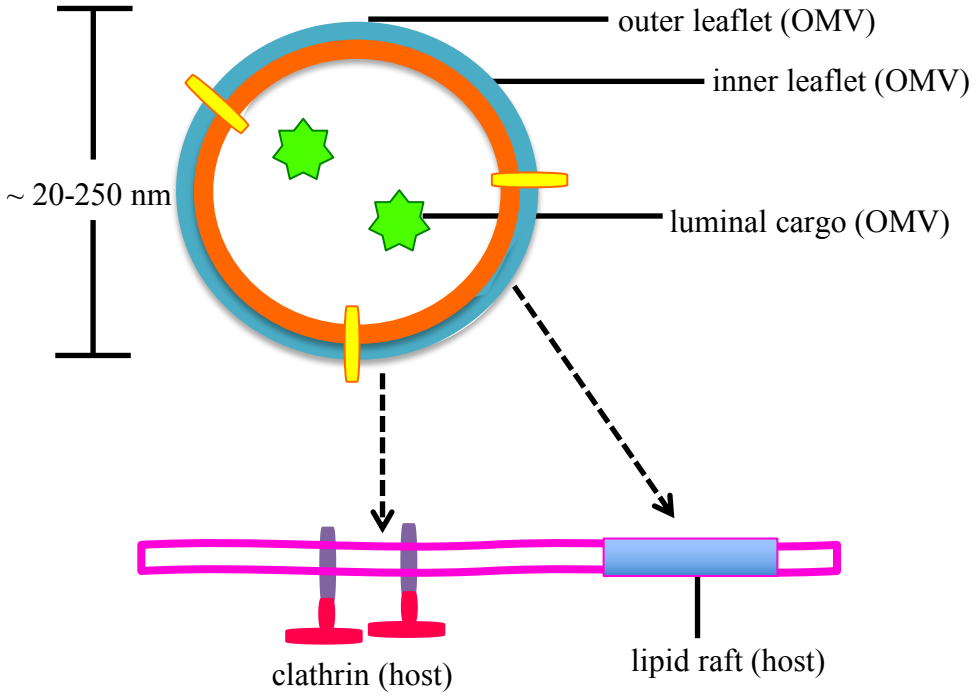

Figure 17. Host-pathogen interface interactions. The OMVs are liposomes that contain an outer leaflet that is predominantly comprised of lipopolysaccharide lipids and an inner leaflet that is predominantly comprised of phospholipids. The OMVs deliver luminal cargo and virulence factors to host cells as they pass through or fuse with the host cell (eukaryotic) plasma membranes. The OMVs can enter cells through clathrin-dependent endocytosis and alternative lipid-mediated internalization uptake pathways that involve lipid rafts, but the precise biomolecular interactions that underpin these processes are not entirely understood. Here, the OMV outer leaflet is cyan, the inner leaflet is orange, the outer membrane proteins are yellow, the host plasma membrane is pink, the lipid raft is blue and the clathrin molecules are purple and red.

1.7 Antimicrobial Peptides

Gram-negative and Gram-positive bacteria are progressively acquiring resistance to last-line antibiotic medication [610-614] and the number of antibiotics that are still effective against infectious diseases is dwindling [593-595]. Without immediate intervention it seems likely that there will soon be few, if any, antibiotics that are suitable for treating the most concerning strains of infectious bacteria [675-678]. We could observe a drastic increase in morbidity and mortality as immunocompromised patients increasingly become infected with debilitating extensively drug-resistant bacterial infections that are unresponsive to any conventional form of chemotherapy.

Antimicrobial peptides (AMPs) are potent broad-spectrum antibiotics that are produced by all classes of life as part of the innate immune response and they can destroy different forms of infectious bacteria [129-137]. AMPs have received significant scientific attention during the last couple of decades because AMPs tend to rather uncommonly, destroy pathogenic microbes by destabilizing the protective lipid-containing cellular membrane. AMPs are effective against multiple different forms of bacteria, fungi, and viruses and it is speculated that novel antibiotics could be manufactured as theoreticians determine the molecular level interactions that underpin the antimicrobial properties of these broad-spectrum AMPs. Chemists could take these molecular level insights and synthesize new medication that is effective against otherwise extensively drug-resistant strains of Gram-negative bacteria [679-682].

Many AMPs have similar chemical characteristics and they have been found to affect membrane permeability via comparable modes of action [683-684]. There are several chemical properties that are common among different types of AMP: (i) the peptides contain cationic moieties and a net positive charge ranging from +2 to +13; (ii) AMPs are primarily comprised of hydrophobic residues such as tryptophan, phenylalanine, and isoleucine; and

(iii) all AMPs are amphipathic [685-689]. The relative abundance of the hydrophilic and hydrophobic moieties determines how the AMPs destabilize the target bacterial membranes and it also determines where the AMPs will reside along the membrane normal axis [690].

The initial contact between AMPs and biological membranes is usually based on attractive electrostatic interactions because the bacterial membrane boundaries contain anionic lipid headgroups and [645] the AMPs always contain positively charged amino acid residues. Early experimental data indicated that biological membranes are disrupted by so-called "barrel-stave", "carpet" or "toroidal-pore" AMP-induced modes of action [687,691-692]. The barrel-stave model mechanism proceeds as follows: the AMPs are initially oriented perpendicular to the bilayer normal but they slowly penetrate into the membrane interior until they are oriented parallel with the encompassing lipid tails (Figure 18B). This transmembrane protein position promotes lateral peptide-peptide interactions and the proteins self-assemble into a transmembrane cylinder whose hollow lumen increases the diffusion of material across the membrane normal axis [693-694]. The toroidal pore model mechanism proceeds as follows: the AMPs initially settle onto the membrane surface and subsequently penetrate the bilayer until they are oriented along the membrane normal axis. The peptides induce local membrane curvature until the peptides and encompassing lipids form a cavernous toroidal pore (Figure 18C) [693,695]. AMPs can additionally disrupt biological membranes through the carpet mechanism, in which the peptides initially adsorb onto the bilayer surface without penetrating into the hydrophobic interior and they collectively form a "carpet" of AMP molecules. The unfavorable interactions between the adsorbed proteins and the underlying lipids affects the local membrane integrity (Figure 18D) [696]. The protein-lipid interactions eventually disrupt the stable lamellar membrane packing and the lipids are prone to break away from the bilayer to form lipid micelles. Indolicidin and cecropin are AMPs that destabilize the bacterial membrane structure through processes that mimic the carpet mechanism [670-672].

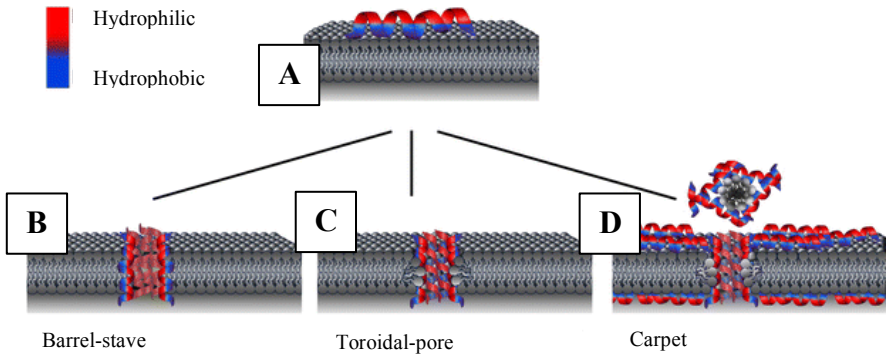

Figure 18. Overview of AMP membrane breakdown processes. (A) The AMPs initially bind to the host membrane surfaces through a combination of electrostatic and hydrophobic protein-lipid interactions. The AMPs adopt orientations that maximize the number of attractive peptide-lipid electrostatic and hydrophobic interactions. (B) In the barrel-stave model the hydrophobic AMP moieties are oriented toward the encompassing acyl chains and this creates a transmembrane water pore. The encompassing acyl chains maintain a transmembrane orientation (i.e. align with the membrane normal axes) and the AMPs oligomerize to effectively form a pore that has one hydrophobic surface and one hydrophilic surface. (C) In the toroidal-pore model the intracellular (inner) and extracellular (outer) monolayers distort when they interact with the oligomerized AMPs and this creates a transmembrane water pore whose surface is comprised of lipid headgroups and protein residues. (D) In the carpet model the AMPs stay on the membrane surface and induce membrane rupture as they change the structure of the membrane. The image source is: 10.1007/s10989-009-9180-5 (DOI) [673].

Keeping in mind that AMPs are known to affect biological membranes and also that molecular dynamics simulation methods have been carefully calibrated over the last few decades to accurately reproduce the interactions of lipids, it should not be particularly surprising that there have been an inordinate number of molecular dynamics simulations that have explored the interactions of AMPs with bacterial membrane mimetics [188,674-677]. The prototypical AMP melittin has been repeatedly simulated with different molecular dynamics simulation forcefields and it has been found that melittin disrupts the stable bilayer structure through the formation of transmembrane water channels according to an unconventional barrel-stave membrane breakdown process [678-682]. It was found via molecular dynamics simulation methods that melittin molecules spread out across transmembrane water pores in different orientations rather than being

neatly aligned along the membrane normal axis, as conventional membrane disruption models had previously assumed [683]. Subsequent molecular dynamics simulations were able to elucidate how the insertion of the N-terminus can contribute to membrane disruption [684] while the C-terminus anchors melittin to the lipid headgroups through hydrogen-bond interactions [685].

The formation of toroidal pores has also been noted in molecular dynamics simulations of magainin AMPs but there were notable differences between the results from the molecular dynamics simulations and predictions from the conventional toroidal pore disruption models. The simulated magainin MG-H2 AMPs induced the formation of a nanometer-sized toroidally shaped pore in DPPC membranes but only one magainin AMP was found near the center of this transmembrane pore while the remaining AMPs remained on the bilayer surface with an orientation that was approximately parallel to the bilayer surface [686]. Later electron paramagnetic resonance spectroscopy studies and molecular dynamics simulations with sum frequency generation vibrational spectroscopic studies would corroborate the inference that magainin molecules tend to predominantly lie on the flat hydrophilic surface of membranes [687-688] rather than immediately cluster to form the simplistic oligomeric transmembrane toroidal pore structures that had been previously hypothesized. Through molecular dynamics simulations it is now clear that magainin AMPs can induce membrane thinning and induce significant membrane perturbation even when they are lying on the flat hydrophilic surfaces of bacterial membrane mimetics [689]. Prior to these interesting molecular dynamics simulations it was assumed that magainin AMPs predominantly disrupted biological membranes by oligomerizing to form conventional transmembrane toroidal pores but it is now becoming clear that the degradative interactions of magainin AMPs are much more complex and it has even been proposed, based on simulation studies [690], that magainin AMPs can only form toroidal pore structures when they co-couple with PGLa (sequence GMASKAGAIAGKIAKVALKAL-NH_2) [691-693] because the molecules are

both a part of the African frog *Xenpus laevis* innate immune response system [694] and consequently they would both be found *in vivo* interacting with the same membrane systems.

Molecular dynamics simulations of the chrys-3 AMP have produced interesting results that in some instances corroborate pore formation models and in other instances corroborate the carpet model. It was found that when chrys-3 peptides were positioned across the membrane normal axis they tended to co-couple and induce the spontaneous production of transmembrane pores, but when chrys-3 peptides were located at the membrane surface they increased membrane curvature and generated membrane protrusions that could be considered micellization intermediates [255]. Molecular dynamics simulations have also demonstrated that the Aurein 1.2 [286], Kalata B1 [695-696], and PA-Pln149 AMPs [697] have the capacity to induce bilayer curvature and affect the membrane integrity. The AMPs had the capacity to increase membrane curvature when they were located at the membrane surface despite minimal insertion of the AMP hydrophobic moieties into the hydrophobic acyl chain domain. Coarse-grained molecular dynamics simulation forcefields have even been applied to demonstrate that cyclic antibacterial peptides can self-assemble at the membrane surface and cause the underlying membrane to extrude lipids as they form micellar aggregates [698]. Taken together, the molecular dynamics simulations reveal that the toroidal, barrel-stave, and carpet models are too simplistic and that molecular dynamics simulations are necessary for revealing otherwise inaccessible molecular level details that underpin the membrane disrupting properties of antibacterial peptides.

1.8 Polymyxin B1

Polymyxin molecules are a class of antimicrobial lipopeptides that are produced by strains of Gram-positive *Paenibacillus polymyxa* bacteria [699-701]. The polymyxin lipopeptides consist of 10 amino acids including six cationic diaminobutyric acid (Dab) residues and a hydrophobic acyl chain

moiety (Figure 19A). Seven of the amino acids are bonded to form the cyclic component of the lipopeptides while the remaining acyl tail and three amino acids comprise the linear chain section [702-703].

Polymyxins are potent antimicrobials that are effective against Gram-negative bacteria [147-150]. The lipopeptides are administered in hospital settings as last-line antibiotics to treat infectious Gram-negative bacterial infections [704-709]. The intravenous application of polymyxin medications is reserved for the most potent and resistant strains of infectious Gram-negative bacteria partly because the antibiotics are considered to be relatively neurotoxic and nephrotoxic [710-716] and partly to suppress the proliferation of multidrug resistant genes [606-612]. The inappropriate application of the polymyxin lipopeptides has the potential to damage renal and neural tissues and at the same time produce extensively drug-resistant strains of Gram-negative bacteria.

It is now well established that polymyxin lipopeptides can kill Gram-negative bacteria by binding to and breaking down the Gram-negative bacterial outer membrane. Polymyxin molecules initially bind to the Gram-negative bacterial outer membrane as the positively charged Dab residues interact with the negatively charged LPS lipid phosphate groups [717-720]. Studies of polymyxin nonpeptide suggest that the acyl chain moiety also affects the membrane breakdown processes. Polymyxin nonapeptide lacks a terminal acyl chain moiety and the molecule is able to bind cationic bacterial membrane surfaces but it is unable to kill pathogenic bacteria [721-724]. The inability of polymyxin nonapeptide to kill pathogenic bacteria indicates that the acyl tail component contributes to the disruption of Gram-negative bacterial cell membranes and this suggests that polymyxin lipopeptides affect Gram-negative bacteria through detergent-like action. It is assumed that the acyl chain portion dissolves into the hydrophobic core of bacterial membranes and that this process disrupts the integrity of the lipid bilayer [725]. It is quite interesting therefore, that in 2018 Lakey et al. used a combination of neutron reflectometry and infrared spectroscopy to show that

polymyxin B acyl chain insertion depends on the phase transition of LPS lipids from the gel to the liquid crystalline state [144].

While the precise antimicrobial interactions that are responsible for Gram-negative bacterial outer membrane breakdown processes are still debated, molecular dynamics simulations are increasingly providing new and interesting molecular level insights that can help us to understand the antibacterial action of polymyxin AMPs. One of the first pioneering publications came from the Khalid group [328] when they revealed, through the application of the GROMOS 53A6 united-atom molecular dynamics simulation forcefield [561-562], that PMB1 molecules affect the movement of LPS lipids in the Gram-negative bacterial outer membrane and additionally, that PMB1 molecules can decrease the inner cytoplasmic bacterial membrane width [328]. Santos et al. later went on to show that the binding of polymyxin molecules to Gram-negative bacterial outer membrane mimetics promotes cation displacement [243] and at the same time, that the antimicrobial promotes spontaneous membrane curvature generation when it interacts with the bacterial membrane mimetic surface. Khondker et al. have also performed all-atom molecular dynamics simulations to better understand how the mobilized colistin resistance (mcr-1) gene confers resistance to colistin, also known as polymyxin E [726]. The mcr-1 phenotype is known to increase membrane packing and at the same time, decrease membrane charge within the Gram-negative bacterial outer membrane. Through the combination of X-ray diffraction analyses, molecular dynamics simulations, electrochemistry, and leakage assays it was shown that increasing membrane surface charge promotes polymyxin molecular penetration and membrane damage, whereas increasing lipid packing decreases penetration and damage.

The undesirable neurotoxic and nephrotoxic effects [710-716] of the polymyxin peptides on mammalian cell membranes have prompted scientists to conduct molecular dynamics simulations to better understand how polymyxin molecules interact with mammalian cell membranes. The SLipids molecular dynamics simulation forcefield [727] was paired with X-ray

diffraction and electrochemistry experiments to understand how polymyxin molecules disrupt mammalian cell membranes [728]. It was found that polymyxin clusters induced bilayer indentation and increased water permeation when they interacted with membranes that were depleted of cholesterol molecules (Figure 19B). The multicomponent membranes were significantly more mechanically robust when they contained high concentrations of cholesterol molecules and significantly more prone to become damaged when they were depleted of cholesterol molecules (Figure 19C). There was less bilayer indentation and less water permeation when the cholesterol content was high and this result suggests that cholesterol molecules can suppress the undesirable neurotoxic and nephrotoxic properties of polymyxin peptides.

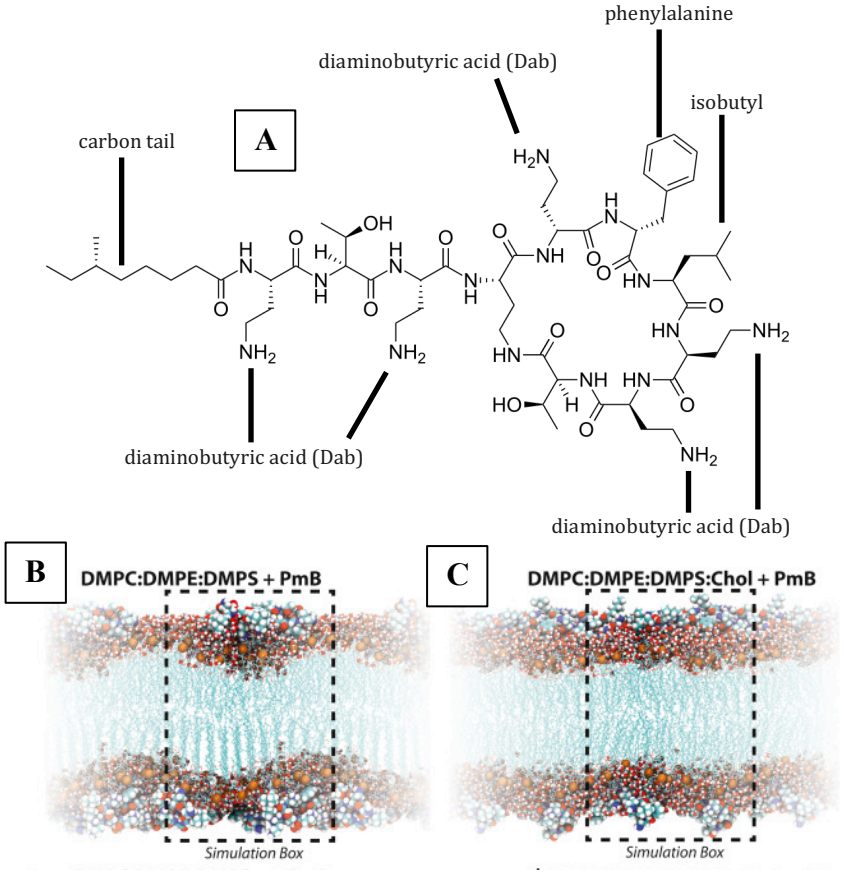

Figure 19. The structure and simulations of the Polymyxin B antimicrobial peptide. (A) The lipopeptide contains a cyclic component that is made of seven amino acids and a non-cyclic section that contains three amino acids with terminal fatty acid chain moiety. The lipopeptide contains five cationic diaminobutyric acid (Dab) residues that impart a net (+5) positive charge to the molecule and this positive electrostatic charge promotes PMB1 interactions with anionic lipids. The fatty acid chain, isobutyl group, and phenylalanine side chains confer hydrophobicity and they promote PMB1 interactions with hydrophobic acyl chain moieties. (B-C) Results from molecular dynamics simulations. The cholesterol concentration affected how the simulated PMB1 peptides interacted with the multicomponent membranes. There was indentation of the bilayers and an overall increase in permeability when the cholesterol content was zero (B). There was significantly less membrane damage when the membranes contained high concentrations of cholesterol (C). The water molecules are red and white, the lipid tails are thin cyan strands, the phosphate groups are orange and the polymyxin molecules are represented using a space-filling van der Waals model. The image sources are: Wikipedia Commons and 10.1016/j.bpj.2017.09.013 (DOI) [728].

Chapter 2: Computational Methods

2.1 Molecular Dynamics

Molecular dynamics simulations consist of the numerical, step-by-step, resolution of the classical equations of motion [729-730], which is described by the equation:

$$\boldsymbol{f}_i = -\frac{\partial}{\partial \boldsymbol{r}_i}\mathcal{U}(\boldsymbol{r}^N)$$

Equation 1

The force $\boldsymbol{f}_i$ acting on each atom is determined from the potential energy of the system $\mathcal{U}(\boldsymbol{r}^N)$ where $\boldsymbol{r}^N = (\boldsymbol{r}_1, \boldsymbol{r}_2 \ldots \boldsymbol{r}_N)$ is the set of N atomic coordinates. The movement of the atoms is simulated by numerically solving Newton's equations of motion:

$$\frac{d^2\boldsymbol{r_i}}{dt^2} = \frac{\boldsymbol{f}_i}{m_i}$$

$$\frac{d\boldsymbol{r_i}}{dt} = \boldsymbol{v_i} \quad ; \quad \frac{d\boldsymbol{v_i}}{dt} = \frac{\boldsymbol{f}_i}{m_i}$$

Equation 2-4

where m_i and $\boldsymbol{v}_i$ are atomic mass and velocity values. By initially defining the potential energy of a simulation system the force acting on the constituent atoms can be resolved, enabling the calculation of updated atomic positions, velocities, accelerations etc. By iteratively updating the position and physical properties of the system particles and the associated total potential energy, the time-dependent trajectory of a biological system can be determined.

In conventional molecular dynamics simulations, the potential energy function is described by a conservative forcefield, which accounts for non-bonded and bonded interactions but ignores electronic transitions. The

conventional molecular dynamics simulation forcefields are a function of atomic positions that discount explicit electronic transitions, although approximations are made for dispersion forces. For a more realistic simulation of biological processes, electronic transitions can be computed through the use of computationally demanding simulation methods that solve the time-dependent electronic Schrödinger equation self-consistently with the classical equations of motions for atoms [731-732].

2.2 Non-Bonded Potentials

The total potential energy of conventional molecular dynamics simulation forcefields consist of a bonded component, which accounts for intramolecular motions and a non-bonded component that includes a van der Waals and Coulomb potential, but additional restraining and/or external forces can also be included. The non-bonded component is derived from the addition of 1-body, 2-body, 3-body…*N*-body terms:

$$\mathcal{U}_{non-bonded}(\boldsymbol{r}^N) = \sum_i u(\boldsymbol{r}_i) + \sum_i \sum_{j>i} v(\boldsymbol{r}_i, \boldsymbol{r}_j) + \ldots$$

Equation 5

The $u(\boldsymbol{r})$ term represents the effects of an externally applied potential field or the effects of the simulation walls; the term is discounted in bulk simulations and in simulations where periodic boundary conditions are applied. For the sake of brevity and a reduction in computational complexity, molecular dynamics programs conventionally focus on the pair potential $v(\boldsymbol{r}_i, \boldsymbol{r}_j) = v(\boldsymbol{r}_{ij})$ while neglecting three-body and higher order interactions.

The van der Waals interactions are generally simulated with the Lennard-Jones potential [733]:

$$v_{LJ}(r) = 4\varepsilon\left[\left(\frac{\sigma}{r}\right)^{12} - \left(\frac{\sigma}{r}\right)^{6}\right]$$

where r represents the distance between the two interacting atoms, σ is the distance where the potential reaches its minimum and ε is the well depth (Figure 20A). The r^{-6} component of the equation approximates the transient attractive interactions that exist between induced dipoles, while the r^{-12} component attempts to account for the repulsive interactions that arise at short distances, where occupied electron orbitals would tend to overlap. The Lennard-Jones parameters are determined for atoms in different chemical environments (hybridization, aromaticity etc.) to enable the simulation of diverse sets of biomolecules.

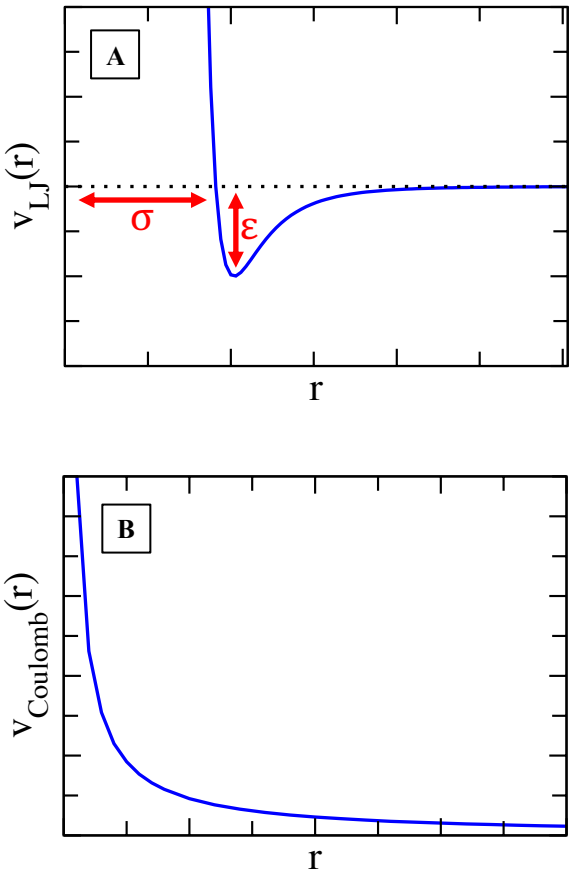

Figure 20. Schematic representation of the non-bonded interaction energy term components. (A) Lennard-Jones component that is used to approximate repulsive electron overlap forces at short-range, and attractive dispersion forces at long-range. The well depth is provided by ε, and σ is the distance where the potential reaches its minimum. (B) Coulombic interaction energy experienced by two point charged particles. Coulomb

forces are appreciable at both short- and long-ranges given that they decay according r^{-1}, where r is the distance between two charged particles.

The choice of 6-12 Lennard-Jones exponents makes simulations computationally efficient, while also providing satisfactory numerical accuracy. But the lack of theoretical justification for the Lennard-Jones potential can warrant the use of alternative mathematical functions to simulate attractive dispersion forces at long ranges and repulsive electron orbital overlap forces at short ranges. The van der Waals interactions can be expressed more generally by the Mie-potential [734-736]:

$$\mathcal{v}_M(r) = \left(\frac{n}{n-m}\right)\left(\frac{n}{m}\right)^{m/(n-m)} \varepsilon\left[\left(\frac{\sigma}{r}\right)^n - \left(\frac{\sigma}{r}\right)^m\right]$$

Equation 7

The exponents n and m can be varied to enable flexible fine-tuning of the steepness of the attractive and repulsive domains of the pairwise potential. Likewise, the Buckingham exponential-6 function [737] can be used in place of the Lennard-Jones potential since it provides a softer repulsive exponential term that is more computationally demanding, but in better accordance with electronic structure theory:

$$\mathcal{v}_B(r) = \varepsilon\left[\frac{6}{\alpha-6}\exp\left(\alpha\left[1-\frac{r}{\sigma}\right]\right) - \frac{\alpha}{\alpha-6}\left(\frac{\sigma}{r}\right)^6\right]$$

Equation 8

Here, α is a free dimensionless parameter that has been optimized to reproduce a realistic interatomic potential. Soft-core van der Waals potential energy functions are sometimes [738-741] used when alchemically transforming molecules, during thermodynamic integration calculations and during energy minimization simulation steps to keep the pairwise interaction energy finite. The soft-core van der Waals potential energy functions have the general functional form:

$$v_{SC}(r,\lambda) = 4\varepsilon\lambda^{a}\left[\left(\frac{1}{\alpha(1-\lambda)^{b}+(r/\sigma)^{c}}\right)^{12/c} - \left(\frac{1}{\alpha(1-\lambda)^{b}+(r/\sigma)^{c}}\right)^{6/c}\right]$$

Equation 9

Here, α controls the softness of the potential energy function, λ is the linear scaling term, and a, b, and c are exponents that control how rapidly the softness is removed. Soft-core potential energy functions are now a part of all the major biomolecular simulation packages. GROMACS and AMBER simulation packages [742-745] provide soft-core van der Waals potential energy functions where $a = 1$, $b = 1$, and $c = 6$, while NAMD [746-747]and CHARMM [748-749] packages provide soft-core potential energy functions where $a = 1$, $b = 1$, and $c = 2$.

The Coulomb potential is used to model the energy between point charge particles that are located at atomic nuclei. The potential energy is described by the equation:

$$v_{Coulomb}(r) = \frac{Q_1 Q_2}{4\pi r \in_0}$$

Equation 10

where Q_1 and Q_2 quantify the charge of two point particles that are separated by a distance of r and $\in_0$ is the permittivity of free space (Figure 20B). Most molecular dynamics simulation packages discount dispersion and electrostatic forces between atoms that are separated by only one or two covalent bonds, however atoms that are separated by at least three bonds are included, albeit with scaling factors to temper the magnitude of the interaction energies. For example, the OPLS (Optimized Potential for Liquid Simulations) forcefield employs a 0.5 scaling factor for the dispersion and electrostatic energies arising from so-called 1-4 interactions [170,750].

The derivation of appropriate partial point charges for molecular dynamics simulations is necessary for accurately mimicking the interactions of all biomolecules. Electrostatic charge is distributed throughout a given simulation biomolecule to accurately mimic data from high-level quantum chemical (*ab initio*) calculations and data obtained from sophisticated experimental analyses [751]. For example, *ab initio* calculations at the LMP2/cc-pVTZ(-f)/HF/6-31G(d) theory level were conducted to optimize partial point charge values for ionic liquids in the OPLS-AA molecular dynamics simulation forcefield [752]. Anions were optimized at the Hartree-Fock (HF) theory level [236] using the 6-31G(d) basis set with single-point energy calculations using the local Møller-Plesset (MP) second-order perturbation method [753] with the correlation-consistent polarized valence cc-pVTZ(-f) basis set [754]. Multiple quantum chemical calculations were used to determine appropriate partial point charge values for each biomolecule, since multiple low-energy configurations exist for each biomolecule due primarily to torsion rotations. Electrostatic potential charges were determined for all of the available energy-minimized stationary points and an average partial charge value for each atom type was determined by appropriately weighting the contribution of each ground-state structure to the overall conformational population. Comparable parameterization schemes have been adopted for the derivation of the OPLS-AA menthol simulation forcefield [755] and for other AMBER [756] and GROMOS forcefields [757-758] but refinement with reference experimental data is also common [759]. The geometry of the menthol molecule was optimized at the HF/6-31G* theory level for the reparameterization of the OPLS-AA menthol forcefield. Following that, single point calculations were performed at the MP2 level using the aug-cc-pVTZ basis set with the f-type function excluded. The reparameterization enabled more accurate simulation of not just the static properties of liquid menthol but also transport properties including the shear viscosity.

The use of partial point charge values is useful for enabling the simulation of diverse biomolecules in standard nonpolarizable (fixed charge) molecular

dynamics simulations, but the lack of theoretical justification for the complete omission of electronic motion can warrant the use of more complex polarizable simulation forcefields [760-762]. Methods can be used to approximate the motion of electrons and ensure that charges within simulated biomolecules display some non-negligible response to their encompassing electrostatically active environment. To be clear, the methods make approximations for electronic motion but the level of theory differs markedly from *ab initio* quantum chemical calculations. The Drude oscillator model mimics induced electronic polarization by introducing an auxiliary particle attached to each polarizable atom via a harmonic spring [763-766]. Drude polarizable forcefields are a simple and intuitive improvement on conventional nonpolarizable forcefields since they preserve the simple particle-particle Coulomb electrostatic interactions that are common in GROMOS, AMBER, OPLS, etc. The AMOEBA (Atomic Multipole Optimized Energetics for Biomolecular Applications) forcefield is considerably more complex and aside from having a different functional form for the bonded potential to most fixed charge molecular dynamics simulation forcefields, it also replaces the fixed partial charge model with polarizable atomic multipoles through the quadrupole moments [767-768]. Rather than merely replicate interaction energies alone, the AMOEBA forcefield replicates molecular polarizabilities and electrostatic potentials. The use of permanent dipoles and quadrupoles enables the AMOEBA forcefield to effectively change molecular charge distributions in response to changing or heterogeneous molecular environments. The energy correlations between AMOEBA and MP2 energies for water-sulfate anion clusters were determined to have correlation coefficients of ~0.9 and predicted AMOEBA solvation free energies had correlation coefficients of ~0.9 when compared with reference experimental values [767]. Polarizable forcefields have been used to simulate relatively few lipid membranes but pronounced differences are already evident e.g. large differences in the dipole across the water/lipid interface between fixed charge and polarizable forcefield simulations [769-771].

2.3 Bonded Potentials

Quantum-chemical calculations are usually performed for most molecular dynamics molecules to estimate appropriate electron density distributions that are then modeled as partial point charges according to Equation 10. The intramolecular bonding potentials are modeled as:

$$\mathcal{U}_{bonded}(r) = \frac{1}{2}\sum_{bonds} k_{ij}^{r}\left(r_{ij} - r_{eq}\right)^2 + \frac{1}{2}\sum_{bend\ angles} k_{ijk}^{\theta}\left(\theta_{ijk} - \theta_{eq}\right)^2 + \frac{1}{2}\sum_{improper\ dihedrals} k_{ijkl}^{\omega}\left(\omega_{ijkl} - \omega_{eq}\right)^2 + \frac{1}{2}\sum_{proper\ dihedrals} k_{ijkl}^{\phi}\left(1 + \cos\left(m\phi_{ijkl} - \gamma_m\right)\right)$$

Equation 11

Here, k_{ij}^{r}, k_{ijk}^{θ}, k_{ijkl}^{ω} and k_{ijkl}^{ϕ} are force constants while r_{eq}, θ_{eq} and ω_{eq} are the equilibrium bond distance, equilibrium valence angle and equilibrium improper torsion angle; m and γ_m are the multiplicity and phase of the proper torsion/dihedral angle term. The value of $1/2$ is placed before each of the bonded potential energy terms because the atomic force is the negative derivative of the scalar potential energy function $\mathcal{U}_{bonded}(r)$. The bonds between adjacent atoms in a molecular framework are usually modeled by a harmonic potential with specified equilibrium separation (Figure 21A), although alternative mathematical functions are also available. The bending angles between two successive bond vectors (or three directly bonded atoms) are described by a harmonic potential with an equilibrium valence angle (Figure 21B). The improper torsion angles usually address out of plane motions such as planarity of aromatic rings; for example, a harmonic potential can be applied to control the angle between two planes (*ijk*) and *(jkl)* where atoms *i, j, k,* and *l* are neighboring atoms (Figure 21C). The proper torsion angle term controls the flexing of planes (*ijk*) and *(jkl)* formed of a consecutively bonded quadruple of atoms (Figure 21D). The proper torsion

angle energy is typically modeled as a Fourier cosine series expression, the number of terms for a given torsion angle ranges between one and six depending on the complexity of the energy profile [772-773].

Significant work is undertaken to determine appropriate bonded parameters for molecular dynamics simulation forcefields. Force constants and equilibrium positions are optimized using reference data from quantum chemical calculations and experimental analysis, most commonly X-ray and neutron scattering studies [750,774-775]. Take for example, the General Amber ForceField (GAFF) [756], which was parameterized for simulations of small organic molecules. GAFF used three sources of information for the parameterization of r_{eq} values: (i) computationally demanding *ab initio* calculations (MP2/6-31G*); (ii) X-ray and neutron diffraction data; and (iii) the suite of Amber protein forcefields [775-776]. The k_{ij}^{r} force constants were derived by designing model molecules and performing high-level *ab initio* vibrational frequencies analysis. The same three data sources were used for the calibration of angle parameters, i.e. the suite of Amber molecular dynamics simulation forcefields, MP2/G-31G* calculations and crystal data. Data were initially collated for different atom types and subsequently averaged to determine appropriate values of θ_{eq}. The torsion energy angle parameters were determined through electronic structure calculations carried out at the MP4/6-311G(d,p)//MP2/6-31G* level. The *Parmscan* automatic engine [777] was used to derive an angle potential that could accurately reproduce the reference *ab initio* rotational profile. The suite of reference AMBER protein forcefields were themselves parameterized according to similar procedures [234]. Equilibrium bond lengths and bond angles were taken from reference crystal structures and adapted to match the normal mode frequencies of peptide fragments, while the torsion force constants were optimized to match torsional energy barriers taken from quantum chemistry calculations.

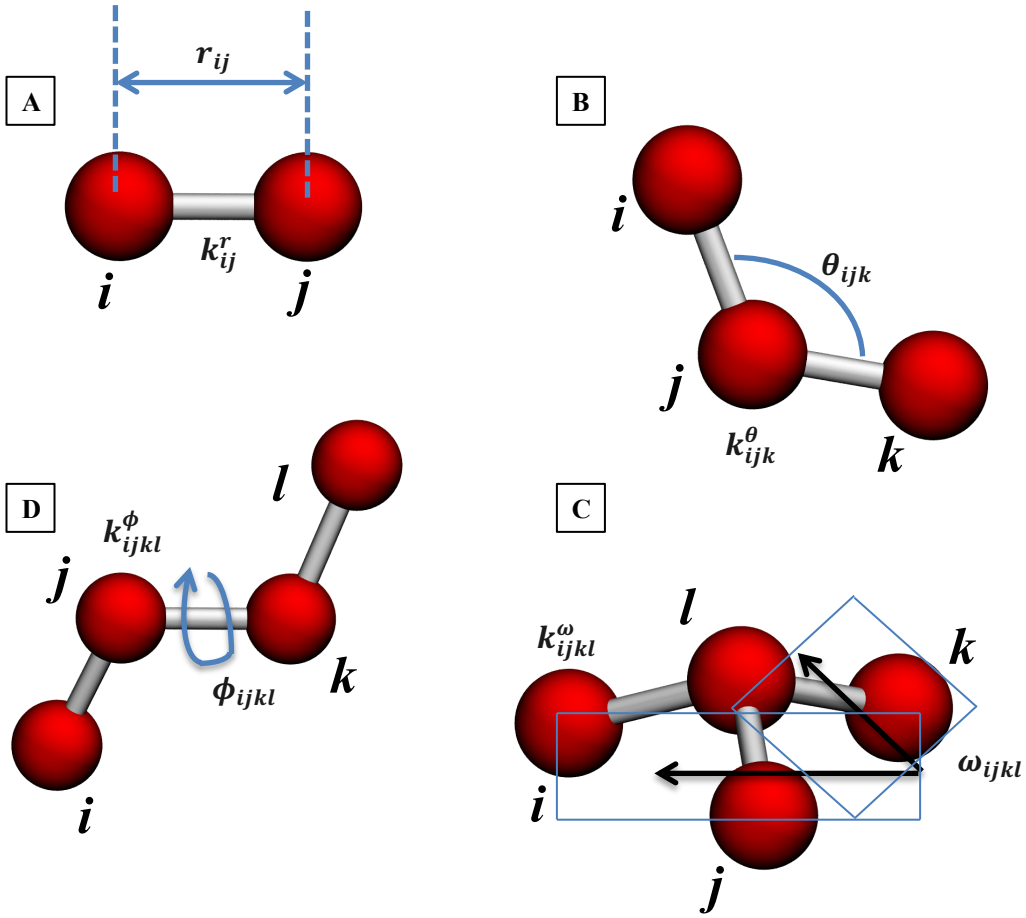

Figure 21. The components of the molecular dynamics forcefield bonded potential. (A) The component for bond stretching: atoms *i* and *j* oscillate about an equilibrium bond distance r_{eq}. (B) The component for valence angles: atoms *i, j,* and *k* flex about an equilibrium valence angle θ_{eq}. (C) The improper torsion angle component: the angle between the two intersecting planes (*ijk*) and (*jkl*) oscillates about an equilibrium improper torsion angle ω_{eq}. (D) The proper dihedral component describes the angular spring between the planes (*ijk*) and (*jkl*) that is formed of four consecutively bonded atoms.

Despite the simple functional form of bonded interaction energy components in class I force fields (including AMBER, OPLS, and GROMOS), they are combined to produce acceptable predictions of thermodynamic data for biophysical systems. To more accurately simulate nanoscopic molecular properties such as molecular geometries or vibrational frequencies, alternative functional forms can be used to model bond stretching motions. In class II force fields for example, bonded interaction energy terms are more

commonly modeled using anharmonic functions such as the Morse potential [778]:

$$\mathcal{U} = D_e\{1 - \exp[-\beta(r - r_{eq})]\}^2$$

Equation 12

where D_e is the dissociation energy and β is an adjustable parameter defined as $\beta = \sqrt{k_{ij}^r/(2D_e)}$. The stretching energies can alternatively be calculated by including higher order polynomial terms and cross-terms to account for the coupling between internal atomic coordinates.

Forcefields specify the size of force constants and sometimes include additional cross-terms for enhanced chemical accuracy. The forcefields and their associated strength parameters are carefully calibrated using quantum mechanical calculations, vibration frequency, thermophysical, and phase coexistence data. The selection of reference data for forcefield calibration is dependent on the intended application of the simulation program.

Scientists do in general, progressively refine molecular dynamics simulation forcefields toward some set of reference experimental data [163]. The progressive fine-tuning of molecular dynamics simulation forcefield parameters enables newer generation forcefields to more accurately reproduce experimental data that has been collated for lipid membranes and proteins. Lindorff-Larsen et al. performed a systematic review to compare eight different protein forcefields with idealized reference experimental data sets [779]. Frist, through the use of experimental NMR data [780-782], the group examined the capacity of each forcefield to describe the structure and fluctuations of folded proteins. Second, the group quantified potential biases toward different secondary structure types through comparison with experimental and simulation data. Third, the group evaluated the capacity of each molecular dynamics simulation forcefield to fold two small proteins, one an α-helix and the other a β-sheet structure (ubiquitin and GB3) [783-786]. It was found through comparative analysis that the simulation forcefields had

improved with time and that newer generation forcefields provided increasingly accurate descriptions of dynamic protein properties. Martin-Garcia et al. [787] stated similarly that newer, reparametrized molecular dynamics simulation forcefields, including variants of AMBER and OPLS, were able to accurately reproduce the displacement properties of proteins (e.g. ubiquitin and Protein G) when compared with reference experimental NMR data [788-791]. However, it was reported that in some instances reparametrizing the molecular dynamics simulation forcefields did not have the intended effect. For example, proteins had similar balances of helical and coil conformations in simulations that were conducted with older less accurate forcefields, and newer generation forcefields that had apparently been specifically reparametrized to ensure that molecular dynamics simulations provided a more accurate balance of the different (helical and coil) protein conformations.

Molecular dynamics simulation forcefields have also been progressively refined to more accurately mimic the properties of lipids and biological membranes. The suite of GROMOS molecular dynamics simulation forcefields is an illustrative example [59]. The now quite dated GROMOS87 forcefield parameters were originally optimized based on calculations of the crystal structures of hydrocarbons and amino acids [792]. The original GROMOS87 forcefield parameter set was later modified and released as the newer and improved GROMOS96 forcefield. The GROMOS96 forcefield was improved in different ways, e.g. aliphatic CH_n groups were reparametrized on the basis of simulations of model liquid alkanes using long (1.4 nm) nonbonded cutoff radii [757]. Newer generation forcefields were optimized after this to make GROMOS forcefields even more accurate for simulating various proteins, sugars, and lipids. The GROMOS54A7 forcefield included adjusted torsional angle terms to more accurately mimic helical propensities [793], the GROMOS53A5 was optimized to reproduce the thermodynamic and solvation free enthalpies of small molecules, the GROMOS53A6 was adjusted to better reproduce hydration free enthalpies in water [794], etc. Lipid forcefields were progressively refined to more accurately reproduce thermodynamic

parameters and other forms of reference experimental data. Fluid membranes were commonly simulated under the isothermal-isobaric ensemble (NPT) and compared with reference area per lipid, membrane thickness, and order parameter data that were primarily determined from X-ray and neutron scattering studies; for example, see: [551,553].

2.4 Atomistic Forcefield

Class I force fields (AMBER, OPLS and GROMOS etc.) that are geared towards the simulation of large biomolecular systems are optimized using a combination of quantum chemical calculations and thermophysical and phase coexistence data. Despite these shared approaches for optimizing simulation parameters, class I force fields can differ markedly in their representation of simulated biomolecules and thereby the number of pairwise intermolecular interactions computed per simulation time step. The constituent atoms of the simulated biomolecules can be explicitly represented to accurately reproduce the complex surface chemistry of proteins and lipids. Within CHARMM for example, carbon and hydrogen atoms are explicitly represented (Figure 22A) and membrane protein dynamics are ordinarily accurately reproduced. Alternatively, neighboring carbon and hydrogen atoms can be clustered into single interaction centers within united-atom packages such as the GROMOS suite of forcefields [793-794], which represent CH_2 and CH_3 hydrocarbon units as single interaction centers (Figure 22B) and thereby reduce the number of computationally demanding pairwise interaction calculations that are computed per time step. As a consequence of reducing the number of interatomic interactions, united-atom forcefields are typically less accurate and less transferable than their all-atom counterparts. For complex biomolecules a compromise is sometimes made e.g. acyl tails can be modeled using a united-atom approach, while aromatic and polar hydrogen atoms are explicitly represented [328].

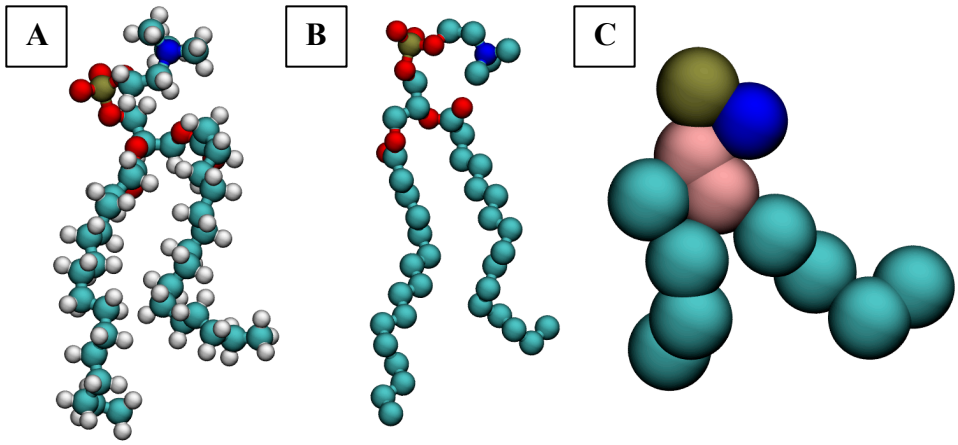

Figure 22. Some of the different resolution levels that can be used in molecular dynamics simulations. (A) An all-atom model for the DPPC lipid. The carbon (cyan), oxygen (red), nitrogen (blue), and hydrogen (white) atoms are represented here explicitly. (B) The GROMOS united-atom forcefield model for the DPPC lipid. The hydrogen atoms are clustered into neighboring carbon atoms to produce a less computationally demanding representation for the DPPC lipid. (C) The coarse-grained Martini forcefield model for the DPPC lipid. Here, multiple neighboring heavy atoms have been clustered into single pseudo-atom interaction centers to substantially reduce the computational load and make the lipid simulations less computationally demanding. The Martini beads have the following color scheme: carbon tail (cyan), glycerol (pink), phosphate (brown), and choline (blue).

2.5 Coarse-Grained Forcefield

Coarse-grained forcefields achieve further reductions in computational complexity by clustering multiple bonded atoms into single interaction centers or "pseudo-atoms" (Figure 22C). By averaging out expensive atomistic detail in this way, coarse-grained forcefields significantly simplify the description of biological systems [795-796], enabling scientists to access spatio-temporal scales that are beyond the scope of CHARMM and GROMOS. Coarse-grained forcefields expand the scope of molecular dynamics simulation methods and reduce the division between molecular modeling programs and conventional experimental techniques. Coarse-grained forcefields are more suitable for exploring protein interactions that occur on mesoscopic length scales and microsecond timescales such as the aggregation of multiple membrane proteins in planar and non-planar lipid geometries [351,496,797-798].

The Martini forcefield [799] was specifically calibrated for the simulation of proteins and lipids and it has been used to simulate different multicomponent membranes. The Martini forcefield is parameterized in a systematic way: non-bonded interactions are based on the reproduction of experimental partitioning free energies, whereas bonded interactions are derived from reference all-atom and united-atom simulations. The model primarily adopts a four-to-one heavy atom mapping scheme to reduce the computational load i.e. on average four heavy atoms and associated hydrogen atoms are represented as a single interaction center, but three-to-one mapping schemes were also made available for the representation of ring-like geometries. Based on the chemical nature of the constituent atoms, the coarse-grained particles are assigned a specific particle type: polar (P), non-polar (N), apolar (C) and charged (Q). Within each category, subtypes are further distinguished by their hydrogen bonding capability or their degree of polarity for the fine-tuning of intermolecular interactions. It is important to note here that the Martini forcefield has now been employed to a study a range of other molecules in addition to proteins and lipids [355,406,800-809].

The primary strength of the Martini coarse-grained forcefield is its capacity to bridge the timescale and length-scale gap between computational and experimental methods using a relatively simple and broadly applicable method for mapping diverse biomolecules from atomistic to coarse-grained resolution [174]. Users can portion complex (atomistic) macromolecules into smaller sub-sections and assign each constituent subdomain a Martini bead type classification based on its specific atomistic composition. For example, one might initially portion a phospholipid headgroup into constituent phosphate, choline, and glycerol sub-sections and assign each segment the following Martini bead type classifications: Qa, Q_0, and Na [428,810]. Rather than optimize the non-bonded parameters of each coarse-grained bead themselves, users can make use of so-called “Martini building-blocks” that have already been carefully calibrated to reproduce experimental partitioning free energies by Marrink et al. [799]. The scope of the Martini

forcefield increased as newer, smaller beads were added to the Martini building-block library including for example, the Tiny Martini bead type that enabled more accurate reproduction of DNA conformational characteristics [805]. The Martini forcefield was originally parameterized for simulations of proteins and lipids alone but is now used to simulate carbon nanotubes [802,811], dendrimers [812-813], C_{60} nanoparticles [301,801], graphite monolayers [800], synthetic hydrocarbon polymers [355], chitin fibers [803], carbohydrates [804], DNA [805], RNA [807], alcohol [406], and more. Users can develop bespoke Martini models by mapping atomistic structures to Martini beads and subsequently optimize the bonded parameter sets through comparisons with reference atomistic simulations.

The second strength of the Martini forcefield is its capacity to reproduce diverse biophysical parameters and provide satisfactory numerical accuracy in biomolecular simulations. There is the reproduction of area per lipid values for most types of phospholipid [814], different components of plasma membrane mimetics [799], and different LPS chemotypes [301,580], to within 0.1 to 0.2 nm^2 of the experimental values. Other than this, the Martini forcefield has been validated through the accurate reproduction of lipid phase diagrams [335], the reproduction of ternary membrane phase behaviour [343-344], the dimerization free energies of transmembrane helices [815] and the capacity of the forcefield to correctly predict protein oligomerization events [115]. There is also the accurate reproduction of the glycophorin A dimer structure [816], the H-NMR quadrupolar splittings of WALP peptides [817], and the relatively accurate binding free energies of pentapeptides at the water-lipid interface [818].

The Martini forcefield can accurately reproduce the partitioning properties of most organic compounds and provide satisfactorily accurate quantitative data for most biomolecular simulations [799,814]. However, there are several limitations that affect the validity of the Martini forcefield and it is important to state some of the most noteworthy inaccuracies here, since the Martini forcefield is used throughout this thesis. First, there is the fact that the Martini

forcefield was parameterized for the fluid phase and is not expected to accurately reproduce the packing, or physical properties of the solid phase [819]. The solid phase generally appears to be too stable in Martini forcefield simulations and this leads to well-known inaccuracies including incorrect freezing temperatures for water [820] and the inaccurate simulation of solid-fluid interfaces. The Lennard-Jones parameters for Martini water bring it into the solid state region of the Lennard-Jones phase diagram (at points of atmospheric pressure and temperature) [819] and in previous publications it was ascertained that the freezing point of Martini water can be as high as 290 ± 5 K [799,814,821]. One can impede Martini water freezing processes by reducing long-range ordering effects, removing obvious ice formation nucleation sites or alternatively, by interspersing so-called "Martini antifreeze" particles throughout areas of Martini simulation water [819].

Second, the Martini forcefield is unsuitable for simulating the partitioning of charged and polar compounds into low dielectric mediums. Coulombic interactions are screened implicitly with a relative dielectric constant ($\varepsilon_{rel} = 15$) in Martini forcefield simulations to account for the omission of explicit partial point charges [822]. Because of this implicit screening effect, polar molecules have unrealistically weak interaction strengths in nonpolarizable solvents. This has affected for example, the capacity of lipids to create transmembrane water pores when they are dragged through biological membrane mimetics [799].

Third, dynamic timescales tend to be different in coarse-grained and analogous atomistic resolution simulation studies. Coarse-grained simulation forcefields average out expensive atomistic detail, leading to smoother intermolecular interaction energy landscapes and less effective intermolecular friction [795-796]. Based on comparisons between coarse-grained simulations and reference data, the effective time sampled in Martini simulations is thought to be three- to eightfold larger than the *in vivo* scenario [818]. In general, it is recommended that Martini simulation timescales be multiplied by a factor of four because Martini water diffuses approximately

four times too fast when compared with experimental data [823]. The fourfold speed-up factor is a reasonably accurate conversion factor for many biomolecular processes in Martini coarse-grained simulations including the permeation rates of water across lipid membranes [814] and the aggregation of lipids into bilayers [814] or vesicles [742]. However, the conversion factor has not been tested systematically for all classes of biomolecules and its applicability is therefore, somewhat limited. Protein dynamics have not been thoroughly tested and it is possible that a fourfold speedup-factor could be inappropriate for describing the effective timescale of Martini protein-lipid interactions. In general, it is recommended that readers should interpret simulation timescales as being semi-quantitatively accurate [818].

Fourth, the Martini forcefield represents ions as Q type Martini beads, which have integer charge values, either ±1 or 2, and mass values of 72 amu (corresponding to four water molecules) [822]. This implicit presentation of ions can make it difficult to accurately reproduce the interactions of realistic lipids and biological membranes. Coarse-grained Martini cations do not effectively establish hydrogen-bonded water networks and this has repeatedly been reported to undesirably impact the properties of Gram-negative bacterial membrane mimetics in Martini forcefield simulations [151,301,329]. There is less water moving through the core saccharide domain of coarse-grained Martini Gram-negative bacterial membranes and the LPS core saccharide domain tends to be much too compressed if measurements are drawn along the membrane normal axis (*z*-axis) [151,580,824]. These inaccuracies will invariably have some undesirable effects on the forthcoming simulations of coarse-grained bacterial membranes.

Coarse-grained simulations generally provide satisfactorily accurate qualitative data, but it is important to appreciate that quantitative errors and inaccuracies are sometimes unavoidable due to the implicit representation of the simulated ions and biomolecules. Coarse-grained Martini forcefield simulations are generally referred to as being “semi-quantitatively” accurate

[822] and no more, or no less, should be expected from the coarse-grained simulations that are conducted throughout this thesis.

2.6 Periodic Boundary Conditions

Molecular dynamics simulations conventionally consider a relatively small portion of bulk macroscopic systems due to computational constraints and the limitations of modern computer hardware. The relatively small size of the simulation cells can introduce unwanted boundary effects as lipid, protein and solvent molecules explore the simulation cell and interact with the simulation cell walls. One can attempt to reduce these unrealistic edge effects by applying periodic boundary conditions. Here, particles are placed within a unit cell that is replicated to infinity by periodic translations; the particles are able to freely traverse the space-filling box and pass through the box borders unabated (Figure 23) [825]. Each particle interacts with its immediate neighbors (including atoms in replicated cells) provided they satisfy user-defined cutoff criteria. Given that each cell is identical to its translated copies, molecular dynamics programs compute the potential energy for a single representation of the periodic system. Due to the introduction of periodic boundary conditions there is no longer an explicit interaction between the system particles and the unit cell borders and this removes the extraneous influence of the simulation cell walls and effectively enables the reproduction of macroscopic physical phenomena with limited computer resources e.g. the self-assembly of lamellar lipid bilayers that serve as suitable surrogates for macroscopic biological membranes.

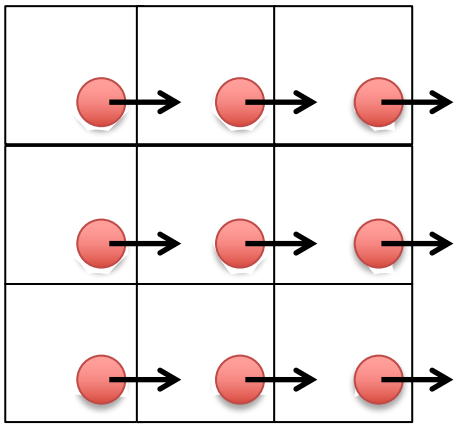

Figure 23. Schematic illustration of a single particle (red circle) passing through the borders of a periodic unit cell (black lines). The use of periodic representations provides a more accurate mimic of bulk systems given the removal of a well-defined, simulation cell boundary. The simulated atoms can freely traverse the space-filling box and as they pass through one border of the unit cell, they instantaneously re-enter through the opposite face.

2.7 Short and Long Interactions

Calculating the nonbonded interactions is generally the most computationally demanding aspect of conventional molecular dynamics simulations. As stated previously, nonbonded interactions are typically decomposed into two components: (i) van der Waals interactions that are used to mimic dispersion and electron orbital overlap; and (ii) explicit electrostatic interactions between partial point charges that are computed according to Coulomb's law. In theory, each particle experiences explicit electrostatic and van der Waals interactions with the entire simulation system (including atoms in replicated cells across periodic boundaries). In practice, approximations are made to reduce the computational load and enable scientists to access larger spatiotemporal scales. The treatment of van der Waals and coulomb forces differs because the van der Waals potential approaches zero rapidly (as r^{-6}) and the electrostatic potential decays relatively slowly (as r^{-1}) [826].

2.8 Short Range Interactions

The coulomb interactions can be computed with the reaction field method [827-828], which assumes a constant dielectric environment beyond a user-defined cutoff distance r_c. For a given dielectric constant of ε_{rf}, the reaction field potential is given as:

$$v_{CRF} = f\frac{q_i q_j}{\varepsilon_r r_{ij}}\left[1 + \frac{\varepsilon_{rf} - \varepsilon_r}{2\varepsilon_{rf} + \varepsilon_r}\frac{r_{ij}^3}{r_c^3}\right] - f\frac{q_i q_j}{\varepsilon_r r_c}\frac{3\varepsilon_{rf}}{2\varepsilon_{rf} + \varepsilon_r}$$

Equation 13

so that the potential reduces to zero at the user-defined cut-off distance. For charged cut-off spheres this corresponds to neutralization with a homogeneous background charge.

Alternatively, the nonbonded potentials can be computed through the use of shift functions that smooth the interaction energies to zero, close to a user-defined cutoff length. The shift functions [829-830] reduce the computational load by effectively discounting the long range nonbonded interactions through the use of cutoff lengths, while simultaneously ensuring that significant truncation errors are not inadvertently introduced; an improvement over straight cut-off methods that can drastically affect system properties. The shift function's effects on the nonbonded interactions must be carefully considered and methods such as Ewald summation [831], must be properly implemented to account for long-range electrostatic interactions that have been left untreated.

The shift function is implemented as:

$$\Phi_\alpha(r) = \frac{1}{r^\alpha} - \frac{A}{3}\left(r - r_{shift}\right)^3 - \frac{B}{4}\left(r - r_{shift}\right)^4 - C; \qquad r_{shift} \le r \le r_{cut}$$

$$\Phi_\alpha(r) = \frac{1}{r^\alpha} - C; \qquad r \le r_{shift}$$

$$A = \frac{\alpha\{(\alpha+1)r_{shift} - (\alpha+4)r_{cut}\}}{r_{cut}^{(\alpha+2)}(r_{cut} - r_{shift})^2}$$

$$B = -\frac{\alpha\{(\alpha+1)r_{shift} - (\alpha+3)r_{cut}\}}{r_{cut}^{(\alpha+2)}(r_{cut} - r_{shift})^3}$$

$$C = \frac{1}{r_{cut}^{\alpha}} - \frac{A}{3}\left(r_{cut} - r_{shift}\right)^3 - \frac{B}{4}\left(r_{cut} - r_{shift}\right)^4$$

Equation 14-18

where α denotes the power for the Coulombic ($\alpha = 1$) and Lennard-Jones ($\alpha = 6{,}12$) terms. The functional form ensures that the nonbonded force is continuous and smoothly decays to zero between r_{shift} and the cut-off distance r_{cut}.

2.9 Long Range Interactions

The electrostatic energy for *N* particles is given by:

$$\mathcal{v} = \frac{f}{2}\sum_{n_x}\sum_{n_y}\sum_{n_{z*}}\sum_{i}^{N}\sum_{j}^{N}\frac{q_i q_j}{\boldsymbol{r}_{ij,\boldsymbol{n}}}$$

Equation 19

where the vector $\mathbf{n} = (n_x, n_y, n_z)$ runs through all the replicated cells of lengths (L_x, L_y, L_z) in the three dimensions. The star indicates that terms with $i = j$ should be omitted when $\left(n_x, n_y, n_z\right) = (0{,}0{,}0)$. The $\boldsymbol{r}_{ij,\boldsymbol{n}}$ term denotes distances between particles within a single simulation cell i.e. not minimum-image distance.

Ewald summation computes the total electrostatic energy for *N* particles by decomposing the slowly converging sum (Equation 19) into two faster converging terms and a constant term:

$$\mathcal{v}_{coulomb} = \mathcal{v}_{direct} + \mathcal{v}_{reciprocal} + \mathcal{v}_{self}$$

$$\mathcal{v}_{direct} = \frac{f}{2}\sum_{i,j}^{N}\sum_{n_x}\sum_{n_y}\sum_{n_{z*}} q_i q_j \frac{erfc(\beta \boldsymbol{r}_{ij,\boldsymbol{n}})}{\boldsymbol{r}_{ij,\boldsymbol{n}}}$$

$$\mathcal{v}_{reciprocal} = \frac{f}{2\pi V}\sum_{i,j}^{N} q_i q_j \sum_{m_x}\sum_{m_y}\sum_{m_{z*}} \frac{exp(-(\pi \boldsymbol{m}/\beta)^2 + 2\pi i \boldsymbol{m}\cdot(\boldsymbol{r}_i - r_j))}{\boldsymbol{m}^2}$$

$$\mathcal{v}_{self} = -\frac{f\beta}{\sqrt{\pi}}\sum_{i}^{N} {q_i}^2$$

Equation 20-23

Here, $\mathbf{m} = (m_x, m_y, m_z)$ and β is an adjustable parameter whose magnitude determines the relative weighting of the direct and reciprocal components of the electrostatic energy. The cost of computing the direct space sum is low, but the reciprocal sum scales as N^2 and therefore the Ewald summation becomes intractable for large simulation systems.

Molecular dynamics programs make use of the Particle mesh Ewald (PME) summation method [832] to reduce the computational load and enable the calculation of the reciprocal sum. PME scales as $N\log(N)$ and is therefore more suitable for simulating medium-to-large systems. PME summation methods assign explicit charge points to a grid that is Fourier transformed with 3D FFT algorithms instead of implicit Fourier transformations.

2.10 Energy Minimization

If the starting configuration for a simulation system is far from equilibrium the inter-atomic forces may be excessively large causing the simulation to become unstable. Energy minimization algorithms can be used to optimize molecular positions and orientations and thereby effectively reduce the total system energy. The energy minimization process reduces unfavorable inter-atomic interactions and removes undesirable steric clash. The optimization algorithms adjust atomic positions to locate minima in the complex

conformational landscape of atomistic or coarse-grained systems. Popular minimization procedures are the steepest descent [833], conjugate gradient [834], and limited-memory Broyden-Fletcher-Goldfarb-Shanno (L-BFGS) [835] optimization algorithms. Energy minimization is sometimes performed with soft-core van der Waals potential energy functions that help to keep pairwise interaction energies finite when conventional energy minimization algorithms would lead to endpoint errors.

The steepest descent method is a robust and easy to implement first-order iterative optimization algorithm. Initially the forces $\boldsymbol{F}$ and potential energy are computed for a given simulation system using a selected simulation forcefield, new positions are subsequently determined using:

$$\boldsymbol{r}^{N+1} = \boldsymbol{r}^{N} + \frac{\boldsymbol{F}_n}{max(|\boldsymbol{F}_n|)} h_n$$

Equation 24

where h_n is the (user-defined) maximum atomic displacement and $\boldsymbol{F}_n$ is the negative gradient of the potential energy function $\mathcal{U}(\boldsymbol{r}^N)$. The forces and energy for the new configuration are resolved and the update is accepted if there is an overall reduction in total potential energy. The algorithm is stopped after a selected number of iterations have been performed or alternatively when the maximum absolute values of the force components are smaller than an arbitrarily defined value [836].

2.11 Integrators

The calibrated force fields can in theory, be used to determine the force acting on each particle within the simulation system and thereby generate a time-dependent trajectory:

$$\boldsymbol{f}_i = -\frac{\partial}{\partial \boldsymbol{r}_i} \mathcal{U}(\boldsymbol{r}^N) = m_i \frac{d^2 \boldsymbol{r}_i}{dt^2}$$

Equation 25

Given however, that the motion of each particle is affected by the position and velocity of all of its neighbors, a numerical finite difference approach must be adopted to overcome the demands of an otherwise intractable many-body problem. The equations of motion are integrated using a small time step Δt while the acceleration ($\boldsymbol{a}$) of each particle is assumed to remain constant. The series of time dependent atomic positions (or the molecular trajectory) is obtained by integrating Newton's equations of motion with respect to time.

$$\boldsymbol{a}(t) = \frac{d^2\boldsymbol{r}(t)}{dt^2}$$

$$\boldsymbol{a}(t)t + \boldsymbol{v}(0) = \frac{d\boldsymbol{r}(t)}{dt}$$

$$\frac{1}{2}\boldsymbol{a}(t)t^2 + \boldsymbol{v}(0)t + \boldsymbol{r}(0) = \boldsymbol{r}(t)$$

Equation 26-28

By integrating Equation 26 from 0 to t we obtain Equation 27, further integration produces Equation 28, which is the Taylor series for atom displacement and is the basis of all molecular dynamics integration methods. Assuming that the forces acting on a particle are constant during a finite time step, new positions at a subsequent step can be determined from the positions, velocities and forces at the previous step. The Verlet algorithm [837] calculates atomic positions at time t + Δt using the current locations of the system particles and their positions during the preceding time step.

$$\boldsymbol{r}(t + \Delta t) = \boldsymbol{r}(t) + \boldsymbol{v}(t)\Delta t + [\boldsymbol{a}(\Delta t)^2/2]$$

$$\boldsymbol{r}(t - \Delta t) = \boldsymbol{r}(t) - \boldsymbol{v}(t)\Delta t + [\boldsymbol{a}(\Delta t)^2/2]$$

$$\boldsymbol{r}(t + \Delta t) = 2\boldsymbol{r}(t) + \boldsymbol{a}(\Delta t)^2 - \boldsymbol{r}(t - \Delta t)$$

Equation 29-31

The Verlet algorithm is straightforward and the storage requirements are modest, however the integration algorithm is of moderate precision and explicit particle velocities are not calculated during the update procedure. An

alternative approach is the leap-frog algorithm [838] that calculates atomic positions and velocities at half time steps.

$$v\left(t+\frac{1}{2}\Delta\mathrm{t}\right)=v\left(t-\frac{1}{2}\Delta\mathrm{t}\right)+a\Delta\mathrm{t}$$
$$\boldsymbol{r}(t+\Delta\mathrm{t})=\boldsymbol{r}(t)+\boldsymbol{v}\left(t+\frac{1}{2}\Delta\mathrm{t}\right)\Delta\mathrm{t}$$

Equation 32-33

Using the leap-frog algorithm, the velocities are calculated at time $t+\frac{1}{2}\Delta\mathrm{t}$ and used to determine the positions at time $t+\Delta\mathrm{t}$. The update algorithm explicitly calculates the velocities at half time steps, while the positions are determined for integer multiples of Δt only (Figure 24). The lack of synchronization between particle positions and velocities can be approximately overcome by estimating the velocity at time t using the relationship:

$$v(t)=\frac{1}{2}\left[v\left(t-\frac{1}{2}\Delta\mathrm{t}\right)+v\left(t+\frac{1}{2}\Delta\mathrm{t}\right)\right]$$

Equation 34

The Verlet and leap-frog algorithms operate by using information of particle positions and velocities disseminated from previous time steps but this data must be manually configured at the start of molecular dynamics simulations. The positions of particles in a crystal can be determined from X-ray diffraction patterns while the positions of particles that make up organic compounds can be determined from nuclear magnetic resonance (NMR) spectroscopy experiments. The particle positions for liquids are not resolved experimentally; the particles are instead usually positioned on a three-dimensional grid whose structure is user-defined. The initial particle speeds can then be estimated from a Maxwell Boltzmann distribution, where the distribution of particle speeds *p(v)* is calculated according to:

$$p(v) = \sqrt{(\frac{m}{2\pi kT})^3} \exp\left[\frac{mv^2}{2kT}\right]$$

Equation 35

where k is Boltzmann's constant and T is the system temperature.

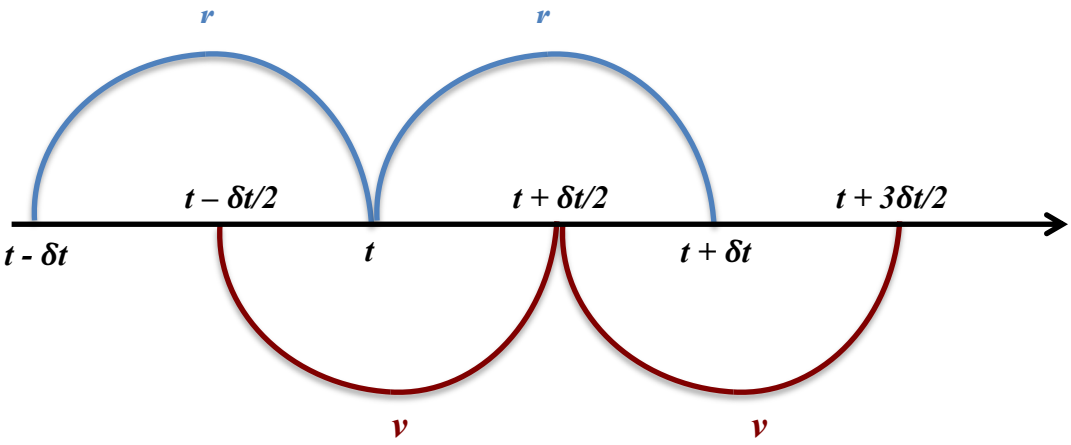

Figure 24. Illustration showing how the leap-frog algorithm operates. The computation of particle positions is shown with a blue line and the computation of particle velocities is shown with a red line. Simulation time is represented with a black arrow; the time step is user-defined and should be calibrated to ensure that molecular dynamics simulations are both efficient and realistic. There is a lack of synchronization between the particle position and velocity calculations: if particle positions are calculated at $t + n\Delta t$, then particle velocities are calculated at $t + \frac{n}{2}\Delta t$, where $n \in \mathbb{N}$.

2.12 Temperature Coupling

The use of molecular dynamics integrators naturally gives rise to the micro-canonical NVE (constant number, constant volume, and constant energy) ensemble but it is usually more desirable to calculate the physical properties of the canonical (NVT) and the isothermal-isobaric (NPT) ensemble. To simulate the canonical and isothermal-isobaric ensembles, it is essential that molecular dynamics programs implement algorithms that enable users to control the system pressure and temperature. The ensemble properties are usually coupled to external heat and pressure baths to accurately modulate their magnitude. Molecular dynamics simulation programs most commonly use the weak-coupling Berendsen scheme [839], the extended ensemble

Nosé-Hoover scheme [840], and the velocity-rescaling scheme to modulate system temperature and correct for unwanted temperature fluctuations and drift that occurs as a result of integration errors, heating due to frictional forces and heating due to external forces.

The Berendsen scheme is an efficient weak-coupling algorithm that uses exponential relaxation to correct for deviations from a user-defined reference temperature according to:

$$\frac{dT(t)}{dt} = \frac{T_0 - T(t)}{\tau}$$

Equation 36

Here, τ is the time constant that determines the strength of coupling between the heat bath T_0 and the simulation system $T(t)$. The Berendsen thermostat controls the system temperature by rescaling particle velocities and thereby suppresses fluctuations in kinetic energy. The algorithm cannot produce trajectories consistent with the canonical ensemble and this affects the magnitude of fluctuation properties such as the heat capacity. The velocity-rescaling thermostat is similar to the Berendsen weak-coupling algorithm but an additional stochastic term is used to ensure a correct kinetic energy distribution by modifying it according to:

$$dK = (K_0 - K)\frac{dt}{\tau_T} + 2\sqrt{\frac{KK_0}{N_f}}\frac{dW}{\sqrt{\tau_T}}$$

Equation 37

where K is the kinetic energy, dW is a Wiener process and N_f is the number of degrees of freedom. The velocity-rescaling thermostat produces a correct canonical ensemble while enabling efficient first-order decay of temperature deviations.

Canonical ensembles can alternatively be simulated with the Nosé-Hoover coupling algorithm, which introduces a frictional term into the equations of

motion. The friction parameter ξ is a dynamic quantity with its own momentum whose magnitude depends on the difference between the current kinetic energies and the reference temperature:

$$\frac{dp_\xi}{dt} = (T - T_0)$$

Equation 38

Under this scheme, the particles of a given simulation system are integrated according to:

$$\frac{d^2\boldsymbol{r_i}}{dt^2} = \frac{\boldsymbol{f}_i}{m_i} - \frac{p_\xi}{Q}\frac{d\boldsymbol{r_i}}{dt}$$

Equation 39

where Q is a constant that is usually termed the mass parameter of the Nosé-Hoover thermal reservoir. Temperature coupling algorithms can be used one after another to facilitate simulation set up e.g. initial equilibration with velocity rescaling thermostats and subsequent production runs with the Nosé-Hoover coupling algorithm.

2.13 Pressure Coupling

Molecular dynamics programs support different methods including the Berendsen algorithm, the extended-ensemble Parrinello-Rahman [841-842] approach and the Martyna-Tuckerman-Tobias-Klein [843] (MTTK) barostat to control system pressure. The Berendsen algorithm modulates system pressure by rescaling the box vectors of the simulation cell every n_{PC} steps with a matrix $\boldsymbol{\mu}$ and this enables first-order relaxation of the system pressure towards the user-defined reference pressure $\mathbf{P}_0$:

$$\frac{d\boldsymbol{P}(t)}{dt} = \frac{\boldsymbol{P}_0 - \boldsymbol{P}(t)}{\tau_p}$$

Equation 40

Here, τ_p is the barostat relaxation time constant. The relaxation algorithm leads to cell size variations where the volume is scaled by a factor η and the coordinates and cell vectors are scaled by $\eta^{1/3}$:

$$\eta(\mathrm{t}) = 1 - \frac{\Delta \mathrm{t}}{\tau_p}\gamma(\boldsymbol{P}_0 - \boldsymbol{P}(t))$$

Equation 50

where γ is the isothermal compressibility of the system. The Berendsen pressure control algorithm yields the correct average pressure for a simulation system, but it does not yield the NPT ensemble. In theory, the exact NPT ensemble can be produced with the Parrinello-Rahman approach, which couples the system pressure to an external pressure bath by adding an additional degree of freedom into the equations of motion. The box vectors are subsequently scaled using their own equations of motion.

$$\frac{d^2\boldsymbol{r_i}}{dt^2} = \frac{\boldsymbol{f}_i}{m_i} - M\frac{d\boldsymbol{r_i}}{dt}$$

$$M = \boldsymbol{b}^{-1}\left[\boldsymbol{b}\frac{d\boldsymbol{b}'}{dt} + \frac{d\boldsymbol{b}}{dt}\boldsymbol{b}'\right]\boldsymbol{b}'^{-1}$$

$$\frac{d\boldsymbol{b}^2}{dt^2} = V\boldsymbol{W}^{-1}\boldsymbol{b}'^{(-1)}(\boldsymbol{P} - \boldsymbol{P}_0)$$

Equation 51-53

Here, $\boldsymbol{b}$ is a matrix of the box vectors, V denotes the volume of the simulation box and $\boldsymbol{W}^{-1}$ determines the coupling strength between the simulation system and the pressure bath. The matrix $\boldsymbol{W}^{-1}$ is calculated using the expression:

$$(\boldsymbol{W}^{-1})_{ij} = \frac{4\pi^2\beta_{ij}}{3{\tau_p}^2 L}$$

Equation 54

Here, L is the largest box vector and β is the isothermal compressibility. Deviations in system pressure are minimized through oscillatory convergence towards the user-defined reference pressure. The Parrinello-Rahman algorithm can lead to large fluctuations in the dimensions of the unit cell if the system pressure is far from equilibrium and these fluctuations can make the simulation system unstable. It is common to first run an equilibration simulation with the weak-coupling Berendsen algorithm to exponentially converge the system pressure and subsequently use the Parrinello-Rahman scheme to yield the correct isothermal-isobaric ensemble.

2.14 Constraints

The choice of integration step is essential for ensuring that simulations are efficient and molecular motions are appropriately sampled. In atomistic simulations the most rapid motions are the bond stretching vibrations of carbon-hydrogen bonds that occur on the timescale of 10 fs and thus limit the simulation time step to ~1 fs. The time step used in molecular dynamics simulations is set to be at least ten times smaller than the carbon-hydrogen bond vibration timescale to ensure that the bonded atoms do not instantaneously overlap, leading to the computation of unrealistically large intermolecular forces and the production of unstable molecular dynamics simulations.

The rapid carbon-hydrogen bond vibrations can be discounted as an alternative approach if they are deemed by the user to be unnecessary for producing relevant biophysical data. Constraint algorithms can be applied to maintain the distance between atomic mass points during simulation time and this enables the use of larger integration time steps and the simulation of longer timescales. The SHAKE [844] and LINCS [845] methods are used quite frequently in united-atom simulations to fix bonds lengths or angles after the integration of forces and effectively enable the use of ~2-4 fs time steps.

The SHAKE algorithm manipulates a set of unconstrained coordinates $\boldsymbol{r}^i$ to produce a set of atomic positions that are in line with selected distance constraints $\boldsymbol{r}^{i\prime}$. The algorithm uses a set reference $\boldsymbol{r}$ to achieve this conversion:

$$SHAKE(r^i \rightarrow r^{i'}\ ;\ \boldsymbol{r})$$

Equation 55

The algorithm functions by solving a set of Lagrange multipliers in the constrained equations of motion. Under this scheme, the equations of motion fulfil a set of *K* holonomic constraints $\sigma_k(\boldsymbol{r}_1, \boldsymbol{r}_2 \ldots \boldsymbol{r}_N) = 0;\ k = 1 \ldots K$, and the forces acting on simulation particles are defined by:

$$-\frac{\partial}{\partial \boldsymbol{r}_i}\left(\mathcal{U} + \sum_{k=1}^{K} \lambda_k \sigma_k\right)$$

Equation 56

where λ_k are Lagrange multipliers that are solved iteratively by the SHAKE algorithm.

The LINCS algorithm is in contrast, non-iterative and can only be used to constrain isolated angles and molecular bonds. The algorithm is faster and more stable than its SHAKE counterpart and for this reason the LINCS approach is generally preferred. For a given simulation system particle acceleration can described by the equation:

$$\frac{d^2\boldsymbol{r}}{dt^2} = \boldsymbol{M}^{-1}\boldsymbol{F}$$

Equation 57

where matrix $\boldsymbol{M}$ contains the atomic masses and $\boldsymbol{F}$ is the *3N* force vector. The system is subject to K constraint equations:

$$g_i(\boldsymbol{r}) = |\boldsymbol{r}_{i1} - \boldsymbol{r}_{i2}| - d_i = 0 \;\; ; \;\; i = 1, 2, .., K$$

Equation 58

where d_i is the constraint distance. The gradient matrix of the constraint equation is:

$$B_{hi} = \frac{\partial g_h}{\partial r_i}$$

Equation 59

The updated constrained positions $\boldsymbol{r}_{n+1}$ are related to the unconstrained positions $\boldsymbol{r}_{n+1}^{unc}$ by:

$$\boldsymbol{r}_{n+1}^{unc} = (\boldsymbol{I} - \boldsymbol{T}_n \boldsymbol{B}_n)\boldsymbol{r}_{n+1}^{unc} + \boldsymbol{T}_n \boldsymbol{d} =$$

$$\boldsymbol{r}_{n+1}^{unc} - \boldsymbol{M}^{-1}\boldsymbol{B}_n(\boldsymbol{B}_n\boldsymbol{M}^{-1}\boldsymbol{B}_n^T)^{-1}(\boldsymbol{B}_n\boldsymbol{r}_{n+1}^{unc} - \boldsymbol{d})$$

Equation 60-61

where $\boldsymbol{T} = \boldsymbol{M^{-1}B^T}(\boldsymbol{BM^{-1}B^T})^{-1}$. This first step projects the new bonds onto the directions of the previous bonds**.** The projection of the bond p_i on the old direction is then set to:

$$p_i = \sqrt{2d_i^2 - l_i^2}$$

Equation 62

where l_i is the bond length after the first projection. The corrected coordinates are:

$$\boldsymbol{r}_{n+1}^{correct} = (\boldsymbol{I} - \boldsymbol{T}_n \boldsymbol{B}_n)\boldsymbol{r}_{n+1} + \boldsymbol{T}_n \boldsymbol{p}$$

Equation 63

2.15 Position Restraints

Molecular dynamics packages enable users to impose restraining forces on specified atoms e.g. membrane protein carbon atoms, to guide biomolecular system construction or steer the simulation through an arbitrary energy pathway. Position restraints are ordinarily implemented according to the following function:

$$V_{pr}(r) = \frac{1}{2} k_{pr} |\boldsymbol{r}_i - \boldsymbol{R}_i|^2$$

Equation 64

where k_{pr} defines the restraining force applied to maintain the fixed reference particle positions $\boldsymbol{R}_i$. The functional form makes the position restraint potential scale with the magnitude of particle position deviation (Figure 25). The position/restraint potential energy function can also be written as:

$$V_{pr}(\boldsymbol{r}_i) = \frac{1}{2}\left[k_{pr}^{x}(x_i - X_i)^2\hat{\boldsymbol{x}} + k_{pr}^{y}(y_i - Y_i)^2\hat{\boldsymbol{y}} + k_{pr}^{z}(z_i - Z_i)^2\hat{\boldsymbol{z}}\right]$$

Equation 65

Users can control the position restraint potential for the *x*, *y*, and *z* dimensions of a simulation cell. Users can define the strength of the harmonic position restraint forces that act along the *x*, *y*, and *z* spatial axis and through the implementation of the restraint potential, users can confine particle positions to arbitrary spheres, planes, or lines within the periodic unit cell. Position restraint forces are regularly used by scientists to equilibrate membranes, micelles, nanodiscs and they have also been used to mimic the action of the cytoskeletal.

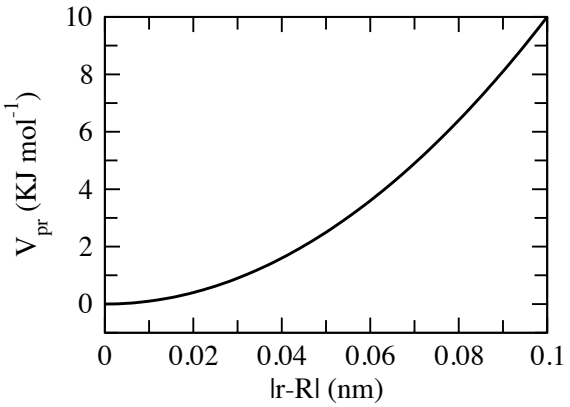

Figure 25. Representative harmonic potential used to enforce (standard) position restraints in molecular dynamics simulations. The potential energy rises as particles drift from a user-defined reference position. The magnitude of the potential energy is a function of the distance between the atom and the user-defined reference position.

2.16 Flat-Bottomed Position Restraints

Alternative functional forms can be used to restrain the position of simulation particles and facilitate simulation set up. Flat-bottomed position restraints subject particles to a harmonic biasing force while they are outside a user-defined volume of the simulation cell and these restraining forces are removed when the particles move back into the arbitrarily selected volume. The flat-bottomed position restraint potential (Figure 14) is computed according to:

$$V_{fb}(\boldsymbol{r}_i) = \frac{1}{2} k_{fb}\left[d_g(\boldsymbol{r}_i; \boldsymbol{R}_i) - r_{fb}\right]^2 H\left[d_g(\boldsymbol{r}_i; \boldsymbol{R}_i) - r_{fb}\right]$$

Equation 66

where $\boldsymbol{R}_i$ is the reference particle position, r_{fb} defines the distance from the center with a flat potential, H is the Heaviside function, and the magnitude of the restraining force is set with k_{fb}. Molecular dynamics simulation packages enable users to apply flat-bottomed position restraint potentials to different types of lipid geometries. Users can for example, apply flat-bottomed position restraint forces to a cylindrical domain of space that spans a simulated

membrane mimetic. Lipids would be able to move unabated within the cylindrical domain of space but their trajectories would be affected outside of the cylinder. Flat-bottomed position restraints can be used with the following geometries:

Spherical: The particle is subjected to a restraining force when it leaves a spherical domain (contained within the unit cell):

$$d_g(\boldsymbol{r}_i; \boldsymbol{R}_i) = |\boldsymbol{r}_i - \boldsymbol{R}_i|$$

Equation 67

Cylindrical: Particles are contained within cylinders that span the *x*, *y*, or *z*-axis simulation cell axes and have user-defined radii. The harmonic biasing force acts toward the cylinder axes and is computed according to the function:

$$d_g(\boldsymbol{r}_i; \boldsymbol{R}_i) = \sqrt{(x_i - X_i)^2 + (y_i - Y_i)^2}$$

Equation 68

In this example the cylindrical restraining force is being imposed along the *z*-axis, but the restraining force can be imposed along the *x* and *y* axes instead. Cylindrical restraints are increasingly being used to facilitate the construction of well-packed lipid vesicles. The CHARMM-GUI Martini Maker Module [151,232] uses flat-bottomed position restraint potentials to maintain cylindrical cavities across the surface of spherical vesicles and thereby enable lipids to transfer between the inner and outer bilayer leaflets. The procedure enables lipids to flip between membrane leaflets and the process can reduce bilayer tension.

Layer: Particle position restraint forces can be applied along the *x*, *y*, or *z*-axis to restrain the motion of selected atoms and subject them to a biasing force as they pass through, and move away from, the borders of user-defined slabs of simulation cell space. Position restraint forces can be applied

simultaneously along the x, y, and z-axes to restrain the motion of selected particles to a cubic volume of the simulation cell. The forces are described as:

$$d_g(\boldsymbol{r}_i; \boldsymbol{R}_i) = |x_i - X_i|, \text{ or } d_g(\boldsymbol{r}_i; \boldsymbol{R}_i) = |y_i - Y_i|, \text{ or } d_g(\boldsymbol{r}_i; \boldsymbol{R}_i) = |z_i - Z_i|$$

Equation 69

2.17 Umbrella Sampling

Large energy barriers can exist between distinct regions of the potential energy landscape in conventional molecular dynamics simulation systems and this can leave molecular configurations poorly sampled or completed neglected. Biased simulation techniques can be used to sample otherwise inaccessible reaction coordinates when the form of the potential energy landscape hinders ergodicity.

The umbrella sampling technique [846-847] enables equal evaluation of all points along a reaction coordinate that separates two well-defined states e.g. the transition of a solute from hydrophilic to hydrophobic solvent. Molecular configuration series are initially generated along a selected reaction coordinate. The starting configurations are most commonly extracted from simulations where a molecule of interest (e.g. a solute) is steered in a user-defined direction through the use of a harmonic biasing potential [848]. Initial configurations are generated through the application of steered molecular dynamics techniques and umbrella potentials and subsequently applied to restrain the center of mass position of the molecule of interest as it interacts with the encompassing molecular environment. The distance that separates the starting configurations is set to be sufficiently small such that there is overlap between adjacent simulation windows and one can therefore produce a single, continuous energy function.

For the user-defined reaction coordinate (ξ), the umbrella potential that is used to restrain the molecular system at the position ξ_i^c $(i = 1, \ldots, N_w)$ with force constant K_i is:

$$w_i(\xi) = K_i/2(\xi - \xi_i^c)^2$$

Equation 70

for a set of N_w separate umbrella simulation windows. The restrained simulations can be used to generate umbrella histograms $h_i(\xi)$ that represent the probability distribution $P_i^b(\xi)$ along the reaction coordinate biased by the umbrella potential.

2.18 Weighted Histogram Analysis Method

The Weighted Histogram Analysis Method [849] (WHAM) can be used to normalize the resulting probability distributions $P_i^b(\xi)$ and resolve the potential of mean force (PMF) function. WHAM operates by estimating the statistical uncertainty of the unbiased probability distribution and subsequently calculates the PMF corresponding to the smallest uncertainty. Thus, the WHAM equations read as:

$$P(\xi) = \frac{\sum_{i=1}^{N_w} {g_i}^{-1} h_i(\xi)}{\sum_{j=1}^{N_w} n_j {g_i}^{-1} \exp\left[-\beta(w_j(\xi) - f_j)\right]}$$

$$\exp(-\beta f_j) = \int d\xi \exp\left[-\beta(w_j(\xi)\right] P(\xi)$$

Equation 71-72

where $\beta = 1/k_B T$, n_j is the number of data points in histogram $h_i(\xi)$ and $g_i = 1 + 2\tau_i$ when τ_i is the autocorrelation time of the umbrella window i. The PMF is related to the unbiased probability distribution by:

$$\mathcal{W}(\xi) = -\beta^{-1}\ln[P(\xi)/P(\xi_0)]$$

Equation 73

Here, ξ_0 defines the position where the PMF reduces to zero. The GROMACS *g_wham* function computes the two unknown elements of Equations 71 and 72, the free energy constants f_j, and the unbiased distribution $P(\xi)$, while

simultaneously allowing for the computation of robust error estimates using bootstrap techniques [850].

2.19 Area per Lipid and Bilayer Thickness

The area per lipid is the average lateral surface area that is occupied by lipids in a biological membrane. The area per lipid can be computed as the product of the *X* and *Y* box vectors divided by half the total number of lipids when the unit cell is cubic and the area per lipid is equivalent in upper and lower bilayer leaflets. The bilayer thickness can be computed as the separation distance between the upper and lower leaflet lipid phosphate groups. These relatively simple methods for analyzing membrane morphology become less accurate when bilayers undulate, when membranes contain many different types of lipid molecules and when bilayer curvature is generated through active processes mediated by specialized proteins, lipids or the cytoskeleton.

Polygon-based tessellation procedures can be used instead as a more generally applicable technique that is appropriate for analyzing the properties of both flat and curved membrane surfaces [851]. The upper and lower membrane leaflets can be partitioned into planes of contiguous polygons based on the distances between adjacent lipid headgroups. The average projected surface area of each tessellated polygon provides a reasonably robust and accurate measure of area per lipid, while the average membrane thickness can be computed as the average distance between tessellated polygons either side of the membrane midplane. Voronoi tessellations segment bilayer surfaces into contiguous planes of convex polygons, whereas Delaunay triangulations decompose bilayer surfaces into contiguous planes of small triangles.

Bhatia et al. [851] compared different Voronoi tessellation and Delaunay triangulation methods for determining the area per lipid fields of distorted plasma membrane mimetics [364]. Comparisons were drawn between three membrane structure analysis tools: *APL@VORO* [852], *FATSLiM* [853] and

MemSurfer [851]. *APL@VORO* determines the area per lipid by projecting three-dimensional coordinates onto two-dimensional surfaces, whereas *FATSLiM* determines area per lipid via iterative and highly localized Voronoi tessellation calculations. *MemSurfer* adopts an altogether different approach and calculates area per lipid through Delaunay triangulation procedures. Visualizations were included in this publication to show how Delaunay triangulation methods manage to capture small undulations within membrane surfaces that are missed by the less accurate Voronoi tessellation tools, i.e. *APL@VORO* and *FATSLiM*. The publication demonstrates that even the more robust polygon-based tessellation procedures are, in some instances, inaccurate and that even seemingly basic membrane properties can be difficult to accurately evaluate in molecular dynamics simulations. Each method has been used to assess area per lipid values for flat membranes of phospholipid-composite and LPS-composite simulation systems to within 0.1 or 0.2 nm^2 of experimental values [151,301,329,851-853]. The tools are suitable for analyzing the properties of flat lipid membrane systems but they are less suitable for studying highly curved membranes that have unusually complex topologies.

Area per lipid and membrane thickness parameters have similarly been evaluated with X-ray and neutron scattering analysis techniques [854]. The most common real-space parameter derived from X-ray and neutron scattering experiments is the membrane thickness. However, there is no single definition of membrane thickness, since one might characterize membrane width as the full extension of the hydrophobic membrane interior or as the distance between terminal hydrophilic headgroup moieties, or then again, some other entirely distinct, but equally valid metric [854]. One relatively simple method for assessing membrane thickness is to initially divide the repeat spacing of (membrane) lamellae stacks into distinct water and lipid regions and subsequently determine membrane width through relatively simple comparative numerical analysis [855]. The divisions between membranes can be ascertained by monitoring the contrast between protiated and deuterated water stacks through neutron scattering

experiments [856-857]. This method makes use of multiple lipid membranes and is expected to provide reasonable numerical accuracy; however, users must be able to precisely quantify both the lipid concentration and the specific volumes of both water and lipid.

X-ray scattering experiments are commonly applied to assess the head-to-head distance, which is defined by the positions of the two maxima in the electron density profiles of lipid bilayer structures [856]. This method has been applied to study the morphology of rough (Re, Rd, Rc, and Ra) LPS lipid membranes [568] and the resulting data were used to validate different LPS molecular dynamics simulation forcefields [301,308,551]. There are many other alternative methods for determining membrane thickness through experimental techniques. Membrane thickness can be evaluated for example, from NMR-derived properties such as the acyl chain carbon-deuterium bond order parameter [858-859]. It is important to appreciate that experimentally derived membrane thickness data usually depend on specific approximations including the tilt of lipid tails and the volume of constituent lipid moieties [856,858,860]. Thickness values for single lipid types can vary substantially and it is consequently desirable to compare computational data with several sets of experimental data.

Experiments have also been performed to assess area per lipid values for different membranes and this data has been used to validate atomistic and coarse-grained molecular dynamics simulation forcefields for the past couple of decades [167,428,822]. Area per lipid data tends to take precedence over membrane thickness magnitudes for molecular dynamics simulation forcefield benchmarking because it is inextricably linked to lipid fluidity and is especially sensitive to the magnitude of intermolecular lipid headgroup attraction and repulsion forces. Petrache et al. [861] proposed that volumetric data and electron density profiles could be combined and used to determine the area per lipid values of single-component bilayers according to the formula:

$$A_L^k = \frac{V_L^k - V_H^0}{D_C^0 + (D_{HH}^k - D_{HH}^0)/2}$$

Equation 74

Here, A_L^k and V_L^k are the area and volume per lipid k within a biological membrane of thickness D_{HH}^k. V_H^0 represents the volume of the headgroup of the lipid of reference in a bilayer of thicknesses D_{HH}^0 and $2D_C^0$. The method makes assumptions that are difficult to prove through experimental analysis e.g. that V_H^0 and D_C^0 can always be accurately estimated. An altogether different approach seeks to determine area per lipid from the values of lipid volume (V_L) and the Luzzati thickness [857]:

$$A_L = \frac{2V_L}{D_B}$$

Equation 75

But it is presumed that one can accurately estimate the magnitude of lipid volumetric parameters [856,862-863], even though this is rarely the case.

Less intuitive approaches have been proposed based on the average NMR order parameters of selected carbon-deuterium bonds. The area per lipid values can be extrapolated from the volume per methylene groups and the orientation of methylene groups with respect to the membrane normal axis (z-axis) [858-860]. It has been found that these experimentally determined area per lipid values can vary significantly; much more so than the area per lipid values that are determined from computer simulations. There tends to be greater differences between lipid packing parameters that are determined with different types of experimental apparatus than the comparative lipid packing parameters that are determined with different molecular dynamics simulation forcefields [854]. This incongruity suggests that there is a systematic bias toward specific lipid packing parameters within molecular dynamics simulations and this calls into question the validity of using such reference metrics for molecular dynamics simulation forcefield validation.

Nonetheless, area per lipid and membrane thickness values are now established as "gold-standards" for assessing the quality of molecular dynamics simulation forcefields and these lipid packing parameters were used quite recently to validate rough (Re and Ra) LPS coarse-grained Martini simulation forcefields [301]. Lipid packing parameters have been used repeatedly in the past to validate biomolecular simulation forcefields; for example, see [408,428,799,814]

2.20 Order Parameter

The acyl tail order parameter quantifies the orientational mobility of lipid acyl tails within a fluid membrane [428,569,864]. The dynamic parameter provides a unique metric to quantify the average order of acyl chains relative to the bilayer normal over the course a molecular dynamics simulation. The order parameter is calculated according to the following equation:

$$S_{CD} = \frac{1}{2} < 3(\cos\Theta)^2 - 1 >$$

Equation 76

Here, Θ is the time-dependent angle between acyl chain bond vectors and the membrane normal reference axis. The magnitude of the computed acyl chain order parameters depends on the resolution level of the molecular dynamics simulation forcefields. Single bond vectors between two coarse-grained beads can represent multiple underlying carbon atoms and consequently the order parameters of comparative coarse-grained and atomistic acyl chains can be significantly different [301].

Comparisons have been made between experimental and computational order parameter data sets to validate molecular dynamics simulation forcefields. Take for example, the recent validation of the hybrid GLYCAM06 [557-559] and Stockholm lipids forcefield (Slipids) [727] that was used to model a *P. aeruginosa* biological membrane mimetic [556]. The molecular dynamics simulation model membrane contained an outer (extracellular)

leaflet of Lipid A molecules and the inner (intracellular) leaflet contained some combination of DPPE, DOPE, DPPG, and DOPG lipids. The averaged acyl chain order parameter was determined to be 0.38 for the simulated Lipid A molecules in these atomistic simulations and for comparison, the acyl chain order parameter for Lipid A molecules was determined to be 0.28 when they were analyzed with Fourier-transform infrared spectroscopy (FT-IR) [865]. Molecular simulations conducted with the GLYCAM and AMBER forcefields reported order parameter values of 0.32 instead [866-868] and these differences demonstrate (i) that molecular dynamics forcefields generally provide satisfactorily accurate predictions for acyl chain order parameter; and (ii) that some atomistic forcefields provide more acceptable predictions of experimental data than others.

2.21 Radius of Gyration

The radius of gyration is used in polymer science to assess how compact a macromolecule is around its center of mass [869]. For a macromolecule composed of n mass elements of mass values $m_i, i = 1,2 \dots n$ located at positions $\boldsymbol{r}_i$ from the center of mass, the radius of gyration is computed as the square-root of the mass average of $\boldsymbol{r}_i^2$ over all mass elements i.e.

$$R_g = (\sum_{i=1}^{n} m_i \boldsymbol{r}_i^2 \Big/ \sum_{i=1}^{n} m_i)^{1/2}$$

Equation 77

Alternatively, one can compute the radius of gyration around the coordinate or principal axes by only summing the radii components orthogonal to each axis:

$$R_{g,x} = (\sum_{i=1}^{n} m_i (\boldsymbol{r}_{i,y}^2 + \boldsymbol{r}_{i,z}^2) \Big/ \sum_{i=1}^{n} m_i)^{1/2}$$

Equation 78

2.22 Root-Mean-Square Deviation

The root-mean-square deviation (RMSD) of atomic/particle positions measures the average distance between the atoms of a dynamic biomolecule relative to a reference structure. The most common application of RMSD computation is for the study of globular protein conformations where the RMSD of carbon-α atomic coordinates is compared for a fluctuating protein relative to a superimposed reference structure [870].

One typically computes the deviation of atomic positions relative to a starting crystal structure within molecular dynamics simulations to evaluate the molecular fluctuation. The RMSD value can alternatively be computed with respect to the structure of a biomolecule at specified simulation time $t_2 = t_1 - \tau$. The functional form of the RMSD is then:

$$RMSD(t_1, t_2) = [\frac{1}{M}\sum_{i=1}^{N} m_i \|\boldsymbol{r}_i(t_1) - \boldsymbol{r}_i(t_2)\|^2]^{\frac{1}{2}}$$

Equation 79

where $M = \sum_{i=1}^{N} m_i$ and $\boldsymbol{r}_i(t)$ is the position of particle *i* at time *t*.

2.23 Radial Distribution Function

The radial distribution function *g(r)* for a dynamic simulation system describes how the density of atoms, molecules, colloids etc. varies around central reference particles and it is determined by partitioning simulation system into a system of concentric circles or spheres. Radial distribution function algorithms compute the probability that molecules are located within concentric spherical shells of user-defined width. In GROMACS [742] the radial distribution function algorithm is implemented as a pair correlation function for atoms of type A and B according to:

$$g_{AB\,(r)} = \frac{\langle \rho_B(r) \rangle}{\langle \rho_B \rangle_{local}} = \frac{1}{\langle \rho_B \rangle_{local}} \frac{1}{N_A} \sum_{i \epsilon A}^{N_A} \sum_{j \epsilon B}^{N_B} \frac{\delta(r_{ij} - r)}{4\pi r^2}$$

Equation 80

Here, $\rho_B(r)$ is the density of particles of type B at a distance r from particles of type A and $\langle \rho_B \rangle_{local}$ is the density of type B particles averaged over all spheres encompassing type A particles.

2.24 Visualization Software

Visual Molecular Dynamics (VMD) [871] is a molecular modeling and visualization computer program that was used throughout this work to set up complex simulation systems. The software was also used to follow stepwise molecular trajectories and for animating and analyzing biomolecular systems through the use of built-in computer scripts. The software was used together with the Tachyon renderer to produce high-resolution images for various biomolecular simulation systems.

Chapter 3: Interactions of Polymyxin B1 with Gram-Negative Bacterial Membranes

3.1 Abstract

Molecular dynamics simulations were conducted in an attempt to understand the interaction of polymyxin B1 (PMB1) peptides with (i) POPE/POPG phospholipid bilayers that are used to mimic the inner membrane of Gram-negative bacteria; and (ii) bilayers of rough (Re mutant) LPS that are used to mimic the extracellular leaflet of the outer membrane of Gram-negative bacteria. The simulations demonstrated that PMB1 peptides promote the formation of anionic (POPG) microdomains when they interact with Gram-negative inner membrane models. The PMB1 peptides also decreased membrane width and it was found that this reduction in membrane thickness was non-uniform across the membrane with some membrane domains being thinner than others. The insights help to clarify how PMB1 peptides make the inner membrane more liable to rupture and how PMB1 peptides can destroy Gram-negative bacteria. The Re LPS membrane simulations revealed that PMB1 peptides have the capacity to modulate the phase behavior of the Gram-negative bacterial outer membrane. This capacity to affect LPS phase properties could help us to understand how PMB1 peptides disrupt the outer membrane of Gram-negative bacteria.

3.2 Introduction

Antibiotic resistance has increased during the past few decades as first-line antimicrobial agents have been applied both excessively and inappropriately [593-595]. The overuse of antibiotics established a selective pressure that promoted the spread of drug-resistant genes and pathogenic bacteria progressively acquired resistance to conventional antibiotics. The problem was then compounded as the drug-resistant genes spread throughout the bacterial communities. The successive transfer of drug-resistant genes progressively produced so-called “superbugs” that are unresponsive to almost all available antibiotic medication [872-876]. Multi-drug resistant

bacteria are now becoming increasingly prevalent and these infectious microbes are increasing our national healthcare costs and the global rates of morbidity and mortality [612-616]. Bacterial infections are becoming increasingly hazardous and there is an urgent need to synthesis new antibiotic medication that can be used to kill the most concerning strains of multi-drug resistant bacteria.

We are now at an interesting precipice where computational simulation methodologies have reached a level of sufficient complexity that we can streamline otherwise laborious methods for identifying novel chemotherapeutic agents and at the same time, use atomic simulation techniques to gain unprecedented molecular level insights into the action of effective antimicrobials [624-629]. Molecular dynamics simulations are increasingly being applied to evaluate the molecular level interactions of effective antimicrobial peptides and to understand how these biomolecules disrupt bacterial membrane systems [630-631]. PMB1 is an unusually effective antimicrobial agent that is used as a last-line therapy to treat multi- or extensively drug-resistant species of Gram-negative bacteria [709-710]. PMB1 molecules have the capacity to kill multi-drug resistant Gram-negative bacterial species that are unresponsive to conventional first-line chemotherapy, but the widespread application of polymyxin medications is limited because the antimicrobial molecules have adverse neurotoxic and nephrotoxic side-effects [710-716]. It is reasoned that chemists could potentially synthesis new polymyxin derivatives in the future that have fewer side-effects but are nonetheless still effective against multi-drug resistant strains of Gram-negative bacteria. Chemists could exploit the insights that are being gained from experimental and computational research and design new antibiotic medication that is relatively harmless to renal and neural tissues but is nonetheless still effective for treating bacterial infections. Molecular dynamics simulations were conducted in this chapter to understand how PMB1 molecules permeabilize bacterial membrane mimetic systems.

The Martini coarse-grained molecular dynamics simulation forcefield was used to understand how PMB1 peptides interact with two symmetric biological membrane mimetics: (i) bilayer membranes of Re LPS lipid; and (ii) bilayers that contained POPE and POPG molecules in a 3:1 number ratio. The first set of simulations was analyzed to understand how PMB1 peptides interact with the outer membrane of Gram-negative. The second set of simulations was analyzed to understand how PMB1 peptides interact with the inner membrane of Gram-negative [645-646,879-880]. The coarse-grained simulations provided important insights that can help us to understand how PMB1 peptides interact with both membranes of the Gram-negative bacterial cell envelope. It was found that PMB1 peptides affect lipid packing parameters and the bilayer organization in a way that has important consequences for membrane structural stability.

When the PMB1 peptides were simulated with the Gram-negative bacterial inner membrane mimetic they preferentially interacted with the POPG lipids and this process promoted lipid demixing and the formation of anionic POPG lipid nanodomains. The PMB1 peptides also decreased membrane width when they were preferentially interacting with the POPG lipids and this increased the membrane width heterogeneity. The results could explain how PMB1 peptides disrupt the inner membrane of Gram-negative bacteria. Preferential interactions between PMB1 and POPG molecules would lead to a non-negligible increase in peptide density at highly localized points along the membrane surface. The PMB1 peptides could become highly localized at specific points along the membrane surface and as these points became increasingly thin, they would become increasingly prone to rupture and break away from the multicomponent membrane [331, 881 16-18]. There would be thin and negatively charged membrane “hotspots” that are prone to induce the formation of transmembrane water pores or other processes that affect the membrane structural stability.

When the PMB1 peptides were simulated with the Re LPS membranes it was found that LPS lipids had unusual biophysical parameters that prevented the

antimicrobial molecules from passing through the LPS core sugar domain. The Re LPS bilayers had glass-like dynamics, high shear viscosity parameters, relatively immobile phosphate groups and a relatively thick domain of hydrophilic core sugar units. Analyses of the unbiased simulations indicated that the interactions between the PMB1 peptides and the Re LPS were not converged even after 5 μs of simulation time. The umbrella sampling simulation technique was used to increase the scope of the simulation study and understand biomolecular interactions on long timescales. The umbrella sampling simulations were used to determine free energy profiles and to understand LPS properties as a function of PMB1 distance from the membrane midplane. It was found that the bilayers became increasingly rigid as the distance between the PMB1 peptides and the host cell membranes was decreased. This PMB1 peptides induced a phase change when they were simulated at the position of the PMF profile minima. The Re LPS bilayers began to behave more like an amorphous solid than a simple and highly fluid lipid membrane. This insight is noteworthy because membrane fluidity affects various important membrane properties such as shape, elastic moduli, tension [884-887] and it also influences biological functions that are crucial for cell viability such as enzymatic action and protein sorting [888-891]. The simulations provided important insights that can help use to understand the PMB1 antibacterial modes of action and the data might help chemists to synthesis new antibiotic medication for Gram-negative bacterial infections.

3.3 Methods

3.3.1 Coarse-Grained Models

The PMB1 peptide (Figure 26A) was clustered into a coarse-grained model so that it could be used with the coarse-grained Martini molecular dynamics simulation forcefield [799]. The bead type classification for each constituent coarse-grained pseudo-atom was selected through comparison with the standard set of Martini coarse-grained building blocks [814]. The terminal acyl chain moiety was modeled as two coarse-grained pseudo-atoms whose

interaction parameters were set to reproduce the experimental partitioning free energies of alkyl groups or saturated lipid tails. An approximate four-to-one heavy atom mapping scheme was used to model most of the constituent PMB1 peptide amino acids. However, smaller S-type Martini coarse-grained beads were used to model the cyclic benzyl group of the phenylalanine residue. The side chain Dab residues were modeled as single cationic beads so that they had more conformational flexibility. There is a total of five positively charged Dab residues on each PMB1 peptide (Figure 19) and the PMB1 coarse-grained model was consequently designed to have an overall positive charge of +5.

The coarse-grained parameters were optimized with the PyCGTOOL [892], which calculates equilibrium distances and force constants for coarse-grained pseudo-atoms directly from reference atomistic molecular dynamics simulation trajectories. PyCGTOOL was initially applied to different coarse-grained mapping schemes and the resulting coarse-grained models were simulated with the Martini simulation forcefield. The simulation results were then compared against the original set of atomistic simulation reference data. In other words, the Python PyCGTOOL program was applied to investigate the accuracy of different multiple atom-to-bead mapping schemes. The most accurate coarse-grained model, and the one used in this chapter, had equilibrium bond distances (r_{ij}) that differed by no more than 0.01 nm from the reference atomistic data; the equilibrium atomistic and coarse-grained angle values (θ_{eq})were equivalent to within 10%. The corresponding force constants (k_{ij}^{r} and k_{ijk}^{θ}) were well matched between the comparative atomistic and coarse-grained parameter sets, i.e. typically within 10%. However, constraints were applied (rather than values of r_{eq} and k_{ij}^{r}) to model the effective lack of bond stretching within the benzyl group of the phenylalanine residue. Analysis of the atomistic simulation reference data demonstrated that the benzyl moiety displayed a small degree of bond-stretching and by association had unusually high force constants that, if transferred into a comparable coarse-grained simulation model, would make the associated coarse-grained simulations unnecessarily unstable.

Constraints were therefore used to mimic the behaviour of the benzyl moiety. Marrink et al. have used comparable constraint options to mimic the dynamic interactions of benzene and cholesterol [799,814,822]. It was found that the average root-mean-square fluctuation values for PMB1 molecules in comparative coarse-grained and atomistic resolution molecular dynamics simulations differed by no more than 0.1 nm.

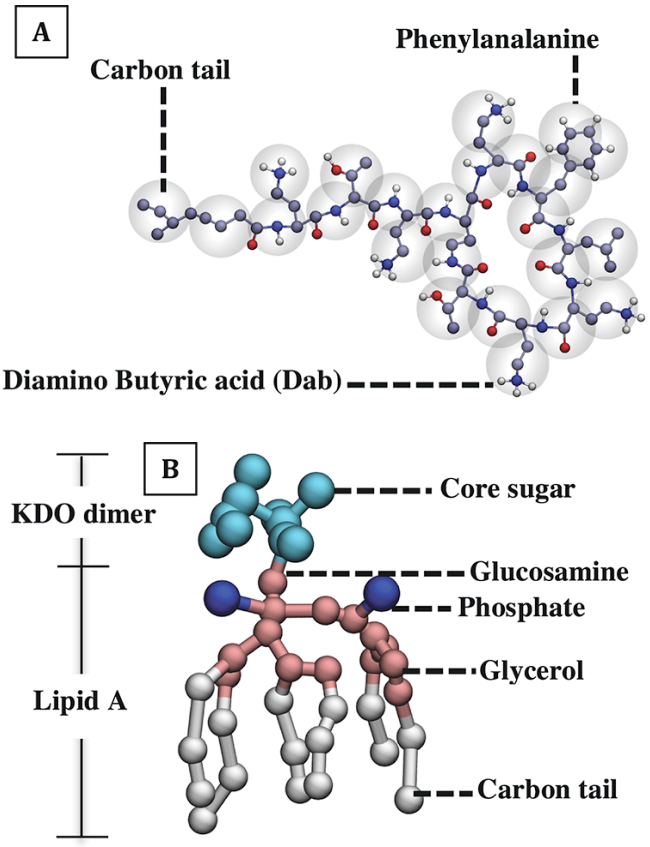

Figure 26. coarse-grained models for PMB1 and Re LPS. (A) coarse-grained model for PMB1. The Martini beads are shown as translucent spheres and the underlying united-atom particles are shown as opaque spheres. The carbon atoms are ice blue, the oxygen atoms are red, the nitrogen atoms are blue and the hydrogen atoms are white. (B) The coarse-grained model for Re LPS. The carbon tails are white, the glucosamine and glycerol groups are pink, the phosphate groups are blue, and the remaining core saccharides are cyan. The Re LPS lipid is divided into its component Lipid A anchor and keto-deoxyoctulosonate acid (Kdo) dimer sections for clarity.

The deep-rough (Re) mutant LPS lipid (Figure 26B), which contains a Lipid A anchor bonded to minimal core oligosaccharide section for bacterial survival (i.e. two keto-deoxyoctulosonate sugars), was modeled using the coarse-

grained Martini forcefield parameter set that is available online as part of the CHARMM-GUI Martini Maker module (http://www.charmm-gui.org) [151]. The POPE and POPG molecule interaction strengths, equilibrium bond distances (r_{ij}), equilibrium angle values (θ_{eq}) and the associated force constant parameters (e.g. k_{ij}^{r} and k_{ijk}^{θ}) were from the standard Martini molecular dynamics simulation forcefield databank.

3.3.2 Membrane Building

The molecular dynamics simulations were conducted with the GROMACS simulation package [742] and the Martini coarse-grained forcefield (version 2.2) [799]. The LPS bilayers were generated with the GROMACS *genconf* utility and the phospholipid bilayers were made with the Martini Python bilayer-building program (*insane.py*) [893]. The bilayers were solvated with enough water to minimize the strength of the interactions between periodic membrane images along the *z*-axis i.e. the bilayer normal axis. The anionic charge of the POPE and POPG phospholipid bilayers was neutralized with monovalent sodium ions (Na^+) and the LPS bilayers were neutralized with either monovalent sodium ions (Na^+) or divalent calcium ions (Ca^{2+}). The phospholipid bilayers were equilibrated for 5 μs at 310 K and the LPS membranes were equilibrated for 10 μs at three different temperatures: 300 K, 310 K, and 320 K. The simulation pressure was maintained at 1 bar with the Parrinello-Rahman barostat [841-842] and the temperature was modulated with the Nosé-Hoover thermostat [840] with a time constant of 1 ps. The shift function was used to smoothly reduce the Lennard-Jones and Coulomb potentials to zero between 0 and 1.2 nm and 0.9 and 1.2 nm, respectively. The simulations were conducted with an integration time step of 10 fs.

It is important to state here how the Martini forcefield represents ions and how this can lead to the inaccurate simulation of proteins and lipids. Coarse-grained ions are represented as Q type Martini beads, which have integer charge values, either ±1 or 2, and mass values of 72 amu (corresponding to

four water molecules) [822]. Monovalent Martini ions were originally based on single atom ions, either sodium, chloride, or choline, with first hydration shell water molecules [799]. Considering how difficult it is to accurately reproduce the interactions of ions with sophisticated united-atom or all-atom forcefields [894-895], it was concluded that ions could only have "semi-qualitatively" accurate interactions in coarse-grained molecular dynamics simulations [822]. Coarse-grained Martini calcium cations are modelled by simply assigning Martini sodium ions two-fold charge making them at best, satisfactory mimics of their atomistic simulation counterparts (i.e. Ca^{2+} ions with first hydration shells), but more often than not, rather crude representations of realistic hydrated calcium ions [151]. The implicit presentation of ions has important consequences for Martini simulations of proteins and lipids, and in particular of LPS macromolecules, which are connected and stabilized by divalent cations in Gram-negative membranes [211-212]. Divalent cations draw water molecules into the LPS core saccharide domain and this helps to support the lamellar lipid packing of LPS lipids [551]. It has been found that the LPS core saccharide domain can be up to three-fold depleted of water molecules in Martini coarse-grained simulations when comparisons are drawn with target atomistic simulations [301]. It has also been found that the LPS core saccharide domain can be compressed by up to 10% in coarse-grained simulations when comparisons are made with target atomistic resolution simulations [301,580]. Coarse-grained molecular dynamics simulations generally provide semi-quantitatively accurate data but it is important to appreciate that errors and inaccuracies are sometimes unavoidable due to the implicit presentation of the coarse-grained ions and biomolecules [822].

3.3.3 Peptide Simulations

The PMB1 peptides were combined with the equilibrated Gram-negative inner and outer membrane mimetics. The number of peptides per unit cell was incrementally increased in different simulations in an attempt to understand how peptide concentration can affect the membrane interactions.

Here it is important to draw comparisons with the clinical usage of PMB1 peptides to determine how realistically these coarse-grained simulations mimic *in vivo* interactions. Therapeutic dosages are administered to exceed pre-determined minimum inhibitory concentrations (MICs), which quantify the lowest drug concentrations that are needed for inhibiting the growth of different species of bacteria [896-897]. The MIC of PMB1 peptide molecules is 0.8 μg/ml for *Haemophilus influenzae*, 0.25 μg/ml – 4 μg/ml for *P. aeruginosa*, and 0.25 μg/ml – 4 μg/ml for *E. coli* bacteria [898-900]. The simulated PMB1 concentrations were at least one order of magnitude larger than these therapeutic MIC values. The PMB1 concentrations were between 50 μg/ml – 400 μg/ml when they were simulated with the LPS lipids and even higher when they were simulated with the two-component POPE and POPG lipid membranes. The disparity between the therapeutic and coarse-grained simulation concentrations is somewhat unavoidable given the constraints of modern computer hardware. Simulation cells must be made small to minimize the computational load and small simulation cells can only contain a limited number of water molecules. The coarse-grained PMB1 peptides were initially positioned at least 5 nm from the lipid phosphate groups to ensure that the initial peptide-lipid interactions were not biased. The orientation of each PMB1 peptide was initially randomized before it interacted with the bacterial membrane lipids to avoid biasing the initial peptide-lipids interactions. The spacing between the peptides was maximized to ensure that the peptides did not overlap at the start of the molecular dynamics simulations. Ions were added to ensure that the systems had an overall (net) neutral electrostatic charge (± 0). Anionic charge values were summed for all LPS and POPG lipids and the total sum value was used to determine the number of Na^{+} or Ca^{2+} ions that were included into each simulation cell or "periodic box". The phospholipid membranes were simulated at a temperature of 310 K and the LPS membranes were simulated at temperatures of 300 K, 310 K, and 320 K. The simulation parameters were adjusted so that they would match the simulation parameters from the membrane equilibration simulations.

3.3.4 Biased Simulations

The umbrella sampling technique and the Weighted Histogram Analysis Method (WHAM) [849] was used to produce the potential of mean force (PMF) profiles. The PMB1 peptides were restrained by applying a harmonic potential with a force constant of 1000 kJ mol^{-1} nm^{-2} along the *z*-axis (membrane normal); movement was unrestrained within the plane of the membrane. The PMF reaction coordinate (length sampled) was 4.3 nm and the distance between the sampling positions was 0.1 nm (along the membrane normal). Each of the umbrella sampling simulations were 1 μs long.

3.3.5 Analysis

Radial distribution functions were analyzed with the GROMACS *g_rdf* utility and the contact analysis data was determined with the *g_mindist* utility. The van Hove correlation functions were computed with the *g_vanhove* program and the lateral diffusion coefficients were determined with the *g_msd* tool. The trajectories of coarse-grained Martini particles were resolved with the *g_traj* utility. The configurational entropy was calculated with the *g_covar* and *g_anaeig* programs. The vector fields were visualized with an MDAnalysis module and the lateral area compressibility moduli were calculated with the equation:

$$K_A = \frac{k_B T A_L}{N_L \langle \delta A_L^2 \rangle}$$

Equation 81

where T is system temperature, A_L is average area per lipid, N_L is the number of lipids per bilayer leaflet, k_B is the Boltzmann constant, and $< \delta A_L^2 >$ is the average value of the squared fluctuation of A_L.

3.4 Results

3.4.1 Effect of Ion Charge on Re LPS Bilayer Properties

It was important to first analyze the properties of the LPS lipids in the presence of both monovalent and divalent ion solutions since it has been demonstrated that LPS lipid interactions depend on the concentration and type of ambient ions [251,901-902]. The symmetric Re LPS membrane systems were simulated with either monovalent (Na^+) or divalent (Ca^{2+}) ion solutions for 10 μs. The Re LPS lipids had a time-averaged area per lipid magnitude of 1.67 ± 0.005 nm^2 when the membranes were simulated with Na^+ ions and a time-averaged area per lipid magnitude of 1.60 ± 0.004 nm^2 when the membranes were simulated with Ca^{2+} ions (Figure 27A-D). To assess the quality of the computed data it is necessary to draw comparisons with previous united-atom and all-atom molecular dynamics simulations of LPS lipid membranes. Let us first compare with all-atom simulations of the Lipid A anchoring domain, which usually contains two phosphate groups, two glucosamine saccharide units, and no more than seven hydrophobic acyl chains [904-905]. Kim et al. used the CHARMM atomistic simulation forcefield to evaluate the area per lipid for Lipid A anchors from twelve different species of bacteria; some containing as few as four acyl chains, and others as many as seven [555]. The area per lipid values were evaluated as being no smaller than 1.50 nm^2 and no larger than 1.68 nm^2 for all of the Lipid A molecules with 6 hydrophobic acyl chain moieties. It is well known that the length of LPS macromolecules is inextricably linked to the magnitude of LPS lateral packing parameters in bacterial membrane simulation systems [212,301,551,555-556]. In general, the longer the LPS molecule is, i.e. the more core and O-antigen sugars it contains, the larger its projected lateral surface area will be. Keeping this in mind, it is expected that longer LPS lipid variants (i.e., Rd LPS, Ra LPS, and especially smooth LPS) will preferentially occupy more lateral surface area within bacterial membrane systems. It was found that semi-rough Rd LPS lipids had area per lipid values of 1.51 nm^2 in atomistic simulations [551] and as expected, that longer Ra LPS lipid variants had an

average area per lipid magnitude of 1.80 nm^2 [211]. When the LPS macromolecules contained long terminal O-antigen chains (i.e. smooth LPS) they tended to occupy even more lateral surface area within bacterial membrane mimetics. For example, smooth LPS lipids had an average area per lipid magnitude of 1.90 nm^2 in all-atom molecular dynamics simulations [211] that were conducted with the CHARMM forcefield. The coarse-grained Re LPS lipid packing parameters that have been calculated within this chapter are quite reasonable when compared with previous computational work e.g. the work performed by Kim et al. [555]. The coarse-grained Re LPS lipid models have time-averaged area per lipid values that are intermediary to the packing parameters that were obtained for short and longer forms of LPS lipids from previous atomistic simulation studies. In addition, there is little mismatch with the experimental values that were obtained by Snyder et al. [568] for LPS lipid variants from *Salmonella Minneso*ta and *Salmonella typhimurium* bacteria. Snyder et al. used X-ray diffraction analysis methods to demonstrate that that LPS lipids had average area per lipid magnitudes of 1.56 nm^2. This value (i.e. 1.56 nm^2) is only 2.5% smaller than the magnitudes that were computed for the coarse-grained Re LPS lipid membrane systems that simulated here in this chapter with divalent calcium (Ca^{2+}) ions.

The distribution of area per lipid values followed an approximate Gaussian distribution when the LPS membrane systems were simulated with the Na^+ ion solvent. The area per lipid values were distributed according to a multi-model non-Gaussian distribution function instead when the LPS lipids were simulated with the Ca^{2+} ion solvent. The multi-modal distribution is indicative of heterogeneous lipid packing, with areas of tightly packed lipids, and areas of more loosely packed lipids. The heterogeneous packing was confirmed via two-dimensional tessellations of the Re LPS phosphate plane. Voronoi tessellations revealed that the phosphate groups were packed similarly to glasses such as defective graphene and sheets of silica. Vitreous and crystal-like fractions were both present within the LPS membranes and this a hallmark of glassy materials [906-908].

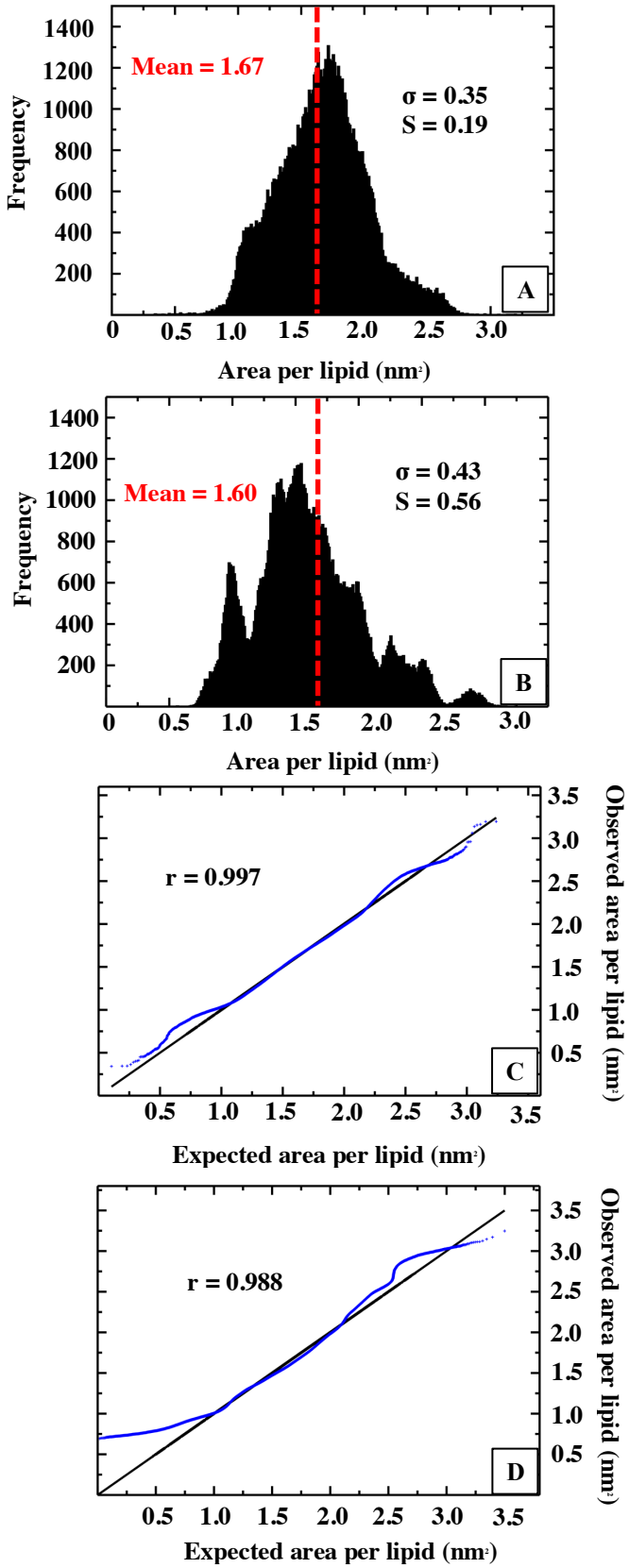

Figure 27. Voronoi tessellation of the Re LPS bilayers that were simulated with either Na^+ or Ca^{2+} ions. (A, B) The two-dimensional Voronoi tessellations were used to determine the projected surface areas distributions for the Re LPS bilayers that were simulated with either (A) Na^+

or (B) Ca^{2+} ions. The mean area values are represented with dashed red lines and the standard deviation (σ) and skew (S) values are shown in the top right-hand corner. (C, D) The observed data sets are compared with Gaussian distributed data sets of equivalent σ and S values. The linear association between the Gaussian (blue) and observed data (black) sets was calculated with the standard Pearson product-moment correlation coefficient (r).

Here it is necessary to provide a characterisation of the viscosity and phase properties of the biological membranes since it appears that cations affect the properties of LPS lipid membranes and as we will see, that PMB1 peptides also affect membrane phase behaviour when they are embedded into the LPS lipid leaflet. If we are to discuss how PMB1 peptides can affect the phase properties of bacterial membranes we should first evaluate the phase properties of bacterial membranes before they interact with PMB1 peptides. We should explore different simulation setups that have different concentrations of ambient ions, i.e. monovalent cations in one instance and divalent cations in the other. Viscosity is a rather simple biophysical parameter that can be used to explore the phase characteristics of different fluids and the metric provides insights into the consistency and internal friction of entire biological membranes or biological membrane components (e.g. the plane of phosphate groups) [909-911]. Radial distribution functions and velocity autocorrelation functions can also provide important insights into the phase behaviour of LPS lipid leaflets [335,912-913]. Viscosity magnitudes, radial distribution functions, and velocity autocorrelation functions can be computed to determine the phase behaviour of the LPS lipid membranes before they are simulated with the PMB1 peptides.

The wave-number dependent viscosity values $\eta(k)$ were computed using transverse current autocorrelation functions (Figure 28A) to assess the coexistence of fluid and static domains in the Re LPS bilayers and to determine the overall phase of the lipids. The data were fit to the Padé approximant used for simulations of three-dimensional liquids: $\eta(k) \propto (1 + \alpha k^2)^{-1}$ [914-915] and the static viscosity values were estimated by subsequent extrapolation to infinite wavelength ($k \to 0$). The viscosity values

were 2.45 (Ca^{2+} system) and 2.11 kg m^{-1} s^{-1} (Na^{+} system). The magnitudes are comparable to the shear viscosity of water at physiological temperatures and atmospheric pressure [916] indicating that the LPS bilayers were as a whole, fluid during simulation time. In contrast, static viscosities of the phosphate plane were extrapolated to values of 8426 and 2562 kg m^{-1} s^{-1} (Figure 28B) and these magnitudes are comparable to the viscosity of molten glass (10^4 – 10^6 kg m^{-1} s^{-1}) [917]. The data demonstrates that the hydrophobic core was highly fluid, whereas the phosphate plane was less mobile and was better described as a relatively rigid viscous glass.

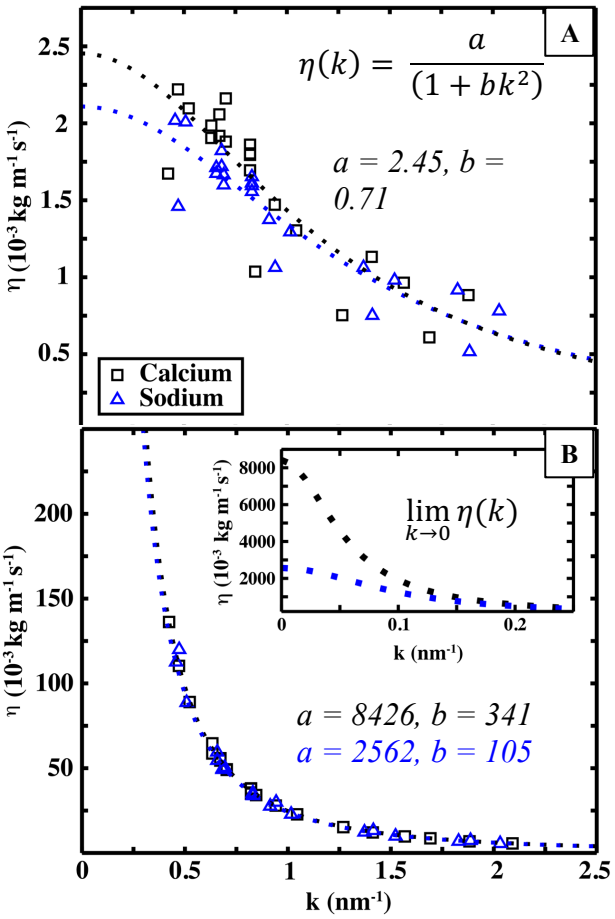

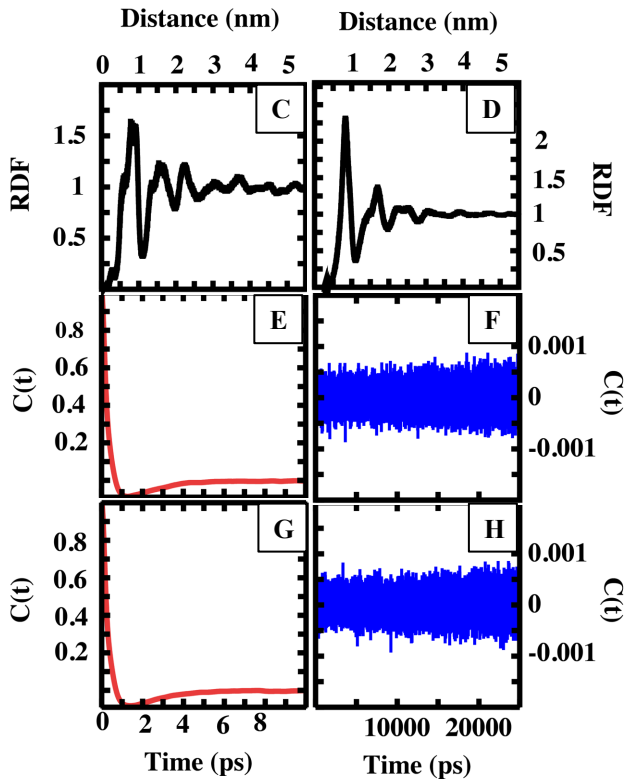

Figure 28. The properties of the Re LPS bilayers that with simulated with either Na^+ or Ca^{2+} ions. (A, B) The wave-number-dependent viscosity η(k) was determined from the transverse current autocorrelation function for the Re LPS bilayers that were simulated with either Na^+ (blue triangles) or Ca^{2+} (black squares) ions. The values of $\eta(k)$ were determined by considering (A) the entire Re LPS lipids in the viscosity calculations or by considering (B) only their phosphate groups. The data were fit to the Padé approximant: $\eta(k) = (1 + bk^2)^{-1}$; the fitting parameters (a, b) are shown with the optimized expressions for η(k) (dashed lines). The inset image shows $\eta(k)$ as $k \rightarrow 0$. Blue lines represent the simulations with Na^+ ions; black lines represent the simulations with Ca^{2+} ions. (C, D) The radial distribution functions (RDF) were determined for the Re LPS phosphate groups in the simulations with (C) Ca^{2+} and (D) Na^+ ions. (E-H) The velocity autocorrelation functions *C(t)* were determined for (E, G) the whole Re LPS lipids or for their (F, H) phosphate groups. The data are presented for the bilayers with either (E, F) Na^+ or (G, H) Ca^{2+} ions.

Radial distribution functions support the assessment that the LPS phosphate plane can be considered to be a relatively rigid viscous glass (Figure 28C-D). The radial distribution functions for the Re LPS phosphate groups were

intermediary to the smooth and jagged profiles one obtains for liquid and crystalline materials. The radial distribution functions for Re LPS phosphate groups were multi-modal and featured long-range order that is indicative of glass-like packing and is atypical of the fluid phase [918-919]. The velocity autocorrelation function is a time dependent metric that quantifies the underlying dynamic processes operating in a molecular system; the function can be used to evaluate molecular fluidity [920]. The velocity autocorrelation functions were typical of three-dimensional fluids when they were computed for the bilayers as a whole (Figure 28E, G) [921]. There was exponential decay to a negative value and subsequent convergence to zero within 10 ps. When auto correlation functions were computed for the phosphate plane (Figure 17F, H) there was rapid fluctuation between positive and negative values that did not dissipate for tens of nanoseconds. The oscillatory behavior is indicative of long-term localization or "caging" of the phosphate groups, whereas the rapid convergence to zero is indicative of a more mobile medium, in which the phosphate groups are caged only briefly. Rheological experiments support the conclusion that Re LPS lipids can form relatively rigid gels when they are interlinked by bridging cations [922].

3.4.2 PMB1 Interaction with Re LPS Bilayers

The PMB1 peptides were simulated with Re LPS lipid bilayers in two different solutions, one containing monovalent cations (Na^+) and another containing divalent (Ca^{2+}) cations. The simulation cells were ~13 x 13 x 20 nm in size and there were no more than 6 PMB1 peptides per periodic box. The PMB1 peptides were initially placed ~5 nm above the Re LPS bilayer center (using their center of mass coordinates for reference). The peptides formed favorable electrostatic interactions (defined as an interatomic separation of $r \leq 0.47$ nm i.e. smaller than the effective diameter of a standard coarse-grained bead) with the peripheral carboxylate groups of the Re LPS lipids after an average time of 60.9 ± 66.2 (s.d.) ns and 80.7 ± 81.6 (s.d.) ns for the systems with Ca^{2+} and Na^+ ions, respectively. The PMB1 peptides moved toward the water-lipid interface after binding to the peripheral core sugars

and electrostatic interactions then formed between the PMB1 Dab residues and the Lipid A phosphate groups. Electrostatic interactions between the Dab residues and the Re LPS phosphate groups were first registered after an average time of 251.4 ± 405.8 (s.d.), and 45.6 ± 149.9 (s.d.) ns for the systems with Ca^{2+} and Na^{+} ions, respectively. The large standard deviations demonstrate that the PMB1 peptides contacted the LPS phosphate groups somewhat sporadically and that the LPS-phosphate contact times differed significantly from one molecular dynamics simulation to another. In one simulation the PMB1 peptides moved through the LPS core saccharide domain relatively quickly and in another instance the PMB1 peptides moved through the LPS core saccharide domain significantly more slowly. But still, these average values demonstrate quite clearly that there was a significant difference between the LPS-phosphate contact times that were sampled for the comparative simulation systems that contained Na^{+} ions in one case and Ca^{2+} ions in another. The number of contacts between the Dab residues and the Re LPS phosphate groups systematically increased after the first LPS-phosphate contacts were registered at the times of 251.4 ± 405.8 (s.d.), and 45.6 ± 149.9 (s.d.) ns (Figure 29A, B). The differences in contact profiles is more apparent when we examine the number of contacts made between the PMB1 Dab residues and the Re LPS phosphate groups as a function of simulation time. It is clear that the number of LPS-phosphate contacts was significantly different in the monovalent and divalent ion simulation systems during the entire 5 μs long molecular dynamics simulations. There were approximately twice as many electrostatic contacts between the Dab residues and the Re LPS phosphate groups when the simulation systems contained monovalent Na^{+} ions compared with the simulation systems that contained divalent Ca^{2+} ions. The data suggests that PMB1 peptides are able to move through the LPS headgroup sugar domain more easily when the LPS lipids are interlinked with monovalent cations. Based on these different interactions it is expected that the distance between the PMB1 peptides and the bilayer center will be smaller in the simulation systems that contain the monovalent (Na^{+}) cations.

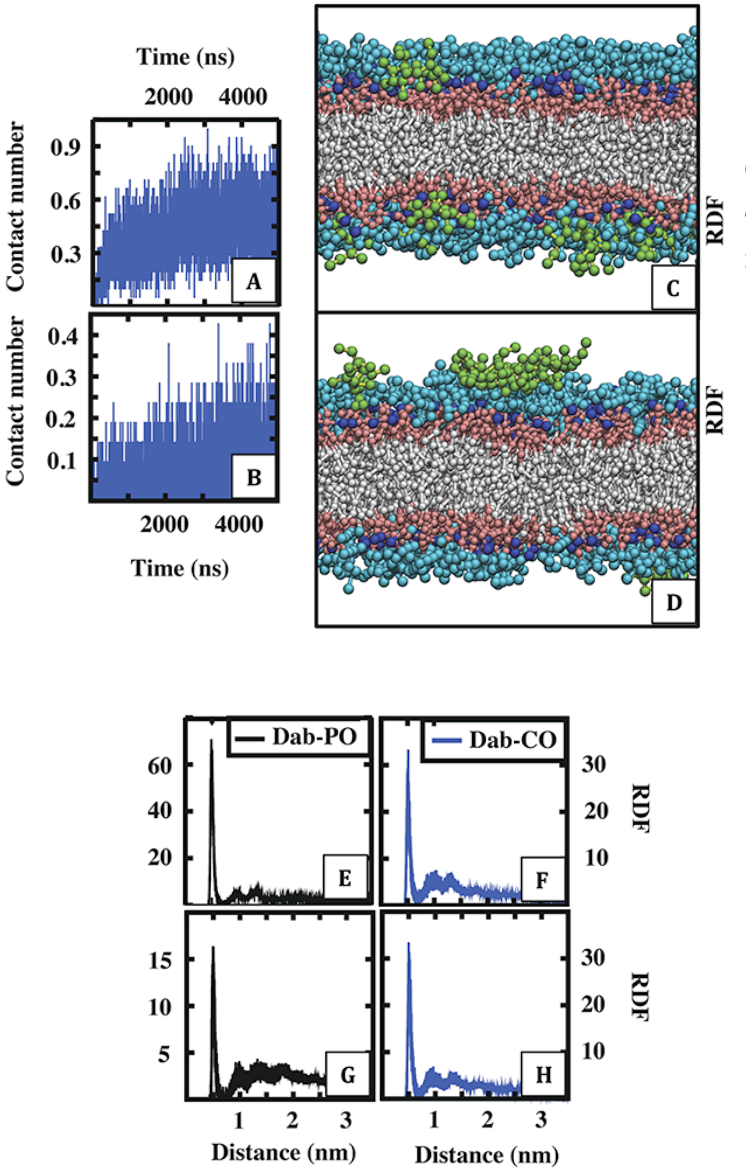

Figure 29. The translocation of the PMB1 peptide through the bacterial membrane mimetic depended on the type of ambient ions that were used to conduct the molecular dynamics simulations. (A, B) The contact number for interactions between the PMB1 Dab residue side chains and the Re LPS lipid phosphate groups as a function of simulation time**.** The cut-off distance was 0.47 nm (the effective size of a coarse-grained Martini bead); data were collated for all of the unbiased simulations. (A) The data for the bilayers that were simulated with Na^+ ions and for (B) the bilayers that were simulated with Ca^{2+} ions. (C, D) The final-frame snapshots of the PMB1 peptides (green) interacting with the Re LPS bilayers that were loaded with (C) Na^+ or (D) Ca^{2+} ions. The Re LPS lipids are colored according to Fig. 26 and the

Na^+, Ca^{2+}, and water particles are omitted for clarity. (E-H) The radial distribution functions for the phosphate (black lines) and carboxylate (blue lines) groups of the Re LPS lipids with respect to the position of the PMB1 Dab residue side chains. The data are shown for both the (E, F) Na^+, and (G, H) Ca^{2+} ion simulation systems. The data were sampled during the last 100 ns of simulation time.

The distance between the PMB1 peptides and the bilayer center was computed by sampling data during the last 100 ns of simulation time. The PMB1 peptides were on average 2.8 ± 0.6 nm above the bilayer center when the LPS lipids were interlinked with Ca^{2+} ions and 2.2 ± 0.6 nm when the LPS lipids were interlinked with Na^+ ions (Figure 29C, D). In other words, the PMB1 peptides bypassed more of the peripheral LPS headgroup sugar domains when the LPS lipids were interlinked with cations of lower charge. Pairwise radial distribution functions (sampled over the final 100 ns of simulation time) provide additional evidence to demonstrate that the PMB1 peptides moved through the LPS lipid headgroups more effectively when the simulation systems contain monovalent Na^+ ions. Pairwise radial distribution functions had first peak values (corresponding to the first coordination shell) of ~30 for the position of peripheral carboxylate groups with respect to the PMB1 Dab residues, regardless of ambient ion type loading. In contrast, the first RDF peak values for the position of Re LPS phosphate groups with respect to PMB1 Dab residues were ~15 when the Re LPS lipids were interlinked with monovalent (Na^+) cations and ~60 when the Re LPS lipids were interlinked with divalent cations (Ca^{2+}) instead (Figure 29E-H). To summarize these data: the PMB1 peptides partially bypassed the LPS headgroups and maximized their interactions with the protected Re LPS phosphate groups at the water-lipid interface. The PMB1 peptides bypassed the Re LPS headgroups more easily and more rapidly when the bilayers contained monovalent Na^+ ions. It must be stressed here that the PMB1 peptides only partially bypassed the carbohydrate headgroup moieties of the LPS lipids. There were interactions between the PMB1 peptides and the Re LPS phosphate groups, but they were limited.

The PMB1 peptides only partially bypassed the LPS lipid headgroups and as a consequence, there was minimal insertion of the PMB1 peptide hydrophobic moieties into the Re LPS lipid core. There were only two instances of any PMB1 hydrophobic moieties completely passing through the phosphate plane to enter into the hydrophobic membrane interior. The isobutyl and benzyl groups bypassed the interfacial phosphate groups of a bilayer that contained Ca^{2+} ions in one instance (Figure 30A) and in the second instance, a single lipid tail slipped through the phosphate groups of a Re LPS bilayer that was simulated with Na^{+} ions. The low number of times that the PMB1 hydrophobic moieties enter into the hydrophobic membrane core can be rationalized through the use of two-dimensional Voronoi tessellations. Voronoi tessellations can be used to understand the distances between LPS lipid headgroups at the water-lipid interface and further how the LPS headgroup packing affects the translocation of hydrophobic moieties into the Re LPS bacterial membrane mimetic core.

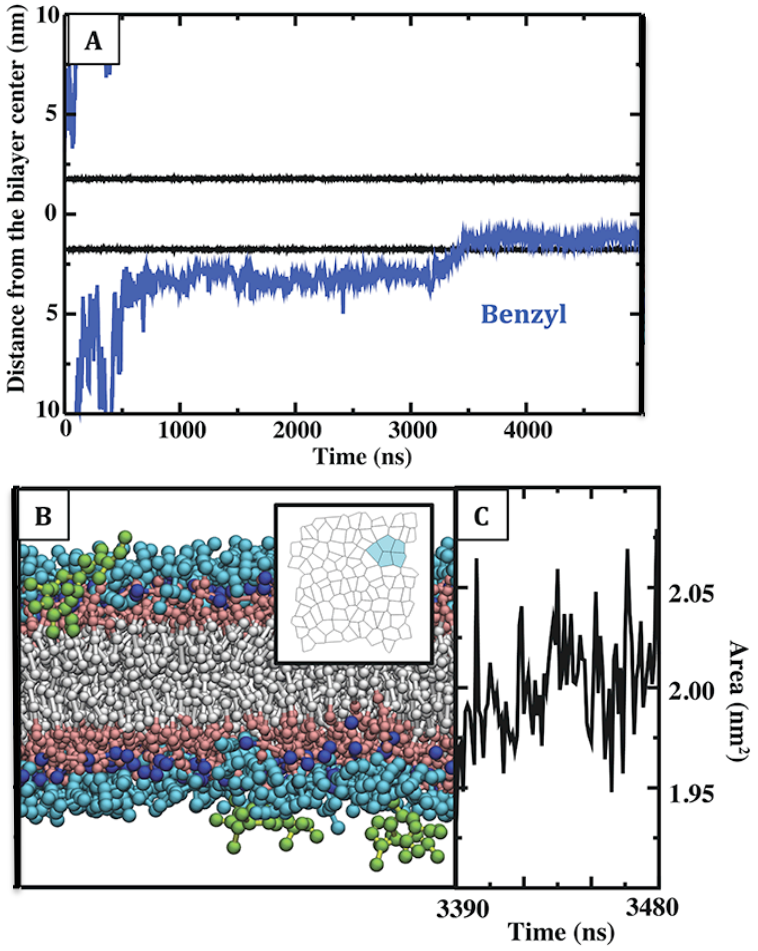

Figure 30. The PMB1 benzyl group penetrates the lipid core. (A) Position of the Re LPS phosphate groups and a single PMB1 benzyl group are shown with black and blue lines, respectively. The coordinates are with respect to the bilayer normal and the distances are relative to the bilayer center. The temperature was 310 K, the pressure was 1 bar and the membranes were simulated with divalent Ca^{2+} ions. (B) Side view snapshot showing how the PMB1 peptide enters into the bacterial membrane mimetic; the perspective is reversed relative to Fig. 30A for clarity. The inset image shows the two-dimensional Voronoi tessellation for the Re LPS headgroups as the PMB1 peptide enters into the lipid core. The projected polygons are colored cyan if they represent lipids that were adjacent to the embedded PMB1 benzyl group. (C) The area per lipid for the five Re LPS lipids that were adjacent to the benzyl group when it moved into the bilayer interior (3390-3480 ns). The average projected surface area of the five Re LPS headgroups was higher than the bilayer average (1.60 ± 0.004 nm^2).

Two-dimensional Voronoi tessellations of the LPS phosphate groups revealed that the PMB1 hydrophobic moieties translocated into the hydrophobic membrane core as “transient micropores” were formed at the bilayer-water

interface (Figure 30B). The phosphate headgroups temporarily moved away from each other when they were interacting with the PMB1 peptides and the alkyl and benzyl groups of the PMB1 peptides were then able to translocate the areas of the bilayer surface that were depleted of hydrophilic lipid headgroup moieties (Figure 30C). Perhaps it is necessary to draw comparisons with previous publications to explain precisely what "transient micropores" are and precisely how hydrophobic penetrants pass through them. Theoretical models hypothesized that hydrophobic penetrants translocated past hydrophilic lipid headgroups and moved into the lipid membrane cores during the spontaneous formation of "transient micropores" within the membrane surface [923-924]. Lipid headgroups continuously jostle back-and-forth within fluid membranes and consequently, their individual projected lateral surface area changes from one moment to the next [925-926]. When there is movement of multiple lipid headgroups away from one central point between them, there is an unusually large interstitial portion of the membrane core that is exposed to the extracellular fluid. The resulting transient micropore is not sufficiently large to be readily tunnelled by multiple water or ion Martini beads, but it is easier for hydrophobic moieties to enter into the membrane core through this point of the membrane surface than most, if not all, other points surrounding it. In other words, it is energetically favorable for hydrophobic penetrants to pass through the hydrophilic headgroup domain and then enter into the membrane interior but there are large energy barriers that can prevent this energetically favorable translocation process from occurring [927]. The energy barriers were hypothesized to be larger when the lipid headgroups were closer together and smaller when they were further apart. The hypothesize was confirmed in previous all-atom simulations that sought to clarify how C_{60} nanoparticles translocate into DPPC lipid membranes [925-926] and was subsequently corroborated by comparable coarse-grained simulations that used bacterial membrane and plasma membrane mimetics instead [301,928]. The formation of the micropores was rationalized here through the use of Voronoi tessellations. Polygon tessellations revealed there was larger than average spacing between adjacent lipid headgroups when the hydrophobic

penetrants were passing in between them. To reiterate, Figure 19B and in particular the small inset image within Figure 19B, shows that six adjacent LPS lipid headgroups had unusually large intermolecular spacing when hydrophobic penetrants were passing in between them (see the association figure caption). The translocation of the hydrophobic penetrants seems to depend on the fluctuations of lipid headgroups here in this chapter, and also in previous computational publications [925,301]. As lipid headgroups jostle back-and-forth they temporarily create "micropores" that enhance the rate at which hydrophobic moieties can pass through the hydrophilic headgroup domain and enter into the hydrophobic membrane core.

However, the formation of these membrane defects or temporary micropores is suppressed by the large lateral area compressibility moduli of the LPS lipid membranes. The compressibility moduli were calculated according to the equation:

$$K_A = \frac{k_B T A_L}{N_L \langle \delta A_L^2 \rangle}$$

where k_B is the Boltzmann constant, T is the system temperature, A_L is the average surface area per lipid, N_L is the number of lipids per membrane leaflet and $< \delta A_L^2 >$ is the average of the squared fluctuation of A_L values. The area compressibility moduli were 1.700 ± 0.003 and 0.673 ± 0.002 Nm^{-1} for the bilayers that were simulated with Ca^{2+} and Na^{+} ions, respectively. The values are significantly larger than the K_A values for DOPC bilayers (0.371 ± 8 Nm^{-1}) that were simulated at a temperature of 300 K and at atmospheric pressure [928], or for DPPC and DMPC membranes (0.234 and 0.231 Nm^{-1}) in X-ray scattering studies [929-930]. The PMB1 peptides were generally unable to pass through the thick hydrophilic core saccharide domain due to the slow dynamics of the LPS lipids and the PMB1 peptides were generally unable to translocate through the Re LPS phosphate plane due to the high lateral compressibility moduli of the Re LPS lipids. It is likely that the final lipid-peptide conformations do not represent global energy minima despite the

microsecond timescales used in this study and it is evident that enhanced sampling techniques (e.g. umbrella sampling) must be used to understand lipid-peptide interactions on long timescales.

3.4.3 Umbrella Sampling, WHAM, and the Thermodynamics of PMB1 Penetration

Potential of mean force profiles (PMFs) were produced to understand the energetics that control the movement of PMB1 peptides from the water domain into the Re LPS bilayer core and also to understand the biomolecular interactions that can occur on long timescales. PMFs were determined using the umbrella sampling technique and the weighted histogram analysis method (WHAM) [849]. PMF profiles were computed for three simulation temperatures: 300 K, 310 K, and 320 K. The energy minima were located at distances of approximately 1.6 nm and 1.9 nm from the bilayer center in the simulation systems that contained divalent (Ca^{2+}) cations and monovalent (Na^{+}) cations, respectively (Figure 31A-B). The PMF minima correspond to positions along the bilayer normal where the PMB1 peptide molecules can interact with cationic phosphate groups while the PMB1 isobutyl, phenylalanine, and acyl chain hydrophobic moieties interact with the hydrophobic acyl chains of the Re LPS.

The accuracy of umbrella sampling calculations is affected by the degree of data convergence and the number of umbrella sampling windows [931-932]. Given the complexity of the simulation systems it was necessary to evaluate the accuracy of the umbrella sampling calculations by evaluating if the reaction coordinates were appropriately sampled and if the PMF profiles were appropriately converged. Sampling was evaluated by studying the overlap of the histograms that were used to produce the PMF curves and the data convergence was evaluated by time-block analysis of the PMF profiles [933]. For each reaction coordinate there was excellent overlap of the histograms and through time-block analyses it was revealed that each data set was converged. Comparable validation methods were used by Khalid et al.

to evaluate the free energies of small solute permeation through the *E. coli* outer membrane [934].

The free energy values (PMFs) were decomposed into enthalpic and entropic contributions (Figure 31C-D) according to the equations:

$$-T\Delta S = T\frac{dG}{dT} \approx \frac{T}{2\Delta T}(G(T+\Delta T) - G(T-\Delta T))$$

$$\Delta H = \Delta G + T\Delta S$$

Equation 82-83

where G is the Gibbs free energy, S is entropy, H is enthalpy, and T is the system temperature [935]. The decomposition of the free energy values revealed that PMB1 permeation was hindered by an unfavorable change in system entropy and that it was driven by favorable changes in system enthalpy. The Schlitter formula and the quasi-harmonic approximations were used to understand the origin of the entropic wall hindering PMB1 permeation. The configurational entropy was computed for the PMB1 peptide as a function of distance along the bilayer normal (Figure 31E). The penetration of the PMB1 into the bilayer interior reduced the peptide configurational entropy by ~0.3 kJ mol^{-1} K^{-1} and this indicates that the significant changes in system entropy were not accounted for solely by changes in peptide conformation. It is apparent that PMB1 penetration was associated with a concomitant change in the conformational behavior of the encompassing lipids.

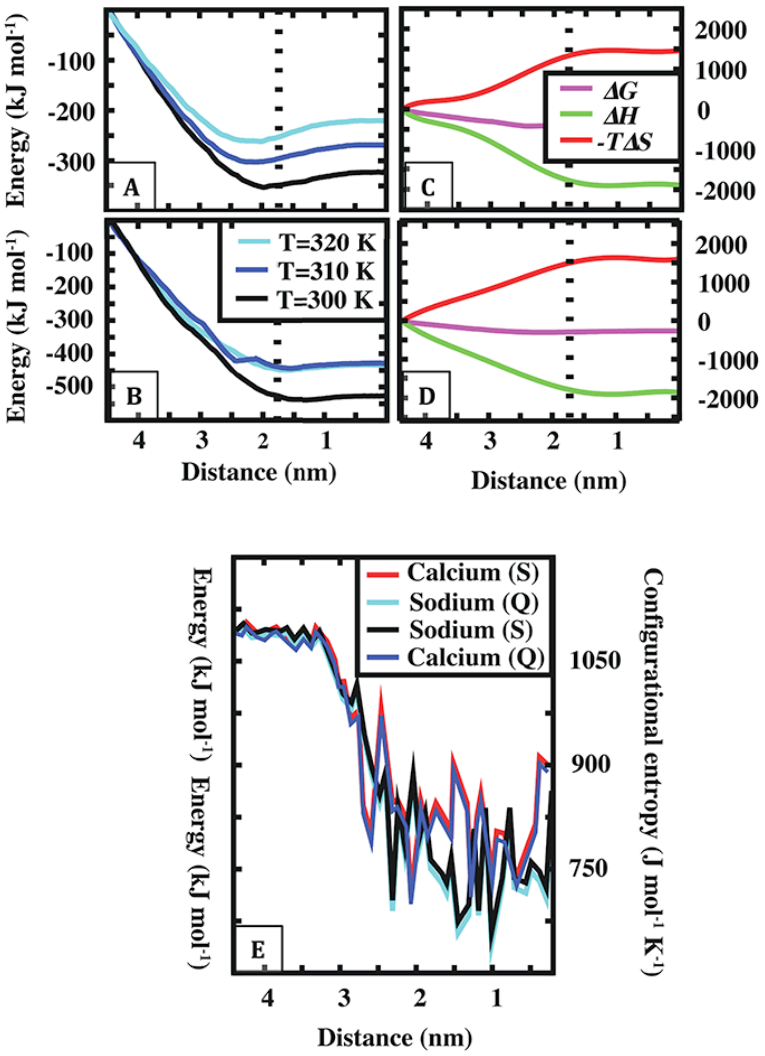

Figure 31. The free energy profile for PMB1 translocation into the membrane interior. The free energy profiles are shown for the simulation systems with (A, C) Na^+ or (B, D) Ca^{2+} ions. (A, B) The PMF profiles for PMB1 as a function of distance from the bilayer center. The PMF profiles are shown for the system temperatures: 320 K (solid cyan lines), 310 K (solid blue lines), and 300 K (solid black lines). (C, D) The free energy profiles ΔG that were computed at 310 K were decomposed into entropic $-T\Delta S$ (solid red lines) and enthalpic ΔH (solid green lines) components. The dashed black lines show the average position of the Re LPS phosphate groups from the bilayer center. (E) The configurational entropy for the PMB1 peptides was evaluated with the Schlitter formula (S) and the quasi-harmonic approximations (Q) as a function of distance from the bilayer center. The cyan and black lines show the data for the simulations with Na^+ ions and the red and blue lines represent the data for simulations with Ca^{2+} ions.

It is important to state here that some of the following data were derived from the umbrella sampling simulations. Data were predominantly sampled when the PMB1 peptides were restrained at distances of 1.6 nm (Ca^{2+} system) and 1.9 nm (Na^{+} system) from the membrane midplane, i.e. the position of the PMF minima. Data were however, sometimes extracted from all of the umbrella sampling simulation windows when it was necessary to understand LPS properties, e.g. lateral diffusion coefficients and heat capacity, as a function of PMB1 distance from the membrane midplane.

The self-part of the van Hove correlation function *G(r,t)* provides the probability that a particle moves a distance *r* from its neighboring particles within a time interval *t*. The metric can be used to quantify the overall dynamic characteristics of Re LPS lipids and demonstrate that as the PMB1 peptides translocate into the membrane interior they affect lipid conformation and the membrane entropy. The van Hove correlation functions, coupled with projections of Re LPS trajectories (during simulation time) and streamlined visualization of lipid motion, is used here to show that the PMB1 peptides changed the lipid conformation and the lipid phase characteristics when they were located at a membrane normal position that corresponds to the location of the PMF minima.

It is first necessary to give some insight into streamline visualisation figures here to provide context for the ensuing LPS lipid trajectory analysis data. Sansom et al. have developed software that enables the easy identification of the correlated movement of lipids within either flat of spherical membrane systems [936]. The software couples the desirable properties of path line visualization techniques and methods for vector field visualization to create an analysis tool that generates an intuitive visualization of both linear and circular nanometer-scale lipid movement patterns. The analysis tool has already been used to study the properties of the Gram-negative bacterial cell envelope and it was shown that LPS lipid trajectories are strongly influenced by the movement of proteins [325]. The analysis tool was created in part to evaluate the nature of lipid diffusion since our model of biological membranes

is currently evolving from the simplistic fluid mosaic model toward a more nuanced view of a laterally heterogeneous patchwork of proteins and lipids [937-938] (see section 1.1). It was also developed to understand if lipids move according to a rattle-in-a-cage diffusion model [164], a flow-like diffusion model [939-941], or some other entirely distinct lipid trajectory scheme.

The evaluation of lipid diffusion patterns is of prime importance within this chapter since diffusion patterns characterize the different phase characteristics of fluid mediums. Heterogeneous relaxation dynamics are a hallmark of amorphous materials and of particles within glassy systems [942-945]. The particles move according to two diffusion processes: (i) cooperatively rattling within small regions of space; and (ii) correlated migrations of particles to neighboring regions of space. The movements mimic clustered continuous-time random walk processes [946], in which particles are momentarily confined to small regions of space before they collectively "jump" into new regions of space. Heterogenous relaxation dynamics are a hallmark of vitreous systems, whereas crystalline materials tend to display more uniform relaxation dynamics. When atoms are confined within a solid material they tend to oscillate back-and-forth within a small region of space, effectively rattling within a small cell and not "jumping" from one cell to another [947].

We will see from Figures 21 and 22 that ions and PMB1 peptides affect the properties of Gram-negative bacterial membranes and in particular, the diffusion behaviour of the LPS lipids. Figure 21 shows that the LPS lipids display heterogeneous relaxation dynamics that are typical of glassy systems but that the precise characteristics of the clustered continuous-time random walk or "blob-and-channel" trajectories depend on the type of ambient ions that are present within the simulation cell. In either instance there is momentary cooperative rattling within small regions of the membrane and after that there is cooperative migration to new regions of space. Figure 22 then shows how PMB1 peptides can affect LPS lipid trajectories during

simulation time. There is not only a significant reduction in the absolute lateral displacement that is quantified here in terms of angstroms, but also the reduction (Na^+ system), or complete removal (Ca^{2+} system), of the "channel" component of the blob-and-channel trajectories. The integration of a PMB1 peptide into the membrane affects the LPS lipid trajectories and they transition from the heterogeneous relaxation dynamic movement patterns of vitreous systems toward the more static, oscillatory movement patterns of solid and crystalline materials. Figures 21A, 21E and Figures 22A, 22E show the trajectories of single LPS lipids over the course of 1 μs long simulations to enable simple identification of single LPS lipid movement patterns and for simple comparison with conventional blob-and-channel and crystalline material trajectories. Figures 21B, 21C and Figures 22F, 22 G are generated using the Flows module developed by Sansom et al. [936]. The figures reveal the differences between each membrane system in terms of correlated lipid trajectories to show that the ions and PMB1 peptides affected all of the LPS lipids and also to quantify the magnitude of the effect in terms of absolute lateral displacement, i.e. angstroms.

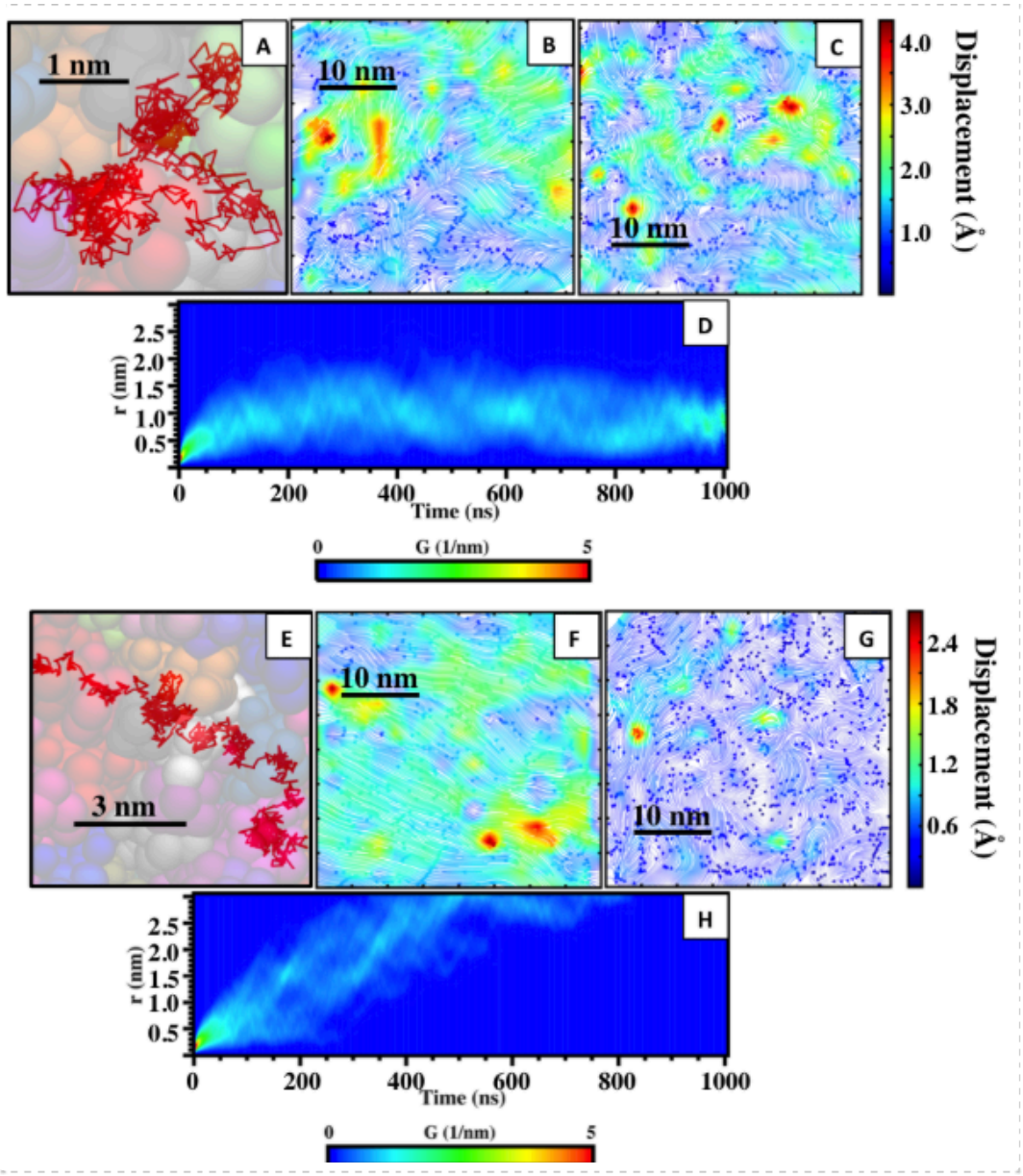

Figure 32. The vitreous dynamics of the Re LPS lipids. The lipid dynamics of the Re LPS lipids were different when they were simulated with (A-D) Na^{+} and (E-H) Ca^{2+} ions. (A, E) The trajectories of single representative Re LPS phosphate groups are presented here as red lines. The background snapshots of the Re LPS lipids are shown with the scale bar to provide a sense of distance. The background snapshots clarify how far the representative Re LPS lipids have moved in Fig. 32A and Fig. 32E or in other words, how long the red line trajectories are. The simulations were conducted with a simulation temperature of 310 K and the analysis was performed for 1 μs. (B-C, F-G) Streamline visualization analysis for arbitrarily selected simulation frames to capture the collective, heterogeneous relaxation dynamics that give rise to the so-called "blob-and-channel" trajectories that are a hallmark of vitreous systems. (D, H) The self-part of the van Hove correlation function that is defined as the probability that a particle that is at r_0 at time zero can be found at position r_0+t at

time t. The figures show how the Re LPS lipid trajectories change when they are simulated with different types of ions.

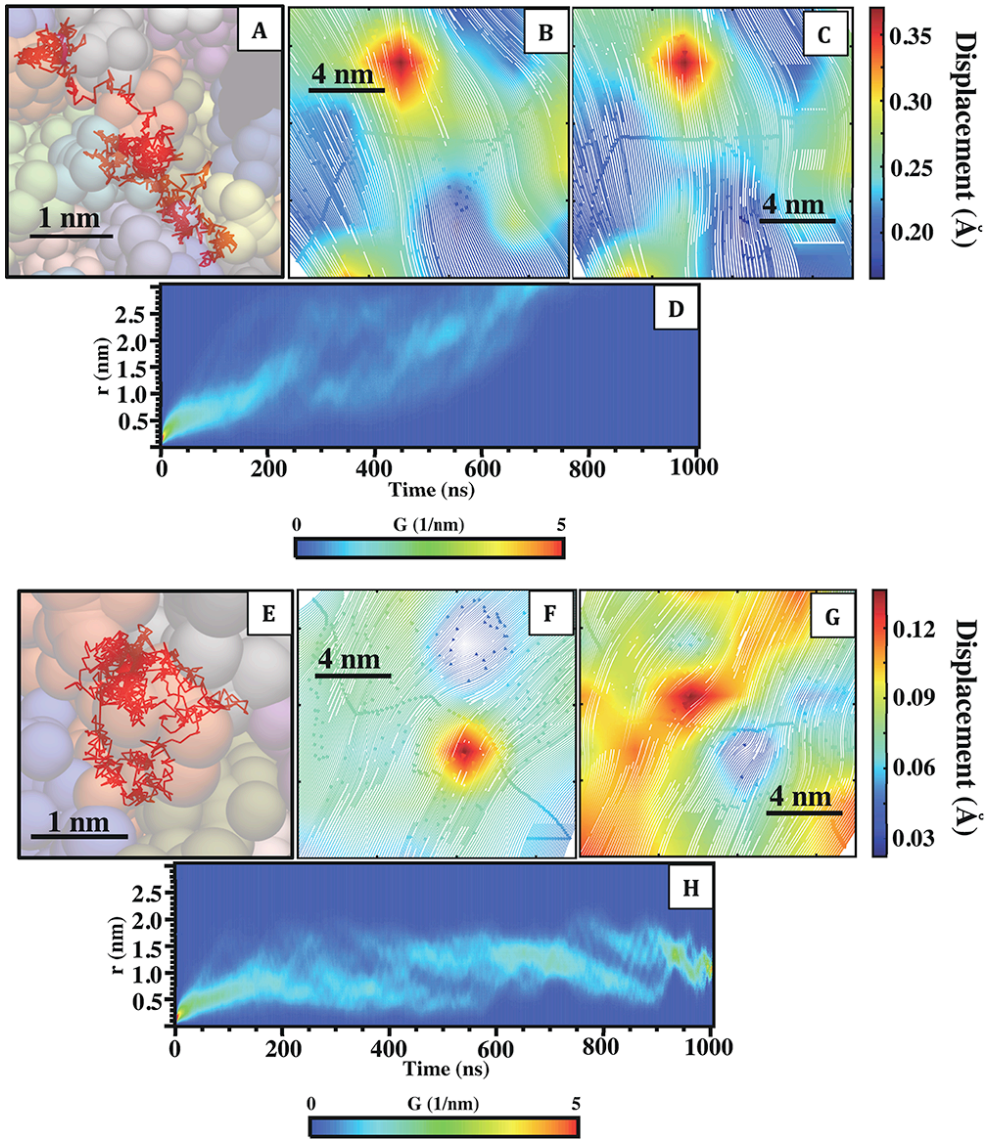

Figure 33. The Re LPS diffusion was affected by the PMB1 peptides. (A, E) The trajectories of single representative Re LPS phosphate groups was visualized over the course of 1 μs long umbrella sampling simulations. The sampled windows correspond to the minimum of the 310 K PMF profiles from Fig. 31A. The trajectories of single representative Re LPS phosphate groups are presented here as red lines. The background snapshots of the Re LPS lipids are shown with the scale bar to provide a sense of distance. The background snapshots clarify how far the representative Re LPS lipids have moved in Fig. 33A and Fig. 33E or in other words, how long the red line

trajectories are. (A) When the Na^+ ion simulation system was simulated with a PMB1 peptide there was a shift away from the clustered-continuous-time-random walk processes (see Figure 32A for comparison) towards the localized oscillatory and rattling motions that have been noted for ions in rigid crystals. (E) When the Ca^{2+} ion simulation system was simulated with a PMB1 peptide there was a more significant shift away from clustered-continuous-time-random walk processes (see Figure 32E for comparison) towards localized oscillatory motions. The Re LPS phosphate groups were confined to membrane domains that were approximately 2 nm^2 during the last 1 μs of simulation time. (B-C, F-G) Streamline visualization analyses of arbitrarily selected simulation frames to clarify the collective Re LPS headgroup relaxation dynamics in the presence of the PMB1 peptide. The Re LPS trajectories are noticeably different from the relaxation dynamics of the Re LPS phosphate groups when they were not simulated with PMB1 peptides (see Figure 32B-C and Figure 32F-G for comparison). There is an approximate order of magnitude reduction in the headgroup displacements per simulation step (see adjoining color bars for clarity). (D, H) Self-part of the van Hove correlation function for the Re LPS phosphate groups. Comparisons between Figure 32D, 32H and Figure 33D, 33H reveal significant differences in the relative mobility of the Re LPS molecules when they interact with a PMB1 peptide.

The visualization of the LPS phosphate group trajectories (void of PMB1 peptides) revealed that the LPS phosphate group diffusion patterns depended on the type of ambient ions that were present. The phosphate groups displayed heterogeneous relaxation dynamics comparable to the now well-established clustered continuous-time random walk processes (Figure 32A-D) [946] when the membranes were simulated with monovalent Na^+ ions. The phosphate groups initially cooperatively traversed a small region of the simulation cell before they moved cooperatively to a new region of the periodic box. Heterogeneous relaxation dynamics were also observed when the phosphate groups were interlinked with Ca^{2+} ions (Figure 32E-H) but the anions were caged within small regions of the simulation cell for less time and a greater number of phosphate groups were involved in the correlated migrations to new regions of space. The van Hove time-space correlation functions for the phosphate groups of single Re LPS leaflets were similarly indicative of heterogeneous relaxation dynamics. The functions had features of both continuous random-walk type diffusion and oscillation type diffusion. The PMB1 peptides changed the LPS lipid diffusion patterns, there was an

overall shift from clustered continuous-time random walk processes to localized oscillatory and rattling motions when the PMB1 peptides were simulated at the PMF membrane minima positions (Figure 33A-H). This inference was supported by orders of magnitude reduction in lipid lateral diffusion coefficients when diffusion coefficients were calculated for PMB1 peptides at positions along the bilayer normal (Figure 34). The Re LPS lipids become increasingly immobile and rigid as the PMB1 peptide was moved from the simulated water domain and into the bilayer interior.

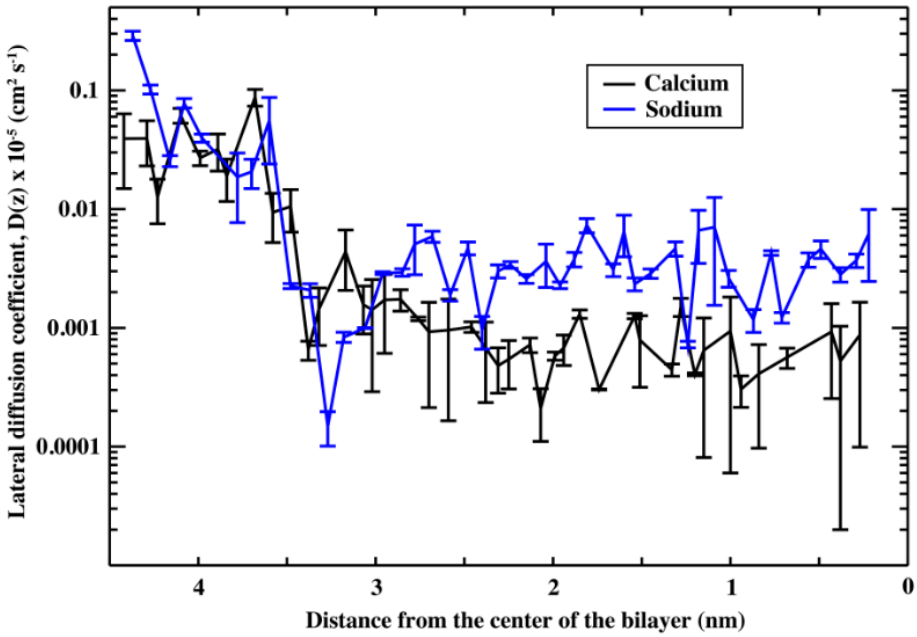

Figure 34. The lateral diffusion coefficients *D(z)* for the Re LPS phosphate groups as a function of PMB1 distance from the bilayer center. The blue line shows the data for the systems with Na^+ ions and the black line shows the data for the systems with Ca^{2+} ions. The diffusion coefficients *D(z)* were determined by linear regression of the mean square displacement and error bars have been included for each data point. The lateral diffusion coefficient axis is logarithmic.

Two-dimensional Voronoi tessellations of the Re LPS phosphate groups was used to clarify the change in lipid dynamics as the PMB1 peptide was restrained at different positions along the membrane normal axis. The Voronoi tessellations revealed that the LPS lipid phosphate groups had projected lateral surface area values of 0.5–0.7 nm^2 and approximate hexagonal coordination when the PMB1 peptide was restrained at the PMF minima (Figure 35A-F). This is similar to the packing of LPS lipid phosphate

groups in nanocrystalline domains for which it was reported that LPS lipids have three LPS lipid neighbors, corresponding to six anionic phosphate groups, and projected lateral surface areas of 0.55 nm^2 [121,948]. The appearance of the crystalline domains in the simulations was not temporary and the rigid lipid fractions were found to be stable for several hundreds of nanoseconds.

The heat capacity profiles provide additional evidence for the inferred crystallization effects. Following the protocol in previous works [935], the heat capacity change was calculated according to:

$$\Delta C_p = -T\frac{d^2G}{dT^2} \approx \frac{T}{\Delta T^2}(\Delta G(T-\Delta T) - 2\Delta G(T) + \Delta G(T+\Delta T))$$

Equation 84

The heat capacity change became increasingly negative as the PMB1 peptide was restrained at positions along the bilayer normal that were closer to the position of the membrane midplane (Figure 35G-H). The heat capacity change profiles are indicative of a transition from disordered to ordered states [949-950]. The data demonstrates that PMB1 peptides changed the dynamic phase behavior of the encompassing Re LPS lipids as they were restrained at positions closer to the membrane midplane. It is well established that PMB1 peptides affect bilayer stability as they displace divalent cations that bridge LPS Lipid A anchors, but these results suggest that PMB1 peptides can additionally change the phase of LPS lipids that surround them. This is important to acknowledge since membrane fluidity affects almost all bilayer properties including elastic moduli, shape, tension, mechanical stress, protein sorting, enzymatic action, and signal transduction [888-890,951-955].

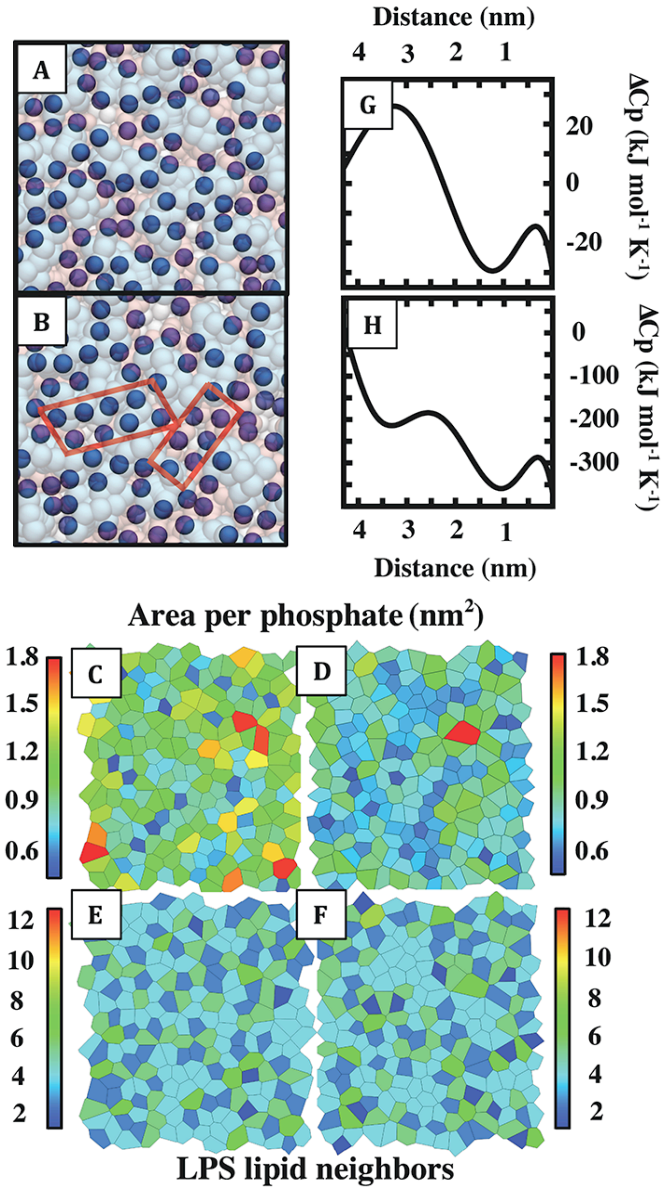

Figure 35. The PMB1 peptide induces the glass-to-crystal transformation. (A, B) Top view snapshots of the Re LPS bilayer when it was simulated with (A) water and ions and (B) when it was simulated with water, ions and a PMB1 peptide. The Re LPS phosphate groups are presented as opaque blue spheres and the other sections of the Re LPS molecules are depicted as translucent spheres. The red quadrilaterals are used to draw attention to the crystalline packing of the Re LPS phosphate groups. These membrane systems were simulated at 310 K with Na^+ ions. (C-F) Voronoi tessellation analyses of the Re LPS phosphate groups when they were simulated (C, E) with water and ions and (D, F) when they were simulated with water, ions and the PMB1 peptide. (D, F) The figures were created by sampling data from the umbrella sampling window that was positioned at the location of the 310 K PMF minimum (see Figure 31A for reference). (C, D) The plots show the area per phosphate group. The color scale bars are used for clarity. It should be noted that each Re LPS lipid has two phosphate groups. (E, F) The plots show the number of whole Re LPS lipids that are counted for each

of the tessellated Voronoi cells (see adjoining color scale bars for clarity). (F) The number of 3 Re LPS neighbors (corresponding to 6 phosphate groups), is indicative of hexagonal packing, which has previously been observed in experimental studies when Gram-negative outer membrane mimetics were strained or placed under high surface pressures [121]. (G, H) The heat capacity change as a function of distance between the PMB1 peptide and the bilayer center. The data are determined for the membrane that with simulated with (G) Na^+ and (H) Ca^{2+} ions.

3.4.4 Cytoplasmic Membrane Simulations

Once PMB1 peptides have passed the Gram-negative bacterial outer membrane they are then able to interact with and disrupt the inner cytoplasmic membrane. PMB1 peptides have been simulated with inner bacterial membrane mimetics once before using atomistic molecular dynamics simulation forcefields [328] and they were simulated here again using the coarse-grained Martini simulation forcefield. The inner membrane of Gram-negative bacteria is known to contain both PE and PG lipids and scientists have used two-component PE/PG lipid bilayers [270,880] as substitutes for the Gram-negative inner membrane. But it is important to appreciate that the inner membrane can be more complex and it can also contain transmembrane proteins, peripheral membrane proteins, cardiolipin, saturated and unsaturated acyl chain moieties etc. [95]. The coarse-grained PMB1 peptide molecules were simulated here with a bilayer that contained POPE and POPG lipids in a 3:1 number ratio in an attempt to understand how PMB1 peptides interact with the inner membrane of Gram-negative bacteria. The bilayer was assembled with the *insane.py* Python tool [893] that divides a periodic box of specified dimensions (here ~12.5 x 12.5 x 10.5 nm) into a contiguous three-dimensional grid and subsequently fills the void cells with user-defined lipids, proteins, and solute particles. The membrane was initially energy minimized and was subsequently simulated for 5 μs to converge the lipid parameters. The PMB1 peptides were placed at least 5 nm from the phosphate plane (based on center of mass separation) and the resulting lipid-peptide systems were simulated for 5 μs each.

It is instructive to first consider the inner Gram-negative bacterial membrane mimetic when it was simulated in water (Figure 36A) before we consider its properties when it interacts with the PMB1 peptides. The POPE and POPG lipids segregated from each other and formed distinct neutrally charged PE and negatively charged PG lipid microdomains when they were simulated with water and ions. Two-dimensional RDFs revealed that the POPG lipids more commonly paired with other POPG lipids than with the neutrally charged POPE molecules. The RDFs were computed for each POPG lipid with respect to every other POPG lipid (POPG-POPG) and also for each POPG lipid with respect to all of the other POPE molecules (POPG-POPE). The pair correlation values were larger in the POPG-POPG RDF than they were in the POPG-POPE RDF despite the fact that the POPG lipids were three times less common. The disparities are presented in terms of two-dimensional projections of lipid number densities for clarity. The POPG number densities were computed by initially splitting the periodic box into a contiguous lattice and subsequently determining how many POPG lipids there were in each (0.2 x 0.2 nm^2) grid cell. The visualization reveals that the POPG lipids preferentially segregated from the encompassing POPE molecules to form nanodomains that contained up to six POPG lipid molecules each (Figure 36B-D). The formation of the small POPG nanodomains can be understood if we consider membrane width, electrostatic interactions and the entropic forces. The association of the POPG lipids is driven in part by the hydrophobic effect: as POPE and POPG lipids are progressively sequestered into distinct domains there is on average a reduction in hydrophobic mismatch [219-221]. There would be more variance in membrane width if the lipids were more evenly distributed throughout the membrane. Electrostatic interactions also contribute: ambient ions bind to negatively charged POPG lipid phosphate groups and effectively screen some of the repulsive electrostatic interactions between the adjacent anionic POPG lipid phosphate groups that would otherwise promote electrostatic repulsion. RDFs were computed for monovalent cations with respect to the POPG phosphate groups to validate this statement. The first peak of the RDF had a magnitude of 25 (sampled during the last 10 ns) and this indicates that the monovalent cations were

interacting with the POPG lipid phosphate groups. Finally, we must also appreciate that entropic forces must have driven the multicomponent membranes towards a state of increased homogeneity [956]; the lipids will segregate, but only partially.

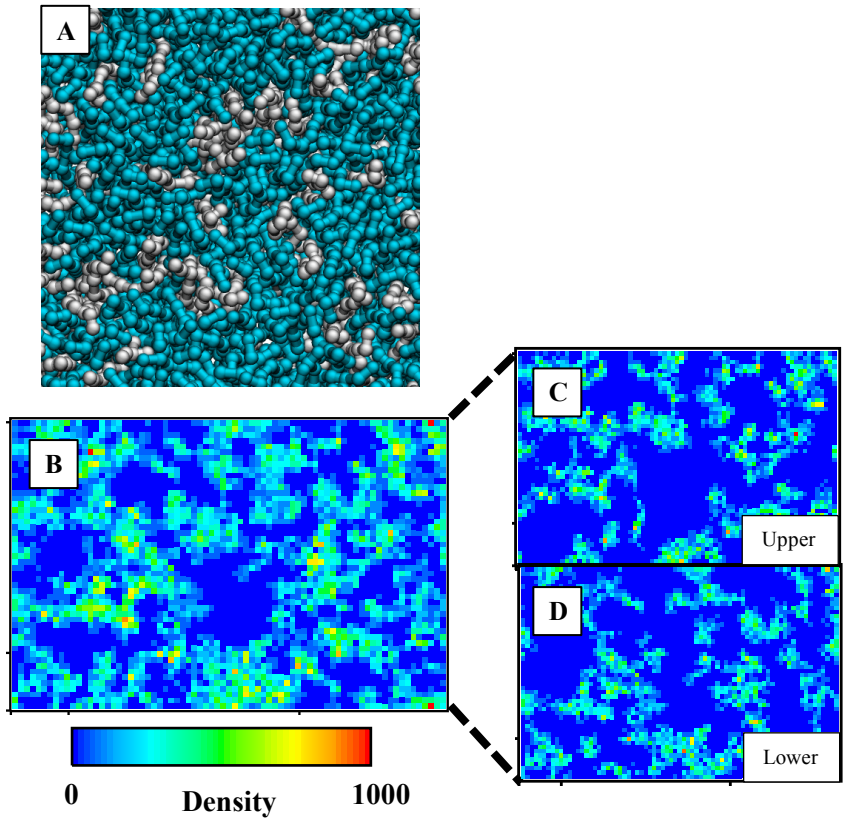

Figure 36. (A) Final frame (top view) snapshot of the Gram-negative inner membrane mimetic. The lipids have the following color scheme: POPE (cyan) and POPG (white). (B) The visualization of the POPG number density during the last 10 ns of the simulation. (C, D) The corresponding visualization of the POPG number densities in the upper (C) and lower (D) bilayer leaflets.

Further decomposition of the total two-dimensional particle number densities revealed that there is also correlation of the (PE/PG) lipid positions across the membrane midplane. There was association of the POPG particle positions in the upper and lower leaflets of the Gram-negative bacterial inner membrane mimetic. This alignment of lipid types about the membrane midplane has been observed in multicomponent membranes but the association is usually noted for plasma membrane mimetics [335,358,957-958] rather than bacterial membrane mimetics. This transversal alignment

reduces the line tension at the interface between the two membrane leaflets. Thus, the formation of small POPG lipid domains and their correlation across the bilayer midplane is due in large part to a complex combination of electrostatic interactions between negatively charged headgroups, hydrophobic mismatch, line tension energies at the phosphate interface and an entropic component that drives multicomponent membranes toward a state of homogeneity.

The center of mass positions of the PMB1 peptides were analyzed in an attempt to understand how the PMB1 peptides moved from the water domain of the simulation cell into the Gram-negative inner bacterial membrane mimetic core (Figure 37A). Representative coordinates are shown for a single PMB1 peptide as it moved along the bilayer normal and passed through the phosphate boundary at 460 ns. The PMB1 peptide moved through the water domain until it came into contact with the surface of the multicomponent membrane. At that moment the PMB1 Dab residues interacted with the phosphate groups of the negatively charged POPG lipid. The hydrophobic alkyl and benzyl groups of the PMB1 peptides progressively entered into the bilayer interior. Two-dimensional Voronoi tessellations of the POPG phosphate groups revealed that the PMB1 hydrophobic moieties passed through the phosphate interface as micropores formed within the membrane surface at the bilayer-water interface (Figure 37B).

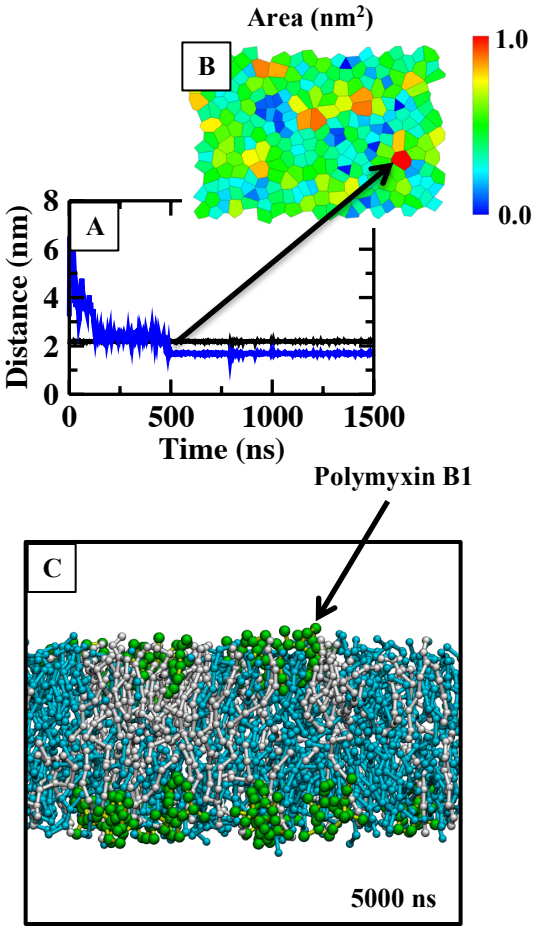

Figure 37. (A) The distance of the upper leaflet POPE and POPG phosphate groups from the membrane midplane is shown with a black line. The distance between a single (representative) PMB1 peptide and the bilayer center is shown with a blue line. (B) The area per lipid for each one of the upper leaflet phosphate group at 460 ns i.e. the time when the PMB1 peptide passed through the phosphate group domain. The arrow shows the pore that the PMB1 peptide tunneled when it moved into the membrane interior. (C) Final frame (side view) snapshot that shows the position of the PMB1 peptides in the Gram-negative inner membrane mimetic.

Temporary defects formed at the bilayer interface due to the fact the constituent lipids ceaselessly move back-and-forth and that this process affects the permeability of the membrane surface. There is at any given time an area of the membrane surface that is relatively depleted of hydrophilic headgroups and other areas that are relatively enriched in hydrophilic headgroups particles. The hydrophobic penetrants can more easily pass through the areas of the membrane surface that are relatively depleted of

hydrophilic headgroups. There was complete immersion of all the alkyl and benzyl groups into the bilayer interior during simulation time and this can be understood if we consider the low lateral area compressibility moduli of the phospholipid membrane (0.673 ± 0.002 Nm^{-1}) and that the fact that the Gram-negative inner membrane mimetic did not contain any saccharide units that could impede the PMB1 peptides. The inner Gram-negative hydrophilic headgroup was much easier to pass through than the coarse-grained Re LPS membrane. The PMB1 peptides were on average 1.6 ± 0.4 nm above the bilayer midplane during the final 100 ns of production time (Figure 37C).

The embedded PMB1 peptides had non-negligible effects on the organization of the membrane lipids and on the overall bilayer packing parameters. Computation of the two-dimensional number densities of the Gram-negative inner membrane mimetics revealed that the PMB1 peptides reduced bilayer homogeneity. There was more pronounced division of the POPE and POPG lipid fractions after the membranes had interacted with the PMB1 molecules (Figure 38A). For example, anionic lipid clusters contained up to 20 POPG molecules in these simulations with the PMB1 peptides and only 6 POPG lipids when the bilayers were simulated with only water and ions. There was lipid aggregation within each membrane leaflet and there was also correlation of the cluster positions across the membrane midplane. This promotion of lipid demixing was associated with a significant reduction in the overall lipid type homogeneity.

Further computation and visualization of the particle number densities demonstrated that the position of the POPG lipid clusters were correlated with the positions of the embedded PMB1 peptides (Figure 38B). The association of the POPG lipid and the PMB1 peptide positions indicates that the embedded PMB1 molecules were directly responsible for the reduction in lipid type homogeneity. The embedded antimicrobials affected the electrostatic interactions between the neighboring POPG lipids and this process enhanced POPG lipid aggregation.

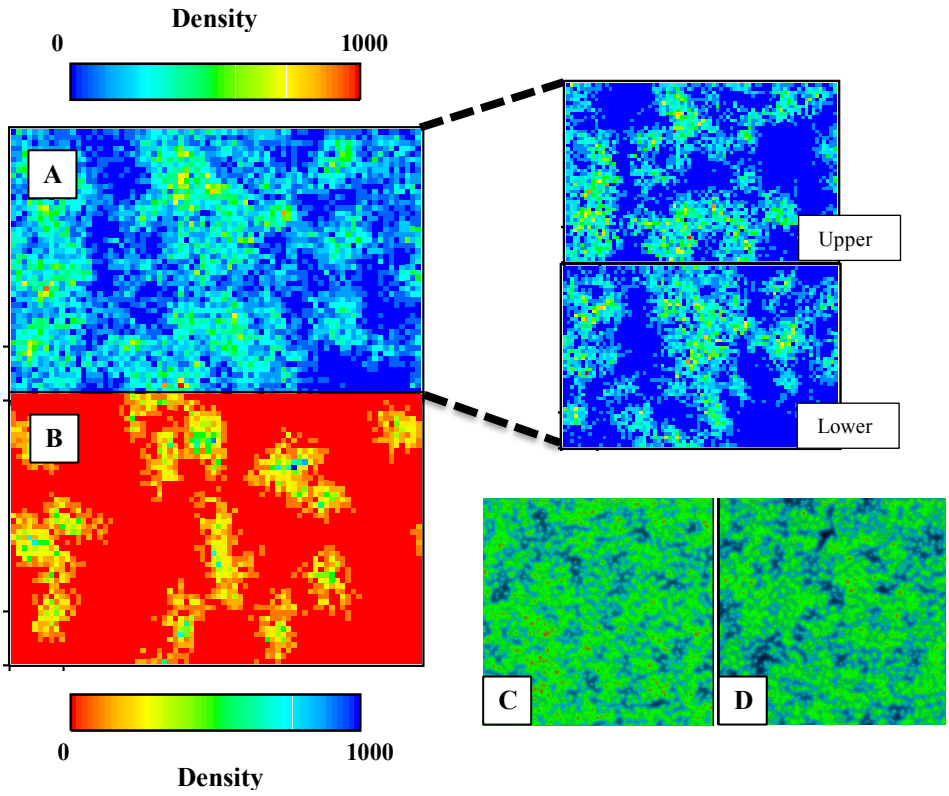

Figure 38. (A) The POPG lipid number density during the last 10 ns of the molecular dynamics simulation. The projected number density map is decomposed into the contributions from the upper and lower leaflets (inset). (B) The associated PMB1 peptide particle number density during the last 10 ns of the molecular dynamics simulation. (C, D) The thickness of the upper bilayer leaflet during the last 10 ns of the molecular dynamics simulation. The figures show thickness data for the simulation systems with water and ions (C) and for the simulation systems with water, ions and peptides. There is approximately one PMB1 peptide for every 27 phospholipids (D).

There was also correlation between the position of the PMB1 peptides and the location of the localized bilayer thinning and this result matched data from comparable united-atom forcefield molecular dynamics simulations [328]. Membrane thickness was reduced in the vicinity of the embedded PMB1 peptides (Figure 38C-D) and affects bilayer stability [959]. Thus, the embedded PMB1 peptides have been shown to promote lipid demixing and at the same they have been found to reduce membrane width. The interactions are not entirely dissimilar to the carpet mechanism that has been proposed to describe how certain AMPs increase membrane permeability and destroy pathogenic bacteria. The PMB1 molecules were found to not only affect membrane organization but also the basic packing parameters that underpin

membrane strength. The structure of the bilayer was affected on the short microsecond timescales that were used here and it would be reasonable to observe more drastic changes to the membrane structure on longer timescales.

At this point, it is necessary to assess the quality of the coarse-grained molecular dynamics simulations and consider if the results were biased by the simulation setup. First, it is important to appreciate that the PMB1 peptides were placed at least 5 nm from the bacterial membrane mimetic surfaces (defined by the position of phosphate groups) before the unbiased molecular dynamics simulations were started at simulation time $t = 0$. Second, we should keep in mind that the initial orientations of the PMB1 peptides were always set to be random before production time. Third, we need to consider that the bacterial membrane mimetics were simulated for at least 5 μs before the membranes were simulated with any PMB1 peptides. Molecular dynamics simulations of AMPs can be biased if the lipid membranes have not been adequately equilibrated as the membranes will not have not reached a converged conformation [960]. It is assumed that converged membrane conformations are more realistic representations of the *in vivo* scenario [59] and therefore, that converged bilayer conformations are necessary for mimicking realistic antimicrobial interactions. The long equilibration timescales that were used in this chapter ensure that the lipid conformations were converged, or close to being converged, before they were simulated with the antimicrobial peptides and we can therefore conclude that at least one of the potential simulation biases was addressed. Another potential biasing procedure is to place antimicrobial peptides too close to the lipid membrane surfaces before the molecular dynamics simulations are conducted [630]. When AMPs are placed too close to the lipid membrane surfaces they are unable to freely change their conformation before they bind the lipid headgroup domain. The initial interactions become highly dependent on the starting configurations and the simulations become less likely to reproduce realistic biomolecular interactions. Considering the initial positions and orientations of the PMB1 peptides, i.e. random and at least 5

nm from the lipid phosphate groups, we can conclude that the other, more obvious simulation biases were also addressed. Overall, it seems that the PMB1 simulations were relatively unaffected by obvious biasing set up procedures but that is not to say the methodology was faultless. More independent repeat simulations could have been conducted to obtain average values that were representative of tens of comparable simulations, rather than just a few. Numerous additional repeat simulations would have indisputably demonstrated that the simulation results were not in any way anomalous.

Perhaps the most convincing evidence that the PMB1 simulations were relatively free from bias is found through comparisons with previous publications. Take for example, the tendency of PMB1 peptides (AMPs) to induce the growth of small PG lipid nanodomains. Previous publications drew comparable conclusions for different types of AMPs [255,270-271,281-283]. It was found that cationic AMPs had the capacity to rearrange Gram-negative bacterial inner membrane mimetics in both atomistic and coarse-grained resolution molecular dynamics simulations. Different AMPs promoted the growth of small PG lipid domains, regardless of the specific structure of the cationic AMPs that were being used to study antimicrobial interactions. The similarities between different publications help to corroborate the inference that these coarse-grained simulations were not in any way anomalous, not highly dependent on the selected starting configurations, that they were representative of realistic biomolecular interactions and that they were relatively free from biases that could significantly affect the simulation results.

The movement of the PMB1 peptides was unbiased both within the plane parallel the lipid membrane surface and also along the membrane normal axis (*z*-axis) throughout the entire duration of the molecular dynamics simulations. There were two reasons for adopting this unbiased setup: (i) not to constrain the PMB1 conformations; and (ii) to ensure that there were similar numbers of PMB1 peptides either side of the membrane midplane.

The lipid bilayer becomes strained when there is mismatch of molecular surface area about the membrane midplane and this can alter almost all membrane properties including lipid aggregation, curvature generation, membrane thickness etc. [428,961-962] The motion of the PMB1 peptides was unbiased along the *z*-axis to minimize the possibility that all of the simulated PMB1 peptides could move into just one-half of the membrane and thereby created mismatch of molecular surface area about the membrane midplane. The PMB1 molecules could freely enter the membrane through either its outer (extracellular) or inner (intracellular) sides. The reasons for this setup are now clear but it is interesting to consider what would be expected if the PMB1 peptides were exposed to just one side of the membrane, i.e. the PMB1 peptide motion was in fact biased along the *z*-axis. The concentration of the PMB1 peptides would become highly concentrated within just one-half of the Gram-negative inner membrane mimetic [695-696] and this side of the bilayer would presumably display significant lipid segregation and more pronounced PG lipid nanodomain formation. The cationic PMB1 peptides would be especially abundant on this single side of the lipid membrane and this bilayer surface would presumably have more significant PG nanodomain formation; more so than anything noted throughout this chapter.

The possibility of performing simulations that would force PMB1 peptides into a single side of the Gram-negative bacterial membrane mimetic are interesting to discuss not only in terms of predicted results, but also in terms of potential implementation. Here we can discuss simulation procedures that would force the PMB1 peptides to interact with just one-half of the inner Gram-negative bacterial membrane mimetic. The discussion would help readers to understand how feasible it would be to perform such simulations for themselves and understand the quality of the simulation output. One method for biasing the movement of biomolecules within periodic simulation cells is to introduce simulation cell "walls" [963-964]. Molecular dynamics simulation packages ordinarily enable users to place walls at the borders of simulation cells that affect all molecules equally, or

some molecules more so than others. The simulation cell walls could stop PMB1 peptides from passing from one side of the simulation cell (e.g. extracellular) into the other (e.g. intracellular). The introduction of simulation cell walls can however, be undesirable since it necessitates the use of unusual simulation options such as periodicity along just two, rather than three coordinate axes. Another option is to "trap" PMB1 peptides between two equivalent inner Gram-negative bacterial membrane mimetics. Ordinarily there is only one planar membrane per simulation cell, but when there are two planar membranes, there are domains within the simulation cell that are relatively inaccessible [965-967]. If PMB1 peptides are placed between the two adjacent membranes, the antimicrobials can only interact with one-half of each multicomponent membrane system. The PMB1 peptides would become concentrated on a single side of each multicomponent membrane and it would be relatively simple to understand how the host membranes are differently perturbed when a single side of the bacterial membranes interact with PMB1 peptides.

3.5 Conclusion

Gram-negative bacteria are developing resistance to last-line antibiotics and this is making many of the most commonly used and readily available antimicrobial medications completely ineffective for treating infectious strains of Gram-negative bacteria [593-600]. Computational simulation methodologies have reached a level of sufficient complexity that they can be used to gain unprecedented molecular level insights into the action of effective antimicrobials [624-629]. Molecular dynamics simulation forcefields are increasingly being applied to understand how some of the most effective AMPs disrupt bacterial membrane mimetics [630-631]. There have been many atomistic resolution molecular dynamics simulations that have attempted to understand how polymyxin molecules interact with bacterial and mammalian membrane mimetics on relatively short (typically less than 1 μs) simulation timescales [243,328,726,728]. The simulations were conducted with the aim of understanding how polymyxin molecules

interact with biological membranes so that these membrane disrupting properties could be duplicated in new antibiotics that are either polymyxin-based derivatives or antibiotics that have an entirely distinct chemical composition. The coarse-grained Martini molecular dynamics simulation forcefield was used here in this chapter to understand the interactions of PMB1 peptides with different Gram-negative bacterial membrane systems on long timescales.

The PMB1 peptides were simulated with a phospholipid membrane that contained POPE and POPG in a 3:1 number ratio and the multicomponent membrane was therefore quite similar to inner membranes of Gram-negative bacteria [270,880]. The PMB1 peptides maintained positions close to the water-lipid interface once the PMB1 hydrophobic moieties (e.g. isobutyl, phenylalanine, terminal acyl tail) entered into the hydrophobic membrane interior. The positively charged (Dab) residues of the PMB1 peptides preferentially interacted with the negatively charged PG lipid headgroups and this induced the formation of negatively charged (PG) nanodomains within the multicomponent Gram-negative inner bacterial membrane mimetic. The PMB1 peptides additionally induced bilayer thinning and decreased the normal distance between the extracellular and intracellular membrane leaflet hydrophilic headgroup boundaries. The membrane thinning effects were highly localized and the locations of the decreased membrane width coincided with the locations of the membrane-active PMB1 peptides. The results closely correspond to data that was obtained from previous simulation studies of membrane-active antimicrobial peptides [117,270-271,281-283,726,728]. It has been demonstrated that the PMB1 peptides did not only reorganize the Gram-negative bacterial multicomponent membrane mimetics but that they also reduced membrane thickness values. The results could help to explain how PMB1 peptides disrupt the inner membrane of Gram-negative bacteria. First, the preferential interactions between the PG lipids and the PMB1 molecules would lead to a local increase in the concentration of the PMB1 peptides at specific points of the membrane surface, i.e. areas enriched with PG lipids. The PMB1 peptides

would then thin the anionic PG lipid nanodomains and these sections of the membrane surface would become less structurally stable and more likely to rupture [959]. There would effectively be anionic “hotspots” that are unusually prone to induce membrane breakdown processes such as micellization processes or the production of transmembrane water pores. It must be appreciated here that the reorganization of the PE and PG lipids would additionally affect the function of membrane proteins because protein-lipid interactions affect protein properties and many important cellular functions [370-371]. PMB1 peptides might hamper the proliferation of pathogenic bacteria by affecting membrane proteins that control bacterial growth and replication. This is speculation based on these interesting molecular dynamics simulation results, but it is important to make some inferences to place the simulation data in context and provide predictions for other scientific research groups.

The PMB1 peptides were also simulated with symmetric Re LPS lipid membrane simulation systems to understand how PMB1 peptide molecules interact with the outer membrane of Gram-negative bacteria. The Re LPS lipids had unusual biophysical parameters that made it difficult for the PMB1 peptides to translocate from the water domain of the simulation cell into the Re LPS lipid membrane core. The Gram-negative bacterial membrane mimetics had glass-like dynamics, high shear viscosities, relatively immobile phosphate groups and a thick wall of hydrophilic core sugar units. The simulation analyses demonstrated that the PMB1-Re LPS interactions were not completely converged even after 5 μs and this lack of simulation convergence was addressed with biased simulation methods. The biased simulation methods were used to increase the scope of the molecular dynamics simulation study and understand how the PMB1 peptides might destabilize the bacterial membrane mimetic on long timescales. The umbrella sampling technique was combined with WHAM to generate PMFs profiles and determine the energetics of PMB1 peptide translocation from the water domain of the simulation cell into the Re LPS lipid membrane core. The umbrella sampling simulations and WHAM analyses demonstrated that the

Re LPS bilayer became increasingly rigid and immobile when the PMB1 peptide was restrained at positions that were closer to the Re LPS membrane midplane. When the PMB1 peptides were restrained at normal distances of 1.6 nm (Ca^{2+} system) and 1.9 nm (Na^{+} system) from the bilayer center (i.e. the position of the PMF minima) they induced changes in the phase behaviour of the bacterial membrane mimetics. The bacterial membrane mimetics became significantly more rigid and the LPS phosphates began to behave as an amorphous solid. This insight is noteworthy because membrane fluidity can affect different bilayer properties such as shape, tension and elastic moduli [884-887]. Membrane fluidity can also affect biological functions that are crucial for cell viability such as enzymatic action and protein sorting [888-891]. Here I have studied the interactions of PMB1 peptides with bacterial membrane mimetics and I have provided some important biomolecular insights that might help chemists to understand how PMB1 peptides can disrupt bacterial membranes and kill Gram-negative bacteria.

Chapter 4: Lipopolysaccharide O-Antigen Chains Modulate the Mechanical Strength of the Gram-Negative Outer Membrane

4.1 Abstract

Lipopolysaccharide (LPS) macromolecules are unusually long lipids that always contain the Lipid A anchor with covalently bonded core saccharide domain and the molecules can additionally contain the repetitive glycan polymer moiety that has been termed the "O-antigen chain". Rough LPS lipids contain the Lipid A anchor with core saccharide sugars alone, whereas smooth LPS lipids additionally contain terminal O-antigen chain moieties. Coarse-grained molecular dynamics simulations were used in this chapter to understand how the interactions between O-antigen chains can affect the mobility and mechanical strength of Gram-negative bacterial outer membrane mimetics. The coarse-grained molecular dynamics simulations demonstrate first of all, that membrane composition affects LPS lipid packing parameters and second of all, that these differences are inextricably linked to membrane mechanical strength. The O-antigen chains had approximate lamellar packing when the outer leaflets of the bacterial membrane mimetics contained smooth LPS lipids alone (i.e. without phospholipids). The O-antigen chains spread out over the membrane surface when the outer leaflets of the bacterial membrane mimetics additionally contained PE and/or rough LPS lipids. When the Gram-negative bacterial membrane mimetics contained an extracellular leaflet that was exclusively comprised of smooth LPS lipids they were able to withstand high surface tensions ($150\ mNm^{-1}$). The Gram-negative bacterial membrane mimetics were able to withstand lower surface tension magnitudes when they contained PE and/or rough LPS lipids in the extracellular leaflet.

4.2 Introduction

The outer membrane of Gram-negative bacteria has an unusual asymmetric structure and unusual biophysical parameters. The extracellular leaflet

contains a high concentration of long LPS macromolecules and the intracellular leaflet contains a high concentration of smaller PE and PG phospholipids [101-103]. The LPS lipids are crossed-linked with stabilizing cations and this combination of positively charged cations and negatively charged LPS lipids creates a relatively rigid barrier that can help the Gram-negative bacteria to resist external stressors [104,968-969]. LPS lipids can affect the basic functioning of individual Gram-negative bacteria and the basic functioning of entire Gram-negative bacterial cell colonies [970-972].

LPS lipids always contain the Lipid A anchor that is covalently bonded to some combination of core saccharide sugars and these sugars can in turn, be bonded to the terminal (repetitive) O-antigen chain glycan polymer [543-545]. The Lipid A moiety is a phosphorylated glucosamine disaccharide that contains between four and seven anchoring acyl chains [555]. The Lipid A moiety is covalently bonded to the core saccharide domain and the core saccharide sugars can in turn, be bonded to the terminal O-antigen chain polymer that has been found in some cases to contain several hundreds of constituent sugars [971]. The appearance of Gram-negative bacterial cell colonies is affected by the length of the LPS lipids that comprise the Gram-negative bacterial cell outer membranes. Gram-negative bacterial colonies appear to be smooth when they contain LPS lipids with terminal O-antigen chains (smooth LPS) and rough when they contain LPS lipids that are capped at the core saccharide domain [972]. LPS nomenclature is based on the appearance of Gram-negative bacterial cell colonies. When LPS lipids contain the Lipid A anchor with variable core saccharide sections they are termed “rough” LPS lipid variants and when the LPS lipids contain the Lipid A anchor with variable core saccharide and terminal O-antigen chain polymer they are termed “smooth” LPS lipid variants.

It was demonstrated that O-antigen chain polymers have the capacity to modulate the structural characteristics of Gram-negative bacterial biofilms. Previous experimental analyses revealed that O-antigen chains have the capacity to affect the instantaneous elasticity of bacterial biofilms or put more

simply, how the bacteria respond to applied mechanical stress [973]. It is interesting to explore the possibility that O-antigen chains might additionally affect the instantaneous elasticity of individual bacteria or even individual Gram-negative bacterial cell membranes. Molecular dynamics simulations were used here in this chapter to determine if O-antigen chain interactions can affect the mechanical strength of Gram-negative bacterial cell membranes. Molecular dynamics simulation forcefields were used here to understand how LPS O-antigen chains interact with each other and how these lipid-lipid interactions can affect membrane tolerance for mechanical stress. Smooth LPS lipids were simulated in asymmetric membranes using the coarse-grained Martini molecular dynamics simulation forcefield. The inner bacterial membrane leaflets contained POPE and POPG lipids in a 9:1 number ratio and the outer leaflets contained different types of lipids (i.e. rough LPS, POPE, and smooth LPS) that were arranged in different number ratios. The membranes were initially simulated at atmospheric pressure and were subsequently simulated with increasing lateral pressure to understand the membrane tolerance for and response to, applied mechanical stress.

The simulations demonstrated that membrane composition affects the organization and aggregation of the LPS O-antigen chains. The O-antigen chains splayed out across the membrane surface when the extracellular leaflet of Gram-negative bacterial membrane mimetics contained smooth LPS lipids with rough LPS and/or POPE molecules. The conformation of the LPS O-antigen chains was different when the extracellular leaflet contained smooth LPS lipids alone. The O-antigen chains had approximate lamellar alignment when the extracellular leaflet of the Gram-negative outer membrane mimetics contained smooth LPS lipids alone and this arrangement of the O-antigen chains promoted strong cohesive intermolecular interactions between the adjacent O-antigen chains. The smooth LPS lipids were significantly less mobile (i.e. smaller lateral diffusion coefficients) when they were incorporated into the extracellular leaflet of the Gram-negative outer membrane mimetic system that was exclusively comprised of smooth

LPS lipids compared with the simulation systems that also included rough LPS lipids and/or POPE molecules in the extracellular leaflet.

The simulations demonstrated that cohesive intermolecular interactions between O-antigen chains can affect membrane tolerance for mechanical stress. The membranes were able to withstand surface tension magnitudes of 150 mNm^{-1} when the extracellular leaflet of the Gram-negative outer membrane mimetics contained smooth LPS lipids alone. The bacterial membranes withstood surface tensions of no more than 100 mNm^{-1} when the extracellular leaflet of the Gram-negative bacterial outer membrane mimetics additionally contained rough LPS, smooth LPS and/or POPE molecules. The data demonstrates that cohesive O-antigen chain interactions can increase the mechanical strength of the outer membrane of Gram-negative bacteria. There are strong intermolecular interactions within bacterial membrane mimetics when the constituent O-antigen chains have approximate lamellar alignment. The cohesive interactions increase the membrane tolerance for mechanical stress and the bacterial membranes become more mechanically robust.

The simulations were then used to rationalize how the bacterial membrane properties changed as the mechanical stress was incrementally increased and the lipid membranes were increasingly driven toward the point of rupture. There were changes to almost all of the membrane parameters when the applied mechanical stress was incrementally increased. The bilayers became thinner, the distances between the lipids increased, and the O-antigen chains packing became less uniform. There was less cohesion between the LPS lipids and the membranes became more flexible. Water molecules were able to penetrate the bilayer interior and they eventually induced the formation of transmembrane water chains that in turn, caused the bilayers to collapse.

4.3 Methods

4.3.1 Parameterization of the Coarse-Grained Smooth LPS Lipid

The parameterization of the smooth LPS lipid was stepwise: the *E. coli* O1 O-antigen chain was simulated with a united-atom forcefield and these atomistic resolution simulation data were then used to optimize parameters for a comparable coarse-grained model of the O1 O-antigen chain. The coarse-grained O-antigen chain was subsequently combined with a coarse-grained model for rough LPS lipid to create a new composite smooth LPS lipid model that contained the Lipid A anchor, core saccharide domain, and the terminal O-antigen chain. This parameterization process is described more thoroughly in the following three paragraphs.

The *E. coli* O1 O-antigen chain was initially simulated with the united-atom GROMOS 53A6 forcefield [561-562]. The glycan polymer was simulated in an orthorhombic unit cell and this cell was filled with SPC water molecules. The pressure was maintained at 1 bar with the Parrinello-Rahman barostat [841-842] and the temperature was maintained at 313 K with the Nosé-Hoover thermostat [840]. The electrostatic interactions were computed with the smooth particle mesh Ewald algorithm [974]; the short-range cutoff value was 0.9 nm. The van der Waals interactions were truncated at 1.4 nm with long-range corrections for the energy and pressure. The simulation bonds were constrained with the LINCS algorithm [845].

The united-atom particles were then mapped to coarse-grained pseudo-atoms in an attempt to produce a coarse-grained model that could mimic the behaviour of the reference united-atom *E. coli* O1 O-antigen chain (Figure 39A-B). Suitable coarse-grained model equilibrium angles (θ_{eq} and ϕ_{ijkl}), equilibrium bond lengths (r_{eq}) and the associated force constant parameters (k_{ij}^{r}, k_{ijk}^{θ} and k_{ijkl}^{ϕ}) were initially derived from the reference atomistic

simulation data. The coarse-grained equilibrium bond lengths and bond angles were determined as the average spacing between the atoms in the united-atom simulations and the corresponding force constants were determined from the variance about these mean average values. The coarse-grained parameters (θ_{eq}, ϕ_{ijkl}, k_{ij}^{r}, k_{ijk}^{θ} and k_{ijkl}^{ϕ}) were then refined after the coarse-grained parameter set was used to generate coarse-grained molecular dynamics simulation data and this new coarse-grained simulation data was compared with the original (reference) atomistic simulation data. To summarize this complex back-and-forth process: I initially determined suitable coarse-grained O1 O-antigen chain simulation parameters from the reference united-atom resolution simulations and then I used these parameters to conduct coarse-grained O1 O-antigen chain polymer molecular dynamics simulations. When I discovered any discrepancies between the united-atom and coarse-grained simulations I would adjust the coarse-grained parameters until these discrepancies were minimized. The coarse-grained parameter set was adjusted until the average O1 O-antigen chain radius of gyration was 0.49 nm for the comparative united-atom and coarse-grained simulations (Figure 39C) and until the average end-to-end O1 O-antigen chain distance differed by no more than 0.03 nm (Figure 39D). The equilibrium bond lengths (r_{eq}) in the coarse-grained and target united-atom simulations (mapped to coarse-grained pseudoatoms) generally differed by no more than 0.01 nm (Figure 39E) and the equilibrium bond angles (both θ_{eq} and ϕ_{ijkl}) were equivalent to within 1° (Figure 39F).

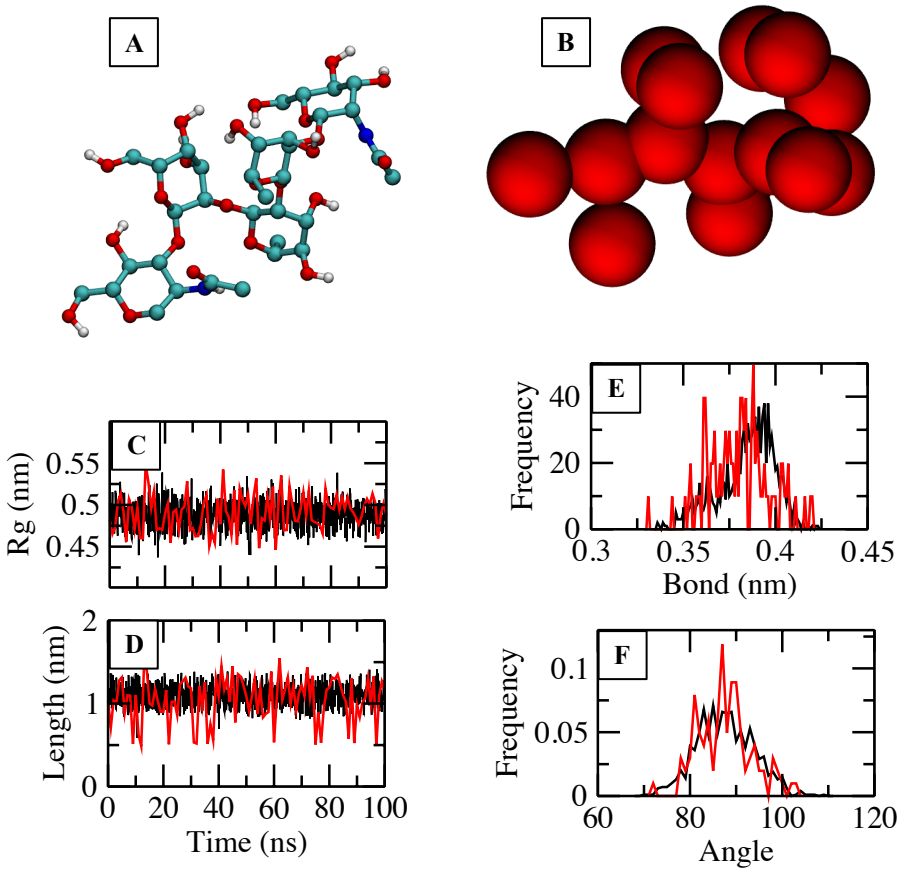

Figure 39. (A) Snapshot of a single unit of the *E. coli* O1 O-antigen chain that was simulated with the GROMOS 53A6 united-atom forcefield. The atoms have the following color scheme: carbon atoms (cyan), nitrogen atoms (blue), oxygen atoms (red) and hydrogen atoms (white). (B) The corresponding coarse-grained Martini forcefield model. (C) Comparison of the radius of gyration values for the O-antigen chain units in the comparative united-atom and coarse-grained molecular dynamics simulations. (D) Comparison of the end-to-end lengths for the O-antigen chain units in the comparative united-atom and coarse-grained molecular dynamics simulations. (E) The probability distribution for a single O-antigen chain bond length in the comparative united-atom and coarse-grained molecular dynamics simulations. (E) The probability distribution for a single angle in the comparative united-atom and coarse-grained molecular dynamics simulations. The united-atom simulation data are presented with black lines and the corresponding coarse-grained molecular dynamics simulation data are presented with red lines.

The coarse-grained O1 O-antigen chain parameter set was combined with a pre-existing coarse-grained model for *E. coli* rough (Ra type) LPS with R3 core sugars and type 1 Lipid A anchor. The resulting smooth LPS model contains

the conserved Lipid A domain with the complete R3 core saccharide sequence and four units of the repetitive O1 O-antigen chain glycan polymer. The O1 O-antigen chain repetitive subunit contains the five saccharides arranged end-to-end: β N-acetyl-D-glucosamine, α D-galactose, α L-rhamnose, α L-rhamnose, β N-acetyl-D-mannosamine. The smooth LPS lipid model was added to the CHARMM-GUI Martini Maker module (http://www.charmm-gui.org/) [151] to simplify the process of constructing asymmetric membrane models that contain different types of lipid (e.g. rough LPS, POPE, and smooth LPS) that are arranged in different number ratios.

4.3.2 Bilayer Simulations

The bacterial membranes were simulated with the coarse-grained Martini forcefield (version 2) [799,814] and the GROMACS simulation package (version 5.1.2) [975]. The simulation systems contained some combination of lipid, water, and ions and they were assembled with the CHARMM-GUI Martini Maker module [151]. The inner (intracellular) leaflets contained POPE and POPG lipids in a 9:1 number ratio and the outer leaflets contained the following lipids: only smooth LPS lipids (OANT), smooth LPS and POPE lipids in a 4:1 ratio (OANT_POPE), smooth LPS and rough LPS lipids in a 1:1 ratio (MIXED), and smooth LPS lipids with rough LPS lipids and POPE molecules in a 2:2:1 ratio (MIXED_POPE). The bilayers were solvated with a column of water that was long enough (~10 nm) to minimize the interaction strengths between one membrane system and its periodic image along the *z*-axis (membrane normal). Divalent cations (Ca^{2+}) were added to neutralize the negative charge of the Lipid A anchors and the remaining system charge was neutralized with monovalent cations (Na^{+}).

The bilayers were initially simulated for 100 ns to equilibrate the lipids. The lipids were then simulated for another 2 μs to understand LPS lipid interactions on microsecond timescales. The temperature was maintained at 313 K using the velocity-rescaling thermostat ($\tau_T = 1.0\ ps$) and the pressure was maintained at 1 bar using the Parrinello-Rahman barostat ($\tau_P = 5.0\ ps$)

[841-842]. The integration time step was 10 fs. The electrostatic interactions were computed with the reaction field method using dielectric constants of 15 and infinity for charge screening in the short-range and long-range regimes. The short-range cutoff for the electrostatic interactions was 1.2 nm. The Lennard-Jones potential was cut off at long ranges using the Potential shift Verlet scheme.

The bilayers were then simulated with lateral pressure magnitudes that were incrementally increased until the membranes ruptured. The lateral pressure was initially set to be -10 bar and the lateral pressure magnitude was subsequently increased to the larger magnitudes of -30 bar, -50 bar, -70 bar etc. thereafter. The lateral pressure (P_L) component was coupled completely separately from the pressure that was being applied along the membrane normal (P_N). Each simulation was 20 μs long because membrane bilayers can undergo significant restructuring when they are subjected to mechanical stress and the membrane restructuring process can be slow, i.e. occur on long microsecond timescales.

The order parameters were computed with the *gmx order* program, the lateral diffusion constants were calculated with the *gmx msd* program and the radial distribution functions were determined with the *gmx rdf* tool. The distances were calculated with the *gmx mindist* program and the angles and radii of gyration were calculated with the *gmx angle* and *gmx gyrate* programs. The area per lipid values were determined via two-dimensional Voronoi tessellations of the lipid phosphate groups. The particle number densities were determined with the *gmx densmap* program.

4.4 Results

Molecular dynamics simulations were conducted to understand the interactions of LPS O-antigen chains within Gram-negative membrane mimetics and to understand how these interactions might affect membrane tolerance for mechanical stress. Four membranes were simulated: systems

OANT, OANT_POPE, MIXED, and MIXED_POPE. In each instance the inner leaflets contained POPE and POPG lipids in a 9:1 ratio and the outer leaflets contained different lipid types (i.e. rough LPS, POPE, and smooth LPS) that were arranged in different number ratios. The composition of the extracellular leaflet was as follows: only smooth LPS lipids (OANT), smooth LPS and POPE molecules in a 4:1 ratio (OANT_POPE), smooth LPS and rough LPS in a 1:1 ratio (MIXED), and smooth LPS, rough LPS and POPE molecules in a 2:2:1 ratio (MIXED_POPE). There was enough divalent calcium (Ca^{2+}) ions within each simulation cell to neutralize the anionic charge that was being generated from the negatively charged LPS Lipid A anchors. The remaining system charge was neutralized with monovalent sodium (Na^{+}) ions. The systems were simulated for 2 μs each and the simulation temperature and pressure were maintained at magnitudes of 313 K and 1 bar.

The orientation of the smooth LPS lipids was affected by the membrane composition. The O-antigen chain sugars had an approximate lamellar alignment in system OANT and this orientation was comparable to the lamellar packing of the LPS anchoring acyl chains (Figure 40A-B). The O-antigen chains tilted more substantially relative to the bilayer normal (Figure 40C-D) within systems OANT_POPE, MIXED and MIXED_POPE. The number of cohesive intermolecular interactions between the O-antigen chain sugars was maximized when the LPS lipid headgroups either aligned with the membrane normal axis (system OANT) or when the O-antigen chains stretched out over the membrane surface (OANT_POPE, MIXED and MIXED_POPE). The specific O-antigen chain orientation depended on the characteristics of the encompassing membrane environment. The O-antigen chains aligned with the membrane normal when the extracellular leaflet of the Gram-negative outer membrane mimetics contained smooth LPS lipids and the O-antigen chains stretched out over the membrane surface when this leaflet additionally contained rough LPS lipids and/or POPE molecules. In one instance the number of cohesive O-antigen chain intermolecular interactions was increased when the smooth LPS lipid O-antigen chain polymer stretched out along the bilayer normal (OANT) and in the others (OANT_POPE, MIXED

and MIXED_POPE) the number of cohesive O-antigen chain intermolecular interactions was increased when the smooth LPS lipid O-antigen chain polymers stretched out over the membrane surface.

The coarse-grained smooth LPS lipid model was parameterized to mimic the interactions of *E. coli* LPS lipid with four units of the repetitive O1 O-antigen chain glycan polymer chain. The simulations provide some important insights into the general conformational characteristics of smooth LPS lipids within Gram-negative bacterial membrane mimetics but it is important to appreciate that O-antigen chain length can vary both among different strains of *E. coli*, and also within single highly heterogeneous Gram-negative membranes [971]. O-antigen chain polymers can contain more than ten repetitive glycan polymer units [976] and, in some circumstances, as many as forty units have been reported [971]. Based on atomistic molecular dynamics simulations of longer smooth LPS lipids (with 10 units of the O6 O-antigen chain) [211] it can be surmised that the splay of O-antigen chains depends on the O-antigen chain length. In previous all-atom molecular dynamics simulations [211-212] it was shown that (i) O-antigen chain subunits tilt relative to the membrane normal, and (ii) that O-antigen chain extension scales with the number of constituent O-antigen sugars. In other words, the O-antigen chains can stretch out over a more substantial portion of the membrane surface when the O-antigen chains contain a greater number of constituent glycan polymer units. It is expected then that the conformational characteristics of these coarse-grained O-antigen chains will differ somewhat from the *in vivo* scenario. Realistic Gram-negative bacterial membranes usually contain longer O-antigen chain polymers [971,976] and longer O-antigen chains are capable of stretching out over more of the membrane surface.

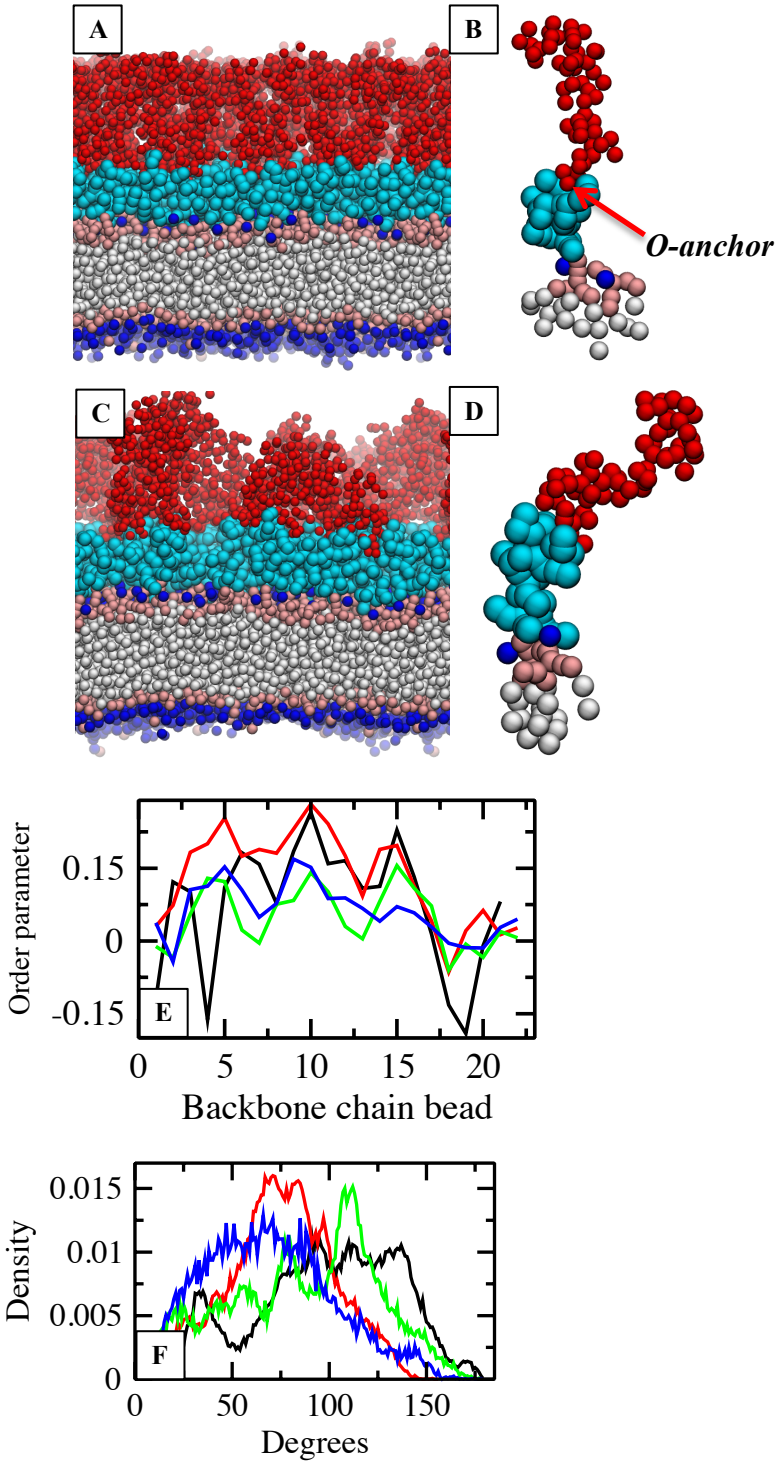

Figure 40. (A) Side view snapshot of system OANT, with (B) a single smooth LPS lipid extracted from the bilayer to show the orientation of the acyl chains and O-antigen chain sugars. The bond that anchors the O-antigen chain to the Lipid A and core sugar domains is termed here as "*O-anchor*" to make the discussion of LPS headgroup orientation clearer. (C) Side view snapshot of system MIXED_POPE, with (D) a single smooth LPS lipid extracted from the bilayer to show the orientation of the smooth LPS acyl chains and O-antigen chain sugars. The acyl tails are white, the phosphate

groups are blue, the glycerol and glucosamine sugars are pink, the core sugars are cyan, the terminal O-antigen chains are red and the water molecules are omitted for clarity. (E) The average order parameters that were calculated for the backbone chain beads of the O-antigen chain sugars in systems OANT (black), OANT_POPE (red), MIXED (green), and MIXED_POPE (blue). (F) The angle distribution for the angle that was formed between the *O-anchor* bond and the terminal O-antigen chain sugar in systems OANT (black), OANT_POPE (red), MIXED (green) and MIXED_POPE (blue).

The acyl tail order parameter can be quantified according to the equation $S = \frac{1}{2}\langle 3(\cos\theta)^2 - 1\rangle$ where θ defines the angle between a bond vector and the bilayer normal (per simulation frame) [569]. The time-averaged equation was applied to compute the average acyl tail order parameter for the smooth LPS lipids during the last 500 ns. The acyl tail order parameter values were as follows: 0.20 ± 0.002 (OANT), 0.20 ± 0.002 (OANT_POPE), 0.24 ± 0.003 (MIXED) and 0.28 ± 0.003 (MIXED_POPE). Order parameters can similarly be computed for the O-antigen chains to assess their average alignment during simulation time. The time-averaged acyl tail order parameters were calculated for the LPS O-antigen chains (Figure 40E) and compared with acyl tail order parameters for glycerophospholipid bilayers. The O-antigen chain order parameter profiles were varied and they contained contrasting troughs and peaks. The shape of the order parameter profile is comparable to the shape of the order parameter profile for the unsaturated acyl chain moiety of POPC lipids [864]. The order parameters of the O-antigen chain and of unsaturated acyl chains are also quite similar. In either instance the magnitude of the order parameters tends to be within the range of 0.05–0.2 [864].

The angle between the bond *O-anchor* (see Figure 40B) and the terminal LPS sugars was computed to understand the average orientation of the smooth LPS lipids and in particular, the orientation of the terminal O-antigen chain polymers (Figure 40F). The angles and the associated standard deviations were calculated using the last 500 ns of simulation time. The values were as follows: 101.2 ± 1.1° (OANT), 75.2 ± 1.0 ° (OANT_POPE), 86.5 ± 1.9 ° (MIXED),

and 68.7 ± 2.8° (MIXED_POPE). The data confirms that the O-antigen chains were tilted more substantially (relative to the anchoring Lipid A domains) when POPE molecules and/or rough LPS lipids were positioned between the smooth LPS lipids. The POPE molecules and rough LPS lipids broke up otherwise contiguous layers of smooth LPS lipids and as a consequence, the terminal O-antigen chains splayed out over the membrane surface. The O-antigen chains came into contact with each other and there was an overall increase in the number of cohesive intermolecular interactions between the terminal LPS carbohydrate moieties. The correlation between membrane composition and O-antigen chain orientation is corroborated by simulations of smooth LPS lipids with O91 or O6 O-antigen chains [211-212]. The O91 O-antigen chains and the O6 O-antigen chains adopted approximate linear conformations when the extracellular leaflet of the Gram-negative outer membrane mimetics only contained LPS lipids and the same O-antigen chains tilted relative to the membrane normal axis when the extracellular leaflet of the Gram-negative outer membrane mimetics additionally contained rough LPS molecules in the extracellular leaflet [211-212]. For reference, the O6 O-antigen chain subunit contains the five saccharides: β D-glucose, β N-acetyl-D-glucosamine, α N-acetyl-D-galactosamine, and two β D-mannose units. The O91 O-antigen chain subunit contains the five saccharide units: β D-galactose, two β N-acetyl-D-glucosamine units, β N-glycine-D-glucosamine, and one unusual 3-amino-3-deoxyquinovose sugar. In other words, each one of the three O-antigen chain polymers (O1, O6, and O91) contains different repetitive chain subunits but they all contain five pentose or five hexose sugars that are aligned end-to-end.

The flexibility of the terminal O-antigen chains promoted smooth LPS lipid clustering within the extracellular leaflets of the Gram-negative outer membrane mimetics. The O-antigen chains splayed out over the membrane surface in systems MIXED and MIXED_POPE and as the O-antigen chains interacted with each other, they progressively formed LPS lipid aggregates. This phenomenon is demonstrated for two smooth LPS lipids that were initially separated by ~4 nm at the start of the MIXED_POPE system

simulation (Figure 41A). The terminal O-antigen chain polymers splayed out over the membrane surface and this led to an increase in the number of cohesive intermolecular interactions between the smooth LPS lipids as they interacted with each other. The cohesive intermolecular interactions induced the formation of a smooth LPS lipid dimer after approximately 30 ns of simulation time (Figure 41B). The dimer then formed a larger smooth LPS lipid aggregate as additional O-antigen chains were intertwined through cohesive carbohydrate-carbohydrate interactions (Figure 41C). The aggregation of multiple smooth LPS lipids occurred in multiple independent coarse-grained molecular dynamics simulations. The repeated observation of the smooth LPS lipid clustering processes suggests that smooth LPS lipid aggregation is energetically favourable.

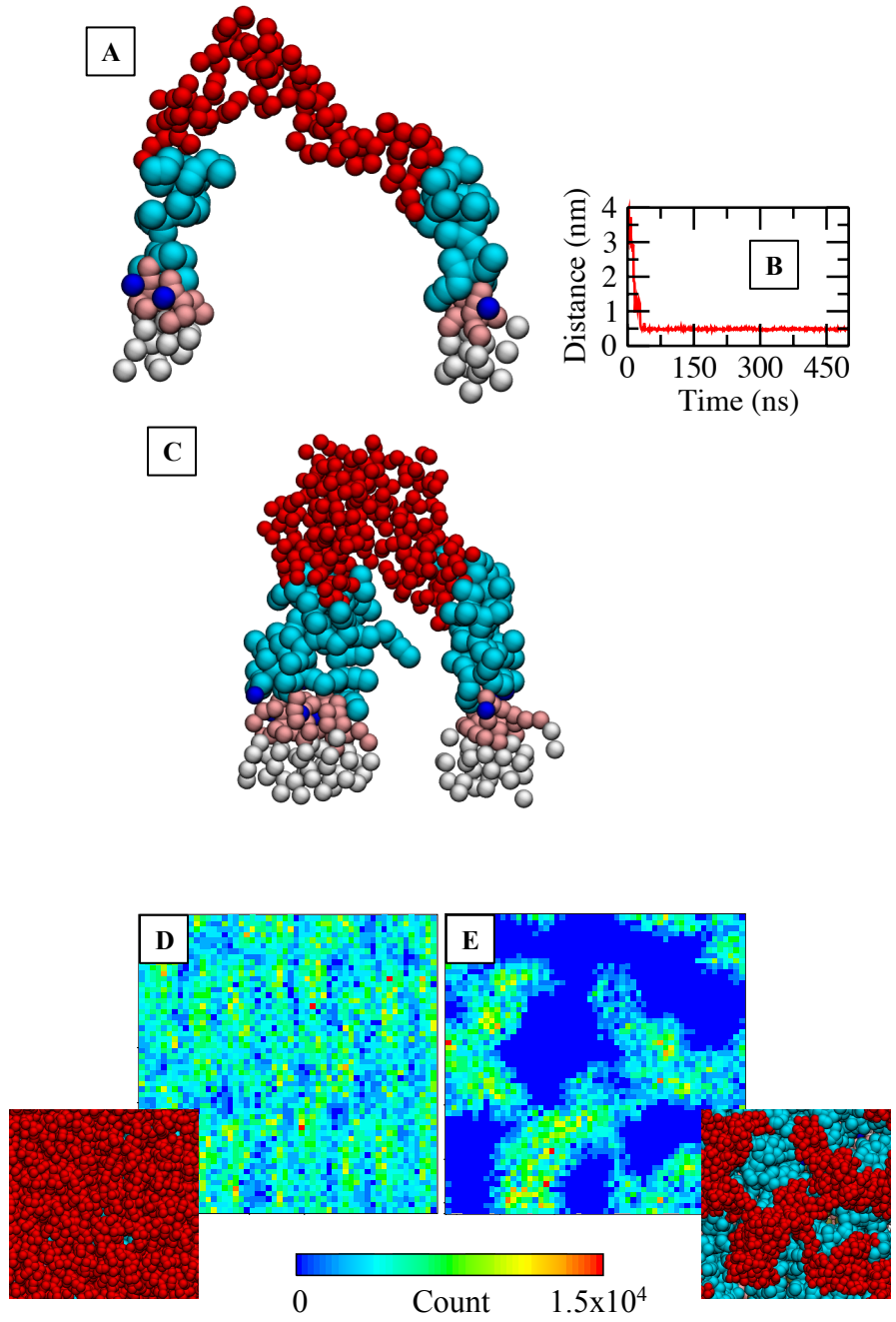

Figure 41. (A) Two smooth LPS lipids from system MIXED_POPE that were initially separated by ~4 nm and subsequently formed a dimer after the flexible O-antigen chains interacted with each other. (B) The corresponding time series that shows the distance between the two smooth LPS lipids as a function of sampled simulation time. (C) Snapshot of the large smooth LPS lipid aggregate that formed after additional smooth LPS lipids interacted with the smooth LPS lipid dimer. (D-E) The O-antigen chain number density in systems OANT (D) and MIXED_POPE (E) after 500 ns. The inset images show the corresponding top view snapshots.

The number density for the LPS lipid O-antigen chains was computed to understand the differences in O-antigen chain splay and clustering. Number densities were evaluated by initially splitting the simulation cells into a contiguous lattice and subsequently determining the number of particles within each grid cell unit (0.2 *x* 0.2 nm^2). The projections reveal how the O-antigen chains were arranged in the extracellular leaflets of the Gram-negative bacterial outer membrane mimetics (Figure 41D-E). The smooth LPS lipids were distributed relatively uniformly in system OANT and there were cohesive intermolecular interactions between the terminal O-antigen chains across the entire width of the periodic simulation cell. The arrangement of the O-antigen chains was significantly different in the extracellular leaflet of the outer membrane mimetic systems (i.e. OANT_POPE, MIXED and MIXED_POPE) compared with the extracellular leaflet that contained smooth LPS lipids alone (i.e. OANT). The O-antigen chains had separated from the encompassing POPE molecules within the OANT_POPE, MIXED, and MIXED_POPE simulation systems and the multicomponent membranes were effectively partitioned into domains with smooth LPS lipid and areas without smooth LPS lipid.

Larger analogues of system MIXED_POPE were simulated for 15 μs to gain additional insights into the segregation of the smooth LPS lipids on larger spatiotemporal scales. The smooth LPS lipids separated from the encompassing rough LPS and POPE lipids and formed a single smooth LPS lipid network that spanned the entire length of the simulation cell (Figure 42A-B). The formation of comparable LPS lipid networks has been noted in previous molecular dynamics simulations that were conducted with coarse-grained molecular dynamics simulation forcefields [301] and this suggests that the clustering of the LPS lipids themselves and the clustering of the LPS O-antigen chains is an energetically favorable process. The smooth LPS lipids formed a single network that spanned the length of the simulation cell (based on a 0.6 nm cut-off distance) and the terminal O-antigen chains formed two distinct domains (Figure 42C-D).

It seems reasonable to assume that LPS lipid co-clustering was not completely converged even after the 15 μs long coarse-grained molecular dynamics simulations and further to assume that the O-antigen chains could form a single unbroken network if the LPS lipids were simulated on a longer timescale. Simulations with the Martini forcefield are generally limited to microsecond timescales but the coupling and decoupling of glycolipids can occur on timescales that are much longer than this [325,498]. In other words, the segregation of the LPS lipids from the phospholipids (e.g. POPE) seemed to transpire quite quickly in these simulations but the segregation of rough and smooth LPS lipids from each other is a slower process that involves large energy barriers [325] and is therefore more challenging to probe with conventional molecular dynamics simulations.

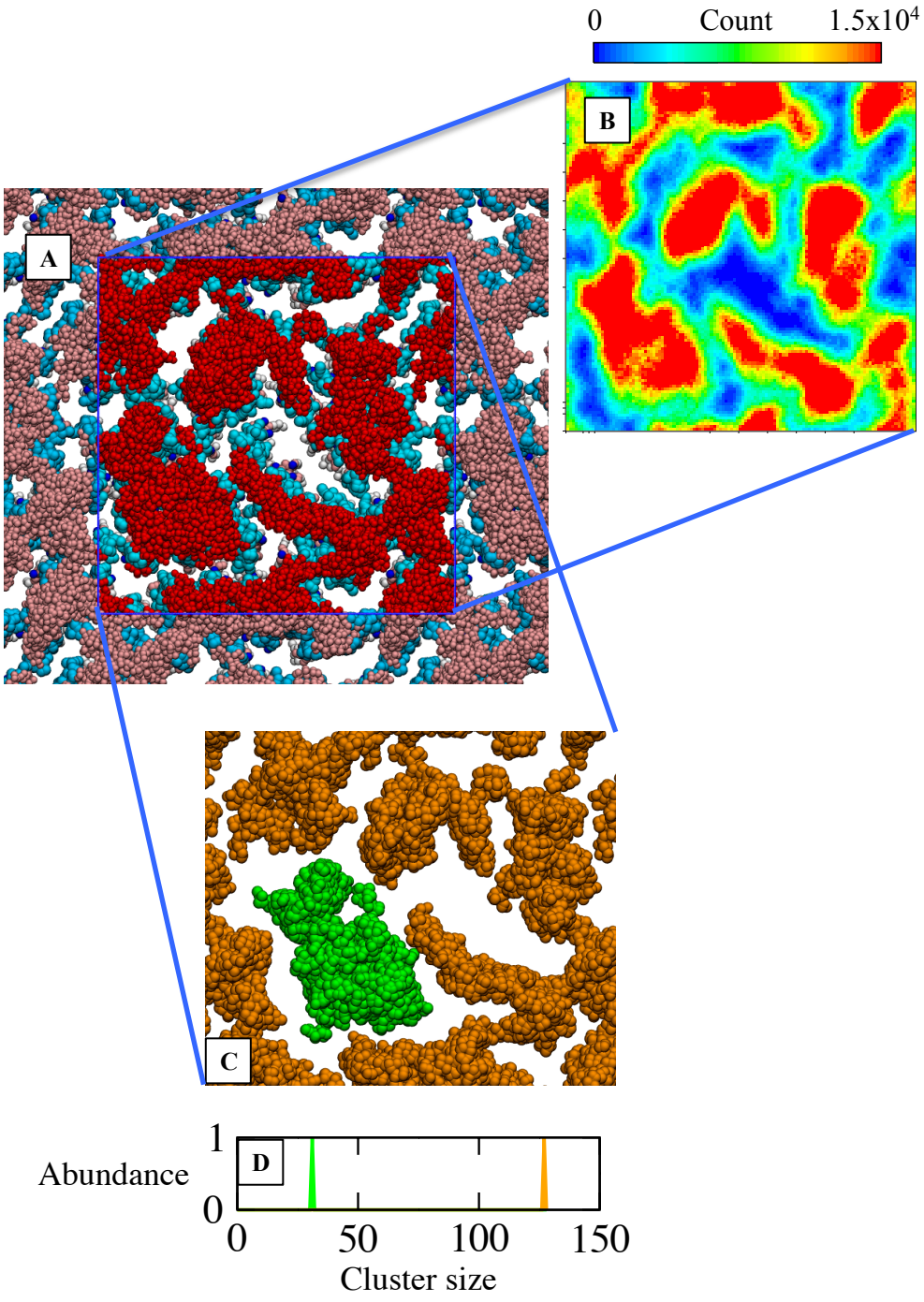

Figure 42. (A) Top view snapshot of a larger analogue of system MIXED_POPE after 15 μs. The POPE and rough LPS lipids are omitted for clarity. The periodic borders are represented with a thin blue line and the periodic images are presented with different shades of red and cyan for clarity. The smooth LPS lipids formed a single contiguous network that spanned the entire length of the simulation cell. (B) The corresponding two-dimensional projection of the O-antigen chain number density (sampled during the last 100 ns). (C) Snapshot of the two O-antigen chain aggregates after 15 μs of simulation time. One of the O-antigen chain aggregates is

green and the other one is orange. (D) The number of glycan polymers in each of these O-antigen chain aggregates.

The differences in the packing of the smooth LPS lipids had important consequences for the lateral mobility of the smooth LPS lipids. The average lateral diffusion rates were computed for smooth LPS lipids in each of the Gram-negative outer membrane systems and the computed values were as follows: 2.1 (OANT), 8.7 (OANT_POPE), 8.0 (MIXED), and 7.0 (MIXED_POPE) $x10^{-8}cm^2/s$. The smooth LPS lipids moved through the extracellular leaflet of the Gram-negative outer membrane mimetics more rapidly when there were POPE molecules and rough LPS lipids embedded throughout. It is interesting to compare the computed lateral mobilities with values from previous publications. The smooth LPS lipids were more mobile than previously simulated rough LPS lipid ($5\ x10^{-9}cm^2/s$) but less mobile than previously simulated B-band O-antigen chains ($2\ x10^{-7}cm^2/s$) [242].

The bilayers were subsequently simulated with lateral pressure values of increasing magnitude until the membranes became unstable and ruptured. The molecular dynamics simulations were conducted in an attempt to understand how the Gram-negative bacterial outer membrane models respond to applied mechanical stress and to determine which membrane systems were the most mechanically robust. The lateral pressure was initially set to be -10 bar and the lateral pressure magnitudes were set to be -30 bar, -50 bar, -70 bar etc. thereafter. The simulations were conducted for 20 μs because membrane breakdown mechanism can occur on long (microsecond) timescales [925].

The surface tension was computed according to the equation:

$$\gamma = L_z\,(P_N - P_L)$$

Equation 85

where L_z was the length of the simulation cell along the z-axis (bilayer normal) and P_N and P_L were defined in terms of the diagonal components of

the pressure tensor (P_{xx} , P_{yy} and P_{zz}) according to $P_N = P_{zz}$ and $P_L = [P_{xx} + P_{yy}]/2$. The areal strain ($\varepsilon_A$) was defined as:

$$\varepsilon_A = \frac{A_i}{A_0} - 1$$

Equation 86

where A_0 was the cross-sectional area of the membrane (along the bilayer normal) when it was simulated at atmospheric pressure and A_i was the cross-sectional area of the membrane when it was subjected to a lateral pressure P_L.

The surface tension-areal strain curves (Figure 43A) revealed that the membrane surface tension increased as the lateral pressure magnitude was incrementally increased. The tolerance of each membrane for lateral area expansion was similar throughout: the membranes ruptured over a critical area strain range of 0.61-0.76. Phospholipid membranes generally have similar tolerance for areal strain in atomistic simulations [977-979] and this similarity in data suggests that there must be similar maximum thresholds for most, if not all, lipid membrane systems.

It is apparent from the tension-areal strain curves that the surface tension magnitudes were largest in system OANT and this indicates that there were stronger intermolecular interactions at the membrane surface of system OANT compared with the OANT_POPE, MIXED, and MIXED_POPE simulation systems. System OANT had increased tolerance for surface tension: system OANT tolerated approximately 60 mNm^{-1} more tension than systems OANT_POPE, MIXED, or MIXED_POPE. System OANT was not only more robust than systems OANT_POPE, MIXED, and MIXED_POPE, it was also much more robust than single-component DPPC bilayers [978]. It seems that O-antigen chain interactions increase membrane mechanical strength. System OANT was the most rigid bilayer at atmospheric pressure and it was also the system that tolerated the largest surface tensions.

There were changes in the physical parameters of each membrane system when the lateral pressure magnitudes were incrementally increased. There was a systematic increase in bilayer surface area (Figure 43B), a systematic decrease in membrane thickness (Figure 43C), and a general reduction in acyl tail order parameters (Figure 43D). The bilayers become thinner and wider in response to the increasing lateral pressure magnitudes and there was a general reduction in the lamellar alignment of the lipid tails. The increasing lateral pressure magnitudes were associated with membrane deformation. The bilayers progressively thinned and expanded outwards (with increasing lateral pressure) until pores appeared along the bilayer normal and these pores caused the membranes to rupture.

It is interesting to compare the degradation and rupture of these complex Gram-negative bacterial membrane models with simpler lipid models that contain some combination of phospholipid and cholesterol molecules. Previous simulation studies assessed the relationship between bilayer areal strain and the magnitudes of different lipid properties including molecular orientation, membrane thickness, and the extent of lipid phase transitions [980]. Two simulation approaches were used: unsteady stretching (US), which involved proportional and temporal scaling of the system box lengths and atom positions [981], and quasistatic stretching (QS), where membranes were simulated at constant temperature (323 K), *z*-axis pressure (1 bar) and various constant bilayer surface areas [981-983]. The averaged instantaneous order parameter was found to monotonically decrease as the areal strain was increased in all of the US and QS simulations of the single-component DPPC lipid bilayers. However, the relationship between areal strain values and the averaged instantaneous order parameter was more complex for the multicomponent membranes that contained both DPPC and cholesterol molecules. Rather than monotonically decrease or monotonically increase, the averaged instantaneous order parameter was found to depend strongly on the range of areal strain magnitudes that was being studied. The averaged instantaneous order parameter was negatively correlated with

areal strain values for one range of ε_A magnitudes and positively correlated for another range of ε_A magnitudes. The relationship between areal strain and membrane thickness values was comparatively less convoluted for the single-component and multicomponent membrane systems [980]. The membrane thickness magnitudes were found to monotonically decrease in both US and QS simulations of either single-component or two-component membranes, for all but the most extreme of ε_A magnitudes.

It can be stated that the effects of increasing areal strain magnitudes are similar for systems OANT, OANT_POPE, MIXED, MIXED_POPE and for the simpler biological membranes that were simulated in previous computational publications [980]. Membrane thickness and acyl tail order parameters were negatively correlated with surface tension and areal strain values in this, and in previous simulation studies. It can be concluded that similar interactions might mediate bilayer breakdown processes, regardless of the specific membrane composition.

It is important to appreciate that the scope of molecular dynamics membrane mechanical strength analyses extends beyond the computation of surface tension magnitudes alone [984-991]. Membrane stiffness parameters are increasingly being characterized in terms of membrane fluctuation properties including bilayer height and thickness fluctuations [992-993]. Helfrich-Canham theory [994-996] can be used to accurately ascertain membrane bending rigidities, but the more accurate bending constants are derived from mesoscopic membrane simulations that include several tens of thousands of lipids and consequently, have both small and large undulatory wavelengths. Alternative schemes, albeit ones based on similar underlying physical models, tend to derive membrane mechanical strength constants from lipid tilting [997-999]. This approach was shown to be appropriate for single-component all-atom lipid bilayers but was deemed to be inappropriate for coarse-grained membrane simulation systems that contained membrane proteins [993]. The coarse-grained membranes that were simulated in this

chapter (i.e. OANT, OANT_POPE, MIXED, MIXED_POPE) lack the size or sophistication that would warrant the use of membrane mechanical strength analyses methods that are based on the Helfrich-Canham theory.

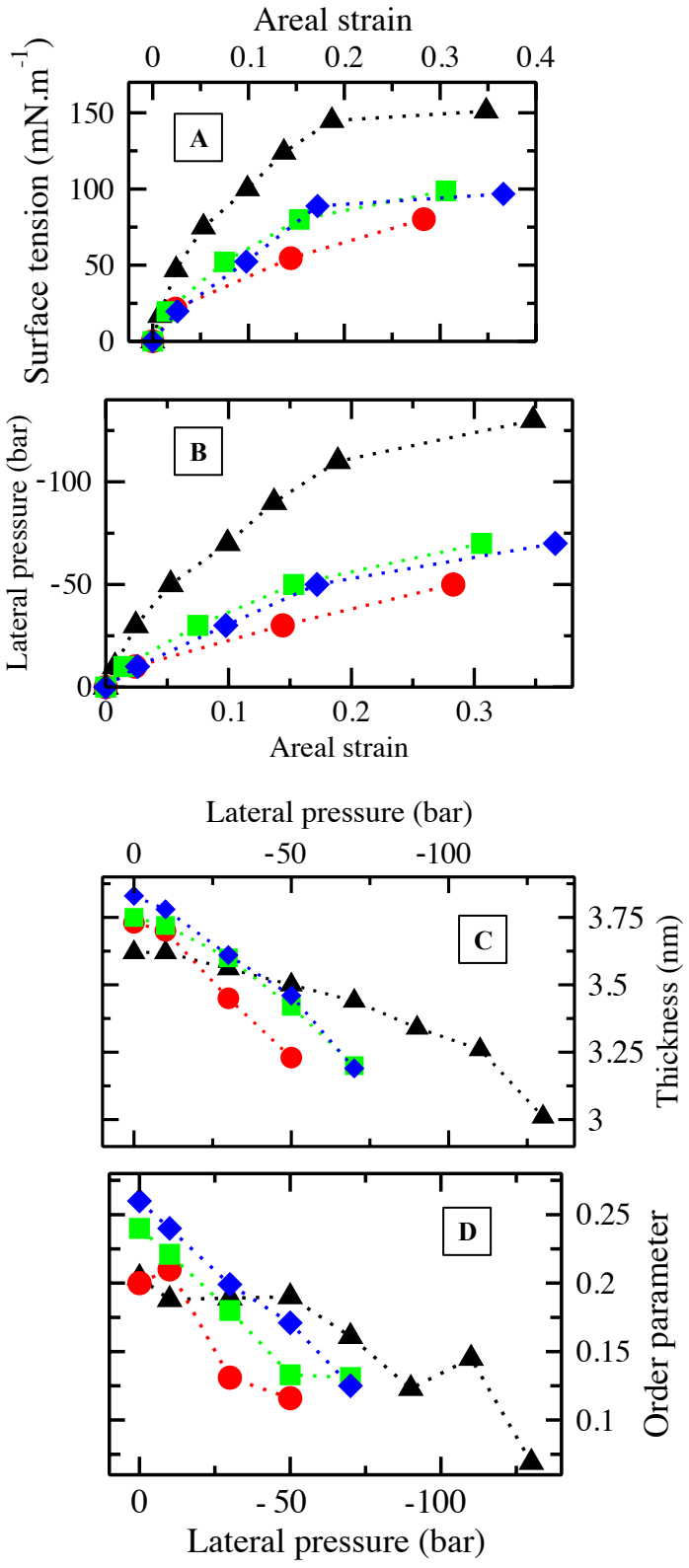

Figure 43. (A) Surface tension-areal strain curves. (B) Lateral pressure against areal strain. (C) Lateral pressure against membrane thickness. (D) Lateral pressure against acyl tail order parameters. Data are shown for the OANT (black), OANT_POPE (red), MIXED (green), and MIXED_POPE (blue) simulation systems. Readers should note that the dependent variables were

plotted on the y-axis in Figure 43A and Figure 43B even though it is customary to plot the independent variable on the x-axis and the dependent variable of the y-axis. The unusual presentation of the simulation data enables readers to more easily identify the relationship between the applied mechanical stress and the membrane stress response. The presentation of the simulation data has been used to study for example, how phospholipid membranes respond to applied mechanical stress [977] and it is therefore easier to compare the data that are presented here with data from previous molecular dynamics simulation studies.

The progressive degradation of system OANT was monitored here to better understand the mechanisms that underpin membrane collapse. The order parameter was computed for the O-antigen chains to understand how the O-antigen chain orientation changed as the lateral pressure was incrementally increased (Figure 44A). There was a general reduction in O-antigen order parameters as the lateral pressure magnitude was incrementally increased and this indicates that the LPS headgroup moieties were becoming less aligned with the membrane normal axes. This conclusion was corroborated when the O-antigen chain tilt angle was computed as a function of lateral pressure magnitude. The tilt angles generally decreased as the lateral pressure was increased e.g. the tilt angle was 9.5 ± 1.5° smaller when system OANT was subjected to a lateral pressure of -130 bar compared with the atmospheric pressure (1 bar) simulations. Two-dimensional projections of the particle number densities revealed that the O-antigen chain distribution became increasingly uneven as the lateral pressure magnitude was incrementally increased (Figure 44B-C).

The increased lateral pressure magnitudes also affected the permeability of the OANT, OANT_POPE, MIXED, and MIXED_POPE simulation systems. One-dimensional partial mass density plots revealed that there was a change in bilayer structure: the distance between the lipid phosphate groups decreased as the magnitude of the lateral pressure was increased (Figure 44D). The bilayer became more permeable as the membrane thickness was reduced and consequently, more water particles were able to pass through the water-lipid interface and flood the extremities of the hydrophobic core. The increase in lateral pressure significantly impacted the bilayer interface: there was no

longer a clear division between the acyl tails and the encompassing solvent. The distance between water particles on the opposing ends of the asymmetric bilayer was reduced as the lateral pressure magnitude was increased and this increased the likelihood that water chains would spontaneously form along the bilayer normal. The critical lateral pressure magnitude for system OANT was -130 bar and water molecules entered into the hydrophobic membrane core when this pressure was applied (Figure 44E). The water molecules spontaneously created a single transmembrane water chain and this led to the formation of larger transmembrane water channels that drastically reduced the membrane integrity and quickly led to the compete loss of basic bilayer structure. It is noteworthy that comparable breakdown processes have been noted in previous mechanical rupture simulations of lipid membranes. Water pores would appear within lipid bilayers after a critical areal strain magnitude was reached and after that, there would generally be a complete loss of lamellar structure as the pore expanded [977-980].

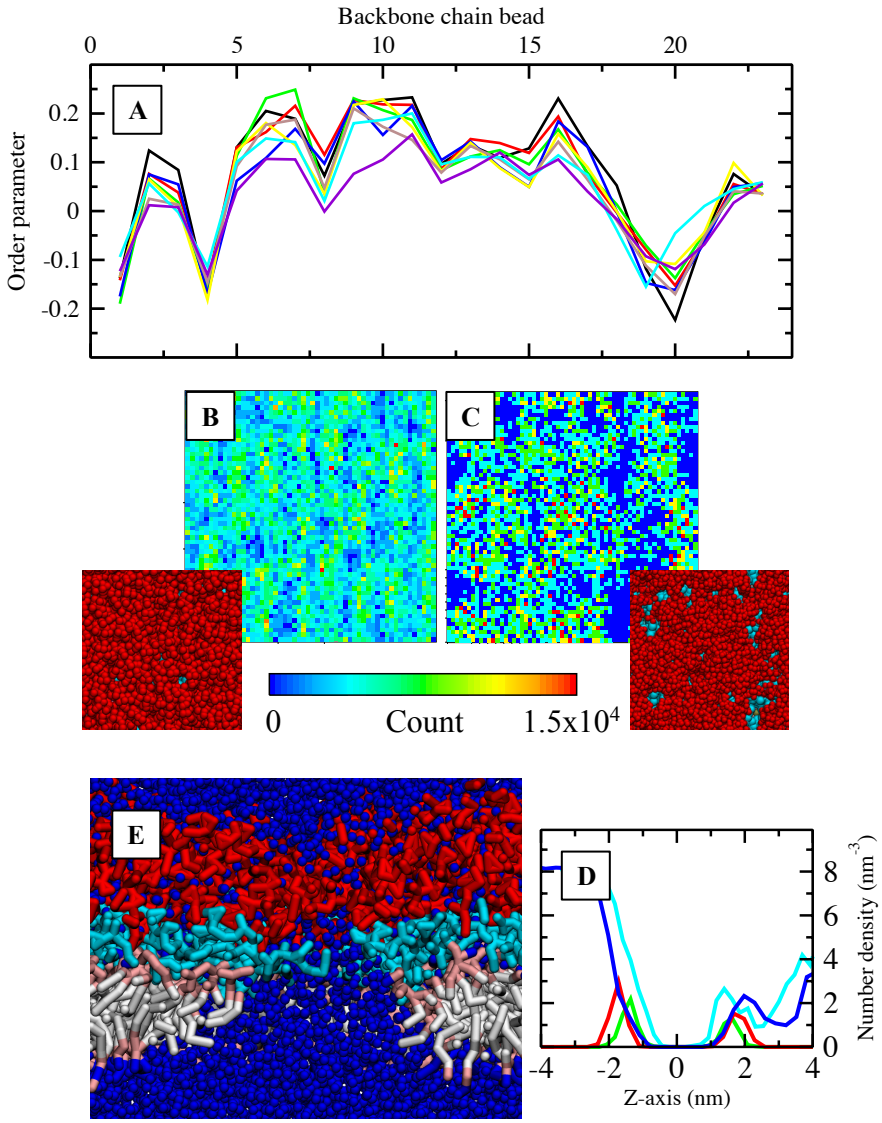

Figure 44. (A) The average order parameters for the O-antigen chains in system OANT as the lateral pressure component magnitude was incrementally increased. The color scheme is as follows: -10 bar (red), -30 bar (green), -50 bar (blue), -70 bar (yellow), -90 bar (brown), -110 bar (cyan) and -130 bar (violet). (B, C) The two-dimensional projection of the O-antigen chain particle number density for system OANT when it was simulated with a lateral pressure magnitude of 1 bar (B) and -130 bar (C). (D) The partial mass density plots for system OANT when it was simulated with a lateral pressure of 1 bar (red and blue lines) and -130 bar (cyan and green lines). The data for the lipid phosphate groups are red and green and the data for the water molecules are blue and cyan. (E) Snapshot that shows the spontaneous formation of a transmembrane pore in system OANT when it is simulated with a lateral pressure magnitude of -150 bar. The water particles are blue and the LPS lipids follow the color scheme of Figure 40.

4.5 Conclusion

LPS lipids are found in the outer membranes of Gram-negative bacteria [95,104-105] and they affect many important biological functions e.g. they regulate nutrient uptake and control processes that are related to OMV biogenesis [576-578,659-660]. The composition of LPS lipids varies widely from one bacterial strain to another and the specific composition of the LPS lipids also depends on bacterial growth conditions [971-972]. The molecules always contain the anchoring Lipid A domain but the size and composition of the carbohydrate headgroup moieties can be strikingly different. Rough LPS lipid variants contain a core domain of sugars, amino acids, ethanolamine, and phosphate groups that are covalently bonded to the Lipid A domain; smooth LPS lipids additionally contain long O-antigen chain polymers [971-972].

It was previously demonstrated that O-antigen chains have the capacity to modulate the structural characteristics of bacterial biofilms. The size of the LPS lipids affected the mechanical and structural properties of *P. aeruginosa* bacterial biofilms [973]. Computer simulations were conducted here within this chapter to explore the possibility that O-antigen chains might additionally affect the elasticity of individual bacterial cell surfaces. Smooth LPS lipids were simulated in membranes that contained different lipid types (i.e. rough LPS, POPE, POPG, and smooth LPS) that were arranged in different number ratios. The intracellular leaflet contained POPE and POPG lipids in a 9:1 number ratio and the extracellular leaflet contained either smooth LPS lipids alone or alternatively some combination of smooth LPS, rough LPS, and POPE molecules. The membranes were initially simulated at atmospheric pressure (1 bar) to understand the magnitude of the lipid packing parameters when the membranes were not strained. The membrane mimetics were then simulated with increasing lateral pressure magnitudes to understand the membrane system tolerance for, and response to, applied mechanical stress.

The simulations revealed that the membrane composition affected the organization of the terminal smooth LPS O-antigen chains. The O-antigen chains splayed out across the membrane surface when there was a mix of rough LPS, smooth LPS and/or POPE molecules in the extracellular leaflet of the Gram-negative bacterial membrane mimetics. In contrast, the O-antigen chains achieved tight lamellar alignment that was associated with higher cohesion forces when the extracellular leaflet was homogeneous and it contained smooth LPS lipids alone. The differences in O-antigen chain interactions affected the membrane tolerance for mechanical strength: the membranes could withstand high surface tension magnitudes (150 mNm^{-1}) and the constituent LPS lipids had low diffusion constants when the extracellular leaflets contained smooth LPS lipids alone. The smooth LPS lipids diffused faster and the membrane tolerance for surface tension was reduced by ~50 mNm^{-1} when there were POPE lipid and/or rough LPS molecules that were embedded throughout the extracellular leaflet of the Gram-negative bacterial outer membrane mimetics. The simulations suggest that cohesive O-antigen chain interactions can make Gram-negative bacterial membranes stiffer and more resilient to external mechanical stress.

The simulations provide interesting insights into the behavior of the LPS O-antigen chains and they also reveal how their collective cohesive intermolecular interactions can enhance the mechanical strength of Gram-negative bacterial membranes. The conclusions have far reaching ramifications if they are reproducible *in vivo* and as such, it is important to consider the limitations of this simulation study and to determine how credible the data are. First, it must be acknowledged that the coarse-grained models omit atomistic detail and that this can affect how accurately LPS conformational landscapes are reproduced in coarse-grained molecular dynamics simulations [174-176]. There is in general satisfactory overlap of the LPS lipid conformational landscapes in comparative united-atom and coarse-grained molecular dynamics simulations but minor discrepancies have been observed e.g. disparities in the full extension of the LPS lipid headgroup moieties [301,580]. Second, it must be acknowledged that cations

are not explicitly represented in coarse-grained molecular dynamics simulations that are conducted with the Martini forcefield [822]. The implicit presentation of cations could affect the accuracy of bridging interactions between Lipid A anchors and this property is important to simulate accurately because it can determine LPS lipid coordination and it can affect the mechanical strength of lipid membranes [551, 866-867]. Third, we must recognize that LPS lipids have unusually slow dynamics [246,866] and by association, that LPS co-clustering was most likely not converged here. Fourth, we must consider that the outer membrane of Gram-negative bacteria is much more complex than these simple simulations would lead readers to believe. Bacterial membranes include a diverse set of lipids and membrane proteins that can affect, at least locally, the properties of the membranes that they are simulated in [213,219-222]. Taken together, we can conclude that the simulations were quite crude and that there were inevitably, minor numerical inaccuracies throughout. It is likely that the cohesion forces were simulated in this work as being either slightly too strong or too weak compared with the *in vivo* scenario. We should not presume that all of the data were quantitatively correct but we can presume that the overarching qualitative conclusions were accurate. The differences in membrane mechanical strength magnitudes was stark and they cannot be accounted for by slight inaccuracies in the computation of cohesive intermolecular interactions alone.

The simulations help us to better understand how the outer membrane of Gram-negative bacteria and more specifically, how interactions between terminal O-antigen chains affect the mechanical properties of Gram-negative bacterial outer membranes. The simulations revealed that when there was tight lamellar alignment of the terminal O-antigen chains, there was an associated increase in membrane rigidity and in the membrane tolerance for surface tension. The simulations suggest that Gram-negative bacterial membranes will be stiff and resilient to different *in vivo* stressors (e.g. osmotic pressure) when there is tight packing of the LPS O-antigen chains. The simulations additionally indicate that the elasticity and shelf stability of OMVs

will be affected by the type of lipids that they are made with. OMVs are spherical liposomes that bud from the outer membrane of Gram-negative bacteria [659-660]. The nanospheres have an outer leaflet that contains a high concentration of LPS lipids and an inner leaflet that contains a high proportion of PE and PG phospholipids. The OMV lipid composition can be modulated [1000] and it can be made to mimic the systems that were simulated in this chapter i.e. OANT, OANT_POPE, MIXED, and MIXED_POPE. We can change the mechanical strength of synthetic OMVs to control their tolerance for *in vitro* and *in vivo* stressors such as turgor pressure, by controlling the relative abundances of smooth LPS lipids and rough LPS in the (OMV) outer leaflet. The length and concentration of the O-antigen chain polymers can be varied and this will change the OMV mechanical strength parameters. This is important since elasticity directly impacts important nanocarrier (or vesicle) properties including how liable nanocarriers are to rupture or fuse, the loading rates of drugs, and the rates of drug uptake at host cell surfaces [1001-1003]. The insights are timely because OMVs have an increasing number of nanomedical functions, e.g. roles as vaccine adjuvants and roles as functional liposomes that can traffic molecular cargo directly into host cell cytoplasm [1004-1006].

Chapter 5: Understanding the Uptake of Outer Membrane Vesicles at Host Cell Surfaces

5.1 Abstract

Outer membrane vesicles (OMVs) are spherical liposomes that are secreted by almost all forms of Gram-negative bacteria. The nanospheres regulate bacterial pathogenesis processes by trafficking molecular cargo from bacterial cell membranes to target cell surfaces at the host-pathogen interface. OMVs were simulated with host cell membranes to understand why lipid-mediated OMV uptake processes depend on the length of constituent lipopolysaccharide (LPS) macromolecules. Coarse-grained molecular dynamics simulation forcefields were used to demonstrate that LPS lipid length affects the shape of OMVs at host cell surfaces. OMVs with long (smooth-type) LPS lipids retained their spherical shape when they interacted with host cell membranes, whereas OMVs with shorter (rough-type) LPS lipids distorted and spread out over the host membrane surface. In addition, it was shown that ganglioside lipid headgroups acted as a zipper to mediate strong adhesion that helped to force the host membranes around the attached OMVs. The differences in shape preservation will affect OMV internalization on long timescales: spherical nanoparticles tend to be completely engulfed by host membranes, whereas lower sphericity nanoparticles tend to remain on the surface of cells.

5.2 Introduction

Outer membrane vesicles (OMVs) are spherical liposomes that bud from the outer membranes of almost all Gram-negative bacteria [46,49]. The nanospheres have an asymmetric architecture: there are glycerophospholipids in the inner (intracellular) leaflet and LPS macromolecules in the outer (extracellular) leaflet [47-49]. The OMVs are enriched with bioactive proteins of two types: (i) integral membrane proteins, which span across the bilayer normal axis; and (ii) peripheral membrane proteins, which are expressed on the OMV surface [51,661-662].

The lumen frequently contains more complex molecular cargo ranging from nucleic acids through to toxins and virulence factors [46-47,1006]. It was initially theorized that OMVs were produced by bacteria as a stress response but it is now recognized that OMVs also traffic molecular cargo between cell surfaces [46-51].

OMVs shuttle molecular cargo across the external milieu and they regulate different forms of intercellular communication, nutrient scavenging, horizontal gene transmission processes, and bacterial pathogenesis [46-52]. Specific virulence factors can be concentrated within the small (20-250 nm) proteoliposomes and this primes them for disease transmission processes [48-49,1007]. Disease transmission occur as follows: the nanospheres bleb from the outer membrane of Gram-negative bacteria, the OMVs then move through the external milieu and latch onto host cell surfaces, the OMVs then pass through the plasma membrane surface and release virulence factors into the host cell cytosol [48-52].

There is evidence that OMVs can enter into host cells via a lipid-mediated uptake pathway that is inextricably linked to the length of LPS macromolecules in the (OMV) outer leaflet [664]. OMVs can enter cells via protein dependent pathways including for example, clathrin-mediated endocytosis [52], but according to Forster Resonance Energy Transfer (FRET) [1008] microscopy analysis techniques, OMVs still manage to pass through host cell membranes even when host membrane protein receptors are inactivated [664]. When OMVs contain short LPS lipids that lack terminal O-antigen chains (rough OMVs) the uptake is relatively inefficient; conversely, when OMVs contain longer LPS lipids (smooth OMVs) they enter cells more effectively [664]. Figure 15 shows the different chemical composition of the coarse-grained smooth and rough *E. coli* LPS lipid models that are used in this chapter to simulate OMVs. The rough (Ra type) LPS lipid contains type 1 Lipid A with R3 core sugar sequence. The smooth LPS lipid contains the type 1 Lipid A anchor with complete R3 core saccharide section and it additionally contains four units of the repetitive O1 O-antigen chain

glycan polymer. The O1 antigen chain repetitive subunit contains the five saccharide units arranged end-to-end: β N-acetyl-D-glucosamine, α D-galactose, α L-rhamnose, α L-rhamnose, β N-acetyl-D-mannosamine.

The processes that underpin lipid-mediated uptake are likely to involve molecular level interactions that are beyond the scope of conventional experimental techniques. Fortunately, computer simulation methods make the smallest spatiotemporal scale accessible; molecular dynamics simulations can be conducted to understand OMV uptake processes at the host-pathogen interface. The coarse-grained Martini molecular dynamics simulation forcefield is used here in this chapter to describe the stepwise biomolecular interactions that drive OMVs into the host cell cytoplasmic matrix. Coarse-grained molecular dynamics simulations are used to understand how the interactions between LPS lipids and host membrane ganglioside molecules (GM3) can contribute to the uptake of OMVs at host cell surfaces. But the question then becomes: how can the simulation results themselves be validated?

Experimental validation techniques can be used to validate most inferences that are ascertained from molecular dynamics simulations. Experimental techniques have been used in the past to validate inferences that were drawn from coarse-grained molecular dynamics simulations of bacterial membrane proteins [115] and it is expected that experimental validation techniques can also be used after this work is published to validate the overarching qualitative conclusions that are drawn from these coarse-grained molecular dynamics simulations of OMVs. Let us consider one of the most important insights that will be drawn from the molecular dynamics simulations that are conducted in this chapter: it is determined here that ganglioside molecules promote wrapping interactions at the host cell surface and that these interactions promote OMV uptake processes. This prediction can be validated by analyzing OMV uptake at host membrane surfaces with experimental analytical techniques. OMVs can be brought into contact with membranes that either lack ganglioside molecules altogether or contain an appreciable

amount of ganglioside molecules e.g. more than 1% of GM1 or GM3 lipids. If ganglioside lipids affect uptake interactions we should expect that the GM1 or GM3 molecules would affect lipid-mediated OMV uptake processes. Membranes that contain ganglioside molecules should promote uptake interactions more effectively than comparative membranes that lack ganglioside molecules. The effects of ganglioside molecules can also be evaluated systematically by varying the ganglioside concentration within a relatively simple membrane mimetic and correlating lipid concentrations with OMV uptake metrics. Some aspects of the OMV uptake processes could also be imaged directly. Imaging techniques could be applied to capture snapshots of OMVs interacting with lipid membranes whose composition is controlled to mimic realistic plasma membranes, or some other lipid composition that affords much needed insights into OMV uptake interactions. There are many possibilities for potentially validating theoretical predictions through experimental analysis techniques and these possibilities are discussed more thoroughly in chapter 6.

Coarse-grained molecular dynamics simulations were used [799,814] here to understand the different entry kinetics of rough and smooth OMVs at the host–pathogen interface [664]. The OMVs were initially simulated in water to determine the OMV lipid packing parameters and the OMVs were then simulated with a single-component POPC bilayer in the first instance, and a multicomponent plasma membrane in the second. The simulations revealed that the shape of OMVs at host cell surfaces is determined by the length of the constituent LPS lipids in the OMV outer leaflet. Smooth OMVs maintained high sphericity at host cell membranes, whereas rough OMVs spread over the host cell surface. This result helps to clarify why smooth OMVs pass through host cell surfaces more readily than comparable rough OMVs. Rigid nanospheres slowly wrap host membrane surfaces and achieve complete encapsulation, whereas lower sphericity nanoparticles generate larger curvatures at the spreading front and this makes endocytosis less likely [1009-1014]. The results are corroborated by the data from Chapter 4 where it was shown that O-antigen chain interactions can make Gram-negative bacterial membranes

more mechanically robust. The O-antigen chain interactions affected the mechanical properties of the OMVs by making them stiffer and we can therefore conclude that smooth OMVs should be more able to retain a higher sphericity value when they interact with host cell surfaces compared with rough OMVs. Smooth OMVs are more likely to retain their spherical shape when they interact with host cell membranes and therefore they will be able to wrap host cell membranes more effectively. Smooth OMVs have smaller energy barriers to surmount during the late stages of nanosphere endocytosis [1010-1013] because they are stiffer.

The simulations also revealed that the host membrane composition affects the OMV wrapping interactions. Ganglioside (GM3) lipid headgroups acted as a zipper to mediate strong OMV-host cell adhesion and lower the energy barriers for host membrane curvature generation. The OMVs affected the organization of the ganglioside lipid headgroup moieties within the host cell membranes and this interaction promoted host membrane wrapping processes. The induced self-assembly of the ganglioside molecules and the associated increase in host membrane wrapping is comparable to the perturbation of host cell membranes by different pathogens (e.g. SV40) and pathogenic products (e.g. Shiga toxin) when they reorganize ganglioside lipids in host cell plasma membranes [537,542,1015-1018]. The sequestered ganglioside lipids formed aggregates within the simulated host cell membranes and this increased the local membrane curvature and it also increased the local abundances of lipids that are associated with raft formation and endocytosis.

Ganglioside lipids seem to control OMV uptake interactions due to the properties of their carbohydrate headgroup moieties e.g. high surface polarity [534] and the tendency to form relatively long-lasting aggregates [498]. Glycoproteins have comparable polar carbohydrate moieties [1019-1020] that must impact, at least partially, OMV uptake interactions at host cell surfaces. Glycoproteins and the glycocalyx (pericellular matrix) [1021-1022] were omitted throughout this chapter to simplify the simulation study and to

make the lipid interactions easier to analyze. The setup enabled the elucidation of lipid processes that seem to drive OMV uptake processes at the host cell surface but the complete omission of the glycocalyx makes the work somewhat crude and the proposed uptake model at best, rudimentary. More refined simulation studies would be necessary for providing a comprehensive understanding of the molecular level interactions that determine OMV uptake processes at host cell surfaces. The simulation study is crude but it does provide novel insights that seem to answer a rather interesting and perplexing question: why does OMV lipid-mediated uptake depend on the cell wall architecture of the parent bacteria [664]?

5.3 Methods

5.3.1 Vesicle Construction Details

The OMVs were assembled with the CHARMM-GUI Martini Maker module [151,232] and simulated with the GROMACS simulation package (version 5.1.2) and the Martini coarse-grained forcefield (version 2) [799,814]. Two types of OMV were produced: smooth and rough. The inner leaflets contained POPE and LPS lipids in a 9:1 number ratio and the outer leaflets contained POPE with either smooth-type, or rough-type LPS lipids in a 1:1 number ratio. The smooth LPS lipids had four units of the *E. coli* O1 O-antigen chain and the rough LPS lipids were modeled without any O-antigen chain units at all. Figure 15 helps to clarify the structural differences between the rough (Ra) and smooth LPS lipid variants that were used here in this chapter to model smooth and rough OMVs. The OMVs were assembled with diameters of 20 nm (based on the position of their hydrophobic midplane). The OMVs were hydrated with standard Martini water particles (W type) and enough calcium ions (Ca^{2+}) to neutralize the anionic system charge. The OMVs were initially energy minimized with the steepest descent algorithm and subsequently subjected to successive equilibration simulations. Position restraints (1000 KJ mol^{-1} nm^{-2}) were applied along the unit cell axes (*x*-, *y*-, and *z*-axes) during these equilibration simulations to create six membrane spanning water pores that facilitated lipid flip-flop processes. The water pores were small; so much

so, that lipid flip-flop processes were facilitated for small glycerophospholipids, while large LPS macromolecules were confined to the extracellular leaflet (Figure 45A). The set up promoted optimal lipid packing while simultaneously ensuring that the OMVs had a realistic, asymmetric distribution of LPS lipids. The water pores were closed over the course of five successive equilibration simulations; the water pore radii were initially set to be 2 nm and were then reduced in size to 1.5 nm, 1.0 nm, 0.5 nm and 0.2 nm. The position restraints were then removed and the OMVs were simulated for an additional 1 μs to ensure that the lipid parameters could converge. The temperature was maintained at 303 K using the V-rescale thermostat and the pressure was maintained at 1 bar. The pressure was modulated with the isotropic Berendsen barostat [839] when the position restraints were enforced along the unit cell axes; the Parrinello-Rahman barostat [841-842] (12.0 ps coupling constant) was applied thereafter. Electrostatic interactions were computed with the reaction field method with dielectric constants of 15 for charge screening in the short-range regime and infinity for the long-range regime. The Lennard-Jones potential was cut off at long-ranges using the Potential-shift-Verlet scheme. The membrane thickness and area per lipid values were used to determine OMV system convergence and ensure that the OMVs had achieved optimal lipid packing before they were simulated with the POPC or plasma membrane bilayers (Figure 45B-E).

The assembled OMVs were highly simplified models that lack, amongst other biomolecules, enzymes, toxins, peptidoglycan, DNA, RNA, OMPs and other bacterial membrane proteins [46-52,661-662]. The omission of the full *in vivo* OMV compositional complexity was intentional. Here I aimed to understand how simple lipid interactions at the host-pathogen interface modulate at least one OMV uptake pathway and consequently, it seemed most appropriate to omit extraneous biomolecular interactions that could make this simulation study needlessly more convoluted. The aim was to determine how the overarching lipid interactions at the host-pathogen interface can regulate lipid-mediated OMV uptake and subsequent simulation studies could then be used to determine how additional OMV compositional complexity further

affects the OMV uptake interactions. This is not to discount the action of scission machinery, adhesion molecules etc. that also invariably impact OMV uptake efficiency [52]. The aims of this chapter were relatively modest and consequently the molecular dynamics simulations were highly simplified.

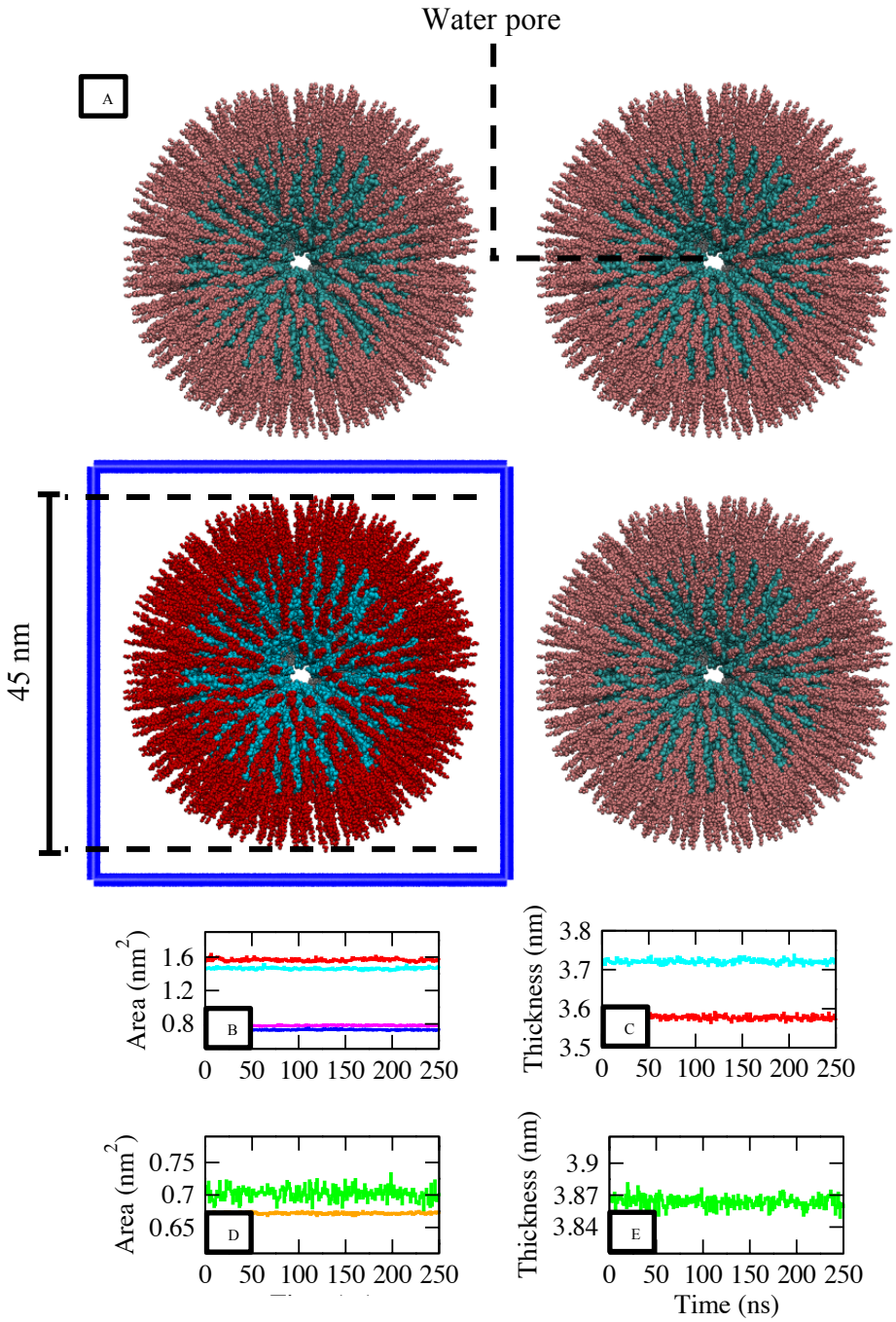

Figure 45. (A) The starting configuration for the smooth OMV equilibration simulations. The POPE and POPG lipids are silver and the LPS lipids have the color scheme: Lipid A and core sugars (cyan) and O-antigen chain (red). The water and ions were removed to make the figure clearer. The periodic cell boundaries are represented with a blue line. The periodic images are shown using different color shades for clarity. The lipids were extended along the bilayer normal to ensure that lipid clustering was not biased during the molecular dynamics simulations. Water pores were maintained along the $(x/y/z)$ coordinate axes to facilitate interleaflet flip-flop for small phospholipids. (B) Area per lipid for LPS (red) and POPE (magenta) lipids in the smooth OMV (during the last 0.25 μs); area per lipid for LPS (cyan) and

POPE (magenta) lipids in the rough OMV. (C) Membrane thickness for the smooth (red) and rough (cyan) OMVs during the last 0.25 μs; the average membrane thickness values were 3.58 ± 0.01 nm (smooth OMV) and 3.72 ± 0.01 nm (rough OMV). (D) Area per lipid for POPE (orange) and POPG (green) lipids in the POPE-POPG phospholipid vesicle during the last 0.25 μs. (E) The corresponding membrane thickness values for the POPE-POPG phospholipid vesicle.

The phospholipid vesicle was made with the CHARMM-GUI Martini Maker module [151,232]. The inner and outer leaflets were both made with POPE and POPG lipids in a 9:1 number ratio. The phospholipid vesicle was assembled with a diameter of 20 nm to make it physically comparable to the smooth and rough OMV simulation systems. The POPE-POPG vesicle was hydrated with Martini water using the *gmx solvate* program and enough calcium ions were added to neutralize the system charge. Position restraints were used to maintain six membrane spanning water pores along the unit cell (*x*, *y*, and *z*) axes. The water pore radius was initially set to be 2 nm and the final water pore radius was 0.2 nm, intermediary radii were 1.5 nm, 1.0 nm, and then 0.5 nm. The vesicle was simulated for an additional 1 μs after the water pores had closed to converge the lipid parameters. The simulation temperature was kept at 303 K using the V-rescale thermostat. The pressure was modulated with the isotropic Berendsen barostat when the position restraints were being enforced along the unit cell axes and the Parrinello-Rahman barostat (12.0 ps coupling constant) [841-842] was applied thereafter. The membrane thickness values and area per lipid magnitudes were used here to assess the POPE-POPG system convergence and ensure that the vesicle was ready for simulations with the single-component POPC and the multicomponent plasma membrane bilayers.

5.3.2 Host Membrane Construction Details

The Palmitoyloleoyl-phosphatidylcholine (POPC) membrane bilayer was made with the *insane.py* script [893]. The initial simulation cell dimensions were 75 x 75 x 20 nm; standard Martini water particles were used to hydrate the lipids within the orthorhombic simulation cell. Position restraints were

applied over the course of five successive equilibration simulations to suppress excessive lipid splay and promote the production of an optimally packed lipid bilayer. Position restraints were used to fix the position of the POPC lipid headgroups and promote lamellar lipid alignment. The force constant was initially set to be 200 KJ mol^{-1} nm^{-2} and this was reduced to 10 KJ mol^{-1} nm^{-2}; the intermediary force constants were 100, 50, and then 20 KJ mol^{-1} nm^{-2}. The bilayer was simulated for an additional 1 μs after this to promote optimal lipid packing. The temperature was maintained at 303 K using the V-rescale thermostat. The pressure was maintained at 1 bar using a semi-isotropic pressure coupling algorithm. The Berendsen barostat was applied when the position restraints were being applied and the Parrinello-Rahman barostat [841-842] was used once the position restraints were removed. The electrostatic interactions were computed with the reaction field method, with dielectric constants of 15 for charge screening in the short-range regime and infinity for the long-range regime. The Lennard-Jones potential was cut off at long-ranges using the Potential-shift-Verlet scheme.

The multicomponent plasma membrane model contained seven different types of lipid that were distributed asymmetrically about the membrane midplane. The lipid abundances for the entire membrane were as follows: POPC (25%), POPE (25%), POPS (7.5%), GM3 lipid (5%), palmitoyl sphingomyelin (7.5%), PIP_2 (5%), and cholesterol (25%). The inner (intracellular) leaflet contained POPE, POPC, POPS, PIP_2 and cholesterol in a 40:10:15:10:25 ratio. The outer (extracellular) leaflet contained POPE, POPC, sphingomyelin, (GM3) ganglioside and cholesterol in a 10:40:15:10:25 ratio. The plasma membrane model was made in previous works by Sansom et al. and the group has simulated the membrane on a multimicrosecond timescale before it was used here in this chapter [76,363,500,993]. The chemical properties of each lipid type can be understood from the following sections: 1.4.1 (PC, PE, and PS phospholipid), 1.4.2 (cholesterol), 1.4.3 (PIP_2), 1.4.4 (sphingomyelin and GM3 lipid). The membrane was produced through a long and seemingly arduous effort where individual constituent lipid types (for

example, see reference [1023]) were initially parameterized to mimic reference atomistic simulation data and these coarse-grained models were then subsequently combined to produce a multicomponent mammalian plasma membrane model. The lipid models have been used to understand amongst other interesting biophysical phenomena, the organization and dynamic interactions of plasma membrane receptor proteins [76].

The plasma membrane model was simulated here for an additional 0.25 μs after it was initially acquired from the Sansom group to correct for small differences in simulation settings. The membrane was simulated with Martini water particles and either monovalent (Na^+) or divalent (Ca^{2+}) cations to systematically determine if the simulation results would be affected by the ambient ion charge density. The semi-isotropic Parrinello-Rahman barostat [841-842] was used to maintain the pressure at 1 bar and the V-rescale thermostat was used to maintain the simulation temperature at 303 K. The electrostatic interactions were computed with the reaction field method and the Lennard-Jones potential was cut off at long-ranges using the Potential-shift-Verlet scheme. At this point, the plasma membrane was combined with vesicles in one instance and simulated independently in another. Ganglioside molecule co-clustering could then be assessed both when OMVs were trapped at the plasma membrane surface and also when the plasma membranes were simulated without OMVs.

It is important to stress here that the plasma membrane was not completely converged when it was first provided by Sansom et al. or even after the subsequent short (0.25 μs) equilibration simulations that were used to correct for difference in simulation settings. Comparable simulations of complex plasma membrane models [498] suggest that converged ganglioside cluster conformations are beyond the scope of the current coarse-grained Martini forcefield, which maps no more than a few heavy atoms to a single interaction center [822]. Marrink et al. created complex plasma membrane models that included up to 63 different lipid types ranging from large ganglioside lipids (e.g. GM3, and GM1 in particular) through to smaller

phosphoinositides, phospholipids and cholesterol [498]. The conformation of the ganglioside molecule aggregates changed continuously over 40 μs and the simulated GM3 and GM1 clusters continuously broke apart and reformed throughout. The plasma membrane contained 63 different lipid types and this level of complexity would have made the equilibration timescales longer, but the slow ganglioside molecule clustering processes cannot be explained by the number of lipids alone. The aggregation of polar glycolipids tends to transpire on unusually long microsecond timescales when the membrane compositional complexity is relatively high [498] and equally when the membrane compositional complexity is relatively low [151,301]. In other words, glycolipid conformations converge on microsecond or even longer (e.g. millisecond) timescales when membranes contain either just a few different types of lipid or up to 63 different types of lipids. The Martini forcefield is optimized for microsecond long molecular dynamics simulations and so we can state that converged glycolipids might well be entirely the scope of the explicit coarse-grained Martini forcefield if it is paired with nothing more than standard high-performance computers.

It is equally important to state that glycolipid molecules are challenging to accurately parameterize in atomistic forcefield simulations [558,1024], but even more so in lower resolution coarse-grained forcefield simulations [1023,1025-1026] that have fewer degrees of freedom. The conformations of glycan polymers can differ markedly in simulations that are conducted with different atomistic resolution forcefields [578] suggesting that at least some, if not many, of the apparently sophisticated atomistic molecular dynamics forcefields fail to satisfactorily reproduce the complex conformational landscapes of bonded saccharide units. While the quality of the reference atomistic simulation data is itself of questionable quality, there is the added problem that coarse-grained ganglioside parameterization schemes can differ from target all-atom molecular dynamics simulations [1025-1026]. Long simulation timescales might promote converged conformations but the precise distribution of the converged glycolipid clusters might not match the *in vivo* scenario. These noted inaccuracies could discredit the forthcoming

conclusions if the wrapping interactions seemed to depend on the precise size or distribution of the simulated ganglioside clusters. This was not the case; host membrane wrapping interactions demanded neither a specific GM3 aggregate size distribution nor a specific ganglioside molecule spatial distribution. The OMVs sequestered GM3 lipids that were in a range of different orientations and states of aggregation and once sequestered, the GM3 molecules almost always contributed to stepwise zippering interactions that promoted the wrapping of the host membranes around the attached OMVs. So, although there is invariably some mismatch between ganglioside lipid interactions here and within realistic cellular membranes, the overarching qualitative conclusions seem to be warranted throughout.

But let us explore a bit more thoroughly what we know and what we do not know about glycolipid clustering and in particular, Martini glycolipid GM1 and GM3 molecule aggregation. It is already well-known that glycosphingolipids tend to co-couple with cholesterol and sphingomyelin in multicomponent plasma membranes and that this aggregation can induce the formation of liquid-ordered nanodomains and lipid rafts [73-79]. The co-clustering processes are complex; glycosphingolipids form gel-like domains in fluid lipid bilayers and sphingomyelin readily associates with cholesterol molecules to form liquid-ordered nanodomains, but glycosphingolipids do not tend to form cholesterol-enriched domains by themselves [1027-1028]. Glycosphingolipid clustering and partitioning also depends on the ceramide backbone structure, the number of sugar units, and the charge of the saccharide headgroups. Although the clustering of glycosphingolipids is evidently quite complex and multifaceted, it is becoming increasingly clear that ganglioside molecules have high affinity for each other within plasma membranes and that ganglioside molecules can form nanodomains *in vitro* and *in vivo* either through attractive self-interactions or through interactions with pathogenic biomolecules [368]. When pathogenic viruses (e.g. SV40) and pathogenic bacterial products (e.g. Shiga toxin) interact with ganglioside lipid headgroups they can induce the formation of curved lipid rafts, or caveolae [537,542,1015-1018]. The ganglioside molecules move to areas of

high positive curvature such as the rim of caveolae where their presence reduces the line tension energy and promotes large-scale membrane reshaping processes [671-673].

Through the application of sophisticated microscopy methods, it was shown that lipid rafts can have a range of different sizes ranging from approximately 10 nm [89] through to 200 nm, i.e. an order of magnitude difference [348,1029]. Coarse-grained molecular dynamics simulations with the Martini forcefield have corroborated the inference that ganglioside molecules can form large lipid rafts when they cluster together [363,497-498]. The coarse-grained Martini molecular dynamics simulations showed that coarse-grained ganglioside lipids can spontaneously self-assemble into clusters that have high intrinsic spontaneous curvature and further, that these glycosphingolipid clusters promote membrane curvature generation [363]. The coarse-grained Martini simulation forcefield correctly predicts that ganglioside molecules can spontaneously self-assemble and form aggregates that have high intrinsic positive curvature but it is assumed that ganglioside conformations and binding profiles are less accurate in coarse-grained molecular dynamics simulations than comparative atomistic simulations [1025-1026]. There are noted difficulties in reproducing the correct conformational landscapes of saccharide units and polymers in atomistic simulations [578] and these problems are compounded in comparative coarse-grained simulations that have fewer degrees of freedom [796]. Although direct benchmarking papers are sparse, it was shown that some Martini forcefield ganglioside molecule binding profiles did not accurately reproduce reference atomistic forcefield simulation data [1026]. Thus, we can state that the Martini forcefield correctly predicts that ganglioside molecules cluster and that they can form aggregates that have high intrinsic spontaneous positive curvature but we should appreciate that the size and state of these clusters may be somewhat inaccurate, e.g. slightly too large or too small, and further that the ganglioside molecules might bind the OMVs somewhat inaccurately, e.g. slightly too tightly or too loosely.

5.3.3 Vesicle-Membrane Simulation Details

The Visual Molecular Dynamics (VMD) module [871] was used to combine the vesicles with the host membrane systems. The position of the vesicles and membranes were positioned within the simulation cells with approximately 5 nm between them. The distance was sufficiently small to promote cohesive interactions between the apposed membranes, while also being wide enough to not drastically bias the initial docking of the vesicles onto the host membrane surfaces. The systems were then hydrated with Martini (W type) water particles with the *gmx solvate* program. The VMD visualization module was used to identify and remove any water particles that were inappropriately inserted into the hydrophobic lipid membrane cores. The *gmx genion* program was applied to add either monovalent (Na^{+}) or divalent (Ca^{2+}) cations to the simulation cells. The steepest descent algorithm was used to optimize the distances between the simulation particles and to minimize the system energy. The vesicle-membrane systems were then simulated for 2 μs each; this timescale is sufficiently long to monitor the full details of the early stage endocytosis interactions that transpire at the host-pathogen interface e.g. the loss of vesicle shape and also to visualize the partial wrapping of the host membranes around the attached OMVs. The simulation temperature was maintained at 303 K using the V-rescale thermostat and the simulation pressure was maintained at 1 bar using the Parrinello-Rahman barostat [841-842]. The box vectors were scaled with a semi-isotropic scheme during the 2 μs long simulations, but isotropic and anisotropic algorithms were also used in shorter 1 μs long simulations to ensure that the loss of vesicle shape was not an artifact of simulation setup. Repeat simulations were performed in all instances to ensure that the simulation results were reproducible.

5.3.4 Lipid Parameter Details

The coarse-grained parameters were calibrated in previous works to reproduce target united-atom molecular dynamics simulation data. The coarse-grained Martini forcefield parameter set for the rough (Ra) LPS lipid

was determined from reference united-atom simulations of Ra-type *E. coli* LPS lipid with R3 core sugar sequence and type 1 Lipid A anchor [301]. The rough LPS lipid parameter set was subsequently expanded by sampling data from united-atom simulations of the *E. coli* O1 O-antigen chain polymer. Data from united-atom simulations of the *E. coli* O1 O-antigen chain were sampled and this data was used to calibrate a coarse-grained O1 O-antigen glycan polymer chain model. The coarse-grained O-antigen chain polymer model was then combined with the coarse-grained model of rough (Ra-type) LPS lipid to create the associated smooth LPS lipid mimetic [579]. The GM3 lipid parameters were optimized according to the same procedure [1023]; atomistic simulation data was used to determine appropriate parameters for a coarse-grained model. The conformations of the GM3 lipid headgroup was analyzed in united-atom simulations and coarse-grained model parameters were selected through comparison. The GM3 and PIP_2 molecules were modeled with a single monounsaturated tail throughout. The POPS, POPC, POPE, POPG, sphingomyelin and cholesterol molecules were based on parameters from the standard Martini molecular dynamics simulation forcefield library.

5.3.5 Simulation Analysis Details

The radii of gyration were computed about the *x*-, *y*-, and *z*-axes to assess vesicle shape during production time. The axes components were computed according to the equation: $R_g(x/y/z) = \sqrt{\sum_i m_i(R_i(y/x/y)^2 + R_i(z/z/x)^2)/\sum_i m_i}$ where m_i were the mass values. The radial extension of the saccharide moieties and the Lipid A phosphate groups were computed using the three-dimensional form of the Pythagorean theorem: $c^2 = x^2 + y^2 + z^2$ where *x*, *y*, and *z* were lengths along the unit cell axes and *c* was the diagonal length between them. The diagonals were measured with respect to vesicle centers throughout and the lengths were assigned a color based on standard VMD color gradients. Voronoi tessellations were performed to compute areas per lipid and simultaneously assess membrane thickness parameters. The lipid phosphate groups were

partitioned into a contiguous grid of polygons whose size and separation were used to determine the lipid-packing parameters. The *gmx select* tool was used to count the number of lipids within an arbitrary cutoff distance e.g. 5 nm from smooth or rough OMVs. Residence times were assessed using a 0.6 nm cutoff distance (GROMAS default) and the results were subsequently assigned a color based on standard VMD color gradients. Vesicle headgroup width was determined by computing radial distribution functions (RDFs) for polar and charged Martini beads with respect to the vesicle centers.

5.4 Results and Discussion

5.4.1 OMV Construction Details

The smooth and rough OMVs were simulated with the coarse-grained Martini forcefield (Figure 46A). The OMVs were made with an inner leaflet of POPE and POPG lipids in a 9:1 number ratio and the outer leaflets contained POPE and LPS molecules in a 1:1 number ratio. The outer leaflet POPE lipids were incorporated to facilitate CHARMM-GUI Martini Maker interleaflet flip-flop processes that can minimize bilayer tension. The inner leaflet composition was set to mimic realistic Gram-negative bacterial outer membrane inner leaflets that have PE and PG lipids distributed in an approximate 9:1 ratio [1031]. It should be stressed here that a limited number of lipid flip-flop events occurred during the equilibration simulations and consequently the lipid abundances were not entirely constant throughout. The lipid ratios were still correct to two significant figures after the equilibration simulations, i.e. a 1.0:1.0 number ratio for POPE and LPS molecules in the OMV outer leaflets, but the number ratios did not precisely match the initial simulation setup, i.e. not an exact 1:1 number ratio.

The rough LPS lipids contained an anchoring Lipid A domain with complete core saccharide section and the smooth LPS lipids additionally contained four units of the *E. coli* O1 O-antigen chain repetitive polymer unit (see Figure 15 for reference). The OMVs had an asymmetric membrane structure and diameters of 20 nm based on the position of the hydrophobic membrane core

midplane. The nanospheres are therefore comparable to the smallest OMVs that are produced *in vivo* [663,1005,1032-1034].

5.4.2 OMVs in Water

It is important to first compute lipid packing parameters for the OMVs when they were simulated in water (Figure 46B) before we can analyze the OMV properties at host membrane surfaces. Data were collated from 1 μs long molecular dynamics simulations of smooth and rough OMVs in Martini coarse-grained water and ions. Voronoi tessellations were used to determine the mean average area per lipid values for each component of the inner and outer membrane leaflets. It is emphasized here that the position of the Lipid A phosphate groups (Figure 46C) was used to characterize the water-lipid interface, while the position of peripheral saccharides was used to assess the full extension of the LPS lipids i.e. the radial length of the molecules with respect to the OMV centers.

The LPS lipids were packed more tightly (less area per lipid) in the OMVs than in comparable flat bacterial bilayers (Table 1). The smooth LPS lipids were packed 17% closer in the OMVs than in reference flat bacterial membrane mimetics and the rough LPS lipids were packed 18% closer than reference flat membrane mimetics [151,301]. The OMV LPS lipids achieved lateral packing comparable to the shortest forms of LPS (Re-type) lipid in flat *E. coli* outer membrane mimetics. This is surprising because the simulated OMV LPS lipids were longer than Re LPS molecules and also that LPS lipid length scales with lateral surface area in flat bacterial membrane simulation systems [151,211,301]. This unusually tight (OMV) lamellar alignment is ascribed to (i) additional fringe volume that affords LPS headgroups more conformational freedom and the capacity to achieve unusually tight lamellar alignment, and (ii) compensatory lateral area expansion of neighboring phospholipids, which pushes the LPS molecules closer together than in flat membranes.

Table 1: Summary of lipid properties for OMVs in solution; data are shown for the inner leaflet (IL) and the outer leaflet (OL). Standard deviations are less than 0.02 for areas per lipids and less than 0.9 for radial heights.

Membrane type	Mean area per lipid (nm^2)				LPS radial height (nm)	
	LPS	POPE (IL)	POPE (OL)	POPG	phosphates	extension
Smooth OMV	1.57	0.55	1.26	0.60	11.63	15.38
Rough OMV	1.46	0.50	1.20	0.53	11.52	12.42
Flat outer membrane	Re-LPS: 1.59	0.62	—	0.61	—	—
	Rough LPS: 1.78					
	Smooth LPS: 1.90					

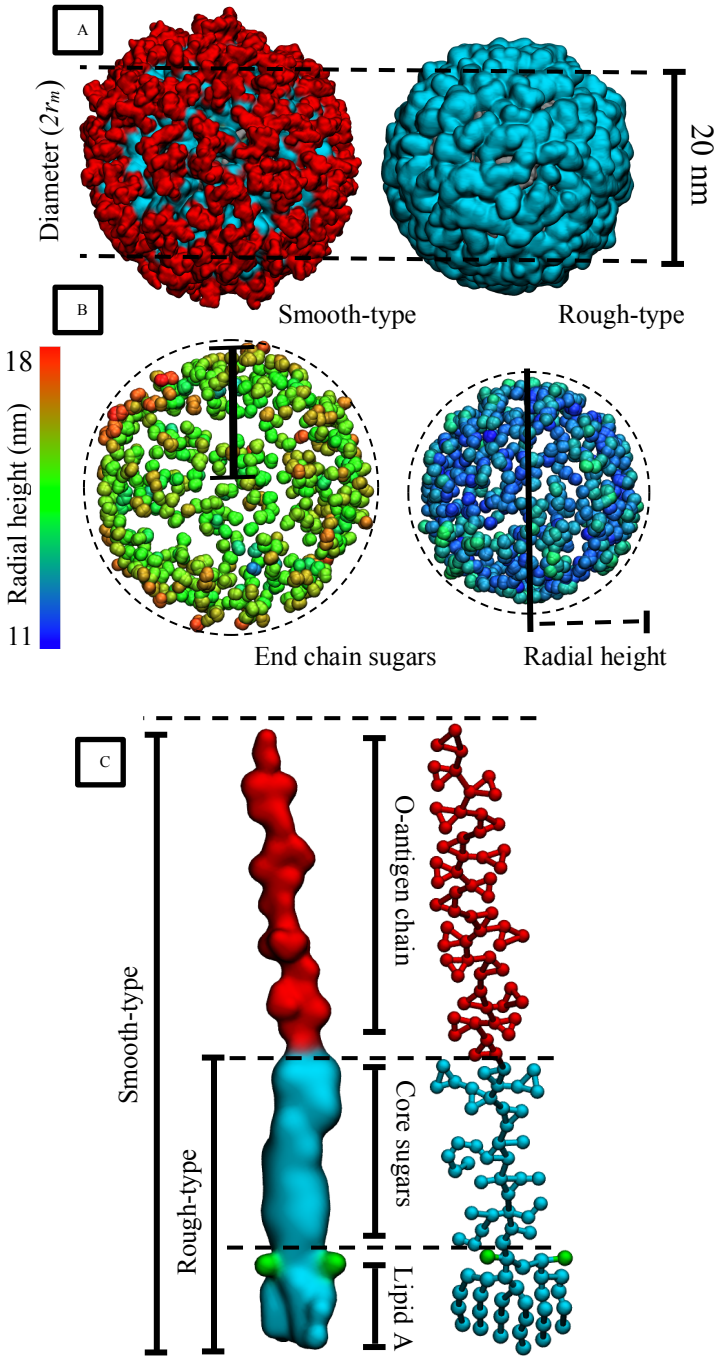

Figure 46. (A) Smooth and rough OMVs—atoms are represented using a volumetric density map. The POPE and POPG lipids are silver and the LPS molecules have the color scheme: Lipid A and core sugars (cyan), O-antigen chain (red). (B) The terminal sugar particles are assigned a BGR color based on their radial height (extension). (C) The LPS molecule is divided into its constituent Lipid A anchor, core sugar domain, and terminal O-antigen chain. The Lipid A phosphate groups are green to clarify the position of the water-lipid interface that is referenced throughout this chapter. The atoms are represented with a volumetric density map (left) and a simpler ball-and-stick model (right).

The smooth and rough OMV surfaces were distinctly different: the smooth OMV was littered with large groves and the rough OMV was comparatively uniform. The surface of the smooth OMV is quite similar to the capsid of the SV40 virus [542,1015-1017], which has grooves that interlink ganglioside lipid receptors in host cell membranes and thereby triggers endocytosis interactions. At this point, it is important to rationalize why the surface of one OMV simulation system is relatively uniform while the other is not. By assessing the surface topologies more thoroughly we will be afforded more general insights into the differences between smooth and rough OMVs and in particular, how their headgroup domains differ in terms of void area and free volume.

The differences in surface topologies will be explained using simple geometric equations and a bare-bones model for the OMVs (Figure 47). The lipids are treated here as axisymmetric cylinders that have constant cross-sectional area along their long-axis.[1] Two more assumptions are made: (i) that lipids align with the membrane normal[2] and (ii) that lipid flip-flop processes can be discounted throughout. Taken together, the assumptions will simplify the ensuing discussion and increase the scope of the conclusions that can be drawn in this section. Given that spherical surface area (A) scales with the square of radial length, i.e. $A = 4\pi r^2$, it is evident that $A_2 > A_1$ and $A_3 \gg A_1$, where $A_N = 4\pi {r_N}^2$ and r_N values are defined in Figure 47. Because the total cross-sectional area is approximately constant along the bilayer normal [211-212] it can be stated that $NA_L + NA_{PE} \approx A_1$; $NA_L + NA_{PE} < A_2$; and $NA_L + NA_{PE} \ll A_3$, where A_L and A_{PE} are the cross-sectional areas of LPS macromolecules and POPE lipids, and N defines the number of these

[1] The approximation of constant cross-sectional area for lipids is reasonable in this case, given that we seek a crude understanding of the disparities in OMV surface topology. The approximation is inappropriate for a detailed understanding of the dynamic interactions of lipids within biological membranes—slight disparities in molecular shape significantly impact almost all bilayer properties, and differences in molecular shape should generally not be ignored.

[2] LPS lipids, to a fair approximation, align with the bilayer normal: there is clear division better Lipid A anchor, core saccharide section, and O-antigen chain polymers along the membrane normal axis [211-212].

molecules in the OMV outer leaflet. If we assume that this system is a reasonable approximation of the structure of OMVs we can extrapolate and state that there is an increasing disparity between the projected surface area ($A = 4\pi r^2$) and the total lipid cross-sectional area ($NA_L + NA_{PE}$) as r is increased beyond the water-lipid interface (r_1). The amount of void area increases exponentially along the LPS macromolecule long-axis ($r_m \leq r \leq r_3$) and as a consequence, smooth OMVs are expected to have more void area at their outer edge than rough OMVs of similar hydrophobic midplane (r_m) diameters. This inference should be correct for almost all OMVs and this could be tested with electron microscopy methods or some other (non-computational) microscopy methods that are suitable for assessing the topology of lipid membrane surfaces.

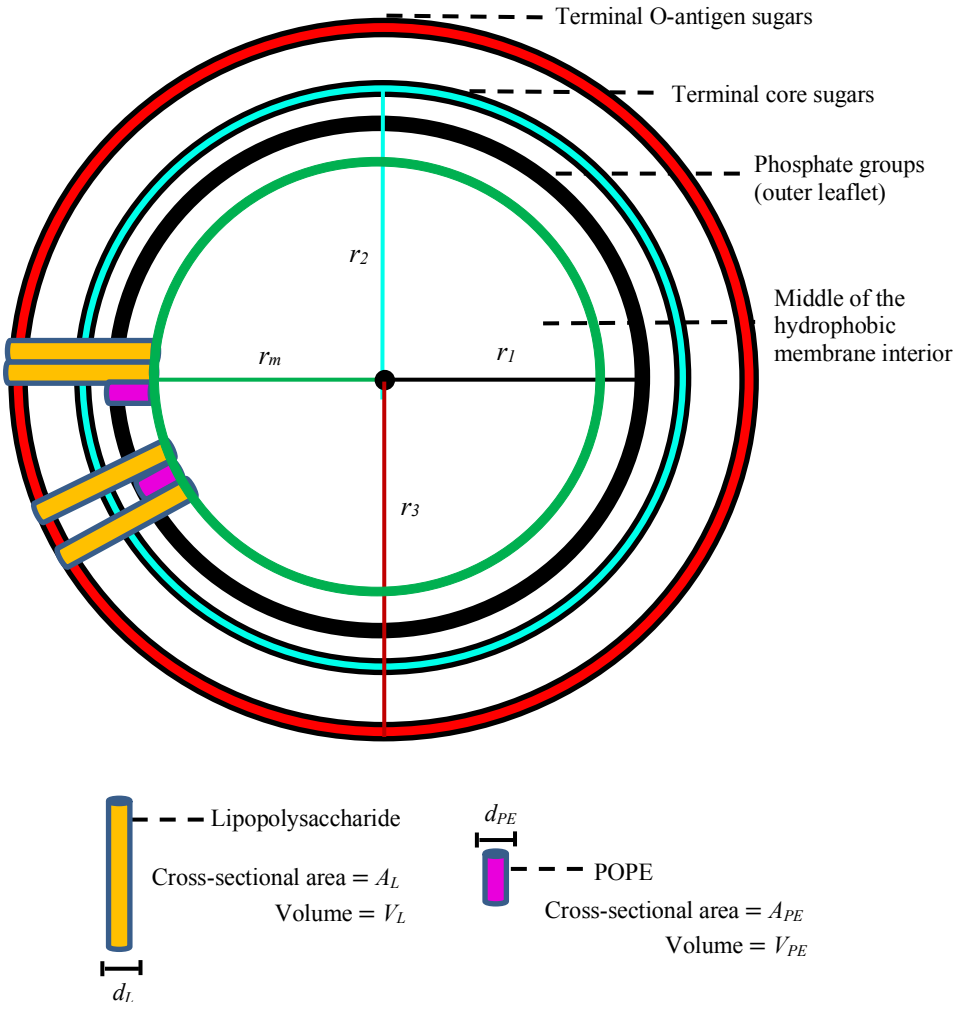

Figure 47. Schematic illustration of the smooth OMV that has been used to understand the different topology of the rough and smooth OMVs. The LPS lipids are orange, the outer leaflet POPE molecules are magenta and inner leaflet lipids are omitted throughout. The radial heights are labelled as follows: r_m (middle of the hydrophobic membrane core), r_1 (outer leaflet phosphate group boundary), r_2 (termini of the LPS core sugars), and r_3 (termini of the LPS O-antigen chains). The lipids are treated as axisymmetric cylinders, for example, the LPS macromolecules have constant cross-sectional area A_L and volume $V_l = \pi(r - r_m)(d_L/2)^2$, where d_L is the cylinder diameter and $r_m \leq r \leq r_3$.

It is appropriate to additionally determine the relationship between "free volume" or solvent-accessible space and the length of LPS lipids in the OMV outer leaflet ($r_m \leq r \leq r_3$). The volume of each LPS lipid is calculated according to the equation: $V_L = \pi(r - r_m)\ (d_L/2)^2$ where d_L is the effective diameter of the LPS lipids. The volume of each POPE lipid (in the outer leaflet) is calculated according to the equation: $V_{PE} = \pi(r - r_m)\ (d_{PE}/2)^2$,

where d_{PE} is the diameter of POPE molecules and $V_{PE} = 0$ beyond the water-lipid interface ($r > r_1$). The relationship between radial length and free volume becomes:

$$V_{fv} = V - (NV_L + NV_{PE})$$

or:

$$V_{fv} = \begin{cases} \left(\frac{4}{3}\pi r^3\right) - \left(N\pi(r - r_m)\left(\frac{d_L}{2}\right)^2 + N\pi(r - r_m)\left(\frac{d_{PE}}{2}\right)^2\right), & r_1 \geq r \geq r_m \\ \left(\frac{4}{3}\pi r^3\right) - \left(N\pi(r - r_m)\left(\frac{d_L}{2}\right)^2\right), & r_3 \geq r \geq r_1 \end{cases}$$

$$V_{fv} = \begin{cases} (ar^3) - \left(b(r - r_m) + c(r - r_m)\right), & r_1 \geq r \geq r_m \\ (ar^3) - \left(b(r - r_m)\right), & r_3 \geq r \geq r_1 \end{cases}$$

Equation 87-88

because the volume of a sphere is defined by the equation: $V = \frac{4}{3}\pi r^3$. Within this equation a, b, and c are constants $\Rightarrow$ that the amount of free volume scales rapidly with r beyond the water-lipid (phosphate group domain) interface for an OMV of radius r_m. The equations explain the disparities in the smooth and rough OMV simulation systems surface topologies: void area and free volume scale rapidly as a function of LPS headgroup length beyond the water-lipid (phosphate group) interface for OMVs of a given ($2r_m$) diameter. There should be stark differences in the surface topology of smooth and rough OMVs that have comparable hydrophobic core midplane diameters regardless of the parent bacteria genera. In other words, smooth OMVs will have rugged surfaces that have contrasting areas of relatively high and low O-antigen chain cluster density *in vivo*, whereas rough OMVs will appear to have much more uniform surfaces.

The disparate surface topologies suggest that rough and smooth OMVs will have different interactions with the headgroup moieties of host cell membrane lipids. The surfaces of smooth and rough OMVs differ markedly and this will affect how they adhere to host cell membrane surfaces. We must also make comparison with simulations from Chapter 4, i.e. Lipopolysaccharide O-antigen Chains Modulate the Mechanical Strength of the Gram-negative Outer Membrane, since it was shown that O-antigen chain interactions increase the strength of (flat) Gram-negative membrane mimetics. It is reasonable to extrapolate from the simulation data that was produced in chapter 4 and state that smooth OMVs must be more mechanically robust and by association stiffer than similarly sized rough OMVs.

We have found then that the smooth and rough OMV surfaces are significantly different. The rough OMV surface is relatively uniform, whereas the smooth OMV is significantly more topologically complex. There are also cohesive O-antigen chain interactions across the smooth OMV surface and these interactions have been shown to increase membrane mechanical strength and make bacterial membranes stiffer and more mechanically robust (see chapter 4). Based on these observations we should expect that the smooth and rough OMVs have significantly different interactions with host cell membranes.

The inference that smooth OMVs should have more topologically complex surfaces than rough OMVs is interesting not only because it has consequences for interactions at the wrapping interface here, but also because it can be tested experimentally. Most conventional experimental analysis methods lack the spatiotemporal resolution that would be necessary for visualizing such small-scale OMV surface features [1035-1038]. However, advanced imaging techniques are increasingly being applied to overcome some of the spatiotemporal restrictions of ordinary microscopy methods [1039-1043]. If sophisticated analytical microscopy methods were used to analyze the surfaces of smooth and rough OMVs they could potentially validate the

inference that smooth OMV surfaces are more topologically complex than comparative rough OMV surfaces. It would be important to mimic the OMV compositions accurately; the inner leaflet should only contain phospholipid molecules and the outer OMV leaflets should both contain phospholipids and LPS macromolecules in an approximate 1:1 number ratio.

5.4.3 OMVs Interacting with POPC Bilayers

The smooth and rough OMVs were simulated with a membrane that contained POPC lipids alone to obtain a rudimentary understanding of OMV interactions at host plasma membrane surfaces (Figure 48A-B). For clarity, the following simulation results are summarized in Table 2: the axis components of the radius of gyration, the radial extension of the Lipid A phosphate groups, the radial extension of the peripheral O-antigen chain saccharides, the number of POPC lipids in contact with LPS lipids, and the percentage of LPS lipids that were in contact with the host membrane POPC lipids (based on a 0.6 nm cutoff). The rough OMV behaved quite similarly to elastic lipid-covered nanoparticles at the host POPC lipid bilayer: the vesicle distorted and spread over the membrane surface (Figure 48C) [1010-1012]. There was approximate axisymmetric compression of the OMV at the bilayer surface and there was also compression of the individual LPS lipids along the membrane normal axes. The average radial extension of the rough LPS lipids was reduced compared with the simulation in water.

Table 2: Summary of OMV properties at the POPC bilayer. Standard deviations for radius of gyration values are less than 0.07 and for heights they are less than 1.74.

OMV type	Radius of gyration (nm)			LPS radial height (nm)		POPC in contact	% LPS bound
	Rg(x)	Rg(y)	Rg(z)	phosphates	extension		
Rough	9.20	8.88	10.07	11.29	12.02	5627	52
Smooth	9.99	10.13	10.13	11.09	16.32	1580	2

The POPC bilayer deformed and partially wrapped around the rough OMV as it distorted at the wrapping interface. It is emphasized here that the degree of host membrane wrapping was quantified according to the number of host membrane lipids that were in contact with the OMVs. There were more than 5000 POPC lipids within 5 nm of the rough OMV after 2 μs and more than 50% of the OMV surface was in contact with host membrane POPC molecules (Figure 48D-F). The correlation coefficient was computed for host membrane wrapping with respect to sampled simulation time to evaluate the likelihood of complete OMV encapsulation on long timescales. The correlation coefficient had a magnitude of -0.55 during the last 250 ns and this indicates that host membrane wrapping peaked at some point before this. Based on the loss of OMV sphericity, the reduction in host membrane wrapping during the last 250 ns, and data from comparable large-scale simulations [1009-1012] it is unlikely that the OMV will be completely enveloped on long timescales.

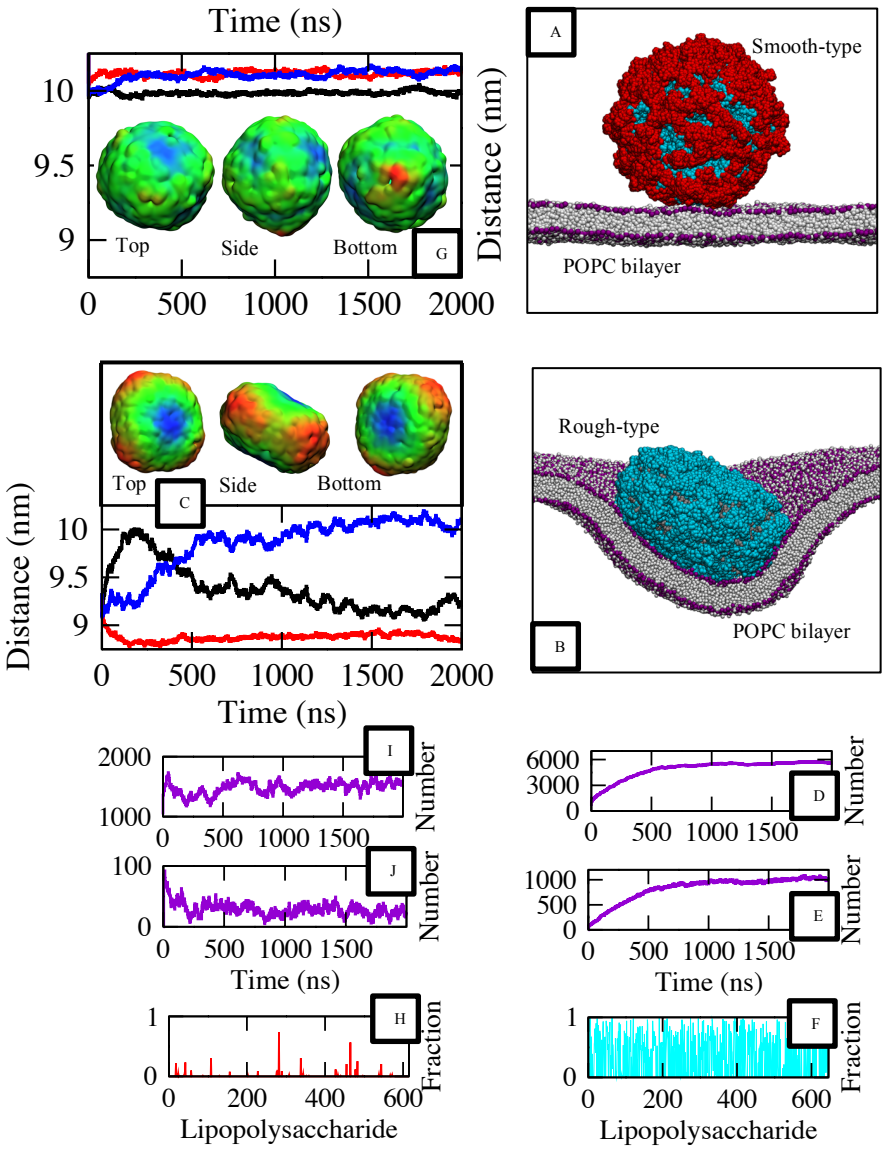

Figure 48. (A-B) Smooth and rough OMVs at the POPC bilayer. (C) The axis components of the radius of gyration for the rough OMV (bottom); the phosphate group (BGR) height map after 2 μs (top). (D) The POPC lipid shell population for the rough OMV (5 nm cutoff). (E) The LPS-POPC contact number (0.6 nm cutoff). (F) The fraction of simulation frames—during the last 0.25 μs—with registered LPS-POPC contacts (per rough LPS molecule). (G) The axis components of the radius of gyration for the smooth OMV (top); the phosphate group (BGR) height map after 2 μs (bottom). (H) The fraction of simulation frames—during the last 0.25 μs—with registered LPS-POPC contacts (per smooth LPS molecule). (I) The POPC lipid shell population for the smooth OMV; (J) the LPS-POPC contact number. Figures I-J and Figures D-E are measured from the point of OMV-host membrane first contact and thus, are non-zero from the start.

In contrast, the smooth OMV was found to maintain high sphericity when it was interacting with the POPC bilayer and did not induce appreciable wrapping upon interaction (Figure 48G). Through theoretical analyses it was

shown that stiff nanospheres gradually promote endocytosis via areal deformation processes [1010-1012]. Voronoi tessellation analyses revealed that the average areas per lipid were different in the upper and lower leaflets of the POPC bilayer after 2 μs. The mean area per lipid in the upper (extracellular) leaflet was 0.54 nm^2—ordinarily 0.68 nm^2 [343-344,1044]—and 0.81 nm^2 in the lower (intracellular) leaflet. The area per lipid was relatively uniform across the length of each lipid monolayer (Figure 49) and this suggests that the entire bilayer was strained rather than there being areas of high strain close to the attached OMV. The data collectively indicate that there were forces promoting areal deformation processes and host membrane wrapping around the smooth OMV. But there was minimal membrane wrapping despite this disparity in lipid packing about the membrane midplane: there were 1580 POPC molecules within 5 nm of the rough OMV and only 2% of the rough LPS lipids were bonded to the POPC lipid headgroups during the last 250 ns of simulation time (Figure 48I-H). Mean squared displacement calculations revealed that the interactions between the rough LPS lipids and the POPC molecules were weak and relatively short-lived. The lateral diffusion constants were 0.063 ± 0.0003 $1x10^{-5}$ cm^2/s for POPC lipids in the intracellular and extracellular leaflets. Collectively, the data indicate that there were forces favoring host membrane wrapping but also that the LPS-POPC bonds were weak and it was difficult for the POPC bilayer to adhere to the arched edge of the smooth OMV and promote gradual endocytosis interactions. The simulations do not preclude the possibility of host membrane wrapping on longer timescales, and as such, an effort has been to explore this possibility.

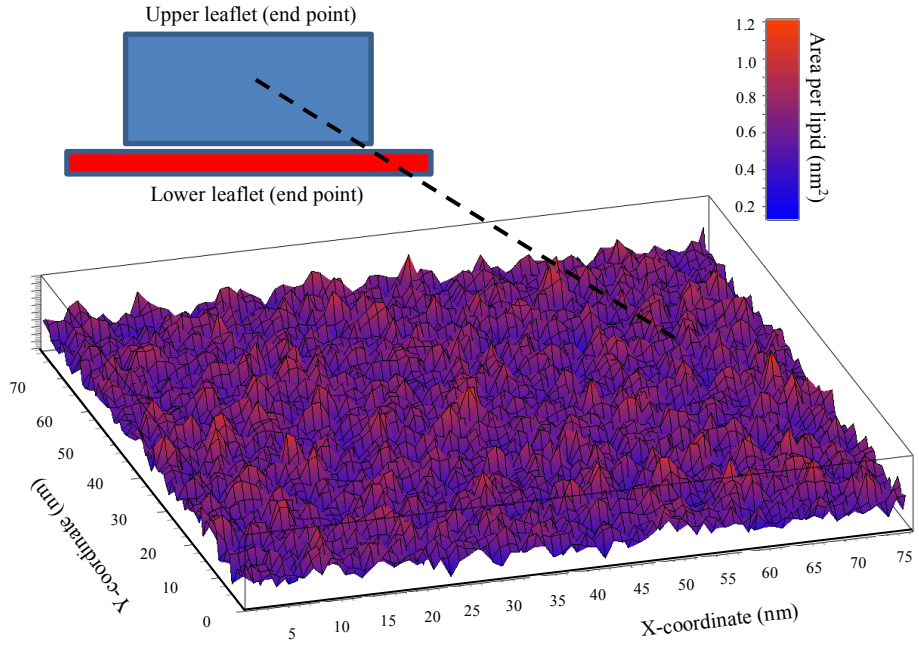

Figure 49. The area per lipid (BPR) color-height map for the upper (extracellular) leaflet of the POPC bilayer after it was simulated with the smooth OMV for 2 μs. The mean area per lipid for this color-height map is 0.54 nm^2; for comparison, the area per lipid is 0.68 nm^2 for POPC membranes that are not strained.

The simulation temperature was increased from 303 K to 330 K in an attempt to address the temporal limitations of conventional molecular dynamics simulations. The process introduced greater kinetic energies into the simulation cell, making it easier for molecules to surmount rate-limiting energy barriers. The simulation was performed for 250 ns and the last 50 ns were used to compute the magnitudes of different simulations parameters. The change did not increase the distortion of the smooth OMV but it did suppress OMV interactions with POPC lipids and the degree to which the host membrane was perturbed. The axis components of the radius of gyration were: 10.03 ± 0.01 (Rg(x)), 10.15 ± 0.01 (Rg(y)), 10.19 ± 0.01 nm (Rg(z)) and the average radial length of the Lipid A phosphate groups was 11.18 ± 0.63 nm. There were fewer interactions between the LPS macromolecules and the POPC lipid headgroup moieties: there were approximately 1500 POPC lipid headgroups within 5 nm of the smooth OMV and only 1% of the LPS lipids

were bound to POPC lipids (based on a 0.6 nm cutoff distance). The host membrane was much less perturbed: the mean area per lipid was 0.65 nm^2 in the upper (extracellular) leaflet and 0.70 nm^2 in the lower (intracellular) leaflet. The analyses suggest that wrapping interactions are not stepwise, they are not controlled by a series of successive energy barriers that are more easily surmounted as greater kinetic energies are introduced into the simulation cell. When particle velocities are increased there are in fact, fewer interactions at the wrapping interface and this loosens the OMV from the host membrane surface and by association, reduces its areal deformation effects. It seems sensible at this point to conduct molecular dynamics simulations with host membranes that contain embedded ganglioside lipids because it was demonstrated in previous publications that adhesion energies affect nanoparticle wrapping interactions [1010-1012].

5.4.4 OMVs Interacting with Realistic Plasma Membranes

The OMVs were simulated with plasma membrane models that incorporate (GM3) ganglioside molecules; this is noteworthy because ganglioside molecules are known to promote strong adhesion energies and at the same time, promote bilayer reshaping processes because the molecules have high intrinsic positive curvature [362-363, 428,1045,536-537]. The plasma membrane contained seven lipid types in total: cholesterol, POPE, POPC, POPS, GM3 lipid, (palmitoyl) sphingomyelin, and PIP_2. The lipids were distributed asymmetrically about the membrane midplane to mimic the *in vivo* scenario, i.e. a realistic asymmetric mammalian plasma membrane composition. The following lipids were set into the upper (extracellular) leaflet: POPE, POPC, sphingomyelin, GM3 lipid, and cholesterol in a 10:40 15:10:25 ratio. The following lipids were set into the inner (intracellular) leaflet: POPE, POPC, POPS, PIP_2, and cholesterol in a 40:10:15:10:25 ratio [76]. The results of these molecular dynamics simulations are presented in Table 3 and Table 4, but the results are also discussed in detail below.

Table 3: Summary of OMV properties at the host plasma membrane. Standard deviations for radius of gyration values are less than 0.01 and for heights they are less than 1.7.

OMV type	Radius of gyration (nm)			LPS radial height (nm)	
	Rg(x)	Rg(y)	Rg(z)	phosphates	extension
Rough	9.83	8.76	9.43	11.22	11.99
Smooth	10.35	10.17	10.12	11.21	14.18

Table 4: Changes in local lipid composition within 5 nm of the OMVs. Data are shown for each lipid type (per bilayer leaflet).

OMV	Enrichment/depletion within 5 nm of the OMV (%)													
	GM3		PIP_2		Cholesterol		Sphingolipid		POPE		POPC		POPS	
	IL	OL	IL	OL	IL	OL	IL	OL	IL	OL	IL	OL	IL	OL
Rough	—	2	2	—	13	2	—	7	2	-11	-12	-1	6	—
Smooth	—	-2[†]	18	—	19	8	—	5	-15	-10	-12	-4	4	—

[†] There was an absolute increase in the number of GM3 lipids (within 5 nm), but a relative reduction in GM3 concentration, given the non-negligible influx of sphingomyelin and cholesterol molecules into the local OMV 'shell'.

The rough OMV lost its spherical shape when it interacted with the plasma membrane: the axis components of the radius of gyration were more than 10% different after 2 μs. Other than this loss of OMV sphericity, there was also compression of the constituent LPS lipids along the membrane normal axes and this indicates that the shapes of both the OMV and its constituent LPS lipids, were perturbed upon interaction. The host membrane had distorted and partially wrapped around the rough OMV to form a concave "pit", or an invagination whose size was computed from the *z*-axis coordinates of lipids within 5 nm of the LPS macromolecules. The concave pit had a depth of 19.1 nm in this simulation and for comparison, the POPC bilayer formed a pit that was 21.0 nm deep when it wrapped around this same rough OMV. The extent to which the rough OMVs and host membranes were deformed seems to be mostly invariant of the specific host membrane composition. In either instance, the rough OMVs spread out over the membrane surface and the host membrane formed a concave pit that was highly curved at the spreading front. Comparable results were obtained from simulations of soft lipid-covered nanoparticles that were interacting with host membranes. The soft

nanospheres rapidly generated large curvatures at the spreading front that suppressed endocytosis on long timescales [1009].

The smooth OMV retained higher sphericity when it was simulated at the surface of the plasma membrane model (Figure 50A). The axis components of the radius of gyration were less than 3% different and the position of the water-lipid interface had only changed by 0.42 nm compared with the reference simulation in water (Figure 50B). However, there was some compression of the O-antigen chains when they interacted with the host plasma membrane model. The average extension of the LPS lipids was 14.18 nm in this simulation (Figure 50C) and for comparison, the extension of the smooth LPS lipids was 15.38 nm in water and 16.32 nm at the surface of the POPC bilayer. The differences in the radial extension of the LPS lipid headgroups is indicative of rather different interactions at the wrapping interface and hence, it is instructive to assess host membrane properties more thoroughly.

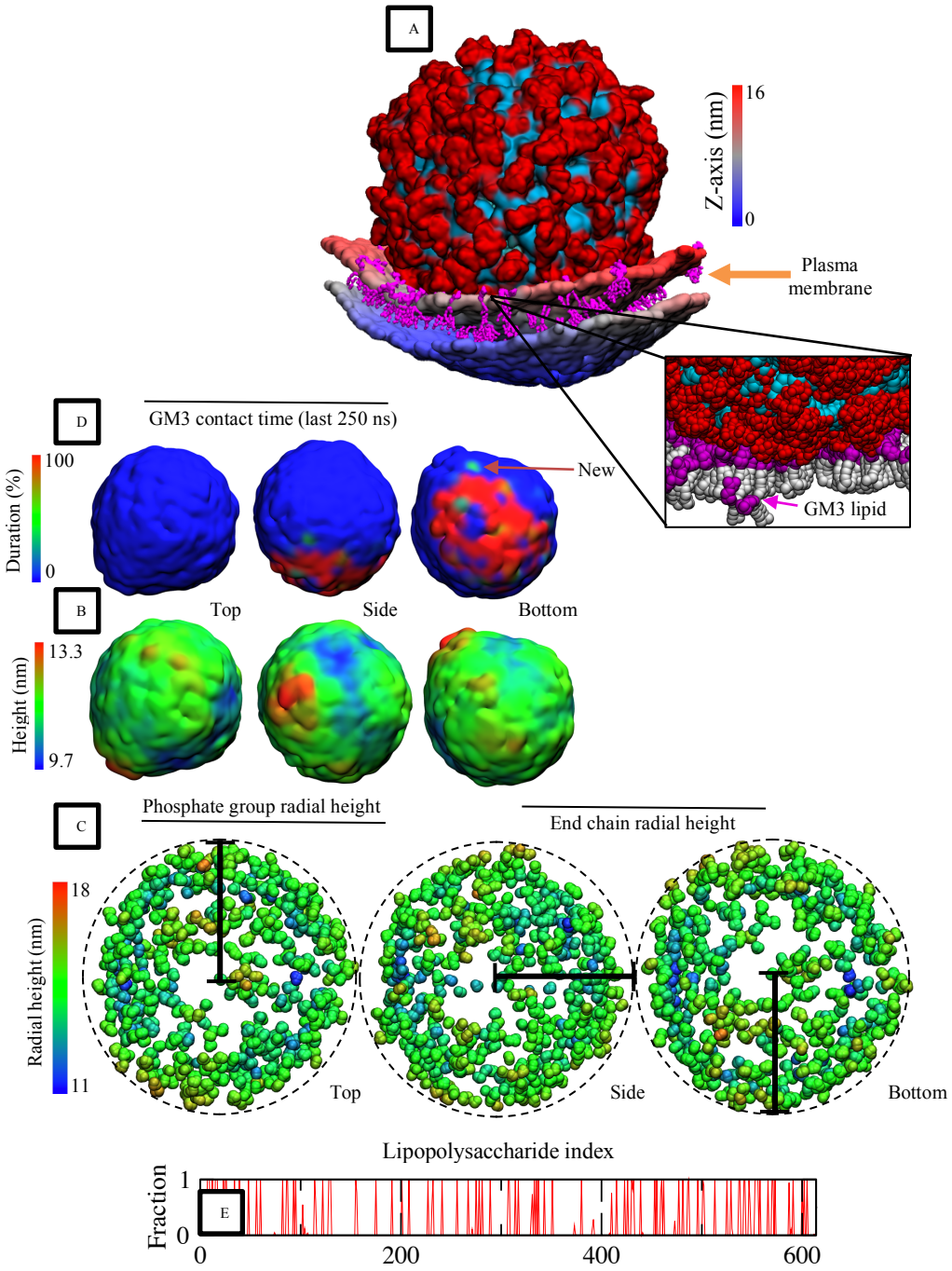

Figure 50. (A) Smooth OMV and the host plasma membrane (5 nm shell). The phosphate groups are assigned a (BSR) color based on their height (*z*-axis coordinate); the ganglioside molecules are magenta. In the inset, the ganglioside head groups are magenta and the lipid tails are white. (B) The phosphate group (BGR) height map after 2 μs. (C) The terminal sugar particles are assigned are a (BGR) color based on their endpoint radial height. (D) The LPS-GM3 contact duration projected onto the phosphate group density map; the data are shown for the last 0.25 μs of simulation time. (E) The fraction of simulation frames—during the last 0.25 μs—that LPS-GM3 contacts were registered for each one of the 615 smooth LPS molecules in the OMV outer leaflet. Put simply, the graph shows the fraction of sampled simulation time that each smooth LPS lipid was bonded to GM3

lipids (based on a 0.6 cutoff). Once the LPS-GM3 interactions were formed they were almost always maintained thereafter.

Up to 15.6% of the LPS lipids were in contact with the GM3 lipids and the bonds between the GM3 lipids and LPS headgroups were strong and long-lived. The GM3 lipid headgroups acted as a zipper and interlinked the LPS lipids to form bonds (based on a 0.6 nm cutoff distanced) that generally remained unbroken thereafter (Figure 50D-E). The process produced a natural ratchet mechanism where the host membrane progressively engulfed the OMV as carbohydrate headgroup moieties were intertwined at the wrapping interface. The ratchet mechanism has membrane-modulating effects: first, there was immobilization of the intertwined GM3 lipids, second, there was local curvature generation, and third, there was a change in the local lipid composition. The ganglioside molecules were progressively sequestered at the OMV contact edge where they formed relatively immobile aggregates (Figure 51) that had high intrinsic positive curvature. The clusters promoted bilayer reshaping processes and facilitated the formation of a small depression in the surface of the plasma membrane. Glycosphingolipid molecule clusters have been noted to promote comparable bilayer reshaping processes in previous computational and experimental publications.

Ganglioside lipids (e.g. GM3) are known to be domain-favoring [362,368,434] molecules and within these molecular dynamics simulations there were non-negligible changes in the composition of the membrane that surrounded the attached OMVs. As the OMV induced ganglioside aggregation there was an associated increase in the concentrations of PIP_2 and cholesterol molecules in the intracellular leaflet and an increase in the concentration of sphingomyelin and cholesterol molecules in the extracellular leaflet. Some of the changes in the local lipid composition can be rationalized by considering lipid shape alone: for example, PIP_2 has an inverted conical structure and it preferentially moved into the expanding intracellular leaflet that is positively curved, while cholesterol lipids are small and have a space-filling role.

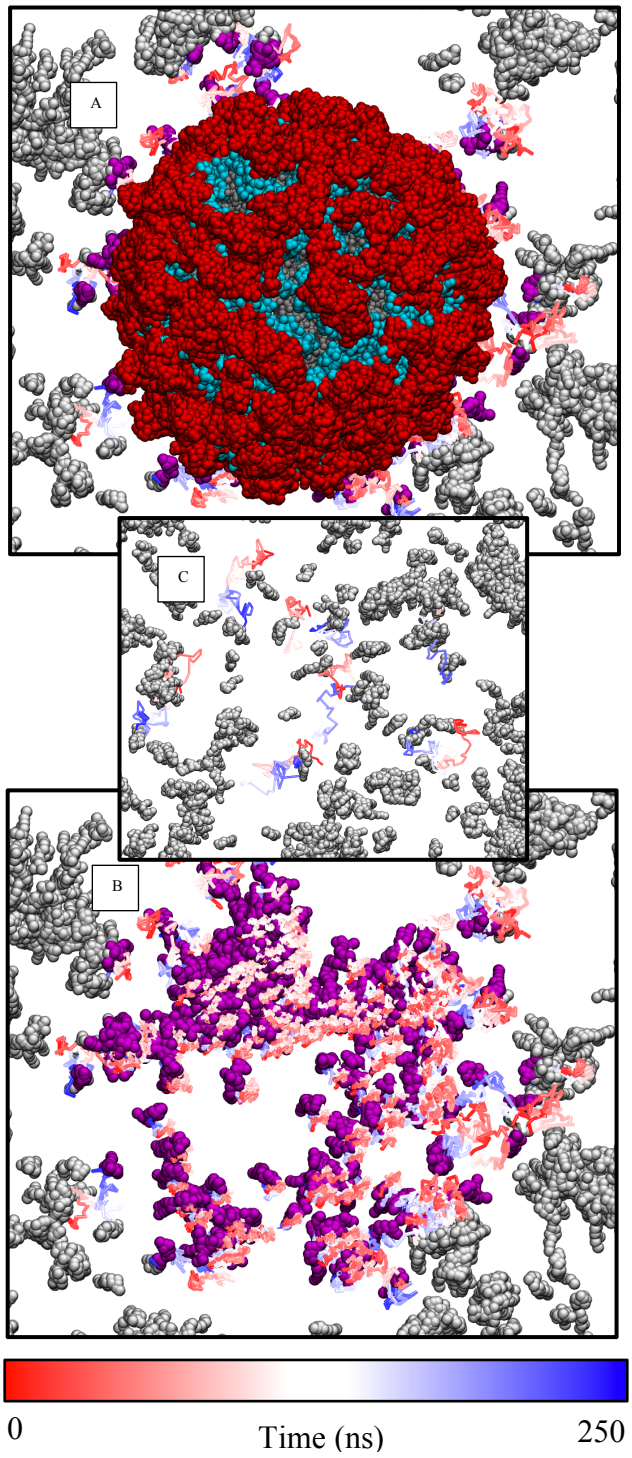

Figure 51. (A) Top view snapshot of the smooth OMV after it was simulated for 2 μs with the multicomponent plasma membrane model. (B) The same top view snapshot with the smooth OMV removed for clarity. The ganglioside lipids within 5 nm of the smooth OMV are magenta and the ganglioside lipids beyond this 5 nm cutoff are white. The POPE, POPC, POPS, PIP_2, cholesterol, and sphingomyelin molecules are omitted throughout. The trajectories are shown for the magenta ganglioside lipids during the last 0.25 μs. The trajectory paths were assigned colors to link the sampled simulation time with lipid diffusion. The early frame positions are red, the

late frame positions are blue and the intermediary frame positions are white. (C) Snapshot of the multicomponent plasma membrane when it was simulated without any OMVs. The trajectories are shown for randomly selected ganglioside lipids during the last 0.25 μs. When Figures A-B are compared with Figure C it becomes apparent that OMVs have the capacity to immobilize ganglioside lipids through zipper-like interlinking at the wrapping interface.

The ratchet mechanism is comparable to the lectin-induced glycosphingolipid clustering processes that can reorganize host plasma membrane lipids and mediate the growth of tubular membrane invaginations [368]. Pathogens (e.g. norovirus and SV40) and pathogenic products (e.g. Shiga toxin) interact with glycosphingolipid headgroups and as they reorganize the host cell membrane lipids they create an asymmetric stress about the membrane midplane [537,542,1015-1018]. The process lowers local bilayer bending moduli and promotes the inward bending of the plasma membrane and by association, the endocytosis of the attached pathogens or pathogenic products. Based on the striking similarities that can be identified between these coarse-grained molecular dynamics simulations and previous endocytosis uptake data it is reasonable to assume that OMVs enter cells as they interact with ganglioside lipid headgroups and progressively sequester the ganglioside molecules into clusters that have high intrinsic positive curvature. The smooth OMVs are spherical and they would generate minimal curvature as they wrapped host plasma membranes, whereas rough OMVs would rapidly generate larger curvatures that are less conducive for endocytosis. It should be stressed here that endocytosis processes have smaller energy barriers when ganglioside molecules have saturated, rather than unsaturated, lipid tails [1015] and theoretically, when ganglioside lipids have more highly branched saccharide headgroup domains. Highly branched ganglioside headgroup domains would support more cohesive carbohydrate-carbohydrate intermolecular interactions at the wrapping interface. Ratchet-like interlinking should occur more readily when plasma membrane mimetics contain larger ganglioside lipids (e.g. GM1) compared with membrane systems that contain smaller ganglioside molecules such as the GM3 lipids that were used here in this simulation study.

5.4.5 Phospholipid Vesicles Interacting with Host Membranes

Control simulations with a glycerophospholipid vesicle were used to understand how the LPS lipid leaflet affects the OMV uptake interactions. The glycerophospholipid vesicle contained POPE and POPG lipids alone. The vesicle was made with POPE and POPG lipids in a 9:1 number ratio per bilayer leaflet. The inner and outer glycerophospholipid vesicle leaflets were comparable to the inner leaflet of the smooth and rough OMV simulation systems. The POPE-POPG vesicle was made a diameter of 20 nm ($2r_m$) in an attempt to make it more similar to the OMVs that were simulated in the previous sections. The results of these simulations are presented as follows: (i) data from the simulations in water; (ii) simulations at the POPC lipid bilayer; and (iii) simulations at the extracellular surface of the plasma membrane model. It must be emphasized here that these data are used to understand how the LPS lipid leaflet affects OMV interactions through comparative analysis. The simulations were not performed to mimic realistic *in vivo* interactions and the simulations should not be considered as realistic representations of OMV uptake processes.

The POPE-POPG vesicle was initially simulated in water (Figure 52A) so that I could determine how the phospholipids were arranged and so that I could compare these data with the lipid packing parameters that were ascertained for the simulations of the rough and smooth OMV simulation systems in water. The squared relation between radial length and spherical surface area (i.e. $A = 4\pi r^2$) states that the spherical surface area scales rapidly with increasing radii and consequently there was an appreciable disparity in the magnitude of the lipid packing parameters about the membrane midplane (Table 5). The mean areas per lipid were larger in the extracellular leaflet than in the intracellular leaflet. The mean areas per lipid in the inner leaflet were as follows: 0. 51 ± 0.01 nm^2 (POPE) and 0.53 ± 0.01 nm^2 (POPG). The mean areas per lipid in the outer leaflet were as follows: 0.78 ± 0.01 nm^2 (POPE) and 0.82 ± 0.01 nm^2 (POPG). The differences in lateral packing parameters was due to the non-uniform projected surface area magnitudes

along the bilayer normal axes. There was less lateral surface area per lipid in the inner leaflet than there was in the outer leaflet. The disparity in area per lipid values was comparable to the disparities that were determined in previous coarse-grained molecular dynamics simulations of glycerophospholipid vesicles by Marrink et al. [1047].

Table 5: Areas per lipid for the POPE-POPG vesicle in water. Standard deviations are less than 0.01 throughout.

Membrane type	Mean area per lipid (nm^2)			
	POPE (IL)	POPG (IL)	POPE (OL)	POPG (OL)
Vesicle	0.51	0.53	0.78	0.82
Flat membrane	0.62	0.61	0.62	0.61

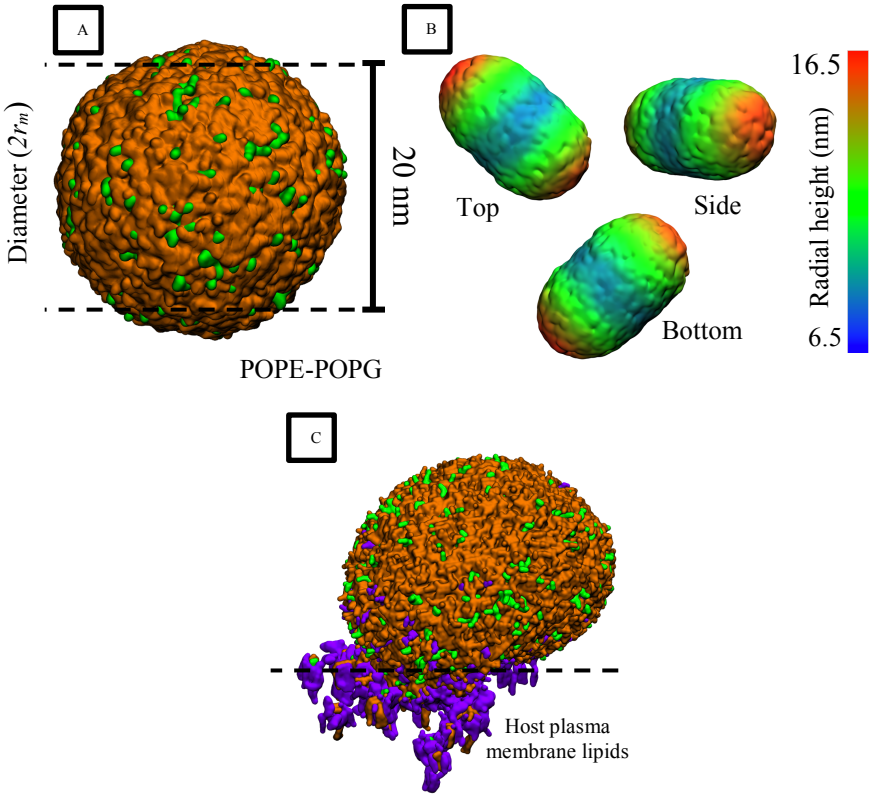

Figure 52. (A) The POPE-POPG vesicle that was used in the control experiments—the atoms are represented using a volumetric density map. The POPE lipids are orange and the POPG lipids are green. (B) The phosphate group (BGR) height map for the POPE-POPG vesicle after it bounced off the host POPC membrane. (C) The endpoint conformation for the simulation of the POPE-POPG vesicle and the multicomponent plasma membrane model. The POPE molecules are orange, the POPG molecules are green, and the host plasma membrane lipids that are within 0.5 nm of these lipids are purple. The vesicle fused with the host plasma membrane to form a lipid-lined pore that promoted lipid exchange between the plasma membrane and the POPE-POPG vesicle.

The vesicles were then simulated with the POPC lipid membrane to provide more data for comparative analysis. The POPE-POPG vesicle moved toward the surface of the POPC membrane at the start of the molecular dynamics simulation but then only made transient contact (approximately 1 ns) with the POPC headgroup moieties before it was pushed backwards. The brief contact was enough to significantly affect the shape of the POPE-POPG vesicle. The axis components of the radius of gyration were up to 13.5% different after 2 μs and the radial heights of the outer leaflet phosphate groups were up to 73% different (Figure 52B). The axisymmetric deformation

demonstrates that even transient contacts with host membranes are enough to warp the shape of vesicles.

There was fusion of the vesicle and plasma membrane model headgroups when the POPE-POPG vesicle was simulated with the multicomponent plasma membrane mimetic. The fusion event was in line with the stalk-pore intermediate model [1048], which describes membrane fusion as a stepwise process that involves hemifusion stalk intermediates. There was initial aggregation of the lipid membranes, association of the apposed bilayers, lipid rearrangement, and subsequent lipid content mixing [670,1049-1051]. There was a lipid-lined pore between the apposed bilayers that facilitated content exchange from the vesicle to the host membrane and also from the host membrane to the vesicle (Figure 52C).

The widths of the hydrophilic headgroups were computed for the POPE-POPG vesicle and the smooth and rough OMVs to understand why fusion was suppressed in certain simulations and facilitated in others. The widths of the hydrophilic headgroup domains were determined by computing RDFs for the hydrophilic headgroup beads with respect to the vesicle centers. The width of the POPE-POPG vesicle headgroup domain was 0.50 ± 0.25 nm and the widths of the hydrophilic headgroup domains were 1.78 ± 0.24 nm and 5.01 ± 0.21 nm for the rough and smooth OMVs, respectively. The data suggests that OMVs will be less likely to achieve direct membrane fusion than comparative phospholipid vesicles because membrane fusion reactions are mediated by pre-stalk transition states. Lipid tails must circumvent a thicker hydrophilic headgroup domain in OMVs to fuse with host membranes compared with phospholipid vesicles. Put simply, OMVs have a thick wall of hydrophilic sugars that obstruct lipid tails and suppress membrane core content mixing, whereas glycerophospholipid vesicles are less encumbered by their hydrophilic headgroup moieties.

It must be stressed here that membrane fusion reactions are multifaceted and that they depend on almost all membrane properties e.g. bilayer curvature,

lipid heterogeneity, and the abundance of POPE molecules, which have intrinsic negative curvature and as such, the capacity to stabilize the negatively curved necks of hemifusion intermediate states [1052-1053]. Indeed, this complexity is evident in these coarse-grained molecular dynamics simulations, the POPE-POPG vesicle fused with one host membrane (plasma membrane) and not the other (POPC bilayer). It is not being stated here that direct membrane fusion reactions are governed by headgroup width alone but rather that OMVs have unusually thick hydrophilic head groups; so much so, that OMVs do not fuse with host membranes regardless of the simulation setup. The data collectively demonstrates that OMVs must enter cells via host cell membrane wrapping processes and because we know that host membrane wrapping processes are more efficient when nanospheres are stiff and cohesion forces are strong, we can explain why smooth OMVs can more effectively enter into cells via lipid-mediated uptake processes and also state that ganglioside molecules should enhance this endocytosis process.

5.5 Conclusion

It has been demonstrated here that the length of LPS lipids affects OMV properties at the host-pathogen interface. When the simulated OMVs contained terminal O-antigen chain polymers (smooth OMVs) they maintained high sphericity when they interacted with host the membranes. When the simulated OMVs contained shorter LPS lipid variants that lacked terminal O-antigen chain polymers (rough OMVs) they spread out over the host membrane surfaces—an event that tends to precede incomplete host membrane wrapping or incomplete encapsulation [1009-1012]. Wrapping interactions were also affected by the composition of the host membrane: ganglioside headgroups acted as a zipper to mediate strong cohesion forces and help force the host membranes around the round OMV surfaces. The process occurred via a natural ratchet mechanism as the carbohydrate headgroup moieties were progressively intertwined at the wrapping interface. The sequestered ganglioside molecules tended to increase the local

bilayer curvature and also increase the concentration of lipids that are associated with raft formation (e.g. sphingomyelin and cholesterol) [79,88] and endocytosis (e.g. PIP_2) [1054-1056]. Importantly, it was observed throughout these molecular dynamics simulations that rough OMVs can deform host membranes more rapidly than comparable smooth OMVs. Smooth OMVs were associated with slow increases in elastic energy that would promote endocytosis processes on long timescales [1010-1013], whereas rough OMVs were associated with faster curvature generation.

The simulations can be used to understand the differences in the uptake efficiency of smooth and rough OMVs at the host-pathogen interface [664]. Interactions between terminal O-antigen chains confer mechanical strength to smooth OMVs [579] and the smooth OMVs are consequently stiff and prone to retain high sphericity at host cell surfaces. When OMVs lack terminal O-antigen chains (rough OMVs) they are less stiff and they tend to lose their spherical shape as they spread out over host cell membranes (Figure 53). The differences in sphericity will affect the magnitude of the late stage energy barriers that are associated with OMV endocytosis. Rigid nanospheres induce minimal curvature generation at the spreading front as they slowly wrap the host membranes. Softer nanospheres tend to be associated with faster increases in elastic energy and the production of larger curvatures at the spreading front and this faster increase in elastic energy makes nanosphere encapsulation much less likely on long timescales [1009-1012]. Put simply, smooth OMVs are stiffer than comparable rough OMVs and consequently, they should be more adept at forcing host membranes around their comparatively highly spheric surface.

It is imperative to appreciate that inferences have been made here through comparisons with previous simulation studies. The simulation data demonstrates that LPS lipid length affects the rigidity and shape of OMVs at host cell surfaces and indeed, the shape of the host cell surfaces themselves. This insight alone appears to explain the differences in the lipid-mediated uptake of smooth and rough OMVs at host cell surfaces [664]. Previous

calculations have demonstrated that endocytosis processes depend on the shape and stiffness of nanoparticles at the wrapping interface. The endocytosis energy barriers are smaller when nanospheres are stiff and round and larger when the nanospheres are soft and non-spherical. The molecular dynamics simulation data is enough to show that endocytosis will be different for rough and smooth OMVs; it is easier for smooth OMVs to enter cells via host membrane wrapping processes because they are stiffer and rounder at host cell surfaces. But nonetheless, the stepwise perturbation of the lipid geometries (both spherical and flat) has been extrapolated here to long timescales and while this seems intuitively reasonable, the proposed uptake models have not been validated outright. To reiterate, an OMV uptake model was proposed here based on the extrapolation of molecular dynamics simulation data rather than a model being proved to be irrefutably accurate.

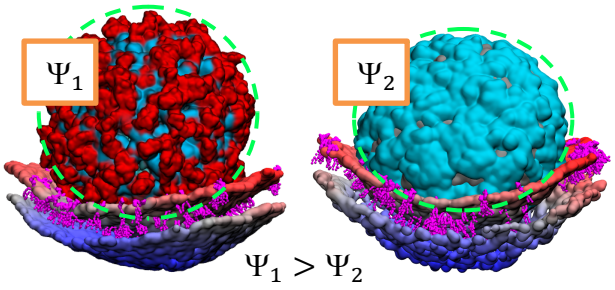

Figure 53. Comparison of the smooth and rough OMVs at the plasma membrane surface at 2 μs of simulation time. The smooth OMV retained its spherical shape and generated moderate curvature and the rough OMV lost its spherical shape and generated larger curvatures at the spreading front. Sphericity is denoted here with the Ψ_n symbols.

The molecular dynamics simulation study dispels the relatively common assumption that OMVs readily pass through host membrane surfaces via direct membrane fusion processes [52]. The molecular dynamics simulation study demonstrated that hydrophilic headgroup width affects membrane fusion reactions. Phospholipid vesicles had a thin hydrophilic headgroup domain and they achieved direct membrane fusion via the formation of stalk-

intermediate states. The OMVs had thicker hydrophilic headgroup domains that obstructed the lipid acyl chains and this impeded membrane association and aggregation. The distance between the OMVs and the host membranes was appreciable throughout the simulations and this made it difficult for the apposed bilayers to fuse at the wrapping interface. The results suggest that OMVs enter cells more readily through host membrane wrapping processes rather than through direct membrane fusion processes. Direct membrane fusion pathways should not be entirely discounted but it is evident that direct membrane fusion is not facile for OMVs. Fusion barriers seem to scale with headgroup width and this implies that direct membrane fusion pathways are hardly accessible for rough OMVs and even less accessible for comparable smooth OMVs.

It was additionally demonstrated that wrapping interactions depend on cohesion energies and the bending moduli of the host membranes. These inferences are not only interesting because they provide important insights for understanding OMV uptake, but also because they are corroborated by predictions from previous theoretical publications [1010-1012]. The smooth OMVs wrapped host membranes that contained ganglioside molecules but these same OMVs were unable to affect the shape of single-component POPC plasma membrane mimetics. POPC lipids do not have high intrinsic positive curvature and the molecules do not strongly interact with pathogens and pathogenic products. Ganglioside molecules contain different carbohydrate headgroup moieties that both promote strong cohesion with pathogens and at the same time, the ganglioside lipids have the capacity to lower bilayer bending moduli (see section 1.4.4). Strong cohesion energies were generated when the LPS headgroup moieties were interlinked with the ganglioside molecule headgroups. The interlinking of the carbohydrate headgroup moieties created a natural ratchet mechanism that helped to force the membrane around the OMV surfaces. The sequestered ganglioside lipids formed clusters that have high intrinsic positive curvature and have been shown to promote bilayer reshaping processes [363,430,1046]. Plasma membrane heterogeneity also impacted the membrane reshaping processes;

the plasma membrane contained seven different lipids types and these lipids were able to change their positions within the plasma membrane mimetic when it was expanding into the intracellular domain of the simulation cell. The constituent lipids changed their relative membrane position as the bilayer shape was changing and this reduced line tension energies and promoted additional membrane reshaping processes. For example, more PIP_2 lipids moved into to the expanding inner leaflet of the plasma membrane model when it was expanding into the intracellular side of the simulation cell. Lipid type heterogeneity has been established as a driving force for membrane reshaping processes in previous simulation studies [364,1057] and it is interesting to see it demonstrated here once again in these coarse-grained molecular dynamics simulations.

The uptake of OMVs at the host-pathogen interface appears to be multifaceted and quite complex. Lipid composition affects the stiffness parameters of OMVs and host membranes and at the same time, the strength of the cohesion forces that are established between them. Furthermore, there is dynamic lipid co-clustering within host plasma membranes that can affect how easy it is for host membranes to wrap around attached OMVs. For clarity, the simulation results are presented here schematically (Figure 54). The figure affords some overarching insights that explain the interaction of the smooth OMVs with the host plasma membrane models and this illustration provides a more general hypothesis for lipid-mediated OMV uptake. It was demonstrated that OMVs preferentially interact with glycosphingolipids within host cell plasma membranes and that this interaction mediates membrane wrapping processes. The interaction between the LPS lipids and the ganglioside molecules is comparable to interactions between pathogenic products (e.g. cholera and Shiga toxin) and host cell membranes and even more similar to the interaction between pathogenic viral particles (e.g. SV40 virus) and host cell membranes [537,542,1015-1018]. Smooth OMVs initially bind ganglioside lipid headgroup moieties and this generates a depression in the host membrane surface that could be considered an endocytosis intermediate [671-673]. The process transpires as unbound ganglioside

lipids move through the plasma membrane mimetic surface and subsequently come into contact with the immobilized OMVs. The ganglioside molecules become trapped at the OMV contact edge and as they progressively change the local membrane composition they affect the local energy barriers for membrane curvature generation (Figure 54). If we extrapolate to longer timescales we would presumably find that the host membrane would be wrapped around much more, if not all, of the smooth OMV surface. The precise degree of host membrane wrapping would depend on specific lipid parameters such as flexural moduli, cohesion energies, and it would also depend on the composition of the host membrane [1010-1012].

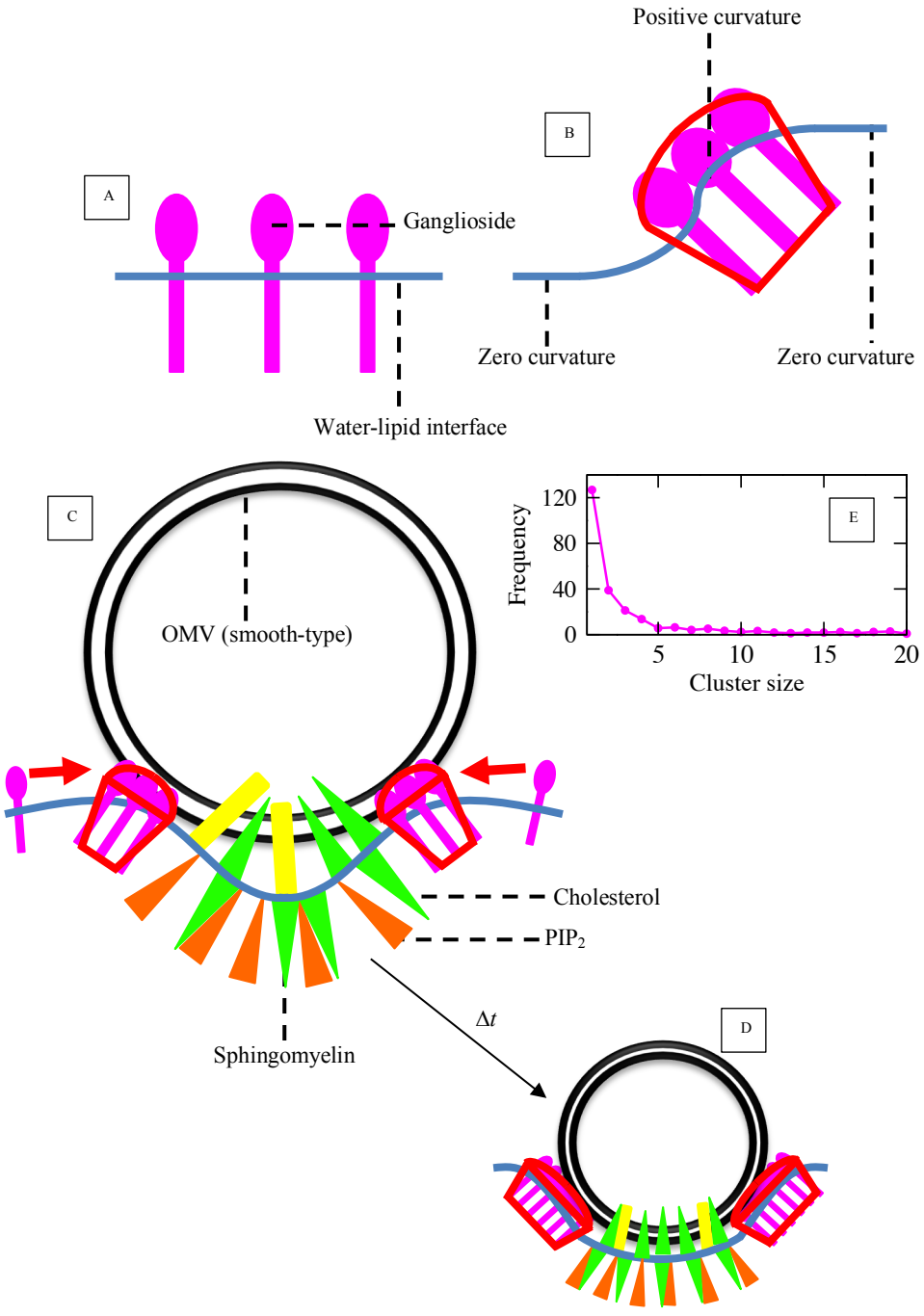

Figure 54. (A) The ganglioside molecules (pink), which are confined to the upper (extracellular) leaflet, create non-negligible stress in plasma membranes that promotes spontaneous bilayer curvature. (B) The energy barriers for bilayer reshaping are reduced when ganglioside molecules aggregate and form clusters that have high intrinsic positive curvature. The ganglioside lipid aggregates can reduce the line tension between membrane domains of different widths due to their conical shape. (C-D) Schematic illustrations showing how smooth OMVs affect bilayer shape and composition. The sphingomyelin are yellow rectangles, the PIP_2 lipids are orange triangles, the cholesterol molecules are inverted green triangles and the POPS, POPC, and POPE lipids are omitted for clarity. After simulation

time of Δt there a significant number of (GM3) ganglioside molecules that have interlinked the smooth LPS lipid headgroups (based on a 0.6 nm cutoff) and consequently, there is a change in the local lipid composition and bilayer curvature. (E) The abundance of ganglioside monomers and aggregates that were detected during the last 100 ns of simulation time when the plasma membrane mimetic was simulated without any OMVs.

The results from this chapter suggest that OMVs can be primed to fully wrap host membranes by increasing the length and concentration of (smooth) LPS lipids within the OMV outer leaflets. This change would increase the mechanical strength of the OMVs and make them more prone to achieve complete encapsulation—explaining why smooth OMVs with longer O-antigen chains more readily exploit lipid-mediated uptake pathways in experimental studies [664]. It can also be discerned from this chapter and from theories of nanosphere encapsulation that the composition of the host membranes can be changed to suppress or promote host membrane wrapping processes [1010-1012]. Constituent membrane lipids have the capacity to affect membrane flexural moduli, adhesion energies and membrane reshaping processes. Ganglioside molecules promoted strong OMV adhesion energies and they also lowered energy barriers for membrane curvature generation. The integration of different lipid types into the host membrane also enhanced membrane reshaping processes as intrinsically negatively curved lipids could move to negatively curved membrane domains and intrinsically positively curved lipids could move to positively curved membrane domains. It is important to note that the membrane mimetics were relatively simplistic and that additional compositional complexity would have further impacted host membrane wrapping interactions. Changes to the plasma membrane composition could either further promote or impede the membrane wrapping processes. For example, integral membrane proteins can make host membranes stiffer and also affect ganglioside co-clustering [496,993,1026]. Stiffer host membranes that contain fewer unconstrained ganglioside headgroups would be less prone to wrap around attached OMVs and lipid-mediated uptake pathways would be suppressed.

The computational study was not comprehensive and the molecular dynamics simulations omitted molecules that could affect OMV uptake processes e.g. membrane proteins. The simulation study does however clarify an interesting question: why does OMV lipid-mediated uptake depend on the cell wall architecture of parent (bacterial) cells [664]? The coarse-grained simulations appear to address this question and thereby make some headway in clarifying some longstanding uncertainties associated with OMV uptake e.g. why the concentration of Filipin, cholesterol, and caveolae affect OMV internalization? And why does LPS lipid modification affect the efficacy of OMV vaccine adjuvants [48,52]? The experimental analyses revealed that LPS lipid length is inexorably linked to membrane parameters that either promote or impede endocytosis. Rough LPS lipid OMVs deformed at host cell surfaces and smooth LPS lipid OMVs retained high sphericity. An OMV uptake model was proposed here based on the extrapolation of molecular dynamics simulation data rather than a model having been proved to be irrefutably accurate. The model proposes precisely how constituent rough and smooth LPS lipids can differently impact lipid-mediated OMV uptake processes. The model is rudimentary and it could be refined to make it more accurate but this does not invalidate the inference that smooth OMVs can more easily enter cells via endocytosis compared with rough OMVs. This conclusion would be true if the proposed uptake model is left unchanged or even if it is refined. Here I have shown that smooth OMVs and stiffer and more round at host cell surfaces than comparative rough OMVs and therefore we can state that it is easier for smooth OMVs to enter into the host cell cytosol via endocytosis.

Before this chapter is concluded it is important to state the limitations of this simulation study to legitimize the conclusions that have been made thus far. The simulations were performed with the coarse-grained Martini forcefield, which omits explicit atomistic detail to reduce the computational load [822]. The coarse-grained Martini molecular dynamics forcefield reduces the number of pairwise interactions that are computed per timestep by mapping approximately four heavy atoms to a single interaction center. The omission of explicit atomistic interactions can negatively impact the accuracy of lipid-

solvent interactions. For example, there is almost always less water moving through the LPS lipid headgroup domain in coarse-grained molecular dynamics simulations compared with comparative atomistic resolution simulations [301,580,824]. Water is explicitly represented in united-atom simulations as tripartite molecules that contain one oxygen atom and two hydrogen atoms. The water molecules are small and they can fill the small cavities that exist between LPS headgroup sugar units. Water is represented in comparative coarse-grained Martini forcefield simulations as large coarse-grained beads or "pseudoatoms" [799] that are less able to fill small cavities between LPS lipid headgroup moieties. Ma et al. found that the coarse-grained *P. aeruginosa* bacterial outer membrane core saccharide domain was depleted of ~25-50% [580] water compared with target atomistic resolution simulations. Van Oosten et al. found that another entirely distinct coarse-grained *P. aeruginosa* bacterial outer membrane core saccharide section was depleted of ~25-50% water in some sections along the bilayer normal [824]. The *E. coli* LPS lipid models that were used here in this chapter have been found to be similarly depleted of water. The Re LPS core saccharide section was found to be up to ~25-50% depleted within some parts of the core saccharide domain and some sections of the Ra LPS core saccharide section were up to three-fold depleted [301]. This is a serious artifact that is essentially unavoidable in Martini coarse-grained molecular dynamics simulations of LPS lipid membranes because hydrogen-bonded water networks cannot be accurately mimicked using implicit coarse-grained bead representations for water and ions [822].

The reduction in atomistic detail additionally makes it difficult to accurately reproduce the complex conformational landscape of lipids, proteins and other complex macromolecules. There generally tends to be satisfactory overlap of LPS lipid conformational landscapes in comparative united-atom and coarse-grained molecular dynamics simulations but minor discrepancies have been observed between the two e.g. disparities in endchain conformations [580]. Let us analyze some of this comparative conformational data quantitatively to explicit define some differences between target

atomistic and model coarse-grained molecular dynamics simulations. Khalid et al. assessed the order parameters of homogeneous Re and Ra LPS lipid membranes in comparative coarse-grained and atomistic molecular dynamics simulations in an attempt to provide some insight into the conformation of the comparative LPS acyl chains [301]. There was a difference of 0.03-0.08 for the simulations with Re LPS lipid acyl chains and a difference of 0.01-0.09 for the simulations with Ra LPS lipid acyl chains. The LPS lipid equilibrium bond length distances (r_{eq}) differed by no more than 0.1 nm between the comparative atomistic and coarse-grained molecular dynamics simulations and the equilibrium bond angles (θ_{eq}) differed by no more than 10%. The corresponding force constants (k_{ijk}^{θ} and k_{ij}^{r}) were well matched for the comparative atomistic and coarse-grained resolution simulations and the bond length and angle distributions generally overlapped to within 20%. The maximum extension of the bacterial membranes differed by no more than 10% but there did appear to be a systematic bias throughout and the coarse-grained LPS lipids were almost always more compressed than the reference atomistic LPS lipids.

The implicit presentation of cations in coarse-grained simulations also affects the accuracy of bridging interactions between Lipid A anchors. Coarse-grained Martini calcium ions do not coordinate multiple neighbouring LPS lipids with each other and with adjacent water molecules. The coarse-grained ions do not connect multiple lipids and water molecules and they do not effectively establish lamellar LPS lipid packing and a hydrogen-bonded network that would otherwise contribute to bacterial membrane stability [551,1058-1059]. The omission of the correct LPS lipid coordination and of the hydrogen bond network negatively impacts the accuracy of the bacterial membrane simulations because these interactions promote lamellar lipid packing and membrane stability.

There were inaccuracies in domain formation and lipid segregation within the multicomponent plasma membrane itself. It has been stated in previous publications that sphingomyelin co-clustering is underestimated in coarse-

grained Martini forcefield simulations relative to reference all-atom molecular dynamics simulations and experimental data [363,993,1023]. The conformation of the coarse-grained ganglioside aggregates must have also been quite inaccurate in these simulations if we consider the spatiotemporal limitations of the Martini coarse-grained forcefield [174]. Simulations of flat plasma membranes had revealed that ganglioside co-clustering proceeds on timescales that are not entirely amenable to conventional molecular dynamics simulations. Ganglioside aggregation was not completely converged even after 40 μs of simulation time [498] and simulation timescales were even shorter here, within this chapter.

These noted conformational, hydration and lipid-solvent inaccuracies inevitably affected the quality of the coarse-grained molecular dynamics simulations that were performed in this chapter. It has been stated previously that the Martini coarse-grained forcefield is generally described as being semi-quantitatively accurate [822] and it should be expected that these coarse-grained simulations were no more, or no less accurate. The simulations likely produced accurate qualitative conclusions but inevitably produced numerical data that was in some places inaccurate. In other words, minor numerical accuracies are to be expected when simulations are conducted with the Martini forcefield but this does not discredit the validity of the overarching qualitative conclusions.

The use of a semi-isotropic coupling algorithm could also potentially bias the deformation of vesicles along a specific plane of the simulation cell. Shorter simulations (1μs) were conducted with isotropic and anisotropic pressure coupling algorithms to modulate the system pressure with alternative simulation cell scaling schemes and thereby ensure that the overarching qualitative conclusions were not an artifact of using inappropriate simulation settings for the modulation of system pressure. There was approximate asymmetric deformation of the rough OMVs about the host membrane normal axes when either of the isotropic and anisotropic pressure coupling algorithms were used to modulate the system pressure and the smooth OMV

always retained its spherical shape. The use of a semi-isotropic pressure coupling algorithm may affect the precise magnitude of the axisymmetric OMV deformation but the general differences in shape preservation seemed to be invariant of the box vector scaling method i.e. isotropic, semi-isotopic, or anisotropic.

Perhaps the most undesirable limitation is the spatiotemporal constraints of modern computer hardware that is paired with nothing more than the coarse-grained Martini simulation forcefield [174]. The Martini forcefield is a relatively sophisticated coarse-grained molecular dynamics simulation forcefield that maps a relatively low number of atoms to each coarse-grained bead and it can be quite computationally demanding. The Martini forcefield maps approximately four heavy atoms to a single interaction center [799] and hence it is challenging to probe simulation timescales that exceed anything more than a few microseconds [59,114]. Simulations were conducted here on a microsecond timescale and this was long enough to show that rough and smooth OMV systems have different shapes at host membrane surfaces. The data were used to infer that this would affect OMV endocytosis processes on long timescales but this was an inference and not something that was proved outright. It would be necessary to use significantly more computational resources or entirely different simulation forcefields to empirically demonstrate that this prediction is indeed correct and that OMVs have different endocytosis uptake efficiencies on long timescales. Comparable simulations were performed with very low resolution solvent-free coarse-grained forcefields and it was shown that complete endocytosis can take as long as 500 μs [1009]. Thus, alternative approaches must be used if we want to access the larger and longer spatiotemporal magnitudes that are necessary for proving some of the predictions that were made in chapter. The non-polarizable coarse-grained Martini molecular dynamics simulation forcefield [799,814] is not suitable, but other lower resolution forcefields [114,174] could be. It is clear then that this simulation study should only be considered as being semi-quantitatively accurate and that some of the simulation settings were non-ideal. But based on comparisons with previous publications [1009-

1012] and the discussions that have been made here we can conclude that the overarching qualitative conclusions were warranted throughout.

Chapter 6: Conclusions

6.1 Abstract

The simulations have presented novel insights that in some places corroborate previous experimental and computational work and in other places propose altogether new explanations for unexplained biological phenomena. Within this chapter I discuss the overarching predictions that were made in chapters 3, 4 and 5 and I attempt to explain how the simulation predictions could be validated through experimental analyses.

6.2 Validating the Predictions from Chapter 5

Perhaps it is most appropriate to start with the primary focus of this thesis: bacterial OMVs. First, it was found that the smooth OMV simulation system surfaces were more topologically complex than the comparative rough OMV simulation system surfaces. The LPS lipid sugars condensed when they were simulated and they formed long approximately linear clusters that were aligned with the bilayer normal axes (Figure 46-47). The smooth LPS lipid headgroups projected further outwards beyond the Lipid A phosphate group domain than the comparative rough LPS lipid headgroups. The radial height of the rough OMV surface was relatively constant, but the smooth OMV surface was less uniform and the radial height differed much more from one point to another. The glycan polymer chain concentration was significantly enriched in some areas of the smooth OMV surface and significantly depleted in others (see Figure 46 for example). The smooth OMV simulation systems were comparable to the CHIKV [1060-1061] and SV40 viral capsids [538-540,1015-1016] that have some surface area noticeably enriched in biomolecular mass and other areas noticeably depleted.

Scientists have used sophisticated electron microscopy analysis techniques to visualize viral particle surfaces [1039-1043] and it is reasonable to think that comparable visualization methods could be used to visualize the surfaces

of rough and smooth OMV systems. The analyses could be used to determine if smooth OMV system surfaces are more topologically complex than comparative rough OMV system surfaces. Sophisticated multistep electron cryotomography imaging analysis methods were already used by experimental research groups to image the shape of OMVs that were approximately 100 nm wide but the imaging methods were not precise enough for determining how the OMV surface height varied from one point to another [1062]. In other words, it seems that experiments have already been conducted to analyze OMV surfaces but the analysis methods have lacked the requisite resolution one needs to visualize differences in lipid height. There are however, more advanced electron microscopy methods that have been used for imaging viral particle surfaces and these methods could potentially be applied in the future to more precisely assess OMV outer leaflet lipid height. It is important that scientists attempt to mimic the OMV simulation system composition as accurately as possible; there should be phospholipids both within the inner and outer OMV leaflets. It would be beneficial for the experimental groups to use an approximate 1:1 number ratio for the number of LPS and phospholipid molecule in the OMV outer leaflet because they could then make more detailed and numerous comparisons with the work from chapter 5. Experimental publications already describe methods that can be used to vary the OMV chemical composition and methods that can be used to generate OMVs with a high concentration of phospholipid molecules in the (OMV) outer leaflet; for example, see [1000,1063-1065].

Second, it was found that the simulated OMVs bind to both flat, single-component POPC lipid bilayers and also to multicomponent plasma membrane mimetics. The molecular dynamics simulations predict that OMVs can adhere to either membrane surface without any action from membrane proteins or the glycocalyx and this proposition should be relatively simple to assess with experimental apparatus. Experimental groups can synthesize flat lipid membrane mimetics and study how these membranes interact with OMVs. The experimental groups can visualize the interactions of OMVs with different biological membrane mimetics and show that OMVs do indeed bind

different host membrane mimetic surfaces. Sophisticated microscopy methods have already been used to visualize the interactions of viral particles with host membrane surfaces and the experimental techniques are now well established and replicable [1066].

The simulations also predicted that ganglioside molecules have the capacity to enhance OMV adhesion energies when they interact with LPS lipid headgroups. The cohesion forces immobilized the simulated OMVs and enhanced the membrane wrapping processes. It was found that SV40 particles have comparable intermolecular interactions when they bind supported membrane bilayers that contain relatively high concentrations of GM1 lipids (i.e. at least 1 mol %). The SV40 virions interacted with the host membrane ganglioside lipids (GM1) and the virus then became trapped at the wrapping interface, wobbling back and forth with a step size of no more than a few nanometers [1067]. This was surprising because the virions were highly mobile when they were attached to membranes that did not include any ganglioside molecules at all [1067-1068]. Comparable experimental studies could be conducted to analyze the properties of OMVs at the surface of host membrane mimetics that contain ganglioside molecules in one instance and do not contain ganglioside molecules in another. The rates of lateral mobility could be determined and used to understand how tightly the OMVs were bound to the host membrane surface. Low lateral mobility parameters would be indicative of strong adhesion energies and higher lateral mobility parameters would be indicative of weaker adhesion energies. If the predictions from the coarse-grained molecular dynamics simulations are accurate then we should expect that the ganglioside-containing membranes support stronger adhesion energies and by association, that OMVs have low lateral mobility parameters when they interact with the ganglioside-containing membrane surface.

Electron microscopy methods were applied in other pioneering publications to visualize vacant space at the wrapping interface when SV40 and mouse polyoma (mPy) viruses were interacting with GM1 lipid containing plasma

membrane mimetics [1069-1071]. Vacant space was found to be minimal due to the tight interlinking of the SV40 capsid proteins and the GM1 lipid headgroups. One could use similar electron microscopy methods to analyze vacant space between OMVs and host membrane surfaces to validate the prediction that there is tight interlinking of the carbohydrate LPS and ganglioside lipid headgroups. Such simple experimental insights would have a high impact factor and they could help us to determine if OMVs can enter cells by sequestering glycosphingolipids. This has already been shown to be true for other pathogens and pathogenic products [368] and our current textbook understanding of the bacterial infection process would have to be changed if it was shown to be true for OMVs.

Third, it was predicted that plasma membranes wrap smooth OMVs and that this creates membrane invaginations or endocytosis intermediate structures. The simulations suggest that the wrapping interactions are mediated by interactions between OMV LPS lipid headgroups and host cell ganglioside lipids. Membrane curvature has been analyzed in previous experimental studies with microscopy methods in an attempt to understand how SV40 particles interact with and perturb host plasma membrane mimetic surfaces [1069-1071]. The experiments revealed that the SV40 viral particles can deform lipid membrane surfaces and create tight-fitting inward bulging "buds". Subsequent studies revealed that the SV40 particle can further deform host membrane surfaces and produce mesoscopic membrane invaginations that morph into elongated membrane tubules on long timescales [1015]. The deformed membrane domains were considered to be endocytosis intermediates that when coupled with for example, scission machinery, would facilitate endocytosis. Similar experiments can be conducted to determine if smooth OMVs generate comparable curvature when they bind ganglioside lipid containing membranes. The experiments would confirm the hypothesis that OMV and host membrane lipid headgroup interactions induce membrane curvature.

6.3 Validating the Predictions from Chapter 4

The synthetic OMVs can be used to validate the primary conclusion from chapter 4: that O-antigen chain interactions increase the mechanical strength of Gram-negative bacterial membranes. OMVs can be created with smooth LPS lipids in one instance, and with rough LPS lipids in another [1000,1063-1065]. Experimental analysis techniques could be used to quantify the strength and durability of the comparative vesicle systems. Comparable studies were conducted to assess the strength of ordinary phospholipid vesicles relative to grafted lipid composites that included for example, polyelectrolyte complexes or amphiphilic block copolymers. Experiments were performed to assess vesicle stability during blood circulation [1072] and to quantify mechanical stability under pH shock [1073-1074]. Membrane durability was similarly assessed in other experimental works by measuring shelf stability and the tendency, or lack thereof, to resist rupture and fusion processes [1072,1075]. Mechanical strength has even been analyzed by quantifying the loading rates of drugs and the rates of drug uptake for single-component lipid vesicles and comparative grafted lipid vesicle composites [1001-1002]. Scientists can systematically assess if LPS O-antigen chains affect membrane mechanical strength by replicating these experiments with synthetic rough and smooth OMVs.

6.4 Validating the Predictions from Chapter 3

Validating the predicted interactions of the PMB1 peptides with the inner and outer Gram-negative bacterial membrane mimetics is expected to be more challenging because scientists would have to evaluate interactions that occur on smaller spatiotemporal scales. Chapter 3 made predictions for small-scale biomolecular processes that in some instances, affected no more than just a few lipids. Here we will first consider the interactions of the PMB1 peptides with the Gram-negative bacterial inner membrane mimetic and for reference, this membrane contained PE and PG lipids in a 3:1 number ratio. It was found that the simulated PMB1 peptides reduced membrane thickness metrics

when they were interacting with the PE and PG phospholipids but importantly, it was also found that this effect dissipated rapidly with distance from the PMB1 peptides. United-atom and all-atom molecular dynamics simulations already corroborate the conclusion that antimicrobial peptides can thin lipid membranes [328,1076-1077] but this effect is significantly more challenging to prove irrefutably through experimental analyses. Bilayer thinning tends to be highly localized in molecular dynamics simulations and the molecular dynamics simulations are generally conducted on relatively short nanosecond or microsecond timescales. Since conventional analytical techniques generally lack the spatiotemporal resolution that one needs for validating highly localized membrane damage directly, it is preferably to infer thickness change through measures of for example, membrane permeability. Electrochemical techniques (e.g. cyclic voltammetry [1078]) can be applied to analyze membrane thickness and bilayer indentation, both before and after interactions with AMPs. Cyclic voltammetry experiments revealed that polymyxin B peptides affect the shape and stability of supported renal membrane mimetics [728]. Comparable experiments could be conducted to analyze the properties of the Gram-negative bacterial inner membrane mimetics before and after interactions with PMB1 peptides. Noticeable increases in water permeability would be indicative of membrane thinning or bilayer indentation processes.

It was also predicted that cationic AMPs (here PMB1 peptides) would preferentially interact with anionic lipids (here PG phospholipids) and this prediction is already corroborated by previous atomistic and coarse-grained molecular dynamics simulation studies [270,281-283,286]. The simulation studies demonstrated that linear and helical AMPs have the capacity to induce the formation of negatively charged lipid nanodomains when the positively charged AMP residues interact with negatively charged lipid headgroup moieties. Analytical experimental techniques (circular dichroism, infrared spectroscopy, NMR etc.) have been used to corroborate these conclusions and they have shown that positively charged AMPs preferentially interact with negatively charged lipids in bacterial membrane mimetics and that these

processes enhance lipid demixing processes and additionally promote the formation of anionic lipid (e.g. PG and CL) nanodomains [275-276,1079-1081]. Comparable experimental techniques could be applied in future studies to evaluate the interactions of PMB1 peptides with the surface of Gram-negative bacterial inner membrane mimetics. The work would not only validate inferences made in chapter 3 but also substantiate hypotheses for various AMP-induced bilayer breakdown pathways being instigated by initial lipid demixing effects.

Other interesting experimental methods such combinations of neutron and X-ray reflectometry, and X-ray diffraction with Brewster angle microscopy could be used to assess the interactions of PMB1 peptides with the outer membrane models. Comparable techniques were used by Lakey et al. to assess the organization of lipids in supported LPS monolayers when they were subjected to applied surface pressures; starting with low values and ending with higher magnitudes [121]. Area per phosphate and LPS coordination numbers were evaluated as the LPS monolayers transitioned, as a stress response, from a fluid state to an ordered crystalline phase. By using similar procedures to analyze rough (Re) LPS leaflets, both before and during interactions with PMB1 peptides, we could systematically assess the lipid modulating effects of the PMB1 peptides on LPS lipids. Readers should note that PMB1 peptides tend to displace stabilizing cations at the LPS Lipid A phosphate plane domain and this process can induce bilayer rupture processes [130,243,1082]. The destabilizing interactions could make it challenging to test the LPS phase modulating properties of the PMB1 peptides. It might be necessary to use LPS chemotypes whose glucosamine sugars were modified to decrement favourable electrostatic interactions between attached LPS phosphate groups and PMB1 Dab residues [726]. Such a setup would ensure that the PMB1 peptides can interact with LPS membrane lipids for a longer amount of time before there is any appreciable loss of membrane structure. Single-particle trafficking procedures could also be used to assess LPS diffusion constants [1083]. Scientists could use these

methods to determine LPS lipid diffusion constants before and during interactions with PMB1 peptides.

It is important to emphasize here that these suggestions are restricted by a personal lack of expertise with biophysical analysis techniques. Experimental groups are much more knowledgeable of advanced experimental tools and it is hoped that readers will be able to design more appropriate experiments for testing the predictions that were made in this thesis.

References

(1) N. J. Yang, M. J. Hinner, Getting Across the Cell Membrane: An Overview for Small Molecules, Peptides and Proteins. Methods Mol. Biol. 2016, 1266, 29-53
(2) J. L. Robertson, The lipid bilayer membrane and its protein constituents. J. Gen. Physiol. 2018, 150, 1472-1483
(3) G. N. Ling, The Membrane Theory and Other Views for Solute Permeability, Distribution, and Transport in Living Cells. Perspect. Biol. Med. 1965, 9, 87-106
(4) J. Lombard, Once Upon a Time the Cell Membranes: 175 Years of Cell Boundary Research. Biol. Direct 2014, 9, 32
(5) R. Whittam, K. P. Wheeler, Transport across cell membranes. Annu. Rev. Physiol. 1970, 32, 21-60
(6) M. J. Chrispeels, C. Maurel, Aquaporins: The Molecular Basis of Facilitated Water Movement Through Living Plant Cells? Plant Physiol. 1994, 105, 9-13
(7) S. T. Cooper, P. L. McNeil, Membrane Repair: Mechanisms and Pathophysiology. Physiol. Rev. 2015, 95, 1205-1240
(8) Y. Miyatake, T. Yamano, R. Hanayama, Myoferlin-Mediated Lysosomal Exocytosis Regulates Cytotoxicity by Phagocytes. J. Immunol. 2018, 201, 3051-3057
(9) JH Soong, R. Hanayama, Mechanisms of Lysosomal Exocytosis by Immune Cells. Chronic inflammation 2016, 369-378
(10) A. L. Koch, Primeval Cells: Possible Energy-Generating and Cell-Division Mechanisms. J. Mol. Evol. 1985, 21, 270-277
(11) J. Lombard, P. Lopez-Garcia, D. Moreira, The Early Evolution of Lipid Membranes and the Three Domains of Life. Nat. Rev. Microbiol. 2012, 10, 507-515
(12) D. Deamer, The Role of Lipid Membranes in Life's Origin. Life (Basel) 2017, 7, 5
(13) G. A. Coleman, R. D. Pancost, T. A. Williams, Investigating the Origins of Membrane Phospholipid Biosynthesis Genes Using Outgroup-Free Rooting. Genome Biol. Evol. 2019, 11, 883-898
(14) G. van Meer, D. R. Voelker, G. W. Feigenson, Membrane Lipids: Where They Are and How They Behave. Nat. Rev. Mol. Cell. Biol. 2008, 9, 112-124
(15) M. Lynch, G. K. Marinov, Membranes, Energetics, and Evolution Across the Prokaryote-Eukaryote Divide. eLife 2018, 7: e35006
(16) M. Pohlschroder, F. Pfeiffer, S. Schulze, M. F. A. Halim, Archaeal Cell Surface Biogenesis. FEMS Microbiol. Rev. 2018, 42, 694-717
(17) J. K. Lee, R. M. Stroud, Unlocking the Eukaryotic Membrane Protein Structural Proteome. Curr. Opin. Struc. Biol. 2010, 20, 464-470
(18) J. G. Almeida, A. J. Preto, P. I. Koukos, A. M. J. J. Bonvin, I. S. Moreira, Membrane Proteins Structures: A Review on Computational Modelling Tools. Biochim. Biophys. Acta Biomembr. 2017, 1859, 2021-2039
(19) L. A. Vega-Cabrera, L. Pardo-Lopez, Membrane Remodelling and Organization: Elements Common to Prokaryotes and Eukaryotes. IUBMB Life 2017, 69, 55-62

(20) T. J. Beveridge, Structures of Gram-Negative Cell Walls and Their Derived Membrane Vesicles. J. Bacteriol. 1999, 181, 4725-4733
(21) S. I. Miller, N. R. Salama, The Gram-Negative Bacterial Periplasm: Size Matters. PLoS Biol. 2018, 16: e2004935
(22) R. M. Epand, C. Walker, R. F. Epand, N. A. Magarvey, Molecular Mechanisms of Membrane Targeting Antibiotics. Biochim. Biophys. Acta 2016, 1858, 980-987
(23) S. Jain, A. Caforio, A. J. M. Driessen, Biosynthesis of Archaeal Membrane Ether Lipids. Front. Microbiol. 2014, 5:641
(24) Y. Koga, Thermal Adaptation of the Archaeal and Bacterial Lipid Membranes. Archaea 2012, 2012:789652
(25) A. Gambacorta, A. Gliozzi, M. De Rosa, Archaeal Lipids and Their Biotechnological Applications. World J. Microb. Biot. 1995, 11, 115-131
(26) H. Xu, D. Ren, Lysosomal Physiology. Annu. Rev. Physiol. 2015, 77, 57-80
(27) M. Schwake, B. Schroder, P. Saftig, Lysosomal Membrane Proteins and Their Central Role in Physiology. Traffic 2013, 14, 739-748
(28) H. Appelqvist, P. Waster, K. Kagedal, K. Ollinger, The Lysosome: From Waste Bag to Potential Therapeutic Target. J. Mol. Cell Biol. 2013, 5, 214-226
(29) L. C. Schenkel, M. Bakovic, Formation and Regulation of Mitochondrial Membranes. Int. J. Cell Biol. 2014, 2014:709828
(30) JW Taanman, The Mitochondrial Genome: Structure, Transcription, Translation and Replication. Biochim. Biophys. Acta 1999, 1410, 103-123
(31) J. R. Friedman, J. Nunnari, Mitochondrial Form and Function. Nature 2014, 505, 335-343
(32) M. D. Esposti, Bioenergetic Evolution in Proteobacteria and Mitochondria. Genome Biol. Evol. 2014, 6, 3238-3251
(33) S. A. Munoz-Gomez, J. G. Widerman, A. J. Roger, C. H. Slamovtis, The Origin of Mitochondrial Cristae from Alphaproteobacteria. Mol. Biol. Evol. 2017, 34, 943-956
(34) W. Kuhlbrandt, Structure and Function of Mitochondrial Membrane Protein Complexes. BMC Biology 2015, 13:89
(35) S. Cogliati, J. A. Enriquez, L. Scorrano, Mitochondrial Cristae: Where Beauty Meets Functionality. Trends Biochem. Sci. 2016, 41, 261-273
(36) M. W. Gray, Mitochondrial Evolution. Cold Spring Harb. Perspect. Biol. 2012, 4:a011403
(37) E. Rideau, R. Dimova, P. Schwille, F. R. Wurm, K. Landfester, Liposomes and Polymersomes: A Comparative Review Towards Cell Mimicking. Chem. Soc. Rev. 2018, 47, 8572-8610
(38) A. Akbarzadeh, R. Rezaei-Sdabady, S. Davaran, SW Joo, N. Zarghami, Y. Hanifehpour, M. Samiei, M. Kouhi, K. Nejati-Koshki, Liposomes: Classification, Preparation, and Applications. Nanoscale Res. Lett. 2013, 8:102
(39) G. Bozzuto, A. Molinari, Liposomes as Nanomedical Devices. Int. J. Nanomedicine 2015, 10: 975-999
(40) D. Perrais, C. J. Merrifield, Dynamics of Endocytic Vesicle Creation. Dev. Cell 2005, 9, 581-592

(41) LG Wu, E. Hamid, W. Shin, HC Chiang, Exocytosis and Endocytosis: Modes, Functions, and Coupling Mechanisms. Annu. Rev. Physiol. 2014, 76, 301-331
(42) Y. Saheki, P. De Camili, Synaptic Vesicle Endocytosis. Cold Spring Harb. Perspect. Biol. 2012, 4:a0005645
(43) M. J. Kennedy, M. D. Ehlers, Mechanisms and Function of Dendritic Exocytosis. Neuron 2011, 69:856-875
(44) N. Jung, V. Haucke, Clathrin-Mediated Endocytosis at Snyapses. Traffic 2007, 8:1129-1136
(45) O. P. Gross, H. von Gersdorff, Recycling at Synapses. Elife 2016, 5:e17692
(46) C. Schwechheimer, M. J. Kuehn, Outer-Membrane Vesicles From Gram-Negative Bacteria: Biogenesis and Functions. Nat. Rev. Microbiol. 2015, 13, 605-619
(47) A. T. Jan, Outer Membrane Vesicles (OMVs) of Gram-Negative Bacteria: A Perspective Update. Front. Microbiol. 2017, 8:1053
(48) J. D. Cecil, N. Sirisaengtaksin, N. M. O'Brien-Simpson, A. M. Krachler, Outer Membrane Vesicle—Host Cell Interactions. Micorbiol. Spectr. 2019, 7
(49) A. Kulp, M. J. Kuehn, Biological Functions and Biogenesis of Secreted Bacterial Outer Membrane Vesicles. Annu. Rev. Microbiol. 2010, 64, 163-184
(50) J. B. Lynch, R. A. Alegado, Spheres of Hope, Packets of Doom: The Good and Bad of Outer Membrane Vesicles in Interspecies and Ecological Dynamics. J. Bacteriol. 2017, 199: e00012-00017
(51) C. Schwechheimer, M. J. Kuehn, Outer-Membrane Vesicles From Gram-Negative Bacteria: Biogenesis and Functions. Nat. Rev. Microbiol. 2015, 13:605-619
(52) E. J. O'Donoghue, A. M. Krachler, Mechanisms of Outer Membrane Vesicle Entry Into Host Cells. Cell Microbiol. 2016, 18:1508-1517
(53) S. Khalid, S. L. Rouse, Simulation of Subcellular Function. Curr. Opin. Struc. Biol. 2020, 61, 167-172
(54) S. G. M. Ong, M. Chitneni, K. S. Lee, L. C. Ming, K. H. Yuen, Evaluation of Extrusion Technique for Nanosizing Liposomes. Pharmaceutics 2016, 8, E36
(55) A. Wagner, Liposome Technology for Industrial Purposes. J. Drug Deliv. 2011, 2011:591325
(56) T. Harayama, H. Riezman, Understanding the Diversity of Membrane Lipid Composition. Nat. Rev. Mol. Cell Biol. 2018, 19, 281-296
(57) E. M. Storck, C. Ozbalci, U. S. Eggert, Lipid Cell Biology: A Focus on Lipids in Cell Division. Annu. Rev. Biochem. 2018, 87, 839-869
(58) M. Eeman, M. Deleu, From Biological Membranes to Biomimetic Model Membranes. Biotechnol. Agron. Soc. Environ. 2012, 14, 719-736
(59) G. Enkavi, M. Javanainen, W. Kulig, T. Rog, I. Vattulainen, Multiscale Simulations of Biological Membranes: The Challenge to Understand Biological Phenomena in a Living Substance. Chem. Rev. 2019, 9, 5607-5774
(60) C. Frantz, K. M. Stewart, V. M. Weaver, The Extracellular Matrix at a Glance. J. Cell Sci. 2010, 123, 4195-4200
(61) G. M. Lee, B. Johnstone, K. Jacobson, B. Caterson, The Dynamic Structure of the Pericellular Matrix on Living Cells. J. Cell Biol. 1993, 123, 1899-1907
(62) A. Wagner, K. Vorauer-Uhl, Liposome Technology for Industrial Purposes. J. Drug Deliv. 2011, 2011:591325

(63) J. B. de la Sema, G. J. Schutz, C. Eggeling, M. Cebecauer, There Is No Simple Model of the Plasma Membrane Organization. Front. Cell Dev. Biol. 2016, 4:106
(64) L. A. Bagatolli, O. G. Mouritsen, Is the Fluid Mosaic (and the Accompanying Raft Hypothesis) a Suitable Model to Describe Fundamental Features of Biological Membranes? What May be Missing? Front. Plant Sci. 2013, 4, 457
(65) G. L. Nicolson, The Fluid-Mosaic Model of Membrane Structure: Still Relevant to Understanding the Structure, Function and Dynamics of Biological Membranes After More Than 40 years. Biochim. Biophys. Acta 2014, 1838, 1451-1466
(66) F. J. Alenghat, D. E. Golan, Membrane Protein Dynamics and Functional Implications in Mammalian Cells. Curr. Top. Membr. 2013, 89-120
(67) G. L. Nicolson, Cell Membrane Fluid-Mosaic Structure and Cancer Metastasis. Cancer Res. 2015, 75, 1169-1176
(68) M. C. Phillips, B. D. Ladbrooke, D. Chapman, Molecular Interactions in Mixed Lecithin Systems. Biochim. Biophys. Acta 1970, 196, 35-44
(69) E. Oldfield, D. Chapman, Dynamics of Lipids in Membranes: Heterogeneity and the Role of Cholesterol. FEBS Lett. 1972, 23, 285-297
(70) E. J. Shimshick, H. M. McConnell, Lateral Phase Separation in Phospholipid Membranes. Biochemistry 1973, 12, 2351-2360
(71) O. G. Mouritsen, M. Bloom, Mattress Model of Lipid-Protein Interactions in Membranes. Biophys. J. 1984, 46, 141-153
(72) E. Sackman, Physical Basis for Trigger Processes and Membrane Structures. In biological membranes 1984, Chapman D. Ed. Academic press London
(73) K. Simons, E. Ikonen, Functional Rafts in Cell Membranes. Nature 1997, 387, 569-572
(74) I. R. Nabi, P. U. Le, Caveolae/Raft-Dependent Endocytosis. J. Cell. Biol. 2003, 161, 673-677
(75) E. Sezgin, I. Levental, S. Mayor, C. Eggeling. The Mystery of Membrane Organization: Composition, Regulation and Role of Lipid Rafts. Nat. Rev. Mol. Cell. Biol. 2017, 18, 361-374
(76) H. Koldso, M. S. P. Sansom, Organization and Dynamics of Receptor Proteins in a Plasma Membrane. J. Am. Chem. Soc. 2015, 137, 14694-14704
(77) J. R. Silvius, Role of Cholesterol in Lipid Raft Formation: Lessons From Lipid Model Systems. Biochim. Biophys. Acta 2003, 1610, 174-183
(78) S. Munro, Lipid Rafts. Cell 2003, 115, 377-388
(79) L. J. Pike, Lipid rafts Bringing Order to Chaos. J. Lipid Res. 2003, 44, 655-667
(80) J. H. Ipsen, G. Karlstrom, O. G. Mourtisen, H. Wennerstrom, M. J. Zuckermann, Phase Equilibria in the Phosphatidylcholine-Cholesterol System. Biochim. Biophys. Acta 1987, 905, 162-172
(81) P. S. Niemela, S. Ollila, M. T. Hyvonen, M. Karttunen, I. Vattulainen, Assessing the Nature of Lipid Raft Membranes. PLoS Comput. Biol. 2007, 3:e34
(82) D. A. Brown, E. London, Structure and Function of Sphingolipid- and Cholesterol-Rich Membrane Rafts. Journal of biological chemistry. J. Biol. Chem. 2000, 275, 17221-17224

(83) K. Simons, Model Systems, Lipid Rafts, and Cell Membranes. Annu. Rev. Biophys. Biomol. Struct. 2004, 33, 269-295
(84) L. J. Pike, Lipid Rafts: Heterogeneity on the High Seas. Biochem. J. 2004, 378, 281-292
(85) P. Varshney, V. Yadav, N. Saini, Lipid Rafts in Immune Signalling: Current Progress and Future Perspective. Immunology. 2016, 149, 13-24
(86) M. A. Alonso, J. Millan, The Role of Lipid Rafts in Signalling and Membrane Trafficking in T Lymphocytes. J. Cell Sci. 2001, 114, 3957-3965
(87) R. G. Parton, Caveolae: structure, function, and relationship to disease. Annu. Rev. Cell Dev. Biol. 2018, 34, 111-136
(88) D. Lingwood, K. Simons, Lipid Rafts as a Membrane-Organizing Principle. Science 2010, 327, 46-50
(89) P. S. Niemela, M. S. Miettinen, L. Monticelli, H. Hammaren, P. Bjelkmar, T. Murtola, E. Lindahl, I. Vattulainen, Membrane Proteins Diffuse as Dynamic complexes With Lipids. J. Am. Chem. Soc. 2010, 132, 7574-7575
(90) A. Kusumi, T. K. Fujiwara, T. A. Tsunoyama, R. S. Kasai, AA Liu, K. M. Hirosawa, M. Kinoshita, N. Matsumori, N. Komura, H. Ando, K. G. N. Suzuki, Defining Raft Domains in the Plasma Membrane. Traffic. 2020, 21, 106-137
(91) A. K. Shishina, E. A. Kovrigina, A. R. Galiakhmetov, R. Rathore, E. L. Kovrigin, Study of Forster Energy Transfer to Lipid Domain Markers Ascertains Partitioning of Semisynthetic Lapidated N-Ras in Lipid Raft Nanodomains. Biochemistry 2018, 57, 872-881
(92) R. M. Epand, R. F. Epand, Lipid Domains in Bacterial Membranes and the Action of Antimicrobial Agents. Biochim. Biophys. Acta 2009, 1788, 289-294
(93) H. Strahl, J. Errington, Bacterial Membranes: Structure, Domains, and Function. Annu. Rev. Microbiol. 2017, 71, 519-538
(94) I. Barak, K. Muchova, The Role of Lipid Domains in Bacterial Cell Processes. Int. J. Mol. Sci. 2013, 14, 4050-4065
(95) T. J. Silhavy, D. Kahne, S. Walker, The Bacterial Cell Envelope. Cold Spring Harb. Perspect. Biol. 2010, 2, a000414
(96) G. K. Auer, D. B. Weibel, Bacterial Cell Mechanics. Biochemistry 2017, 56, 3710-3724
(97) R. Guerrero, C. Pedros-Alio, I. Esteve, J. Mas, D. Chase, L. Margulis, Predatory Prokaryotes: Predation and Primary Consumption Evolved in Bacteria. Proc. Natl. Acad. Sci. U. S. A. 1986, 83, 2138-2142
(98) G. Reshes, S. Vanounou, I. Fishov, M. Feingold, Cell Shape Dynamics in Escherichia coli. Biophysical J. 2008, 94, 251-264
(99) M. H. Saier, M. Saier, M. V. Bogdanov, Membranous Organelles in Bacteria. J. Mol. Microb. Biotech. 2013, 23, 5-12
(100) C. R. Grant, J. Wan, A. Komeili, Organelle Formation in Bacteria and Archaea. Annu. Rev. Cell Dev. Biol. 2018, 34, 217-238
(101) F. Duong, J. Eichler, A. Price, M. R. Leonard, W. Wickner, Biogenesis of the Gram-Negative Bacterial Envelope. Cell 1997, 91, 567-573
(102) A. Filloux, C. Whitfield, Editorial: The Many Wonders of the Bacterial Cell Surface. FEMS Microbiol. Rev. 2016, 40, 161-163
(103) C. Sohlenkamp, O. Geiger, Bacterial Membrane Lipids: Diversity in Structures and Pathways. FEMS Microbiol. Rev. 2016, 40, 133-159

(104) W. Im, S. Khalid, Molecular Simulations of Gram-Negative Bacterial Membranes Come of Age. Annual review of physical chemistry. Annu. Rev. Phys. Chem. 2020, 12:11
(105) S. Khalid, T. J. Piggot, F. Samsudin, Atomistic and Coarse Grain Simulations of the Cell Envelope of Gram-Negative Bacteria: What Have we Learned? Acc. Chem. Res. 2019, 52, 180-188
(106) R. G. Huber, T. S. Carpenter, N. Dube, D. A. Holdbrook, H. I. Ingolfsson, W. A. Irvine, J. K. Marzinek, F. Samsudin, J. R. Allison, S. Khlaid, P. J. Bond, Multiscale Modelling and Simulation Approaches to Lipid-Protein Interactions. Methods Mol. Biol. 2019, 2003, 1-30
(107) R. D. Turner, S. Mesnage, J. K. Hobbs, S. J. Foster, Molecular Imaging of Glycan Chains Couples Cell-Wall Polysaccharide Architecture to Bacterial Cell Morphology. Nat. Commun. 2018, 9, 1263
(108) R. D. Turner, J. K. Hobbs, S. J. Foster, Atomic Force Microscopy Analysis of Bacterial Cell Wall Peptidoglycan Architecture. Bacterial cell wall homeostasis. Methods Mol. Biol. 1440, 3-9
(109) W. Vollmer, D. Blanot, M. A. De Pedro, Peptidoglycan Structure and Architecture. FEMS Microbiol. Rev. 2008, 32, 149-167
(110) W. Vollmer, JV Holtje, The Architecture of the Murein (Peptidoglycan) in Gram-Negative Bacteria: Vertical Scaffold or Horizontal Layer(s)? J. Bacteriol. 2004, 186, 5978-5987
(111) H. Zhao, V. Patel, J. D. Helmann, T. Dorr, Don't Let Sleeping Dogmas Lie: New Views of Peptidoglycan Synthesis and Regulation. Mol. Microbiol. 2017, 106, 847-860
(112) A. L. Lovering, S. S. Safadi, N. C. J. Strynadka, Structural Perspectives of Peptidoglycan Biosynthesis and Assembly. Annu. Rev. Biochem. 81, 451-478
(113) A. Boags, PC Hsu, F. Samsudin, P. J. Bond, S. Khalid, Progress in Molecular Dynamics Simulations of Gram-Negative Bacterial Cell Envelopes. J. Phys. Chem. Lett. 2017, 8, 2513-2518
(114) S. J. Marrink, V. Corradi, P. C. T. Souza, H. I. Ingolfsson, D. P. Tieleman, M. S. P. Sansom, Computational Modelling of Realistic Cell Membranes. Chem. Rev. 2019, 119, 6184-6226
(115) M. Chavent, A. L. Duncan, P. Rassam, O. Birkholz, J. Helie, T. Reddy, D. Beliaev, B. Hambly, J. Piehler, C. Kleanthous, M. S. P. Sansom, How Nanoscale Protein Interactions Determine the Mesoscale Dynamic Organisation of Bacterial Outer Membrane Proteins. Nat. Commun. 2018, 9, 2846
(116) J. Parkin, M. Chavent, S. Khalid, Molecular Simulations of Gram-Negative Bacterial Membranes: A Vignette of Some Recent Successes. Biophys. J. 2015, 109, 461-468
(117) S. Khalid, N. A. Berglund, D. A. Holdbrook, J. Parkin, The Membranes of Gram-Negative Bacteria: Progress in Molecular Modelling and Simulation. Biochem. Soc. Trans. 2015, 43, 162-167
(118) J. C. Henderson, S. M. Zimmerman, A. A. Crofts, J. M. Boll, L. G. Kuhns, C. M. Herrerra, M. S. Trent, The Power of Asymmetry: Architecture and Assembly of the Gram-Negative Outer Membrane Lipid Bilayer. Annu. Rev. Microbiol. 2016, 70, 255-278
(119) L. A. Clifton, S. A. Holt, A. V. Hughes, E. L. Dalton, W. Arunmanee, F. Heinrich, S. Khalid, D. Jefferies, T. R. Charlton, J. R. Webster, C. J. Kinane, J. H.

Lakey, An Accurate In Vitro Model of the E. coli Envelope. Angew. Chem. Weinheim Bergstr. Ger. 2015, 127, 12120-12123
(120) L. A. Clifton, S. A. Holt, A. V. Hughes, E. L. Dalton, W. Arunmanee, F. Heinrich, S. Khalid, D. Jefferies, T. R. Charlton, J. R. Webster, C. J. Kinane, J. H. Lakey, An Accurate In Vitro Model of the E. coli Envelope. Angew. Chem. Int. Ed. Engl. 2015, 54, 11952-11955
(121) A. P. Le Brun, L. A. Clifton, C. E. Halbert, B. Lin, M. Meron, P. J. Holden, J. H. Lakey, S. A. Holt, Structural Characterization of a Model Gram-Negative Bacterial Surface Using Lipopolysaccharides From Rough Strains of Escherichia Coli. Biomacromolecules 2013, 14, 2014-2022
(122) I. T. Roe, S. M. Selbach, S. K. Schnell, Crystal Structure Influences Migration Along Li and Mg Surfaces. J. Phys. Chem. Lett. 2020, 2891-2895
(123) D. Huo, Z. Cao, J. Li, M. Xie, J. Tao, Y. Xia, Seed-Mediated Growth of Au Nanospheres Into Hexagonal Stars and the Emergence of a Hexagonal Close-Packed Phase. Nano Lett. 2019, 19, 3115-3121
(124) M. Herrmann, E. Schneck, T. Gutsmann, K. Brandenburg, M. Tanaka, Bacterial Lipopolysaccharide Form Physically Cross-Linked, Two-Dimensional Gels in the Presence of Divalent Cations. Soft Matter 2015, 11, 6037-6044
(125) L. A. Clifton, M. W. A. Skoda, E. L. Daulton, A. V. Hughes, A. P. Le Brun, J. H. Lakey, S. A. Holt, Asymmetric Phospholipid: Lipopolysaccharide Bilayers; a Gram-Negative Bacterial Outer Membrane Mimic. J. R. Soc. Interface 2013, 10, 20130810
(126) A. Steimle, I. B. Autenrieth, JS Frick, Structure and Function: Lipid A Modifications in Commercials and Pathogens. Int. J. Med. Microbiol. 2016, 306, 290-301
(127) M. Vaara, M. Nurminen, Outer Membrane Permeability Barrier in Escherichia Coli Mutants That Are Defective in the Late Acyltransferases of Lipid A Biosynthesis. Antimicrob. Agents Chemother. 1999, 43, 1459-1462
(128) E. Schneck, R. G. Oliveira, F. Rehfeldt, B. Deme, K. Brandenburg, U. Seydel, M. Tanaka, Mechanical Properties of Interacting Lipopolysaccharide Membranes From Bacteria Mutants Studied by Specular and Off-Specular Neutron Scattering. Phys. Rev. E 2009, 80, 041929
(129) J. Li, JJ Koh, S. Liu, R. Lakshminarayanan, C. S. Verma, R. W. Beuerman, Membrane Active Antimicrobial Peptides: Translating Mechanistic Insights to Design. Front. Neurosci. 2017, 11,73
(130) M. J. Trimble, P. Mlynarcik, M. Kolar, R. E. W. Hancock, Polymyxin: Alternative Mechanisms of Action and Resistance. Cold Spring Harb. Perspect. Med. 2016, 6, a025288
(131) F. F. Han, Y. H. Gao, C. Luan, Y. G. Xie, Y. F. Liu, Y. Z. Wang, Comparing Bacterial Membrane Interactions and Antimicrobial Activity of Procine Lactoferricin-Derived Peptides. J. Dairy Sci. 96, 3471-4387
(132) P. Durai, Y. Lee, J. Kim, D. Jeon, Y. Kim, Biophysical Studies Reveal Key Interactions Between Papiliocin-Derived papN and Lipopolysaccharide in Gram-Negative Bacteria. J. Microbiol. Biotechnol. 2018, 28, 671-678
(133) W. C. Wimley, Describing the Mechanism of Antimicrobial Peptide Action with the Interfacial Activity Model. ACS Chem. Biol. 2010, 5, 905-917

(134) N. Raheem, S. K. Straus, Mechanisms of Action for Antimicrobial Peptides With Antibacterial and Antibiofilm Functions. Front. Microbiol. 2019, 10, 2866
(135) B. Bechinger, S. U. Gorr, Antimicrobial Peptides: Mechanisms of Action and Resistance. J. Dent. Res. 2017, 96, 254-260
(136) M. Yasir, D. Dutta, M. D. P. Willcox, Comparative Mode of Action of the Antimicrobial Peptide Melimine and Its Derivative Mel4 Agaisnt Pseudomonas Aeuruginosa. Sci. Rep. 2019, 9, 7063
(137) L. A. Clifton, F. Ciesielski, M. V. Skoda, N. Paracini, S. A. Holt, J. H. Lakey, The Effect of Lipopolysaccharide Core Oligosaccharide Size on the Electrostatic Binding of Antimicrobial Proteins to Models of the Gram Negative Bacterial Outer Membrane. Langmuir 2016, 32, 3485-3494
(138) T. G. Baboolal, M. J. Conroy, K. Gill, H. Ridley, V. Visudtiphole, P. A. Bullough, J. H. Lakey, Colicin N Binds to the Periphery of Its Receptor and Translocator, Outer Membrane Protein F. Structure 2008, 371-379
(139) O. Hecht, H. Ridley, J. H. Lakey, G. R. Moore, A Common Interaction for the Entry of Colicin N and Filamentous Phage Into Escherichia Coli. J. Mol. Biol. 2009, 388, 880-893
(140) C. L. Johnson, H. Ridley, R. J. Pengelly, M. Z. Salleh, J. H. Lakey, The Unstructured Domain of Colicin K Kills Escherichia Coli. Mol. Microbiol. 2013, 89, 84-95
(141) C. L. Johnson, H. Ridley, R. Marchetti, A. Silipo, D. C. Griffin, L. Crawford, B. Bonev, A. Molinaro, J. H. Lakey, The Antibacterial Colicin N Binds to the Inner Core of Lipopolysaccharide and Close to Its Translocator Protein. Mol. Microbiol. 2014, 92, 440-452
(142) C. L. Johnson, A. S. Solovyova, O. Hecht, C. Macdonald, H. Waller, J. G. Grossman, G. R. Moore, J. H. Lakey, The Two-State Prehensile Tail of the Antibacterial Toxin Colicin N. Biophys. J. 2017, 113, 1673-1684
(143) Y Huang, A. Soliakov, A. P. Le Brun, C. Macdonald, C. L. Johnson, A. S. Solovyova, H. Waller, G. R. Moore, J. H. Lakey, Helix N-cap Residues Drive the Acid Unfolding That Is Essential in the Action of the Toxin Colicin A. Biochemistry 2019, 58, 4882-4892
(144) N. Paracini, L. A. Clifton, M. W. A. Skoda, J. H. Lakey, Liquid Crystalline Bacterial Outer Membranes Are Critical for Antibiotic Susceptibility. Proc. Natl. Acad. Sci. U. S. A. 2018, 115, E7587-E7594
(145) J. H. Lakey, Recent Advances in Neutron Reflectivity Studies of Biological Membranes. Curr. Opin. Colloid Interface Sci. 2019, 42, 33-40
(146) M. W. A. Skoda, Recent Developments in the Application of X-ray and Neutron Reflectivity to Soft-Matter Systems. Curr. Opin. Colloid Interface Sci. 2019, 42, 41-54
(147) Z. Yu, W. Qin, J. Lin, S. Fang, J. Qiu, Antibacterial Mechanisms of Polymyxin and Bacterial Resistance. Biomed. Res. Int. 2015, 679109
(148) C. C. H. Chen, D. S. Feingold, Mechanism of Polymyxin B Action and Selectivity Toward Biologic Membranes. Biochemistry 1973, 12, 2105-2111
(149) L. Poirel, A. Jayol, P. Nordmann. Polymyxins: Antibacterial Activity, Susceptibility Testing, and Resistance Mechanisms Encoded by Plasmids or Chromosomes. Clin. Microbiol. Rev. 2017, 30, 557-596

(150) T. Velkov, K. D. Roberts, P. E. Thompson, J. Li. Polymyxins: A New Hope in Combating Gram-Negative Superbugs? Future Med. Chem. 2016, 8, 1017-1025
(151) PC Hsu, B. M. H. Bruininks, D. Jefferies, P. Cesar Telles de Souza, J. Lee, D. S. Patel, SJ Marrink, Y. Qi, S. Khalid, W. Im. CHARMM-GUI Martini Maker for Modelling and Simulation of Complex Bacterial Membranes With Lipopolysaccharide. J. Comput. Chem. 2017, 38, 2354-2363
(152) B. J. Alder, T. E. Wainwright. Phase Transition for a Hard Sphere System. J. Chem. Phys. 1957, 27, 1208-1209
(153) A. Rahman, Correlations in the Motion of Atoms in Liquid Argon. Phys. Rev. 1964, 136, A405-A411
(154) J. A. McCammon, B. R. Gelin, M. Karplus. Dynamics of Folded Proteins. Nature 1977, 267, 585-590
(155) Y. Duan, P. A. Kollman, Pathways to a Protein Folding Intermediate Observed in a 1-Microsecond Simulation in Aqueous Solution. Science 1998, 282, 740-744
(156) J. Wu, YL Shen, K. Reinhardt, H. Szu, B. Dong, A Nanotechnology Enhancement to Moore's Law. Applied computational intelligence and soft computing 2012, 2013, 426962
(157) P. van der Ploeg, H. J. C. Berendsen, Molecular Dynamics Simulation of a Bilayer Membrane. J. Chem. Phys. 1982, 76, 3271-3276
(158) A. J. Kox, J. P. J. Michels, F. W. Wiegel, Simulation of a Lipid Monolayer Using Molecular Dynamics. Nature 1980, 287, 317-319
(159) B. Jonsson, O. Edholm, O. Teleman, Molecular Dynamics Simulations of a Sodium Octanoate Micelle in Aqueous Solution. J. Chem. Phys. 1986, 85, 2259-2271
(160) L. H. Scott. Lipid-Cholesterol Interactions. Monte Carlo simulations and theory. Biophys. J. 1991, 59, 445-455
(161) S. W. Chiu, E. Jakobsson, H. L. Scott, Combined Monte Carlo and Molecular Dynamics Simulation of Hydrated Lipid-Cholesterol Lipid Bilayers at Low Cholesterol Concentration. Biophys. J. 2001, 80, 1104-1114
(162) S. Chiu, E. Jakobsson, S. Subramaniam, H. L. Scott. Combined Monte Carlo and Molecular Dynamics Simulation of Fully Hydrated Dioleyl and Palmitoyl-Oleyl Phosphatidylcholine Lipid Bilayers. Biophys. J. 1999, 77, 2462-2469
(163) A. P. Lyubartsev, A. L. Rabinovich. Force Field Development for Lipid Membrane Simulations. Biochim. Biophys. Acta 2016, 1858, 2483-2497
(164) I. Vattulainen, T. Rog. Lipid Simulations: A Perspective on Lipids in Action. Cold Spring Harb. Perspect. Biol. 2011, 3, a004655
(165) T. Mori, N. Miyashita, W. Im, M. Feig, Y. Sugita, Molecular Dynamics Simulations of Biological Membranes and Membrane Proteins Using Enhanced Conformational Sampling Algorithms. Biochim. Biophys. Acta 2016, 1858, 1635-1651
(166) S. A. Hollingsworth, R. O. Dror, molecular Dynamics Simulation for All. Neuron 99, Neuron 2018, 99, 1129-1143
(167) H. Chu, L. Cao, X. Peng, G. Li, Polarizable Force Field Development for Lipids and Their Efficient Applications in Membrane Proteins. WIREs Comput. Mol. Sci. 2017, 7, e1312

(168) E. Egberts, SJ Marrink, H. J. C. Berendsen, Molecular Dynamics Simulation of a Phospholipid Membrane. Eur. Biophys. J. 1994, 22, 423-436
(169) O. Berger, O. Edholm, F. Jahnig. Molecular Dynamics Simulations of a Fluid Bilayer of Dipalmitoylphosphatidylcholine at Full Hydration, Constant Pressure, and Constant Temperature. Biophys. J. 1997, 72, 2002-2013
(170) W. L. Jorgensen, D. S. Maxwell, J. Tirado-Rives, Development and Testing of the OPLS All-Atom Force Field on Conformational Energetics and Properties of Organic Liquids. J. Am. Chem. Soc. 1996, 45, 11225-11236
(171) J. W. Essex, M. M. Hann, W. G. Richards, Molecular Dynamics Simulation of a Hydrated Phospholipid Bilayer. Philos. Trans. R. Soc. London B. Biol. Sci. 1994, 344, 239-260
(172) R. W. Pastor, A. D. MacKerell, Development of the CHARMM Force Field for Lipids. J. Phys. Chem. Lett. 2011, 2, 1526-1532
(173) F. Sajadi, C. N. Rowley. Simulations of Lipid Bilayers Using the CHARMM36 Force Field With the TIP3P-FB and TIP4P-FB Water Models. Peer J. 2018, 6, e5472
(174) H. I. Ingolfsson, C. Arnarez, X. Periole, SJ Marrink. Computational 'Microscopy' of Cellular Membranes. J. Cell. Sci. 2016, 129, 257-268
(175) N. Singh, W. Li, Recent Advances in Coarse-Grained Models for Biomolecules and Their Applications. Int. J. Mol. Sci. 2019, 20, 3774
(176) H. I. Ingolfsson, C. A. Lopez, J. J. Uusitalo, D. H. de Jong, S. M. Gopal, X. Periole, SJ Marrink, The Power of Coarse Graining in Biomolecular Simulations. Wiley Interdiscip. Rev. Comput. Mol. Sci. 2014, 4, 225-248
(177) K. R. Hadley, C. McCabe, Coarse-Grained Molecular Models of Water: A Review. Mol. Simulat. 2012, 28, 671-681
(178) C. Arnarez, J. J. Uusitalo, M. F. Masman, H. I. Ingolfsson, D. H. de Jong, M. N. Melo, X. Periole, A. H. de Vries, SJ. Marrink, Dry Martini, a Coarse-Grained Force Field for Lipid Membrane Simulations With Implicit Solvent. J. Chem. Theory Comput. 2015, 11, 260-275
(179) D Jefferies, S. Khalid. Atomistic and Coarse-Grained Simulations of Membrane Proteins: A Practical Guide. Methods 2020, S1046-2023, 30229
(180) S. Khalid, N. A. Berglund, D. A. Holdbrook, Y. M. Leung, J. Parkin, The Membranes of Gram-Negative Bacteria: Progress in Molecular Modelling and Simulation. Biochem. Soc. Trans. 2015, 43, 162-167
(181) M. R. Machado, A. Zeida, L. Darre, S. Pantano, From Quantum to Subcellular Scales: Multi-Scale Simulation Approaches and the SIRAH Force Field. Interface Focus 2019, 9, 21080085
(182) R. M. Venable, A. Kramer, R. W. Pastor, Molecular Dynamics Simulations of Membrane Permeability. Chem. Rev. 2019, 119, 5954-5997
(183) I. Vattulainen, T. Rog, Lipid Membranes: Theory and Simulations Bridged to Experiments. Biochim. Biophys. Acta 2016, 1858, 2251-2253
(184) S. Moradi, A. Nowroozi, M. Shahlaie, Shedding Light on the Structural Properties of Lipid Bilayers using Molecular Dynamics Simulation: A Review Study. RSC Adv. 2019, 8
(185) M. Takaharu, N. Miyashita, W. Im, M. Feig, Y. Sugita, Molecular Dynamics Simulations of Biological Membranes and Membrane Proteins Using Enhanced Conformational Sampling Algorithms. Biochim. Biophys. Acta 2016, 1858, 1635-1651

(186) E. Lindahl, M. S. P. Sansom, Membrane Proteins: Molecular Dynamics Simulations. Curr. Opin. Struc. Biol. 2008, 18, 425-431
(187) E. Matyus, C. Kandt, D. P. Tieleman, Computer Simulation of Antimicrobial Peptides. Curr. Med. Chem. 2007, 14, 2789-2798
(188) R. Lipkin, T. Lazaridis, Computational Studies of Peptide-Induced Membrane Pore Formation. Phil. Trans. R. Soc. B 372, 20160219
(189) A. D. Mackerell, D. Bashford, M. Bellott, R. L. Dunbrack, J. D. Evanseck, M. J. Field, S. Fischer, J. Gao, H. Guo, S. Ha, D. Joseph-McCarthy, L. Kuchnir, K. Kuczera, F. T. Lau, C. Mattos, S. Michnick, T. Ngo, D. T. Nguyen, B. Prodhom, W. E. Reiher, B. Roux, M. Schlenkrich, J. C. Smith, R. Stote, J. Straub, M. Watanabe, J. Wiorkiewicz-Kuczera, D. Yin, M. Karplus. All-Atom Empirical Potential for Molecular Modelling and Dynamics Studies of Proteins. J. Phys. Chem. B 1998, 102, 3586-3616
(190) A. D. Mackerell, M. Feig, C. L. Brooks, Extending the Treatment of Backbone Energetics in Protein Force Fields: Limitations of Gas-Phase Quantum Mechanics in Reproducing Protein Conformational Distributions in Molecular Dynamics Simulations. J. Comput. Chem. 2004, 25, 1400-1415
(191) C. L. Brooks, J. Chen, W. Im, Balancing Solvation and Intramolecular Interactions: Toward a Consistent Generalized Born Force Field. J. Am. Chem. Soc. 2006, 128, 3728-3736
(192) A. D. Mackerell, N. Banavali, N. Foloppe, Development and Current Status of the CHARMM Force Field for Nucleic Acids. Biopolymers 2001, 56, 257-265
(193) K. Vanommeslaeghe, E. Hatcher, C. Acharya, S. Kundu, S. Zhong, J. Shim, E. Darian, O. Guvench, P. Lopes, I. Vorobyov, A. D. Mackerell, CHARMM General Force Field: A Force Field for Drug-Like Molecules Compatible with the CHARMM All-Atom Additive Biological Force Fields. J. Comput. Chem. 2009, 31, 671-690
(194) S. Patel, C. L. Brooks, CHARMM Fluctuating Charge Force Field for Proteins: I Parameterization and Application to Bulk Organic Liquid Simulations. J. Comput. Chem. 2004, 25, 1-15
(195) S. Patel, A. D. Mackerell, C. L. Brooks, CHARMM Fluctuating Charge Force Field for Proteins: II Protein/Solvent Properties from Molecular Dynamics Simulations Using a Nonadditive Electrostatic Model. J. Comput. Chem. 2004, 25, 1504-1514
(196) G. Lamoureux, B. Roux, Modeling Induced Polarization With Classical Drude Oscillators: Theory and Molecular Dynamics Simulation Algorithm. J. Chem. Phys. 2003, 119, 3025-3039
(197) G. Lamoureux, E. Harder, I. V. Vorobyov, B. Roux, A. D. Mackerell, A Polarizable Model of Water for Molecular Dynamics Simulations of Biomolecules. Chem. Phys. Lett. 2006, 418, 245-249
(198) D. S. Patel, Y. Qi, W. Im, Modeling and Simulation of Bacterial Outer Membranes and Interactions With Membrane Proteins. Curr. Opin. Struct. Biol. 2017, 43, 131-140
(199) A. V. Hughes, D. S. Patel, G. Widmalm, J. B. Klauda, L. A. Clifton, W. Im. Physical Properties of Bacterial Outer Membrane Models: Neutron Reflectometry & Molecular Simulation. Biophys. J. 2019, 116, 1095-1104
(200) N. R. Kern, H. S. Lee, E. L. Wu, S. Park, K. Vanommeslaeghe, A. D. MacKerell, J. B. Klauda, S. Jo, W. Im, Lipid-Linked Oligosaccharides in

Membrane Sample Conformations That Facilitate Binding to Oligosaccharyltransferase. Biophys. J. 2014, 107, 1885-1895
(201) K. A. Matthias, M. B. Strader, H. F. Nawar, Y. S. Gao, J. Lee, D. S. Patel, W. Im, M. C. Bash, Heterogeneity in Non-Epitope Loop Sequence and Outer Membrane Protein Complexes Alters Antibody Binding to the Major Porin Protein PorB in Serogroup B Neisseria Meningitidis. Mol. Microbiol. 2017, 105, 934-953
(202) P. J. Felming, D. S. Patel, E. L. Wu, Y. Qi, M. S. Yeom, M. C. Sousa, K. G. Fleming, W. Im, BamA POTRA Domain Interacts With a Native Lipid Membrane Surface. Biophys. J. 2016, 110, 2698-2709
(203) S. Kim, M. M. Pires, W. Im, Insight Into Elongation Stages of Peptidoglycan Processing in Bacterial Cytoplasmic Membranes. Sci. Rep. 2018, 8, 17704
(204) J. Lee, K. R. Pothula, U. Kleinekathofer, W. Im, Simulation Study of Occk5 Functional Properties in Pseudomonas Aeruginosa Outer Membranes. J. Phys. Chem B 2018, 122, 8185-8192
(205) H. Yao, H. Rui, R. Kumar, K. Eshelman, S. Lovell, K. P. Battaile, W. Im, M. Rivera, Concerted Motions Networking Pores and Distant Ferroxidase Centers Enable Bacterioferritin Function and Iron Traffic. Biochemistry 2015, 54, 1611-1627
(206) B. Roux, T. Allen, S. Berneche, W. Im, Theoretical and Computational Models of Biological Ion Channels. Q. Rev. Biophys. 2004, 37, 15-103
(207) G. Jepkorir, J. C. Rodriguez, H. Rui, W. Im, S. Lovell, K. P. Battaile, A. Y. Alongtaga, E. T. Yukl, P. Moenne-Loccoz, M. Rivera, Structural, NMR Spectroscopic, and Computational Investigation of Hemin Loading in the Hemophore HasAp From Pseudomonas Aeruginosa. J. Am. Chem. Soc. 2010, 132, 9857-9872
(208) Z. Ren, J. Lee, M. M. Moosa, Y. Nian, L. Hu, Z. Xu, J. G. McCoy, A. C. M. Ferreon, W. Im, M. Zhou, Structure of an EIIC Sugar Transporter Trapped in an Inward-Facing Conformation. Proc. Natl. Acad. Sci. U. S. A. 2018, 115, 5962-5967
(209) W. Im, J. Liang, A. Olson, H. X. Zhou, S. Vajda, I. A. Vakser, Challenges in Structural Approaches to Cell Modelling. J. Mol. Biol. 2016, 428, 2943-2964
(210) J. Lee, D. S. Patel, I. Kucharska, L. K. Tamm, W. Im, Refinement of OprH-LPS Interactions by Molecular Simulations. Biophys. J. 2017, 112, 346-355
(211) E. L. Wu, O. Engstrom, S. Jo, D. Stuhlsatz, M. S. Yeom, J. B. Klauda, G. Windmalm, W. Im. Molecular dynamics and NMR Spectroscopy Studies of E. Coli Lipopolysaccharide Structure and Dynamics. Biophys. J. 2013, 105, 1444-1455
(212) B. Pilar, D. S. Patel, O. Engstrom, W. Im, G. Widmalm, Conformational Dynamics of the Lipopolysaccharide from Escherichia coli O91 Revealed by Nuclear Magnetic Resonance Spectroscopy and Molecular Simulations. Biochemistry 2017, 56, 3826-3839
(213) E. L. Wu, P. J. Fleming, M. S. Yeom, G. Widmalm, J. B. Klauda, K. G. Fleming, W. Im, E. Coli Outer Membrane and Interactions with OmpLA. Biophys. J. 2014, 106, 2493-2502
(214) N. Dekker, Outer-Membrane Phospholipase A: Known Structure, Unknown Biological Function. Mol. Microbiol. 2000, 35, 711-717

(215) R. G. Brok, A. P. Boots, N. Dekker, H. M. Verheij, J. Tommassen, Sequence Comparison of Outer Membrane Phospholipoases A: Implications for Structure and for the Catalytic Mechanism. Res. Microbiol. 1998, 149, 703-710
(216) H. J. Snijder, B. W. Dijkstra, Bacterial Phospholipase A: Structure and Function of an Integral Membrane Phospholipase. Biochim. Biophys. Acta 2000, 1488, 91-101
(217) R. L. Kingma, H. J. Snijder, B. W. Dijkstra, N. Dekker, M. R. Egmond, Functional Importance of Calcium Binding Sites in Outer Membrane Phospholipase A. Biochim. Biophys. Acta 2002, 156, 230-237
(218) A. M. Stanley, P. Chuawong, T. L. Hendrickson, K. G. Fleming, Energetics of Outer Membrane Phospholipase A (OMPLA) Dimerization. J. Mol. Biol. 2006, 358, 120-131
(219) T. Kim, K. I. Lee, P. Morris, R. W. Pastor, O. S. Andersen, W. Im, Influence of Hydrophobic Mismatch on Structures and Dynamics of Gramicidin A and Lipid Bilayers. Biophys. J. 2012, 102, 1551-1560
(220) J. A. Killian, Hydrophobic Mismatch Between Proteins and Lipids in Membranes. Biochim. Biophys. Acta 1998, 1376, 401-415
(221) T. Kim, W. Im, Revisiting Hydrophobic Mismatch With Free Energy Simulation Studies of Transmembrane Helix Tilt and Rotation. Biophys. J. 2010, 99, 175-183
(222) H. Rui, R. Kumar, W. Im, Membrane Tension, Lipid Adaptation, Conformational Changes, and Energetics in MscL Gating. Biophys. J. 2011, 101, 1671-679
(223) S. Jo, E. L. Wu, D. Stuhlsatz, J. B. Klauda, A. D. Mackerell, G. Widmalm, W. Im, Lipopolysaccharide Membrane Building and Simulation. Methods Mol. Biol. 2015, 1273, 391-406
(224) S. Jo, T. Kim, V. G. Iyer, W. Im, CHARMM-GUI: A Web-Based Graphical User Interface for CHARMM. J. Comput. Chem. 2008, 29, 1859-1865
(225) J. Lee, X. Cheng, J. M. Swails, M. S. Yeom, P. K. Eastman, J. A. Lemkul, S. Wei, J. Buckner, J. C. Jeong, Y. Qi, S. Jo, V. S. Pande, D. A. Case, C. L. Brooks, A. D. Mackerell, J. B. Klauda, W. Im, CHARMM-GUI Input Generator for NAMD, GROMACS, AMBER, OpenMM, and CHARMM/OpenMM Simulations Using the CHARMM36 Additive Force Field. J. Chem. Theory Comput. 2016, 12, 405-413
(226) S. Jo, X. Cheng, S. M. Islam, L. Huang, H. Rui, A. Zhu, H. S. Lee, Y. Qi, W. Han, K. Vanommeslaeghe, A. D. Mackerell, B. Roux, W. Im, CHARMM-GUI PDB Manipulator for Advanced Modelling and Simulations of Proteins Containing Nonstandard Residues. Adv. Protein Chem. Struct. Biol. 2014, 96, 235-265
(227) S. J. Park, J. Lee, Y. Qi, N. R. Kern, H. S. Lee, S. Jo, I. Joung, K. Joo, J. Lee, W. Im, CHARMM-GUI Glycan Modeler for Modelling and Simulation of Carbohydrates and Glycoconjugates. Glycobiology 2019, 29, 320-331
(228) E. L. Wu, X. Cheng, S. Jo, H. Rui, K. C. Song, E. M. Davila-Contreras, Y. Qi, J. Lee, V. Monje-Galvan, R. M. Venable, J. B. Klauda, W. Im, CHARMM-GUI Membrane Builder Toward Realistic Biological Membrane Simulations. J. Comput. Chem. 2014, 35, 1997-2004
(229) J. Lee, D. S. Patel, J. Stahle, S. J. Park, N. R. Kern, S. Kim, J. Lee, X. Cheng, M. A. Valvano, O. Holst, Y. A. Knirel, Y. Qi, S. Jo, J. B. Klauda, G. Widmalm, W. Im, CHARMM-GUI Membrane Builder for Complex Biological Membrane

Simulations With Glycolipids and Lipoglycans. J. Chem. Theory Comput. 2019, 15, 775-786
(230) S. Jo, J. B. Lim, J. B. Klauda, W. Im, CHARMM-GUI Membrane Builder for Mixed Bilayers and Its Application to Yeast Membranes. Biophys. J. 2009, 97, 50-58
(231) S. Jo, X. Cheng, J. Lee, S. Kim, S. J. Park, D. S. Patel, A. H. Beaven, K. I. Lee, H. Rui, S. Park, H. S. Lee, B. Roux, A. D. Mackerell, J. B. Klauda, Y. Qi, W. Im, CHARMM-GUI 10 years for Biomolecular Modelling and Simulation. J. Comput. Chem. 2017, 38, 1114-1124
(232) Y. Qi, H. I. Ingolfsson, X. Cheng, J. Lee, SJ Marrink, W. Im, CHARMM-GUI Martini Maker for Coarse-Grained Simulations With the Martini Force Field. J. Chem. Theory Comput. 2015, 11, 4486-4494
(233) R. D. Lins, T. P. Straatsma, Computer Simulation of the Rough Lipopolysaccharide Membrane of Pseudomonas Aeruginosa. Biophys. J. 2001, 81, 1037-1046
(234) W. D. Cornell, P. Cieplak, C. I. Bayly, I. R. Gould, K. M. Merz, D. M. Ferguson, D. C. Spellmeyer, T. Fox, J. W. Caldwell, P. A. Kollman, A Second Generation Force Field for the Simulation of Proteins, Nucleic Acids, and Organic Molecules. J. Am. Chem. Soc. 1995, 117, 5179-5197
(235) R. J. Woods, R. A. Dwek, C. J. Edge, B. Fraser-Reid, Molecular Mechanical and Molecular Dynamical Simulations of Glycoproteins and Oligosaccharides. 1. GLYCAM 93 Parameter Development. J. Phys. Chem. 1995, 99, 3832-3846
(236) P. Echenique, J. L. Alonso, A Mathematical and Computational Review of Hartree-Fock SCF Methods in Quantum Chemistry. Molecular physics 2007, 105, 3057-3098
(237) I. Alkorta, J. J. Perez, Approximations in the Computation of Molecular Polarization Maps. Electron. J. Theor. Chem. 1995, 1, 26-37
(238) A. Karton, A Computational Chemist's Guide to Accurate Thermochemistry for Organic Molecules. WIREs Comput. Mol. Sci. 2016, 6, 292-310
(239) W. S. Ohlinger, P. E. Klunzinger, B. J. Deppmeier, W. J. Hehre, Efficient Calculation of Heats of Formation. J. Phys. Chem. A 2009, 113, 2165-2175
(240) E. Schneck, T. Schubert, O. V. Konovalov, B. E. Quinn, T. Gutsmann, K. Brandenburg, R. G. Oliveira, D. A. Pink, M. Tanaka, Quantitative Determination of Ion Distributions in Bacterial Lipopolysaccharide Membranes by Grazing-Incidence X-Ray Fluorescence. Proc. Natl. Acad. Sci. U. S. A. 2010, 107, 9147-9151
(241) R. D. Lins, E. R. Vorpagel, M. Guglielmi, T. P. Straatsma, Computer Simulation of Uranyl Uptake by the Rough Lipopolysaccharide Membrane of Pseudomonas Aeruginosa. Biomacromolecules 2008, 9, 29-35
(242) T. A. Soares, T. P. Straatsma, R. D. Lins, Influence of the B-band O-Antigen Chain in the Structure and Electrostatics of the Lipopolysaccharide Membrane of Psedudomonas Aeruginosa. J. Braz. Chem. Soc. 2008, 19, 312-320
(243) D. E. S. Santos, L. Pol-Fachin, R. D. Lins, T. A. Soares, Polymyxin Binding to the Bacterial Outer Membrane Reveals Cation Displacement and Increasing Membrane Curvature in Susceptible but Not in Resistant Lipopolysaccharide Chemotypes. J. Chem. Inf. Model. 2017, 57, 2182-2193

(244) M. A. Apicella, Lipid A Is More Than Acyl Chains. Infect. Immun. 2014, 82, 2160-2161
(245) A. Anandan, G. L. Evans, K. Condic-Jurkic, M. L. O'Mara, C. M. John, N. J. Phillips, G. A. Jarvis, S. S. Wills, K. A. Stubbs, I. Moraes, C. M. Kahler, A. Vrielink, Structure of a Lipid a Phosphoethanolamine Transferase Suggests How Conformational Changes Govern Substrate Binding. Proc. Natl. Acad. Sci. U. S. A. 2017, 114, 2218-2223
(246) K. N. Kirschner, R. D. Lins, A Maass, T. A. Soares, A Glycam-Based Force Field for Simulations of Lipopolysaccharide Membranes: Parameterization and Validation. J. Chem. Theory Comput. 2012, 8, 4719-4731
(247) V. H. Rusu, V. A. Horta, B. A. Horta, R. D. Lins, R. Baron, MDWiZ: A Platform for the Automated Translation of Molecular Dynamics Simulations. J. Mol. Graph. Model. 2014, 48, 80-86
(248) L. Pol-Fachin, H. Verli, R. D. Lins, Extension and Validation of the GROMOS 53A6(GLYC) Parameter Set for Glycoproteins. J. Comput. Chem. 2014, 35, 2087-2095
(249) V. H. Rusu, R. Baron, R. D. Lins, PITOMBA: Parameter Interface for Oligosaccharide Molecules Based on Atoms. J. Chem. Theory Comput. 2014, 10, 5068-5080
(250) D. E. S. Santos, F. J. S. Pontes, R. D. Lins, K. Coutinho, T. A. Soares, SuAVE: A Tool for Analysing Curvature-Dependent Properties in Chemical Interfaces. J. Chem. Inf. Model 2020, 60, 473-484
(251) A. Nascimento, F. J. Pontes, R. D. Lins, T. A. Soaresm, Hydration, Ionic Valence and Cross-Linking Propensities of Cations Determine the Stability of Lipopolysaccharide (LPS) Membranes. Chem. Commun. (Camb). 2014, 50, 231-233
(252) F. J. Pontes, V. H. Rusu, T. A. Soares, R. D. Lins, The Effect of Temperature, Cations, and Number of Acyl Chains on the Lamellar to Non-Lamellar Transition in Lipid-A Membranes: A Microscopic View. J. Chem. Theory Comput. 2012, 8, 3830-3838
(253) T. Saitoh, Y. Seto, Y. Fujikawa, N. Iijma, Distribution of Three Isoforms of Antimicrobial Peptide, Chrysophin-1, -2, and -3, in the Red Sea Bream, Pagrus (Chrysophrys) major. Anal. Biochem. 2019, 566, 13-15
(254) N. Iijma, N. Tanimoto, Y. Emoto, Y. Morita, K. Uematsu, T. Murakami, T. Naki, Purification and Characterization of Three Isoforms of Chrysophsin, a Novel Antimicrobial Peptide in the Gills of the Red Sea Bream, Chrysophrys Major. Eur. J. Biochem. 2003, 270, 675-686
(255) A Catte, M. R. Wilson, M. Walker, V. S. Oganesyan, Antimicrobial Action of the Cationic Peptide, Chrysophsin-3: A Coarse-Grained Molecular Dynamics Study. Soft Matter 2018, 14, 2796-2807
(256) S. Esteban-Martin, H. J. Risselada, J. Salgado, SJ Marrink, Stabilty of Asymmetric Bilayers Assessed by Molecular Dynamics Simulations. J. Am. Chem. Soc. 2009, 131, 15194-151202
(257) T. V. Tolpekina, W. K. den Otter, W. J. Briels, Nucleation Free Energy of Pore Formation in an Amphiohilic Bilayer Studied by Molecular Dynamics Simulations. J. Chem. Phys. 2004, 121, 12060-12066
(258) D. J. Bicout, E. Kats, Rupture of a Biomembrane Under Dynamic Surface Tension. Phys. Rev. E Stat. Nonlin. Soft Matter Phys. 2012, 85, 031905

(259) F. Franz, C. Aponte-Santamaria, C. Daday, V. Miletic, F. Grater, Stability of Biological Membranes Upon Mechanical Identation. J. Phys. Chem. B 2018, 122, 7073-7079
(260) P. A. Pinzon-Arango, R. Nagarajan, T. A. Camesano, Interactions of Antimicrobial Peptide Chrysophsin-3 With Bacillus Anthracis in Sporulated, Germinated, and Vegetative States. J. Phys. Chem. B 2013, 117, 6364-6372
(261) A. J. Mason, P. Bertani, G. Moulay, A. Marquette, B. Perone, A. F. Drake, A. Kichler, B. Bechinger, Membrane Interaction of Chrysophsin-1, a Histidine-Rich Antimicrobial Peptide From Red Sea Bream. Biochemistry 2007, 46, 15175-15187
(262) K. F. Wang, R. Nagarajan, C. M. Mello, T. A. Camesano, Characterization of Supported Lipid Bilayer Disruption by Chrysophin-3 Using QCM-D. J. Phys. Chem B 2011, 115, 15228-15238
(263) L. D. Lozeau, T. E. Alexander, T. A. Camesano, Proposed Mechanisms of Tethered Antimicrobial Peptide Chrysophsin-1 as a Function of Tether Length Using QCM-D. J. Phys. Chem. B 2015, 119, 13142-13151
(264) K. F. Wang, R. Nagarajan, T. A. Camesano, Differentiating Antimicrobial Peptides Interacting With Lipid Bilayer: Molecular Signatures Derived From Quartz Crystal Microbalance With Dissipation Monitoring. Biophys. Chem. 2015, 196, 53-67
(265) H. Syed, M. Tauseef, Z. Ahmad, A Connection Between Antimicrobial Properties of Venom Peptides and Microbial ATP Synthase. Int. J. Biol. Macromol. 2018, 119, 23-31
(266) S. A. Kozlov, A. A. Vassilevski, A. V. Feofanov, A. Y. Surovoy, D. V. Karpunin, E. V. Grishin, Latarcins, Antimicrobial and Cytolytic Peptides From the Venom of the Spider Lachesana Tarabaevi (Zodariidae) That Exemplify Biomolecular Diversity. J. Biol. Chem. 2006, 28, 20983-20992
(267) H. A. Rothan, H. Bahrani, N. A. Rahman, R. Yusof, Identification of Natural Antimicrobial Agents to Treat Dengue Infection: In Vitro Analysis of Latarcin Peptide Activity Against Dengue Virus. BMC Microbiol. 2014, 14, 140
(268) Y. M. Shlyapnikov, Y. A. Andreev, S. A. Kozlov, A. A. Vassilevski, E. V. Grishin, Bacterial Production of Latarcin 2a, a Potent Antimicrobial Peptide From Spider Venom. Protein Expr. Purif. 2008, 60, 89-95
(269) H. A. Rothan, H. Bahrani, E. M. Shankar, N. A. Rahman, R. Yusof, Inhibitory Effects of a Peptide-Fusion Protein (Latarcin-PAP1-Thanatin) Against Chikungunya Virus. Antiviral Res. 2014, 108, 173-180
(270) A. A. Polyansky, R. Ramaswamy, P. E. Volynsky, I. F. Sbalzarini, SJ. Marrink, R. G. Efremov, Antimicrobial Peptides Induce Growth of Phosphatidylglycerol Domains in a Model Bacterial Membrane. J. Phys. Chem. Lett. 2010, 1, 3108-3111
(271) P. V. Dubovskii, A. A. Ignatova, P. E. Volynsky, I. A. Ivanov, M. N. Zhmak, A. V. Feofanov, R. G. Efremov, Improving Therapeutic Potential of Antibacterial Spider Venom Peptides: Coarse-Grained Molecular Dynamics Guided Approach. Future Med. Chem. 2018, 10, 2309-2322
(272) R. F. Epand, J. E. Pollard, J. O. Wright, P. B. Savage, R. M. Epand, Depolarization, Bacterial Membrane Composition, and the Antimicrobial Action of Ceragenins. Antimicrob. Agents Chemther. 2010, 54, 3708-3713

(273) R. D. Barker, L. E. McKinley, S. Titmuss, Neutron Reflectivity as a Tool for Physics-Based Studies of Model Bacterial Membranes. Adv. Exp. Med. Biol. 2016, 915, 261-282
(274) L. Davydova, S. Bakholdina, M. Barkina, P. Velansky, M. Bogdanov, N. Sanina, Effects of Elevated Growth Temperature and Heat Shock on the Lipid Composition of the Inner and Outer Membranes of Yersinia Pseudotuberculosis. Biochimie. 2016, 123, 103-109
(275) A. Won, A. Ruscito, A. Lanoul, Imaging the Membrane Lytic Activity of Bioactive Peptide Latarcin 2a. Biochim. Biophys. Acta 2012, 1818, 3072-3080
(276) A. S. Kuznetsov, P. V. Dubovskii, O. V. Vorontsova, A. V. Feofanov, R. G. Efremov, Interaction of Linear Cationic Peptides With Phospholipid Membranes and Polymers of Sialic Acid. Biochemistry (Mosc) 2014, 79, 459-468
(277) D. P. Budagavi, A. Chugh, Antibacterial Properties of Latarcin 1 Derived Cell-Penetrating Peptides. Eur. J. Pharm. Sci. 2018, 115, 43-49
(278) G. Idiong, A. Won, A. Ruscito, B. O. Leung, A. P. Hitchcock, A. Ianoul, Investigating the Effect of a Single Glycine to Alanine Substitution on Interactions of Antimicrobial Peptide Latarcin 2a With a Lipid Membrane. Eur. Biophys. J. 2011, 40, 1087-1100
(279) O. V. Vorontsova, N. S. Egorova, A. S. Arseniev, A. V. Feofanov, Haemolytic and Cytotoxic Action of Latarcin Ltc2a. Biochimie 2011, 93, 227-241
(280) P. V. Dubovskii, P. E. Volynsky, A. A. Polyansky, D. V. Karpunin, D. V. Karpunin, V. V. Chupin, R. G. Efremov, A. S. Arseniev, Three-Dimensional Structure/Hydrophobicity of Latarcins Specifies Their Mode of Membrane Activity. Biochemistry 2008, 47, 3525-3533
(281) D. Lin, A. Grossfield, Thermodynamics of Antimicrobial Lipopeptide Binding to Membranes: Origins of Affinity and Selectivity. Biophys. J. 2014, 107, 1862-1872
(282) J. N. Horn, J. D. Sengillo, D. Lin, T. D. Romo, A. Grossfield, Characterization of a Potent Antimicrobial Lipopeptide via Coarse-Grained Molecular Dynamics. Biochim. Biophys. Acta 2012, 1818, 212-218
(283) J. N. Horn, T. D. Romo, A. Grossfield, Simulating the Mechanism of Antimicrobial Lipopeptides With All-Atom Molecular Dynamics. Biochemistry 2013, 52, 5604-5610
(284) L. H. Eckhard, A. Sol, E. Abtew, Y. Shai, A. J. Domb, G. Bachrach, N. Beyth, Biohybrid Polymer-Antimicrobial Peptide Medium Against Enterococcus Faecalis. PLoS One 2014, 9, e109413
(285) G. N. Serrano, G. G. Zhanel, F. Schweizer, Antibacterial Activity of Ultrashort Cationic Lipo-Beta-Peptides. Antimicrob. Agents Chemother. 2009, 53, 2215-2217
(286) D. Poger, S. Poyry, A. E. Mark, Could Cardiolipin Protect Membranes Against the Action of Certin Antimicrobial Peptides? Aurein 1.2, a Case Study. ACS Omega 2018, 3, 16453-16464
(287) T. Zhang, J. K. Muraih, N. Tishbi, J. Herskowitz, R. L. Victor, J. Silverman, A. Uwumarenogie, S. D. Taylor, M. Palmer, E. Mintzer, Cardiolipin Prevents Membrane Translocation and Permeabilization by Daptomycin. J. Biol. Chem. 2014, 289, 11584-11591

(288) Y. F. Chen, T. L. Sun, Y. Sun, H. W. Huang, Interaction of Daptomycin With Lipid Bilayers: A Lipid Extracting Effect. Biochemistry 2014, 53, 5384-5392
(289) D. Beriashvili, R. Taylor, B. Kralt, N. Abu Mazen, S. D. Taylor, M. Palmer, Mechanistic Studies on the Effect of Membrane Lipid Acyl Chain Composition on Daptomycin Pore Formation. Chem. Phys. Lipids 2018, 216, 73-79
(290) M. Davlieva, W. Zhang, C. A. Arias, Y. Shamoo, Biochemical Characterization of Cardiolipin Synthase Mutations Associated With Daptomycin Resistance in Enterococci. Antimicrob. Agents Chemother. 2013, 57, 289-296
(291) K. M. Hines, A. Waalkes, K. Penewit, E. A. Holmes, S. J. Salipante, B. J. Werth, L. Xu, Characterization of the Mechanisms of Daptomycin Resistance Among Gram-Positive Bacterial Pathogens by Multidimensional Lipidomis. mSphere 2017, 2, e00492-00417
(292) Z. Sajjadiyan, N. Cheraghi, S. Mohammadinejad, L. Hassani, Interaction of Aurein 1.2 and Its Analogue With DPPC Lipid Bilayer. J. Biol. Phys. 2017, 43, 127-137
(293) G. E. Balatti, M. F. Martini, M. Pickholz, A Coarse-Grained Approach to Studying the Interactions of the Antimicrobial Peptides Aurein 1.2 and Maculatin 1.1 With POPG/POPE Lipid Mixtures. J. Mol. Model. 2018, 24, 208
(294) D. K. Rai, S. Qian, Interaction of the Antimicrobial Peptide Aurein 1.2 and Charged Lipid Bilayer. Sci. Rep. 2017, 7, 3719
(295) M. Shahmiri, M. Enciso, A. Mechler, Controls and Constrains of the Membrane Disrupting Action of Aurein 1.2. Sci. Rep. 2015, 5, 16378
(296) E. N. Lorenzon, K. A. Riske, G. F. Troiano, G. C. Da Hora, T. A. Soares, E. M. Cilli, Effect of Dimerization on the Mechanism of Action of Aurein 1.2. Biochim. Biophys. Acta 2016, 1858, 1129-1138
(297) C. T. Jafvert, P. P. Kulkarni, Buckminsterfullerene's (C60) Octanol-Water Partition Coefficient (Kow) and Aqueous Solubility. Environ. Sci. Technol. 2008, 42, 5945-5950
(298) Y. P. Galvan, I. Alperovich, P. Zolotukhin, E. Prazdnova, M. Mazanko, A. Belanova, V. Chistyakov, Fullerenes as Anti-Aging Antioxidants. Curr. Aging Sci. 2017, 10, 56-67
(299) H. Kazemzadeh, M. Mozafari, Fullerene-Based Delivery Systems. Drug Discov. Today 2019, 24, 898-905
(300) PC. Hsu, Focussing the Computational Microscope on the E. Coli Cell Envelope: Model Development and Simulation Studies. 2017, University of Southampton, Doctoral Thesis
(301) PC. Hsu, D. Jefferies, S. Khalid, Molecular Dynamics Simulations Predict the Pathways via Which Pristine Fullerenes Penetrate Bacterial Membranes. J. Phys. Chem. B 2016, 120, 11179
(302) C. M. Rosetti, G. G. Montich, C. Pastorino, Molecular Insight Into the Line Tension of Bilayer Membranes Containing Hybrid Polyunsaturated Lipids. J. Phys. Chem. B 2017, 121, 1587-1600
(303) Z. Li, A. A. Gorfe, Modulation of a Small Two-Domain Lipid Vesicle by Linactants. J. Phys. Chem. B 2014, 118, 9028-9036

(304) F. Schmid, Physical Mechanisms of Micro- and Nanodomain Formation in Multicomponent Lipid Membranes. Biochim. Biophys. Acta Biomembr. 2017, 1859, 509-528
(305) J. Gumbart, Y. Wang, A. Aksimentiev, E. Tajkhorshid, K. Schulten, Molecular Dynamics Simulations of Proteins in Lipid Bilayers. Curr. Opin. Struct. Biol. 2005, 15, 423-431
(306) F. Khalili-Araghi, J. Gumbart, P. C. Wen, M. Sotomayor, E. Tajkhorshid, K. Schulten, Molecular Dynamics Simulations of Membrane Channels and Transporters. Curr. Opin, Struct. Biol. 2009, 19, 128-137
(307) N. Noinaj, J. C. Gumbart, S. K. Buchanan, The β-Barrel Assembly Machinery in Motion. Nat. Rev. Microbiol. 2017, 15, 197-204
(308) A. Pavlova, H. Hwang, K. Lundquist, C. Balusek, J. C. Gumbart, Living on the Edge: Simulations of Bacterial Outer-Membrane Proteins. Biochim. Biophys. Acta 2016, 1858, 1753-1759
(309) J. C. Gumbart, M. Beeby, G. J. Jensen, B. Roux, Escherichia Coli Peptidoglycan Structure and Mechanics as Predicted by Atomic-Scale Simulations. PLoS Comput. Biol. 2014, 10, e1003475
(310) L. T. Nguyen, J. C. Gumbart, G. J. Jensen, Coarse-Grained Molecular Dynamics Simulations of the Bacterial Cell Wall. Methods Mol. Biol. 2016, 1440, 247-270
(311) L. T. Nguyen, J. C. Gumbart, M. Beeby, G. J. Jensen, Coarse-Grained Simulations of Bacterial Cell Wall Growth Reveal That Local Coordination Alone Can Be Sufficient to Maintain Rod Shape. Proc. Natl. Acad. Sci. U. S. A. 2015, 112, E3689-E3698
(312) H. Hwang, N. Paracini, J. M. Parks, J. H. Lakey, J. C. Gumbart, Distribution of Mechanical Stress in the Escherichia Coli Cell Envelope. Biochim. Biophys. Acta Biomembr. 2018, 1860, 2566-2575
(313) R. M. Venable, F. L. H. Brown, R. W. Pastor, Mechanical Properties of Lipid Bilayers From Molecular Dynamics Simulation. Chem. Phys. Lipids 2015, 192, 60-74
(314) N. K. Khadka, P. Teng, J. Cai, J. Pan, Modulation of Lipid Membrane Structural and Mechanical Properties by a Peptidomimetic Derived From Reduced Amide Scaffold. Biochim. Biophys. Acta Biomembr. 2017, 1859, 734-744
(315) J. Shearer, D. Jefferies, S. Khalid, Outer Membrane Proteins OmpA, FhuA, OmpF, EstA, BtuB, and OmpX Have Unique Lipopolysaccharide Fingerprints. J. Chem. Theory Comput. 2019, 15, 2608-2619
(316) F. Samsudin, M. L. Ortiz-Suarez, T. J. Piggot, P. J. Bond, S. Khalid, OmpA: A Flexible Clamp for Bacterial Cell Wall Attachment. Structure 2016, 24, 2227-2235
(317) F. Samsudin, S. Khalid, Movement of Arginine Through OprD: The Energetics of Permeation and the Role of Lipopolysaccharide in Directing Arginine to the Protein. J. Phys. Chem. B 2019, 123, 2824-2832
(318) D. A. Holdbrook, R. G. Huber, T. J. Piggot, P. J. Bond, S. Khalid, Dynamics of Crowded Vesicles: Local and Global Responses to Membrane Composition. PLoS One 2016, 11, e0156963
(319) J. Parkin, S. Khalid, Atomstic Molecular-Dynamics Simulations Enable Prediction of the Arginine Permeation Pathway Through OccD1/OprD From Pseudomonas Aeruginosa. Biophys. J. 2014, 107, 1853-1861

(320) F. Samsudin, A. Boags, T. J. Piggot, S. Khalid, Braun's Lipoprotein Facilitates OmpA Interaction With the Escherichia Coli Cell Wall. Biophys. J. 2017, 113, 1496-1504
(321) A. T. Boags, F. Samsudin, S. Khalid, Binding From Both Sides: TolR and Full-Length OmpA Bind and Maintain the Local Structure of the E. Coli Cell Wall. Structure 2019, 27, 713-742
(322) P. J. Bond, S. Khalid, Antimicrobial and Cell-Penetrating Peptides: Structure, Assembly and Mechanisms of Membrane Lysis via Atomistic and Coarse-Grained Molecular Dynamics Simulations. Protein Pept. Lett. 2010, 17, 1313-1327
(323) H. Venter, R. Mowla, T. Ohene-Agyei, S. Ma, RND-Type Drug Efflux Pumps From Gram-Negative Bacteria: Molecular Mechanism and Inhibition. Front. Microbiol. 2015, 6, 1-11
(324) A. Yamaguchi, R. Nakashima, K. Sakurai, Structural Basis of RND-Type Multidrug Exporters. Front. Microbiol. 2015, 6, 1-19
(325) PC. Hsu, F. Samsudin, J. Shearer, S. Khalid, It Is Complicated: Curvature, Diffusion, and Lipid Sorting Within the Two Membranes of Escherichia Coli. J. Phys. Chem. Lett. 2017, 8, 5513-5518
(326) G. Calamita, W. R. Bishai, G. M. Preston, W. B. Guggino, P. Agre, Molecular Cloning and Characterization of AqpZ, a Water Channel From Escherichia Coli. J. Biol. Chem. 1995, 270, 29063-29066
(327) V. Schmidt, M. Sidore, C. Bechara, J. P. Duneau, J. N. Sturgis, The Lipid Environment of Escherichia Coli Aquaporin Z. Biochim. Biophys. Acta Biomembr. 2019, 1861, 431-440
(328) N. A. Berglund, T. J. Piggot, D. Jefferies, R. B. Sessions, P. J. Bond, S. Khalid, Interaction of the Antimicrobial Peptide Polymyxin B1 With Both Membranes of E. Coli: A Molecular Dynamics Study. PLoS Comput. Biol. 2015, 11, e1004180
(329) D Jefferies, PC. Hsu, S. Khalid, Through the Lipopolysaccharide Glass: A Potent Antimicrobial Peptide Induces Phase Changes in Membranes. Biochemistry 2017, 56, 1672-1679
(330) K. Koshiyama, T. Kodama, T. Yano, S. Fujikawa, Structural Change in Lipid Bilayers and Water Penetration Induced by Shock Waves: Molecular Dynamics Simulations. Biophys. J. 2006, 91, 2198-2205
(331) L. Thogersen, B. Schiott, T. Vosegaard, N. C. Nielsen, E. Tajkhorshid, Peptide Aggregation and Pore Formation in a Lipid Bilayer: A Combined Coarse-Grained and All Atom Molecular Dynamics Study. Biophys. J. 2008, 95, 4337-4347
(332) F. G. Dupuy, I. Pagano, K. Andenoro, M. F. Peralta, Y. Elhady, F. Heinrich, S. Tristam-Nagle, Selective Interaction of Colistin With Lipid Model Membranes. Biophys. J. 2018, 114, 919-928
(333) B. Palmieri, M. Grant, S. A. Safran, Prediction of the Dependence of the Line Tension on the Composition of Linactants and the Temperature in Phase Separated Membranes. Langmuir 2014, 30, 11734-11745
(334) S. M. Malone, S. Trabelsi, S. Zhang, T. R. Lee, D. K. Schwartz, Self-Assembly of Linactants: Micelles and Lyotropic Liquid Crystals in Two Dimensions. J. Phys. Chem. B 2010, 114, 8616-8620
(335) H. J. Risselada, SJ. Marrink, The Molecular Face of Lipid Rafts in Model Membranes. Proc. Natl. Acad. Sci. U. S. A. 2008, 105, 17367-17372

(336) S. Mishra, P. G. Joshi, Lipid Raft Heterogeneity: An Enigma, J. Neurochem. 2007, 103, 135-142
(337) J. A. Allen, R. A. Halverson-Tamboli, M. M. Rasenick, Lipid Raft Microdomains and Neurotransmitter Signalling. Nat. Rev. Neurosci. 2007, 8, 128-140
(338) J. R. Silvius, Role of Cholesterol in Lipid Raft Formation: Lessons From Lipid Model Systems. Biochim. Biophys. Acta 2003, 1610, 174-1783
(339) J. M. Lopez Marti, N. J. English, M. G. Del Popolo, Elucidating Mysteries of Phase-Segregated Membranes: Mobile-Lipid Recruitment Facilitates Pores' Passage to the Fluid Phase. Phys. Chem. Chem. Phys. 2018, 20, 19234-19239
(340) S. A. Pandit, E. Jakobsson, H. L. Scott, Simulation of the Early Stages of Nano-Domain Formation in Mixed Bilayers, of Sphingomyelin, Cholesterol, and Dioleylphosphatidylcholine. Biophys. J. 2004, 87, 3312-3322
(341) C. Arnarez, A. Webb, E. Rouviere, E. Lyman, Hysteries and the Cholesterol Dependent Phase Transition in Binary Lipid Mixtures With the Martini Model. J. Phys. Chem. B 2016, 120, 13086-13093
(342) Y. Wang, P. Gkeka, J. E. Fuchs, K. R. Liedle, Z. Cournia, DPPC-Cholesterol Phase Diagram Using Coarse-Grained Molecular Dynamics Simulations. Biochim. Biophys. Acta Biomembr. 2016, 1858, 2846-2857
(343) T. S. Carpenter, C. A. Lopez, C. Neale, C. Montour, H. I. Ingolfsson, F. Natale, F. C. Lightstone, S. Gnanakaran, Capturing Phase Behaviour of Ternary Lipid Mixtures With a Refined Martini Coarse-Grained Force Field. J. Chem. Theory Comput. 2018, 14, 6050-6062
(344) T. S. Carpenter, C. A. Lopez, C. Neale, C. Montour, H. I. Ingolfsson, D. Di Natale, F. C. Lightstone, S. Gnanakaran, Capturing Phase Behaviour of Ternary Lipid Mixtures With a Refined Martini Coarse-Grained Force Field. J. Chem. Theory Comput. 2018, 14, 6050-6062
(345) P. Uppamoochikkal S. Tristram-Nagle, J. F. Nagle, Orientation of Tie-lines in the Phase Diagram of DOPC/DPPC/Cholesterol Model Biomembranes. Langmuir 2010, 26, 17363-17368
(346) E. Bieberich, Sphingolipids and Lipid Rafts: Novel Concepts and Methods of Analysis. Chem. Phys. Lipids 2018, 216, 114-131
(347) E. Klotzsch, G. J. Schutz, A Critical Survey of Methods to Detect Plasma Membrane Rafts. Philos. Trans. R Soc. Lond. B Biol. Sci. 2012, 368, 20120033
(348) L. J. Pike, The Challenge of Lipid Rafts. J. Lipid Res. 2009, 50, S323-S328
(349) R. S. Davis, P. B. S. Kumar, M. M. Sperotto, M. Laradji, Predictions of Phase Separation in Three-Component Lipid Membranes by the Martini Force Field. J. Phys. Chem. B 2013, 117, 4072-4080
(350) C. Rosetti, C. Pastorino, Comparison of Ternary Bilayer Mixtures With Asymmetric or Symmetric Unsaturated Phosphatidylcholine Lipids by Coarse Grained Molecular Dynamics Simulations. J. Phys. Chem. B 2012, 116, 3525-3537
(351) J. Domanski, SJ. Marrink, L. V. Schafer, Transmembrane Helices Can Induce Domain Formation in Crowded Model Membranes. Biochim. Biophys. Acta Biomembr. 2012, 1818, 984-994

(352) X. Lin, J. H. Lorent, A. D. Skinkle, K. R. Levental, M. N. Waxham, A. A. Gorfe, I. Levental, Domain Stability in Biomimetic Membranes Driven by Lipid Polyunsaturation. J. Phys. Chem. B 2016, 120, 11930-11941
(353) D. Hakobyan, A. Heuer, Key Molecular Requirements for Raft Formation in Lipid/Cholesterol Membranes. PLoS One 2014, 9, e87369
(354) P. W. Fowler, J. J. Williamson, M. S. Sansom, P. D. Olmsted, Roles of Interleaflet Coupling and Hydrophobic Mismatch in Lipid Membranes Phase-Separation Kinetics. J. Am. Chem. Soc. 2016, 138, 11633-11642
(355) J. Barnoud, G. Rossi, SJ. Marrink, L. Monticelli, Hydrophobic Compounds Reshape Membrane Domains. PLoS Comp. Biol. 2014, 10, e1003873
(356) R. Reigada, Alteration of Interleaflet Coupling Due to Compounds Displaying Rapid Translocation in Lipid Membranes. Sci. Rep. 2016, 6, 32934
(357) D. G. Ackerman, G. W. Feigenson, Effects of Transmembrane α-Helix Length and Concentration on Phase Behaviour in Four-Component Lipid Mixtures: A Molecular Dynamics Study. J. Phys. Chem. B 2016, 120, 4064-4077
(358) L. V. Schafer, D. H. de Jong, A. Holt, A. J. Rzepiela, A. H. de Vries, B. Poolman, J. A. Kilian, SJ. Marrink, Lipid Packing Drives the Segregation of Transmembrane Helices Into Disordered Lipid Domains in Model Membranes. Proc. Natl. Acad. Sci. U. S. A. 2011, 108, 1343-1348
(359) S. Thallmair, H. I. Ingolfsson, SJ. Marrink, Cholesterol Flip-Flop Impacts Domain Registration in Plasma Membrane Models. J. Phys. Chem. Lett. 2018, 9, 5527-5533
(360) RX. Gu, S. Baoukina, D. P. Tieleman, Cholesterol Flip-Flop in Heterogeneous Membranes. J. Chem. Theory Comput. 2019, 15, 2064-2070
(361) Y. Liu, J. Barnoud, SJ. Marrink, Gangliosides Destabilize Lipid Phase Separation in Multicomponent Membranes. Biophys. J. 2019, 117, 1215-1223
(362) D. S. Patel, S. Park, E. L. Wu, M. S. Yeom, G. Widmalm, J. B. Klauda, W. Im, Influence of Ganglioside GM1 Concentration on Lipid Clustering and Membrane Properties and Curvature. Biophys. J. 2016, 111, 1987-1999
(363) H. Koldso, D. Shorthouse, J. Helie, M. S. P. Sansom, Lipid Clustering Correlates With Membrane Curvature as Revealed by Molecular Dynamics Simulations of Complex Lipid Bilayers. PLoS Comput. Biol. 2014, 10, e1003911
(364) S. Baoukina, H. I. Ingolfsson, SJ. Marrink, D. P. Tieleman, Curvature-Induced Sorting of Lipids in Plasma Membrane Tethers. Adv. Theory Simul. 2018, 1, 1800034
(365) P. Marina, B. Joseph, A. Ferraretto, D. Ravasi, P. Palestini, M. Masserini, Use of a Photoactivable GM1 Ganglioside Analogue to Assess Lipid Distribution in Caveolae Bilayer. Glycoconjugate 2000, 17, 215-222
(366) T. E. Hutchinson, H. Hu, J. M. Patel, Cell Penetrating Peptide-Mediated Caveolae-Dependent Activation of Lung Endothelial Nitric Oxide Synthase. Protein Pept. Lett. 2016, 23, 169-175
(367) S. Sonnino, A. Prinetti, Sphingolipids and Membrane Environments for Caveolin. FEBS Letters 2009, 583, 597-606

(368) T. Sych, Y. Mely, W. Romer, Lipid Self-Assembly and Lectin-Induced Reorganization of the Plasma Membrane. Philos. Trans. R. Soc. B 2018, 373, 20170117
(369) M. Chavent, A. L. Duncan, M. S. P. Sansom, Molecular Dynamics Simulations of Membrane Proteins and Their Interactions: From Nanoscale to Mesoscale. Curr. Opin. Struct. Biol 2016, 40, 8-16
(370) M. P. Muller, T. Jiang, C. Sun, M. Lihan, S. Pant, P. Mahinthichaichan, A. Trifan, E. Tajkhorshid, Characterization of Lipid-Protein Interactions and Lipid-Mediated Modulation of Membrane Protein Function Through Molecular Simulation. Chem. Rev. 2019, 119, 6086-6161
(371) V. Corradi, B. I. Sejdiu, H. Mesa-Galloso, H. Abdizadeh, S. Y. Noskov, SJ. Marrink, D. P. Tieleman, Emerging Diversity in Lipid-Protein Interactions. Chem. Rev. 2019, 119, 5775-5848
(372) K. Pluhackova, R. A. Bockmann, Biomembranes in Atomistic and Coarse-Grained Simulations. J. Phys. Condens. Matter 2015, 27, 323103
(373) T. A. Wassenaar, K. Pluhackova, R. A. Bockmann, SJ. Marrink, D. P. Tieleman, Going Backward: A Flexible Geometric Approach to Reverse Transformation From Coarse Grained to Atomistic Models. J. Chem. Theory Comput. 2014, 10, 676-690
(374) C. Arnarez, JP, Mazat, J. Elezgaray, SJ. Marrink, X. Periole, Evidence for Cardiolipin Binding Sites on the Membrane-Exposed Surface of the Cytochrome bc1. J. Am. Chem. Soc. 2013, 135, 3112-3120
(375) M. R. Schmidt, P. J. Stansfeld, S. J. Tucker, M. S. P. Sansom, Simulation-Based Prediction of Phosphatidylinositol 4,5-Bisphosphate Binding to an Ion Channel. Biochemistry 2013, 52, 279-281
(376) P. J. Stansfeld, R. Hopkinson, F. M. Ashcroft, M. S. P. Sansom, PIP2-Binding Site in Kir Channels: Definition by Multiscale Biomolecular Simulations. Biochemistry 2009, 48, 10926-10933
(377) C. N. Lumb, M. S. P. Sansom, Finding a Needle in a Haystack: The Role of Electrostatics in Target Lipid Recognition by PH Domains. PLoS Comp. Biol. 2012, 8, e1002617
(378) G. van den Bogaart, K. Meyenberg, H. J. Risselada, H. Jelger, H. Amin, K. I. Willig, B. E. Hubrich, M. Dier, S. W. Hell, H. Grubmueller, U. Diederichsen, R. Jahn, Membrane Protein Sequestering by Ionic Protein-Lipid Interactions. Nature 2011, 479, 552-555
(379) X. Periole, T. Huber, SJ. Marrink, T. P. G. Sakmar, Protein-Coupled Receptors Self-Assemble in Dynamics Simulations of Model Bilayers. J. Am. Chem. Soc. 2007, 129, 10126-10132
(380) J. Li, X. Wang, T. Zhang, C. Wang, Z. Huang, X. Luo, Y. Deng, A Review of Phospholipids and Their Main Applications in Drug Delivery Systems. Asian J. Pharm. Sci. 2015, 10, 81-98
(381) M. Alagumuthu, D. Dahiya, P. S. Nigam, Phospholipid—The Dynamic Structure Between Living and Non-Living World; a Much Obligatory Supramolecule for Present and Future. AIMS Mol. Sci. 2019, 6, 1-19
(382) L. A. Colin, Y. Jailais, Phospholipids Across Scales: Lipid Patterns and Plant Development. Curr. Opin. Plant Biol. 2020, 53, 1-9
(383) C. Botella, J. Jouhet, M. A. Block, Importance of Phosphatidylcholine on the Chloroplast Surface. Prog. Lipid Res. 2017, 65, 12-23

(384) T. Skotland, K. Sandvig, The role of PS 18:0/18:1 in Membrane Function. Nat. Commun. 2019, 10, 2752
(385) P. A. Leventis, S. Grinstein, The Distribution and Function of Phosphatidylserine in Cellular Membranes. Annu. Rev. Biophys. 2010, 39, 407-427
(386) E. M. Bevers, P. L. Williamson, Getting to the Outer Leaflet: Physiology of Phosphatidylserine Exposure at the Plasma Membrane. Physiol Rev. 2016, 96, 605-645
(387) J. Pan, X. Cheng, L. Monticelli, F. A. Heberle, N. Kucerka, D. P. Tieleman, J. Katsaras, The Molecular Structure of a Phosphatidylserine Bilayer Determined by Scattering and Molecular Dynamics Simulations. Soft Matter 2014, 10, 3716-3725
(388) R. Dawaliby, C. Trubbia, C. Delporte, C. Noyon, J. M. Ruysschaert, P. Van Antwerpen, C. Govaerts, Phosphatidylethanolamine is a Key Regulator of Membrane Fluidity in Eukaryotic Cells. J. Biol. Chem. 2016, 291, 3658-3667
(389) N. Sun, J. Chen, Z Bao, D. Wang, B. An, S. Lin, Egg Yolk Phosphatidylethanolamine: Extraction Optimization, Antioxidative Activity, and Molecular Structure Profiling. J. Food Sci. 2019, 84, 1002-1011
(390) G. Shahane, W. Ding, M. Palaiokostas, M. Orsi, Physical Properties of Model Biological Lipid Bilayers: Insights From All-Atom Molecular Dynamics Simulations. J. Mol. Model. 25, 76
(391) K. Kobayashi, K. Endo, H. Wada, Specific Distribution of Phosphatidylglycerol to Photosystem Complexes in the Thylakoid Membrane. Front. Plant Sci. 2017, 8, 1991
(392) R. Pan, J. Hu, Plant Mitochondrial Dynamics and the Role of Membrane Lipids. Plant. Signal Behav. 2015, 10, e1050573
(393) S. E. Horvath, G. Daum, Lipids of Mitochondria, Prog. Lipid Res. 2013, 52, 590-614
(394) S. Vanounou, A. H. Parola, I. Fishov, Phosphatidylethanolamine and Phosphatidylglycerol Are Segregated Into Different Domains in Bacterial Membranes. A Study With Pyrene-Labelled Phospholipids. Mol. Microlbiol. 2003, 49, 1067-1079
(395) J. M. Wood, Perspective: Challenges and Opportunities for the Study of Cardiolipin, a Key Player in Bacterial Cell Structure and Function. Curr. Genet. 2018, 64, 795-798
(396) A. Musatov, E. Sedlak, Role of Cardiolipin in Stability of Integral Membrane Proteins. Biochimie 2017, 102-111
(397) H. Bareli, B. Antonny, Lipid Unsaturation and Organelle Dynamics. Curr. Opin. Cell Biol. 2016, 41, 25-32
(398) Y. Xu, Z. Zhao, W. Tong, Y. Ding, B. Liu, Y. Shi, J. Wang, S. Sun, M. Liu, Y. Wang, Q. Qi, M. Xian, G. Zhao, An Acid-Tolerance Response System Protecting Exponentially Growing Escherichia Coli. Nat. Commun. 2020, 11, 1496
(399) Y. Tu, M. Lv, P. Xiu, T. Huynh, M. Zhang, M. Castelli, Z. Liu, Q. Huang, C. Fan, H. Fang, R. Zhou, Destructive Extraction of Phospholipids From Escherichia Coli Membranes by Graphene Nanosheets. Nat. Nanotechnol. 2013, 8, 594-601

(400) J. Wang, Y. Wei, X. Shi, H. Gao, Cellular Entry of Graphene Nanosheets: The Role of Thickness, Oxidation and Surface Adsorption. RSC Adv. 2013, 3, 15776-15782
(401) L. Monticelli, E. Salonen, P. C. Ke, I. Vattulainen, Effects of Carbon Nanoparticles on Lipid Membranes: A Molecular Simulation Perspective. Soft Matter 2009, 5, 4433-4445
(402) S. Kanchi, M. Gosika, K. G. Ayappa, P. K. Maiti, Dendrimer Interactions With Lipid Bilayer: Comparison of Force Field and Effect of Implicit vs Explicit Solvation. J. Chem. Theory Comput. 2018, 14, 3825-3839
(403) X. He, M. Lin, B. Sha, S. Feng, X. Shi, Z. Qu, F. Xu, Coarse-Grained Molecular Dynamics Studies of the Translocation Mechanism of Polyarginines Across Asymmetric Membrane Under Tension. Sci. Rep. 2015, 5, 12808
(404) J. Kapla, B. Stevensson, A. Maliniak, Coarse-Grained Molecular Dynamics Simulations of Membrane-Trehalose Interactions. J. Phys. Chem. B 2016, 120, 9621-9631
(405) J. Kapla, J. Wohlert, B. Stevensson, O. Engstrom, G. Widmalm, A. Maliniak, Molecular Dynamics Simulations of Membrane-Sugar Interactions. J. Phys. Chem. B 2013, 117, 6667-6673
(406) T. Kondela, J. Gallova, T. Haub, J. Barnoud, SJ. Marrink, N. Kucerka, Alcohol Interactions With Lipid Bilayers. Molecules 2017, 22, E2078
(407) S. M. Hanson, S. Newstead, K. J. Swartz, M. S. P. Sansom, Capsaicin Interaction With TRPV1 Channels in a Lipid Bilayer: Molecular Dynamics Simulation. Biophys. J. 2015, 108, 1425-1434
(408) J. B. Klauda, R. M. Venable J. A. Freites, J. W. O'Connor, D. J. Tobias, C. Mondragon-Ramirez, I. Vorobyov, A. D. Mackerell, R. W. Pastor, Update of the CHARMM All-Atom Additive Force Field for Lipids: Validation on Six Lipid Types. J. Phys. Chem. B 2010, 114, 7830-7843
(409) N. Kucerka, J. F. Nagle, J. N. Sachs, S. E. Feller, J. Pencer, A. Jackson, J. Katsaras, Lipid Bilayer Structure Determined by the Simultaneous Analysis of Neutron and X-Ray Scattering Data. Biophys. J. 2008, 95, 2356-2367
(410) N. Kucerka, Y. Liu, N. Chu, H. I. Petrache, S. Tristam-Nagle, J. F. Nagle, Structure of Fully Hydrated Fluid Phase DMPC and DLPC Lipid Bilayers Using X-Ray Scattering From Oriented Multilamellar Arrays and From Unilamellar Vesicles. Biophys. J. 2005, 88, 2626-2637
(411) M. C. Wiener, S. H. White, Structure of a Fluid Dioleoylphosphatidylcholine Bilayer Determined by Joint Refinement of X-Ray and Neutron Diffraction Data. II. Distribution and Packing of Terminal Methyl Groups. Biophys. J. 1992, 61, 428-433
(412) J. B. Klauda, N. Kucerka, B. R. Brooks, R. W. Pastor, J. F. Nagle, Simulation-Based Methods for Interpreting X-Ray Data From Lipid Bilayers. Biophys. J. 2006, 90, 2796-2807
(413) N. Kucerka, S. Tristam-Nagle, J. F. Nagle, Structure of Fully Hydrated Fluid Phase Lipid Bilayers With Monounsaturated Chains. J. Membr. Biol. 2005, 208, 193-202
(414) S. R. Shaikh, M. R. Brzustowica, N. Gustafson, W. Stillwell, S. R. Wassall, Monounsaturated PE Does Not Phase-Separate From the Lipid Raft Molecules Sphingomyelin and Cholesterol: Role for Polyunsaturation? Biochemistry 2002, 41, 10593-10602

(415) A. Seelig, J. Seelig, The Dynamic Structure of Fatty Acid Chains in a Phospholipid Bilayer Measured by Deuterium Magnetic Resonance. Biochemistry 1974, 13, 4839-4845
(416) A. Seelig, J. Seelig, Dynamic Structure of Fatty Acyl Chains in a Phospholipid Bilayer Measured by Deuterium Magnetic Resonance. Biochemistry 1974, 13, 4839-4845
(417) J. B. Klauda, N. V. Eldho, K. Gawrisch, B. R. Brooks, R. W. Pastor, Collective and Noncollective Models of NMR Relaxation in Lipid Vesicles and Multilayers. J. Phys. Chem. B 2008, 112, 5924-5929
(418) M. C. Wiener. G. I. King, S. H. White, Structure of a Fluid Dioleoylphosphatidylcholine Bilayer Determined by Joint Refinement of X-Ray and Neutron Diffraction Data. I. Scaling of Neutron Data and the Distributions of Double Bonds and Water. Biophys. J. 1991, 60, 568-576
(419) E. J. Dufourc, Sterols and Membrane Dynamics. J. Chem. Biol. 2008, 1, 63-77
(420) W. K. Subczynski, M. Pasenkiewicz_Gierula, J. Widomska, L. Mainali, M. Raguz, High Cholesterol/Low Cholesterol: Effects in Biological Membranes Review. Cell Biochem. Biophys. 2017, 75, 369-385
(421) F. Abe, T. Hiraki, Mechanistic Role of Ergosterol in Membrane Rigidity and Cycloheximide Resistance in Saccharomyces Cerevisiae. Biochim. Biophys. Acta Biomembr. 2009, 1788, 743-752
(422) P. V. Welander, R. C. Hunter, L. Zhang, A. L. Sessions, R. E. Summons, D. K. Newman, Hopanoids Play a Role in Membrane Integrity and pH Homeostasis in Rhodopseudomonas Palustris TIE-1. J. Bacteriol. 2009, 191, 6145-6156
(423) K. Bloch, Sterol Molecule: Structure, Biosynthesis, and Function. Steroids 1992, 57, 378-383
(424) D. A. Mannock, R. N. Lewis, T. P. McMullen, R. N. McElhaney, The Effect of Variations in Phospholipid and Sterol Structure on the Nature of Lipid-Sterol Interactions in Lipid Bilayer Model Membranes. Chem. Phys. Lipids 2010, 163, 403-448
(425) K Bloch, Sterol Structure and Function. Steroids 1989, 53, 261-270
(426) U. Krengel, P. Bousquet, Molecular Recognition of Gangliosides and Their Potential for Cancer Immunotherapies. Front. Immunol. 2014, 5, 325
(427) K. Simons, E. Ikonen, How Cells Handle Cholesterol. Science 2000, 290, 1721-1726
(428) A. N. Leonard, E. Wang, V. Monje-Galvan, J. B. Klauda, Developing and Testing of Lipid Force Fields with Applications to Modelling Cellular Membranes. Chem. Rev. 2019, 6227-6269
(429) I. A. Barragan, M. Muller, Generalization of the Swelling Method to Measure the Intrinsic Curvature of Lipids. J. Chem. Phys. 2017, 147, 224902
(430) YS. Ryu, IH. Lee, JH. Suh, S. C. Park, S. Oh, L. R. Jordan, N. J. Wittenberg, SH. Oh, N. L. Jeon, B. Lee, A. N. Parikh, SD. Lee, Reconstituting Ring-Rafts in Bud-Mimicking Topography of Model Membranes. Nat. Commun. 2014, 5, 4507
(431) J. Grouleff, S. J. Irudayam, K. K. Skeby, B. Schiott, The Influence of Cholesterol on Membrane Protein Structure, Function, and Dynamics Studied by Molecular Dynamics Simulations. Biochim. Biophys. Acta 2015, 1848, 1783-1795

(432) D. Sengupta, A. Chattopadhyay, Molecular Dynamics Simulations of GPCR-Cholesterol Interaction: An Emerging Paradigm. Biochim. Biophys. Acta 2015, 1848, 1775-1782
(433) M. L. Berkowitz, Detailed Molecular Dynamics Simulations of Model Biological Membranes Containing Cholesterol. Biochim. Biophys. Acta 2009, 1788, 86-96
(434) T. Rog, I. Vattulainen, Cholesterol, Sphingolipids, and Glycolipids: What Do We Know About Their Role in Raft-Like Membranes? Chem. Phys. Lipids 2014, 184, 82-104
(435) H. L. Scott, Modeling the Lipid Component of Membranes. Curr. Opin. Struct. Biol. 2002, 12, 495-502
(436) C. M. Macdermaid, H. K. Kashyap, R. H. Devane, W. Shinoda, J. B. Klauda, M. L. Klein, G. Fiorin, Molecular Dynamics Simulations of Cholesterol-Rich Membranes Using a Coarse-Grained Force Field for Cyclic Alkanes. J. Chem. Phys. 2015, 143, 243144
(437) W. F. D. Bennett, J. L. MacCallum, M. J. Hinner, SJ. Marrink, D. P. Tieleman, Molecular View of Cholesterol Flip-Flop and Chemical Potential in Different Membrane Environments. J. Am. Chem. Soc. 2009, 131, 12714-12720
(438) J. Dai, M. Alwarawrah, J. Huang, Instability of Cholesterol Clusters in Lipid Bilayers and the Cholesterol's Umbrella Effect. J. Phys. Chem. B 2010, 114, 840-848
(439) N. Yandrapalli, D. Muriaux, C. Favard, Lipid Domains in HIV-1 Assembly. Front. Microbiol. 2014, 5, 220
(440) S. Mukherjee, F. R. Maxfield, Membrane Domains, Annu. Rev. Cell Dev. Biol. 2004, 20, 839-866
(441) M. Bu, H. Li, H. Wang, J. Wang, Y. Lin, Y. Ma, Synthesis of Ergosterol Peroxide Conjugates as Mitochondrial Targeting Probes for Enhanced Anticancer Activity. Molecules 2019, 24, 3307
(442) K. A. Solanko, M. Modzel, L. M. Solanko, D. Wustner, Fluorescent Sterols and Cholesteryl Esters as Probes for Intracellular Cholesterol Transport. Lipid Insights 2015, 8, 95-114
(443) HY. Wu, FL. Yang, LH. Li, Y. K. Rao, TC. Ju, WT. Wong, CY. Hsieh, M. V. Pivkin, KF. Hua, SH. Wu, Ergosterol Peroxide From Marine Fungus Phoma Sp. Induces ROS-Dependent Apoptosis and Autophagy in Human Lung Adenocarcinoma Cells. Sci. Rep. 2018, 8, 17956
(444) F. J. Barrantes, J. Fantini, From Hopanoids to Cholesterol: Molecular Clocks of Pentameric Ligand-Gated Ion Channels. Prog. Lipid Res. 2016, 63, 1-13
(445) B. Caron, A. E. Mark, D Poger, Some Like It Hot: The Effect of Sterols and Hopanoids on Lipid Ordering at High Temperature. J. Phys. Chem. Lett. 2014, 5, 3953-3957
(446) J. P. Saenz, E. Sezgin, P. Schwille, K. Simons, Functional Convergence of Hopanoids and Sterols in Membrane Ordering. Proc. Natl. Acad. Sci. U. S. A. 2012, 109, 14236-14240
(447) A. Mangiarotti, D. M. Genovese, C. A. Naumann, M. R. Monti, N. Wilke, Hopanoids, Like Sterols, Modulate Dynamics, Compaction, Phase Segregation and Permeability of Membranes. Biochim. Biophys. Acta Biomembr. 2019, 1861, 183060

(448) C. H. Wu, L. Kong, M. Bialecka-Fornal, S. Park, A. L. Thompson, G. Kulkarni, S. J. Conway, D. K. Newman, Quantitative Hopanoid Analysis Enables Robust Pattern Detection and Comparison Between Laboratories. Geobiology 2015, 13, 391-407
(449) A. Mangiarotti, V. V. Galassi, E. N. Puentas, R. G. Oliveira, M. G. Del Popolo, N. Wilke, Hopanoids Like Sterols form Compact but Fluid Films. Langmuir 2019, 35, 9848-9857
(450) J. P. Saenz, D. Grossner, A. S. Bradley, T. J. Lagny, O. Lavrynenko, M. Broda, K. Simons, Hopanoids As Functional Analogues of Cholesterol in Bacterial Membranes. Proc. Natl. Acad. Sci. U. S. A. 2015, 112, 11971-11976
(451) M. N. Melo, H. I. Ingolfsson, SJ. Marrink, Paramters for Martini Sterols and Hopanoids Based on a Virtual-Site Description. J. Chem. Phys. 2015, 143, 243152
(452) R. A. Hill, J. D. Connolly, Trierpenoids. Nat. Prod. Rep. 2018, 35, 1294-1329
(453) N. A. J. C. Furtado, L. Prison, H. Edelberg, L. M. Miranda, C. Loira-Pastoriza, V. Preat, Y. Larondelle, C. M. Andre, Pentacyclic Triterpene Bioavailability: An Overview of In Vitro and In Vivo Studies. Molecules 2017, 22, E400
(454) B. Dinda, S. Debnath, B. C. Mohanta, Y. Harigaya, Naturally Occurring Triterpenoid Saponins. Chem. Biodivers. 2010, 7, 2327-2580
(455) J. M. Renoux, M. Rohmer, Prokaryotic Triterpenoids. New Bacteriohopanetetrol Cyclitol Ethers From the Methylotrophic Bacterium Methylobacterium Organophilum. Eur. J. Biochem. 1985, 151, 405-410
(456) D. Poger, A. E. Mark, The Relative Effect of Sterols and Hopanoids on Lipid Bilayers: When Comparable Is Not Identical. J. Phys. Chem. B 2013, 117, 16129-16140
(457) M. P. Czech, PIP2 and PIP3: Complex Roles at the Cell Surface. Cell 2000, 100, 603-606
(458) J. O. De Craene, D. L. Bertazzi, S. Bar, S. Friant, Phosphoinositides, Major Actors in Membrane Trafficking and Lipid Signalling Pathways. Int. J. Mol. Sci. 2017, 18, E634
(459) S. B. Hansen, Lipid Agonism: the PIP2 Paradigm of Ligand-Gated Ion Channels. Biochim. Biophys. Acta 2015, 1851, 620-628
(460) B. C. Suh, B. Hille, PIP2 Is a Necessary Cofactor for Ion Channel Function: How and Why? Annu. Rev. Biophys. 2008, 37, 175-195
(461) O. T. Le, T. T. Nguyen, S. Y. Lee, Phosphoinositide Turnover in Toll-Like Signalling and Trafficking. BMB Rep. 2014, 47, 361-368
(462) J. P. Kukkonen, Lipid Signalling Cascades of Orexin/Hypocretin Receptors. Biochimie 2014, 96, 158-165
(463) G. Godlee, M. Kaksonen, Review Series: From Uncertain Beginnings: Initiation Mechanisms of Clathrin-Mediated Endocytosis. J. Cell. Biol. 2013, 203, 717-725
(464) Y. Posor, M. Eichhorn-Grunig, V. Haucke, Phosphoinositides in Endocytosis. Biochim. Biophys. Acta 2015, 1851, 794-804
(465) K. Takei, Y. Yoshida, H. Yamada, Regulatory Mechanisms of Dynamin-Dependent Endocytosis. J. Biochem. 2005, 137, 243-247
(466) T. F. Martin, PI(4,5)$_2$P -Binding Effector Proteins for Vesicle Exocytosis. Biochim. Biophys. Acta 2015, 1851, 785-793

(467) L. E. Rameh, K. Tolias, B. C. Duckworth, L. C. Cantley, A New Pathway for Synthesis of Phosphatydilinositol-4,5-Biphosphate, Nature 390, 192-196
(468) D. Barneda, S. Cosulich, L. Stephens, P. Hawkins, How Is the Acyl Chain Composition of Phosphoinositides Created and Does It Matter? Biochem. Soc. Trans. 2019, 47, 1291-1305
(469) A. Koizumi, S. Narita, H. Nakanishi, M. Ishikawa, S. Eguchi, H. Kimura, S. Takasuga, M. Huang, T. Inoue, J. Sasaki, T. Yoshioka, T. Habuchi, T. Sasaki, Increased Fatty Acyl Saturation of Phosphatidylinositol Phosphates in Prostate Cancer Progression. Sci. Rep. 2019, 9, 13257
(470) M. R. Schmidt, P. J. Stansfeld, S, J. Tucker, M. S. P. Sansom, Simulation-Based Prediction of PIP_2 Binding to an Ion Channel. Biochemistry 2013, 52, 279-281
(471) L. H. Xie, S. A. John, B. Ribalet, J. N. Weiss, Activation of Inwardly Rectifying Potassium (Kir) Channels by Phosphatidylinositol-4,5-Bisphosphate (PIP2): Interaction With Other Regulatory Ligands. Prog. Biophys. Mol. Biol. 2007, 94, 320-335
(472) A. N. Bukiya, A. Rosenhouse-Dantsker, Synergistic Activation of G Protein-Gated Inwardly Rectifying Potassium Channels by Cholesterol and $PI(4,5)P_2$. Biochim. Biophys. Acta Biomembr. 2017, 1859, 1233-1241
(473) D. E. Logothetis, H. Zhang, Gating of G Protein-Sensitive Inwardly Rectifying K+ Channels Through Phosphatidylinositol 4,5-Bisphosphate. J. Physiol. 1999, 520, 630
(474) D. E. Logothetis, T. Jin, D. Lupyan, A. Rosenhouse-Dantsker, Phosphoinositide-Deiated Gating of Inwardly Rectifying K(+) Channels. Pflugers Arch. 2007, 455, 83-95
(475) HY. Yen, K. K. hoi, I. Liko, G. Hedger, M. R. Horrell, W. Song, D. Wu, P. Heine, T. Warne, Y. Lee, B. Carpenter, A. Pluckthun, C. G. Tate, M. S. P. Sansom, C. V. Robinson, $PtdIns(4,5)P_2$ Stabilizes Active States of GPCRs and Enhances Selectivity of G-Protein Coupling. Nature 2018, 559, 423-427
(476) J. A. Pitcher, Z. L. Fredericks, W. C. Stone, R. T. Premont, R. H. Stoffel, W. J. Koch, R. J. Lefkowitz, Phosphatidylinositol 4,5-Biphosphate (PIP2)-Enhanced G Protein-Coupled Receptor Kinase (GRK) Activity. Location, Structure, and Regulation of the PIP2 Binding Site Distinguishes the GRK Subfamilies. J. Biol. Chem. 1996, 271, 24907-24913
(477) A. L. Dunacan, W. Song, M. S. P. Sansom, Lipid-Dependent Regulation of Ion Channels and G Protein-Coupled Receptors: Insights From Structures and Simulations. Annu. Rev. Pharmacol. Toxicol. 2020, 60, 31-50
(478) P. Yang, K. T. Homan, Y. Li, O. Cruz-rodriguez, J. J. G. Tesmer, Z. Chen, Effect of Lipid Composition on Membrane Orientation of the G Protein-Coupled Receptor Kinase 2-Gβ1γ2 Complex. Biochemistry 2016, 55, 2841-2848
(479) H. Q. Sun, M. Yamamoto, M. Mejillano, H. L. yin, Gelsolin, a Multifunctional Actin Regulatory Protein. J. Biol. Chem. 1999, 274, 33179-33182
(480) D. A. Eberhard, C. L. Cooper, M. G. Low, R. W. Holz, Evidence That the Inositol Phospholipids Are Necessary for Exocytosis. Loss of Inositol Phospholipids and Inhibition of Secretion in Permeabilized Cells Caused by a Bacterial Phospholipase C and Removal of ATP. Biochem. J. 1990, 268, 15-25

(481) J. C. Hay, T. F. J. Martin, Phosphatidylinositol Transfer Protein Required for ATP-Dependent Priming of Ca2+-Activated Secretion. Nature 1993, 366, 572-575
(482) J. C. Hay, P. L. Fisette, G. H. Jenkins, K. Fukami, T. Takenawa, R. A. Anderson, T. F. J. Martin, ATP-Dependent Inositide Phosphorylation Required for Ca2+-Activated Secretion. Nature 1995, 374, 173-177
(483) Z. Li, R. M. Venable, L. A. Rogers, D. Murray, R. W. Pastor, Molecular Dynamics Simulations of PIP2 and PIP3 in Lipid Bilayers: Determination of Ring Orientation, and the Effects of Surface Roughness on a Poisson-Boltzmann Description. Biophys. J. 2009, 97, 155-163
(484) J. P. Bradshaw, R. J. Bushby, C. C. Giles, M. R. Saunders, D. G. Reid, Neutron Diffraction Reveals the Orientation of the Headgroup of Inositol Lipids in Model Membranes. Nat. Struct. Biol. 1996, 3, 125-127
(485) R. V. McDaniel, T. J. McIntosh, Neutron and X-ray Diffraction Structural Analysis of Phosphatidylinositol Bilayers. Biochim. Biophys. Acta Biomembr. 1989, 983, 241-246
(486) D. R. Slochower, P. J. Huwe, R. Radhakrishnan, P. A. Janmey, Quantum and All-Atom Molecular Dynamics Simulations of Protonation and Divalent Ion Binding to Phosphatidylinositol 4,5-Bisphosphate (PIP2). J. Phys. Chem. B 2013, 117, 8322-8329
(487) D. Lupyan, M. Mezei, D. E. Logothetis, R. Osman, A Molecular Dynamis Investigation of Lipid Bilayer Perturbation by PIP2. Biophys. J. 2010, 98, 240-247
(488) K. B. A. Halim, H. Koldso, M. S. P. Sansom, Interactions of the EGFR Juxtamembrane Domain With PIP2-Containing Lipid Bilayers: Insights From Multiscale Molecular Dynamics Simulations. Biochim. Biophys. Acta Biomembr. 2015, 1850, 1017-1025
(489) M. A. Kasimova, M. Tarek, A. K. Shaytan, K. V. Shaitan, L. Delemotte, Voltage-Gated Ion Channel Modulation by Lipids: Insights From Molecular Dynamics Simulations. Biochim. Biophys. Acta Biomembr. 2014, 1838, 1322-1331
(490) F. Sun, C. F. E. Scroer, L. Xu, H. Yin, SJ. Marrink, SZ Luo, Molecular Dynamics of the Association of L-selectin and FERM Regulated by PIP2. Biophys. J. 2018, 114, 1858-1868
(491) ZL. Li, M. Buck, Computational Modelling Reveals That Signalling Lipids Modulate the Orientation of K-Ras4A at the Membrane Reflecting Protein Topology. Structure 2017, 25, 679-689
(492) F. A. Herzog, L. Braun, I. Schoen, V. Vogel, Improved Side Chain Dynamics in MARTINI Simulations of Protein-Lipid Interfaces. J. Chem. Theory Comput. 2016, 12, 2446-2458
(493) S. Sharma, B. N. Kim, P. J. Stansfeld, M. S. Sansom, M. Lindau, A Coarse Grained Model for a Lipid Membrane With Physiological Composition and Leaflet Asymmetry. PLoS One 2015, 10, e0144814
(494) F. A. Herzog, L. Braun, I. Schoen, V. Vogel, Structural Insights How PIP2 Imposes Preferred Binding Orientations of FAK at Lipid Membranes. J. Phys. Chem. B 2017, 121, 3523-3535
(495) F. Sun, C. F. E. Schroer, L. Xu, H. Yin, SJ. Marrink, SZ. Luo, Molecular Dynamics of the Association of L-selectin and FERM Regulated by PIP2. Biophys. J. 2018, 114, 1858-1868

(496) V. Corradi, E. Mendez-Villuendas, H. I Ingolfsson, RX. Gu, I. Siuda, M. N. Melo, A. Moussatova, L. J. DeGagne, B. I. Sejdiu, G. Singh, T. A. Wassenaar, K. D. Magnero, SJ. Marrink, D. P. Tieleman, Lipid-Protein Interactions Are Unique Fingerprints for Membrane Proteins. ACS Cent. Sci. 2018, 4, 709-717
(497) H. I. Ingolfsson, T. S. Carpenter, H. Bhatia, PT. Bremer, SJ. Marrink, F. C. Lightstone, Computational Lipidomic of the Neuronal Plasma Membrane. Biophys. J. 2017, 113, 2271-2280
(498) H. I. Ingolfsson, M. N. Melo, F. J. van Eerden, C. Arnarez, C. A. Lopez, T. A. Wassenaar, X. Periole, A. H. de Vries, D. P. Tieleman, SJ. Marrink, Lipid Organization of the Plasma Membrane. J. Am. Chem. Soc. 2014, 136, 14554-14559
(499) X. Periole, Interplay of G Protein-Coupled Receptors With the Membrane: Insights From Supra-Atomic Coarse Grain Molecular Dynamics Simulations. Chem. Rev. 2017, 117, 156-185
(500) A. L. Duncan, T. Reddy, H. Koldso, J. Helie, P. W. Fowler, M. Chavent, M. S. P. Sansom, Protein Crowding and Lipid Complexity Influence the Nanoscale Dynamic Organization of Ion Channels in Cell Membranes. Sci. Rep. 2017, 7, 16647
(501) A. L. Duncan, R. A. Corey, M. S. P. Sansom, Defining How Multiple Lipid Species Interact With Inward Rectifier Potassium (Kir2) Channels. Proc. Natl. Acad. Sci. U. S. A. 2020, 117, 7803-7813
(502) D. M. Zajonc, E. Girardi, Recognition of Microbial Glycolipids by Natural Killer T Cells. Front. Immunol. 2015, 6, 400
(503) A. J. Thompson, R. P. de Vries, J. C. Paulson, Virus Recognition of Glycan Receptors. Curr. Opin Virol. 2019, 34, 117-129
(504) F. Ding, Y. Zhang, Biomedical Applications of Glycoconjugates. Mini Rev. Med. Chem. 2018, 18, 1508-1523
(505) K. Mendelson, T. Evans, T Hla, Sphingosine 1-Phosphate Signalling, Development 2014, 141, 5-9
(506) A. Kutlar, S. H. Embury, Cellular Adhesion and the Endothelium: P-selectin. Hematol. Oncol. Clin. Nort Am. 2014, 28, 323-339
(507) R. D. Cummings, “Stuck on Sugars – How Carbohydrates Regulate Cell Adhesion, Recognition, and Signalling”. Glycoconj. J. 2019, 36, 241-257
(508) R. K. Yu, T. A. Koerner, J. N. Scarsdale, J. H. Prestegard, Elucidation of Glycolipid Structure by Proton Nuclear Magnetic Resonance Spectroscopy. Chem. Phys. Lipids 1986, 42, 27-48
(509) H. J. Gabius, The Sugar Code: Why Glycans Are So Important. Biosystems 2018, 164, 102-111
(510) M. Ines, G. Dhouha, Glycolipid Biosurfactants: Potential Related Biomedical and Biotechnological Applications. Carbohydr. Res. 2015, 416, 59-69
(511) K. Fujikawa, S. Suzuki, R. Nagase, S. Ikeda, S. Mori, K. Nomura, K. I. Nishiyama, K. Shimamoto, Syntheses and Activities of the Functional Structures of a Glycolipid Essential for Membrane Protein Integration. ACS Chem. Biol. 2018, 13, 2719-2727
(512) S. Groux-Degroote, Y. Guerardel, P. Delannoy, Gangliosides: Structures, Biosynthesis, Analysis, and Roles in Cancer. Chembiochem. 2017, 18, 1146-1154

(513) R. L. Schnaar, The Biology of Gangliosides. Adv. Carbohydr. Chem. Biochem. 2019, 76, 113-148
(514) R. Sano, V. M. Trindade, A. Tessitore, A. d'Azzo, M. B. Vieira, R. Giugliani, J. C. Coelho. G(M1)-Ganglioside Degradation and Biosynthesis in Human and Murine G(M1)-Gangliosidosis. Clin. Chem. Acta 2005, 354, 131-139
(515) G. K. Chacko, G. M. Villegas, F. V. Barnola, R. Villegas, D. E. Goldman, The Polypeptide and the Phospholipid Components of Axon Plasma Membranes. Biochim. Biophys. Acta 1976, 443, 19-32
(516) G. van Echten-Deckert, S. Alam, Sphingolipid Metabolism – An Ambiguous Regulator of Autophagy in the Brain. Biol. Chem. 2018, 399, 837-850
(517) A. Piccinotti, G. Benaglia, R. Bresciani, D. Zizioli, M. Presta, A. Preti, S. Marhesini, Nerve Growth Factor Induces Sphingomyelin Accumulation in Pheochromocytoma Cells. FEBS Lett. 2000, 472, 143-147
(518) J. Kurniawan, J. Ventrici, G. Kittleson, T. L. Kuhl, Interaction Forces Between Lipid Rafts. Langmuir 2017, 33, 382-387
(519) R. H. Gensure, M. L. Zeidel, W. G. Hill, Lipid Raft Components Cholesterol and Sphingomyelin Increase H+/OH- Permeabilty of Phosphatidylcholine Membranes. Biochem. J. 2006, 398, 485-495
(520) R. S. Petruzielo, F. A. Heberle, P. Drazba, J. Katsaras, G. W. Feigenson, Phase Behaviour and Domain Size in Sphingomyelin-Containing Lipid Bilayers. Biochim. Biophys. Acta 2013, 1828, 1302-1313
(521) T. K. Nyholm, D. Lindroos, B. Westerlund, J. P. Slotte, Construction of a DOPC.PSM/cholesterol Phase Diagram Based on the Fluorescence Properties of Trans-Parinaric Acid. Langmuir 2011, 27, 8339-8350
(522) O. Engberg, H. A. Scheidt, T. K. M. Nyholm, J. P. Slotte, D. Huster, Membrane Localization and Lipid Interactions of Common Lipid-Conjugated Fluorescence Probes. Langmuir 2019, 35, 11902-11911
(523) T. A. Enoki, F. A. Heberle, G. W. Feigenson, FRET Detects the Size of Nanodomains for Coexisting Liquid-Disordered and Liquid-Disordered Phases. Biophys. J. 2018, 114, 1921-1935
(524) P. R. Maulik, G. G. Shipley, N-Palmitoyl Sphingomyelin Bilayers: Structure and Interactions With Cholesterol and Dipalmitoylphosphatidylcholine. Biochemistry 1996, 35, 8025-8034
(525) I. Bera, J. B. Klauda, Molecular Simulations of Mixed Lipid Bilayers With Sphingomyelin, Glycerophospholipids, and Cholesterol. J. Phys. Chem. B 2017, 121, 5197-5208
(526) P. Kumari, S. Kaur, S. Sharma, H. K. Hashyap, Impact of Amphiphilic Molecules on the Structure and Stability of Homogeneous Sphingomyelin Bilayer: Insights From Atomistic Simulations. J. Chem. Phys. 2018, 148, 165102
(527) H. A. Filipe, D. Bowman, T. Palmeira, R. M. Cardoso, L. M. Loura, M. J. Moreno, Interaction of NBD-Labelled Fatty Amines With Liquid-Ordered Membranes: A Combined Molecular Dynamics Simulation and Fluorescence Spectroscopy Study. Phys. Chem. Chem. Phys. 2015, 17, 27534-27547
(528) R. M. Venable, A. J. Sodt, B. Rogaski, H. Rui, E. Hatcher, A. D. MacKereil, R. W. Pastor, J. B. Klauda, CHARMM All-Atom Additive Force Field for

Sphingomyelin: Elucidation of Hydrogen Bonding and of Positive Curvature. Biophys. J. 2014, 107, 134-145
(529) C. Zhang, M. Terreni, M. Sollogoub, Y. Zhang, Ganglioside GM3 and Its Role in Cancer. Curr. Med. Chem. 2019, 26, 2933-2947
(530) J. I. Inokuchi, K. I. Inamori, K. Kabayama, M. Nagafuku, S. Uemura, S. Go, A. Suzuki, I. Ohno, H. Kanoh, F. Shishido, Biology of GM3 Ganglioside. Prog. Mol. Biol. Transl. Sci. 2018, 156, 151-195
(531) K. G. N. Suzuki, H. Ando, N. Komura, M. Konishi, A. Imamura, H. Ishida, M. Kiso, T. K. Fujiwara, A. Kusumi, Revealing the Raft Domain Organization in the Plasma Membrane by Single-Molecule Imaging of Fluorescent Ganglioside Analogs. Methods Enzymol. 2018, 598, 267-282
(532) P. Mukherjee, A. C. Faber, L. M. Shelton, R. C. Baek, T. C. Chiles, T. N. Seyfried, Thematic Review Series: Sphingolipids, Ganglioside GM3 Suppresses the Proangiogenic Effects of Vascular Endothelial Growth Factor and Ganglioside GD1a. J. Lipid Res. 2008, 49, 929-938
(533) C. Zheng, M. Terreni, M. Sollogoub, Y. Zhang, Ganglioside GM3 and Its Role in Cancer. Curr. Med. Chem. 2019, 26, 2933-2947
(534) R. K. Yu, YT. Tsai, T. Ariga, M. Yanagisawa, Structures, Biosynthesis, and Functions of Gangliosides—An Overview. J. Oleo Sci. 60, 537-544
(535) K. Banda, G. Kang, A. Varki, 'Sialidase Sensitivity' of Rotaviruses Revisitied. Nat. Che. Biol. 2009, 5, 71-72
(536) R. Dasgupta, M. S. Miettinen, N. Fricke, R. Lipowsky, R. Dimova, The Glycolipid GM1 Reshapes Asymmetric Biomembranes and Giant Vesicles by Curvature Generation. Proc. Natl. Acad. Sci. U. S. A. 2018, 115, 5756-5761
(537) W. Pezeshkian, L. J. Nabo, J. H. Ipsen, Cholera Toxin B Subunit Induces Local Curvature on Lipid Bilayers. FEBS Open Bio. 2017, 7, 1638-1645
(538) H. Ewers, W. Romer, S. Dmitrieff, L. Berland, GM1 Structure Determines SV40-Induced Membrane Invagination and Infection. Nat. Cell Biol. 2009, 12, 11-18
(539) YJ. Chen, X. Liu, B. Tsai, SV40 Hijacks Cellular Transport, Membrane Penetration, and Disassembly Machineries to Promote Infection. Viruses 2019, 11, 917
(540) R. Kociurzynski, S. D. Beck, J. B. Bouhon, W. Romer, V. Knecht, Binding of SV40's Viral Capsid Protein VP1 to Glycosphingolipid Receptor GM1 Induces Negative Membrane Curvature: A Molecular Dynamics Study. Langmuir 2019, 35, 3534-3544
(541) C. A. Lingwood, B. Boyd, A. Nutikka, Analysis of Interactions Between Glycosphingolipids and Microbial Toxins. Methods Enzymol. 2000, 312, 459-473
(542) H. Ewers, A. Helenius, Lipid-Mediated Endocytosis. Cold Spring Harbor Perspectives in biology. Cold Spring Harb. Perspect. Biol. 2011, 3, a004721
(543) C. R. Raetz, C. Whitfield, Lipopolysaccharide Endotoxins. Annu. Rev. Biochem. 2002, 71, 635-700
(544) X. Wang, P. J. Quinn, Lipopolysaccharide: Biosynthetic Pathway and Structure Modification. Prog. Lipid Res. 2010, 49, 97-107
(545) H. Li, T. Liao, A. W. Debowski, H. Tang, H. O. Nilsson, K. A. Stubbs, B. J. Marshall, M. Benghezal, Lipopolysaccharide Structure and Biosynthesis in Helicobacter Pylori. Helicobacter. 2016, 21, 445-461

(546) C. R. Raetz, C. M. Reynolds, M. S. Trent, R. E. Bishop, Lipid A Modification Systems in Gram-Negative Bacteria. Annu. Rev. Biochem. 2007, 76, 295-329
(547) C. R. Raetz, Biochemistry of Endotoxins. Annu. Rev. Biochem. 1990, 59, 129-170
(548) C. R. Raetz, R. J. Ulevitch, S. D. Wright, C. H. Sibley, A. Ding, C. F. Nathan, Gram-Negative Endotoxin: An Extraordinary Lipid With Profound Effects on Eukaryotic Signal Transduction. FASEB J. 1991, 5, 2652-2660
(549) X. Wang, A. A. Ribeiro, Z. Guan, S. C. McGrath, R. J. Cotter, C. R. Raetz, Structure and Biosynthesis of Free Lipid A Molecules That Replace Lipopolysaccharide in Francisella Tularensis Subsp. Novicida. Biochemistry 2006, 45, 14427-14440
(550) Z. Zhou, A. A. Ribeiro, S. Lin, R. J. Cotter, S. I. Miller, C. R. Raetz, Lipid A Modification in Polymyxin-Resistant Salmonella Typhimurium: PMRA-Dependent 4-Amino-4-Deoxy-L-Arabinose, and Phosphoethanolamine Incorporation. J. Biol. Chem. 2001, 276, 43111-43121
(551) T. J. Piggot, D. A. Holdbrook, S. Khalid, Electroporation of the E. Coli and S. Aureus Membranes: Molecular Dynamics Simulations of Complex Bacterial Membranes. J. Phys. Chem. B 2011, 115, 13381-13388
(552) J. A. Garate, C. Oostenbrink, Lipid A From Lipopolysaccharide Recognition: Structure, Dynamics and Cooperativity by Molecular Dynamics Simulations. Proteins 2013, 81, 658-674
(553) S. Lee, A. Tran, M. Allsopp, J. B. Lim, J. Henin, J. B. Klauda, CHARMM36 United Atom Chain Models for Lipids and Surfactants. J. Phys. Chem. B 2014, 118, 547-556
(554) J. Huang, A. D. Mackerell, CHARMM36 All-Atom Additive Protein Force Field: Validation Based on Comparison NMR Data. J. Comput. Chem. 2013, 34, 2135-2145
(555) S. Kim, D. S. Patel, S. Park, J. Slusky, J. B. Klauda, G. Widmalm, W. Im, Bilayer Properties of Lipid A From Various Gram-Negative Bacteria. Biophys. J. 2016, 111, 1750-1760
(556) A. Li, J. W. Schertzer, X. Yong, Molecular Dynamics Modelling of Pseudomonas Aeruginosa Outer Membranes. Phys. Chem. Chem. Phys. 2018, 20, 23635-23648
(557) K. N. Kirschner, A. B. Yongye, S. M. Tschampel, J. Gonzalez-Outeirino, C. R. Daniels, B. L. Foley, R. J. Woods, GLYCAM06: A Generalizable Biomolecular Force Field. Carbohydrates. J. Comput. Chem. 2008, 29, 622-655
(558) M. B. Tessier, M. L. Demarco, A. B. Yongye, R. J. Woods, Extension of the GLYCAM06 Biomolecular Force Field to Lipids. Lipid Bilayers and Glycolipids. Mol. Simul. 2008, 34, 349-363
(559) W. K. Lay, M. S. Miller, A. H. Elcock, Optimizing Solute-Solute Interactions in the GLYCAM06 and CHARMM36 Carbohydrate Force Fields Using Osmotic Pressure Measurements. J. Chem. Theory Comput. 2016, 12, 1401-1407
(560) R. Lakshminarayanan, W. X. Tan, T. T. Aung, E. T. Goh, N. Muruganantham, J. Li, J. Y. Chang, N. Dikshit, P. Saraswathi, R. R. Lim, T. S. Kang, V. Balamuralidhar, B. Sukumaran, C. S. Verma, J. Sivaraman, S. S. Chaurasia, S. Liu, R. W. Beuerman, Branched Peptide, B2088, Disrupts the

Supramolecular Organization of Lipopolysaccharides and Sensitizes the Gram-Negative Bacteria. Sci. Rep. 2016, 6, 25905
(561) C. Oostenbrink, A. Villa, A. E. Mark, W. F. Gunsteren, A biomolecular force field based on the free enthalpy of hydration and solvation: the GROMOS force-field parameter sets 53A5 and 53A6. J. Comput. Chem. 2004, 25, 1656-1676
(562) C. Oostenbrink, T. A. Soares, N. F. van der Vegt, W. F. van Gunsteren, Validation of the 53A6 GROMOS Force Field. Eur. Biophys. J. 2005, 34, 273-284
(563) J. Lodowska, D. Wolny, L. Weglarz, The Sugar 3-Deoxy-D-Manno-Oct-2-Ulosonic Acid (Kdo) as a Characteristic Component of Bacterial Endotoxin – A Review of Its Biosynthesis, Function, and Placement in the Lipopolysaccharide Core. Can. J. Microbiol. 2013, 59, 645-655
(564) D. Kocincova, J. S. Lam, Structural Diversity of the Core Oligosaccharide Domain of Pseudomonas Aeruginosa Lipopolysaccharide. Biochemistry (Mosc.) 2011, 76, 755-760
(565) N. Kato, T. Sugiyama, S. Naito, Y. Arakawa, H. Ito, N. Kido, M. Ohta, K. Sasaki, Molecular Structure of Bacterial Endotoxin (Escherichia Coli Re Lipooplysaccharide): Implications for Formation of a Novel Heterogeneous Lattice Structure. Mol. Microbiol. 2000, 36, 796-805
(566) H. W. Wollenweber, K. W. Broady, O. Luderitz, E. T. Rietschel, The Chemical Structure of Lipid A. Demonstration of Amide-Linked 3-Acyloxyacyl Residues in Salmonella Minnesota Re Lipopolysaccharide. Eur. J. Biochem. 1982, 124, 191-198
(567) U. Seydel, M. H. Koch, K. Brandenburg, Structural Polymorphisms of Rough Mutant Lipopolysaccharide Rd to Ra From Salmonella Minnesota. J. Struct. Biol. 1993, 110, 232-243
(568) S. Snyder, D. Kim, T. J. McIntosh, Lipopolysaccharide Bilayer Structure: Effect of Chemotype, Core Mutations, Divalent Cations, and Temperature. Biochemistry 1996, 38, 10758-10767
(569) L. S. Vermeer, B. L. De Groot, V. Reat, A. Milon, J. Czaplicki, Acyl Chain Order Parameter Profiles in Phospholipid Bilayers: Computation From Molecular Dynamics Simulations and Comparison With 2 H NMR Experiments. Eur. Biophys. J. 2007, 36, 919-931
(570) J. Gumbart, M. C. Wiener, E. Tajkorshid, Mechanics of Force Propagation in TonB-Dependent Outer Membrane Transport. Biophys. J. 2007, 93, 496-504
(571) J. D. Faraldo-Gomez, G. R. Smith, M. S. P. Sansom, Molecular Dynamics Simulations of the Bacterial Outer Membrane Protein FhuA: A Comparative Study of the Ferrichrome-Free and Bound States. Biophys. J. 2003, 85, 1406-1420
(572) J. Gumbart, W. C. Wiener, E. Tajkhorshid, Coupling of Calcium and Substrate Binding Through Loop Alignment in the Outer Membrane Transporter BtuB. J. Mol. Biol. 2009, 393, 1129-1142
(573) N. Noinaj A. J. Kuszak, J. C. Gumbart, P. Lukacik, H. Chang, N. C. Easley, T. Lithgow, S. K. Buchanan, structural Insight Into the Biogenesis of β-Barrel Membrane Proteins. Nature 2013, 501, 385-390

(574) J. Shearer, S. Khalid, Communication Between the Leaflets of Asymmetric Membranes Revealed From Coarse-Grain Molecular Dynamics Simulations. Sci. Rep. 2018, 8, 1805
(575) T. Steffens, FJ. Vorholter, M. Giampa, G. Hublik, A. Puhler, K. Niehaus, The Influence of a Modified Lipopolysaccharide O-antigen on the Biosynthesis Ox Xanthan in Xanthomonas Campestris pv. Campestris B100. BMC Microbiol. 2016, 16, 93
(576) L. Mazgaeen, P. Gurung, Recent Advances in Lipopolysaccharide Recognition Systems. Intl. J. Mol. Sci. 2020, 21, 379
(577) B. Bertani, N. Ruiz, Function and Biogenesis of Lipopolysaccharides. EcoSal Plus. 2018, 8
(578) T. Galochkina, D. Zlenko, A. Nesterenko, I. Kovalenko, M. Strakhovskaya, A. Averyanov, A. Rubin, Conformational Dynamics of the Single Lipopolysaccharide O-Antigen in Solution. Chemphyschem. 2016, 17, 2839-2853
(579) D. Jefferies, J. Shearer, S. Khalid, Role of O-Antigen in Response to Mechanical Stress of the E. Coli Outer Membrane: Insights From Coarse-Grained MD Simulations. J. Phys. Chem. B 2019, 123, 3567-3575
(580) H. Ma, F. J. Irudayanathan, W. Jiang, S. Nangia, Simulating Gram-Negative Bacterial Outer Membrane: A Coarse Grain Model. J. Phys. Chem. B 2015, 119, 14668-14682
(581) H. Ma, D. C. Cummins, N. B. Edelstein, J. Gomez, A. Khan, M. D. Llewellyn, T. Picudella, S. R. Willsey, S. Nangia, Modeling Diversity in Structures of Bacterial Outer Membrane Lipids. J. Chem. Theory Comput. 2017, 13, 811-824
(582) D. Ribet, P. Cossart, How Bacterial Pathogens Colonize Their Hosts and Invade Deeper Tissues. Microbes Infect. 2015, 17, 173-183
(583) S. J. Siegel, J. N. Weisser, Mechanisms of Bacterial Colonization of the Respiratory Tract. Annu. Rev. Microbiol. 2015, 69, 425-444
(584) J. N. Weiser, D. M. Ferreira, J. C. Paton, Streptococcus Pneumoniae: Transmission, Colonization and Invasion. Nat. Rev. Microbiol. 2018, 16, 355-367
(585) M. Meena, P. Swapnil, T. Barupal, K. Sharma, A Review on Infectious Pathogens and Mode of Transmission. J. Plant Pathol. Microbiol. 2019, 10,1000472
(586) E. S. Donkor, Understanding the Pneumococcus: Transmission and Evolution. Front. Cell. Infect. Microbiol. 2013, 3, 7
(587) T. J. Foster, J. A. Geoghegan, V. K. Ganesh, M. Hook, Adhesion, Invasion and Evasion: The Many Functions of the Surface Proteins of Staphylococcus Aureus. Nat. Rev. Microbiol. 2014, 12, 49-62
(588) C. R. Hauck, F. Agerer, P. Muenzner, T. Schmitter, Cellular Adhesion Molecules as Targets for Bacterial Infection. Eur. J. Cell. Biol. 2006, 85, 235-242
(589) C. R. Hauck, Cell Adhesion Receptors – Signalling Capacity and Exploitation by Bacterial Pathogens. Med. Microbiol. Immunol. 2002, 191, 55-62
(590) P. J. Sansonetti, Bacterial pathogens, From Adherence to Invasion: Comparative Strategies. Med. Microbiol. Immunol. 1993, 182, 223-232

(591) M. S. Glickman, W. R. Jacobs, Microbial Pathogenesis of Mycobacterium Tuberculosis: Dawn of a Discipline. Cell 2001, 104, 477-485
(592) M. E. Ohl, S. I. Miller, Salmonella: A Model for Bacterial Pathogenesis. Annu. Rev. Med. 2001, 52, 259-274
(593) R. I. Aminov, A Brief History of the Antibiotic Era: Lessons Learned and Challenges for the Future. Front. Microbiol. 2010, 1 134
(594) K. Gould, Antibiotics: From Prehistory to the Present Day. J. Antimicrob. Chemother. 2016, 71, 572-575
(595) D. E. Fry, The Unintended Consequences of Antibiotic Use. Surg. Infect. (Larchmt). 2016, 17, 623-624
(596) C. E. Luyt, N. Brechot, J. L. Trouillet, J. Chastre, Antibiotic Stewardship in the Intensive Care Unit. Crit. Care 2014, 18, 480
(597) K. E. Rollins, K. K. Varadhan, K. R. Neal, D. N. Lobo, Antibiotics Versus Appendicectomy for the Treatment of Uncomplicated Acute Appendicitis: An Updated Meta-Analysis of Randomised Controlled Trials. World J. Surg. 2016, 40, 2305-2318
(598) J. Gallaher, C. MacDougall, Antibiotics Simplified. Jones & Bartlett 2011, 15-17
(599) E. J. Bow, Infection in Neutropenic Patients With Cancer. Crit. Care Clin. 2013, 29, 411-441
(600) C. Kirchhelle, Swan Song: Antibiotic Regulation in British Livestock Production (1953-2006). Bull. Hist. Med. 2018, 92, 317-350
(601) K. A. de Souza, R. F. Cooke, K. M. Schubach, A. P. Brandao, T. F. Schumaher, I. N. Prado, R. S. Marques, D. W. Bohnert, performance, Health and Physiological Responses of Newly Weaned Feedlot Cattle Supplemented With Feed-Grade Antibiotics or Alternative Feed Ingredients. Animal 2018, 12, 2521-2528
(602) M. K. Chattopadhyay, Use of Antibiotics as Feed Additives: A Burning Question. Front. Microbiol. 2014, 5, 334
(603) G. M. Rizal, J. Gyeltshen, K. Namgay, Evaluation of Animal Feeds for the Presence of Three Important Antibiotic Classes in Bhutan. J. Glob. Antimicrob. Resist. 2018, 15, 228-231
(604) J. O. Buntyn, T. B. Schmidt, D. J. Nisbet, T. R. Callaway, The Role of Direct-Fed Microbials in Conventional Production. Annu. Rev. Anim. Biosci. 2016, 4, 335-355
(605) D. R. Dodds, Antibiotic Resistance: A Current Epilogue. Biochem. Pharmacol. 2017, 134, 139-146
(606) R. K. Shaffer, The Challenge of Antibiotic-Resistant Staphylococcus: Lessons From Hospital Nurseries in the Mid-20th Century. Yale J. Biol. Med. 2013, 86, 261-270
(607) J. L. Martinez, F. Baquero, Emergence and Spread of Antibiotic Resistance: Setting a Parameter Space. Ups. J. Med. Sci. 2014, 119, 68-77
(608) N. A. Lerminiaux, A. D. S. Cameron, Horizontal Transfer of Antibiotic Resistance Genes in Clinical Environments. Can. J. Microbbiol. 2019, 65, 34-44
(609) J. M. Munita, C. A. Arias, Mechanisms of Antibiotic Resistance. Microbiol. Spectr. 2016, 4
(610) L. Sowole, D. K. Ming, F. Davies. Multidrug-Resistant Bacteria. Br. J. Hosp. Med. (Lond.) 2018, 79, C66-C69

(611) S. De Valliere, Multidrug-Resistant Bacteria and Travel. Rev. Med. Suisse 2017, 13, 944-947
(612) E. Medina, D. H. Pieper, Tackling Threats and Future Problems of Multidrug-Resistant Bacteria. Curr. Top. Microbiol. Immunol. 2016, 398, 3-33
(613) P. Tatarelli, M. Mikulska, Multidrug-Resistant Bacteria in Hematology Patients: Emerging Threats. Future Microbiol. 2016, 11, 767-780
(614) C. Huebner, M. Roggelin, S. Flessa, Economic Burden of Multidrug-Resistant Bacteria in Nursing Homes in Germany: A Cost Analysis Based on Empirical Data. BMJ Open 2016, 6, e008458
(615) C. Lange, D. Chesov, J. Heyckendorf, C. C. Leung, Z. Udwadia, K. Dheda, Drug-Resistant Tuberculosis: An Update on Disease Burden, Diagnosis and Treatment. Respirology 2018, 23, 656-673
(616) J. M. Pogue, K. S. Kaye, Infections Caused by Resistant Gram-Negative Bacteria: Epidemiology and Management. Pharmacotherapy 2015, 35, 949-962
(617) G. Domagk, Ein Beitrag Zur Chemotherapies Der Bakteriellen Infektionen. Dtsch. Med. Wochenschr. 1935, 61, 250
(618) J. Davies, D. Davies, Origins and Evolution of Antibiotic Resistance. Microbiol. Mol. Biol. Rev. 2010, 74, 417-433
(619) H. Landecker, Antimicrobials Before Antibiotics: War, Peace, and Disinfectants. Palgrave commun. 2019, 5, 45
(620) H. Otten, Domagk and the Development of the Sulphonamides. J. Antimicrob. Chemother. 1986, 17, 689-696
(621) O. Skold, Sulfonamide Resistance: Mechanisms and Trends. Drug Resist. Update 2000, 3, 155-160
(622) T. K. Burki, Superbugs: An Arms Race Against Bacteria. Lancet Resp. Med. 2018, 6, 668
(623) K. Hede, Antibiotic Resistance: An Infectious Arms Race. Nature 2014, 5097, S2-3
(624) D. W. Borhani, D. E. Shaw, The Future of Molecular Dynamics Simulaitons in Drug Discovery. J. Comput. Aided Mol. Des. 2012, 26, 15-26
(625) T. S. Crofts, A. J. Gasparrini, G. Dantas, Next-Generation Approaches to Understand and Combat the Antibiotic Resistome. Nat. Rev. Microbiol. 2017, 15, 422-423
(626) J. D. Durrant, R. E. Amaro, Machine-Learning Techniques Applied to Antibacterial Drug Discovery. Chem. Biol. Drug Des. 2015, 85, 14-21
(627) J. M. Stokes, K. Yang, K. Swanson, W. Jin, A. Cubillos-Ruiz, N. M. Donghia, C. R. MacNair, S. French, L. A. Carfrae, Z. Bloom-Ackerman, V. M. Tran, A, Chiappino-Pepe, A. H. Badran, I. W. Andrews, E. J. Chory, G. M. Church, E. D. Brown, T. S. Jaakkola, R. Brazilay, J. J. Collins, A Deep Learning Approach to Antibiotic Discovery. Cell 2020, 180, 688-702
(628) V. R. Bacot-Davis, A. V. Bassenden, A. M. Berghuis, Drug-Target Networks in Aminoglycoside Resistance: Hierarchy of Priority in Structural Drug Design. MedChemComm 2016, 7, 103-113
(629) A. Bansal, P. A. Srivastava, T. Singh, An Integrative Approach to Develop Computational Pipeline for Drug-Target Interaction Network Analysis. Sci. Rep. 2018, 8, 10238

(630) A. Langham, Y. N. Kaznessis, Molecular Simulations of Antimicrobial Peptides. Methods Mol. Biol. 2011, 618, 267-285
(631) J. Mondal, A Brief Appraisal of Computational Modelling of Antimicrobial Peptide's Activity. Drug Dev. Res. 2019, 80, 28-32
(632) R. Colco, Gram Staining. Curr. Protoc. Microbiol. 2006, 00, A.3C.1-A.3C.2
(633) G. J. Hucker, H. J. Conn, Methods of Gram Staining. N. Y Agric Exp. Station Tech. Bull 1923, 93, 3-37
(634) T. J. Beveridge, J. A. Davies, Cellular Responses of Bacillus Subtilis and Escherichia Coli to the Gram Stain. J. Bacteriol. 1983, 156, 846-858
(635) R. B. Thomson, One Small Step for the Gram Stain, One Giant Leap for Clinical Microbiology. J. Clin. Microbiol. 2016, 54, 1416-1417
(636) T. J. Beveridge, Use of the Gram Stain in Microbiology. Biotech. Histochem. 2001, 76, 111-118
(637) M. Rajagopal, S. Walker, Envelope Structures of Gram-Positive Bacteria. Curr. Top. Microbiol. Immunol. 2017, 404, 1-44
(638) S. D. Siegel, J. Liu, H. Ton-That, Biogenesis of the Gram-Positive Bacterial Cell Envelope. Curr. Opin. Microbiol. 2016, 34, 31-37
(639) M. Rohde, The Gram-Positive Bacterial Cell Wall. Microbiol. Spectr. 2019, 7
(640) W. Vollmer, B. Joris, P. Charlier, S. Foster, Bacterial Peptidoglycan (Murein) Hydrolases. FEMS Microbiol. Rev. 2008, 32, 259-286
(641) M. Pazos, K. Peters, Peptidoglycan. Subcell. Biochem. 2019, 92, 127-168
(642) W. Vollmer, D. Blandot, M. A. de Pedro, Peptidoglycan Structure and Architecture. FEMS Microbiol. Rev. 2008, 32, 149-167
(643) W. Vollmer, U. Bertsche, Murein (Peptidoglycan) Structure, Architecture and Biosynthesis in Escherichia Coli. Biochim. Biophys. Acta 2008, 1778, 1714-1734
(644) A. Purcell, Bacteria. Basic Biology 2016
(645) J. Hoyo, J. Torrent-Burgues, T. Tzanov, Physical States and Thermodynamic Properties of Model Gram-Negative Bacterial Inner Membranes. Chem. Phys. Lipids 2019, 218, 57-64
(646) A. Shokri, G. Larsson, Characterisation of the Escherichia Coli Membrane Structure and Function During Fedbatch Cultivation. Microb. Cell Fact. 2004, 3, 9
(647) P. L. Yeagle, The Membrane of Cells. Academic Press-Elsevier, San Diego, California 2016
(648) J. Jiang, B. V. Daniels, D. Fu, Crystal Structure of AqpZ Tetramer Reveals Two Distinct Arg-189 Conformations Associated With Water Permeation Through the Narrowest Constriction of the Water-Conducting Channel. J. Biol. Chem. 2006, 281, 454-460
(649) J. Abramson, I. Smirnova, V. Kasho, G. Verner, H. R. Kaback, S. Iwata, Structure and Mechanism of the Lactose Permease of Escherichia Coli. Science 2003, 301, 610-616
(650) G. E. Fanucci, N. Cadieux, C. A. Piedmont, R. J. Kadner, D. S. Cafiso, Structure and Dynamics of the Beta-Barrel of the Membrane Transporter BtuB by Site-Directed Spin Labelling. Biochemistry 2002, 41, 11543-11551

(651) B. Y. Wei, C. Bradbeer, R. J. Kadner, Conserved Structural and Regulatory Regions in the Salmonella Typhimurium btuB Gene for the Outer Membrane Vitamin B12 Transport Protein. Res. Microbiol. 1992, 143, 459-466
(652) M. S. P. Sansom, Membrane Proteins: A Tale of Barrels and Corks. Curr. Biol. 1999, R254-R257
(653) S. Dramsi, S. Magnet, S. Davison, M. Arthur, Covalent Attachment of Proteins to Peptidoglycan. FEMS microbiol. Rev. 2008, 32, 307-320
(654) A. Konovalova, T. J. Silhavy, Outer Membrane Lipoprotein Biogenesis: Lol Is Not the End. Philos. Trans. R. Soc. Lond. B Biol. Sci. 2015, 370, 1679
(655) A. Kovacs-Simon, R. W. Titball, S. L. Mitchell, Lipoproteins of Bacterial Pathogens. Infect. Immun. 2011, 79, 548-561
(656) L. T. Nguyen, C. M. Oikonomou, H. J. Ding, M. Kaplan, Q. Yao, YW. Chang, M. Beeby, G. J. Jensen, Simulations Suggest a Constrictive Force Is Required for Gram-Negative Bacterial Cell Division. Nat. Commun. 2019, 10, 1259
(657) A. T. Asmar, J. F. Collet, Lpp, the Braun Lipoprotein, Turns 50-Major Achievements and Remaining Issues. FEMS Microbiol. Lett. 2018, 365
(658) M. J. Kuehn, N. C. Kesty, Bacterial Outer Membrane Vesicles and the Host-Pathogen Interaction. Genes Dev. 2005, 19, 2645-2655
(659) R. D. Pathirana, M. Kaparakis-Liaskos, Bacterial Membrane Vesicles: Biogenesis, Immune Regulation and Pathogenesis. Cell. Microbiol. 2016, 18, 1518-1524
(660) J. H. Kim, J. Lee, J. Park, Y. S. Gho, Gram-Negative and Gram-Positive Bacterial Extracellular Vesicles. Semin. Cell. Dev. Biol. 2015, 40, 97-104
(661) L. van der Pol, M. Stork, P. van der Ley, Outer Membrane Vesicles as Platform Vaccine Technology. Biotechnol. J. 2015, 10, 1689-1706
(662) J. Lee, O. Y. Kim, Y. S. Gho, Proteomic Profiling of Gram-Negative Bacterial Outer Membrane Vesicles: Current Perspectives. Proteomics Clin. Appl. 2016, 10, 897-909
(663) K. E. Bonnington, M. J. Kuehn, Protein Selection and Export via Outer Membrane Vesicles. Biochim. Biophys. Acta 2014, 1843, 1612-1619
(664) E. J. O'Donoghue, N. Sirisaengtaksin, D. F. Browning, E. Bielska, M. Hadis, F. Fernandez-Trillo, L. Alderwick, S. Jabbari, A. M. Krachler, Lipopolysaccharide Structure Impacts the Entry Kinetics of Bacterial Outer Membrane Vesicles Into Host Cells. PLoS Pathog. 2017, 13, e1006760
(665) N. J. Bitto, M. Kaparakis-Liaskos, The Therapeutic Benefit of Bacterial Membrane Vesicles. Int. J. Mol. Sci. 2017, 18, E1287
(666) V. Gujrati, S. Kim, S. H. Kim, J. J. Min, H. E. Choy, S. C. Kim, S. Jon, Bioengineered Bacterial Outer Membrane Vesicles as Cell-Specific Drug-Delivery Vehicles for Cancer Therapy. ACS Nano 2014, 8, 1525-1537
(667) F. Farjadin, M. Moghoofei, S. Mirkiani, A. Ghasemi, N. Rabiee, S. Hadifar, A. Beyzavi, M. Karimi, M. R. Hamblin, Bacterial Components as Naturally Inspired Nano-Carriers for Drug/Gene Delivery and Immunization: Set the Bugs to Works? Biotechnol. Adv. 2018, 36, 968-985
(668) S. K. Vanaja, A. J. Russo, B. Behl, I. Banerjee, M. Yankova, S. D. Deshmukh, V. A. K. Rathinam, Bacterial Outer Membrane Vesicles Mediate Cytosolic Localization of LPS and Caspase-11 Activation. Cell 2016, 165, 1106-1119

(669) S. Saffarian, E. Cocucci, T. Kirchhausen, Distinct Dynamics of Endocytic Clathrin-Coated Pits and Coated Plaques. PLoS Biol. 2009, 7, e1000191
(670) H. J. Risselada, Membrane Fusion Stalks and Lipid Rafts: A Love-Hate Relationship. Biophys. J. 2017, 112, 2475-2478
(671) E. Shvets, A. Ludwig, B. J. Nicholes, News From the Caves: Update on the Structure and Function of Caveolae. Curr. Opin. Cell Biol. 2014, 29, 99-106
(672) R. G. Parton, K. Simons, The Multiple Faces of Caveolae. Nat. Rev. Mol. Cell Biol. 2007, 8, 185-194
(673) M. Pitto, J. Brunner, A. Ferraretto, D. Ravasi, P. Palestini, M. Masserini. Use of a Photoactive GM1 Ganglioside Analogue to Assess Lipid Distribution in Caveolae Bilayer. Glycoconj. J. 2000, 17, 215-222
(674) J. Mercer, M. Schelhaas, A. Helenius, Virus Entry by Endocytosis. Annu. Rev. Biochem. 2010, 79, 803-833
(675) I. Karaiskos, A. Antoniadou, H. Giamarellou, Combination Therapy for Extensively-Drug Resistant Gram-Negative Bacteria. Expert. Rev. Anti. Infect. Ther. 2017, 15, 1123-1140
(676) U. Theuretzbacher, M. Paul, Developing a New Antibiotic for Extensively Drug-Resistant Pathogens: The Case of Plasomicin. Clin. Microbiol. Infect. 2018, 24, 1231-1233
(677) A. Jain, R. Mondal. Extensively Drug-Resistant Tuberculosis: Current Challenges and Threats. FEMS Immunol. Med. Microbiol. 2008, 53, 145-150
(678) G. Gunther, Multidrug-Resistant and Extensively Drug-Resistant Tuberculosis: a Review of Current Concepts and Future Challenges. Clin. Med. (Lond.) 2014, 14, 279-285
(679) M. Ashby, A. Petkova, J. Gani, R. Mikut, K. Hilpert, Use of Peptide Libraries for Identification and Optimization of Novel Antimicrobial Peptides. Curr. Top. Med. Chem. 2017, 17, 537-553
(680) K. E. Greber, M. Dawgul, Antimicrobial Peptides Under Clinical Trials. Curr. Top. Med. Chem. 2017, 17, 620-628
(681) L. T. Nguyen, E. F. Haney, H. J. Vogel, The Expanding Scope of Antimicrobial Peptide Structures and Their Modes of Action. Trends Biotechnol. 2011, 29, 464-472
(682) M. Tonk, A. Vilcinskas, The Medical Potential of Antimicrobial Peptides from Insects. Curr. Top. Med. Chem. 2017, 17, 554-575
(683) T. H. Lee, K. N. Hall, M. I. Aguilar, Antimicrobial Peptide Structure and Mechanism of Action: A Focus on the Role of Membrane Structure. Curr. Top. Med. Chem. 2016, 16, 25-39
(684) M. R. Yeaman, N. Y. Yount, Mechanisms of Antimicrobial Peptide Action and Resistance. Pharmacol. Rev. 2003, 55,27-55
(685) H. Jenssen, P. Hamil, R. E. W. Hancock, Peptide Antimicrobial Agents. Clin. Microbiol. Rev. 2006, 19, 491-511
(686) M. Zasloff, Antimicrobial Peptides of Multicellular Organisms. Nature 2002, 415, 389-395
(687) P. Kumar, J. N. Kizhakkedathu, S. K. Straus, Antimicrobial Peptides: Diversity, Mechanism of Action and Strategies to Improve the Activity and Biocompatibility In Vivo. Biomolecules 2018, 4, 4, 8

(688) P. Baindara, S. Korpole, V. Grover, Bacteriocins: Perspective for the Development of Novel Anticancer Drugs. Appl. Microbiol. Biotechnol. 2018, 102, 10393-10408
(689) G. Wang, Database-Guided Discovery of Potent Peptides to Combat HIV-1 or Superbugs. Pharmaceuticals 2013, 6, 728-758
(690) N. Papo, Y. Shai, Host Defense Peptides as New Weapons in Cancer Treatment. Cell. Mol. Life Sci. CMLS 2005, 62, 784-790
(691) J. M. Sanderson, Resolving the Kinetics of Lipid, Protein and Peptide Diffusion in Membranes. Mol. Membr. Biol. 2012, 29, 118-143
(692) M. Gestin, M. Dowaidar, U. Langel, Uptake Mechanism of Cell-Penetrating Peptides. Adv. Exp. Med. Biol. 2017, 255-264
(693) L. Yang, T. A. Harroun, T. M. Weiss, L. Ding, H. W. Huang, Barrel-Stave Model or Toroidal Model? A Case Study on Melittin Pores. Biophys. J. 2001, 81, 1475-1485
(694) J. E. Lopez-Meza, A. Ochoa-Zarzosa, J. A. Aguilar, P. D. Loeza-Lara, Antimicrobial Peptides: Diversity and Perspectives for Their Biomedical Application, Biomedical Engineering, Trends, Research and Technologies. In Biomedical Engineering, Trends, Research and Technologies, M. A. Komorowska and S. Olsztynska-Janus, Eds. pp. 275-304, Intech, Rijeka, Croatia, 2011
(695) D. Sengupta, H. Leontiadou, A. E. Mark, SJ. Marrink, Toroidal Pores formed by Antimicrobial Peptides Show Significant Disorder. Biochim. Biophys. Acta 2008, 1778, 2308-2317
(696) Y. Shai, Mode of Action of Membrane Active Antimicrobial Peptides. Biopolymers 2002, 66, 236-248
(670) N. Shagaghi, E. A. Palombo, A. H. Clayton, M. Bhave, Archetypal Tryptophan-Rich Antimicrobial Peptides: Properties and Applications. World J. Microbiol. Biotechnol. 2016, 32, 31
(671) Q. Wu, J. Patocka, K. Kuca, Insect Antimicrobial Peptides, a Mini Review. Toxins (Basel) 2018, 10, E461
(672) A. Agrawal, J. C. Weisshaar, Effects of Alterations of the E. Coli Lipopolysaccharide Layer on Membrane Permeabilization Events Induced by Cecropin A. Biochim. Biophys. Acta Biomembr. 2018, 18607, 1470-1479
(673) P. F. Zipfel, M. Reuter, Complement Activation Products C3a and C4a as Endogenous Antimicrobial Peptides. Int. J. Pept. Res. Ther. 2009, 15
(674) V. S. de Paula, A. P. Valente, A Dynamic Overview of Antimicrobial Peptides and Their Complexes. Molecules 2018, 23, E2040
(675) D. S. Bolintineanu, Y. N. Kaznessis, Computational Studies of Protegrin Antimicrobial Peptides: A Review. Peptides 2011, 32, 188-201
(676) P. J. Bond, S. Khalid, Antimicrobial and Cell-Penetrating Peptides: Structure, Assembly and Mechanisms of Membrane Lysis via Atomistic and Coarse-Grained Molecular Dynamics Simulations. Protein Pept. Lett. 2010, 17, 1313-1327
(677) A. A. Polyansky, A. O. Chugunov, A. A. Vassilevski, E. V. Grishin, R. G. Efremov, Recent Advances in Computational Modelling of α-Helical Membrane-Active Peptides. Curr. Protein Pept. Sci. 2012, 13, 644-657
(678) Y. Wang, T. Zhao, D. Wei, E. Strandberg, A. S. Ulrich, J. P. Ulmschneider, How Reliable Are Molecular Dynamics Simulations of Membrane Active Antimicrobial Peptides? Biochim. Biophys. Acta 2014, 1838, 2280-2288

(679) S. Berneche, M. Nina, B. Roux, Molecular Dynamics Simulation of Melittin in a Dimyristoylphosphatidylcholine Bilayer Membrane. Biophys. J. 1998, 75, 1603-1618
(680) L. Chen, X. Li, L. Gao, W. Fang, Theoretical Insight Into the Relationship Between the Structures of Antimicrobial Peptides and Their Actions on Bacterial Membranes. J. Phys. Chem. B 2015, 119, 850-860
(681) S. J. Irudayam, M. L. Berkowitz, Binding and Reorientation of Melittin in a POPC Bilayer: Computer Simulations. Biochim. Biophys. Acta 2012, 1818, 2975-2981
(682) X. Wu, A. K. Singh, X. Wu, Y. Lyu, A. K. Bhunia, G. Narsimhan, Characterization of Antimicrobial Activity Against Listeria and Cytotoxicity of Native Melittin and Its Mutant Variants. Colloids and surfaces B: Biointerfaces 2016, 143, 194-205
(683) D. Sengupta, H. Leontiadou, A. E. Mark, SJ. Marrink, Toroidal Pores Formed by Antimicrobial Peptides Show Significant Disorder. Biochim. Biophys. Acta 2008, 1778, 2308-2317
(684) D. Sun, J. Forsman, C. E. Woodward, Molecular Simulations of Melittin-Induced Pores. J. Phys. Chem. B 2017, 121, 10209-10214
(685) A. Glattli, I. Chandrasekhar, W. F. van Gunsteren, A Molecular Dynamics Study of the Bee Venom Melittin in Aqueous Solution, in Methanol, and Inserted in a Phospholipid Bilayer. Eur. Biophys. J. 2006, 35, 255-267
(686) H. Leontiadou, A. E. Mark, SJ. Marrink, Antimicrobial Peptides in Action. J. Am. Chem. Soc. 2006, 128, 12156-12161
(687) A. P. Boughton, I. Andricioaei, Z. Chan, Surface Orientation of Magainin 2: Molecular Dynamics Simulation and Sum Frequency Generation Vibrational Spectroscopic Studies. Langmuir 2010, 26, 16031-16036
(688) D. J. Mayo, I. D. Sahu, G. A. Lorigan, Assessing Topology and Surface Orientation of an Antimicrobial Peptide Magainin 2 Using Mechanically Aligned Bilayers and Electron Paramagnetic Resonance Spectroscopy. Chem. Phys. Lipids 2018, 213, 124-130
(689) M. Packler, I. Kabelka, MS. Appavou, K. Lohner, R. Vacha, G. Pabst, Magainin 2 and PGLa in Bacterial Membrane Mimics I: Peptide-Peptide and Lipid-Peptide Interactions. Biophys. J. 2019, 117, 1858-1869
(690) E. Strandberg, D. Horn, S. Reiber, J. Zerweck, P. Wadhwani, A. S. Ulrich, ^{2}H-NMR and MD Simulations Reveal Membrane-Bound Conformation of Magainin 2 and Its Synergy With PGLa. Biophys. J. 2016, 111, 2149-2161
(691) H. V. Westerhoff, M. Zasloff, J. L. Rosner, R. W. Hendler, A. De Waal, A. Vaz Gommes, P. M. Jongsma, A. Rithorst, D. Juretic, Functional Synergism of the Magainins PGLa and Magainin-2 in Escherichia Coli, Tumor Cells and Liposomes. Eur. J. Biochem. 1995, 228, 257-264
(692) E. F. Haney, H. N. Hunter, K. Matsuzaki, H. J. Vogel, Solution NMR Studies of Amphibian Antimicrobial Peptides: Linking Structure to Function? Biochim. Biophys. Acta 2009, 1788, 1639-1655
(693) E. Strandberg, P. Tremouilhac, P. Wadhwani, A. S. Ulrich, Synergistic Transmembrane Insertion of the Heterodimeric PGLa/Magainin 2 Complex Studied by Solid-State NMR. Biochim. Biophys. Acta 2009, 1788, 1667-1679
(694) D. Juretic, Antimicrobial Peptides of the Magainin Family: Depolarization Studies on E. coli and Cytochrome Oxidase Liposomes. Stud. Biophy. 1990, 138, 79-86

(695) W. Nawae, S. Hannongbua, M. Ruengjitchatchawalya, Defining the Membrane Disruption Mechanism of Kalata B1 via Coarse-Grained Molecular Dynamics Simulations. Sci. Rep. 2014, 4, 3933
(696) W. Nawae, S. Hannongbua, M. Ruengjitchatchawalya, Dynamic Scenario of Membrane Binding Process of Kalata b1. PLoS One 2014, 9, e114473
(697) G. C. A. da Hora, N. L. Archiha, J. L. S. Lopes, D. M. Muller, K. Coutinho, R. Itri, T. A. Soares, Membrane Negative Curvature Induced by a Hybrid Peptide From Pediocin PA-1 and Plantaricin 149 as Revealed by Atomistic Molecular Dynamics Simulations. Soft Matter 2016, 12, 8884-8898
(698) A. Khalfa, M. Tarek, On the Antibacterial Action of Cyclic Peptides: Insights From Coarse-Grained MD Simulations. J. Phys. Chem. B 2010, 114, 2676-2684
(699) Z. Yu, Z. Sun, J. Yin, J. Qiu, Enhanced Production of Polymyxin E in Paenibacillus Polymyxa by Replacement of Glucose by Starch. Biomed. Res. Int. 2018, 2018, 1934309
(700) C. A. Galea, M. Han, Y. Zhu, K. Roberts, J. Wang, P. E. Thompson, J. L, T. Velkov, Characterization of the Polymyxin D Synthetase Biosynthetic Cluster and Product Profile of Paenibacillus Polymyxa ATCC 10401. J. Nat. Prod. 2017, 80, 1264-1274
(701) E. N. Grady, J. MacDonald, L. Liu, A. Richman, Z. C. Yuan, Current Knowledge and Perspectives of Paenibacillus: A Review. Microb. Cell. Fact. 2016, 15, 203
(702) A. Kwa, S. K. Kasiakou, V. H. Tam, M. E. Falagas, Polymyxin B: Similarities to and Differences from Colistin (Polymyxin E). Expert Rev. Anti. Infect. Ther. 2007, 5, 811-821
(703) J. A. Orwa, C. Govaerts, R. Busson, E. Roets, A. van Schepdael, J. Hoogmartens, Isolation Structural Characterization of Polymyxin B Components. J. Chromatogr. A 2001, 912, 369-373
(704) M. Vaara, Polymyxin Derivatives That Sensitize Gram-Negative Bacteria to Other Antibiotics. Molecules 2019, 24, E249
(705) S. Chatterjee, D. Agrawal, Multi-Drug Pseudomonas Aeruginosa Keratitis and Its Effective Treatment With Topical Colistimethate. Indian J. Opthalmol. 2016, 64, 153-157
(706) N. Martis, S. Leroy, V. Blanc, Colistin in Mutli-Drug Resistant Pseudomonas Aeruginosa Blood-Stream Infections: A Narrative Review for the Clinician. J. Infect. 2014, 69, 1-12
(707) A. R. Brochado, A. Telzerow, J. Bobonis, M. Banzhaf, A. Mateus, J. Selkrig, E. Huth, S. Basseler, J. Zamarreno Beas, M. Zietek, N. Ng, S. Foerster, B. Ezraty, B. Py, F. Barras, M. M. Savitski, P. Bork, S. Gottig, A. Typas, Species-Specific Activity of Antibacterial Drug Combinations. Nature 2018, 559, 259-263
(708) L. Peyclit, S. A. Baron, J. M. Rolain, Drug Repurposing to Fight Colistin and Carbapenem-Resistant Bacteria. Front. Cell Infect. Microbiol. 2019, 9, 193
(709) M. Z. Doymaz, E. Karaaslan, Comparison of Antibacterial Activities of Polymyxin B and Colistin Against Multidrug Resistant Gram Negative Bacteria. Infect. Dis. (Lond.) 2019, 51, 676-682

(710) A. P. Zavascki, R. L. Nation, Nephrotoxicity of Polymyxins: Is There Any Difference Between Colistimethate and Polymyxin B? Antimicrob. Agents Chemother. 2017, 61, e02319-16
(711) R. L. Nation, M. H. P. Rigatto, D. R. Falci, A. P. Zavascki, Polymyxin Acute Kidney Injury: Dosing and Other Strategies to Reduce Toxicity. Antibiotics (Basel) 2019, 8, E24
(712) M. A. K. Azad, R. L. Nation, T. Velkov, J. Li, Mechanisms of Polymyxin-Induced Nephrotoxicity. Adv. Exp. Med. Biol. 2019, 1145, 305-319
(713) J. R. Lenhard, Z. P. Bulman, B. T. Tsuji, K. S. Kaye, Shifting Gears: The Future of Polymyxin Antibiotics. Antibiotics (Basel) 2019, 8, E42
(714) T. Kelesidis, M. E. Falagas, The Safety of Polymyxin Antibiotics. Expert Opin. Drug. Saf. 2015, 14, 1687-1701
(715) C. Dai, X. Xiao, J. Li, G. D. Ciccotosto, R. Cappai, S. Tang, E. K. Schneider-Futschik, D. Hoyer, T. Velkov, J. Shen, Molecular Mechanisms of Neurotoxicity Induced by Polymyxins and Chemoprevention. ACS Chem. Neurosci. 2019, 10, 120-131
(716) J. A. Justo, J. A. Bosso, Adverse Reactions Associated With Systemic Polymyxin Therapy. Pharmacotherapy 2015, 35, 28033
(717) J. H. Moffatt, M. Harper, J. D. Boyce, Mechanisms of Polymyxin Resistance. Adv. Exp. Med. Biol. 2019, 1145, 55-71
(718) A. O. Olaitan, S. Morand, J. M. Rolain, Mechanisms of Polymyxin Resistance: Acquired and Intrinsic Resistance in Bacteria. Front. Microbiol. 2014, 5, 643
(719) J. H. Moffatt, M. Harper, J. D. Boyce, Mechanisms of Polymyxin Resistance. Adv. Exp. Med. Biol. 2019, 1145, 55-71
(720) M. L. Han, T. Velkov, Y. Zhu, K. D. Roberts, A. P. Le Brun, S. H. Chow, A. D. Gutu, S. M. Moskowitz, H. H. Shen, J. Li, Polymyxin-Induced Lipid A Diacylation in Pseudomonas Aeruginosa Perturbs Polymyxin Penetration and Confers High-Level Resistance. ACS Chem. Biol. 2018, 13, 121-130
(721) R. L. Danner, K. A. Joiner, M. Rubin, W. H. Patterson, N. Johnson, K. M. Ayers, J. E. Parrillo, Purification, Toxicity, and Antiendotoxin Activity of Polymyxin B Nonapeptide. Antimicrob. Agents Chemother. 1989, 33, 1428-1434
(722) N. Yin, R. L. Marshall, S. Matheson, P. B. Savage, Synthesis of Lipid A Derivatives and Their Interactions with Polymyxin B and Polyxin B Nonapeptide. J. Am. Chem. Soc. 2003, 125, 2425-2435
(723) R. A. Dixon, I. Chopra, Polymyxin B and Polymyxin B Nonapeptide Alter Cytoplasmic Membrane Permeability in Escherichia Coli. J. Antimicrob. Chemother. 1986, 18, 557-563
(724) P. Viljanen, M. Vaara, Susceptibility of Gram-Negative Bacteria to Polymyxin B Nonapeptide. Antimicrob. Agents Chemother. 1984, 25, 701-705
(725) H. Tsubery, I. Ofek, S. Cohen, M. Fridkin, Structure Activity Relationship Study of Polymyxin B Nonapeptide. Adv. Exp. Med. Biol. 2000, 479, 219-222
(726) A. Khondker, A. K. Dhaliwal, S. Saem, A. Mahmood, C. Fradin, J. Moran-Mirabal, M. C. Rheinstadter, Membrane Charge and Lipid Packing Determine Polymyxin-Induced Membrane Damage. Commun. Biol. 2019, 2, 67

(727) I. Ermilova, A. P. Lyubartsev, Extension of the Slipids Force Field to Polyunsaturated Lipids. J. Phys. Chem. B 2016, 120, 12826-12842
(728) A. Khondker, R. J. Alsop, A. Dhaliwal, S. Saem, J. M. Moran-Mirabal, M. C. Rheinstadter, Membrane Cholesterol Reduces Polymyxin B Nephrotoxicity in Renal Membrane Analogs. Biophys. J. 2017, 113, 2016-2028
(729) M. Karplus, J. A. McCammon, Molecular Dynamics Simulations of Biomolecules. Nat. Struct. Biol. 2002, 9, 646-652
(730) H. C. Andersen, Molecular Dynamics Simulations at Constant Pressure and/or Temperature. J. Chem. Phys. 1980, 72, 2384-2393
(731) J. C. Tully, Molecular Dynamics With Electronic Transitions. J. Chem. Phys. 1990, 93, 1061
(732) S. Hammes-Schiffer, J. C. Tully, Proton Transfer in Solution: Molecular Dynamics With Quantum Transitions. J. Chem. Phys. 1994, 101, 4657
(733) J. E. Jonesn, On the Determination of Molecular Fields. -II. From the Equation of State of a Gas. Proc. R. Soc. A Math. Phys. Eng. Sci. 1924, 106, 463-477
(734) G. Mie, Zur Kinetischen Theorie Der Einatomigen Korper. Ann. Phys. 1903, 316, 657-697
(735) E. Gruneisen, Theorie des festen Zustandes einatomiger Elemente. Annalen der physic. 1912, 344, 257-306
(736) J. E. Lennard-Jones, Wave Functions of Many-Electron Atoms. Proc. Phys. Soc. 1931, 27, 469
(737) R. A. Buckingham, The Classical Equation of State of Gaseous Helium, Neon and Argon. Proc. R. Soc. Lond. A, 1938, 168, 264-283
(738) J. W. Pitera, W. F. van Gunsteren, A Comparison of Non-Bonded Scaling Approaches for Free Energy Calculations. Mol. Simul. 2002, 28, 45-65
(739) M. Zacharias, T. P. Straatsma, J. A. McCammon, Separation-Shifted Scaling, a New Scaling Method for Lennard-Jones Interactions in Thermodynamic Integration. J. Chem. Phys. 1994, 100, 9025
(740) T. C. Beutler, A. E. Mark, R. C. Vanschaik, P. R. Gerber, W. F. Vangunsteren, Avoiding Singularities and Numerical Instabilities in Free Energy Calculations Based on Molecular Simulations. Chem. Phys. Lett. 1994, 222, 529-539
(741) T. T. Pham, M. R. Shirts, Optimal Pairwise and Non-Pairwise Alchemical Pathways for Free Energy Calculations of Molecular Transformation in Solution Phase. J. Chem. Phys. 2012, 136, 124120
(742) D. Van Der Spoel, E. Lindahl, B. Hess, G. Groenhof, A. E. Mark, H. J. Berendsen, GROMACS: Fast, Flexible, and Free. J. Comput. Chem. 2005, 26, 1701-1718
(743) S. Pronk, S. Pall, R. Schulz, P. Larsson, P. Bjelkmar, R. Apostolov, M. R. Shirts, J. C. Smith, P. M. Kasson, D. Van Der Spoel, B. Hess, E. Lindahl, GROMACS 4.5: A High-Throughput and Highly Parallel Open Source Molecular Simulation Toolkit. Bioinformatics 2013, 29, 845-854
(744) D. A. Pearlman, D. A. Case, J. W. Caldwell, W. S. Ross, T. E. Cheatha, S. DeBolt, D. Ferguson, G. Seibel, P. Kollman, AMBER, a Package of Computer Programs for Applying Molecular Mechanics, Normal Mode Analysis, Molecular Dynamics and Free Energy Calculations to Stimulate the

Structural and Energetic Properties of Molecules. Comput. Phys. Commun. 1995, 91, 1-41
(745) T. Steinbrecher, D. L. Mobley, D. A. Case, Nonlinear Scaling for Lennard-Jones Interactions in Free Energy Calculations. J. Chem. Phys. 2007, 127, 214108
(746) M. T. Nelson, W. Humphrey, A. Gursoy, A. Dalke, L. V. kale, R. D. Skeel, K. Schulten, NAMD: A Parallel, Object-Oriented Molecular Dynamics Program. Int. J. High Perform. Comput. Appl. 1996, 10, 251-268
(747) J. C. Phillips, R. Braun, W. Wang, J. Gumbart, E. Tajkhorshid, E. Villa, C. Chipot, R. D. Skeel, L. Kale, K. Schulten, Scalable Molecular Dynamics With NAMD. J. Comput. Chem. 2005, 26, 1781-1802
(748) A. D. Mackerell, N. Banavali, N. Foloppe, Development and Current Status of the CHARMM Force Field for Nucleic Acids. Biopolymers 2000, 56, 257-265
(749) B. R. Brooks, C. L. Brooks III, A. D. Mackerell, L. Nilsson, R. J. Petrella, B. Roux, Y. Won, G. Archontis, C. Bartels, S. Boresch, A. Caflisch, L. Caves, Q. Cui, A. R. Dinner, M. Feig, S. Fischer, J. Gao, M. Hodoscek, W. Im, K. Kuczera, T. Lazaridis, J. Ma, V. Ovchinnikov, E. Paci, R. W. Pastor, C. B. Post, J. Z. Pu, M. Schaefer, B. Tidor, R. M. Venable, H. L. Woodcock, X. Wu, W. Yang, D. M. York, M. Karplus, CHARMM: The Biomolecular Simulation Program. J. Comput. Chem. 2009, 30, 1545-1614
(750) M. A. Gonzalez, Force Fields and Molecular Dynamics Simulations. Collection SFN 2011, 12, 169-200
(751) A. J. Stone, A. J. Misquitta, Atom-Atom Potentials From Ab Initio Calculations. Int. Rev. Phys. Chem. 2007, 26, 193-222
(752) S. V. Sambasivarao, O. Acevedo, Development of OPLS-AA Force Field Parameters for 68 Unique Ionic Liquids. J. Chem. Theory Comput. 2009, 5, 1038-1050
(753) D. Yamaki, H. Koch, S. Ten-no, Basis Set Limits of the Second Order Moller-Plesset Correlation Energies of Water, Methane, Acetylene, Ethylene, and Benzene. J. Chem. Phys. 2007, 127, 144104
(754) W. An, Y. Gao, S. Bulusu, X. C. Zeng, Ab Initio Calculation of Bowl, Cage, and Ring Isomers of C20 and C20-. J. Chem. Phys. 2005, 122, 204109
(755) M. Jasik, B. Szefczyk, Parameterization and Optimization of the Menthol Force Field for Molecular Dynamics Simulations. J. Mol. Model. 2016, 22, 234
(756) J. Wang, R. M. Wolf, J. W. Caldwell, P. A. Kollman, D. A. Case, Development and Testing of a General Amber Force Field. J. Comput. Chem. 2004, 25, 1157-1174
(757) L. D. Schuler, X. Daura, W. F. van Gunsteren, An Improved GROMOS96 Force Field for Aliphatic Hydrocarbons in the Condensed Phase. J. Comput. Chem. 2001, 22, 1205-1218
(758) K. Nester, K. Gaweda, W. Plazinski, A Gromos Force Field for Furanose-Based Carbohydrates. J. Chem. Theory Comput. 2019, 15, 1168-1186
(759) D. Vlachakis, E. Bencurova, N. Papangelopoulos, S. Kossida, Current State-of-the-Art Molecular Dynamics Methods and Applications. Adv. Protein Chem. Struct. Biol. 2014, 94, 269-313

(760) P. E. Lopes, O. Guvench, A. D. Mackerell, Current Status of Protein Force Fields for Molecular Dynamics Simulations. Methods Mol. Biol. 2015, 1215, 47-71
(761) J. A. Lemkul, Pairwise-Additive and Polarizable Atomistic Force Fields for Molecular Dynamics Simulations Proteins. Prog. Mol. Biol. Transl. Sci. 2020, 170, 1-71
(762) Z. Jing, C. Liu, S. Y. Cheng, B. D. Walker, J. P. Piquemal, P. Ren, Polarizable Force Fields for Biomolecular Simulations: Recent Advances and Applications. Annu. Rev. Biophys. 2019, 48, 371-394
(763) J. A. Lemkul, J. Huang, B. Roux, A. D. Mackerell, An Empirical Polarizable Force Field Based on the Classical Drude Oscillator Model: Development History and Recent Applications. Chem. Rev. 2016, 116, 4983-5013
(764) A. Savelyev, A. D. Mackerell, All-Atom Polarizable Force Field for DNA Based on the Classical Drude Oscillator Mode. J. Comput. Chem. 2014, 35, 1219-1239
(765) F. Y. Lin, A. D. Mackerell, Force Fields for Small Molecules. Methods Mol. Biol. 2019, 2022, 21-54
(766) H. Li, J. Chowdhary, L. Huang, X. He, A. D. Mackerell, B. Roux, Drude Polarizable Force Field for Molecular Dynamics Simulations of Saturated and Unsaturated Zwitterionic Lipids. J. Chem. Theory Comput. 2017, 13, 4535-4552
(767) J. W. Ponder, C. Wu, P. Ren, V. S. Pande, J. D. Chodera, M. J. Schnieders, I. Haque, D. L. Mobley, D. S. Lambrecht, R. A. Distasio, M. Head-gordon, G. N. I. Clark, M. E. Johnson, T. Head-Gordon, Current Status of the AMOEBA Polarizable Force Field. J. Phys. Chem. B 2010, 114, 2549-2564
(768) Y. Shi, Z. Xia, J. Zhang, R. Best, C. Wu, J. W. Ponder, P. Ren, The Polarizable Atomic Multipole-Based AMOEBA Force Field for Proteins. J. Chem. Theory Comput. 2013, 9, 4046-4063
(769) H. Chu, L. Cao, X. Peng, G. Li, Polarizable Force Field Development for Lipids and Their Efficient Applications in Membrane Proteins. WIREs Comput. Mol. Sci. 2017, 7, e1312
(770) T. R. Lucas, B. A. Bauer, S. Patel, Charge Equilibrium Force Fields for Molecular Dynamics Simulations of Lipids, Bilayers, and Integral Membrane Protein Systems. Biochim. Biophys. Acta 2012, 1818, 318-329
(771) J. Chowdhary, E. Harder, P. E. M. Lopes, L. Huang, A. D. Mackerell, B. Roux, A Polarizable Force Field of Dipalmitoylphosphatidylcholine Based on the Classical Drude Model for Molecular Dynamics Simulations of Lipids. J. Phys. Chem. B 2013, 117, 9142-9160
(772) L. Monticelli, D. P. Tieleman, Force Fields for Classical Molecular Dynamics. Methods Mol. Biol. 2013, 924, 197-213
(773) K. Vanommeslaeghe, O. Guvench, A. S. Mackerell, Molecular Mechanics. Curr. Pharm. Des. 2014, 20, 3281-3292
(774) J. W. Ponder, D. A. Case, Force Fields for Protein Simulations. Adv. Protein Chem. 2003, 66, 27-85
(775) Y. Li, H. Li, F. C. Pickard, B. Narayanan, F. Sen, M. K. Y. Chan, S. Sankaranarayanan, B. R. Brooks, B. Roux, Machine Learning Force Field Parameters from Ab Inito Data. J. Chem. Theory Comput. 2017, 13, 4492-4503

(776) V. Hornak, R. Abel, A. Okur, B. Strockbine, A. Roitberg, C. Simmerling, Comparison of Multiple AMBER Force Fields and Development of Improved Protein Backbone Parameters. Proteins 2006, 65, 712-725
(777) J. Wang, P. A. Kollman, Automatic Parameterization of Force Field by Systematic Search and Genetic Algorithms. J. Comput. Chem. 2001, 22, 1219-1228
(778) P. M. Morse, Diatomic Molecules According to the Wave Mechanics. II. Vibrational Levels. Phys. Rev. 1929, 57-64
(779) K. Lindorff-Larsen, P. Maragakis, S. Piana, M. P. Eastwood, R. O. Dror, D. E. Shaw, Systematic Validation of Protein Force Fields Against Experimental Data. PLoS One 2012, 7, e32131
(780) O. F. Lange, D. van der Spoel, B. L. de Groot, Scrutinizing Molecular Mechanics Force Fields on the Submicrosecond Timescale With NMR Data. Biophys. J. 2010, 99, 647-655
(781) P. R. Markwick, G. Bouvignies, M. Blackledge, Exploring Multiple Timescale Motions in Protein GB3 Using Accelerated Molecular Dynamics and NMR Spectroscopy. J. Am. Chem.Soc. 2007, 129, 4724-4730
(782) R. B. Fenwick, S. Esteban-Martin, B. Richter, D. Lee, K. F. Walter, D. Milovanovic, S. Becker, N. A. Lakomek, C. Griesinger, X. Salvatella, Weak Long-Range Correlated Motions in a Surface Patch of Ubiquitin Involved in Molecular Recognition. J. Am. Chem. Soc. 2011, 133, 10336-10339
(783) M. Akutsu, I. Dikic, A. Bremm, Ubiquitin Chain Diversity at a Glance. J. Cell. Sci. 2016, 129, 875-880
(784) Y. Kazansky, M. Y. Lai, R. K. Singh, D. Fushman, Impact of Different Ionization States of Phosphorylated Serine-65 on Ubiquitin Structure and Interactions. Sci. Rep. 2018, 8, 2651
(785) A. Berg, O. Kukharenko, M. Scheffner, C. Peter, Towards a Molecular Basis of Ubiquitin Signalling: A Dual-Scale Simulation Study of Ubiquitin Dimers. PLoS Comput. Biol. 2018, 14, e1006589
(786) T. S. Ulmer, B. E. Ramirez, F. Delaglio, A. Bax, Evaluation of Backbone Proton Positions and Dynamics in a Small Protein by Liquid Crystal NMR Spectroscopy. J. Am. Chem. Soc. 2003, 125, 9179-9191
(787) F. Martin-Garcia, E. Papaleo, P. Gomez-Puertas, W. Boomsma, K. Lindorff-Larsen, Comparing Molecular Dynamics Force Fields in the Essential Subspace. PLoS One 2015, 10, e0121114
(788) R. B. Best, X. Zhu, J. Shim, P. E. M. Lopes, J. Mittal, M. Feig, A. D. Mackerell, Optimization of the Additive CHARMM All-Atom Protein Force Field Targeting Improved Sampling of the Backbone ϕ, ψ and Side-Chain X^1 and X^2 Dihedral Angles. J. Chem. Theory Comput. 2012, 8, 3257-3273
(789) P. Kuhrova, A. De Simone, M. Otyepka, R. B. Best, Force-Field Dependence of Chignolin Folding and Misfolding: Comparison With Experiment and Redesign. Biophys. J. 2012, 102, 1897-1906
(790) O. F. Lange, D. van der Spoel, B. L. de Groot, Scrutinizing Molecular Mechanics Force Fields on the Submicrosecond Timescale With NMR data. Biophys. J. 2010, 99, 647-655
(791) S. A. Showalter, E. Johnson, M. Rance, R. Bruschweiler, Toward Quantitative Interpretation of Methyl Side-Chain Dynamics NMR by Molecular Dynamics Simulations. J. Am. Chem. Soc. 2007, 129, 14146-14147

(792) W. F. van Gunsteren, H. J. C. Berendsen, Groningen Molecular Simulation (GROMOS) Library Manual, Biomos., Groningen, The Netherlands, 1987, pp. 1-221
(793) N. Schmid, A. P. Eichenberger, A. Choutko, S. Riniker, M. Winger, A. E. Mark, W. F. van Gunsteren, Definition and Testing of the GROMOS Force-Field Versions 54A7 and 54B7. Eur. Biophys. J. 2011, 40, 843-856
(794) C. Oostenbrink, A. Villa, A. E. Mark, W. F. van Gunsteren, A Biomolecular Force Field Based on the Free Enthalpy of Hydration and Solvation: The GROMOS Force-Field Parameter Sets 53A5 and 53A6. J. Comput. Chem. 2004, 25, 1656-1676
(795) B. A. Merchant, J. D. Madura, A Review of Coarse-Grained Molecular Dynamics Techniques to Access Extended Spatial and Temporal Scales in Biomolecular Simulations. Annual reports in computational chemistry 2011, 7, 67-87
(796) M. G. Saunders, G. A. Voth, Coarse-Graining Methods for Computational Biology. Annu. Rev. Biophys. 2013, 42, 73-93
(797) D. A. Holdbrook, R. G. Huber, T. J. Piggot, P. J. Bond, S. Khalid, Dynamics of Crowded Vesicles: Local and Global Responses to Membrane Composition. PLoS One 2016, 11, e0156963
(798) D. L. Parton, J. W. Klingelhoefer, M. S. Sansom, Aggregation of Model Membrane Proteins, Modulated by Hydrophobic Mismatch, Membrane Curvature, and Protein Class. Biophys. J. 2011, 101, 691-699
(799) SJ. Marrink, J. Risselada, S. Yefimov, D. P. Tieleman, A. H. de Vries, The Martini Force Field: Coarse Grained Model for Biomolecular Simulations. J. Phys. Chem. B 2007, 111, 7812-7824
(800) T. K. Piskorz, C. Gobbo, SJ. Marrink, S. De Feyter, A. H. De Vries, N. H. van Esch, Nucleation Mechanisms of Self-Assembled Physisorbed Monolayers on Graphite. J. Phys. Chem. C 2019, 123, 17510-17520
(801) R. S. D'Rozario, C. L. Wee, E. J. Wallace, M. S. Sansom, The Interaction of C60 and Its Derivatives With a Lipid Bilayer via Molecular Dynamics Simulations. Nanotechnology 2009, 20, 115102
(802) E. J. Wallace, M. S. Sansom, Carbon Nanotube/Detergent Interactions via Coarse-Grained Molecular Dynamics. Nano Lett. 2007, 7, 1923-1928
(803) Z. Yu, D. Lau, Development of a Coarse-Grained α-Chitin Model on the Basis of MARTINI Forcefield. J. Mol. Model. 2015, 21, 128
(804) C. A. Lopez, A. J. Rzepiela, A. H. de Vries, L. Dijkhuizen, P. H. Hunenberger, SJ. Marrink, Martini Coarse-Grained Force Field: Extension to Carbohydrates. J. Chem. Theory Comput. 2009, 5, 3195-3210
(805) J. J. Uusitalo, H. I. Ingolfsson, P. Akhshi, D. P. Tieleman, SJ. Marrink, Martini Coarse-Grained Force Field: Extension to DNA. J. Chem. Theory Comput. 2015, 11, 3932-3945
(806) M. Xue, L. Cheng, I. Faustino, W. Guo, SJ. Marrink, Molecular Mechanism of Lipid Nanodisc Formation by Styrene-Maleic Acid Copolymers. Biophys. J. 2018, 115, 494-502
(807) J. J. Uusitalo, H. I. Ingolfsson, SJ. Marrink, I. Faustino, Martini Coarse-Grained Force Field: Extension to RNA. Biophys. J. 2017, 113, 246-256
(808) S. Salassi, F. Simonelli, A. Bartocci, G. Rossi, A Martini Coarse-Grained Model of the Calcein Fluorescent Dye. J. Phys. D: Appl. Phys. 2018, 51

(809) P. Gkeka, P. Angelikopoulos, L. Sarkisov, Z. Cournia, Membrane Partitioning of Anionic, Ligand-Coated Nanoparticles Is Accompanied by Ligand Snorkelling, Local Disordering, and Cholesterol Depletion. PLoS Computational biology 2014, 10, e1003917
(810) J. Barnoud, L. Monticelli, Coarse-Grained Force Fields for Molecular Simulations. Methods Mol. Biol. 2015, 1215, 125-149
(811) I. Lado Tourino, A. C. Naranjo, V. Negri, S. Cerdan, P. Ballesteros, Coarse-Grained Molecular Dynamics Simulation of Water Diffusion in the Presence of Carbon Nanotubes. J. Mol. Graph. Model. 2015, 62, 69-73
(812) L. Chong, F. Aydin, M. Dutt, Implicit Solvent Coarse-Grained Model of Polyamidoamine Dendrimers: Role of Generation and pH. J. Comput. Chem. 2016, 37, 920-926
(813) S. Kavynani, M. Dadvar, H. Modarress, S. Amjad-Iranagh, A Coarse Grained Molecular Dynamics Simulation Study on the Structural Properties of Carbon Nanotube-Dendrimer Composites. Soft Matter 2018, 14, 3151-3163
(814) SJ. Marrink, A. H. de Vries, A. E. Mark, Coarse Grained Model for Semiquantitative Lipid Simulations. J. Phys. Chem. B 2004, 108, 750-760
(815) L. Monticelli, D. P. Tieleman, P. F. J. Fuchs, Interpretation of 2H-NMR Experiments on the Orientation of the Transmembrane Helix WALP23 by Computer Simulations. Biophys. J. 2010, 99, 1455-1464
(816) D. Sengupta, SJ. Marrink, Lipid-Mediated Interactions Tune the Association of Glycophorin A Helix and Its Disruptive Mutants in Membranes. Phys. Chem. Chem. Phys. 2010, 12, 12987-12996
(817) N. Castilo, L. Monticelli, J. Barnoud, D. P. Tieleman, Free Energy of WALP23 Dimer Association in DMPC, DPPC, and DOPC Bilayers. Chem. Phys. Lipids 2013, 169, 95-105
(818) G. Singh, D. P. Tieleman, Using the Wimley-White Hydrophobicity Scale as a Direct Quantitative Test of Force Fields: The Martini Coarse-Grained Model. J. Chem. Theory Comput. 2011, 7, 2316-2324
(819) X. Periole, SJ. Marrink, The Martini Coarse-Grained Force Field. Biomolecular simulations 2012, 533-565
(820) M. Winger, D. Trzesniak, R. Baron, W. F. van Gunsteren. On Using a Too Large Integration Time Step in Molecular Dynamics Simulations of Coarse-Grained Molecular Models. Phys. Chem. Chem. Phys. 2009, 11, 1934-1941
(821) M. Winger, D. Trzesniak, R. Baron, W. F. van Gunsteren. On Using a Too Large Integration Time Step in Molecular Dynamics Simulations of Coarse-Grained Molecular Models. Phys. Chem. Chem. Phys. 2009, 11, 1934-1941
(822) SJ. Marrink, D. P. Tieleman, Perspective on the Martini Model. Chem. Soc. Rev. 2013, 42, 6801-6822
(823) S. O. Yesylevskyy, L. V. Schafer, D. Sengupta, SJ. Marrink, Polarizable Water Model for the Coarse-Grained MARTINI Force Field. PLoS Comput. Biol. 2010, 6, e10000810
(824) B. van Oosten, T. A. Harroun, A MARTINI Extension for Pseudomonas Aeruginosa PAO1 Lipooplysaccharide. J. Mol. Graph. Model. 2016, 63, 125-133
(825) O. N. de Souza, R. L. Ornstein, Effect of Periodic Box Size on Aqueous Molecular Dynamics Simulations of a DNA Dodecamer With Particle-Mesh Ewald Methods. Biophys. J. 1997, 72, 2395-2397

(826) R. S. Varekova, J. Koca, CG. Zhan, Complexity and Convergence of Electrostatic and Van der Waals Energies Within PME and Cutoff Methods. Int. J. Mol. Sci. 2004, 5, 154-173
(827) I. Fukuda, H. Nakamura, Non-Ewald Methods: Theory and Applications to Molecular Systems. Biophys. Rev. 2012, 4, 161-170
(828) I. G. Tironi, A Generalized Reaction Field Method for Molecular Dynamics Simulations. J. Chem. Phys. 1995, 102, 5451
(829) C. J. Fennell, J. D. Gezelter, Is the Ewald Summation Still Necessary? Pairwise Alternatives to the Accepted Standard for Long-Range Electrostatics. J. Chem. Phys. 2006, 124, 234104
(830) S. R. Toxvaerd, J. C. Dyre, Communication: Shifted Forces in Molecular Dynamics. J. Chem. Phys. 2011, 134, 081102
(831) B. A. Wells, A. L. Chaffee, Ewald Summation for Molecular Simulaitons. J. Chem. Theory Comput. 2015, 11, 3684-3695
(832) T. Darden, D. York, L. Pedersen, Particle Mesh Ewald: An N·log(N) Method for Ewald Sums in Large Systems. J. Chem. Phys. 1993, 98, 10089-10092
(833) A. A. Goldstein, Convex Programming and Optimal Control. SIAM J. Appl. Math. 1965, 3, 147-151
(834) R. Fletcher, C. M. Reeves, Function Minimization by Conjugate Gradients. Comput. J. 1964, 7, 149-154
(835) D. C. Liu, J. Nocedal, On the Limited Memory BFGS Method for Large Scale Optimization. Math. Program. 1989, 45, 503-528
(836) A. R. Leach, Molecular Modelling: Principles and Applications. Harlow, England: Prentice Hall, 2001
(837) M. P. Allen, D. J. Tildesley, Computer Simulations of Liquids, clarendon press, oxford, 1989
(838) W. F. van Gunsteren, H. J. C. Berendsen, A Leap-Frog Algorithm for Stochastic Dynamics. Mol. Simulat. 1988, 1, 173-185
(839) H. J. C. Berendsen, J. P. M. Postma, W. F. van Gunsteren, J. R. Haak, Molecular Dynamics With Coupling to an External Bath. J. Chem. Phys. 1984, 81, 3684
(840) W. G. Hoover, Canonical Dynamics: Equilibrium Phase-Space Distributions. Phys. Rev. A 1985, 31, 1695-1697
(841) M. Parrinello, A. Rahman, Crystal Structure and Pair Potentials: A Molecular-Dynamics Study. Phys. Rev. Lett. 1980, 45, 1196
(842) M. Parrinello, A. Rahman, Polymorphic Transitions in Single Crystals: A New Molecular Dynamics Method. J. Appl. Phys. 1981, 52, 7182-7190
(843) G. J. Martyna, D. J. Tobias, M. L. Klein, Constant Pressure Molecular Dynamics Algorithms. J. Chem. Phys. 1994, 101, 4177
(844) J. P. Ryckaert, G. Ciccotti, H. J. C. Berendsen, Numerical Integration of the Cartesian Equations of Motion of a System With Constraints: Molecular Dynamics of n-Alkanes. J. Comput. Phys. 1977, 23, 327-341
(845) B. Hess, H. Bekker, H. J. C. Berendsen, J. G. E. M. Fraaije, LINCS: A Linear Constraint Solver for Molecular Simulations. J. Comput. Chem. 1997, 18, 1463-1472
(846) J. Kastner, Umbrella Sampling, WIREs Computat. Mol. Sci. 2011, 1, 932-942

(847) G. M. Torrie, J. P. Valleau, Nonphysical Sampling Distribtuions in Monte Carlo Free-Energy Estimation: Umbrella Sampling. J. Comput. Phys. 1977, 23, 187-199
(848) F. M. Boubeta, R. M. C. Garcia, E. N. Lorenzo, L. Boechi, D. Estrin, M. Arrar, Lessons Learned About Steered Molecular Dynamics Simulations and Free Energy Calculations. Chem. Biol. Drug Des. 2019, 93, 1129-1138
(849) S. Kumar, J. M. Rosenberg, D. Bouzida, R. H. Swendsen, P. A. Kollman, Multidimensional Free-Energy Calculations Using the Weighted Histogram Analysis Method. J. Computat. Chem. 1995, 16, 1339-1350
(850) A. K. Jain, R. C. Dubes, CC. Chen, Bootstrap Techniques for Error Estimation. IEEE T. Pattern Anal. 1987, 9, 628-633
(851) H. Bhatia, H. I. Ingolfsson, T. S. Carpenter, F. C. Lightstone, PT. Bremer, MemSurfer: A Tool for Robust Computation and Characterization of Curved Membranes. J. Chem. Theory Comput. 2019, 15, 6411-6421
(852) G. Lukat, J. Kruger, B. Sommer, APL@Voro: A Voronoi-Based Membrane Analysis Tool for GROMACS Trajectories. J. Chem. Inf. Model. 2013, 53, 2908-2925
(853) S. Buchoux, FATSLiM: A Fast and Robust Software to Analyse MD Simulations of Membranes. Bioinformatics 2017, 33, 133-134
(854) D. Poger, B. Caron, A. E. Mark, Validating Lipid Force Fields Against Experimental Data: Progress, Challenges and Perspectives. Biochim. Biophys. Acta 2016, 1858, 1556-1565
(855) V. Luzzati, H. Mustacchi, A. Skoulios, F. Husson, La Structure Des Colloides D'association. I. Les Phases Liquid-Cristallines des Systems Amphiphile-Eau. Acta Crystallogr. 1960, 13, 660-667
(856) J. F. Nagle, S. Tristram-Nagle, Structure of Lipid Bilayers. Biochim. Biophys. Acta 2000, 1469, 159-195
(857) N. Kucerka, J. Gallova, D. Uhrikova, P. Balgavy, M. Bulacu, SJ. Marrink, J. Katsaras, Areas of Monounsaturated Diacylphosphatidylcholines. Biophys. J. 2009, 97, 1926-1932
(858) H. I. Petrache, S. W. Dodd, M. F. Brown, Area per Lipid and Acyl Length Distributions in Fluid Phosphatidylcholines Determined by 2H-NMR Spectroscopy. Biophys. J. 2000, 79, 3172-3192
(859) A. Leftin, M. F. Brown, An NMR Database for Simulations of Membrane Dynamics. Biochim. Biophys. Acta 2011, 1808, 818-839
(860) H. I. Petrache, K. Tu, J. F. Nagle, Analysis of Simulated NMR Order Parameters for Lipid Bilayer Structure Determination. Biophys. J. 1999, 76, 2479-2487
(861) H. I. Petrache, S. Tristam-Nagle, J. F. Nagle, Fluid Phase Structure of EPC and DMPC Bilayers. Chem. Phys. Lipids 1998, 95, 83-94
(862) D. Uhrikova, P. Rybar, T. Hianik, P. Balgavy, Component Volumes of Unsaturated Phosphatidylcholines in Fluid Bilayers: A Densitometric Study. Chem. Phys. Lipids 2007, 145, 97-105
(863) D. Marsh, Molecular Volumes of Phospholipids and Glycolipids in Membranes. Chem. Phys. Lipids, 2010, 163, 667-677
(864) T. J. Piggot, J. R. Allison, R. B. Sessions, J. W. Essex, On the Calculation of Acyl Chain Order Parameters From Lipid Simulations. J. Chem. Theory Comput. 2017, 13, 5683-5696

(865) K. Brandenburg, J. Andra, M. Muller, M. H. J. Koch, P. Garidel, Physicochemical Properties of Bacterial Glycopolymers in Relation to Bioactivity. Barbohydr. Res. 2003, 338, 2477-2489
(866) T. A. Soares, T. P. Straatsma, Assessment of the Convergence of Molecular Dynamics Simulations of Lipopolysaccharide Membranes. Mol. Simul. 2008, 34, 295-307
(867) R. P. Dias, G. C. A. da Hora, M. Remstedt, T. A. Soares, Outer Membrane Remodelling: The Structural Dynamics and Electrostatics of Rough Lipopolysaccharide Chemotypes. J. Chem. Theory Comput. 2014, 10, 2488-2497
(868) S. Leekumjorn, A. K. Sum, Molecular Studies of the Gel to Liquid-Crystlline Phase Transition for Fully Hydrated DPPC and DPPE Bilayers. Biochim. Biophys. Acta 2007, 1768, 354-365
(869) M. Fixman, Radius of Gyration of Polymer Chains. J. Chem. Phys. 1962, 36, 306
(870) I. Kufareva, R. Abagyan, Methods of Protein Structure Comparison. Methods Mol. Biol. 2012, 857, 231-257
(871) W. Humphrey, A. Dalke, K. Schulten, VMD: Visual Molecular Dynamics. J. Mol. Graph. 1996, 14, 33-38
(872) A. Bravo, S. Ruiz-Cruz, I. Alkorta, M. Espinosa, When Humans Met Superbugs: Strategies to Tackle Bacterial Resistance to Antibiotics. Biomol. Concepts 2018, 9, 216-226
(873) J. Mwangi, X. Hao, R. Lai, ZY. Zhang, Antimicrobial Peptides: New Hope in the War Against Multidrug Resistance. Zool. Res. 2019, 40, 488-505
(874) P. J. Planet, Life After USA300: The Rise and Fall of a Superbug. J. Infect. Dis. 2017, 215, S71-S77
(875) E. K. Schneider, F. Reyes-Ortega, T. Velkov, J. Li, Antibiotic-Non-Antibiotic Combinations for Combating Extremely Drug-Resistant Gram-Negative 'Superbugs'. Essays Biochem. 2017, 61, 115-125
(876) A. C. Mehta, L. F. Muscarella, Bronchoscope-Related "Superbug" Infections. Chest 2020, 157, 454-469
(877) YW. Lin, H. H. Yu, J. Zhao, ML. Han, Y. Zhu, J. Akter, H. Wickremasinghe, H. Walpola, V. Wirth, G. G. Rao, A. Forrest, T. Velkov, J. Li, Polymyxin B in Combinations With Enrofloxacin Exerts Synergistic Killing Against Extensively Drug-Resistant Pseudomonas Aeruginosa. Antimicrob. Agents Chemother. 2018, 62, e00028-18
(878) V. M. Thomas, R. M. Brown, D. S. Ashcraft, G. A. Pankey, Synergistic Effect Between Nisin and Polymyxin B Against Pandrug-Resistant and Extensively Drug-Resistant Acinetobacter Baumannii. Int. J. Antimicrob. Agents 2019, 53, 663-668
(879) E. Glukhov, M. Stark, L. L. Burrows, C. M. Deber, Basis for Selectiveity of Cationic Antimicrobial Peptides for Bacterial Versus Mammalian Membranes. J. Biol. Chem. 2005, 280, 33960-33967
(880) K. Murzyn, T. Rog, M. Pasenkiewicz-Gierula, Phosphatidylethanolamine-Phosphatidylglycerol Bilayer as a Model of the Inner Bacterial Membrane. Biophys. J. 2005, 88, 1091-1103
(881) MT. Lee, WC. Hung, FY. Chen, H. W. Huang, Mechanism and Kinetics of Pore Formation in Membranes by Water-Soluble Amphipathic Peptides. Proc. Natl. Acad. Sci. U. S. A. 2008, 105, 5087-5092

(882) S. A. Akimov, P. E. Volynsky, T. R. Galimzyanov, P. I. Kuzmin, K. V. Pavlov, O. V. Batishchev, Pore Formation in Lipid Membrane I: Continuous Reversible Trajectory from Intact Bilayer Through Hydrophobic Defect to Transversal Pore. Sci. Rep. 2017, 7, 12152
(883) S. A. Akimov, P. E. Volynsky, T. R. Galimzyanov, P. I. Kuzmin, K. V. Pavlov, O. V. Batishchev, Pore Formation in Lipid Membrane II: Energy Landscape Under External Stress. Sci. Rep. 2017, 7, 12509
(884) H. J. Risselada, SJ. Marrink. M. Muller, Curvature-Dependent Elastic Properties of Liquid-Ordered Domains Result in Inverted Domain Sorting on Uniaxially Compressed Vesicles. Phys. Rev. Lett. 2011, 106, 148102
(885) S. Tristam-Nagle, J. F. Nagle, Lipid Bilayers: Thermodynamics, Structure, Fluctuations, and Interactions. Chem. Phys. Lipids 2004, 127, 3-14
(886) J. H. Ipsen, O. G. Mouritsen, M. Bloom, Relationships Between Lipid Membrane Area, Hydrophobic Thickness, and Acyl-Chain Orientational Order. The Effects of Cholesterol. Biophys. J. 1990, 57, 405-412
(887) B. A. Lewis, D. M. Engelman, Lipid Bilayer Thickenss Varies Linearly With Acyl Chain Length in Fluid Phosphatidylcholine Vesicles. J. Mol. Biol. 1982, 166, 211-217
(888) G. Deliconstantinos, L. Kopeikina-Tsiboukidou, V. Villiotou, Evaluation of Membrane Fluidity Effects and Enzyme Alterations in Adrianmycin Neurotoxicity. Biochem. Pharmacol. 1987, 36, 1153-1161
(889) A. H. Pande, S. Qin, S. A. Tatulian, Membrane Fluidity Is a Key Modulator of Membrane Binding, Insertion, and Activity of 5-Lipoxygenase. Biophys. J. 2005, 88, 4084-4094
(890) J. D. Petit, F. Immel, L. Lins, E. M. Bayer, Lipids or Proteins: Who Is Leading the Dance at Membrane Contact Sites? Front. Plant Sci. 2019, 10, 198
(891) C. Le Grimellec, G. Friedlander, E. H. el Yandouzi, P. Zlatkine, M. C. Giocondi, Membrane Fluidity and Transport Properties in Epithelia. Kidney Int. 1992, 42, 825-836
(892) J. A. Graham, J. W. Essex, S. Khalid, PyCGTOOL: Automated Generation of Coarse-Grained Molecular Dynamics Models From Atomistic Trajectories. J. Chem. Inf. Model. 2017, 57, 650-656
(893) T. A. Wassenaar, H. I. Ingolfsson, R. A. Bockmann, D. P. Tieleman, SJ. Marrink, Computational Lipidomics With Insane: A Versatile Tool for Generating Custom Membranes for Molecular Simulations. J. Chem. Theory Comput. 2015, 11, 2144-2155
(894) D. Bedrov, JP. Piquemal, O. Borodin, A. D. Mackerell, B. Roux, C. Schroder, Molecular Dynamics Simulations of Ionic Liquids and Electrolytes Using Polarizable Force Fields. Chem. Rev. 2019, 119, 7940-7995
(895) F. Paesani, P. Bajaj, M. Riera, Chemical Accuracy in Modelling Halide Ion Hydration From Many-Body Representations. Adv. Phys. X 2019, 4, 1631212
(896) J. M. Andrews, Determination of Minimum Inhibitory Concentrations. J. Antimicrob. Chemother. 2001, 1, 5-16
(897) J. E. McKie, J. Seo, J. N. Arvesen, Rapid Determination of Minimum Inhibitory Concentrations of Antimicrobial Agents by Regression Analysis of Light Scattering Data. Antimicrob. Agents Chemther. 1980, 17, 813-823

(898) B. Behera, J. Jana, P. Kar, S. Mohanty, A. Mahapatra, Deciphering Polymyxin B Minimum Inhibitory Concentration From Colistin Minimum Inhibitory Concentration and Vice Versa: An Analysis of 156 Carbapenem-Resistant Enterobacteriaceae Isolates. Indian J. Med. Microbiol. 2018, 36, 587-589
(899) S. Simar, D. Sibley, D. Ashcraft, G. Pankey, Colistin and Polymyxin B Minimal Inhibitory Concentrations Determined by Etest Found Unreliable for Gram-Negative Bacilli. Ochsner J. 2017, 17, 239-242
(900) Polymyxin B Sulfate: Susceptibility and Minimum Inhibitory Concentration (MIC) data. (Toku-e.com)
(901) A. Rahnamoun, K. Kim, J. A. Pedersen, R. Harnandez, Ionic Environment Affects Bacterial Lipopolysaccharide Packing and Function. Langmuir 2020, 36, 3149-3158
(903) P. J. Bond, M. S. P. Sansom, The Simulation Approach to Bacterial Outer Membrane Proteins (Review). Mol. Membr. Biol. 2004, 21, 151-161
(904) A. Steimle, I. B. Autenrieth, JS. Frick, Structure and Function: Lipid A Modifications in Commensals and Pathogens. Int. J. Med. Microbiol. 2016, 306, 290-301
(905) K. V. Korneev, N. P. arbatsky, A. Molinaro, A. Palmigiano, R. Z. Shaikhutdinova, M. M. Shneider, G. B. Pier, A. N. Kondakova, E. N. Sviriaeva, L. Sturiale, D. Garozzo, A. A. Kruglov, S. A. Nedospasov, M. S. Drutskaya, Y. A. Knirel, D. V. Kuprash, Structural Relationship of the Lipid A Acyl Groups to Activation of Murine Toll-Like Receptor 4 by Lipopolysaccharides From Pathogenic Strains of Burkholderia Malleli, Acinetobacter Baumannii, and Pseudomonas Aeruginosa. Front. Immunol. 2015, 6, 595
(906) J. Kotakoski, A. V. Krasheninnikov, U. Kaiser, J. C. Meyer, From Point Defects in Graphene to Two-Dimensional Amorphous Carbon. Phys. Rev. Lett. 2011, 106, 105505
(907) L. Lichtenstein, C. Buchner, B. Yang, S. Shaikhutdinov, M. Heyde, M. Sierka, R. Wlodarczyk, J. Sauer, HJ. Freund, The Atomic Structure of a Metal-Supported Virtreous Thin Silica Film. Angew. Chem. Int. Ed. Engl. 2012, 51, 404-407
(908) P. Y. Huang, S. Kurasch, A. Srivastava, V. Skakalova, J. Kotakoski, A. V. Krasheninnikov, R. Hovden. Q. Mao, J. C. Meyer, J. Smet, D. A. Muller, U. Kaiser, Direct Imaging of a Two-Dimensional Silica Glass on Graphene. Nano Lett. 2012, 12, 1081-1086
(909) J. T. Milka, A. J. Thompson, M. R. Dent, N. J. Brooks, J. Michiels, J. Hofkens, M. K. Kuimova, Measuring the Viscosity of the Escherichia Coli Plasma Membrane Using Molecular Rotors. Biophys. J. 2016, 111, 1528-1540
(910) G. Espinosa, I. Lopez-Montero, F. Monroy, D. Langevin, Shear Rheology of Lipid Monolayers and Insights on Membrane Fluidity. Proc. Natl. Acad. Sci. U. S. A. 2011, 108, 6008-6013
(911) C. W. Harland, M. J. Bradley, R. Parthasarathy, Phospholipid Bilayers are Viscoelastic. Proc. Natl. Acad. Sci. U. S. A. 2010, 107, 19146-19150
(912) S. Moradi, A. Nowroozi, M. Shahlaei, Shedding Light on the Structural Properties of Lipid Bilayers Using Molecular Dynamics Simulation: A Review Study. RSC Adv. 2019, 9, 4644-4658

(913) Q. Waheed, R. Tjornhammar, O. Edholm, Phase Transitions in Coarse-Grained Lipid Bilayers Containing Cholesterol by Molecular Dynamics Simulations. Biophys. J. 2012, 103, 2125-2133
(914) U. Balucani, J. P. Brodholt, P. Jedlovszky, R. Vallauri, Viscosity of Liquid Water From Computer Simulations With a Polarizable Potential Model. Phys. Rev. E 2000, 62, 2971
(915) W. E. Alley, B. J. Alder, Generalized Transport Coefficients for Hard Spheres. Phys. Rev. A 1983, 27, 3158-3173
(916) J. Kestin, M. Sokolov, W. A. Wakeham, Viscosity of Liquid Water in the Range -8 °C to 150 °C. J. Phys. Chem. Ref. Data 1978, 7, 941
(917) D. R. LIde, CRC Handbook of Chemistry and Physics 86th ed. CRC press, 2005
(918) D. Errandonea, Can Metals Be a Liquid Glass? Nat. Mater. 2009, 8, 170-171
(919) N. C. Karayiannis, K. Foteinopoulou, M. Laso, Spotaneous Crystallization in Athermal Polymer Packings. Int. J. Mol. Sci. 2013, 14, 332-358
(920) S. Bellissima, M. Neumann, E. Guarini, U. Bafile, F. Barocchi, Time Dependence of the Velocity Autocorrelation Function of a Fluid: An Eigenmode Analysis of Dynamical Processes. Phys. Rev. E 2015, 92, 042166
(921) J. A. Leegwater, Velocity Autocorrelation Function of Lennard-Jones. J. Chem. Phys. 1991, 94, 7402
(922) M. Herrmann, E. Schneck, T. Gutsmann, K. Brandenburg, M. Tanaka, Bacterial Lipopolysaccharide Form Physically Cross-Linked, Two-Dimensional Gels in the Presence of Divalent Cations. Soft Matter 2015, 11, 6037-6044
(923) R. Qiao, A. P. Roberts, A. S. Mount, S. J. Klaine, P. C. Ke, Translocation of C60 and Its Derivatives Across a Lipid Bilayer. Nano Lett. 2007, 7, 614-619
(924) X. Lin, Y. Li, N. Gu, Nanoparticle's Size Effect on Its Translocation Across a Lipid Bilayer: A Molecular Dynamics Simulation. J. Comput. Theor. Nanos. 2010, 7, 269-276
(925) J. Y. Xie, G. H. Ding, M. Karttunen, Molecular Dynamics Simulations of Lipid Membranes With Lateral Force: Rupture and Dynamic Properties. Biochim. Biophys. Acta 2014, 1838, 994-1002
(926) R. Reigada, Atomistic Study of Lipid Membranes Containing Chloroform: Looking for a Lipid-Mediated Mechanism of Anesthesia. PLoS One 2013, 8, e52631
(927) E. Awoonor-Williams, C. N. Rowley, Molecular Simulation of Nonfaciliated Membrane Permeation. Biochim. Biophys. Acta 2016, 1858, 1672-1687
(928) J. Wong-ekkabut, S. Baoukina, W. Triampo, IM. Tang, D. P. Tieleman, L. Monticelli, Computer Simulation Study of Fullerene Translocation Through Lipid Membranes. Nat. Nanotechnol. 2008, 3, 363-368
(929) N. Kucerka, Y. Liu, N. Chu, H. I. Petrache, S. Tristram-Nagle, J. F. Nagle, Structure of Fully Hydrated Fluid Phase DMPC and DLPC Lipid Bilayers Using X-Ray Scattering From Oriented Multilamellar Arrays and From Unilamellar Vesicles. Biophys. J. 2005, 88, 2626-2637

(930) S. D. Guler, D. D. Ghosh, J. Pan, J. C. Mathai, M. L. Zeidel, J. F. Nagle, S. Tristram-Nagle, Effects of Ether vs. Ester Linkage on Lipid Bilayer Structure and Water Permeability. Chem. Phys. Lipids 2009, 160, 33-44
(931) Y. I. Yang, Q. Shao, J. Zhang. L. Yang, Y. Q. Gao, Enhanced Sampling in Molecular Dynamics. J. Chem. Phys. 2019, 151, 070902
(932) W. You, Z. Tang, CE. A. Chang, Potential Mean Force From Umbrella Sampling Simulations: What Can We Learn and What Is Missed? J. Chem. Theory Comput. 2019, 15, 2433-2443
(933) A. Grossfield, D. M. Zuckerman, Quantifying Uncertainty and Sampling Quality in Biomolecular Simulations. Annu. Rep. Comput. Chem. 2009, 5, 23-48
(934) T. S. Carpenter, J. Parkin, S. Khalid, The Free Energy of Small Solute Permeation Through the Escherichia Coli Outer Membrane Has a Distinctly Asymmetric Profile. J. Phys. Chem. Lett. 2016, 7, 3446-3451
(935) J. L. MacCallum, D. P. Tieleman, Computer Simulation of the Distribution of Hexane in a Lipid Bilayer: Spatially Resolved Free Energy, Entropy, and Enthalpy Profiles. J. Am. Chem. Soc. 2006, 128, 125-130
(936) M. Chavent, T. Reddy, J. Goose, A. C. Dahl, J. E. Stone, B. Jobard, M. S. Sansom, Methodologies for the Analysis of Instantaneous Lipid Diffusion in MD Simulations of Large Membrane Systems. Faraday Discuss. 2014, 169, 455-475
(937) D. M. Engelman, Membranes Are More Mosaic Than Fluid. Nature 2005, 438, 578-589
(938) F. Spira, N. S. Mueller, G. Beck, P. von Olshausen, J. Beig, R. Wedlich-Soldner, Patchwork Organization of the Yeast Plasma Membrane Into Numerous Coexisting Domains. Nat. Cell. Biol. 2012, 14, 640-648
(939) E. Falck, T. Rog, M. Karttunen, I. Vattulainen, Lateral Diffusion in Lipid Membranes Through Collective Flows. J. Am. Chem. Soc. 2008, 130, 44-45
(940) T. Apajalahti, P. Niemela, P. N. Govindan, M. S. Miettinen, E. Salonen, SJ. Marrink, I. Vattulainen, Concerted Diffusion of Lipids in Raft-Like Membranes. Faraday Discuss. 2010, 144, 411-430
(941) S. Busch, C. Smuda, L. C. Pardo, T. Unruh, Molecualar Mechanism of Long-Range Diffusion in Phospholipid Membranes Studied by Quasielastic Neutron Scattering. J. Am. Chem. Soc. 2010, 132, 3232-3233
(942) N. V. Priezjev, Heterogeneous Relaxation Dynamics in Amorphous Materials Under Cyclic Loading. Phys. Rev. E 2013, 87, 052302
(943) T. Zhang, AL. Wu, TK. Gu, H. Liu, Relaxation Dynamics in Liquid and Amorphous Copper. Comp. Mater. Sci. 2008, 42, 130-138
(944) P. Zhang, J. J. Maldonis, Z. Liu, J. Schroers, P. M. Voyles, Spatially Heterogeneous Dynamics in a Metallic Glass Forming Liquid Imaged by Electron Correlation Microscopy. Nat. Commun. 2018, 9, 1129
(945) W. Zhang, J. F. Douglas, F. W. Starr, Dynamical Heterogeneity in a Vapor-Deposited Polymer Glass. J. Chem. Phys. 2017, 146, 203310
(946) K. Weron, A. Stanislavsky, A. Jurlewicz, M. M. Meerschaert, HP. Scheffler, Clustered Continuous-Time Random Walks: Diffusion and Relaxation Consequences. Proc. R. Soc. 2012, 468, 1615-1628
(947) M. Klenk, W. Lai, Local Structure and Dynamics of Lithium Garnet Ionic Conductors: Tetragonal and Cubic Li7La3Zr2O7. Phys. Chem. Chem. Phys. 2015, 17, 8758-8768

(948) C. Jeworrek, F. Evers, J. Howe, K. Brandenburg, M. Tolan, R. Winter, Effects of Specific Versus Nonspecific Ionic Interactions on the Structure and Lateral Organization of Lipopolysaccharides. Biophys. J. 2011, 100, 2169-2177
(949) S. Wei, I. Gallino, R. Busch, C. A. Angell, Glass Transition With Decreasing Correlation Length During Cooling of $Fe_{50}Co_{50}$ Superlattice and Strong Liquids. Nat. Phys. 2011, 7, 178-182
(950) F. Angeli, O. Villain, S. Schuller, T. Charpentier, D. de Ligny, L. Bressel, L. Wondraczek, Effect of Temperature and Thermal History on Borosilicate Glass Structure. Phys. Rev. B 2012, 85, 054110
(951) G. Khelashvili, B. Kollmitzer, P. Heftberger, G. Pabst, D. Harries, Calculating the Bending Modulus for Multicomponent Lipid Membranes in Different Thermodynamic Phases. J. Chem. Theory Comput. 2013, 9, 3866-3871
(952) V. A. Frolov, A. V. Shnyrova, J. Zimmerberg, Lipid Polymorphisms and Membrane Shape. Cold Spring Harb. Perspect. Biol. 2011, 3, a004747
(953) W. K. Subczynski, M. Pasenkiewicz-Gierula, J. Widomska, L. Mainali, M. Raguz, High Cholesterol/Low Cholesterol: Effects in Biological Membranes: A Review. Cell. Biochem. Biophys. 2017, 75, 369-385
(954) W. E. M. Lands, F. S. Davis, Fluidity of Membrane Lipids. In: M. Kates, L. A. Manson, (eds) Membrane fluidity. Biomembranes, vol 12. Springer, Boston, MA
(955) K. M. Eyster, The Membrane and Lipids as Integral Participants in Signal Transduction: Lipid Signal Transduction for the Non-Lipid Biochemist. Adv. Physiol. Educ. 2007, 31, 5-16
(956) P. F. F. Almeida, Thermodynamics of Lipid Interactions in Complex Bilayers. Biochim. Biophys. Acta 2009, 1788, 72-85
(957) D. H. de Jong, C. A. Lopez, SJ. Marrink, Molecular View on Protein Sorting Into Liquid-Ordered Membrane Domains Mediated by Gangliosides and Lipid Anchors. Faraday Discuss. 2013, 161, 347-363
(958) T. Devanand, S. Krishnaswamy, S. Vemparala, Interdigitation Induced by Membrane-Active Proteins. J. Membr. Biol. 2019, 252, 331-342
(959) T. Shigematsu, K. Koshiyama, S. Wada, Effects of Stretching Speed on Mechanical Rupture of Phospholipid/Cholesterol Bilayers: Molecular Dynamics Simulation. Sci. Rep. 2015, 5, 15369
(960) L. Zhao, Z. Cao, Y. Bian, G. Hu, J. Wang, Y. Zhou, Molecular Dynamics Simulations of Human Antimicrobial Peptide LL-37 in Model POPC and POPG Lipid Bilayers. Int. J. Mol. Sci. 2018, 19, 1186
(961) S. Park, A. H. Beaven, J. B. Klauda, W. Im, How Tolerant Are Membrane Simulations With Mismatch in Area per Lipid Between Leaflets? J. Chem. Theory Comput. 2015, 11, 3466-3477
(962) P. W. Fowler, J. J. Williamson, M. S. P. Sansom, P. D. Olmsted, Roles of Interleaflet Coupling and Hydrophobic Mismatch in Lipid Membrane Phase-Seperation Kinetics. J. Am. Chem. Soc. 2016, 138, 11633-11642
(963) M. Abraham, B. Hess, D. van der Spoel, E. Lindahl, GROMACS reference manual version 2016
(964) R. Bernardi, M. Bhandarkar, A. Bhatele, E. Bohm, R. Brunner, F. Buelens, C. Chipot, A. Dalke, S. Dixit, G. Fiorin, P. Freddolino, H. Fu, P. Grayson, J. Gullingsrud, A. Gursoy, D. Hardy, C. Harrison, J. Henin, W.

Humphrey, D. Hurwitz, A. Hynninen, N. Jain, N. Krawetz, S. Kumar, D. Kunzman, J. Lai, C. Lee, J. Maia, R. McGreevy, C. Mei, M. Melo, M. Nelson, J. Phillips, B. Radak, T. Rudack, O. Sarood, A. Shinozaki, D. Tanner, D. Wells, G. Zheng, F. Zhu, NAMD User's Guide Version 2.13
(965) P. T. Vernier, M. J. Ziegler, Y. Sun, M. A. Gundersen, D. P. Tieleman, Nanopore-Facilitated, Voltage-Driven Phosphatidylserine Translocation in Lipid Bilayers—In Cells and In Silico. Phys. Biol. 2006, 3, 233-247
(966) M. D. Kaye, K. Schmalzl, V. C. Nibali, M. Tarek, M. C. Rheinstadter, Ethanol Enhances Collective Dynamics of Lipid Membranes. Phys. Rev. E 2011, 83, 050907
(967) J. A. Killian, Hydrophobic Mismatch Between Proteins and Lipids in Membranes. Biochim. Biophys. Acta 1998 1376, 401-415
(968) R. D. Booker, A. K. Sum, Biophysical Changes Induced by Xenon on Phospholipid Bilayers. Biochim. Biophys. Acta 2013, 1828, 1347-1356
(969) S. Wang, R. G. Larson, Water Channel Formation and Ion Transport in Linear and Branched Lipid Bilayers. Phys. Chem. Chem. Phys. 2014, 16, 7251-7262
(967) B. Rozycki, R. Lipowsky, Spontaneous Curvature of Bilayer Membranes From Molecular Simulations: Asymmetric Lipid Densities and Asymmetric Adsorption. J. Chem. Phys. 2015, 142, 054101
(968) K. L. May, M. Grabowicz, The Bacterial Outer Membrane Is an Evolving Antibiotic Barrier. Proc. Natl. Acad. Sci. U. S. A. 2018, 115, 8852-8854
(969) M. R. J. Slaton, Structure and Function of Bacterial Cell Membranes. Annu. Rev. Microbiol. 1967, 21, 417-442
(970) G. Zhang, T. C. Meredith, D. Kahne, On the Essentiality of Lipopolysaccharide to Gram-Negative Bacteria. Curr. Opin. Microbiol. 2013, 16, 779-785
(971) I. Lerouge, J. Vanderleyden, O-Antigen Structural Variation: Mechanisms and Possible Roles in Animal/Plant-Microbe Interactions. FEMS Microbiol. Rev. 2002, 26, 17-47
(972) P. J. Hitchcock, L. Leive, P. H. Makela, E. T. Rietschel, W. Strittmatter, D. C. Morrison, Lipopolysaccharide Nomenclature—Past, Present, and Future. J. Bacteriol. 1986, 166, 699-705
(973) P. C. Y. Lau, T. Lindhout, T. J. Beveridge, J. R. Dutcher, J. S. Lam, Differential Lipopolysaccharide Core Capping Leads to Quantitative and Correlated Modifications of Mechanical and Structural Properties in Pseudomonas Aeruginosa Biofilms. J. Bacteriol. 2009, 191, 6618-6631
(974) U. Essman, L. Perera, M. L. Berkowitz, A Smooth Particle Mesh Ewald Method. J. Chem. Phys. 1995, 103, 8577
(975) M. J. Abraham, T. Murtola, R. Schulz, S. Pall, J. C. Smith, B. Hess, E. Lindahl, GROMACS: High Performance Molecular Simulations Through Multi-Level Parallelism From Laptops to Supercomputers. SoftwareX 2015, 1-2, 19-25
(976) J. D. King, S. Berry, B. R. Clarke, R. J. Morris, C. Whitfield, Lipopolysaccharide O Antigen Size Distribution Is Determined by a Chain Extension Complex of Variable Stoichiometry in Escherichia Coli O9a. Proc. Natl. Acad. Sci. U. S. A. 2014, 111, 6407-6412

(977) A. M. Zaki, P. Carbone, How the Incorporation of Pluronic Block Copolymers Modulates the Response of Lipid Membranes to Mechanical Stress. Langmuir 2017, 33, 13284-13294
(978) M. D. Tomasini, C. Rinaldi, M. S. Tomassone, Molecular Dynamics Simulations of Rupture in Lipid Bilayers. Exp. Biol. Med. (Maywood) 2010, 235, 181-188
(979) H. Leontiadou, A. E. Mark, SJ. Marrink, Molecular Dynamics Simulations of Hydrophilic Pores in Lipid Bilayers. Biophys. J. 2004, 86, 74275-742277
(980) T. Shigematsu, K. Koshiyama, S. Wada, Effects of Stretching Speed on Mechanical Rupture of Phospholipid/Cholesterol Bilayers: Molecular Dynamics Simulation. Sci. Rep. 2015, 5, 15369
(981) K. Koshiyama, S. Wada, Molecular Dynamics Simulations of Pore Formation Dynamics During the Rupture Process of a Phospholipid Bilayer Caused by High-Speed Equibiaxial Stretching. J. Biomech. 2011, 44, 2053-2058
(982) T. Shigematsu, K. Koshiyama, S. Wada, Molecular Dynamics Simulations of Pore Formation in Stretched Phospholipid/Cholesterol Bilayers. Chem. Phys. Lipids 2014, 183, 43-49
(983) A. Gauthier, B. Jose, Stretching Effects on the Permeability of Water Molecules Across a Lipid Bilayer. J. Chem. Phys. 2007, 127, 105104
(984) R. Goetz, G. Gompper, R. Lipowsky, Mobility and Elasticity of Self-Assembled Membranes. Phys. Rev. Lett. 1999, 82, 221
(985) E. Lindahl, O. Edholm, Mesoscopic Undulations and Thickness Fluctuations in Lipid Bilayers From Molecular Dynamics Simulations. Biophys. J. 2000, 79, 426-433
(986) SJ. Marrink, A. E. Mark, Effect of Undulations on Surface Tension in Simulated Bilayers. J. Phys. Chem. B 2001, 105, 6122-6127
(987) S. W. Chiu, S. Vasudevan, E. Jakobsson, R. J. Mashl, H. L. Scott, Structure of Sphingomyelin Bilayers: A Simulation Study. Biophys. J. 2003, 85, 3624-3635
(988) A. J. Sodt, R. W. Pastor, Bending Free Energy From Simulation: Correspondence of Planar and Inverse Hexagonal Lipid Phases. Biophys. J. 2013, 104, 2202-2211
(989) M. C. Watson, E. G. Brandt, P. M. Welch, F. L. H. Brown, Determining Biomembrane Bending Rigidities From Simulations of Modest Size. Phys. Rev. Lett. 2012, 109, 028102
(990) G. Kelashvili, D. Harries, How Cholesterol Tilt Modulates the Mechanical Properties of Saturated and Unsaturated Lipid Membranes. J. Phys. Chem. B 2013, 117, 2411-2421
(991) A. R. Braun, J. N. Sachs, α −Synuclein Reduces Tension and Increases Undulations in Simulations of Small Unilamellar Vesicles. Biophys. J. 2015, 108, 1848-1851
(992) A. R. Braun, J. N. Sachs, Determining Structural and Mechanical Properties From Molecular Dynamics Simulations of Lipid Vesicles. J. Chem. Theory Comput. 2014, 10, 4160-4168
(993) P. W. Fowler, J. Helie, A. Duncan, M. Chavent, H. Koldso, M. S. P. Sansom, Membrane Stiffness Is Modified by Integral Membrane Proteins. Soft Matter 2016, 12, 7792-7803

(994) F. L. H. Brown, Elastic Modelling of Biomembranes and Lipid Bilayers. Annu. Rev. Phys. Chem. 2008, 59, 685-712
(995) M. Deserno, Fluid Lipid Membranes: From Differential Geometry to Curvature Stresses. Chem. Phys. Lipids 2015, 185, 11-45
(996) F. Campelo, C. Arnarez, SJ. Marrink, M. M. Kozlov, Helfrich Model of Membrane Bending: From Gibbs Theory of Liquid Interfaces to Membranes As Thick Anisotropic Elastic Layers. Adv. Colloid Interface Sci. 2014, 208, 25-33
(997) Z. A. Levine, R. M. Venable, M. C. Watson, M. G. Lerner, JE. Shea, R. W. Pastor, F. L. H. Brown, Determination of Biomembrane Bending Moduli in Fully Atomistic Simulations. J. Am. Chem. Soc. 2014, 136, 13582-13585
(998) E. R. May, A. Narang, D. I. Kopelevich, Role of Molecular Tilt in Thermal Fluctuations of Lipid Membranes. Phys. Rev. E 2007, 76, 021913
(999) M. C. Watson, E. S. Penev, P. M. Welch, F. L. H. Brown, Thermal Fluctuations in Shape, Thickness, and Molecular Orientation in Lipid Bilayers. J. Chem. Phys. 2011, 135, 244701
(1000) S. Roier, F. Zingl, F. Cakar, S. Durakovic, P. Kohl, T. O. Eichman, L. Klug, B. Gadermaier, K. Weinzerl, R. Prassl, A. Lass, G. Daum, J. Reidl, M. Feldman, S. Schild, A Novel Mechanism for the Biogenesis of Outer Membrane Vesicles in Gram-Negative Bacteria. Nat. Commun. 2016, 7, 10515
(1001) B. Mandal, H. Bhattacharjee, N. Mittal, H. Sah, P. Balabathula, L. A. Thoma, G. C. Wood, Core-Shell-Type Lipid-Polymer Hybrid Nanoparticles as a Drug Delivery Platform. Nanomedicine 2013, 9, 474-491
(1002) D. Chen, M. M. Santore, Hybrid Copolymer-Phospholipid Vesicles: Phase Separation Resembling Mixed Phospholipid Lamellae, but With Mechanical Stability and Control. Soft Matter 2015, 11, 2617-2626
(1003) R. X. Zhang, P. Cai, T. Zhang, K. Chen, J. Li, J. Cheng, S. Pang, H. A. Adissu, A. M. Rauth, X. Y. Wu, Polymer-Lipid Hybrid Nanoparticles Synchronize Pharmacokinetics of Co-Encapsulated Doxorubicin-Mitomycon C and Enable Their Spatiotemporal Co-Delivery and Local Bioavailability in Breast Tumor. Nanomedicine 2016, 12, 1279-1290
(1004) K. Tan, R. Li, X. Huang, Q. Liu, Outer Membrane Vesicles: Current Status and Future Direction of These Novel Vaccine Adjuvants. Front. Microbiol. 2018, 26, 783
(1005) D. Anand, A. Chaudhuri, Bacterial Outer Membrane Vesicles: New Insights and Applications. Mol. Membr. Biol. 2016, 33, 125-137
(1006) N. J. Bitto, R. Chapman, S. Pidot, A. Costin, C. Lo, J. Choi, T. D'Cruze, E. C. Reynolds, S. G. Dashper, L. Turnbull, C. B. Whitchurch, T. P. Stinear, K. J. Stacey, R. L. Ferrero, Bacterial Membrane Vesicles Transport Their DNA Cargo Into Host Cells. Sci. Rep. 2017, 7, 7072
(1007) T. N. Ellis, M. J. Kuehn, Virulence and Immunomodulatory Roles of Bacterial Outer Membrane Vesicles. Microbiol. Mol. Biol. Rev. 2010, 74, 81-94
(1008) J. A. Broussard, K. J. Green, Research Techniques Made Simple: methodology and Applications of Forster Resonance Energy Transfer (FRET) Microscopy. J. Invest. Dermatol. 2017, 137, e185-e191
(1009) J. Sun, L. Zhang, J. Wang, Q. Feng, D. Liu, Q. Yin, D. Xu, Y. Wei, B. Ding, X. Shi, X. Jiang, Tunable Rigidity of (Polymeric Core)-(Lipid Shell)

Nanoparticles for Regulated Cellular Uptake. Adv. Mater. 2015, 27, 1402-1407
(1010) X. Yi, X. Shi, H. Gao, Cellular Uptake of Elastic Nanoparticles. Phys. Rev. Lett. 2011, 107, 098101
(1011) X. Yi, H. Gao, Cell Membrane Wrapping of a Spherical Thin Elastic Shell. Soft Matter 2015, 11, 1107-1115
(1012) X. Yi, H. Gao, Kinetics of Receptor-Mediated Endocytosis of Elastic Nanoparticles. Nanoscale 2017, 9, 454-463
(1013) J. Zhao, M. H. Stenzel, Entry of Nanoparticles Into Cells: The Importance of Nanoparticle Properties. Polym. Chem. 2018, 9, 259-272
(1014) Z. Shen, MP. Nieh, Y. Li, Decorating Nanoparticles Surface for Targeted Drug Delivery: Opportunites and Challenges. Polymers (Basel) 2016, 8, 83
(1015) H. Ewers, W. Romer, A. E. Smith, K. Bacia, S. Dmitrieff, W. Chai, R. Mancini, J. Kartenbeck, V. Chambon, L. Berland, A. Oppenheim, G. Schwarzmann, T. Feizi, P. Schwille, P. Sens, A. Helenius, L. Johannes, GM1 Structure Determines SV40-Induced Membrane Invagination and Infection. Nat. Cell Biol. 2010, 12, 11-18
(1016) B. Tsai, J. M. Gilbert, T. Stehle, W. Lencer, T. L. Benjamin, T. A. Rapoport, Gangliosides Are Receptors for Murine Polyoma Virus and SV40. EMBO J. 2003, 22, 4346-4355
(1017) M. A. Campanero-Rhodes, A. Smith, W. Chai, S. Sonnino, L. Mauri, R. A. Childs, Y. Zhang, H. Ewers, A. Helenius, A. Imberty, T. Feizi, N-Glycolyl GM1 Ganglioside as a Receptor for Simian Virus 40. J. Virol. 2007, 81, 12846-12858
(1018) G. Hall, S. Kurosawa, D. J. Stearns-Kurosawa, Shiga Toxin Therapeutics: Beyond Neutralization. Toxins (Basel) 2017, 9, 291
(1019) J. E. Nettleship, Structural Biology of Glycoproteins. 2012, INTECH, Rijeka, Croatia
(1020) R. Kornfeld, S. Kornfeld, Comparative Aspects of Glycoprotein Structure. Annual review of biochemistry 1976, 45, 217-238
(1021) P. Strzyz, Bend it Like Glycocalyx. Nat. Rev. Mol. Cell Biol. 2019, 20, 388
(1022) S. Weinbaum, J. M. Tarbell, E. R. Damiano, The Structure and Function of the Endothelial Glycocalyx Layer. Annu. Rev. Biomed. Eng. 2007, 9, 121-167
(1023) D. Shorthouse, G. Hedger, H. Koldso, M. S. P. Sansom, Molecular Simulations of Glycolipids: Towards Mammalian Cell Membrane Models. Biochimie 2015, 120, 105-109
(1024) L. Pol-Fachin, V. H. Rusu, H. Verli, R. D. Lins, GROMOS 53A6 GLYC, an Improved GROMOS Force Field for Hexopyranose-Based Carbohydrates. J. Chem. Theory Comput. 2012, 8, 4681-4690
(1025) C. A. Lopez, Z. Sovova, F. J. van Eerden, A. H. de Vries, SJ. Marrink, Martini Force Field Parameters for Glycolipids. J. Chem. Theory Comput. 2013, 9, 1694-1708
(1026) RX. Gu, H. I. Ingolfsson, A. H. de Vries, SJ. Marrink, D. P. Tieleman, Ganglioside-Lipid and Ganglioside-Protein Interactions Revealed by Coarse-Grained and Atomistic Molecular Dynamics Simulations. J. Phys. Chem. B 2017, 121, 3262-3275

(1027) A. Prinetti, N. Loberto, V. Chigorno, S. Sonnino, Glycosphingolipid Behaviour in Complex Membranes. Biochim. Biophys. Acta 2009, 1788, 184-193
(1028) B. Westerlund, J. P. Slotte, How the Molecular Features of Glycosphingolipids Affect Domain Formation in Fluid Membranes. Biochim. Biophys. Acta 2009, 1788, 194-201
(1029) K. Gaus, E. Gratton, E. P. W. Kable, A. S. Jones, I. Gelissen, L. Kritharides, W. Jessup, Visualizing Lipid Structure and Raft Domains in Living Cells With Two-Photon Microscopy. Proc. Natl. Acad. Sci. U. S. A. 2003, 100, 15554-15559
(1030) K. Ilic, B. Auer, K. Mlinac-Jerkovic, R. Herrera-Molina, Neuronal Signalling by Thy-1 in Nanodomains With Specific Ganglioside Composition: Shall We Open the Door to a New Complexity? Front. Cell Dev. Biol. 2019, 7, 27
(1031) E. J. J. Lugtenberg, R. Peters, Distribution of Lipids in Cytoplasmic and Outer Membranes of Escherichia Coli K12. Biochim. Biophys. Acta 1976, 441, 38-47
(1032) H. M. Kulkarni, M. V. Jagannadham, Biogenesis and Multifaceted Roles of Outer Membrane Vesicles From Gram-Negative Bacteria. Microbiology 2014, 160, 2109-2121
(1033) M. F. Haurat, W. Elhenawy, M. F. Feldman, Prokaryotic Membrane Vesicles: New Insights on Biogenesis and Biological Roles. Biol. Chem. 2015, 396, 95-109
(1034) K. Roy, D. J. Hamilton, G. P. Munson, J. M. Fleckenstein, Outer Membrane Vesicles Induce Immune Responses to Virulence Proteins and Protect Against Colonization by Enterotoxigenic Escherichia Coli. Clin. Vaccine Immunol. 2011, 18, 1803-1808
(1035) J. D. Morris, C. K. Payne, Microscopy and Cell Biology: New Methods and New Questions. Annu. Rev. Phys. Chem. 2019, 70, 199-218
(1036) A. T. Wassie, Y. Zhao, E. S. Boyden, Expansion Microscopy: Principles and Uses in Biological Research. Nat. Methods 2019, 16, 33-41
(1037) D. B. Schmolze, C. Standley, K. E. Fogarty, A. H. Fischer, Advances in Microscopy Techniques. Arch. Pathol. Lab. Med. 2011, 135, 255-263
(1038) K. R. Richert-Poggeler, K. Franzke, K. Hipp, R. G. Kleespies, Electron Microscopy Methods for Virus Diagnosis and High Resolution Analysis of Viruses. Front. Microbiol. 2019, 9, 3255
(1039) F. Guo, W. Jiang, Single Particle Cryo-Electron Microscopy and 3-D Reconstruction of Viruses. Methods Mol. Biol. 2014, 1117, 401-443
(1040) S. Cao, W. Zhang, Characterization of an Early-Stage Fusion Intermediate of Sindbis Virus Using Cryoelectron Microscopy. Proc. Natl. Sci. U. S. A. 2013, 110, 13362-13367
(1041) R. H. Rochat, X. Liu, K. Murata, K. Nagayama, F. Rixon, W. Chiu, Seeing the Portal in Herpes Simplex Virus Type 1 B Capsids. J. Virol. 2011, 85, 1871-1874
(1042) K. Miranda, W. Girard-Dias, M. Attias, W. De Souza, I. Ramos, Three Dimensional Reconstruction by Electron Microscopy in the Life Sciences: An Introduction for Cell and Tissue Biologists. Mol. Reprod. Dev. 2015, 82, 530-547

(1043) D. H. Hall, Chapter 17 Electron Microscopy and Three-Dimensional Image Reconstruction. Method. Cell Biol. 1995, 48, 395-436
(1044) T. Rog, A. Koivuniemi, The Biophysical Properties of Ethanolamine Plasmalogens Revealed by Atomistic Molecular Dynamics Simulations. Biochim. Biophys. Acta 2016, 1858,97-103
(1045) L. Han, M. Tan, M. Xia, E. N. Kitova, X. Jiang, J. S. Klassen, Gangliosides Are Ligands for Human Noroviruses. J. Am. Chem. Soc. 2014, 136, 12631-12637
(1046) A. Sreekumari, R. Lipowsky, Lipids With Bulky Head Groups Generate Large Membrane Curvatures by Small Compositional Asymmetries. J. Chem. Phys. 2018, 149, 084901
(1047) SJ. Marrink, A. E. Mark, Molecular Dynamics Simulation of the Formation, Structure, and Dynamics of Small Phospholipid Vesicles. J. Am. Chem. Soc. 2003, 125, 15233-15242
(1048) V. S. Markin, J. P. Albanesi, Membrane Fusion: Stalk Model Revisited. Biophys. J. 2002, 82, 693-712
(1049) S. Kawamoto, M. L. Klein, W. Shinoda, Coarse-Grained Molecular Dynamics Study of Membrane Fusion: Curvature Effects on Free Energy Barriers Along the Stalk Mechanism. J. Chem. Phys. 2015, 143, 243112
(1050) SJ. Marrink, A. E. Mark, The Mechanism of Vesicle Fusion As Revleaed by Molecular Dynamics Simulations. J. Am. Chem. Soc. 2003, 125, 11144-11145
(1051) H. J. Risselada, G. Marelli, M. Fuhrmans, Y. G. Smirnova, H. Grubmuller, SJ. Marrink, M. Muller, Line-Tension Controlled Mechanism for Influenza Fusion. PLoS One 2012, 7, e38302
(1052) P. M. Kasson, V. S. Pande, Control of Membrane Fusion Mechanism by Lipid Composition: Predictions From Ensemble Molecular Dynamics. PLoS Comput. Biol. 2007, 3, e220
(1053) C. Allollio, A. Magarkar, P. Jurkiewicz, K. Baxova, M. Javanainen, P. E. Mason, R. Sachl, M. Cebecauer, M. Hof, D. Horinek, V. Heinz, R. Rachel, C. M. Ziegler, A. Schrofel, P. Jungwirth, Arginine-Rich Cell-Penetrating Peptides Induce Membrane Multilamellarity and Subsequently Enter via Formation of a Fusion Pore. Proc. Natl. Acad. Sci. U. S. A. 2018, 115, 11923-11928
(1054) C. N. Antonescu, F. Aguet, G. Danuser, S. L. Schmid, Phosphatidylinositol-(4,5)-Bisphosphate Regulates Clathrin-Coated Pit Initiation, Stabilization, and Size. Mol. Biol. Cell. 2011, 22, 2588-2600
(1055) R. Williams, PIP_2 in Endocytosis. J. Cell. Biol. 2007, 177, 185
(1056) S. Mayor, R. G. Parton, J. G. Donaldson, Clathrin-Independent Pathways of Endocytosis. Cold Spring Harb. Perspect. Biol. 2014, 6, a016758
(1057) H. T. McMahon, E. Boucrot, Membrane Curvature at a Glance. J. Cell Sci. 2015, 128, 1065-1070
(1058) I. Rodriguez, V. Latza, G. Fragneto, E. Schneck, Conformation of Single and Interacting Lipopolysaccharide Surfaces Bearing O-Side Chains. Biophys. J. 2018, 114, 1624-1635
(1059) P. G. Adams, L. Lamoureux, K. L. Swingle, H. Mukundan, G. A. Montano, Lipopolysaccharide-Induced Dynamic Lipid Membrane Reorganization: Tubules, Perforations, and Stacks. Biophys. J. 2014, 106, 2395-2407

(1060) M. L. Yap, T. Klose, A. Urakami, S. S. Hasan, W. Akahata, M. G. Rossman, Structural Studies of Chikungunya Virus Maturation. Proc. Natl. Acad. Sci. U. S. A. 2017, 114, 13703-13707
(1061) J. Jin, M. B. Sherman, D. Chafets, N. Dinglasan, K. Lu, TH. Lee, LA. Carlson, An Attenuated Replication-Competent Chikungunya Virus With a Fluorescently Tagged Envelope. PLoS Negl. Trop. Dis. 2018, 12, e0006693
(1062) M. Toyofuku, N. Nomura, L. Eberl, Types and Origins of Bacterial Membrane Vesicles. Nat. Rev. Microbiol. 2018, 17, 13-24
(1063) T. Henry, S. Pommier, L. Journet, A. Bernadac, J. P. Gorvel, R. Lloubes, Improved Methods for Producing Outer Membrane Vesicles in Gram-Negative Bacteria. Res. Microbiol. 2004, 155, 437-446
(1064) C. Schwechheimer, A. Kulp, M. J. Kuehn, Modulation of Bacterial Outer Membrane Vesicle Production by Envelope Structure and Content. BMC Microbiol. 2014, 14, 324
(1065) G. Qing, N. Gong, X. Chen, J. Chen, H. Zhang, Y. Wang, R. Wang, S. Zhang, Z. Zhang, X. Zhao, Y. Luo, XJ. Liang, Natural and Engineered Bacterial Outer Membrane Vesicles. Biophys. Rep. 2019, 5, 184-198
(1066) M. Marsh, A. Helenius, Virus Entry: Open Sesame. Cell 2006, 124, 729-740
(1067) P. Kukura, H. Ewers, C. Muller, A. Renn, A. Helenius, V. Sandoghdar, High-Speed Nanoscopic Tracking of the Position and Orientation of a Single Virus. Nat. Methods 2009, 6, 923-927
(1068) H. Ewers, A. E. Smith, I. F. Sbalzarini, H. Lilie, P. Koumoutsakos, A. Helenius, Single-Particle Tracking of Murine Polyoma Virus-Like Particles on Live Cells and Artificial Membranes. Proc. Natl. Acad. Sci. U. S. A. 2005, 102, 15110-15115
(1069) K. Hummeler, N. Tomassini, F. Sokol, Morphological Aspects of the Uptake of Simian Virus 40 by Permissive Cells. J. Virol. 1970, 87-93
(1070) R. L. MacKay, R. A. Consigli, Early Events in Polyoma Virus Infection: Attachment, Penetration, and Nuclear Entry. J. Virol. 1976, 19, 620-636
(1071) G. G. Maul, G. Rovera, A. Vorbrodt, J. Abramczuk, Membrane Fusion as a Mechanism of Simian Virus 40 Entry into Different Cellular Compartments. J. Virol. 1978, 28, 936-944
(1072) W. Shen, J. Hu, X. Hu, Impact of Amphiphilic Triblock Copolymers on Stability and Permeability of Phospholipid/Polymer Hybrid Vesicles. Chem. Phys. Lett. 2014, 600, 56-61
(1073) F. Quemeneur, M. Rinaudo, B. Pepin-Donat, Influence of Polyelectrolyte Chemical Structure on Their Interaction With Lipid Membrane of Zwitterionic Liposomes. Biomacromolecules 2008, 9, 2237-2243
(1074) F. Quemeneur, M. Rinaudo, G. Maret, B. Pepin-Donat, Decoration of Lipid Vesicles by Polyelectrolytes: Mechanism and Structure. Soft Matter 2010, 6, 4471-4481
(1075) R. M. A. Sullan, W. Shi, H. Chan, J. K. Li, G. C. Walker, Mechanical Stability of Phase-Segregated Multicomponent Lipid Bilayers Enhanced by PS-b-PEO Diblock Copolymers. Soft Matter 2013, 9, 6245-6253
(1076) S. Bobone, Y. Gerelli, M. De Zotti, G. Bocchinfuso, A. Farrotti, B. Orioni, F. Sebastiani, E. Latter, J. Penfold, R. Senesi, F. Formaggio, A. Palleschi, C. Toniolo, G. Fragneto, L. Stella, Membrane Thickness and the Mechanism of

Action of the Short Peptaibol Trichogen GA IV. Biochim. Biophys. Acta 2013, 1828, 1013-1024
(1077) J. Li, S. Liu, R. Lakshminarayanan, Y. Bai, K. Pervushin, C. Verma, R. W. Beuerman, Molecular Simulations Suggest How a Branched Antimicrobial Peptide Perturbs a Bacterial Membrane and Enhances Permeability. Biochim. Biophys. Acta 2013, 1828, 1112-1121
(1078) N. Elgrishi, K. J. Rountree, B. D. McCarthy, E. S. Rountree, T. T. Eisenhart, J. L. Dempsey, A Practical Beginer's Guide to Cyclic Voltammetry. J. Chem. Educ. 2018, 95, 197-206
(1079) D. Ciumac, R. A. Campbell, H. Xu, L. A. Clifton, A. V. Hughes, J. R. P. Webster, J. R. Lu, Implications of Lipid Monolayer Charge Characteristics on Their Selective Interactions With a Short Antimicrobial Peptide. Colloids Surf. B Biointerfaces 2017, 150, 308-316
(1080) K. A. Reid, C. M. Davis, R. B. Dyer, J. T. Kindt, Binding, Folding and Insertion of a β-Hairpin Peptide at a Lipid Bilayer Surface: Influence of Electrostatics and Lipid Tail Packing. Biochim. Biophys. Acta Biomembr. 2017, 1860, 792-800
(1081) T. Ebenhan, O. Gheysens, H. G. Kruger, J. R. Zeevaart, M. M. Sathekge, Antimicrobial Peptides: Their Role As Infection-Selective Tracers for Molecular Imaging. Biomed. Res. Int. 2014, 867381
(1082) T. I. Nicas, R. E. W. Hancock, Alteration of Susceptibility to EDTA, Polymyxin B and Gentamicin in Pseudomonas Aeruginosa by Divalent Cation Regulation of Outer Membrane Protein H1. J. Gen. Microbiol. 1983, 129, 509-517
(1083) H. Shen, L. J. Tauzin, R. Baiyasi, W. Wang, N. Moringo, B. Shuang, C. F. Landes, Single Particle Tracking: From Theory to Biophysical Applications. Chem. Rev. 2017, 117, 7331-7376